Electron re-collision dynamics in strong mid-IR fields for diffraction imaging of molecular structure and its fragmentation

DISSERTATION

submitted in partial fulfilment of the
requirements for the degree of
Doctor of Philosophy
by

Benjamin Wolter

ICFO - Institut de Ciències Fotòniques
UPC - Universitat Politècnica de Catalunya

Thesis Advisor: Prof. Dr. Jens Biegert

Barcelona, January 2017

Abstract

One of the grand challenges of modern science is to image chemical reactions and biological functions while they are taking place. These *molecular movies*, where the exact spatio-temporal trajectories of the constituent atoms are tracked, would provide a multitude of valuable insights into how nature works. To realize a molecular movie, experimental techniques need to resolve the relevant molecular motions on their natural dimensions, namely sub-atomic ($\lesssim 10^{-10}$ m) spatial dimensions and in few- to hundreds of femtoseconds (10^{-15} s) in duration.

A developing molecular imaging technique is based on *laser-induced electron diffraction* (LIED). Here, an intense electric field is used to liberate an electron from the target molecule before being accelerated and driven back to its parent ion by the same laser field. Upon return the electron wave packet re-scatters off the target nuclei and an imprint of the molecular structure is encoded in the resultant diffraction pattern. LIED follows similar principles to those used in conventional electron diffraction techniques but occurs in the presence of a strong laser field. Due to the single optical cycle nature of the strong-field induced re-collision process, LIED inherits an intrinsic temporal resolution that fundamentally lies in the sub-femtosecond temporal regime.

In this thesis, a novel experimental approach is presented that allows us to use the LIED technique for dynamic imaging of polyatomic molecular systems, a feat that had never before been realized. Our method involves combining an intense mid-IR field with 3D coincidence momentum detection. On the one hand, the mid-IR laser allows the creation of high energy re-collision electrons, and ionization within the quasi-static regime, hence permitting semi-classical treatment of the process. On the other hand, coincidence detection imaging of the entire momentum space allows for a selective assignment of the molecular reaction channel with sufficient signal-to-noise. Both points have been the main drawbacks to use LIED as a readily available and resilient method that can be utilized for structurally imaging of ultrafast processes in gas phase molecular systems.

The experiments conducted throughout this thesis are divided in two main parts with both harnessing the benefits of combining an ultrafast, 160 kHz, mid-IR source with a “reaction microscope” detection system:

First, the interaction of intense mid-IR waveforms with atomic and molecular targets is investigated and tested against established theories. Here, we measured the photo electron spectrum for very low energies with high resolution and for the first time in full 3D. Thereby, we observed various orders of the recently found “ionization surprise” being electrons bunching for specifically low energies when crossing the ionization threshold. They predominantly exist when tunnel-ionized at longer

wavelength ($\lambda \gtrsim 1\,\mu$m). We studied the electron structures as a function of pulse duration of our mid-IR driver. Next, mid-IR induced double ionization was investigated for xenon atoms as an example of a many-electron system. By probing the transition between different ionization regimes as a function of intensity, we found divergent behavior as compared to 800 nm driving fields. These initial experiments serve as a foundation and confirmation that the main parts of strong-field interactions with mid-IR lasers can be accurately modeled with classical simulations. More importantly, this re-insures the interpretation of LIED as re-scattering electrons on classical trajectories which sets the scene for our work on molecular imaging with LIED.

Then in the second part, mid-IR LIED imaging is implemented with our experimental methodology. This allowed us to image aligned acetylene (C_2H_2) molecules and generate enough momentum transfer to successfully probe its entire structure with few picometer spatial resolution. Acetylene offers reaction channels of prototypical, ultrafast molecular dynamics like e.g. dissociation and isomerization. In order to investigate the combined spatio-temporal capabilities of mid-IR LIED, we conducted measurements to image the molecule while it undergoes a breakup of one of its carbon-hydrogen bonds. These snapshots of a proton escape are taken on a time scale below 10 fs after population of the dissociating state.

Resumen

Uno de los grandes desafíos de la ciencia moderna es captar reacciones químicas y funciones biológicas mientras están teniendo lugar. Estas *películas moleculares*, donde se rastrearían las trayectorias espacio-temporales exactas de los átomos constituyentes, proporcionaría una multitud de perspectivas viables sobre cómo funciona la naturaleza. Para realizar una película molecular, las técnicas experimentales necesitan medir los movimientos moleculares relevantes en sus magnitudes naturales - las distancias subatómicas ($\lesssim 10^{-10}$ m) y duraciones desde unos pocos a cientos de femtosegundos (10^{-15} s).

Una técnica para captar imágenes moleculares en desarrollo se basa en la *difracción de electrones inducida por láser* (LIED, en inglés: laser-induced electron diffraction). Aquí, un campo eléctrico intenso se utiliza para liberar un electrón de un átomo o molécula antes de ser acelerado y conducido de nuevo a su ión de origen por el mismo campo de láser. Al volver, el paquete de ondas de electrones interactúa con los núcleos objetivos, quienes dejan su huella en el patrón de difracción. LIED sigue principios similares a los utilizados en técnicas convencionales de difracción de electrones, pero ocurre en presencia de un campo láser fuerte. Debido a que la re-colisión inducida por el laser ocurre en una escala menor a la duración de un período, LIED hereda una resolución temporal intrínseca, que se encuentra fundamentalmente en una escala menor a un femtosegundo.

En esta tesis se presenta un nuevo enfoque experimental que nos permite utilizar la técnica LIED para captar de sistemas moleculas poliatómicas y dinámicas que nunca antes se había realizado. Nuestro método consiste en combinar un intenso laser de infrarrojo medio con detección 3D de iónes y electrónes en coincidencia. Por un lado, esto permite la creación de electrones de re-colisión de alta energía que operan dentro del régimen cuasi-estático, el cual a la vez atmite un tratamiento semiclasico del proceso de la ionizacón. Por otra parte, la detección en coincidencia de todo el espacio de momento de los partículas permite determinar selectivamente el canal de reacción molecular correspondiente con suficiente relación señal - ruido. Ambos puntos han sido hasta ahora las principales limitaciones al utilizar LIED como un método de imagen fiable y robusto que puede ser utilizado para la imagen de estructuras de moléculas durante procesos ultra-rápidos.

Los experimentos llevados a cabo a lo largo de esta tesis se dividen en dos partes principales, ambos aprovechando los beneficios de una fuente infrarroja ultrarápida de 160 kHz, combinada con un sistema de detección de “microscopio de reacción”.

En primer lugar, se presenta y analiza la interacción de las formas de onda infrarroja de alta intensidad con objetivos atómicos y moleculares respecto a las teorías

establecidas. Aquí, medimos el espectro fotoelectrónico a muy bajas energías con una alta resolución y por primera vez completamente en 3D. En ello, hemos observado varios órdenes de la recientemente encontrada "sorpresa de ionisación", es decir, electrones agrupados para energías específicamente bajas al cruzar el umbral de ionización. Estos existen predominantemente cuando se ioniza a través de ionización-efecto-túnel con longitudes de onda más larga ($\lambda \gtrsim 1\,\mu$m). Estudiamos estás "estructuras de electrones" en función de la duración del pulso del infrarrojo medio. A continuación, se investigó el proceso de ionización doble inducida por el infrarrojo medio en átomos de xenón, como modelo de un sistema de muchos electrones. Midiendo la transición entre diferentes regímenes de ionización en función de la intensidad, encontramos un comportamiento divergente en comparación con campos de 800 nm.

En segundo lugar, la tecníca de LIED con campos infrarrojos medios fue implementado con nuestra metodología experimental. Esto nos permitió realizar imágenes de moléculas de acetileno (C_2H_2) alineadas y generar suficiente transferencia de momento para medir con éxito su estructura con una resolución espacial de unos pocos picómetros. El acetileno ofrece canales de reacción de dinámicas moleculares prototípicas y ultrarrápidos como disociación e isomerización. Para investigar la combinación de las capacidades espacio-temporales de LIED, obtuvimos imágenes de la molécula durante la ruptura de uno de sus enlaces carbono-hidrógeno. Estas imágenes instantáneas del escape de protones son tomadas en una escala de tiempo por debajo de los 10 fs después de que el estado de disociación se ha poblado.

Zusammenfassung

Eine der größten Herausforderungen der modernen Wissenschaft besteht darin, chemische Reaktionen und biologische Funktionen zu visualisieren, während sie stattfinden. Diese *molekularen Filme*, in denen die exakten Bahnen der einzelnen Atome räumlich und zeitlich verfolgt werden, würden eine Vielzahl von wertvollen Einblicken in die Funktionsweise der Natur liefern. Um einen molekularen Film realisieren zu können, müssen experimentelle Techniken entwickelt werden, die molekulare Bewegungen in ihren natürlichen Dimensionen auflösen können. Dazu wird eine subatomare räumliche Auflösung ($\lesssim 10^{-10}$ m) benötigt, sowie zeitliche Rasterung binnen weniger Hunderte von Femtosekunden (10^{-15} s).

Eine molekulare Bildgebungstechnik, die viel Potential in sich birgt, basiert auf *laserinduzierter Elektronenbeugung* (*engl.* laser-induced electron diffraction [LIED]). Dabei wird ein intensives elektrisches Laserfeld verwendet, um ein Elektron aus dem Molekül der Wahl freizusetzen, es zu mit Hilfe desselben Laserfeldes zu beschleunigen und danach zu seinem Mutterion zurückzubringen. Bei seiner Rückkehr streut das Elektronenwellenpaket an den Molekülkernen, und ein Abdruck der Molekülstruktur wird im resultierenden Beugungsmuster einkodiert. LIED folgt ähnlichen Prinzipien wie denen konventioneller Elektronenbeugungstechniken, tritt jedoch in Gegenwart eines starken Laserfeldes auf. Aufgrund der Natur des Rekollisionsprozesses, welcher innerhalb eines Zyklusses des starken Laserfeldes stattfindet, weist LIED eine intrinsische zeitliche Auflösung im Subfemtosekundenbereich auf.

In dieser Arbeit wird ein neuartiger experimenteller Ansatz vorgestellt, der es uns erlaubt, die LIED-Technik für die dynamische Bildgebung von mehratomigen molekularen Systemen zu verwenden. Dies konnte bisher noch nie erreicht werden. Die angewandte experimentelle Methodik zeichnet sich durch die Kombination eines intensiven mittleren infraroten Laserfeldes mit 3D-Koinzidenzimpulsdetektion aus. Auf der einen Seite erlaubt das mittlere infrarote Laserfeld die Erzeugung von hochenergetischen Rekollisionselektronen sowie einer Ionisation innerhalb des Tunnel- oder quasi-statischen Regimes, wodurch eine semiklassische theoretische Beschreibung des Prozesses möglich wird. Auf der anderen Seite gewärt die Koinzidenzdetektion des gesamten Impulsraums eine selektive Zuordnung der molekularen Reaktionskanäle bei einem ausreichendem Signal-Rausch-Verhältnis. Beide Punkte waren bisher die Haupthindernisse, LIED als standardmäßiges Verfahren zur Abbildung ultraschnellerProzesse in molekularen Systemen zu verwenden.

Die in dieser Dissertation durchgeführten Experimente sind in zwei Hauptteile gegliedert, wobei beide die Vorteile der Kombination einer ultraschnellen Laser-

quelle im mittleren infraroten Wellenlängenbereich mit einem “Reaktionsmikroskops” nutzen:

Im ersten Teil der Arbeit wird die Wechselwirkung von Wellenformen im mittleren infraroten Wellenlängenbereich mit atomaren und molekularen Targets untersucht und mit etablierten Theorien verglichen. Dabei konnten wir erstmals ein Photoelektronenspektrum für sehr niedrige Energien mit hoher Auflösung und in 3D messen. Hierbei fanden wir verschiedene Ordnungen der erst kürzlich entdeckten “Ionisationsüberraschung” (*engl.* ionization surprise), bei der sich niederenergetische Elektronen beim Überschreiten der Ionisationsschwelle zusammenbündeln. Diese gebündelten Elektronenstrukturen treten hauptsächlich auf, wenn sie mit langwelligen Laserfeldern erzeugt werden ($\lambda \gtrsim 1\,\mu\text{m}$). Weiterhin untersuchten wir die Elektronenstrukturen als eine Funktion der Laserpulsdauer. Als Nächstes fokussierten wir uns auf die Doppelionisation von Xenonatomen durch langwellige Laserfelder. Xenon gilt als Beispiel für ein Vielelektronensystem. Unser Fokus lag hierbei auf dem Übergang zwischen verschiedenen Ionisationsregimen als Funktion der Laserintensität. Dabei fanden wir ein divergentes Verhalten im Vergleich zu Laserfeldern mit einer Wellenlänge von 800 nm. Diese ersten Experimente dienen als Grundlage und Bestätigung dafür, dass die Wechselwirkung von Atomen mit starken mittleren infraroten Laserfeldern anhand von klassischen Theorien genau beschrieben werden können. Umso wichtiger ist, dass diese Erkenntnisse die Interpretation von LIED als streuende Elektronen auf klassischen Bahnen sicherstellt, welche die Grundlage für unsere Experimente zur molekularen Bildgebung bildet.

Im zweiten Teil widmen wir uns dann der Implementierung von LIED als molekulare Bildgebungsmethodik mit Hilfe von mittleren infraroten Laserfeldern. Unser Ziel war es Acetylen (C_2H_2) Moleküle abzubilden und dabei mittels genügend Impulsübertragung ihre komplette Struktur mit einer räumlichen Auflösung von wenigen Pikometern zu untersuchen. Acetylen ist interessant, da es via verschiedener ultraschneller und prototypischer Kanäle wie z. B. Dissoziation und Isomerisierung reagieren kann. Um die Leistungsfähigkeit von LIED im Sinne ihrer gleichzeitigen räumlichen und zeitlichen Auflösung zu überpüfen, haben wir Messungen durchgeführt, die das Acetylenmolekül abbilden, während eine seiner Kohlenstoff-Wasserstoff-Bindungen aufbricht. Diese Schnappschüsse einer “Protonenflucht” wurden in einem Zeitraum von weniger als 10 fs nach der Besetzung des spezifischen dissoziierenden Zustands aufgenommen.

Publications

Publications with immediate connection to this work

- M. G. Pullen, **B. Wolter**, X. Wang, Xiao-Ming Tong, M. Sclafani, M. Baudisch, H. Pires, C. D. Schröter, J. Ullrich, T. Pfeifer, R. Moshammer, J. H. Eberly, and J. Biegert,
  "Transition from non-sequential to sequential double ionisation in many-electron systems," **Phys. Rev. A 96**, 033401 (2017).
- **B. Wolter***, M. G. Pullen*, A.-T. Le, M. Baudisch, K. Doblhoff-Dier, A. Senftleben, M. Hemmer, C. D. Schröter, J. Ullrich, T. Pfeifer, R. Moshammer, S. Gräfe, O. Vendrell, CD Lin, and J. Biegert,
  "Ultrafast electron diffraction imaging of bond breaking in acetylene," **Science 354**, 308-312 (2016).
  - Highlighted with a Perspective Article by Chong-Yu Ruan, "Molecular imaging at 1-femtosecond resolution," **Science 354**, 283-284 (2016).
- M. G. Pullen, **B. Wolter**, A.-T. Le, M. Baudisch, M. Hemmer, A. Senftleben, C. D. Schröter, J. Ullrich, R. Moshammer, CD Lin, and J. Biegert,
  "Laser-Induced Electron Diffraction to Image Molecular Structure," **Optics & Photonics News**, Issue December 2015.
- **B. Wolter***, M. G. Pullen*, M. Baudisch, M. Sclafani, M. Hemmer, A. Senftleben, C. D. Schröter, J. Ullrich, R. Moshammer, and J. Biegert,
  "Strong-Field Physics with Mid-IR Fields," **Phys. Rev. X 5**, 021034 (2015).
  - Highlighted with a Synopsis in APS Physics.
- M. G. Pullen*, **B. Wolter***, A.-T. Le, M. Baudisch, M. Hemmer, A. Senftleben, C. D. Schröter, J. Ullrich, R. Moshammer, CD Lin, and J. Biegert,
  "Imaging an aligned polyatomic molecule with laser-induced electron diffraction," **Nat. Commun. 6**, 7262 (2015).
- **B. Wolter**, C. Lemell, M. Baudisch, M. G. Pullen, Xiao-Min Tong, M. Hemmer, A. Senftleben, C. D. Schröter, J. Ullrich, R. Moshammer, J. Biegert, and J. Burgdörfer,
  "Formation of very-low-energy states crossing the ionization threshold of argon atoms in strong mid-infrared fields," **Phys. Rev. A 90**, 063424 (2014).
- M. G. Pullen, J. Durá, **B. Wolter**, M. Baudisch, M. Hemmer, N. Camus, A. Senftleben, C. D. Schröter, R. Moshammer, J. Ullrich, and J. Biegert,
  "Kinematically complete measurements of strong field ionization with mid-IR pulses," **J. Phys. B: At. Mol. Opt. Phys. 47**, 204010 (2014).

* The authors contributed equally.

Other publications

- N. Suarez, A. Chacón, M. F. Chiappina, **B. Wolter**, J. Biegert, and M. Lewenstein,
"Above-threshold ionization and laser-induced electron diffraction in diatomic molecules," **Phys. Rev. A 94**, 043423 (2016).
- M. Baudisch, **B. Wolter**, M. G. Pullen, M. Hemmer, and J. Biegert,
"High power multi-color OPCPA source with simultaneous femtosecond deep-UV to mid-IR outputs," **Opt. Lett. 41**, 3583-3586 (2016).
- M. G. Pullen, **B. Wolter**, A.-T. Le, M. Baudisch, M. Sclafani, H. Pires, C. D. Schröter, J. Ullrich, R. Moshammer, T. Pfeifer, CD Lin, and J. Biegert,
"Influence of orbital symmetry on diffraction imaging with rescattering electron wave packets," **Nat. Commun. 7**, 11922 (2016).

Acknowledgement indications

- M. García-Matos and L. Torner, "The Wonders of Light," Cambridge University Press, 1st edition (2015).
- A. Merz, J. Siller, R. Schittny, C. Krämmer H. Kalt, and M. Hetterich, "Fast electron spin resonance controlled manipulation of spin injection into quantum dots," **Appl. Phys. Lett. 104**, 252401 (2014).

To my parents.

Contents

Publications 9

List of Figures 17

List of Tables 21

1 Introduction 23

I Fundamentals 31

2 Fundamentals of Strong-field Physics 33
2.1 Ionization of atoms in strong laser fields 34
2.1.1 Keldysh theory 34
2.1.2 Quantitative models for tunneling ionization 39
2.1.3 Limits of strong-field tunneling models 43
2.2 Propagation and return of the quasi-free electron 44
2.2.1 Re-collision model 46
2.2.2 Physics upon re-collision 51
2.3 Molecules in strong laser fields 55
2.3.1 Fundamentals of molecular orbitals 56
2.3.2 Strong-field induced processes in molecules 59
2.3.3 Molecular ADK theory 60
2.3.4 Laser-induced molecular alignment 62
2.4 Benefits and challenges of strong-field physics with mid-IR fields . . 65

3 Experimental Methodology 71
3.1 Generation of intense, ultrashort, mid-IR pulses 71
3.1.1 Fundamentals of ultrafast laser pulses 72
3.1.2 Mid-IR OPCPA source at 160 kHz repetition rate 77
3.1.3 Intensity determination 79
3.1.4 On the importance of high repetition rates 83
3.2 Reaction Microscope 85
3.2.1 Working principle and setup 85
3.2.2 Data analysis 98
3.2.3 Capabilities of the system 109

II Strong-field Ionization in Mid-IR Fields 113

4 Energy Bunching for Electrons crossing the Ionization Threshold 115
4.1 Low-energy structures: state-of-the-Art . . . 116
4.2 Multiple orders of low-energy structures in 3D momentum space . 120
4.2.1 Experimental parameters . . . 121
4.2.2 Theoretical methods: classical and quantum simulations . . 123
4.2.3 Experimental results in comparison with CTMC simulations 125
4.3 LESs: dependence on pulse duration . . . 130
4.4 VLES: analysis of the V-shape . . . 133
4.5 ZES: mechanism and quantitative analysis . . . 137
4.6 Universality of the structures . . . 141

5 Double Ionization of Xenon atoms in Strong Mid-IR Fields 143
5.1 Basics of non-sequential and sequential double ionization . . . 144
5.2 NSDI and SDI of xenon atoms: state-of-the-art . . . 149
5.3 Transition from NSDI to SDI of Xe atoms with mid-IR fields . . . 152
5.3.1 Theoretical methods . . . 152
5.3.2 Ion yield . . . 155
5.3.3 Dication momentum distribtion . . . 160
5.3.4 Electron correlation distribution . . . 162
5.4 Overcoming shielding effects of inner-shell electrons in NSDI of xenon 166

III Imaging of Molecular Structure and Dynamics 167

6 Retrieval of Structural Information from Polyatomic Molecules with Laser-Induced Electron Diffraction 169
6.1 Capabilities and limitations of X-ray and conventional electron diffraction . . . 170
6.2 Imaging molecular structure with LIED . . . 173
6.2.1 Basic requirements and capabilities . . . 174
6.2.2 Intrinsic sub-optical cycle temporal resolution . . . 179
6.2.3 State-of-the-Art . . . 181
6.3 Theoretical concepts . . . 183
6.3.1 Quantitative re-scattering (QRS) theory . . . 184
6.3.2 Independent atom model (IAM) . . . 185
6.4 Calibration experiment of mid-IR LIED on Xenon atoms . . . 187
6.4.1 Experimental parameters and detection . . . 187
6.4.2 Extraction of differential cross-sections (DCSs) . . . 189
6.4.3 Doubly differential cross-section compared to NIST data . . 191
6.4.4 Intensity insensitivity of DCS extraction via QRS theory . . . 193
6.4.5 Dominance of long trajectories in LIED . . . 193
6.5 Extraction of multiple bond lengths of aligned acetylene . . . 196
6.5.1 Challenges of imaging polyatomic, hetero-nuclear molecules via LIED . . . 196
6.5.2 Acetylene C_2H_2 as molecular target . . . 196

6.5.3 Impulsive molecular alignment of C_2H_2 198
6.5.4 Experimental parameters and bond extraction fitting routine 201
6.5.5 Importance of ion-electron coincidence detection for LIED imaging 205
6.5.6 Complete experimental results 207

7 Imaging and Control of Selected Molecular Fragmentation 211
7.1 Preparation and isolation of the deprotonation pathway of $C_2H_2^{++}$ 212
7.1.1 Potential energy landscape of acetylene 213
7.1.2 Double ionization regimes of acetylene in mid-IR fields . . . 215
7.1.3 Sequential ionization pathways of dication states 217
7.1.4 Photo-ion photo-ion coincidence (PiPiCo) analysis 222
7.2 Spatio-temporal imaging molecular structure during deprotonation 224
7.2.1 Experimental parameters 225
7.2.2 Measurement of bond lengths during deprotonation 226
7.2.3 Theoretical modeling of the deprotonation dynamics 230
7.2.4 Control over field-enhanced and field-free deprotonation . . 233
7.2.5 Spatio-temporal snapshots of the deprotonation reaction . . 234

8 Conclusions and Outlook 239

A Relevant Physical Quantities in SI and Atomic Units 249

B Derivation of the intensity threshold of over-the-barrier ionization 251

C Additional information about the supersonic gas jet 252
C.1 Empirical model to determine the Mach number and the off-axis particle number density in the gas jet 252
C.2 Derivation of jet momentum from Mach number 253

D Electronic trigger scheme 255

Acronyms 259

References 263

Acknowledgements 293

List of Figures

1.1 Illustration of a pump-probe measurement. 24
1.2 Illustration of LIED imaging of molecules. 27

2.1 Keldysh parameter. 35
2.2 Ionization mechanisms. 37
2.3 Comparison of PPT, ADK and TDSE ionization rates (taken from [1]). 41
2.4 Re-collison model. 47
2.5 Long and short trajectories. 50
2.6 Re-collison model. 54
2.7 Molecular orbitals and potential energy curves of H_2. 58
2.8 3D alignment distributions. 63
2.9 Time evolution of the degree of alignment from Torres *et al.* [2]. . . 65
2.10 Re-collison model. 68

3.1 Concept of chirped pulse amplification. 75
3.2 Concept of optical parametric amplification. 76
3.3 Mid-IR OPCPA setup. 78
3.4 Intensity distribution in the focal volume and peak intensity determination. 81
3.5 Data aquisition time. 83
3.6 Setup of a reaction microscope. 86
3.7 Supersonic gas jet in ultra-high vacuum. 88
3.8 Electric field spectrometer. 92
3.9 MCP detector and delay line. 95
3.10 Timing and electronic trigger scheme. 98
3.11 GENERiC signal flow chart. 99
3.12 Convention of coordinate system. 100
3.13 Electron cyclotron trajectory. 102
3.14 Analysis steps to calibrate experimental conditions (Part I). 105
3.15 Analysis steps to calibrate experimental conditions (Part II). 107
3.16 Momentum conservation and “loose” coincidence. 109

4.1 LESs: state-of-the-art. 117
4.2 Momentum resolution with two magnetic fields. 121
4.3 Detection of multiple LESs, VLES and ZES in 3D momentum space. 127
4.4 Kinetic energy spectra at ToF-like cuts. 128
4.5 Projection of PtPl onto E-L plane. 129

4.6 Dependence of LESs on pulse duration. . . . 132
4.7 Comparison of experiment and CTMC calculations around the center of PtPl. . . . 134
4.8 Comparison of width of center structure. . . . 135
4.9 Quantum orbit analysis of VLES and LESs. . . . 136
4.10 Energy distribution of bound electrons from CTMC and TDSE calculations. . . . 138
4.11 LES, VLES and ZES detected for xenon. . . . 142

5.1 Milestones of experimental discoveries of NSDI. . . . 145
5.2 Basic DI mechanisms and characteristic behavior of experimental observables. . . . 147
5.3 Particular findings of Sun *et al.* [3] on NSDI of Xe atoms. . . . 151
5.4 Distributions of Xe ion yields and respective ratios. . . . 157
5.5 Determination of saturation intensity. . . . 159
5.6 ToF spectra of five Xe dications for different intensities. . . . 160
5.7 Recoil-ion momenta of $^{129}Xe^{2+}$ and $^{129}Xe^{3+}$ for different intensities. 162
5.8 Experimental and semi-classical electron correlation distributions for moderate and high intensity. . . . 163
5.9 Representative trajectories for both moderate and high intensity from semi-classical model. . . . 165

6.1 Illustration of LIED imaging of molecules. . . . 174
6.2 Momentum transfer as a function of scattering angle. . . . 176
6.3 Ratio of scattering cross-sections of hydrogen and carbon. . . . 178
6.4 Intrinsic sub-cycle temporal resolution. . . . 180
6.5 Electron momentum resolutions for high static fields. . . . 188
6.6 Extraction of elastic DCSs of electrons re-scattering off Xe atoms with mid-IR LIED. . . . 190
6.7 Doubly differential cross-section of mid-IR LIED on Xe atoms. . . . 192
6.8 Demonstration of intensity insensitivity in LIED. . . . 194
6.9 Demonstration of dominance of long trajectories in LIED. . . . 195
6.10 Time-of-Flight distribution of acetylene interacting with 3 μm pulses. 197
6.11 Impulsive molecular alignment of C_2H_2. . . . 199
6.12 Ionization rate as a function of alignment angle of the HOMO of C_2H_2. . . . 200
6.13 Electron momentum distributions of all channels and corresponding to C_2H_2. . . . 201
6.14 Extraction of molecular structure from electron momentum distributions. . . . 204
6.15 χ^2 solution maps of the fitting routine. . . . 205
6.16 Coincidence imaging enabling accurate bond length extraction. . . . 206
6.17 Accurate $C_2H_2^+$ bond length extraction. . . . 207
6.18 Extraction of all 3 individual $C_2H_2^2$ bond lengths. . . . 210

7.1 Potential energy landscape of acetylene. . . . 214

7.2 Transition from NSDI to SDI of acetylene with mid-IR pulses. . . . 216
7.3 Molecular orbitals of the neutral ground state of acetylene. 218
7.4 Relevant potential energy curves of acetylene and pathways to populate dication states. 219
7.5 Angular ionization yield dependence of HOMO and HOMO-1. . . . 220
7.6 PiPiCo distributions for aligned and anti-aligned acetylene. 223
7.7 Kinetic energy release. 224
7.8 MCF extraction. 227
7.9 3D χ^2 solution space of LIED imaging of the $^3\Pi_u$ and $^1\Pi_u$ states for two alignments. 229
7.10 PES of the acetylene dication dressed with the mid-IR LIED field. . 233
7.11 Comparison between experiment and theory of the presence of the nuclear wave packet in the $^3\Pi_u$ and $^1\Pi_u$ states. 235
7.12 Temporal dynamics of acetylene resolved for the different bonds and as function of orientation. 237

D.1 Electronic trigger scheme. 256
D.2 Electronic trigger signals. 257

List of Tables

2.1 Ionization regime conditions. 38

3.1 Technical parameters of our jet and vacuum system. 90
3.2 Properties of our supersonic jet for target species used in this thesis. 91

6.1 Overview of properties of various diffraction imaging techniques. . 172

A.1 Conversion of basic physical quantities and constants between atomic and SI units. 250

Chapter 1

Introduction

Modern technology offers everybody the possibility to shoot their own movies since every smartphone nowadays has a video camera function. The most vital bit of information conveyed in a movie is the behavior of an object over time. From a technological point of view, in order to record a sequence of frames of a dynamic process like a moving object, a camera needs to fulfill two basic requirements: 1) it needs to resolve that object spatially *plus* 2) its shutter speed must be faster than a fraction of the total time of the dynamic process itself.

Scientists have always been curious to visualize ever faster processes of ever smaller objects in order to study and understand their behavior and function. Popular examples for this endeavor can be found at many points in history. At the end of the 19th century, rapid processes of macroscopic objects prompted questions as they could not be resolved by the "human camera shutter" being the blink of an eye combined with the information bandwidth between the eye and the brain (at $\sim$0.1 s) [4]. This included the questions whether a horse completely lifts off ground during its gallop or how a cat quickly turns around during a fall off to land on its feet. Respectively, the inventors and photographers Eadweard Muybridge (1878) [5] and Etienne-Jules Marey (1894) developed photographic devices with shutter speeds on the ms - level. These cameras were able to resolve and *freeze* instances of these rapid motions in time and helped to answer the questions. Another popular example is the work of Harold Edgerton (mid-1900s) who combined stroboscopic light flashes with photography to resolve, among others, bullets passing through various objects like e.g. an apple with µs temporal resolution [4].

This "stop-motion" technique, i.e. the idea of taking pictures using light flashes faster than the actual process of interest, laid out the principle ideas for modern research using time-resolved measurements in physics, chemistry and biology. Here, the crucial challenge is the ability to investigate chemical reactions and biological functions by "freezing their constituent molecules in time". This allows to better understand their working principles [4, 6] and hence to potentially control their underlying processes. The universal "tool" of modern science is the *laser*[1] which was first experimentally realized by Theodore H. Maiman [7] in 1960 in the visible spectrum[2]. Initially the concept was established six years earlier for microwaves

[1] **l**ight **a**mplification by **s**timulated **e**mission of **r**adiation
[2] $\lambda = 380\,\text{nm}$ to $750\,\text{nm}$ or $E_\lambda = 3.26\,\text{eV}$ to $1.65\,\text{eV}$

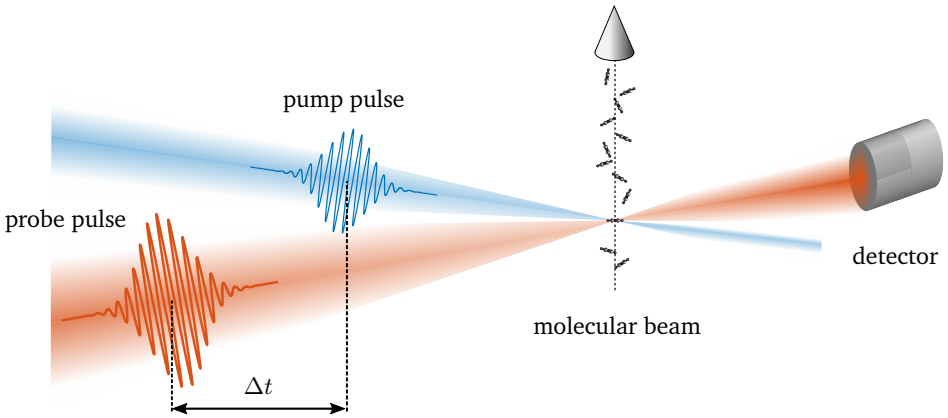

Figure 1.1: Illustration of a pump-probe measurement.

with the *maser*[3] by the Nobel laureate in Physics Charles H. Townes. Shortly after, techniques were developed to generate pulsed, coherent electro-magnetic waveforms from the laser output (i.e. *mode-locking* [8], see Sec. 3.1.1). The continuous advancement of pulsed laser systems evolved from initial pulse durations in the nanosecond (ns = 10^{-9} s) to 100s of picoseconds (ps = 10^{-12} s) regime (historical overview given in [8]) to nowadays standardly generated laser pulses of a few femtoseconds (fs = 10^{-15} s) duration, dubbed as *ultrafast* laser sources. This paved the way for modern research fields like ultrafast optics and spectroscopy [8–11] which in the end followed the historical trend of researchers striving to grasp processes that are faster than they can record and understand.

With the tool of ultrafast laser pulses at hand, the field of ultrafast or *femtochemistry* [4] was developed in order to overcome the limits hindering the possibility to probe "immeasurably fast reactions" as stated by the Nobel laureate in Chemistry Manfred Eigen in 1967 [12, 13]. The work of the group of Ahmed Zewail in the 1980s and 1990s greatly contributed to the development of femtochemistry by making use of ultrafast laser pulses of generally tens to 100s of femtoseconds duration as their "flashes of light" to investigate the evolution of chemical processes. Hereby, they pioneered *pump-probe* type time-resolved measurements, where a molecular system is excited or *pumped* by a fs-laser pulse to reach a dynamic state of interest so that it can be projected afterwards onto a final state of the molecular system by applying a second fs-pulse serving as a *probe* of the outcome of the system. A typical pump-probe setup is illustrated in Fig. 1.1. By step-wise variation of the temporal difference between both fs-pulses, the evolution of the dynamic reaction of the molecule can be studied. Zewail was awarded the Nobel prize in Chemistry in 1999 for this work [4] on "real-time chemistry" [14][4].

The vivid interplay between the motion of electrons and nuclei within a molecular

[3] **m**icrowave **a**mplification by **s**timulated **e**mission of **r**adiation

[4] The beginning of this introduction was inspired by his exciting Nobel lecture article published in [4] i.a.

system is ultimately the basis of all chemistry [15]. As a matter of fact, chemical reactions are triggered by the dynamic alteration of the *coupled* electronic and nuclear structure of the participating molecules. Within atoms and molecules different processes happen at different timescales [4, Fig. 2]: (non-)radiative decays between different energy levels have characteristic lifetimes on the μs to ns - level; rotational motions of molecules[5] occur on ns to ps - time scales; vibrational motions and dissociation reactions of molecular wave packets evolve on the level of several 100s of fs [15]; the dynamics of valence electrons and holes fundamentally occur on the sub-fs namely several 100s of attoseconds (as = 10^{-18}) level [16]. Thus, the chemical process of interest defines the necessary temporal resolution of a spectroscopic methodology or a required imaging technique.

Ideally, capturing the microscopic motion of all electronic and nuclear constituents during a chemical reaction is key to understand the process. In order to do so, it is desirable to utilize imaging techniques that can detect the motion of the relevant particles on their natural time-scales. Therefore, sub-atomic resolution in both space (picometers) and time (attoseconds) [14] needs to be provided.

On the one hand, the dynamics of valence electrons in atomic and molecular systems can be interrogated by attosecond duration waveforms [13–16]. This allows the study of charge migration dynamics in molecules [17, 18] that alter a chemical process including the position of their nuclei. Nowadays, attosecond pulses in the extreme ultraviolet (EUV) and soft-x-ray regime[6] are readily generated via the non-linear frequency up-conversion process of high harmonic generation (HHG) [20–23]. Conclusions about subsequent nuclear motion can indirectly be drawn via the before mentioned coupling of electrons and nuclei (see e.g. [24]).

On the other hand, the ability to *directly* observe and track the nuclear motion in molecular compounds would give information about the "precise nature of the structural rearrangement" [25] during a chemical reaction. In order to provide insights into dynamics of molecular structure, a structural imaging method needs sub-Ångström spatial and few- to sub-femtosecond temporal resolutions [15]. The simultaneous achievement of such challenging requirements would allow the possibility of directly imaging key problems in physical chemistry, such as transition states [26], proton migration or isomerization [27]. Furthermore, rapid dynamics at critical intervals in a chemical reaction could be resolved. Here, nuclear wave packets are moving along a "molecular crossroad" between two electronic energy surfaces, i.e. *conical intersections* [28]. Reactions and rearrangements on the electronic level at these crossroads directly decide the outcome of the chemical reaction guiding the nuclei to one or another final state [15]. The capability of imaging the motions of the atomic constituents during these processes with the above mentioned spatio-temporal resolutions would represent a paradigm shift in modern physics and chemistry.

Prominent approaches to achieve such dynamic nuclear imaging are based on elec-

[5] as utilized in impulsive molecular alignment, see Secs. 2.3 and 6.5.3.

[6] The EUV spectral region ranges from $\lambda \sim$ 121-10 nm equivalent to $E_\lambda \sim$10.25-124 eV while the soft-x-ray region ranges from $\lambda \sim$ 10-0.25 nm equivalent to $E_\lambda \sim$125-5 keV [19].

tron [29, 30] and X-ray [31, 32] diffraction. In the last decades, both methods have been developed into promising techniques that could provide the necessary sub-atomic spatio-temporal resolutions[7] [33–35]. To-date, enormous efforts are undertaken by the scientific community in order to conduct experiments that utilize the simultaneous spatio-temporal resolution capabilities to image dynamics of single molecules. *Laser-induced electron diffraction* (LIED) [36,37] is an alternative, table-top method that provides the combined spatio-temporal resolutions for imaging of gas-phase structural molecular dynamics. Here, a strong laser field triggers a self-diffraction event via photo ionization as sketched in Fig. 1.2. The process offers intriguing intrinsic temporal probabilities on the sub-fs level. Challenges in establishing LIED as a reliable molecular imaging technique lie in simultaneously fulfilling stringent experimental conditions in order to provide highly energetic electrons that offer sufficient momentum transfer when colliding with the atomic or molecular system to be looked at. Moreover, the effect of the strong laser field on the nuclei during the LIED process need to be closely investigated and understood as it can have implications on the measured final state of the target. So far, LIED has only been applied to extract structural information from small diatomic molecules, i.e. nitrogen N_2 and oxygen O_2 molecules [38, 39]. In order to become a consistent and robust method towards imaging ultrafast processes in gas-phase molecular systems, LIED needs to be applied to and tested on larger, more complex molecular systems. So far, this has not been achieved due to experimental limitations partially addressed above. A central part of this thesis is dedicated to overcoming those limitations (see Part III). This also necessitated to primarily study the influence of the strong laser field on the atomic and molecular systems (see Part II).

Both the process of HHG and LIED are applications of the general field of strong-field physics (SFP) which is concerned with the effects related to the interaction of intense electric fields with matter. Here, "intense" means that the electric field is non–negligible compared to the binding fields within matter. Since these field strengths are most easily attained with intense ultrashort laser pulses, most of the effects and observations stem from the interaction with these laser fields. The physics behind the process of *strong-field ionization* (SFI) can be described by the semi-classical *re-collision model*[8] which was first elaborately described by Paul B. Corkum in 1993 [23]. In brief, tunneling ionization of an atomic or molecular target is followed by the acceleration of the detached photo electron and its return to the parent ion. Upon return, the electron (wave packet) holds probabilities to either recombine with the parent ion system leading to the emission of attosecond bursts of EUV photons (HHG), or to elastically re-scatter off its parent ion thereby acquiring a diffraction imprint of the target (LIED, as illustrated in Fig. 1.2). Moreover, inelastic re-scattering can occur where the returning electron further ionizes the target ion, also known as *non-sequential double* (or multiple) *ionization* (NSDI). All mechanisms rely on the attained kinetic energy of the accelerated electron wave trajectory away and back towards the ion that is scaling linearly with the intensity

[7] few-picometer spatial and few- to sub-femtosecond temporal resolution [14]
[8] also known as *Simple-Man's Model* or *three-step model*

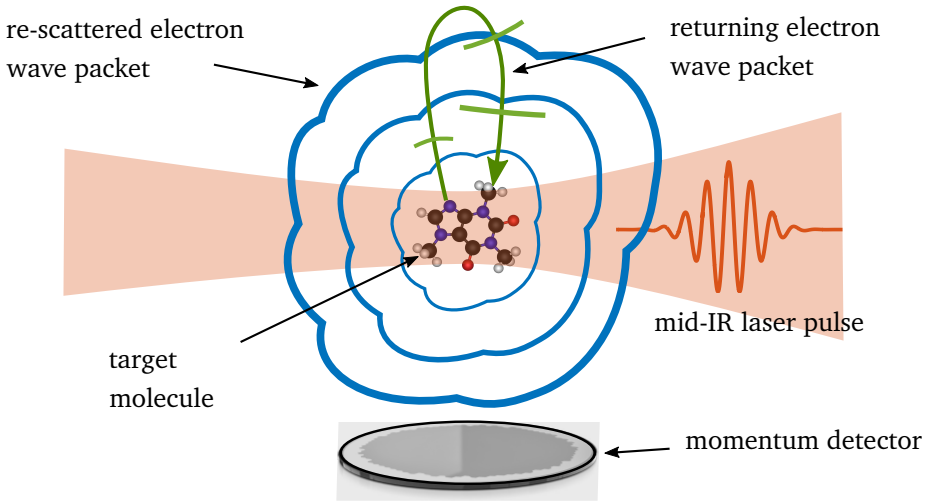

Figure 1.2: Illustration of LIED imaging of molecules. A target molecule is tunnel-ionized by a long wavelength electric laser field (red) to accelerate the liberated electron on a long excursion (green) before driving it back to the parent ion. Upon return the electron elastically re-scatters in all directions (blue), henceforth containing a diffraction imprint of the positions of the single atomic scatterers. This diffraction information is perceptible in the 3D detected momentum distribution as the Fourier transform in the far-field.

I and quadratically with the wavelength λ^2 of the driving laser pulses. A distinct feature of the re-collision model is that the electrons can be described as classical particles allowing for an attribution of energy dependent timing of each electron trajectory. This then allows for sub-optical cycle temporal properties (hence on the order of tens to hundreds of attoseconds) of all SFI mechanisms. An important characteristic of the field of *attosecond science*[9] is that "[...] attosecond optical pulses" (HHG) "are always accompanied by an attosecond electron pulse" (LIED) as both are possible outcomes of the re-collision process. "Thus, the technology of electron physics" that has been established for decades, "can be integrated with optical technology. The electron gives attosecond science access to spatial resolution determined by electron wavelength ($\sim$1 Å), and optics gives electron-collision physics a systematic method for measuring dynamics. [...]" as pointed out by Corkum in [14].

In parallel with the advancement of ultrafast laser science, strong-field physics has developed into a mature field of research that is now capable of tracking electronic dynamics on the attosecond timescales [24, 40–43]. This advancement of SFP and attoscience has, in turn, generated an upsurge in the development of ultrafast *mid-*

[9] Attosecond science and strong-field physics are obviously closely related. For clarity, in this thesis, the term attoscience is used in general for any mechnism based on the SFI induced re-scattering model involving an electron wave packet returning to the parent ion on sub-optical cycle / sub-fs time scales. Hence, not only HHG but also LIED is defined as an attosecond science effect.

infrared (mid-IR) laser sources due to the possibilities of driving strong-field re-collision with long wavelengths [44–47]. Mid-IR sources present many benefits for the SFI process compared to the ubiquitous 0.8 μm radiation of Ti:Sapphire based laser systems. Some of the most relevant to this study are:

1. the unambiguous creation of interaction conditions that are conducive for classical interpretations of experimental results, also in terms of the intrinsic temporal resolution;
2. strong-field re-collision at low peak intensity in order to avoid appreciable ground state depletion; and
3. the ability to create high energy re-collision electrons for imaging applications (HHG, LIED).

However, long wavelength (ponderomotive) scaling comes at the cost of a dramatically reduced signal [44–47], which translates into reduced statistics or long data acquisition times. This problem is exacerbated by the fact that traditional electron detection techniques only detect a small fraction of the entire momentum space. Experiments will eventually become untenable due to the required acquisition times exceeding the stability of a measurement apparatus. These points are often overlooked but they present a significant roadblock to the advancement of strong-field physics.

In this thesis, I am specifically interested in exploiting the benefits of the long-wavelength scaling of the SFI process in order to establish LIED as a readily available technique for structurally imaging ultrafast processes in gas phase molecules. More specifically, higher kinetic energy returning electrons will be used to achieve spatial resolutions comparable with sub-Å capabilities of conventional electron diffraction. LIED combines its spatial resolution with unique intrinsic temporal capabilities of sub-optical cycle scales paving the way to an ideal structural imaging technique with few-fs to as - time scales. This would provide an enticing basis towards the possibility of dynamically imaging the position of nuclei in chemical bonds while they break, form, or geometrically rearrange [4] on their natural time scales during transient states. This potential holds impacts well beyond physics, influencing chemistry, biology and future technologies [14].

On a more fundamental level, the laws and mechanisms of SFI process need to be verified and benchmarked when driven with long-wavelength sources, as to-date only a minority of investigations have been conducted due to a lack of available sources. With the recent availability of intense long-wavelength sources [48–57] surprising peculiarities and features have been found in SFI spectra [58–61] that neither have not been existent in the near-IR analogue nor have they been predicted by the commonly used theoretical ionization models. The features in SFI spectra at long wavelength need to be fully understood since a complete knowledge of the SFI process for any laser condition is crucial to further advance the research process on the field.

Here, an experimental methodology is employed that harnesses the benefits of long-wavelength SFI while overcoming the accompanied limitations of the long-

wavelength scaling by combining two tools:

1. an intense and high repetition rate optical parametric chirped pulse amplification (OPCPA) based mid-IR (3.1 μm) source [49–56] pioneered and developed in the last decade in our group being the *Attoscience and Ultrafast Optics* (AUO) group at ICFO - The Institute of Photonic Sciences in Barcelona, Spain; and

2. a reaction microscope (ReMi) detection system [62, 63] that can image the three-dimensional (3D) momentum space of the interaction in full particle coincidence, which was built up in our laboratory in collaboration with the Max Planck Institute for Nuclear Physics of Heidelberg, Germany.

Our interest lies in resolving specifically the momentum spectrum of all charged particles of mid-IR SFI events for the fundamental reason that "[...] atoms and molecules are *de-localized* according to the laws of quantum mechanics. Location *and* time [of quantum particles] are no observables in a singular measurement. Momenta of quantum particles, however, are measurable observables at any point in time. [...]" [64] as pointed out by Horst Schmidt-Böcking, one of the pioneers of ReMi detection systems.

This thesis is structured in three main parts. In part I, the fundamentals are established. First, an introduction to the physics behind the interaction of strong laser fields with atoms and molecules is given in Ch. 2. In doing so, the re-collision model, i.e. the basis of all physics discussed within the thesis, is defined. Also, the benefits and challenges of driving SFI with mid-IR fields are laid out in more detail. Then, the experimental methodology is presented in Ch. 3 including the working principles and setup of both our high repetition rate, mid-IR OPCPA source and the ReMi detection system.

Afterwards, the experimental results of this thesis are presented, divided into two main topics. In part II, mid-IR driven SFI is tested against established theories. In Ch. 4, the recently found "ionization surprise" [65] is elucidated which arises at low kinetic energy and was not predicted by theory neither detected in previous experimental investigations. Therefore, the SFI induced photo electron momentum spectrum is probed for very low energies with high resolution and for the first time in full 3D. Combining the experimental results with accurate theoretical calculations, the behavior of different types of low energy structures (LESs) as a function of pulse duration is investigated. This sheds light on the mechanisms behind and differences between them. In Ch. 5, double ionization (DI) dynamics in strong mid-IR fields are examined in detail. By probing the transition between different ionization regimes as a function of intensity, xenon atoms are investigated as a precursor for multi-electron molecular systems as they have shown anomalous behavior when investigated with 800 nm laser pulses.

In part III of the thesis, the combined temporal and spatial resolutions of LIED imaging are harnessed with our experimental methodology of the mid-IR laser pulses and 3D momentum coincidence detection. As pointed out earlier, the mid-IR driving wavelength allows the operation of LIED in the quasi-static regime which

permits scrutinizing experiments closest to classical treatments. This allows us to extract field-free (re-)scattering information which are tested on xenon atoms in Ch. 6. The resulting cross-sections are put in contrast with the most up-to-date data from NIST[10] in order to calibrate our mid-IR LIED technique. Then, mid-IR LIED imaging is applied to aligned acetylene (C_2H_2) molecules in order to extract its full structure. Structural imaging of polyatomic molecules with LIED, i.e. systems with three or more atoms, had not been successfully achieved before. Acetylene is an interesting target molecule as it exhibits channels of full prototypical molecular dynamics like e.g. dissociation [66] and isomerization [27] reactions. Lastly, in Ch. 7, the combined spatio-temporal capabilities of mid-IR LIED are utilized to image the acetylene molecules while they undergo the ultrafast process of a breakup of one of its carbon-hydrogen bonds. The snapshots of the proton escape are taken on a time scale below 10 fs after population of the dissociating state.

Finally the results of all experiments presented in this thesis are summarized in Ch. 8. In addition, an outlook on possible future investigations and perspectives on the individual experiments is given.

[10] **N**ational **I**nstitute of **S**tandards and **T**echnology

Part I

Fundamentals

Chapter 2

Fundamentals of Strong-field Physics

One of the goals of strong-field physics is to acquire an understanding of the interaction between strong laser fields and matter. The first question that needs to be asked is at what magnitude an electro-magnetic field is considered *strong* enough to perturb an atomic or a molecular compound. The rule-of-thumb is that an electric field is regarded as *strong* when it is non-negligible in comparison with the Coulomb field that is experienced by an electron in its atomic orbital. In case of the simplest atom, hydrogen, the electron is held in its orbit around the proton at the distance of a Bohr radius $a_0 \approx 0.529 \times 10^{-10}\,\mathrm{m} = 0.529\,\text{Å} \stackrel{!}{=} 1\,\mathrm{a.u.}$[1] with an electric field strength of

$$|\vec{\mathcal{E}_0}| = \frac{1}{4\pi\epsilon_0}\frac{e}{a_0^2} \approx 5.142 \times 10^{11}\,\frac{V}{m} \stackrel{!}{=} 1\,a.u.\,. \tag{2.1}$$

The Coulomb field experienced by the s-electron is comparable with the electric field of a laser source at a peak intensity of

$$I = \frac{1}{2}\,\epsilon_0\,c\,\mathcal{E}_0^2 = 3.509\,\times\,10^{16}\,\frac{W}{cm^2} \stackrel{!}{=} 1\,a.u.\,.^{2} \tag{2.2}$$

For multi-electron atomic systems, the electric field experienced by the outer valence shell electron is lower due to a larger distance to the nucleus ($|\vec{\mathcal{E}_\omega}| \lesssim |\vec{\mathcal{E}_0}|$) because of the $1/r^2$ scaling of the Coulomb field and screening effects by the inner shell electrons. Nowadays, ultrafast laser sources readily provide electric waveforms with comparable field amplitudes in form of ultrashort laser pulses ranging from sub-100 fs ($< 100 \times 10^{-15}$ s) duration down to the few-cycle[3] regime. The electric field of a linearly polarized, pulsed waveform is defined (e.g. in [8, 68]) as

$$\mathcal{E}(t) = \mathcal{E}_0(t)\cdot\cos(\omega t + \phi_{\mathrm{CE}}) = \mathcal{E}_0\exp(-\frac{t^2}{2\,\sigma^2})\cdot\cos(\omega t + \phi_{\mathrm{CE}}) \tag{2.3}$$

with the laser frequency ω and the time-dependent amplitude $\mathcal{E}_0(t)$ usually being described by a Gaussian envelope function. Here $\sigma = \tau_{\mathcal{E}}/(2\sqrt{2\ln 2})$ is one

[1] This corresponds to one atomic unit 1 a.u. of length. An overview of atomic units together with their conversion into the SI unit system can be found in appendix A.

[2] The relation between peak electric field strength $\mathcal{E}_0$ and peak intensity I of an electromagnetic wave includes the vacuum permittivity ϵ_0 and the speed of light c.

[3] The duration of one laser electric field cycle depends on the carrier wavelength(s) and can be estimated as $\tau_{\text{cycle}} = \frac{\lambda_0}{c}$ with λ_0 being the central wavelength of the pulse . A *few-cycle* pulse contains less than three optical cycles [67].

standard deviation of the Gaussian envelope of the electric field and $\tau_{\mathcal{E}}$ its full-width half maximum (FWHM), which can be considered as the laser pulse duration. Generally, the pulse durations of laser pulses in literature are given in terms of the FWHM of the laser intensity envelope τ_I according to the time-dependent analogue of Eq. 2.2. The relation between both FWHM values can be derived as $\tau_I = \tau_{\mathcal{E}}/\sqrt{2} \approx 0.707\,\tau_{\mathcal{E}}$. In this thesis, pulse durations are also given in terms of τ_I (FWHM of $I(t)$). The *carrier-envelope phase* (CEP) ϕ_{CE} stands for the offset between the peak of electric field envelope and the next neighboring peak of the oscillating carrier field.

In this chapter, the basic concepts developed in the last decades describing the behavior of atoms and molecules in strong laser fields are explained.

2.1 Ionization of atoms in strong laser fields

In quantum physics, an electromagnetic wave is also described as a quantized particle - a *photon*. The commonly accepted wave-particle duality permits describing a photon both as a particle and a wave with respective properties. Hence, one ascribes an energy to the photon according to the frequency/wavelength of its corresponding electromagnetic waveform: $E = \hbar\omega = \frac{hc}{\lambda}$.

Photo ionization is the consequence of the interaction of an electromagnetic wave / photon with an atomic (or molecular) system [69]. In its simplest form, a single photon with an energy $E_{1\omega}$ greater than the ionization potential I_{P} ($E_{1\omega} > I_{\mathrm{P}}$) results in emission of an electron from the ground state of the system to a continuum state and an ion. The ionization rate of this *linear ionization* process [70, Ch. 4.3] is directly proportional to the intensity I and a probability factor in form of the cross section $\sigma_{1\omega}$ of the absorption process

$$\Gamma \propto \sigma_{1\omega} I \,. \tag{2.4}$$

In the case that the photon energy is smaller than the ionization potential ($E_{1\omega} < I_{\mathrm{P}}$), ionization is only possible with *strong fields* ($|\vec{\mathcal{E}_{\mathrm{n}\omega}}| \lesssim |\vec{\mathcal{E}_0}|$) via *non-linear ionization* processes [71].

2.1.1 Keldysh theory

A framework to model non-linear ionization via strong-field interactions was proposed by Keldysh in his seminal work from 1965 [72] where he introduced the dimensionless adiabaticity parameter γ, defined as

$$\gamma := \frac{\omega\sqrt{2m_e I_{\mathrm{P}}}}{e\mathcal{E}} \propto \frac{1}{\sqrt{I}\lambda} \,. \tag{2.5}$$

The *Keldysh parameter* γ is dependent on the laser frequency ω, the ionization potential I_{P} and the electric field amplitude $\mathcal{E}$. Moreover, it can be expressed as

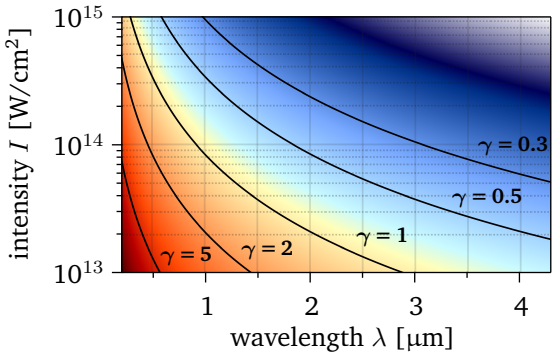

Figure 2.1: Keldysh parameter. Distribution of the Keldysh parameter γ (logarithmic color scale) as a function of intensity I and wavelength λ of a laser field interacting with argon atoms. Black contour lines highlight Keldysh parameters of $\gamma = 0.3, 0.5$ for the tunneling regime, $\gamma = 1$ in the transition region, and $\gamma = 2, 5$ for the multi-photon regime.

a function of the *ponderomotive energy* U_P being the cycle-average quiver energy experienced by a free electron in the time-varying laser electric field [70, Eq. 8.128] defined as

$$U_\mathrm{P} := \overline{\frac{1}{2} m_e v^2} = \frac{e^2\,\mathcal{E}^2}{4\,m_e\,\omega^2} = \frac{I\,e^2}{2\,m_e\,\epsilon_0\,c\,\omega^2} = \frac{I\,e^2\,\lambda^2}{8\,\pi^2\,m_e \epsilon_0 c^3} \propto I\lambda^2 \tag{2.6}$$

using in anticipation Eq. 2.38 (as velocity in SI units) and Eq. 2.2, leading to

$$\gamma = \sqrt{\frac{I_\mathrm{P}}{2U_\mathrm{P}}}\,. \tag{2.7}$$

The conventional interpretation of γ is as a metric to distinguish between the two main regimes of strong-field ionization:

1. the *multi-photon* ionization (MPI) regime for $\gamma > 1$,
2. the *tunneling* ionization (TI) or *quasi-static* (QS) regime for $\gamma \ll 1$,

It is important to realize that γ should only be used as an approximate orientation to determine whether a process is predominantly governed by MPI or TI. The case when $\gamma \approx 1$ is known as the *transition* regime where ionization features characteristics from both multi-photon and tunneling ionization [73]. The scaling of the Keldysh parameter as a function of intensity I and wavelength λ of the driving field interacting with an argon (Ar) atom ($I_\mathrm{P} \approx 15.76$ eV) is presented in Fig. 2.1. Both, an increase of the intensity or the wavelength from the visible (380 nm - 750 nm) to the mid-IR ($\lambda > 3$ μm) spectral regime leads to a decrease of the Keldysh parameter and hence to a ionization regime change between MPI and TI. Important to note here is that the Keldysh parameter has a stronger dependence on wavelength than intensity, so the influence of the laser field on the atomic system is higher with longer wavelength.

In the following, the most common ionization mechanisms within the two main regimes are presented sorted by its dependence on field intensity. This ranges from lower I ($\gamma > 1$), described in the particle picture, to higher I ($\gamma \ll 1$), described in the wave picture.

Multi-photon ionization ($\gamma > 1$)

When an atom is exposed to a laser field at low intensities ($I \lesssim 10^{13}\,\frac{W}{cm^2}$), and in the limit of a high density of photons, an electron can be liberated by absorption of n photons of $E_{1\omega} < I_P$[4]. This mechanism is sketched in Fig. 2.2 (a), where the sum of absorbed photons (green arrows) yields a combined energy greater than the ionization potential $n \cdot E_\omega > I_P$ needed to lift an electron (purple dot) from the ground state of the unperturbed Coulomb potential V_C [blue solid line in Fig. 2.2 (a)] to the continuum ($V_C > 0$). By applying n$^{\text{th}}$-order perturbation theory the ionization rate of MPI [70, Ch. 5.5] can be determined as

$$\Gamma_n \propto \sigma_{n\omega}\, I^n \propto \sigma_{n\omega}\, \mathcal{E}^{2n}\,, \tag{2.8}$$

where $\sigma_{n\omega}$ is the generalized absorption cross-section of n photons. For the case that more photons are absorbed than needed for overcoming the ionization potential, the excess energy is shared by both kinetic energy and ponderomotive energy of the detached electron [74]

$$n \cdot E_\omega - I_P = E_{kin} + U_P\,. \tag{2.9}$$

This special case of MPI dubbed *above threshold ionization* (ATI) was first experimentally observed in 1979 by Agostini et al. [75] in experiments on six-photon ionization of xenon atoms. As a peculiarity of ATI it was found that the integrated kinetic energy spectrum of the liberated electron shows s characteristic peaks equally spaced by the photon energy E_ω according to the s additionally absorbed photons. The ionization rate of ATI is analogously calculated by

$$\Gamma_{n+s} \propto \sigma_{(n+s)\omega}\, I^{n+s}\,. \tag{2.10}$$

A review of theoretical and experimental investigations on ATI following the initial observations of [75] can be found in [76]. Next to the equally spaced ATI peaks, the kinetic energy spectrum can additionally contain further characteristic features. These result from the influence of the electric field on the bound states of the atomic (or molecular) system leading to Stark-shift [77,78] or channel-closing [79] induced resonances during the ATI process.

Tunneling ionization ($\gamma \ll 1$)

By increasing the laser intensity, the applied oscillating electric field reaches a strength comparable with the binding Coulomb field (dashed blue lines in Fig. 2.2)

[4] We consider photons in the infrared (IR) wavelength range here.

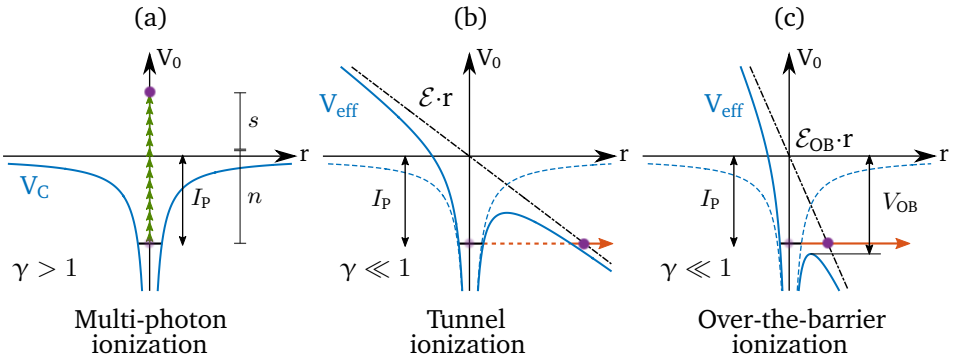

Figure 2.2: Nonlinear ionization mechanisms. Nonlinear ionization mechanisms occur for photon energies smaller than the ionization potential of the atomic system ($\hbar\omega < I_\mathrm{P}$). **(a)** *Multi-photon ionization:* For lower intensities ($I \lesssim 10^{13}\, W\,/\,cm^2$) an electron can be liberated by absorption of $n+s$ photons (green arrows), where n photons are needed to account for I_P and s photons result in the kinetic energy E_kin of the detached electron. The latter process is specified as *above threshold ionization*. **(b)** *Tunneling ionization:* For higher intensities, the electric field distorts the Coulomb potential V_C, resulting in a bent effective potential V_eff which can be overcome by the electron wave packet via tunneling (red dashed arrow). **(c)** *Over-the-barrier ionization:* When the distortion of the field reaches the point that the tunneling barrier is completely suppressed, the electron wave packet can escape quasi-freely (red arrow).

which results in a distortion of the Coulomb potential V_C. At the instant of a local field maximum, the quasi-static electric field that can be considered effectively linear, bends the Coulomb potential leading to a *barrier suppression* as experienced by the bound electron. The resulting potential V_eff [70, Ch. 8.5] [blue line in Fig. 2.2 (b)] can be calculated as

$$V_\mathrm{eff}(r, t_0) = -\frac{Z_\mathrm{eff}\, e^2}{4\,\pi\,\epsilon_0\, r} - e\,\mathcal{E}(t_0) r\,, \tag{2.11}$$

with Z_eff being the effective nuclear charge of the ion residue. Rather than taking the "vertical ionization channel" [73] of MPI, the electron now is more likely to *tunnel* through the classically forbidden region being the suppressed potential barrier ($V_\mathrm{eff} > 0$) via a "horizontal ionization channel". Originally Keldysh [72] expressed γ as the ratio between the frequency of the electric field ω and the frequency of an electron tunneling through the potential barrier ω_T [80]

$$\gamma \propto \frac{\omega}{\omega_\mathrm{T}}\,. \tag{2.12}$$

Hence, low electric field frequencies allow for $\gamma \ll 1$. Under this consideration, tunneling can be understood as an *adiabatic process* [81, Ch. 16] occurring for quasi-static field conditions. Since the electric field has a significant influence on the atomic system, the application of perturbation theory is invalid. Instead

Keldysh shows that in the adiabatic limit ($\gamma \ll 1$) the transition rate grows exponentially and is described as [72]:

$$\Gamma_{\mathrm{T}} \propto \exp\left(-\frac{4\sqrt{2\,m}\,I_{\mathrm{P}}^{3/2}}{3\,e\,\hbar\,\mathcal{E}}\right) \text{ (for } \omega \to 0\text{)}. \tag{2.13}$$

An overview over the most established tunneling models is given in the following Sec. 2.1.2.

Over-the-barrier ionization / Field ionization

As the intensity I of the ionizing electric waveform is increased further, the effective potential V_{eff} is bent to the point where the peak of the potential barrier is equal to the ionization potential I_{P} of the bound electron state. Hence, the electron wave packet encounters no barrier and can quasi-freely escape. This process is known as *field-* or *over-the-barrier* ionization [70] and is exemplarily sketched in Fig. 2.2 (c). In order to field-ionize bound states of an atom and to bend the effective potential by the amount of the ionization potential $V_{\mathrm{OB}} \geq I_{\mathrm{P}}$ (or more), the intensity I has to succeed the critical intensity limit

$$I_{\mathrm{OB}} = \frac{\epsilon_0^3\,\pi^2\,c\,I_{\mathrm{P}}^4}{2\,Z_{\mathrm{eff}}^2\,e^6}\ ^{5}. \tag{2.14}$$

The quartic scaling of the critical intensity I_{OB} with ionization potential I_P clearly shows that higher lying electron states have a high probability of field ionization.

Conditions for different ionization effects

In the following the different ionization regimes are listed in terms of their characteristic energy condition which strongly depends on the driving laser pulse parameters.

ionization regime	condition
single-photon	$\hbar\omega > I_{\mathrm{P}} \gg U_{\mathrm{P}}$
multi-photon	$I_{\mathrm{P}} > \hbar\omega \gg U_{\mathrm{P}}$
above-threshold	$I_{\mathrm{P}} > U_{\mathrm{P}} > \hbar\omega$
tunneling	$U_{\mathrm{P}} \gtrsim I_{\mathrm{P}} > \hbar\omega$
over-the-barrier / field	$U_{\mathrm{P}} \gg V_{\mathrm{OB}} \geq I_{\mathrm{P}}$

Table 2.1: Ionization regime conditions.

The table shows that the validity of different ionization effects is clearly connected to the properties of the laser pulses in comparison to the ionization potential I_{P}. In general, the trend from linear towards highly non-linear ionization is related with decreasing photon energies $\hbar\omega$ and at the same time increasing peak intensities leading to an increase of the ponderomotive energy U_{P}.

[5] A derivation of the critical intensity I_{OB} is shown in App. B.

2.1.2 Quantitative models for tunneling ionization

In this subsection, a short overview of the most established tunneling ionization models is presented. The overview raises no claim to (historical) completeness of all the different approaches to model the tunneling process. A more detailed overview is given in e.g. [80, 82–84]. From here on, atomic units (see App. A) are used unless indicated otherwise.

Keldysh like models: PPT and ADK theory

Shortly after the work of Keldysh was published in 1965, further models on the basis of his ideas were developed. Nikishov and Ritus [85] calculated the transitions rates of an electromagnetic wave interacting with atomic systems built up of short-range potential barriers. The rates were investigated according to their angular distributions and polarization dependence. At the same time, the work of Perelomov, Popov and Terent'ev [86–88], today better known as the *PPT model*, was published that included Coulomb forces to calculate tunneling transition rates. According to the PPT model, the ionization rate of an atomic target for linearly polarized monochromatic field is proportional to [86]

$$\Gamma_{\mathrm{PPT}} \propto \exp\left(-\frac{2}{3}\frac{\mathcal{E}_0}{\mathcal{E}}\, g(\gamma)\right) \tag{2.15}$$

with $\mathcal{E}_0 = (2\,I_\mathrm{P})^{3/2}$ and as a function of the Keldysh parameter γ. Hence, the PPT model describes the ionization process as a function of wavelength and is valid not only in the tunneling regime ($\gamma \ll 1$). The multiplication factor $g(\gamma)$ can be expressed as (e.g. from [1])

$$g(\gamma) = \frac{3}{2\,\gamma}\left[(1+\frac{1}{2\,\gamma^2})\,\sinh^{-1}(\gamma) - \frac{\sqrt{1+\gamma^2}}{2\,\gamma}\right] . \tag{2.16}$$

The complete PPT model contains a series of integrals and prefactors which are given in the original work [86–88].

In 1986, these Keldysh like models were further refined and generalized for any complex atom (i.e. more complex than hydrogen) by Ammosov, Delone and Krainov [89]. Due to its simplicity, the *ADK model* is nowadays widely used mostly amongst experimentalist as a pure tunnel ionization model at the quasi-static limit ($\gamma \ll 1$) independent of the driving wavelength λ. Considering a monochromatic electric field in linear polarization, the ADK model predicts an ionization rate [89, 90] of

$$\Gamma_{\mathrm{ADK}} = \frac{\mathcal{E}\,D^2}{8\,\pi\,Z_\mathrm{eff}}\sqrt{\frac{3\,n^{*3}\,\mathcal{E}}{\pi\,Z_\mathrm{eff}^3}}\,\exp\left(-\frac{2\,Z_\mathrm{eff}^3}{3\,n^{*3}\,\mathcal{E}}\right) , \tag{2.17}$$

averaged over all momentum vectors. The principal quantum number n is substituted here with the *effective quantum number*

$$n^* := \frac{Z_\mathrm{eff}}{\sqrt{2\,I_\mathrm{P}}} , \tag{2.18}$$

while D is defined for simplification of the formula as

$$D := \left(\frac{4\, e\, Z_{\text{eff}}^3}{\mathcal{E}\, n^{*4}} \right)^{n^*} . \tag{2.19}$$

The given formula represents an s-state of the regarded atomic system. For higher orbital states, the m,l - dependent ADK rates are given in the original work [89]. In typical strong-field ionization experiments, laser pulses are utilized to achieve high electric field amplitudes. Note that a laser pulse is associated with a spectrum of multiple frequencies and that the ionization rate of such a polychromatic waveform is typically greater for identical intensity compared to the monochromatic case [90, 91]. Many times it is useful to express the ADK rates as a function of the momentum vector $\vec{p} = (p_\parallel, p_\perp)$[6] of the liberated electron

$$\Gamma(p_\parallel, p_\perp) = \Gamma_0 \, \exp\left(-\frac{p_\parallel^2\, \omega^2\, (2\, I_\text{P})^{3/2}}{3\, \mathcal{E}^3} - \frac{p_\perp^2\, (2\, I_\text{P})^{1/2}}{\mathcal{E}} \right) , \tag{2.20}$$

$$\text{with} \quad \Gamma_0 = \frac{|\vec{p}|\, \omega^2\, D^2}{8\, \pi^3\, n^*\, \mathcal{E}} \, \exp\left(-\frac{2\, (2\, I_\text{P})^{3/2}}{3\, \mathcal{E}} \right) . \tag{2.21}$$

Important to realize is that the electron momentum vector $\vec{p}$ stands for the final experimental observable. It is derived not only for the momentum related to the tunneling process itself but also for the classical motion of the detached electron at the maximum of the laser electric field [90]. Moreover, the prefactor Γ_0 takes the influence of the Coulomb field on the electron into account. This opens up the possibility to fit Eq. 2.20 against an experimental electron momentum distribution (Gaussian-like distribution around $|\vec{p}| = 0$) in order to calibrate the peak intensity of the driving laser (see Subsec. 3.1.3).

While the ADK model is widely used, it should be mentioned that the PPT model generally results in a more accurate description of the ionization process. This can be shown by comparing the PPT and ADK rates with the results of the direct solution of the TDSE being the most accurate description. Such a study was conducted e.g. by Yan-Zhuo *et al.* [1]. In Fig. 2.3 (directly taken from [1]), a comparison between the all three descriptions of the ionization process is plotted for atomic hydrogen as a function of peak intensity and in case of PPT and TDSE for different wavelengths [λ = 600 nm (red), 800 nm (blue), 1200 nm (orange)]. It is apparent that the ionization probabilities according to the PPT model lie close to the ones of the TDSE solution for all used intensities. The ADK-based calculation only coincides with the ones of PPT and TDSE towards $\gamma \ll 1$, as expected, while it deviates up to two orders of magnitude on the $\gamma > 1$ side. This is the benefit of using a PPT based model over ADK as it also accurately describes the SFI process around for $\gamma \lesssim 1$ and above.

An extended PPT model was proposed by Popruzhenko *et al.* [92], which even more accurately allows to calculate ionization rates for arbitrary Keldysh parameter and

[6] given in cylindrical coordinates as photo electron momentum spectra generally contain an azimuthal symmetry

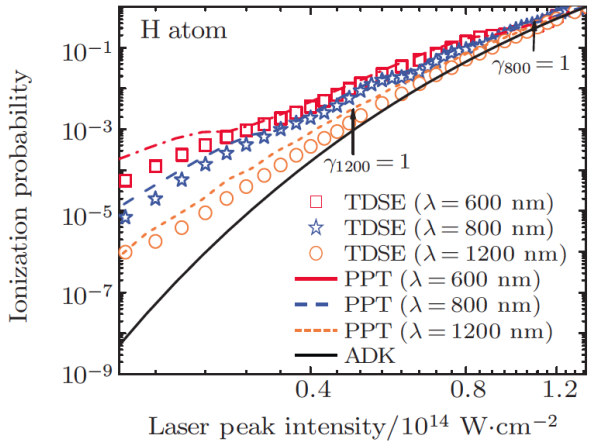

Figure 2.3: Comparison of PPT, ADK and TDSE ionization rates (taken from [1]). Normalized ionization probabilities of atomic hydrogen calculated as a function of laser intensity at three different laser wavelengths λ =600 nm (red), 800 nm (blue), 1200 nm (orange) according to the ADK model (black solid line), the PPT model (dashed lines) and the TDSE solution (markers).

wavelength over a wide range of intensities (agreeing with respective TDSE rates from $I = 10^{12}$ W/cm^2 to $I = 10^{18}$ W/cm^2 [92]).

KFR theory / Strong-field approximation (SFA)

Another, entirely analytical approach to describe the ionization process in strong electric fields was proposed in a "different, but unquestionably related" [82] manner by Faisal [93] and Reiss [94]. The idea behind the *KFR theory*[7] is to solve the time-dependent Schrödinger equation (TDSE, see e.g. [95, Ch. 5] and [73])

$$i\frac{\partial}{\partial t}\,|\Psi(t)\rangle = \hat{H}(t)\,|\Psi(t)\rangle \ , \tag{2.22}$$

for adequate approximations. Its formal solution is

$$|\Psi(t)\rangle = \exp(-i\int_0^t \hat{H}(t')\,\mathrm{d}t')\,|\Psi(t=0)\rangle = \exp(-i\int_0^t \hat{H}(t')\,\mathrm{d}t')\,|\Phi_i\rangle \ , \tag{2.23}$$

describing an external plane-wave electromagnetic field interacting with an electron bound in a finite atomic potential via the S-matrix formalism of quantum mechanical scattering theory[8]. Here the transition of an initial state $\Phi_i(t)$ of the

[7] The KFR model is abbreviated after its three authors **K**eldysh, **F**aisal and **R**eiss.

[8] A nice and compact explanation of the use of S-matrix amplitudes to solve the time-dependent Schrödinger equation for strong-field ionization problems can be found in [73] or [96].

field-free system $\hat{H}_0$ to a final state $\Psi_i(t)$ through interaction with the electromagnetic field $\hat{H}_\mathrm{I}(t)$ can expressed via a transition amplitude

$$(S-1)_{fi} = -i \int_{-\infty}^{+\infty} \mathrm{d}t \, \langle \Psi_f(t) | \, \hat{H}_0 + \hat{H}_\mathrm{I}(t) \, | \Phi_i(t) \rangle \ . \tag{2.24}$$

In order to solve this equation analytically one needs to simplify the problem. Faisal [93] and Reiss [94] achieved this by adapting the idea of Keldysh [72] through a *strong-field approximation* (SFA): the influence of field is strong compared to the influence of the long-range Coulomb potential so that the latter can be considered a small perturbation and is neglected ($\gamma \ll 1$). In order to put this physical picture into the mathematical description of Eq. 2.24, the final continuum state of the electron $\langle \Psi_i(t) |$ is replaced with the analytically exact *Volkov solution* $\langle \Psi_f^\mathrm{V}(t) |$ for a free electron in the time-varying electric field thus neglecting any Coulomb field influence. This was originally proposed by Reiss in 1962 [97]. Note that the Hamiltonian of the field-free system $\hat{H}_0$ contributes negligibly to the transition amplitude since it has no contribution to the ionization. The initial state $|\Phi_i(t)\rangle$ is kept exact. This results in the *SFA transition amplitude* [96]

$$(S-1)_{fi}^\mathrm{SFA} = -i \int_{-\infty}^{+\infty} \mathrm{d}t \, \langle \Psi_f^\mathrm{V}(t) | \, \hat{H}_\mathrm{I}(t) \, | \Phi_i(t) \rangle \ . \tag{2.25}$$

This treatment is valid under quasi-static conditions, i.e. $\gamma \ll 1$. Here, the Hamiltonian describing the electron-field interaction is given in velocity gauge[9] as [98]

$$\hat{H}_\mathrm{I}(t) = -\vec{p} \cdot \vec{A}(t) + \frac{\vec{A}^2(t)}{2} \ , \tag{2.26}$$

while the Volkov wave function is expressed as [98]

$$\langle \vec{r} | \Psi_f^\mathrm{V}(t) \rangle = \frac{1}{(2\pi)^{3/2}} \ \exp\left(i\vec{p}\vec{r} - \frac{i}{2} \int_0^t \mathrm{d}t' [\vec{p} - \vec{A}(t')]^2 \right) \ . \tag{2.27}$$

$\vec{A}(t)$ is the time-dependent vector potential of the electromagnetic field. Finally, the ionization rate is given by the transition probability which relates as

$$\Gamma_\mathrm{SFA} \propto \left| (S-1)_{fi}^\mathrm{SFA} \right|^2 \ . \tag{2.28}$$

Direct integration of the three-dimensional Schrödinger equation

The numerical solution of the TDSE (see eq. 2.22 and 2.23) of an atomic or molecular system in an intense, pulsed electromagnetic waveform is the most complete

[9] The choice of gauge in SFA has led to many discussions (e.g. [96,98]) since the initial SFA after KFR theory lacks gauge invariance. As a result, gauge-invariant descriptions of the SFA have been proposed, like e.g. in [99].

description of the strong-field ionization process since it incorporates all possible physical outcomes and effects. Yet, the *ab initio* nature of this method limits the insight one can have in comparison with models where one can in- and exclude different physical effects. Solving the TDSE can be very demanding in terms of time and computing capacity which is why approximations are being made. Hence, a common simplification is the *single active electron* (SAE) approximation [100] where the ionization process is described as a pure one-electron transition while the remaining electrons are considered "frozen spectators" [101]. The SAE approach has been shown to give accurate descriptions even of molecular ionization yet completely neglects e.g. electron-electron correlations which can be important for specific underlying ionization dynamics [102]. An overview of common numerical methods to solve the TDSE is given in [103].

2.1.3 Limits of strong-field tunneling models

All approximate descriptions assume conditions of tunneling that is the quasi-static limit of electron emission, in which the field oscillates non-noticeably compared to the electron wavepacket motion. The tunneling or adiabatic limit is described mathematically as $\gamma \to 0$. Per definition of the Keldysh parameter (see Eq. 2.5) the tunneling limit is reached both by increasing the intensity $I \to \infty$ and decreasing the frequency $\omega \to 0$[10] of the field as shown in Fig. 2.1. This already indicates a more complex interplay between variables which is not correctly classified by simply one parameter, the Keldysh parameter γ. This argument was brought forward early on by H. R. Reiss [82, 104–107] and was already mentioned in his initial description of the SFA in 1980 [94]. He defined three intensity parameters z, z_1 and z_f which permit classifying different fundamental boundaries of tunneling.

The original tunneling limit described by the Keldysh parameter $\gamma \ll 1$ is expressed by

$$z_1 := \frac{2\,U_\mathrm{P}}{I_\mathrm{P}} \gg 1\,. \tag{2.29}$$

Hence $z_1 = 1/\gamma^2$ is basically another representation of the Keldysh parameter (see Eq. 2.7) describing the relation between the ponderomotive energy U_P of the liberated electron and the ionization potential I_P of the atomic system for tunneling (see Tab. 2.1). Although technologically not trivial, an unlimited increase of I or decrease of ω would stretch the validity of the tunneling picture. An indefinite increase of I leads to a relativistic behaviour of the electron, where the interplay of both electric and magnetic fields of the electromagnetic waveform become vital. A tunneling theory that only considers the electric field in this regime would fail for obvious reasons [106][11] The intensity parameter that describes the relativistic

[10] The angular frequency ω is used here instead of the wavelength λ and in atomic units.
[11] Note that tunneling theories consider longitudinal fields only, which is already an issue.

behaviour of an electron is defined as

$$z_\mathrm{f} := \frac{2\,U_\mathrm{P}}{m_e\,c^2}\ ^{12}. \tag{2.30}$$

An electron behaves relativistically when its ponderomotive energy U_P becomes comparable to the rest kinetic energy of a relativistic electron $E_0 = mc^2$. Hence the relativistic behavior starts to be prominent for $z_\mathrm{f} \approx 1$ so that non-relativistic behavior occurs for the ratio $I/w^2 \ll 2\,c^2$ [13].

Already in an intermediate regime between clear non-relativistic and relativistic electron behavior, the magnetic field of the laser field has an influence on the tunneling process [104]. This influence causes the propagation of the electron in the laser field to change from a linear, one-dimensional, dipole-like motion to a *figure-8 motion* [82, 104] where the mayor axis lies parallel to the electric field component $\vec{\mathcal{E}}$ and the minor axis points along the magnetic field component $\vec{\mathcal{B}}$. Larger magnetic field magnitudes $|\vec{\mathcal{B}}|$ result in a non-negligible amount of the minor axis of the figure-8 motion defined as

$$\beta_0 = \frac{z}{2\,c\,(1+z_\mathrm{f})} \approx \frac{z}{2\,c}\ . \tag{2.31}$$

The minor axis amplitude β_0 is dependent on the third intensity parameter defined as

$$z := \frac{U_\mathrm{P}}{\omega}\ . \tag{2.32}$$

In [104], Reiss defined the onset of the departure from a dipole-like behavior of the electron motion when the minor amplitude reaches the magnitude of an atom $\beta_0 \approx 1$ a.u. This sets the limit for the validity of the dipole approximation which is important in many tunneling models to $z \ll 2c$.

In summary, next to requiring nonlinear ionization $\omega \ll I_\mathrm{P}$ and the quasi-static condition $\gamma \ll 1$ or $z_1 \gg 1$, it is equally important to consider the validity of the dipole approximation $z \ll 2c$ and non-relativistic electron behavior $z_\mathrm{f} \ll 1$. This defines the strong-field ionization process and hence permits to estimate the ionization probability according to the appropriate tunneling model.

2.2 Propagation and return of the quasi-free electron

An essential part of the ionization process of atomic systems in strong laser fields is the propagation of the electron wave packet after tunneling. While the tunneling process is described quantum-mechanically, the post-tunneling behavior of the

[12] The electron mass m is used here to highlight the rest kinetic energy mc^2 of a relativistic electron. In atomic units the electron mass equals 1.

[13] The speed of light results as $c = 137\,a.u.$ in atomic units (see App. A).

electron wave packet in the oscillating electric field can be modeled with classical electrodynamics. According to the SFA, the influence of the Coulomb potential on the tunneled electron, compared to the strong laser field, is considered to be negligible, so that the electron propagates quasi-freely in this oscillating field. As described previously, the electron is considered to not gain any kinetic energy ($\vec{v}_0 \approx 0$) while[14] tunneling through the suppressed potential barrier.

After tunneling, the electron undergoes an oscillating or quiver motion attributed to the electric force and resulting acceleration by the time-varying electric field[15]

$$\vec{\mathcal{E}}(t) = \mathcal{E}_0(t) \begin{pmatrix} 0 \\ -\epsilon \sin(\omega t) \\ \cos(\omega t) \end{pmatrix} , \tag{2.33}$$

(being Eq. 2.3 generalized in three dimensions with $\phi_{\text{CE}} = 0$) where ϵ is the ellipticity parameter ($\epsilon = 0$ for linear, $\epsilon = \pm 1$ for circular polarization) and $\mathcal{E}_0(t)$ the amplitude envelope of the electric field (also defined in Eq. 2.3). The classical motion of the electron is described by[16]

$$\vec{F} = \vec{a}(t) = -\vec{\mathcal{E}}(t) . \tag{2.34}$$

Hence the momentum of the quasi-free electron in the oscillating electric field follows as (from e.g. [108, 109])

$$\vec{p}(t, t_\text{i}) = -\int_{t_\text{i}}^{t} \vec{\mathcal{E}}(t')\text{d}t' = \vec{A}(t_\text{i}) - \vec{A}(t) \tag{2.35}$$

with t_i being the time the electron exits the tunneling barrier and $\vec{A}(t) = \int \vec{\mathcal{E}}(t')\text{d}t'$[17] being the vector potential of the laser field. After the pulse, and hence in the state as it reaches the detector at $t \to \infty$, the electron is left with the momentum obtained initially by the vector potential of the laser field

$$\vec{p}_\text{str}(t_\text{i}) = \vec{p}(t \to \infty, t_\text{i}) = -\int_{t_\text{i}}^{\infty} \vec{\mathcal{E}}(t')\text{d}t' = \vec{A}(t_\text{i}) , \tag{2.36}$$

when assuming that the vector potential after the pulse vanishes $\vec{A}(t \to \pm\infty) = 0$. In other words, the electron remains with a propulsion or "kick" by the laser field. This effect is better known as *streaking* of the electron in the community.

[14] Again let's define the tunneling process to happen instantaneously.

[15] The magnetic field component of the laser field is ignored here. It is assumed to operate in an ionization regime where the dipole approximation is applicable, and hence the influence of the magnetic field on the electron is negligible (see Subsec. 2.1.3).

[16] Again atomic units are utilized here.

[17] Note that the vector potential $\vec{A}(t)$ is defined differently throughout the literature, either with or without a *minus* sign. Important to be considered here is that *either* the expression for $\vec{A}(t)$ *or* Eq. 2.34 should be defined with a *minus* sign. Throughout this chapter the definition of Eq. 2.34 with a *minus* sign and $\vec{A}(t)$ without according to [25, 108, 110] is followed. The opposite definition is taken e.g. in [74, 111]. The final relations give identical results.

The following considerations are made assuming the laser pulse to consist of multiple cycles, hence the amplitudes of subsequent carrier field maxima around the center of the pulse can be approximated constant $\mathcal{E}_0(t) = \mathcal{E}_0$ [black line in Fig. 2.4 (a)]. For linear polarization $\epsilon = 0$, the electron streaking momentum is reduced to one dimension and is given as

$$p_{\text{str}}(t_\text{i}) = A(t_\text{i}) = -\int_{t_\text{i}}^{\infty} \mathcal{E}_0 \cos(\omega t')\text{d}t' = p_{\text{str,max}} \sin(\omega t_\text{i}) \tag{2.37}$$

with

$$p_{\text{str,max}} := \frac{\mathcal{E}_0}{\omega} = 2\sqrt{U_\text{P}}\,. \tag{2.38}$$

According to Eq. 2.37, a tunneling electron with a negligible velocity at the tunnel exit that is subsequently *streaked* by the strong oscillating laser field, can gain a maximum kinetic energy of

$$E_{\text{str,max}} = \frac{p_{\text{str,max}}^2}{2} = 2\,U_\text{P}\,. \tag{2.39}$$

This applies for all electrons that directly oscillate away from the parent ion without any further interaction upon reaching the detector which is why they are commonly dubbed *direct electrons*.

2.2.1 Re-collision model

The classical quiver motion of the electron holds the possibility, under specific circumstances, to re-encounter and possibly interact with the parent ion before eventually drifting.The possibility of a return and interaction of the tunnel electron to its parent ion was first suggested by Kuchiev [112] and was then further discussed in [113–115]. Yet, Paul B. Corkum was the first to formulate the idea of a purely classically electron return [23], nowadays better known as the *re-collision*, *three step* or *simple man's model* (SMM).

The re-collision model starts with the basic classical equation of motion as beforehand described in Eq. 2.34. The electric field amplitude is approximated as $\mathcal{E}_0 = \text{const.}$. For a generalized electric field (see Eq. 2.33), the velocity (and momentum[18]) of the electron follows as

$$\vec{v}(t,t_\text{i}) = \vec{p}(t,t_\text{i}) = p_{\text{str,max}} \begin{pmatrix} 0 \\ \epsilon[\cos(\omega t_\text{i}) - \cos(\omega t)] \\ \sin(\omega t_\text{i}) - \sin(\omega t) \end{pmatrix} + \vec{v}_0\,. \tag{2.40}$$

The integration constant $\vec{v}_0$ is the initial velocity of the electron which is assumed to be zero at the tunnel exit ($\vec{v}_0 = 0$). Further, the position of the electron in three-dimensions (with the parent ion sitting at the origin) is derived as

$$\vec{x}(t,t_\text{i}) = \frac{p_{\text{str,max}}}{\omega} \begin{pmatrix} 0 \\ \epsilon[\cos(\omega t_\text{i})(\omega\Delta t) - \sin(\omega t) + \sin(\omega t_\text{i})] \\ \sin(\omega t_\text{i})(\omega\Delta t) + \cos(\omega t) - \cos(\omega t_\text{i}) \end{pmatrix} + \vec{v}_0\Delta t + \vec{x}_0 \tag{2.41}$$

[18] in atomic units calculated similarly

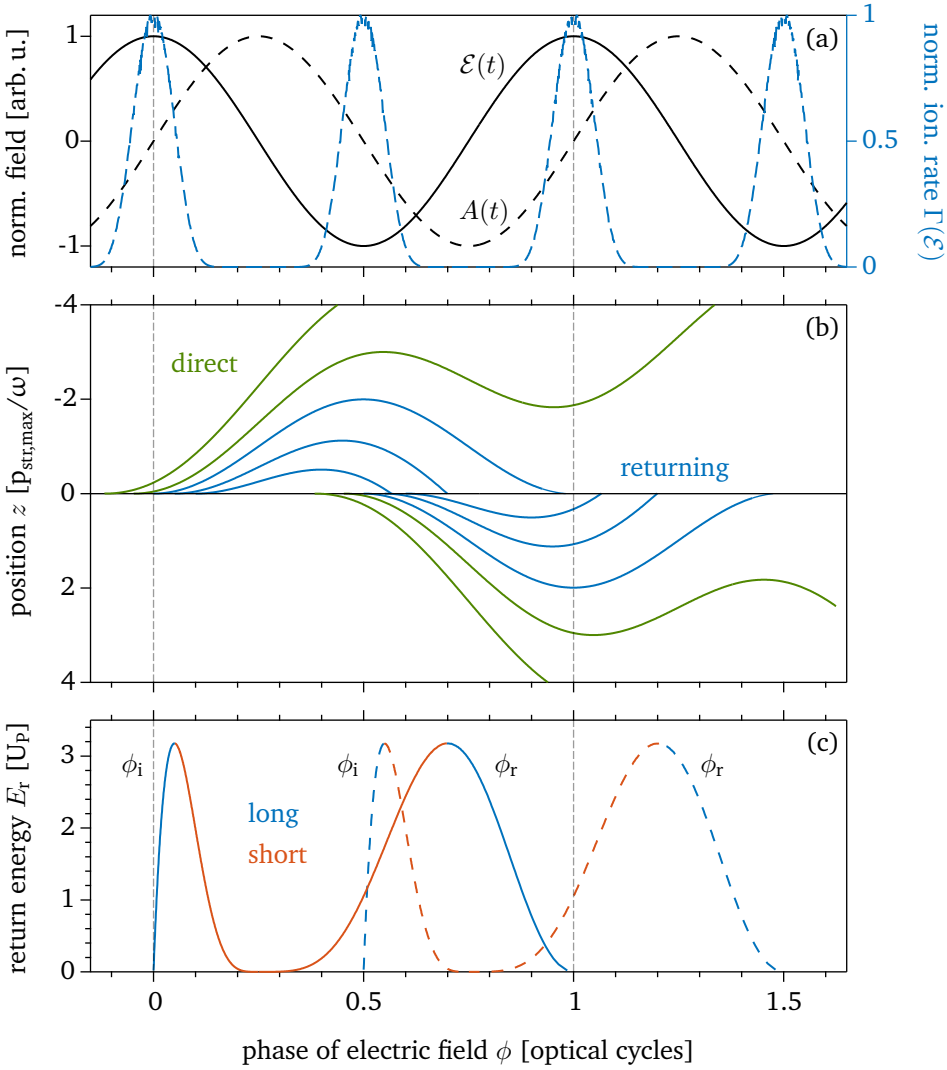

Figure 2.4: Re-collision model. All distributions are plotted as a function of the phase of the laser electric field ϕ in optical cycles ($[\frac{1}{360°}]$ or $[\frac{1}{2\pi}]$ or $[\frac{1}{\lambda}]$). **(a)** Normalized electric field $\mathcal{E}$ (black solid line) and its corresponding vector potential $A = \int E\,\mathrm{d}t$ (black dashed line); normalized instantaneous ionization rate $\Gamma(\mathcal{E})$ (blue dashed line) shows a symmetric distribution around the local electric field maxima. **(b)** Exemplarily selected electron trajectories $z(t, t_\mathrm{i})$ directly quivering towards the detector (green lines) or returning (at least once) to the parent ion (blue lines). **(c)** The accumulated electron return energy distribution for both ionization ϕ_i and return ϕ_r phases plotted for the first (solid lines) and second (dashed lines) half cycle. The maximum energy $E_\mathrm{r,max} = 3.2\,U_\mathrm{P}$ is found for $\phi_\mathrm{i,max} \approx 0.05, 0.55$, etc. and $\phi_\mathrm{r,max} \approx 0.70, 1.20$, etc. Moreover, long (blue) and short (red) trajectories are distinguished according to the flight time $\Delta\phi = \phi_\mathrm{r} - \phi_\mathrm{r} \gtrless \phi_\mathrm{r,max} - \phi_\mathrm{i,max}$, respectively.

with $\Delta t = t - t_\mathrm{i}$. Here, $\vec{x}_0$ stands for the initial position of the electron at the tunnel exit. In the re-collision model it is assumed that the atom is small compared to the electron trajectories and hence $\vec{x}_0 \approx 0$ [23].
Mathematically an electron's return can be expressed as

$$\vec{x}(t_\mathrm{r}, t_\mathrm{i}) \stackrel{!}{=} 0 \tag{2.42}$$

at the return time t_r. By taking a closer look at Eq. 2.41, it becomes clear that this occurs when the laser field is linearly polarized ($\epsilon = 0$). More complicated solutions are also possible for the combination of several non-linear fields [116][19]. Here, we will restrict our description to the simplest case of a single linearly polarized field and the re-turning problem being one-dimensional. In order to calculate the pairs of ionization t_i and return time t_r that correspond to a returning electron trajectory, the following simplified equation needs to be solved numerically:

$$\sin\phi_\mathrm{i}\Delta\phi + \cos\phi_\mathrm{r} - \cos\phi_\mathrm{i} \stackrel{!}{=} 0 \tag{2.43}$$

with $\phi = \omega t$ as the phase of the carrier field cycle and $\Delta\phi = \phi_\mathrm{r} - \phi_\mathrm{i}$. Solutions of Eq. 2.43 are found for electrons tunneling between $0° \leq \phi_\mathrm{i} \leq 90°$ and returning between $90° \leq \phi_\mathrm{r} \leq 360°$ corresponding to a cosine-like electric field [see left y-axis of Fig. 2.5 (a)]. Electron trajectories starting before the electric field maximum $-90° \leq \phi_\mathrm{i} < 0°$ do not have causal ($\phi_\mathrm{i} < \phi_\mathrm{r}$) solutions. Hence these electrons do not return to the parent ion and result in a direct trajectory. All scenarios are depicted in Fig. 2.4.

The electric field is plotted as a black solid line in Fig. 2.4 (a). Its corresponding vector potential (black dashed line) is shown according to their relation in Eq. 2.35. Fig. 2.4 (b) shows examples of trajectories $z(t, t_\mathrm{i})$[20] (from Eq. 2.41 in polarization direction) for direct (green solid lines) and returning (blue solid lines) electrons initialized before and after the local field maximum ($\phi_\mathrm{i} = 0$), respectively. The relative probability of an electron tunneling around the field maximum is illustrated by the normalized instantaneous ionization rate $\Gamma(\mathcal{E}(t))$ [21] [blue dashed lines in Fig. 2.4 (a)]. The ionization probability is distributed symmetrically around the field maximum ($\phi = 0$) which implies that half of all electrons ionized by the linearly polarized field return at least once to the parent ion [23] while the other half directly quivers towards the detector.

In general there are causal solutions of Eq. 2.43 for $k\pi \leq \phi_\mathrm{i} \leq (k + 0.5)\pi$ and $(k + 0.5)\pi \leq \phi_\mathrm{r} \leq (k + 2)\pi$ (for $k \in \mathbb{Z}$) for a field maximum of any successive half cycle around the peak of the center of the pulse envelope. This is emphasized in Fig. 2.4 (a) with the ionization rates around every half cycle maximum, and in

[19] Recently, the concept of returning electrons for $\epsilon \neq 0$ was introduced by utilizing the combination of two counter-rotating circularly polarized fields at different wavelength [117–121],

[20] Note that the y-Axis is mirrored along the x-Axis for reasons of display.

[21] The ionization rate is calculated according to an improved PPT model [92] which yields the instantaneous ionization rate analytically for arbitrary values of the Keldysh parameter and as a function of laser frequency. The latter differentiates the model from standard ADK rates. Exemplarily the calculation is performed here for Hydrogen atoms with an $I_\mathrm{P} = 13.6\,\mathrm{eV}$ interacting with laser field with $\lambda = 3100\,\mathrm{nm}$ at an intensity of $I = 10^{14}\,\mathrm{W/cm^2}$.

Fig. 2.4 (b) by plotting trajectories corresponding to the second half cycle (a) which are a mirror image of the trajectories of the first half cycle.

The kinetic energy an electron accumulated upon return can be calculated via Eqs. 2.38 and 2.40 as

$$E_{\mathrm{r}}(\phi_{\mathrm{r}}[\phi_{\mathrm{i}}],\phi_{\mathrm{i}}) = \frac{p(\phi_{\mathrm{r}},\phi_{\mathrm{i}})^2}{2} = 2\,U_{\mathrm{P}}(\sin\phi_{\mathrm{i}} - \sin\phi_{\mathrm{r}})^2\,. \tag{2.44}$$

In Fig. 2.4 (c) the return energy distribution is plotted as a function for both ionization ϕ_{i} and return phases ϕ_{r} for the first (solid lines) and second (dashed lines) half cycle, respectively. The electron trajectory starting at $\phi_{\mathrm{i,Er,max}} \approx 18.0° \approx 0.05\,\tau_{\mathrm{cycle}}$ and returning at $\phi_{\mathrm{r,Er,max}} \approx 251.7° \approx 0.70\,\tau_{\mathrm{cycle}}$[22] results in the maximum return momentum

$$p_{\mathrm{r,max}} = 1.26\,p_{\mathrm{str,max}} = 2.52\,\sqrt{U_{\mathrm{P}}}\,, \tag{2.45}$$

corresponding to an energy $E_{\mathrm{r,max}} = 3.175\,U_{\mathrm{P}}$. The trajectories with maximum return momenta of other half cycles initiate at $\phi_{\mathrm{i,Er,max}} \approx k\cdot 180° + 18.0° \approx (k\cdot 0.5 + 0.05)\,\tau_{\mathrm{cycle}}$ and return at $\phi_{\mathrm{r,Er,max}} \approx k\cdot 180° + 251.7° \approx (k\cdot 0.5 + 0.70)\,\tau_{\mathrm{cycle}}$ ($k \in \mathbb{Z}$).

Another important property of the electron trajectories is revealed in the energy distribution of Fig. 2.4 (c). Here, a given return energy can be achieved by two different trajectories ionizing and returning at distinct times. These trajectories are classified as *long* (blue lines), ionizing at $\phi_{\mathrm{i,long}} < \phi_{\mathrm{i,Er,max}}$ and returning at $\phi_{\mathrm{r,long}} > \phi_{\mathrm{r,Er,max}}$, and *short* (red lines) which exist for $\phi_{\mathrm{i,short}} > \phi_{\mathrm{i,Er,max}}$ and returning at $\phi_{\mathrm{r,short}} < \phi_{\mathrm{r,Er,max}}$. The naming is chosen after the overall time the electron spends on its trajectory $t_{\mathrm{traj.}} = t_{\mathrm{r}} - t_{\mathrm{i}}$.

The context is further illustrated in Fig. 2.5. In Fig. 2.5 (a) on the left axis, the ionization - return phase pairs are plotted for both long (blue line) and short (red line) trajectories. On the right y-axis in Fig. 2.5 (a), the corresponding vector potential $A(\phi_{\mathrm{r}})$[23] is plotted which after Eq. 2.36 is directly connected to the streaking momentum p_{str} of an electron at the point of return. The correlation between the streaking momentum p_{str} and return momentum p_{r} for long (blue line) and short (red line) electron trajectories is shown in Fig. 2.5 (b) which will play a role for the description of the elastic re-scattering process of the returning electron.As calculated before, the maximum return momentum is $p_{r,max} = 2.52\,\sqrt{U_{\mathrm{P}}}$.

The relative probability of both long and short trajectories is addressed in Fig. 2.5 (c). On the right axis, the normalized instantaneous PPT rate [92] is calculated [similarly to Fig. 2.4 (a)] as a function of return energy for both long and short trajectories. Due to the fact that the long trajectories are initialized closer to the local field maximum, they generally reveal a higher ionization rate than the short trajectories. This leads to a distribution of the relative probability ratio from $\frac{\Gamma_{\mathrm{long}}}{\Gamma_{\mathrm{short}}} > 10^4$

[22] Note that in the literature the values for the ionization and return times can differ slightly due to different rounding in the numerical solution. E.g. $\phi_{\mathrm{i,Er,max}} \approx 17°$ in the original publication by Corkum [23].

[23] Note the mirrored y-axis for display reasons.

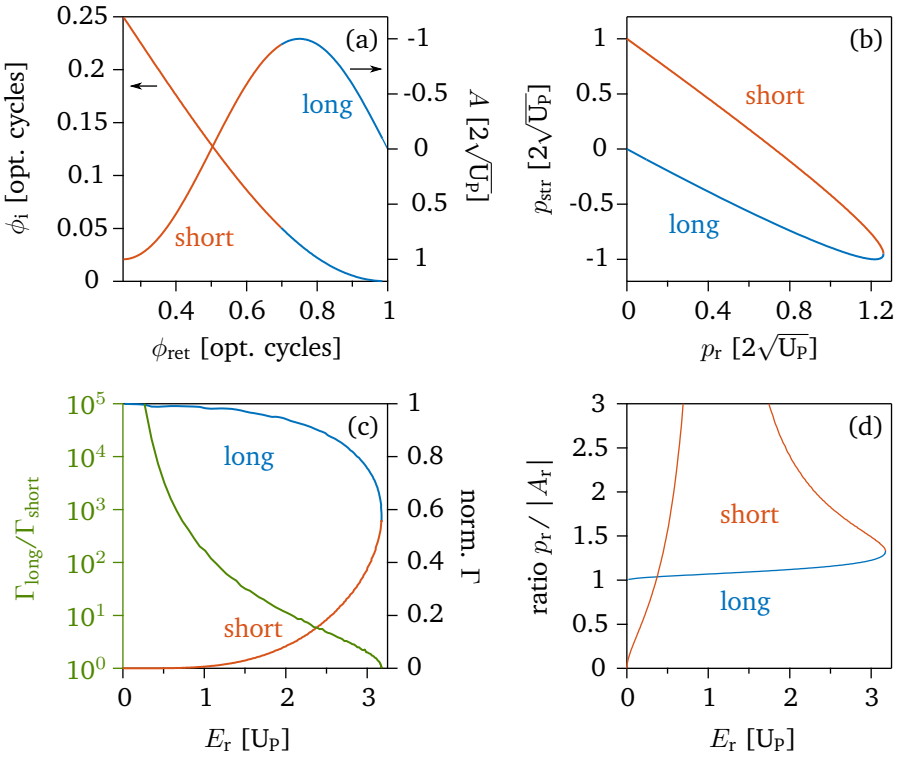

Figure 2.5: Long and short trajectories. (a) The solutions of Eq. 2.43 are plotted on the left axis in terms of ionization phase ϕ_i vs. return phase ϕ_r. The trajectories can be divided in *long* (blue lines, $\phi_{i,long} < \phi_{i,Er,max}$ and $\phi_{r,long} > \phi_{r,Er,max}$) and *short* (red lines, $\phi_{i,short} > \phi_{i,Er,max}$ and $\phi_{r,short} < \phi_{r,Er,max}$) depending on their propagation time compared to the trajectory yielding the maximum kinetic energy $E_{r,max}$. The right axis shows the corresponding vector potential A at the point of return ϕ_r. **(b)** The streaking momentum p_{str} is shown as a function of resulting return momentum p_r. **(c)** The normalized instantaneous ionization rate is shown as a function of return energy E_r for both long (blue line) and short (red line) trajectories. Clearly the long trajectories have a higher yield due to their ionization time closer to the local field maximum, which is expressed by the ratio $\frac{\Gamma_{long}}{\Gamma_{short}}$ (green line). **(d)** The ratio of the return momentum p_r on the absolute value of the vector potential $|A_{\phi_r}|$ at the point the electron's return as a function of the return energy E_r is plotted for long (blue) and short (red) trajectories.

for return energies $E_r < 0.5\,U_P$ to an equal ratio of $\frac{\Gamma_{long}}{\Gamma_{short}} = 1$ at the maximum return energy $E_r \approx 3.2\,U_P$ (green solid line).

Additionally, the ratio $p_r\,/\,|A_{\phi_r}|$ of the return momentum and the absolute value of the vector potential at the point of return is plotted as a function of return energy for both long and short trajectories in Fig. 2.5 (d). The ratio is relatively flat for long trajectories with values between 1 - 1.32 while ratio for short trajectories is

more complex with singularity around $E_r \approx 1\,U_P$ due to the zero crossing of $A(\phi_r)$.

2.2.2 Physics upon re-collision

After tunnel ionization and acceleration of the electron wave packet, the third step of Corkum's three-step model constitutes the re-collision of the accelerated electron with its parent ion. There are three main physical processes that can take place upon re-collision. The returning electron wave packet either 1) re-combines with the parent ion leading to the emission of a high-energy photon, re-scatters 2) inelastically thereby passing kinetic energy to the parent atomic system, or 3) elastically with energy loss. The recombination-induced UV photon emission (1) is better known as the process of *high-harmonic generation*. In the simplest case, inelastic re-scattering (2) can lead to further ionization of the parent atomic system which is also known as the $(e, 2e)$ process of *non-sequential double ionization* (NSDI). The case of elastic re-collision (3) where the momentum and kinetic energy is conserved is combined with the re-scattered electron gaining kinetic energy by the laser field of up to $10\,U_P$ [sometimes labeled as *high-energy ATI* (HATI)]. Moreover, these elastically re-scattered electrons capture a diffraction imprint of the parent ion target which is utilized in *laser-induced electron diffraction* (LIED). In Part III of this thesis, LIED is studied and further developed in detail. The importance of the semi-classical re-collision model [23] shall be stressed since it was able to describe all three types of phenomena (HHG, NSDI, HATI) which were experimentally discovered beforehand, however they could not be fully understood. General reviews on all three topics can be found in [14, 108, 122].

2.2.2.1 Re-combination

The returning electron holds the possibility to re-collide and re-combine with its parent ion leading to the generation of a high energy photon in the extreme ultraviolet (XUV) and soft-x-ray regime[24]. In this manner a photon is generated every half cycle of the laser pulse, so that their corresponding wave packets interfere, thus yielding periodic modulations of a high harmonic (HH) spectral distribution [122]. Hence, this coherent frequency up-conversion process leads to regular bursts of radiation which are separated as odd[25] multiples of the driving laser frequency. The HHG process was first observed experimentally by McPherson et *al.* in 1987 [20] and Ferray et *al.* in 1988 [21]. The maximum photon energy generated by an infrared laser pulse is achieved by the electron with a maximum return energy leading to a harmonic cutoff energy of $E_{\mathrm{HHG,c}} = I_P + 3.2\,U_P$ [22]. I_P is the ionization potential of the recombined state. In 1994, Lewenstein et *al.* [123] developed an analytic and fully quantum-mechanical model describing the HHG process where the harmonic cutoff-law was expressed more accurately.

[24] The XUV spectral region ranges from $\lambda \sim$ 121-10 nm equivalent to $E_\lambda \sim$10.25-124 eV while the soft-x-ray region ranges from $\lambda \sim$ 10-0.25 nm equivalent to $E_\lambda \sim$125-5 keV [19].

[25] due to parity conservation

The emission of HH photons every half cycle, thus yielding a coherent harmonic frequency spectrum gives rise to the temporal structure of HHG [108]. HH spectra potentially offer sub-cycle temporal properties that lead to attosecond bursts of light [124, 125]. In case of multi-cycle laser pulses, these bursts are generated as *trains* of attosecond pulses. Yet, when utilizing few-cycle pulses or specific gating techniques single isolated attosecond pulses can be generated[26]. A review on the physics involving attosecond pulses can be found in [126]. Our group recently generated, for the first time, isolated attosecond pulses in the *water window* spectral region[27] [127, 128].

2.2.2.2 Inelastic Re-scattering

Another possible outcome of the electron's re-collision with its parent ion is an inelastic re-scattering process. Here, some kinetic energy Q is transfered from the returning electron to the ionic system thereby promoting a second electron to a continuum state while the overall momentum is conserved. This aspect of double ionization (DI) of atoms and molecules was discovered in the early 1980s for xenon atoms by l'Huillier et *al.* [129] and later in other noble gases [130–132] or small molecules [133, 134]. In these experiments, the second ionization step was expected to behave as a sequential tunnel ionization step and so the yield of the dications as a function of intensity was assumed to follow standard tunneling rates (i.e. PPT or ADK models). Yet, the yield of dications for intensities below the single ionization saturation threshold was much higher than expected from two sequential tunneling events. This unexpected, enhanced yield of the dications, also known as a "knee" structure [109] in the intensity dependent yield distribution, was ascribed to inelastic re-collision events and dubbed NSDI[28].

The NSDI process which is intricately linked to the re-collision of the first electron (e_1) can proceed via two routes that lead to the promotion of the second electron (e_2) to the continuum: 1) e_2 can be directly promoted to the continuum by the impact energy of the returning e_1, which is the so-called *(e,2e)* mechanism, or 2) it can be resonantly lifted to an excited cation state by the impact of e_1. The excited ion system can subsequently be tunnel ionized at a succesive half cycle maximum of the laser electric field. The latter process is better known as *re-collision excitation with subsequent ionization* (RESI). Some reviews over double or multiple ionization processes via inelastic electron re-scattering can be found in [74, 102, 109, 135]. In chapter 5 the transition from the non-sequential to sequential double ionization

[26] A recent review on the generation of isolated attosecond pulses and its application in spectroscopy of electron dynamic can be found in [16].

[27] The water window spectral region is defined by the K-absorption edge of oxygen at a wavelength of 2.34 nm and the K-absorption edge of carbon at 4.4 nm which correspond to soft X-ray photons between 530 and 280 eV, respectively. Photons in that region are almost not absorbed by water.

[28] The re-scattering related DI process was named *nonsequential* because it was behaving not like the expected two *sequential* tunneling processes. This name-giving might be misleading since in the sequential DI process both electron emissions are independent of each other, and in the NSDI process the second electron is only emitted by the impact of the first electron so it is dependent on the first electron.

regime of xenon atoms interacting with intense, mid-IR fields is investigated where the most important characteristics of both regimes will be described in detail.

2.2.2.3 Elastic Re-scattering

The third possibility is that the returning electrons elastically scatter off the parent ion without exchanging energy with the target system. Yet, the electron wave packet diffracts with the target atom(s) retaining a diffraction image thereafter. In case of molecular targets, the angle dependent diffraction amplitude, carried by the scattered electron wave, contains the relative structural coordinates of the single atomic scatterers of the molecule. This information is analyzed as a LIED information to image molecular systems. The possibility to use the LIED technique to image polyatomic, hetero-nuclear molecules will be presented in detail in Part III of this thesis.

Characteristic of the elastic re-scattering process is the fact that the returning electron is streaked by the laser field at the point of return, hence receiving an additional momentum kick $p_{\mathrm{str}}(\phi_{\mathrm{r}}) = A(\phi_{\mathrm{r}})$ in polarization direction. This was described earlier with Eq. 2.37. The re-scattered electrons can accumulate a final kinetic energy which is much bigger than the maximum energy of the direct electrons ($E_{\mathrm{resc}} > E_{\mathrm{str,max}} = 2\,U_{\mathrm{P}}$). This opens the possibility to distinguish between re-scattered and direct electrons via the detected kinetic energy or momentum distribution. The scenario is sketched in Fig. 2.6 (a) where the 3D electron momentum space[29] is represented with its perpendicular momentum components $p_{\perp}$ over parallel components $p_{\parallel}$ relative to the laser polarization direction $\vec{\mathcal{E}}$. The accelerated electron (purple trajectory) returns to the parent ion (origin of the coordinate system) and subsequently scatters at an angle Θ_{r}[30] while conserving all its momentum $\vec{p}_{\mathrm{r}}$ (blue dashed arrow). Taking into account the additional streaking momentum $\vec{A}(\phi_{\mathrm{r}})$ (red dashed arrow) obtained by the laser field upon return, the overall re-scattering momentum vector $\vec{p}_{\mathrm{resc}}$ (green solid arrow) yields an effective angle $\Theta^{'}$[31]. The relation between p_{r} and $A(\phi_{\mathrm{r}})$ is plotted in Fig. 2.5 (d). Hence, this final electron momentum $\vec{p}_{\mathrm{resc}}$ at the time $t \gg t_{\mathrm{r}}$ is dependent on both the time and momentum of the returning electron; i.e. on the initial phase ϕ_{i} of the electron entering the laser field, as well as the scattering angle Θ_r of the electron upon re-collision with respect to its direction of motion [111]. In every re-scattering event, the electron can be considered to scatter within a two-dimensional ρ-z-plane [25, 111] so that the final momentum from Eq. 2.37 and 2.40 (for linear

[29] Cylindrical coordinates are assumed here, where the three-dimensional momentum space has been integrated around the full azimuthal angle.

[30] The field-free scattering angle Θ_{r} spans clock-wise between the vector of incoming electron and the field-free electron vector after scattering $\measuredangle(\vec{e}^{\,*}, \vec{p}_{\mathrm{r}})$ [blue in Fig. 2.6 (a)].

[31] The overall field-dressed scattering angle $\Theta^{'}$ is different from the field-free scattering angle Θ_{r} and spans clock-wise between the vector of incoming electron and the overall re-scattering electron vector $\measuredangle(\vec{e}^{\,*}, \vec{p}_{\mathrm{resc}})$ [green in Fig. 2.6 (a)].

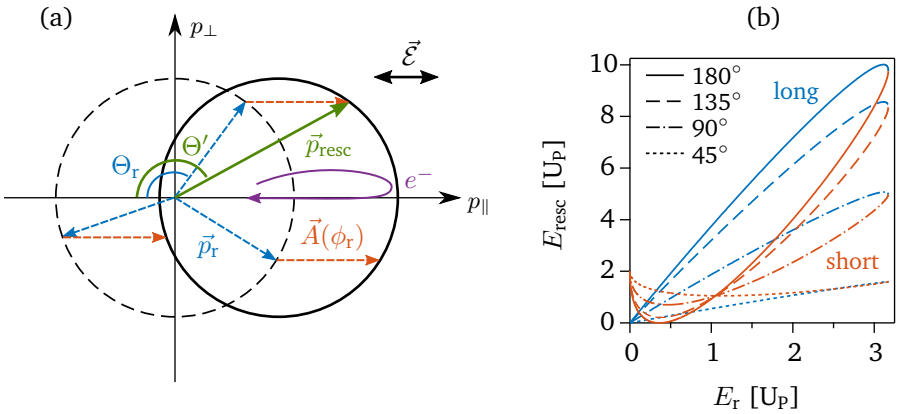

Figure 2.6: Laser-induced elastic re-scattering. (a) The re-scattering process is sketched in vectorized form. After acceleration in the laser field, the tunnel ionized electron returns (purple trajectory) to the parent ion (origin of the coordinate system) and elastically re-scatters at an angle of Θ_r (blue angle) with its complete return momentum $\vec{p}_r$ (blue dashed arrow). Upon return, the electron experiences a kick by the laser field of the magnitude of the vector potential at the point of return $A(\phi_r)$. This adds up to the overall re-scattering momentum vector $\vec{p}_{resc}$ (green solid arrow). **(b)** The final kinetic energy of the electron after re-scattering E_{resc} is plotted as a function of return momentum for various scattering angles Θ_r for both long and short trajectories.

polarization $\epsilon = 0$)[32] is:

$$\vec{p}_{resc} := \vec{p}(\infty, \phi_i, \phi_r[\phi_i]) = p_{str,max}\,(\sin\phi_i - \sin\phi_r)\begin{pmatrix}\cos\Theta_r\\ \sin\Theta_r\end{pmatrix} + \begin{pmatrix}p_{str,max}\sin\phi_r\\ 0\end{pmatrix}. \tag{2.46}$$

The first term includes the momentum accumulated before the return, folded with the influence of the scattering direction/angle, while the second term adds the streaking momentum upon return. This leads to a final kinetic energy of the electron (as detected long after the pulse) of

$$E_{resc}(\phi_i, \phi_r[\phi_i], \Theta_r) = 2\,U_P[\sin^2\phi_i + 2\sin\phi_r(1-\cos\Theta_r)(\sin\phi_r - \sin\phi_i)]\,, \tag{2.47}$$

which is plotted in Fig. 2.6 (b) for various scattering angles $\Theta_r = 45°, 90°, 135°, 180°$ (for both long and short trajectories). The returning electron trajectory resulting in maximum kinetic energies after re-scattering $E_{resc,max}(\Theta_r)$ is determined numerically to be initiated at $\phi_{i,Eresc,max} \approx 15.0° \approx 0.04\,\tau_{cycle}$ and returning to re-scatter at $\phi_{r,Eresc,max} \approx 261.5° \approx 0.73\,\tau_{cycle}$. Hence, the overall maximum kinetic energy is achieved for electrons scattering at angles of $\Theta_r = 180°$, the so-called *back-scattering* electrons, resulting in

$$E_{resc,max}(180°) \approx 10\,U_P\,. \tag{2.48}$$

[32] Note that the electron momentum vectors are considered in the coordinate system of the returning electron (purple returning trajectory) and so in $-\vec{p}_\parallel$.

It should be noted that the trajectories resulting in a maximum re-scattering energy are not the ones that return to the parent ion with a maximum (return) energy $E_{\mathrm{r,max}} \approx 3.2\,U_\mathrm{P}$. This is reflected in Fig. 2.6 (b), where $E_\mathrm{resc}(\Theta_\mathrm{r})$ is maximizing for $E_\mathrm{r} < E_{\mathrm{r,max}}$. As mentioned previously, the elastically re-scattered electrons can be discerned from the direct electrons in the kinetic energy spectrum for energies of $2\,U_\mathrm{P} \leq E_\mathrm{resc} \leq 10\,U_\mathrm{P}$. This part of the spectrum appears *plateau*-like and was initially investigated by Paulus *et al.* [111, 136]. The final, field-dressed re-scattering angle can be derived from Eq. 2.46 as

$$\tan(\Theta') = \frac{\sin(\Theta_\mathrm{r})}{\cos(\Theta_\mathrm{r}) + \frac{\sin(\phi_\mathrm{r})}{\sin(\phi_\mathrm{i}) - \sin(\phi_\mathrm{r})}} \,. \tag{2.49}$$

2.3 Molecules in strong laser fields

Strong-field physics in atomic target systems presents a challenging topic, but the scenario gets significantly more complex when considering strong-field ionization in molecular systems. Molecules are a compound of two or more atoms in which the core potentials as well as the electronic orbitals merge into a stable equilibrium. This results generally in lower ionization potentials I_P[33] plus a higher density and complexity of electronic states. Moreover, molecules offer $3N$ ($N =$ number of atoms) *degrees of freedom* (DoF) as every included atom contributes with its three translational DoFs. The overall number of DoFs consist of the three DoFs of the center of mass and the rotational DoFs which are two for *linear molecules* and three for *non-linear molecules*. The remaining DoFs can be summarized as vibrational DoFs being $3N-5$ for linear and $3N-6$ for non-linear molecules [137].

A massive challenge in physics is to describe molecular systems due to the large number of interacting particles [138] even without an external laser field. The addition of a dressing field just exacerbates the description of molecular electronic and nuclear structure to a level where the problem becomes untreatable. The reason for that lies in the complexity of the resulting time-(in-)dependent Schrödinger equation due to the intricacy of all individual ingredients which cannot be solved analytically without drastic approximations. Even with the intention of finding numerical solutions, the challenge exceeds modern modeling as well as computational capabilities (in terms of resources). Hence, to be able to explain experimental results, feasible approximations need to be performed and vice versa to develop novel theoretical model approximations, experimental benchmarks need to be included.

The aim of this section is to explain some very basics of molecular physics as well as their behavior in strong laser fields, and to motivate general aspects of the topic in order to follow parts of this thesis. This section raises no claim to completeness and should serve to define the necessary terminology used especially in Part III of

[33] A rule-of-thumb suggests that I_P decreases the more atoms that are involved (with exceptions like e.g. CO_2)

this thesis. The content of this section is collected from standard literature [137][34] and selected dissertations [138–140].

2.3.1 Fundamentals of molecular orbitals

The coherent motion of nuclear and electronic wave packets in molecular systems can be accurately described by solving the Schrödinger equation. To keep things simple, the focus here lies on the static case described by time-independent Schrödinger equation (TISE)

$$\hat{H}_{\mathrm{M}}(\vec{r},\vec{R})\,\Psi_{\mathrm{M}}(\vec{r},\vec{R}) = E_{\mathrm{M}}\,\Psi_{\mathrm{M}}(\vec{r},\vec{R})\;; \tag{2.50}$$

$\hat{H}_{\mathrm{M}}(\vec{r},\vec{R})$ is the general molecular Hamiltonian and $\Psi_{\mathrm{M}}(\vec{r},\vec{R})$ the total wave function of the system. The constituents of Eq. 2.50 depend both on the coordinates corresponding to the electrons $\vec{r}$ and to the nuclei $\vec{R}$. The Hamiltonian consists of

$$H_{\mathrm{M}} \equiv T_e(\vec{p}_e) + V_e(\vec{r}) + T_{\mathrm{N}}(\vec{p}_{\mathrm{N}}) + V_{\mathrm{N}}(\vec{R}) + V_{e,\mathrm{N}}(\vec{r},\vec{R}) \tag{2.51}$$

describing the kinetic energy of electron $T_e(\vec{p}_e)$ and nuclei $T_{\mathrm{N}}(\vec{p}_{\mathrm{N}})$ as well as the interaction potentials for electrons $V_e(\vec{r})$, nuclei $V_{\mathrm{N}}(\vec{R})$ and electron-nucleus correlations $V_{e,\mathrm{N}}(\vec{r},\vec{R})$ [138].

In order to solve the TISE for the spatial evolution of a molecular system, a widely used approach is taken by applying the *Born-Oppenheimer approximation* (BOA) [141] which suggests to decouple the motion and hence the interaction between the electrons and nuclei. Thus, the nuclear frame is considered stationary in first approximation based on the fact that the nuclei have a bigger mass than electrons ($m_{\mathrm{Proton}}/m_e \approx 1836$). Hence, the nuclei move on longer time scales due to a smaller energy. On the other hand, the electrons adapt quasi-instantaneously to changes in the Coulomb potential of the nuclei [139]. This implicates that the total wave function of the molecular system can be separated into an electronic $\psi_e(\vec{r},\vec{R})$ and a nuclear $\psi_N(\vec{R})$ part

$$\Psi_{\mathrm{M}}(\vec{r},\vec{R}) = \psi_e(\vec{r},\vec{R})\cdot\psi_N(\vec{R})\;. \tag{2.52}$$

Consequently, the TISE of Eq. 2.50 can be solved separately for the electrons and the nuclei and hence the molecular energy levels can be separated in an electronic, vibrational and rotational contribution [138]

$$E_{\mathrm{M}} = E_e + E_{\mathrm{vib}} + E_{\mathrm{rot}}\;. \tag{2.53}$$

For the moving electron (cloud), the nuclear frame appears “frozen” [139], so that the complete TISE (Eq. 2.50) can be reduced and calculated for fixed internuclear distances $\vec{R}_{i,\mathrm{fix}}$ as [138]

$$\hat{H}_e(\vec{r},\vec{R}_{\mathrm{fix}})\,\psi_e(\vec{r},\vec{R}_{\mathrm{fix}}) = [T_e(\vec{p}_e)+V_e(\vec{r})+V_{e,\mathrm{N}}(\vec{r},\vec{R}_{\mathrm{fix}})]\,\psi_e(\vec{r},\vec{R}_{\mathrm{fix}}) = E_e(\vec{R}_{\mathrm{fix}})\,\psi_e(\vec{r},\vec{R}_{\mathrm{fix}})\;. \tag{2.54}$$

[34] The book series of Prof. Demtröder serves as a standard for experimental physics in undergraduate programs in Physics in many German Universities.

Both the energy eigenstates $E_e(\vec{R}_{\text{fix}})$ and the orbital wave functions $\psi_e(\vec{r}, \vec{R}_{\text{fix}})$ depend on a set of quantum numbers describing the orbital and the internuclear distance(s) $R_{i,\text{fix}}$ of the molecule. Hence, the eigenstates can be extracted as a function of $R_{i,\text{fix}}$ by solving Eq. 2.54 for sets of adequate orbital wave functions, resulting in the *potential energy landscape* of the molecule. This consists of the potential energy distribution as a function of $R_{i,\text{fix}}$, namely *potential energy curves* (PECs) for the individual bonds or multi-dimensional *potential energy surfaces* (PESs) along all geometrical coordinates, bonds, etc. The minimum eigenstates $E_e(\vec{R}_{\text{fix}})$ can be found by solving Eq. 2.54 for an approximated orbital wave function via a minimization routine like [137, 139]

$$E_e(\vec{R}_{\text{fix}}) = \min \frac{\int \psi^\star \, \hat{H} \, \psi \, \partial^3 r}{\int \psi^\star \, \psi \, \partial^3 r} \; . \tag{2.55}$$

The orbital wave functions $\psi_{\text{A,i}}$ are complex and can only be exactly obtained for the simplest molecule $H_2{}^+$. In order to determine the wave functions of other molecules, various approximations have been developed in the past, with a well known approximation being the construction of the wave function as a *linear combination of atomic orbitals* (LCAO) [137, Ch. 9]

$$\psi_{\text{LCAO}} = \sum_i c_i \cdot \psi_{\text{A},i} \; . \tag{2.56}$$

The construction of possible molecular orbital wave functions by a LCAO can be exemplified when looking at $H_2{}^+$. Combining the two s-orbitals of the H-atoms $\psi_{\text{A,B}}$ results in two possible wave functions [137, Ch. 9]

$$\psi_{\text{S,A}} = c_{\text{S,A}}(\psi_{\text{A}} \pm \psi_{\text{B}}) \tag{2.57}$$

with $c_{\text{S,A}}$ being the amplitude coefficients of the linear combination as is illustrated in Fig. 2.7 (a, taken from [137, Fig. 9.8 (a)]). Hence, the orbital consists of a symmetric wave function ψ_{S} where the individual atomic wave functions interfere constructively (red line) and an asymmetric wave function ψ_{A} (black line) for destructive interference. Both resulting wave functions are cylindrically symmetric around the molecular axis between the nuclei A and B. Generally, a molecular orbital is considered to be *bonding* between two nuclei when the respective electron probability density $|\psi^2|$ is non-zero and *anti-bonding* for zero probability density. These regions around the nuclei that have a zero likelihood of finding electrons are also known as a *nodal plane*. In our example, both electron probability densities $|\psi_{\text{S}}^2|$ (red line) and $|\psi_{\text{A}}^2|$ (black line) are plotted in Fig. 2.7 (b, taken from [137, Fig. 9.8 (b)]). The respective 2D probabilities (cylindrical symmetry) are sketched in the respective insets showing the non-zero and zero density for the bonding and anti-bonding H_2 bonds, respectively. In molecular physics, two (anti-)bonding s-orbitals are considered a σ-type orbital, while two e.g. (anti-)bonding p-orbitals combine to a π-type orbital (see e.g. Sec. 7.1.1 for the case of acetylene) [140]. In the case of H_2, both existing electrons completely fill the σ orbital[35] which makes it the *highest occupied molecular orbital* (HOMO) of the hydrogen molecule.

[35] every orbital can hold two electrons of opposite spin

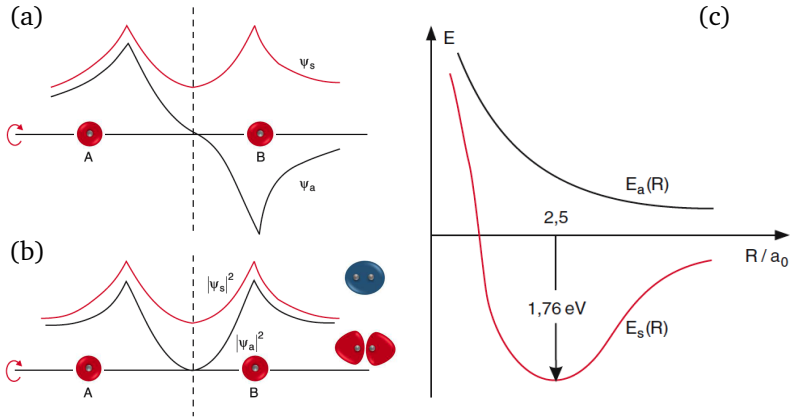

Figure 2.7: Molecular orbitals and potential energy curves of H_2. The plots are taken from [137, Fig. 9.8 & 9.9]. **(a)** Cut through the symmetric ψ_S (red line) and asymmetric ψ_A (black line) molecular orbital wave functions of H_2 that are cylindrically symmetric (indicated by the circular arrow). **(b)** The respective electron probability densities $|\psi_S|$ (red line) and $|\psi_A|$ (black line reveal the constructive and destructive interference of the s-orbitals leading to a bonding (non-zero) and anti-bonding (zero) H_2 molecule. **(c)** The PECs E_s (red line) and E_a (black line) resulting from solving the electronic TISE using the orbital wave functions for different "frozen" nuclei distances R.

As mentioned before, using the approximated orbital wave functions $\psi_{S,A}$, the respective energy eigenstates can be calculated according Eq. 2.55. By varying the nuclear distances, the eigenstates can be determined as function of $R_{fix,i}$. The results for our example of H_2 are plotted in Fig. 2.7 (c, taken from [137, Fig. 9.9]) for the symmetric case $E_{e,S}(R)$ (red line) and the asymmetric case $E_{e,A}(R)$. The curves are clearly different as $E_{e,S}(R)$ shows a local minimum at $R_0 = 2.5$ a.u. which is the equilibrium bond length of the stable molecule. On the other hand, the anti-bonding state $E_{e,A}(R)$ shows a monotonically decrease for increasing bond lengths revealing a non-stable, dissociating H_2 molecule. The local minimum of the stable orbital can be overcome by applying energy (e.g. electrically or optically) to the system to lift the population above the energy barrier, thus forcing dissociation of the molecule.

In the field of quantum chemistry, much more advanced approaches are taken to approximate the molecular orbitals, and hence to calculate the PESs. A commonly used software package that includes various different approximations is *GAMESS* [142] which allows to perform *ab initio* calculations of molecular orbitals. Another possibility to quantum-mechanically model the electronic structure of many-body systems is to use *density-functional theory* (DFT) [143, 144].

Next to the electronic energy eigenstates E_e, the solution of the overall TISE offers contributions of the vibrational E_{vib} and the rotational E_{rot} motion of the nuclei which according to the BOA can be regarded individually as described in Eq. 2.53.

These contributions can be computed subsequently with the TISE when neglecting the influence of the electronic wave function on the nuclear coordinates according to BOA. This results as [138]

$$\hat{H}_{\mathrm{M}}(\vec{R})\,\psi_N(\vec{R}) = [T_{\mathrm{N}}(\vec{p}_{\mathrm{N}}) + V_{\mathrm{N}}(\vec{R}) + E_e]\,\psi_N(\vec{R}) = E_{\mathrm{M}}\,\psi_N(\vec{R})\ . \tag{2.58}$$

The resulting vibrational and rotational energy eigenstates can be superimposed on the PESs resulting in individual fine structures [138].

Finally, it should be added that the BOA works nicely for slow nuclear processes that can clearly be separated from the respective electron behavior. For reaction that move faster, the physics can not be approximated [15]. An example is the influence of the particles' spins on the motion of the molecule via *spin-orbit coupling* (SOC) which can significantly alter a molecular reaction. SOC processes can happen on fast temporal scales which can only be described in a non-adiabatic, and hence a non-BOA manner [145].

2.3.2 Strong-field induced processes in molecules

When applying a laser field to a molecule, transitions between different states are induced similarly to the atomic case. These transitions lead to excitation and ionization, with possibly complex dynamics.

Higher-lying PEC can be populated e.g. via single photon ionization. In the process, vibrational states in the ionic PEC can be excited [139] via a vertical transition between the initial state ψ_i and the final state ψ_f. This interpretation is called the *Franck-Condon principle* [146, 147] which can be described in a simple semi-classical picture [139]. The photo absorption and ionization process occurs on a much faster timescale than nuclear motion, thus the interaction can be described as instantaneous. Hence the transition between the PECs curves appears vertical. Excess energy of the photon interaction is converted in vibrational energy. The momentum of the photon can be considered small compared to the molecular vibrations.
The Franck-Condon process is described quantum-mechanically by a transition amplitude [137, Sec. 9.6.4]

$$A_{f,i} = \langle \Psi_f | \hat{H}_{\mathrm{D}} | \Psi_i \rangle = \langle \psi_{e,f}, \psi_{\mathrm{N},f} | \hat{H}_{\mathrm{D}} | \psi_{e,i}, \psi_{\mathrm{N},i} \rangle \tag{2.59}$$

with the interaction Hamiltonian in dipole approximation $\hat{H}_{\mathrm{D}} = -r\,\mathcal{E}\,\cos(\omega_0\,t)$ [137, 139]. With the dipole transition matrix element [137, 139]

$$M_{f,i}(R) = \langle \psi_{e,f}(\vec{r}, R), \hat{H}_{\mathrm{D}}, \psi_{e,i}(\vec{r}, R) \rangle \tag{2.60}$$

varying only slowly with R, the electronic wave functions and the vibrational, nuclear wave functions can be separated and the transition amplitude can be simplified to

$$A_{f,i} = M_{f,i}\ \langle \psi_{\mathrm{N},f}(R), \psi_{\mathrm{N},i}(R) \rangle\ . \tag{2.61}$$

A measure for the strength of the transition is given by the *Franck-Condon factor* which is defined by the overlap integral as [137, Eq. 9.92]

$$FC(\nu_f \leftrightarrow \nu_i) = \left|\langle \psi_{\mathrm{N},f}(R), \psi_{\mathrm{N},i}(R)\rangle\right|^2 . \tag{2.62}$$

In contrary to weak-field interaction where the laser electric field does not alter the the molecular states, as described above, the interaction of strong-fields with molecules demands an inclusion of the laser field in the calculation. Hence, the non-perturbative approach of solving the TDSE describes the strong-field interaction most accurately. Here, the Hamiltonian includes the time-independent, field-free molecular part $\hat{H}_{\mathrm{M}}$, the laser field $\hat{H}_{\mathrm{L}}$ and the time-dependent dipole interaction between the molecular system and the laser field [138]

$$\hat{H}_{\mathrm{tot}} = \hat{H}_{\mathrm{M}} + \hat{H}_{\mathrm{L}} + \vec{\mu} \cdot \vec{\mathcal{E}}_{\mathrm{L}} . \tag{2.63}$$

Similarly to the atomic case, different strong-field regimes are classified by the Keldysh parameter. Technically, a modified Keldysh parameter should be deployed which takes the complexities of the orbital shapes into account together with the reduced ionization potentials [148]. Before addressing molecular tunnel ionization in the next Sec. 2.3.3, a few peculiarities about molecular multi-photon ionization should be pointed out. When a long laser pulse (e.g. $>$ 10 optical cycles) is applied to a molecular system, the dipole interaction between two molecular states can be considered periodically as well [138]. In the energy domain, this oscillating laser-driven dipole interaction can be considered a set of coherent states that are separated by the photon energy $\hbar\omega$ of the applied field which is superimposed onto the molecular orbital landscape. This phenomenon is described by the *Floquet theorem* which states that a field-free molecular system can be *dressed* with the photon states which effectively lifts or lowers the respective states by $n \times \hbar\omega$. This leads to intersections between various PECs where a *resonant crossing* or mixing of the eigenstates occurs [138]. This process can open up various dissociation channels within a molecular system as potential boundaries are decreased - a process which has been named *bond softening*. Likewise, potential barriers can emerge. This is called *bond hardening*. Both processes have been widely studied in literature starting since the 1990s [149, 150].

2.3.3 Molecular ADK theory

In the tunneling or quasi-static regime, molecules can be ionized or excited similarly to atomic systems. Yet, the additional DoF as well as the non-spherical electronic structure alters the process compared to atomic systems and hence the related ionization models and rates. The complexity of molecular tunnel ionization is reflected by the fact that experimental tunnel ionization rates of some molecular systems are suppressed compared to their "atomic sibling", which is an atom with similar ionization potential: e.g. Ar ($I_{\mathrm{P}} = 15.76\,\mathrm{eV}$) and D_2 ($I_{\mathrm{P}} = 15.467\,\mathrm{eV}$), Xe ($I_{\mathrm{P}} = 12.13\,\mathrm{eV}$) and O_2 ($I_{\mathrm{P}} = 12.06\,\mathrm{eV}$), etc., while other atomic siblings have similar ionization rates, like e.g. Ar and N_2 ($I_{\mathrm{P}} = 15.58\,\mathrm{eV}$), Ar and F_2 ($I_{\mathrm{P}} = 15.697\,\mathrm{eV}$), Kr ($I_{\mathrm{P}} = 14.00\,\mathrm{eV}$) and CO ($I_{\mathrm{P}} = 14.01\,\mathrm{eV}$) [151].

One attempt to describe the anisotropic tunnel ionization rates of molecules was proposed by Xiao Min Tong, Z. X. Zhao and Chi-Dong Lin[36] [151] in 2002 with their modified ADK rates for molecular systems better known as the *molecular ADK theory* (MO-ADK). The modifications account for the additional DoFs of the molecular systems compared to atoms including rotational and vibrational motion [151]. The principle idea of the MO-ADK is to combine the individual tunneling rates from specific sets of atomic states in a coherent superposition. This is achieved by expressing the asymptotic wave function of the valence electron as a superposition of spherical harmonics [151] and leads to a field- and alignment-dependent static tunneling rate defined as

$$\Gamma^{\text{static}}_{\text{MO-ADK}}(\mathcal{E},\Omega_{\text{M}}) = \sum_{m'} \frac{B^2(m',\Omega_{\text{M}})}{2^{|m'|}\,|m'|!} \frac{1}{\kappa^{\frac{2\,Z_{\text{eff}}}{\kappa}-1}} \left(\frac{2\,\kappa^3}{\mathcal{E}}\right)^{\frac{2\,Z_{\text{eff}}}{\kappa}-|m'|-1} \exp\left(-\frac{2\,\kappa^3}{3\,\mathcal{E}}\right) . \tag{2.64}$$

$\mathcal{E}$ is the laser electric field, Ω_{M} the alignment angle between the molecular axis and the polarization direction of the laser field, Z_{eff} the effective ion charge, $\kappa = \sqrt{2\,I_{\text{P}}}$ and $m' = 0,1,2,\ldots$ the projection of the angular momentum onto the molecular axis of the state to be ionized. Moreover, $B(m',\Omega_{\text{M}})$ is defined as

$$B(m',\Omega_{\text{M}}) = \sum_{l\geq m} C_l\, D^l_{m',m}(\Omega_{\text{M}})\, Q(l,m') , \tag{2.65}$$

where C_l are normalization coefficients (see [151, Table 1 & 2]), and $D^l_{m',m}(\Omega_{\text{M}})$ the rotation matrix that determines the actual projection of the angular momentum defined as [151, 152]

$$D^l_{m',m}(\Omega_{\text{M}}) = \sum_j (-1)^j \frac{\sqrt{(l+m)!\,(l-m)!\,(l+m')!\,(l-m')!}}{(l-m'-j)!\,(l+m-j)!\,j!\,(l+m'-m)!} \cdot \left(\cos\frac{\Omega_{\text{M}}}{2}\right)^{2l+m-m'-2j} \left(\sin\frac{\Omega_{\text{M}}}{2}\right)^{2j+m'-m} . \tag{2.66}$$

The sum is valid for all integers of j for arguments of the factorials are positive or zero [151, 152]. The coefficients of the spherical harmonics $Y_{l,m}$ are summarized as

$$Q(l,m) = (-1)^m \sqrt{\frac{(2l+1)(l+|m|)!}{2(l-|m|)!}} . \tag{2.67}$$

The factor $B^2(m',\Omega_{\text{M}})$ contains all information about the electron density of the orbital of interest in the region around the tunneling exit along the direction of the electric field [151,152]. This alters the ADK rates for the specific molecular system. As Eq. 2.64 describes the MO-ADK rates for a static field, the ionzation rates are extended for a low frequency ac field by [151]

$$\Gamma_{\text{MO-ADK}}(\mathcal{E},\Omega_{\text{M}}) = \sqrt{\frac{3\,\mathcal{E}}{\pi\,\kappa^3}}\, \Gamma^{\text{static}}_{\text{MO-ADK}}(\mathcal{E},\Omega_{\text{M}}) \tag{2.68}$$

[36] XMT and CDL are collaborating with us on projects within this thesis.

A benefit of the MO-ADK model is that the ionization rates can be calculated universally for all molecular targets, both as a function of electric field $\mathcal{E}$ and the alignment angle of the molecules Ω_{M}, and also for different orbitals of the molecule. The latter point is important, as not only the HOMO of a molecule contributes to the overall tunneling ionization rate, but also TI from lower lying orbitals HOMO-n can play a distinctive role in the overall TI rates. This has been found experimentally in various investigations [153–157].

2.3.4 Laser-induced molecular alignment

Another very vital property of molecules in strong laser fields, is the ability to control the alignment and/or orientation of molecular systems within the laboratory frame. Generally, gas-phase molecules are randomly aligned/oriented within their ensemble without any external influence. The interaction of the individual molecular systems with a linearly polarized laser field can change the average overall alignment of the ensemble towards the direction of the laser polarization. This becomes quite useful in investigations on resolving molecular structure within dynamical processes, as we will investigate in Part III since observables that are dependent on the molecular structure become clearer. This is why the use of strong laser fields for *laser-induced molecular alignment* has developed into a routine method used in many laboratories nowadays. The section serves to give a basic overview over the essentials of laser-induced molecular alignment. Detailed information is given in literature, like e.g. [2, 158, 159] as well as in selected dissertations, e.g. [138, 160].

The idea behind laser-induced molecular alignment is that a laser pulse induces a torque to a molecular system in order to force it into a rotational motion[37]. This rotational kick is perceived by a molecule that possesses an *anisotropic polarizability* $\vec{\alpha}$, so that the laser field induces anisotropical dipole towards the laser polarization [138] and effectively aligns the mayor molecular axis along the polarization axis. From a quantum mechanical perspective, the laser field couples to the rotational states of the molecules. The molecules initially orient along the laser polarization axis upon first interaction. In specific cases the molecule then rotates in seemingly random direction to *revive* at specific points in time to its alignment positions. This revival time is defined as $T_{\mathrm{R}} = 1/(2\,B_0\,c)$ where B_0 is the rotational constant of the molecule which is characteristic for each type of molecule.

In the simplest case, the quality of the alignment is characterized by a $\langle\cos^2\Theta\rangle$ factor, where Θ is the angle between the molecular axis and the polarization axis, previously defined as Ω_{M}. Perfect alignment of the molecular parallel to the polarization axis is achieved for $\langle\cos^2\Theta\rangle = 1$, perfect anti-alignment perpendicular to the polarization axis for $\langle\cos^2\Theta\rangle = 0$. The ensemble is isotropically distributed for $\langle\cos^2\Theta\rangle = 0.33$. The experimentally achievable alignment distributions usually lie somewhere between the extrema. The resulting the 3D alignment distributions for exemplary experimental alignment degrees are plotted in

[37] The intensity of the pulse should be just not enough to ionize the molecular system

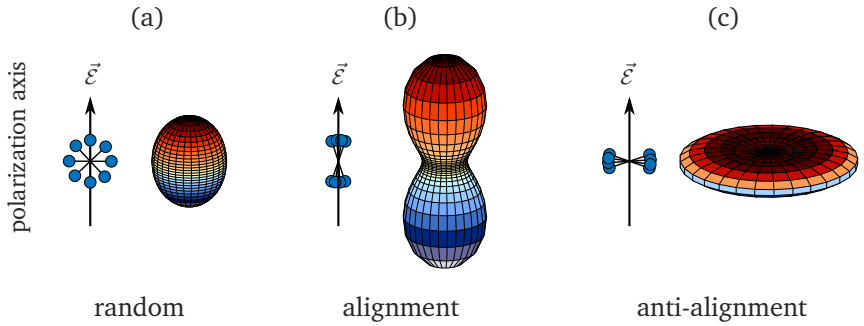

Figure 2.8: 3D alignment distributions. The individual alignment distributions are shown for the three characteristic cases as calculated according to [161]. **(a)** Random alignment of the ensemble of molecules. **(b)** In the alignment case, the molecules oscillate around the polarization axis for small angles. **(c)** In the anti-alignment case, the molecules oscillate around the polarization axis for angles around 90°.

Figs. 2.8 (a-c) which were calculated according to [161][38]. In Fig. 2.8 (a) random alignment ($\langle\cos^2\Theta\rangle = 0.33$) is displayed where all molecules of the ensemble are distributed isotropically as sketched in the inset. For (non-perfect) alignment ($0.33 < \langle\cos^2\Theta\rangle < 1$) as shown in Fig. 2.8 (b), the molecules rotate around the polarization axis for small angles towards the individual molecules' axes. In Fig. 2.8 (c), (non-perfect) anti-alignment ($0 < \langle\cos^2\Theta\rangle < 0.33$) is shown, where the individual molecules oscillate around the polarization axis for angles of around 90° towards their own axes.

In general, laser-induced molecular alignment can be divided into two main regimes, namely *adiabatic* and *impulsive* alignment. In the adiabatic regime, the pulse duration of the alignment pulse is chosen to be far longer that the revival time of the molecule $\tau \gg T_{\mathrm{R}}$. Hence, the molecule "feels" the influence of the laser field adiabatically, which effectively aligns the molecular axis along the polarization axis for the whole interaction time. As T_{R} usually lies in the singles to tens of ps – regime, the pulse duration of adiabatic alignment needs to be chosen around tens to hundreds of ps. Due to the constant laser interaction, the adiabatic regime is characterized by high degrees of alignment for adequate anisotropic polarizabilities of the molecular target.
On the other hand, ultrashort pulses are utilized to impulsively align molecules that are distinctly shorter than the rotational period $\tau \ll T_{\mathrm{R}}$. Here, the laser pulse coherently couples to the rotational states of the molecule, thereby creating a rotational wave packet that initially aligns the molecule upon interaction, before it then rotates towards de- and rephasing for every T_{R} as well as fractions of the rotational period T_{R}/n [138]. These periodic revivals of the alignment states of the

[38] The distributions are extracted from a Matlab script of Markus Gühr that was programmed on the basis of [161] in order to generate 3D alignment distribution as a function of the rotational period. The code was available until recently on his old webpage at the FU Berlin (http://users.physik.fu-berlin.de/∼guehr/).

rotational wave packet continues until the coherence of the wave packet is eventually lost [138]. The benefit of impulsive alignment is that the molecular ensemble can reach (anti-)alignment when no laser field is present. This *field-free* alignment is especially useful for investigations on molecular reactions that could be altered by an applied field.

The characteristic alignment distributions of both regimes as well as an *intermediate regime* are nicely shown in the work of Torres *et al.* [2, Fig. 1] which is replotted in Figs. 2.9. Here, Fig. 2.9 (a) shows a characteristic impulsive alignment trace calculated for N_2 ($T_R = 8.38$ ps) for $\tau = 50$ fs and an intensity of $I = 2.5 \times 10^{13}$ W/cm^2. Both the full T_R and the half-revival $T_R/2$ are clearly visible showing alignment and anti-alignment responses on out-of-phase positions. Also, two quarter revivals at $T_R/4$ and $3T_R/4$ are visible. On the other hand, the adiabatic alignment trace in Fig. 2.9 (c) shows a broad Gaussian alignment distribution over the whole pulse duration being here $\tau = 50$ ps ($I = 2.5 \times 10^{12}$ W/cm^2). The intermediate regime in Fig. 2.9 (b) shows broad, "washed-out" revivals calculated for $\tau = 1$ ps and $I = 2.5 \times 10^{12}$ W/cm^2.

In Sec. 6.5.3 of Ch. 6, we will compare an experimental alignment distribution as a function of revival time with a theoretical model calculation for our target system of interest being acetylene C_2H_2. The theoretical model will be explained in that Sec. 6.5.3.

As mentioned before, optical molecular alignment has evolved in a standard technique applied to studying molecular systems. Applying a linearly polarized laser pulse generally serve for alignment of a molecule in one dimension. This is sufficient when looking a linear molecules with only two rotational degrees of freedom. For more complex, non-linear molecules like e.g. asymmetric top molecules [160], the alignment in 1D is not sufficient anymore to achieve a clear spectroscopic view of the molecule so that alignment in 3D needs to be applied. This can be achieved by e.g. applying elliptically polarized laser pulses that are able to apply a torque onto the molecule in two orthogonal directions [160]. To apply two forces in orthogonal directions onto the rotational wave packet of a molecule, a possibility is using two orthogonally polarized fs-laser pulses [162]. Similarly, a long (adiabatic alignment) pulse is overlayed with a short (impulsive alignment) pulse at the peak of each pulse, in order to reach 3D alignment [160].

It should be noted that linear asymmetric molecules like e.g. carbonyl sulfide (OCS) can be aligned in 1D leading to random orientation of the molecule. Desirably, the orientation in this case should be controlled. Therefore, all-optical orientation schemes have been proposed that involves two long (adiabatic) laser pulses of different colors (fundamental and its second-harmonic) [163]. The orientation is controlled in this scheme by the relative phase of both waveforms.

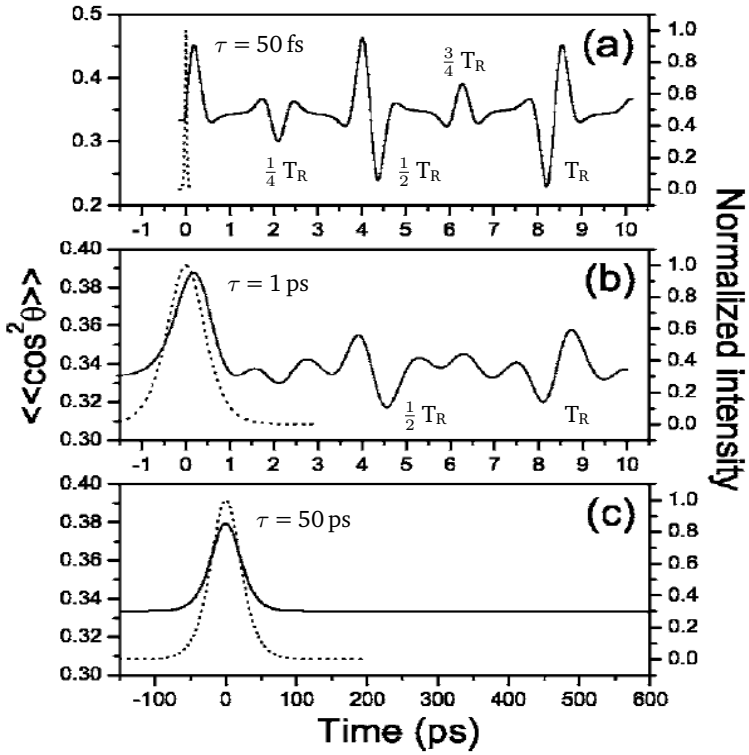

Figure 2.9: Time evolution of the degree of alignment from Torres *et al.* [2]. The alignment degree $\langle \cos^2 \Theta \rangle$ is calculated for nitrogen molecules N_2 for different laser pulses as a function of time over the course of one revival $T_R = 8.38\,\text{ps}$. The plots are taken from [2, Fig. 1]. **(a)** The impulsive alignment regime is reached for $\tau = 50\,\text{fs}$ pulses at an intensity of $I = 2.5 \times 10^{13}$ W/cm^2 showing clear full, half and quarter revivals. **(b)** An intermediate is reached for $\tau = 1\,\text{ps}$ and $I = 2.5 \times 10^{12}$ W/cm^2 leading to "washed out" revivals. **(c)** The adiabatic regime results for pulses around $\tau = 50\,\text{ps}$ ($I = 2.5 \times 10^{12}$ W/cm^2) showing alignment over the course of the laser pulse (dotted line).

2.4 Benefits and challenges of strong-field physics with mid-IR fields

Electron re-collision, leading to HHG based waveforms as well as electron re-scattering (elastically and inelastically), is entirely controlled by the characteristics of the driving electromagnetic waveform (see Sec. 2.2). Consequently, the advancement of the field of SFP has always been strongly correlated with the technological progress of ultrafast laser science. For instance, an impactful step forward was the development of sources that are able to generate laser pulses as short as a few- (less than three [67]) optical cycles. Consequently one had the ability to de-

tect and investigate single returning electron trajectories at constant relative CEP positions within the laser pulse [8, 67] in order to verify and refine the re-collision model.

Since the early 2000s, the idea has been discussed to drive attosecond and strong-field physics with laser pulses at *longer wavelength* [164–167], i.e. longer than the standardly utilized near-infrared light pulses which are provided by e.g. Ti:Sapphire based laser systems at $\lambda \approx 800\,\text{nm}$. The advantages of using mid-infrared (mid-IR, $\lambda \geq 3\,\mu\text{m}$ [168]) electromagnetic fields are described in our publication [169]: (1) the unambiguous creation of interaction conditions that are conducive for classical interpretations of experimental results, (2) strong-field recollision at low peak intensity in order to avoid appreciable ground-state depletion, and (3) the ability to create high-energy recollision electrons for imaging applications. However, a hindrance of driving the re-collision process in the mid-IR is certainly the fact that the probability of an electron re-colliding with its parent ion decreases with increasing wavelength [45]. Due to outweighing benefits, the non-trivial development of high intensity and ultrafast sources at central wavelengths towards the mid-IR was expedited in the last decade [57] and led to first experimental investigations on HHG [45], HATI [45, 166] and NSDI [170, 171] towards the end of the last decade. In the following, the mentioned benefits and challenges are discussed in more detail. This section follows our publication [169].

Scaling the Keldysh parameter towards tunnel ionization conditions

As discussed in Sec. 2.2, an important prerequisite of the semi-classical re-collision model is the ionization step to occur in the tunneling regime. Here, the electron can be assumed to have no initial velocity at the tunnel exit ($\vec{v}_0 = 0$) and hence its post-tunneling behavior can be approximated being purely dependent on the time-varying laser electric field as derived in Subsec. 2.2.1. The importance of this point cannot be stressed enough since the fact that most of the strong-field phenomena can be explained with the (semi-)classical re-collision model is beneficial when modeling any new strong-field or re-collision based time-resolved investigation. This desire to accurately match experimental findings without requiring resource[39] intensive modeling is an important general aspect.

An effective way of assuring tunnel ionization conditions is upscaling the driving wavelength. This is apparent by looking at the definition of the Keldysh parameter (see Eq. 2.5) which scales with $\gamma \propto 1/(\sqrt{I}\lambda)$ and hence stronger with wavelength as visualized in Fig. 2.1. Experimentally the step towards applying SFP in the mid-IR has not been easily realizable due to a lack of adequate sources.

Interestingly, first experimental studies on the photo ionization of noble gas atoms and small diatomic molecules utilizing $\lambda > 2\,\mu\text{m}$ sources revealed unexpected structures appearing in the photo electron spectrum for energies $E \ll U_\text{P}$ [58, 59]. Those *low energy structures* (LESs) were not anticipated by common theoretical models including the SFA. Considering these findings, it was stated in [169] that

[39] computationally speaking

"as these models are utilized to interpret many experimental results, including attosecond science experiments, it was worrying that such obvious features could evade prediction and detection for so long". Only by including the Coulomb field influence on the tunneled electrons, initially neglected in the SFA, the experimental findings could be reproduced and explained. This shows the importance of interrogating strong-field interactions unambiguously in the tunneling / quasi-static regime. In Ch. 4 of Part II of this thesis, we investigate the 3D photo electron momentum spectrum close to the tunnel exit ($E \gtrsim 10\,\text{meV}$) where we find various orders of LESs.

Re-collision without ionization saturation

Increasing the radiation intensity in order to reach the $\gamma \ll 1$ regime is only applicable up to the limit of ionization saturation where the population of the target (ground-)state is depleted. This intensity limit is defined as the *saturation intensity* I_{sat} which is determined by the ionization potential I_{P} of the target (valence state) as well as on laser wavelength and pulse duration [170]. In the tunneling regime, the saturation intensity can be estimated as the over-the-barrier ionization intensity limit defined in Eq. 2.14 for which the laser electric field $\mathcal{E}_{\text{OB}} \geq \frac{I_{\text{P}}^2}{4Z^2}$ suppresses the effective potential barrier of the target by the amount of I_{P} (or more). Hence, I_{sat} is the maximum effective intensity that can ionize the target [170]. This means that for pulses with peak intensities of $I > I_{\text{sat}}$ the target ground state is already fully depleted on the leading edge of the pulse. Moreover, I_{sat} as the maximum effective intensity also limits the ponderomotive energy of the tunnel electrons that might re-scatter with the parent ion which limits the final kinetic energy of these electrons upon return. Therefore, it is disadvantageous for experiments that rely on the electron re-collisions to be conducted in ionization saturation $I > I_{\text{sat}}$.

In order to prevent ionization saturation, the ionization fraction I_{F} of a target ground state should be kept much lower than unity. In Fig. 2.10 (a), the ionization fraction I_{F}[40] is plotted as a function of λ for different target atoms and molecules for 6-cycle laser pulses at peak intensities providing tunneling conditions at a constant $\gamma = 0.3$. The relation between λ and the peak intensity I for constant γ is shown for argon atoms in Fig. 2.1. The considered target systems are the argon atom (blue line) with an $I_{\text{P}} = 15.76\,\text{eV}$, comparable to the I_{P} of a nitrogen molecule N_2, the xenon atom (red line) with an $I_{\text{P}} = 12.13\,\text{eV}$, comparable to the I_{P} of an oxygen molecule O_2, the smallest organic molecule acetylene C_2H_2 (green line) with an $I_{\text{P}} = 11.4\,\text{eV}$, as well as larger polyatomic molecular systems like e.g. naphtalene $C_{10}H_8$ (yellow line) with an $I_{\text{P}} = 8.12\,\text{eV}$ and the fullerene C_{60} (purple line) with an $I_{\text{P}} = 7.58\,\text{eV}$. The ionization fraction is unity for 0.8 µm-radiation in case of all targets. The intensities needed here to provide a constant $\gamma = 0.3$ ranges from $I = 15 \times 10^{14}\,\text{W/cm}^2$ in case of argon to $I = 7.0 \times 10^{14}\,\text{W/cm}^2$ for C_{60}. When

[40] Again the ionization fraction/rate is calculated with the improved PPT model of [92] which can be applied for arbitrary values of γ and more importantly as a function of wavelength. The model is derived for atomic targets and so technically not suitable for molecules. For elucidation of our argument, we use the model here in approximation also for molecular targets with their specific I_{P}.

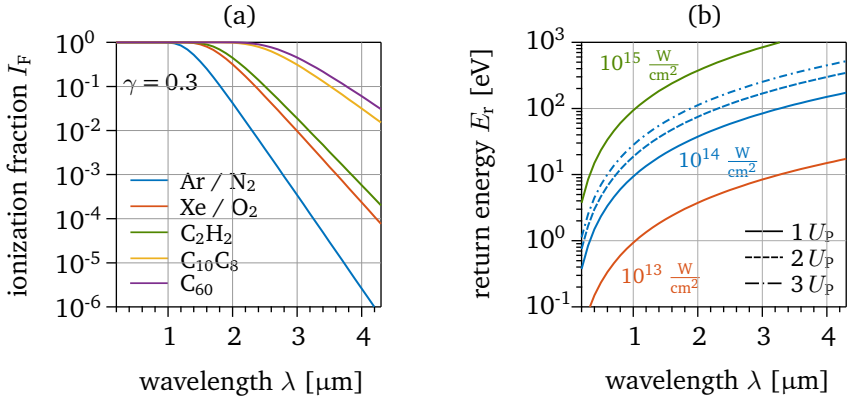

Figure 2.10: Benefits of mid-IR driving fields. (a) The ionization fraction I_F of ground state of various atoms and molecules is calculated as a function of wavelength λ according to [92] for 6-cycle laser pulses with peak intensities assuring a constant $\gamma = 0.3$ (for each wavelength case). The targets are argon (blue line) with an $I_P = 15.76$ eV, comparable to the I_P of nitrogen N_2, xenon (red line) with an $I_P = 12.13$ eV, comparable to the I_P of oxygen O_2, acetylene C_2H_2 (green line) with an $I_P = 11.4$ eV, naphtalene $C_{10}H_8$ (yellow line) with an $I_P = 8.12$ eV and the fullerene C_{60} (purple line) with an $I_P = 7.58$ eV. I_F decreases when shifting to mid-IR driving wavelengths, hence preventing ionization saturation while providing tunnel ionization conditions ($\gamma \ll 1$). **(b)** Longer driving wavelengths lead to higher electron return energies E_r plotted here as a function of λ for three different intensities $I = [10^{13}, 10^{14}, 10^{15}]$ W/cm^2 (in red, blue and green, respectively). Exemplarily different levels of return energies are shown as the distributions of U_P (solid line), $2\,U_P$ (dashed line) and $3\,U_P$ (dash-dotted line).

shifting to longer driving wavelength the ionization fraction decreases, more radically for the targets with a higher I_P. In order to reach ionization fractions of $I_F < 0.1$ at $\gamma = 0.3$, a driving wavelength of 1.80 μm (at $I = 2.9 \times 10^{14}$ W/cm^2) is needed for argon atoms while $\lambda \approx 3.75$ μm (at $I = 0.32 \times 10^{14}$ W/cm^2) is needed for C_{60}. This analysis demonstrates how mid-IR sources are favorable in order to provide tunneling conditions ($\gamma \ll 1$) in SFI while preventing ionization saturation that limits the effective U_P and hence kinetic energy of the returning electrons. As just shown, this is especially important when investigating electron re-collision on molecular targets due to their lower I_P.

High energy re-collision electrons

Another important benefit from using long wavelength sources for SFP is the quadratic dependence of the ponderomotive energy on wavelength: $U_P \propto \lambda^2$. Hence, an increase of the driving laser wavelength results in a quadratic increase of the energy of the re-colliding electron according to the re-collision model. This relation can be understood in terms of the longer time an electron is accelerated in the electric field during a longer optical cycle away from and towards the parent

ion. The dependence of the electron's return energy E_r on the driving wavelength λ is shown in Fig. 2.10 (b) for different intensities $I = [10^{13}, 10^{14}, 10^{15}]$ W/cm^2 (in red, blue and green, respectively). Comparing $\lambda = 0.8\,\mu$m and $\lambda = 3\,\mu$m, an increase in return energy by a factor of 14 can be achieved. This means that in case of those two examples, the maximum return energy $E_{r,max} \approx 3\,U_P$ (dash-dotted line) is enhanced from $E_{r,max,0.8} = 18$ eV to $E_{r,max,3.0} = 252$ eV for an intensity of $I = 10^{14}$ W/cm^2. Such ponderomotive scaling of the electron return energy opens various possibilities. On the one hand the cut-off energy of HHG is enhanced [172]. Moreover multiple ionization steps via NSDI not only from the valence shell but also from inner shells can be generated [173]. Also the electrons with higher return energies can be utilized for LIED to probe the nuclear rather than the electronic structure of the target ion due to a higher momentum transfer [169, 174]. The latter point is going to be explained in more detail in Sec. 6.2 of Part III.

Unfavorable scaling of re-collision probability

During the excursion in the oscillating electric field, the liberated electron wave packet generally spreads in both its lateral and transversal extent due to quantum diffusion [8]. The wave packet grows at a typical rate of around 1 nm/fs [8]. Hence, this effect is enhanced during the (longer) optical cycle of a mid-IR driving field. An extended wave packet yields a lower probability for re-collision. This unfavorable dependence is quantified as λ^{-2} according to [45] taking into account the transverse extend, and as λ^{-3} according to [47] for the overall wave packet spread. Moreover, by adding the dependence of the number of returning electrons on wavelength as λ^{-2} [45], the overall ratio of re-colliding and hence re-scattering electrons scales with $\lambda^{-(4\,\text{to}\,5)}$ (for long trajectories). This was experimentally confirmed in [45]. Thus, the ratio of re-scattered ($E_{kin} > 2\,U_P$) compared to direct electrons ($E_{kin} < 2\,U_P$) differs by a factor of 200 when comparing the driving wavelengths of 0.8 μm and 3.0 μm. Practically speaking, an experiment takes 200 times longer when changing the wavelength from the near- to the mid-IR for otherwise equal laser parameters. A possible compensation can be obtained by scaling up the repetition rate of the laser system, which will be discussed in Sec. 3.1.4. The more complex re-combination process of HHG scales even stronger with wavelength since the yield dependence of HHG can be calculated as $\lambda^{-(5\,\text{to}\,6)}$ [44, 46] while the extent of the high photon energy cut-off scales with λ^{-9} [47].

Reduced curvature of the returning electron wave front

The enhanced wave packet spread due to quantum diffusion [8] on the longer excursions of a mid-IR field also holds benefits for re-collision induced physics. Upon return to the parent ion, the wave front of a larger wave packet appears effectively less curved than a smaller wave packet that returns earlier to the ion. Hence, one can argue that longer wavelength drivers support returning wave packets with close-to-plane wave fronts. This fact makes theoretical modeling of your experimental results easier as the *plane-wave approximation* can be applied. Examples

are theoretical models describing SFI processes using SFA, where a plane wave is assumed for any outgoing electron wave packet (described before in Sec. 2.1.2). Also, the interpretation of elastic scattering and diffraction of returning electrons as used in LIED benefits from close-to-plane wave fronts in terms of cleanliness and hence interpretability of the diffraction patterns.

Chapter 3

Experimental Methodology

In this chapter, our experimental methodology is introduced. The key components are two independent systems. On the one hand, we make use of a home-built, high repetition rate *optical parametric chirped pulse amplification* (OPCPA)-based mid-IR (at a central wavelength $\lambda_C = 3.1\mu m$) source allowing to trigger SFI events in the tunnel regime providing all benefits suggested in Sec. 2.4. On the other hand, we use a *reaction microscope* (ReMi) detection system to resolve the 3D momentum vectors of all charged particle during ionization in coincidence. The *combination* of both of these experimental tools has proven to be of vital importance when utilizing mid-IR re-collision physics in order to study atomic and molecular dynamics.
The chapter includes the most important aspects about the experimental methodology behind the investigations in this thesis. First, the key aspects for the generation of intense, ultrashort mid-IR pulses including the working principle of our system are presented in Sec. 3.1. Then, the ReMi detection system is introduced in Sec. 3.2 with specification of its defining components as well as the data analysis steps after accumulation of SFI events are explained to show the path from *raw* detected time signals to the momentum space information of all detected particles in coincidence.

3.1 Generation of intense, ultrashort, mid-IR pulses

The generation of strong laser fields is the prerequisite for our investigations as they trigger the ionization reaction, steer the re-collision electrons and influence the atomic or molecular target system. Generally, highly intense electric laser fields are generated and utilized as a pulsed waveform in order to achieve high peak intensities without requiring too high average laser powers. These could not be maintained throughout a laser system due to heat-sensitive dependencies, like e.g. thermal lensing. Thus, high peak powers can be achieved for shorter pulse time durations at a constant pulse energy and average power. Moreover, short pulse durations, nowadays preferentially in the regime of tens to a few femtoseconds, also dubbed as ultrashort pulses[1], are essential for various areas of atomic, molecular and optical (AMO)[2] physics SFP. Examples are, the above mentioned

[1] Pulses were initially considered as *ultrashort* with pulse durations on the level of tens of picoseconds [9], yet over time and with technical advancement nowadays pulse durations from hundreds down to a few femtoseconds are readily possible and used [10, 11, 175].

[2] general term for the research field of matter-matter and light-matter interactions

strong-field processes, i.e. HHG or re-collision physics [122], or also time-resolved spectroscopy where molecular dynamics such as bond dissociations and vibrations that occur on fs to ps - timescales [176, 177], are investigated.

The generation of intense, ultrashort laser pulses and development of novel sources is a complex field of optics in itself so that a detailed summary would extend the scope of this chapter. Here, merely a compact overview of the fundamentals of ultrafast lasing is given, while concentrating on the generation of mid-IR pulses via the OPCPA technique used in our laser source. Then, the non-trivial subject of laser intensity calibration [178] is discussed by showing the methods used within this thesis. Finally, the importance of the generation of reproducible, mid-IR pulses at a high repetition rate is commented on.

3.1.1 Fundamentals of ultrafast laser pulses

The basic knowledge about ultrafast laser physics is fundamental in most modern AUO laboratory nowadays. This section mainly is for completeness, to give an overview of the technical aspects of our laser system and serves the purpose to refresh the memory of the non-specialist reader. The content of this section can be read up on in the standard literature such as e.g. [8, 179, 180].

Every laser pulse is initially generated in the oscillator being the principal component of any laser system. Here, light at distinct frequencies can be guided and contained within a cavity while being amplified via stimulated emission in a pumped gain medium in every cavity round trip. Without relative phase relation, the different electromagnetic modes form a continuous wave (*cw*). The properties of the gain medium (e.g. crystalline material, gas, or dye) defines the emitted electromagnetic spectrum and is chosen accordingly.

Mode-locking

Laser pulses can be generated within the laser cavity via a process called *mode-locking*. Here spectrally different, oscillating eigenstates of the cavity round trip (modes) are synchronized (or locked) in phase to interfere constructively at several points in time during the cavity round trip in order to form a pulse while keeping the signal to zero at other times [8]. Like this all energy oscillating within the cavity is confined within the pulse envelope. Laser modes can be locked *actively* by externally synchronizing cavity loss e.g. with an acousto-optic modulator to discard non-contributing modes while enhancing the contributing frequencies of the pulse [9]. However more standardly used nowadays are *passively* mode-locked (PML) lasers where an optical element placed within the laser cavity triggers the pulse shaping. Most commonly used for passively mode-locking are materials with nonlinear optical properties like *saturable absorption* and the *optical nonlinear Kerr effect* [8, 11].
A common example of making use of saturable absorption for PML is the introduc-

tion of semiconductor saturable absorber mirrors (SESAMs) [181]. SESAMs contain a semi-conductor material in front of a Bragg reflector. The semi-conductor absorbs low intense laser light yet decreases the absorption with increasing intensity due to excitation saturation of the initial state for a distinct fluence[3] of photons acting as a saturable absorber (SA). Without being absorbed, only the higher intense part of a pulse and so the constructively interfering modes get reflected building up a shorter waveform in every round trip. Using materials with different band gaps, SESAMs can be scaled over different frequency ranges.
The most widely used and commercially available laser systems in the field are based on Titanium doped sapphire[4] (Ti:Sa) as a gain[5] medium. Next to supporting a wide range of frequencies around its central wavelength of $\lambda_C \approx 800\,\text{nm}$ [8, 9] in terms of gain, Ti:Sa crystals trigger PML without an additional SA due to a nonlinear self-focusing effect based on the optical Kerr effect, dubbed *Kerr-lens modelocking* (KLM). The optical Kerr-effect leads to a fast, intensity dependent refractive index change [8]

$$n(\vec{r}, t, \lambda) = n_0(\lambda) + n_2(\lambda)\, I(\vec{r}, t) \tag{3.1}$$

with n_2 being the nonlinear refractive index of the medium and $I(\vec{r}, t)$ the spatially and temporally dependent intensity distribution of the pulse. The change $\Delta n = n - n_0$ leads to a lensing effect (for $n_2 > 0$) which reshapes the radial distribution of the Gaussian beam profile enhancing the higher intense central part, also known as *self-amplitude modulation* (SAM). As a consequence, locked modes within the laser cavity reaching the Ti:Sa crystal as a pulsed waveform get Kerr-lens focused, reaching a higher intensity. Thus, theses modes can be separated by a *hard aperture* from the non-locked, cw modes in order to enhance the pulse in every round trip. Another possibility is to use KLM in a *soft aperture* configuration where the fact is exploited that the effective gain in the pumped laser medium is increased with enhanced intensity [11]. Thus, again only the locked modes get amplified in every round trip leading up to an enhanced pulse.
While Kerr lensing by SAM influences the spatial intensity distribution of a laser pulse, its time-domain analogy known as *self-phase modulation* (SPM) causes a time-dependent phase perturbation resulting in a frequency shift for different parts of the spectral profile of the pulse [8]:

$$\Delta\omega(t) = -\frac{\partial\phi(t)}{\partial t} = -\frac{\omega\, n_2\, L}{c}\frac{\partial I(t)}{\partial t}\,, \tag{3.2}$$

with the absolute phase of the carrier electromagnetic field $\phi(t)$ and the propagation length in the gain medium L. As from Eq. 3.2, the leading edge of a pulse ($\frac{\partial I(t)}{\partial t} > 0$) experiences a red-shift[6], effectively stretching the electric field oscillations, while analogously the trailing edge ($\frac{\partial I(t)}{\partial t} < 0$) is blue-shifted [7], resulting in compressed electric field oscillations. Consequently, the time-dependent phase

[3] optical energy per unit area
[4] Ti^{3+}:Al_2O_3
[5] amplification mechanism by the pumped medium when passing energy to the emitted electromagnetic field
[6] red shift: wavelength λ increases
[7] blue shift: wavelength λ decreases

variation throughout the pulse introduced via SPM results in an overall spectral broadening and hence a potential shorter pulse.
The pulse formation and enhancement due to mode-locking generally builds up until saturation of the specific effect, yet stabilizes in saturation. The shortest pulse that can be achieved by any mode-locking technique depends on how many modes can be phase-locked which is strongly dependent on the frequencies that are supported by the laser gain material. The effective spectral bandwidth $\Delta\omega$ of phase-locked frequencies sets the limit for the minimum pulse duration $\Delta\tau$ better known as *bandwidth* or *Fourier limit* [179]:

$$\Delta\omega\,\Delta\tau \geq 2\pi c_{\mathrm{B}} \tag{3.3}$$

with c_{B} being a numerical constant depending on the pulse shape[8].

Chirped pulse amplification

As of Eq. 3.1, any dispersive medium introduces a different refractive index change $\Delta n(\omega)$ depending on the carrier frequency / wavelength. In other words, different frequencies travel through the medium at different relative velocities, gather different relative phases and hence drift apart. This temporal variation of frequencies throughout the pulse, also known as *chirp*, leads to an overall stretch of the pulse envelope [8]. For the case of *positive dispersion* higher frequencies are delayed more than lower ones, and for *negative dispersion* the opposite case occurs. The beforehand discussed effect of spectral broadening via SPM is always accompanied by a positive chirp of the pulse (for media with $n_2 > 0$). In order to compensate for that, the pulse can be guided through a medium with the opposite, in this case negative, chirp. An opposite chirp can be compensated for via prism, grating or chirped mirror compression, where different frequency components of the pulse are delayed accordingly [8, 11].
In general, laser pulses from a mode-locked oscillator are generated on a relatively low pulse energy level compared to what is required for strong-field experiments. A typical Ti:Sa based oscillator provides pulses on the order of single nJ [182] at repetition rates of 60 - 100 MHz[9]. Pulse energies can be further increased in one or several additional amplification stages. A problem with enhancing fs-pulses within a gain media is that the focused pulses result in high intensities that can lead to non-linear distortions like e.g. thermal lensing or even material damage when overcoming the damage threshold of the crystal [8]. A solution for this problem was introduced in [183] in 1985 with a *chirped pulse amplification* (CPA) scheme sketched in Fig. 3.1. Here, the fs laser pulses are temporally stretched to the order of several picoseconds by adding chirp (with e.g. a dispersive medium or a grating) before getting amplified in another pumped gain medium. Like this the pulses feature a low peak intensity during the amplification process preventing catastrophic

[8] Gaussian pulse shape: $c_{\mathrm{B}} = 0.441$; Lorentzian pulse shape: $c_{\mathrm{B}} = 0.142$.

[9] The repetition rate of an oscillator depends on the length of one cavity round trip: $RR = c/2L_{\mathrm{cav}}$. So cavity length are usually of the order of L_{cav} = 1.5 - 2.5 m.

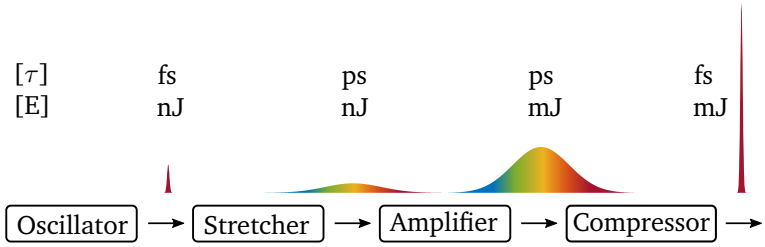

Figure 3.1: Concept of chirped pulse amplification. In order to avoid non-linear beam distortions or material damage during the amplification process, fs pulses that are generated from the oscillator on a relatively low peak energy level (i.e. nJ), get temporally stretched by adding chirp. Then, the pulses are amplified to higher peak energies (e.g. mJ) in one or multiple amplification stages without yielding material damaging peak intensities. Finally, the pulses are re-compressed to the fs-level by applying the opposite temporal chirp.

effects [8]. Afterwards, the amplified pulses can be re-compressed to the femtosecond level by applying then again an opposite chirp, hence offering pulse energies of up to several mJ [182].

Optical parametric amplification

The spectral properties of a laser output are generally determined by the spectral properties of the gain medium. As mentioned earlier, laser systems based on Ti:Sa are widely used because they are able to amplify a broad bandwidth of $\Delta\lambda_{\text{Ti:Sa}} \approx 800\,\text{nm} \pm 200\,\text{nm}$. Other examples of gain media are e.g. Nd:YAG[10] emitting around $\lambda_{\text{C,Nd:YAG}} \approx 1064\,\text{nm}$ or Er:glass[11] with $\lambda_{\text{C,Er:glass}} \approx 1535\,\text{nm}$ [137, Chapter 8]. Next to ultrafast sources generating pulses in the NIR spectral region, there is great demand for ultrafast sources in the mid-IR spectral region not just in the AMO community, but also in biology or medical research [184]. The benefits of using ultrafast mid-IR sources for SFP were stated in Sec. 2.4. Unfortunately not many solid-state gain media supporting broad spectral bandwidth for short pulses are available in the mid-IR [57].
As a solution, *nonlinear optical frequency conversion* phenomena in suitable materials are standardly utilized to generate intense, coherent and ultrafast pulses for mid-IR wavelength. Here, next to the linear response of the dielectric polarization of a material $\mathcal{P} = \epsilon_0 \chi^{(1)} \mathcal{E}(t)$ on the optical electric field, with the electric permitivity in free space ϵ_0 and the linear susceptibility $\chi^{(1)}$, nonlinear media also feature a non-linear polarization response scaling with higher orders of the electric field [180]:

$$\mathcal{P} = \epsilon_0 [\chi^{(1)} \mathcal{E}(t) + \chi^{(2)} \mathcal{E}^2(t)] + \chi^{(3)} \mathcal{E}^3(t) + ...] \tag{3.4}$$

with $\chi^{(2)}$ and $\chi^{(3)}$ as the second- and third-order non-linear optical susceptibility. These non-linear properties allow wave-mixing processes which generate new fre-

[10] neodymium-doped yttrium aluminium garnet: $Nd^{3+}:Y_3Al_5O_{12}$
[11] erbium-doped silica: $Er^{3+}:SiO_2$

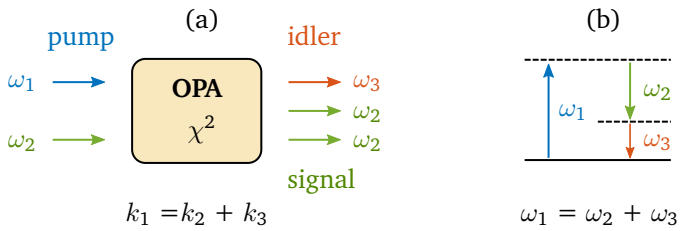

Figure 3.2: Concept of optical parametric amplification. Non-linear three-wave mixing processes are triggered by focusing two laser beams into a non-linear optical medium ($\chi^{(2)} > 0$) as sketched in **(a)**. Under selected phase-matching conditions ($\Delta k = 0$), a difference-frequency generation (DFG) scenario is triggered where two incident photon frequencies ($\omega_1 > \omega_2$) are subtracted to create a third frequency ω_3. Since the energy is conserved in this process as shown in **(b)**, the *pump* photon ω_1 is split into the *idler* photon ω_3 and an additional photon of the *signal* frequency ω_2. Hence, the signal beam is amplified in the process, which is why the process is called OPA.

quency components dependent on the incoming frequencies, their incident angles as well as the strength of the non-linear susceptibility of the material. An important characteristic of all frequency conversion processes is the conservation of photon energies $\Delta\omega = 0$ as well as the conservation of wave vectors $\Delta k = 0$, also known as *phase matching* [180].
The most prominent examples of non-linear frequency conversion processes are *second-harmonic generation* (SHG), *sum-* (SFG) and *difference-frequency generation* (DFG). In SHG two incident photons ω_0 are converted into one photon $\omega_1 = 2\,\omega_0$, effectively dividing the wavelength in half. In SFG and DFG, two incident photons $\omega_1 > \omega_2$ are added and subtracted $\omega_3 = \omega_1 \pm \omega_2$, respectively, to generate a new frequency component ω_3. At first glance, SFG and DFG seem similar, yet DFG offers an important property as sketched in Fig. 3.2. In order to fulfill energy conservation [see Fig. 3.2 (b)], the incident photon with the larger energy ω_1 needs to be split into ω_2 and ω_3. This means that the smaller incident photon ω_2 gets effectively amplified in the conversion process [180]. This mechanism is better known as *optical parametric amplification* (OPA) [sketched in Fig. 3.2 (a)] and serves as a common amplification procedure especially in the mid-IR spectral range. In practice, the incident beam at larger frequency $\omega_1 = \omega_\mathrm{P}$ usually is called the *pump* frequency, the second and amplified frequency $\omega_2 = \omega_\mathrm{S}$ is known as the *signal* frequency and the third, resulting frequency $\omega_3 = \omega_\mathrm{I}$ is known as the *idler*. It should be added that Fig. 3.2 (a) shows the OPA process with perfect efficiency. In reality, the the pump is usually not fully converted into signal and idler leading to a *rest pump* leaking out of the nonlinear medium.

One approach to effectively generate intense, ultrafast pulses in the mid-IR spectral region is the combination of the two preceding amplification schemes CPA and OPA. This idea was introduced in the 1990s [185,186] as *optical parametric chirped pulse amplification* (OPCPA). The strength of the OPCPA concept is the possibility to directly amplify broad bandwidth pulses at any wavelength down to the few-cycle

regime, potentially CEP stable and at relatively high repetition rates of hundreds of kHz [49,52] compared to Ti:Sa based laser systems usually operating at 1 - 10 kHz. OPCPA sources at longer wavelength have been realized in the 2 μm spectral region by e.g. Fuji *et al.* [48] and in the mid-IR at a central wavelength of $\lambda_C = 3.2\,\mu m$ by Chalus *et al.* in 2009 [50]. The latter source was developed within our group and is a predecessor of the source used within this thesis which presented in the following Subsec. 3.1.2.

3.1.2 Mid-IR OPCPA source at 160 kHz repetition rate

Our home-built, mid-IR source used for the investigations within the scope of this thesis is based on the above described OPCPA concept. Our table-top system is able to generate passively CEP stable pulses of three optical cycles duration (FWHM) with a center wavelength of $\lambda_C \approx 3.07\,\mu m$ at a repetition rate of 160 kHz with pulse energies of up to 20 μJ. Moreover, the system generates a second output at $\lambda_C \approx 1.63\,\mu m$ with 18 cycles duration (FWHM) at a 15 μJ pulse energy.

The working principle of the source [Fig. 3.3 (a)] has been engineered over the last couple of years and is well documented in various publications [50–52,55,56]. The version used in this thesis is closest to [56]. The *mid-IR front-end* consists of a commercial two-color fiber laser and a DFG stage. The Erbium-based fiber laser (*Toptica Photonics AG*) generates and amplifies two broadband outputs at $\lambda_1 = 1050\,nm$ and $\lambda_2 = 1550\,nm$ at a repetition rate of 100 MHz. The first output λ_1 is the Erbium related oscillator wavelength and exhibits a pulse duration of $\tau_1 = 60\,fs$ and a pulse energy of $E_{p,1} = 0.16\,nJ$. λ_2 is generated in an additional highly non-linear fiber (HNLF) with $\tau_2 = 90\,fs$ and $E_{p,2} = 2.5\,nJ$. Hence, both frequencies originate from the same oscillator. The two outputs are focused into a non-linear crystal[12] and converted via DFG to broadband mid-IR radiation at 3.07 μm center wavelength spanning a spectrum of over $\Delta\lambda = 900\,nm$ which supports a transform-limited pulse of $\tau_{TL} = 27\,fs$ (∼2.6 optical cycles). The DFG stage is a crucial component of the OPCPA system as it provides passive CEP stability without any additional electronically stabilizing components. Next, the mid-IR pulses with a pulse energy of $E_{p,3} = 10\,pJ$ are temporally stretched to a duration of 3 ps by propagating through a 5 cm long sapphire rod. Then, the stretched pulses are successively amplified in a *chain of four OPA stages*. An additional temporal stretch is applied between OPA 1 and OPA 2 by an extra 2 cm sapphire rod. The system is pumped by a commercial Neodymium-based power amplifier system (*Coherent GmbH*) emitting pulses with $\tau_P = 9.5\,ps$ centered at 1064 nm wavelength. The high-power pump system generates pulses at a repetition rate of 160 kHz with an overall pulse energy of $E_P = 1\,mJ$. In order to warrant consistent temporal overlap between the pump and the mid-IR signal pulses, the repetition rates of both outputs are electronically synchronized. After the amplification stage, the left-over pump beam as well as the residual idler wave are filtered out with a dichroic optic after every OPA stage. After OPA 4, the system provides both amplified outputs of the signal ($\lambda_S = 1.63\,\mu m$)

[12] magnesium oxide-doped, periodically poled lithium niobate (MgO:PPLN)

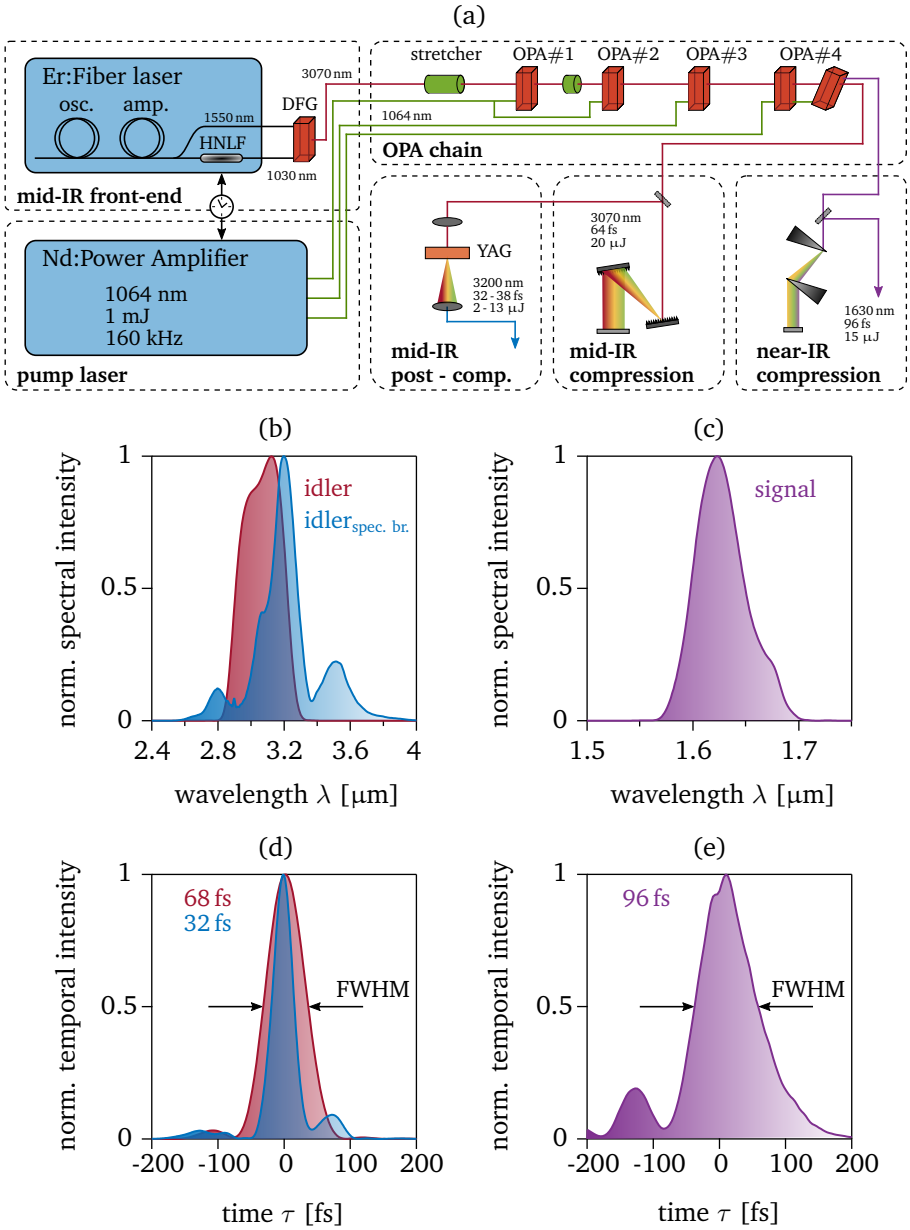

Figure 3.3: Mid-IR OPCPA setup. (a) The system architecture is sketched based on [56]. For details see text. The normalized spectral intensity for **(b)** the compressed idler output at 3.07 µm (ruby) and the spectrally broadened pulses at 3.2 µm (blue) as well as **(c)** the signal output at 1.62 µm (purple) as detected via FROG. **(d,e)** The respective normalized temporal intensities as retrieved from the FROG trace with resulting pulse durations (FWHM).

and idler ($\lambda_I = 3.07\,\mu m$) radiation at $E_S = 60\,\mu J$ and $E_I = 40\,\mu J$, respectively. Both outputs are individually compressed leading to a 3 µm-pulse with a duration of $\tau_I = 68\,fs$[13] at a pulse energy of $E_P = 20\,\mu J$ and a 1.6 µm-pulse with $\tau_S = 96\,fs$ at $E_P = 15\,\mu J$. In Fig. 3.4 (b,c) the spectral intensity of both the idler (b, ruby) and the signal (c, purple) are plotted as detected via the frequency-resolved optical gating (FROG) technique[14]. The respective temporal intensities as retrieved from the FROG traces are shown in Fig. 3.4 (d,e). The mid-IR output stability was measured via a long-term measurement to fluctuations of below 1 % rms over the course of 12.5 hours [56], while its CEP stability as inherited from the initial DFG stage was measured as better than 250 mrad over 11 min [51].
Additionally, the duration of the mid-IR pulse can be further reduced by focussing in a non-linear YAG plate leading to filamentation induced spectral broadening and simultaneously temporal self-compression [54] [named mid-IR post compression in Fig. 3.4 (a)]. Thus, the mid-IR pulse can be compressed to a duration of 38 fs (3.7 optical cycles) with a remaining pulse energy of 13 µJ, and even to 32 fs (2.9 optical cycles) with an energy of 2 µJ [54]. The spectral and temporal FROG retrieval of the latter pulse is shown in blue in Fig. 3.4 (b,d). The central wavelength of the spectrum is slightly shifted to $\lambda_{I,spec.br.} = 3.20\,\mu m$ in the self-compression process.

3.1.3 Intensity determination

Light-matter interactions strongly depend on the field strength of the incident light. Therefore, the detailed knowledge about the field amplitude and in this sense the intensity[15] distribution of the focused laser pulses used in an experiment is crucial to scale and interpret experimental results when e.g. comparing them to theoretical models. When focused to a well-defined spot, the intensity distribution of the focused laser beam strongly depends on the size and the shape of the focal volume. Hence, not only the peak intensity $I_{peak} = I_{max}$ at the center of the focal volume ("focal spot") contributes to e.g. the ionization of an atomic or molecular target, yet also other atoms or molecules at different positions within the focal volume will be ionized at lower intensities.

Pulsed laser sources generally generate output beams with an intensity profile that can be described by a Gaussian distribution. Therefore, the intensity distribution in the focal volume can be expressed according to Gaussian optics [68, Ch. 17]:

$$I(z,r) = I_{peak}\left[\frac{w_0^2}{w^2(z)}\right]\exp\left[-\frac{2\,r^2}{w^2(z)}\right], \tag{3.5}$$

[13] Without extra spectral broadening steps, the shortest achieved pulse duration of the OPCPA system was 55 fs [56]. In this thesis, we generally used pulse durations around 65 fs to 75 fs.

[14] The FROG technique is a method to characterize ultrashort pulses and was developed by Daniel J. Kane [187] and Rick Trebino [187, 188]. By detecting the complete spectral bandwidth of a pulse at each temporal position of an autocorrelation, the phase of the pulse can be iteratively retrieved by an algorithm. This results in the spectral intensity and phase of the pulse allowing to calculate the temporal intensity and hence the duration of the pulse.

[15] as a reminder: $I = \frac{1}{2}\,\epsilon_0\,c\,\mathcal{E}^2$

as function of the distance z from the focal spot parallel to the beam propagation direction $\vec{e}_z$ and the transverse distance r from the focal spot perpendicular to $\vec{e}_z$. The peak intensity of a cylindrical Gaussian beam can be calculated as

$$I_{\text{peak}} = \frac{2\,E_P}{\tau\,\pi\,w_0^2} = \frac{2\,P}{f_{\text{rep}}\,\tau\,\pi\,w_0^2}\,, \tag{3.6}$$

with the pulse energy E_P, the pulse duration τ (FWHM) and the beam waist (half the diameter at $1/e^2$ amplitude) at the position of the focal spot $w_0 = w(z = 0)$. More practical in the laboratory is actually the measurement parameter of the laser power $P = E \cdot f_{\text{rep}}$ which can be expressed by the pulse energy and the repetition rate f_{rep} of the pulsed laser system. For the parameters achievable with our laser system, as described in the Sec. 3.1.2 before, a maximum peak intensity of $I_{\text{peak}} \sim 3.6 \times 10^{14}\,\text{W/cm}^2$ is feasible. In the experiments of this thesis, we generally focus our collimated laser beam with a focal length of $d_f = 50\,\text{mm}$ to a focal spot with a waist of $\omega_0 = 7\,\mu\text{m}$.

The intensity distribution of Eq. 3.5 further contains the beam waist of the focused beam along the propagation axis

$$w(z) = w_0\sqrt{1 + \left(\frac{z}{z_R}\right)^2} \tag{3.7}$$

with the Rayleigh range z_R which is defined as the distance from the focal spot at which the intensity has decreased to half the peak intensity $I(z_R) = I_{\text{peak}}\,/\,2$. Both ω_0 and z_R can be expressed with laser and optical parameters:

$$w_0 = \frac{\lambda\,d_f}{\pi\,R}\,, \tag{3.8}$$

$$z_R = \frac{w_0^2\,\pi}{\lambda}\,. \tag{3.9}$$

Here, d_f is the focal length of the mirror or lens, while R is the radius of the collimated beam incident on the focusing optic. According to Eq. 3.8, the minimum waist w_0 of the focal volume decreases for decreasing laser wavelength. The intensity distribution $I(z, r)$ is plotted in Fig. 3.4 (a) for parameters of our laser system as used in the experiments of this thesis. The 2D intensity distribution is normalized to the peak intensity I_{peak}. It spans a volume with a longitudinal width of roughly $z_{1/e^2} \approx \pm 127\,\mu\text{m}$ considering a minimum intensity of $I_{\text{min}} = I(z_{1/e^2}, 0) = 1/e^2 \cdot I_{\text{peak}}$[16]. The contour of I_{min} as the outline of the focal volume is plotted as a green line, while the beam waist $w(z)$ is shown as a red line.

In equations 3.5 - 3.9, the beam shape is considered to have a *perfect* Gaussian distribution. In reality, laser beams tend to suffer from optical aberrations accumulated in the generation process and/or during propagation that can change the beam profile in the focus. This is accounted for by the *beam quality factor* $M^2 \geq 1$ [189] which is added as a multiplication factor to λ. A perfect Gaussian

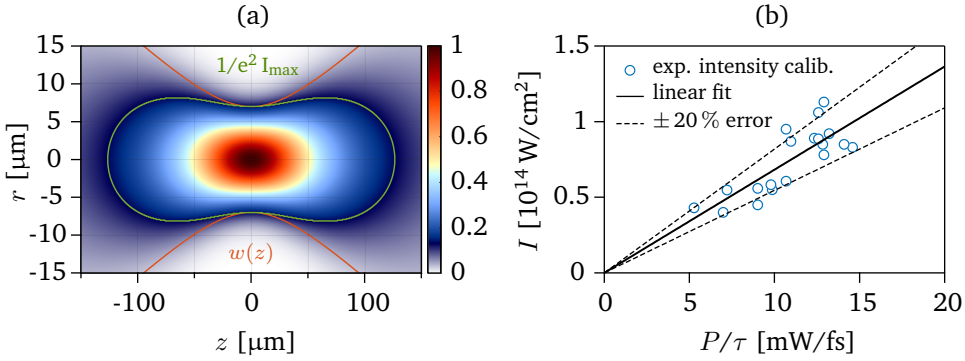

Figure 3.4: Intensity distribution in the focal volume and peak intensity determination. (a) The normalized intensity distribution $I(z,r)$ of the focal volume of our laser pulse is calculated according to Eg. 3.5. The beam is considered to have a perfect Gaussian distribution and an $M^2 = 1$. The green contour signalizes the intensity dropping from the peak intensity to a value of $1/e^2$ of I_{peak}. **(b)** The peak intensity values of experiments within this thesis were determined by various methods (see bullet points in text). The extracted intensity values (blue circles) are plotted as a function of the ratio of laser power to pulse duration P/τ and compared. The values agree within error to a fitted linear regression of $I_{peak} = 6.82 \times 10^{12} \cdot P/\tau$ [mW/fs] $\pm$ 20 % W/cm^2.

distribution has $M^2 = 1$. Hence, aberrations lead to a bigger focal volume and hence a smaller peak intensity when keeping all other parameters constant.

Any theoretical model should include the intensity distribution of the focal volume, also referred to as *focal averaging*, in order to realistically compare with experimental results. Moreover, the value for the peak intensity I_{peak} needs to be estimated as accurate as possible. All measurement parameters of Eq. 3.6 necessary to calculate I_{peak} are generally determined with errors of 1 - 10 % each [178] which can accumulate to a large error. The biggest uncertainty in our case depicts the waist w_0 in the focus because we operate in the ultrahigh vacuum chamber of a ReMi (see Sec. 3.2) without beam profile diagnostics available. Hence, the determination of the peak intensity with a high accuracy is difficult, and should ideally be derived directly from physical measurables of an experiment. Within this thesis we utilized the following methods to determine I_{peak} of our experiments:

- **Longitudinal momentum spread compared to ADK theory.**
  The longitudinal ion and electron momentum distribution of a single ionization event of an atomic target induced by a linearly polarized laser field is compared with the momentum dependent ionization rate calculated after ADK theory [90]. Therefore, Eq. 2.20 can be fitted against the experimental data in order to extract the maximum electric field $\mathcal{E}$ and hence the peak intensity I_{peak}.

[16] $1/e^2 \approx 0.1352$

- **$2\,U_\mathrm{P}$ and $10\,U_\mathrm{P}$ cutoffs.**
  As described in Sec. 2.2, electrons in SFI can either propagate directly to the detector or elastically re-scatter with their parent ion beforehand. The different electrons can be distinguished by their final kinetic energy, since electrons gain kinetic energy in the re-scattering process and only return with a probability on the few percent level or less depending on the wavelength [45]. Accordingly, the kinetic energy distribution for SFI events offers two characteristic features marking the cutoff of direct electrons at $E_\mathrm{kin} = 2\,U_\mathrm{P}$ and the cutoff of re-scattered electrons at $E_\mathrm{kin} = 10\,U_\mathrm{P}$. After extracting both cutoff features, the peak intensity is extracted via the formula for the ponderomotive energy U_P as stated in Eq. 2.6.

- **Comparison of differential cross sections from LIED with theory.**
  According to the quantitative re-scattering (QRS) theory [110, 190, 191], the electron momentum distribution of only the re-scattered or HATI electrons is composed of the field-dependent momentum of the electron wave packet plus the field-free differential cross-section (DCS) of the elastic scattering events. Hence, by considering classical behavior of the electron in the laser field (as described in Sec. 2.2), the DCS of electrons with a specific return energy E_r can be extracted from an experimental 2D[17] photo electron momentum distribution. A detailed introduction of QRS theory as well as the DCS extraction can be found in Ch. 6.3.1. The experimental DCS is compared to a theoretical DCS calculated e.g. via quantum-mechanical scattering theory (described e.g. in [95, Ch. 7]) , or the independent atom model (IAM) (decribed e.g. in [29, Ch. 2]) which is standardly used in conventional electron diffraction (CED). Optionally the experimental DCS can also be directly compared to CED data. By varying the electrons' return energy and vector potential at the point of return to achieve an agreement with theory, the laser conditions driving the electron on its trajectory can be deduced. The peak intensity I_peak is derived from p_r and $A(t_\mathrm{r})$ via classical considerations as in Sec. 2.2. Yet, this method is not as accurate as others, since the LIED extraction is fairly insensitive on intensity (see Sec. 6.4.4).

The intensities in each of the experiments conducted within this thesis were determined using at least one of the three methods. All resulting values for I_peak are summarized in Fig. 3.4 (b) as a function of the ratio between laser power and pulse duration P/τ [mW/fs]. The comparison can be justified since 1.) all experiments were conducted with the same version of our OPCPA source, 2.) with the same beam conditions plus 3.) all experiments were aligned in the same manner by maximizing the ion count rate in order to warrant equal focusing conditions. By linear regression, an overall intensity calibration for all investigations can be derived to:

$$I_\mathrm{peak} = \left\{ 6.82 \times 10^{12} \left(\frac{P}{\tau}\,[\mathrm{mW/fs}] \right) \pm 20\,\% \right\}\,[\mathrm{W/cm^2}]. \,. \tag{3.10}$$

[17] considering cylindrical coordinates and integrated over the azimuthal angle plus applying the appropriate Jacobian

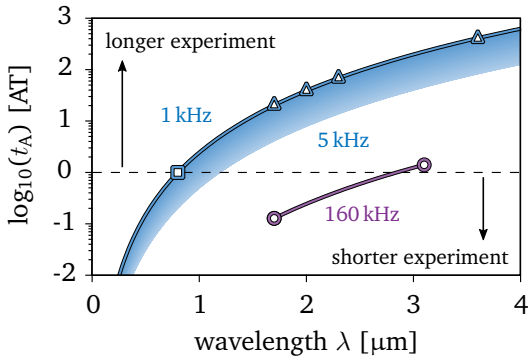

Figure 3.5: Comparison of data acquisition time. The number of "acquisition times" ATs (as defined in the text) required for a range of driving wavelengths after accounting for the λ^{-4} scaling of electron re-scattering. Typical 1 kHz systems based on Ti:Sapphire technology (Ref. [39] - blue triangles) are limited as total acquisition times become untenable. Even the expected repetition rate upper limit of 5 kHz is not fast enough to compensate for the decrease of signal (blue shaded region). Using a 160 kHz system such as our mid-IR OPCPA system, on the other hand, allows much shorter acquisition times (purple circles). The figure is adapted from our publication [169].

The statistical error of the linear fit lies at $\sim$4 % (1σ) while a realistic error bar of $\pm 20\,\%$ is applied here for the before mentioned uncertainties of the involved measurables.
For the sake of completeness, it should be mentioned that the peak intensity can be determined by various other methods which are nicely listed and explained in [192], yet were not used within this thesis: a) comparison of the ratio of dications to cations Γ^{++}/Γ^{+} which scales differently with intensity (transition from NSDI to SDI) and wavelength, b) electron momentum distribution of SFI with circularly polarized light resulting in a distinctive donut (in 2D) or double-peak (in 1D) shape where the radius directly proportional to the laser electric field, or c) comparison of branching ratios of molecular fragmentation processes. The most accurate peak intensity determination can be achieved by d) SFI of atomic hydrogen and comparison to exactly solved TDSE calculations. An accuracy on the $1\,\%$ level has been achieved in this way [178].

3.1.4 On the importance of high repetition rates

A major challenge in performing SFP experiments with long wavelength sources is quantum diffusion [8] as already described in Sec. 2.4. Here the electron wave packet experiences larger longitudinal and transverse spreading with increasing wavelength due to the longer excursion time. Consequently, the larger extent of the re-colliding wave packet results in a smaller re-combination or re-collision cross-section which manifests in reduced count rate when driving SFP at longer wavelength [44, 46]. Experimental evidence shows that the ratio of re-scattered to

directly ionized electrons scales roughly as λ^{-4} [45].

We highlighted this crucial point for experimental investigations in our publication [169] by defining an arbitrary standard unit of "acquisition time" (AT) shown in Fig. 3.5 . AT stands for the time required to reach a certain signal-to-noise ratio of re-scattered electrons when using a standard 1 kHz, 0.8 μm radiation source (dashed black line). Using the above mentioned λ^{-4} scaling and assuming all other experimental parameters stay constant, the number of standard ATs that are required to reach the identical signal-to-noise ratio, can be estimated as a function of driving wavelength. The results of this calculation are presented in Fig. 3.5 for 1 kHz sources (blue curve) that are e.g. frequency down-converted based on a Ti:Sa system. The triangular data points represent the wavelength of some sources that have recently been used to study electron re-collisions with longer wavelength [45, 58, 127, 128, 193]. The required ATs for accumulated counts with identical signal-to-noise scale rapidly with wavelength. Compared with 0.8 μm radiation a one and two orders of magnitude increase for 1.4 μm and 2.5 μm radiation can be predicted, respectively. At a wavelength of 3.6 μm over 400 ATs are required. Let's put these arbitrarily defined ATs and the quoted numbers into perspective: if a standard AT is equal to one hour of integration time then the new experimental time would be over 17 days at 3.6 μm. Clearly, the unfavorable wavelength scaling of SFP must be addressed to ensure continual advancement of the field.

An obvious solution to this dilemma is to increase the repetition rate of the driving laser [49, 50, 194, 195]. Ti:Sapphire based laser systems [45, 58, 59, 196] are typically limited to a few kHz. The range of acquisition times that can realistically be achieved with such systems is represented by the blue shaded region in Fig. 3.5. Mid-IR sources at much higher repetition rates, i.e. above several tens to hundreds of kilohertz, can be realized with a range of techniques but so far only OPCPA has provided a viable solution. High average power fiber laser sources are operational at MHz repetition rates, but additional down conversion into the mid-IR carries a sacrifice in pulse energy. Another approach could be based on passive enhancement cavities [197] in the mid-IR but such apparatuses are extremely challenging to contain broad bandwidths for few-cycle pulses and are yet to be implemented outside of the near-IR. These technical problems are overcome with the concept of OPCPA. As described in Subsec. 3.1.2, our mid-IR OPCPA source offers *the combination* of mid-IR wavelength (3.1 μm), few-cycle pulses at a hight repetition rate of 160 kHz with a long term power stability ($\leq 1\%$ rms over 12 hours) [56]. Additionally, pulses are parasitically generated at wavelength of the OPCPA system's signal at 1.7 μm at the same repetition rate. When the above AT analysis is applied to the two wavelengths of our system it is found that the required experimental time is actually an order of magnitude less than a standard AT for the 1.7 μm output and a factor 1.4 longer for 3.1 μm (the purple circles in Fig. 3.5). Combining these points with the benefits of operating in the mid-IR as shown in Sec. 2.4, it is clear that high repetition rate, mid-IR OPCPA schemes solve the problems of studying SFP at longer wavelengths.

3.2 Reaction Microscope

The interaction between a strong laser field and matter happens inherently in three dimensions. Therefore, it is important to capture all products of an ionization - in case of molecules potentially fragmentation - process in all three dimensions in order to grasp the entirety of the physical process(es) during an experimental investigation. A necessary approach on the detection side is to determine the 3D momentum information of all resulting particles during SFI events. This is because atoms, molecules and electrons are quantum objects being *de-localized* according to the laws of quantum mechanics (Heisenberg's uncertainty principle). Hence, since location and time are no observables in a singular measurement, the momenta of quantum particles are the measurable observables at any point in time [64].
A reaction microscope (ReMi)allows the detection of momenta of both electrons and ions or ionic fragments in full 4π solid angle for a large range of energies providing at the same time unprecedented resolution. The key feature of a ReMi is the possibility to detect electrons and parent ions in coincidence. This is possible despite their intrinsically large mass difference because a ReMi operates on a single particle level.

The ReMi used for the experiments conducted in the scope of this thesis was built up in our AUO laboratory in collaboration with the group(s) of Robert Moshammer and Joachim Ullrich of the Max Planck Institut für Kernphysik (MPIK, Max Planck Institute for Nuclear Physics) in Heidelberg, Germany. This groups' principal investigators designed and developed the ReMis in the nineties by combining for the first time the concept of *cold target recoil ion momentum spectroscopy* (COLTRIMS) [198] with an electron analyzer with 4π solid angle acceptance in order to look at recoil-ion and electrons at the same time [62]. The technique has been further advanced and led to a multitude of discoveries in the field of atomic and molecular physics which can found in many review articles [62, 63, 198–201]. In this section, the basic setup and working principle of our system is outlined (Subsec. 3.2.1). Then, the data analysis from the initial raw time signals to the momentum space of the detected events is explained (Subsec. 3.2.2), before the performance of the ReMi is presented (Subsec. 3.2.3).

3.2.1 Working principle and setup

Our ReMi is similar to the one in Heidelberg described in [202, 203]. In general, a ReMi can be used to investigate *particle collisions* of any kind of projectiles (e.g. electrons, ions, or in our case photons) interacting with a target (e.g. a gas jet of atoms or molecules), thereby resolving the resulting momentum space of all originated ionic particles (or particle fragments) and their corresponding electrons. Our experimental procedure of a strong-field experiment is sketched in Fig. 3.6: the target is prepared as a gas jet cooled via supersonic expansion (dark green) which intersects with the focused mid-IR laser beam (red). Hence, the target is ionized in the focal or *reaction volume* (as described in Subsec. 3.1.3) creating at least one

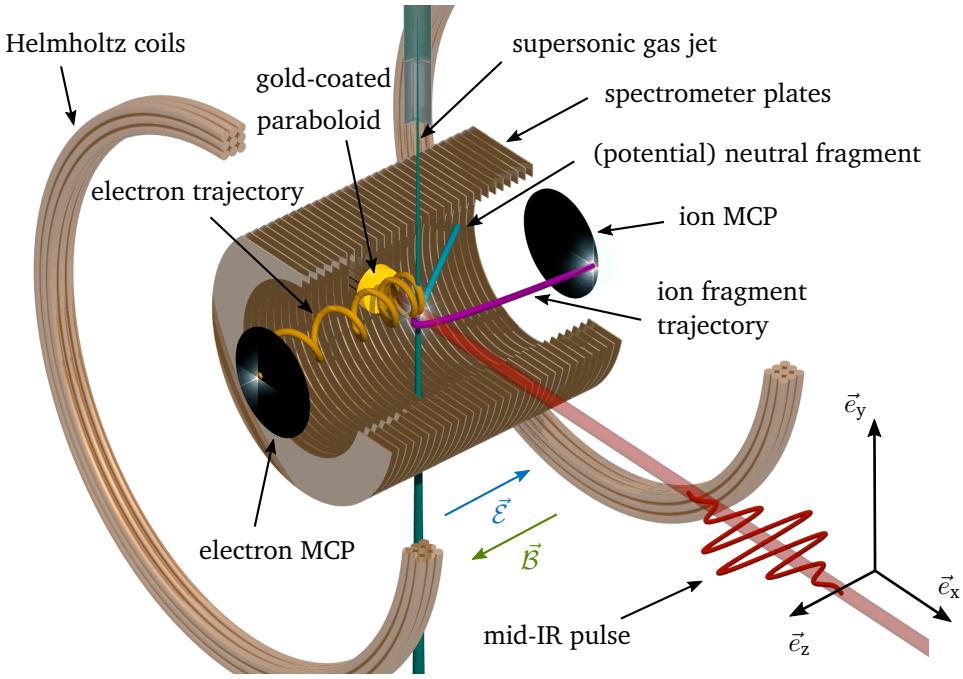

Figure 3.6: Setup of a reaction microscope. Sketch of the ReMi used in this thesis adapted with kind permission from Phillip Cörlin [139]. The target atoms and molecules are supersonically expanded into an ultra-high vacuum chamber where the gas jet (dark green) intersects with our mid-IR laser beam (red). The charged SFI products as in electrons (orange) and ions (purple) are guided onto two position-sensitive multi-channel plate (MCP) detectors by anti-collinear electric (blue, via spectrometer plates) and magnetic fields (light green, via Helmholtz coils). The 3D momentum vector of ions and electrons can be extracted from the ToF (1D) and detector impact position (2D) information in coincidence.

ion and one electron. Upon SFI, a combination of static electric ($\vec{\mathcal{E}}$, blue) and magnetic ($\vec{B}$, light green) extraction fields that are aligned anti-collinear along the spectrometer axis, directs all charged particles to two opposing large-scale time- and position-sensitive detectors. The $\vec{\mathcal{E}}$ field is generated via spectrometer plates holding linearly increasing potentials, while the $\vec{\mathcal{B}}$ field is created via a Helmholtz coil pair. The trajectories of a negatively charged electron and positively charged ion fragment are presented in orange and purple arrows, respectively. A potential neutral fragment is sketched in turquoise. The resulting 3D momentum vectors of ions (and electrons) extend along the z-axis with $+\vec{e}_z$ along the direction of the static electric field $_{(-)}\vec{\mathcal{E}}$, respectively, while the x-axis $+\vec{e}_x$ ranges along the laser propagation direction $_{(-)}\vec{k}$ and the y-axis $+\vec{e}_y$ anti-parallel to the direction of the gas jet. The coordinate system is indicated in Fig. 3.6. Its origin is the reaction volume.

3.2.1.1 Supersonic gas jet in ultra-high vacuum

The target in our ReMi is prepared in gas-phase in form of a gas jet which has the benefit over fixed targets that the investigated atoms or molecules are constantly renewed and so never altered e.g. by radiative heating. The key to achieve high resolutions in momentum spectroscopy when imaging collision induced atomic or molecular reactions is to keep secondary momentum uncertainties at a minimum in order to be able to resolve the momenta of the products of the actual reaction. Therefore, the target particles need to be prepared with minimum possible initial momentum spread[18]. This becomes clear when comparing the recoil momenta of ions and electrons that are transferred via strong-field induced photoionization and that can range over several orders of magnitude from the level of $\ll 1$ a.u. (e.g. close to the ionization threshold as discussed in Ch. 4) to tens of a.u., with the mean momentum spread $\bar{p}$ of an ensemble of atoms in an ideal gas. The latter can be derived from the Maxwell-Boltzmann distribution of an ideal gas [204, Ch. 7] which can be regarded in one dimension effectively as a Gaussian distribution [204, Eq. 7.24]. The longitudinal momentum spread of the gas jet in propagation direction can be regarded as the standard deviation of $\bar{p}$ (one σ) being

$$\Delta p = \sqrt{k_\mathrm{B}\, T\, m}\,. \tag{3.11}$$

with the Boltzmann constant k_B[19] and temperature T. At room temperature $T_0 = 300\,\mathrm{K}$ noble gas atoms yield $\Delta p_{300\mathrm{K}} \approx 10$ a.u. and hence on the order of the momenta achieved in SFI events. The transverse momentum spread is determined by geometrical dimensions of the setup (explained in the following). For accurate resolution of the SFI events, the temperature of the gas target atoms or molecules needs to be kept at a minimum. A way to achieve that is by cooling the gas target via *adiabatic expansion* to form a *supersonic gas jet*[20]. The following paragraphs describe the realization and the properties of a supersonic gas jet. Their information is mostly based on the book chapter "Free Jet Sources" by *David R. Miller* [205], with a summary of its most important formulas compiled from [139, 206, 207].

The technical *realization of a supersonic jet* as shown in Fig. 3.7 (a) is achieved by a differential pumping scheme. When the target gas with an initial temperature of $T_0 = 300\,\mathrm{K}$ and an initial pressure P_0 is expanded through a narrow nozzle with diameter d into a chamber with much lower pressure $P_1 \ll P_0$, the gas particles are accelerated and adiabatically expanded while effectively being cooled. The temperature loss is established by the transition from an *uncorrelated* thermal motion of the gas into a *directional* motion in form of a jet thereby converting thermal energy into translational energy under adiabatic conditions (see [205] and [207, Subsec. 4.1.1]). This decreases the thermal energy and effectively the gas jet temperature $T_1 \ll T_0$. In the process, the translational velocity of the particles can exceed the speed of sound c_S, which is why is the process is dubbed as

[18] In SFI experiments the momentum of the incident photon is negligible [63].

[19] $k_\mathrm{B} = 8.6173324(78) \cdot 10^{-5}\ \frac{eV}{K}$

[20] Another possibility to cool the target particles is to use a *magneto-optical trap* (MOT) which was implemented with MOTRIMS [63, Subsec. 3.2.2].

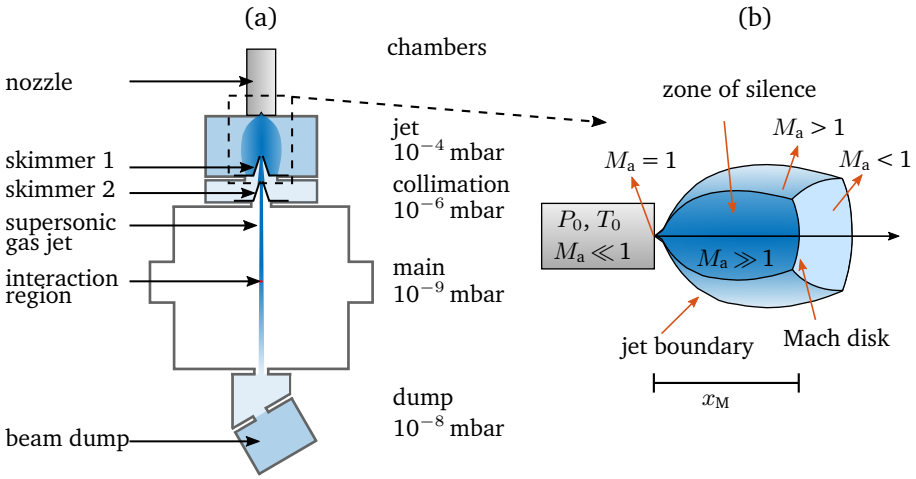

Figure 3.7: Supersonic gas jet in ultra-high vacuum. (a) The target gas expands through a nozzle into the differentially pumped vaccuum chambers of the ReMi. According to the theory of free gas expansion, the gas is cooled in the process turning thermal energy into kinetic energy while escaping through the nozzle. **(b)** After the nozzle, the gas forms a Mach cone with the coldest region being the *zone of silence* in the center. Two skimmers [see **(a)**] isolate the coolest part of the gas and form a gas jet which is guided into the main chamber to intersect with the focussed laser beam. Afterward the interaction with the laser in the main chamber, the gas jet is picked off by a beam-dump [see **(a)**] to reduce the overall gas pressure in the main chamber.

a supersonic gas expansion [205]. In gas flow dynamics, the relation between the gas velocity v to c_S is expressed by the *Mach number* [208, Sec. 3.3][21]

$$M_a = \frac{v}{c_S} = \sqrt{\frac{2}{\kappa - 1}\left(\frac{T_0}{T_1} - 1\right)} = \sqrt{\frac{2}{\kappa - 1}\left[\left(\frac{P_0}{P_1}\right)^{(\kappa-1)/\kappa} - 1\right]} \tag{3.12}$$

with the specific heats ratio[22]

$$\kappa = \frac{c_P}{c_V} = 1 + \frac{2}{f}\,. \tag{3.13}$$

Here, f stands for the degrees of freedom of an ideal gas particle. Atoms hold $f = 3$ translational degrees of freedom, while linear molecules have $f = 5$, for extra 2 rotational degrees of freedom. The Mach number can also be determined as a function of the distance x from the nozzle by an empirical model [205,209], which

[21] Temperature, pressure and number density ratios of an ideal gas are connected as $\left(\frac{P_1}{P_0}\right) = \left(\frac{T_1}{T_0}\right)^{\kappa/(\kappa-1)} = \left(\frac{n_1}{n_0}\right)^{\kappa}$.

[22] The specific heat ratio includes the specific heat at constant-volume c_V and constant-pressure c_P.

is outlined in App. C.
The transition point where the gas jet velocity equals the speed of sound is hence characterized by $M_a = 1$. Consequentially, the low jet temperatures T_1 are accomplished by high jet velocity v or a Mach number $M_a \gg 1$, which is achieved by a large pressure difference. This is evident when re-organizing Eq. 3.12 leading to

$$\frac{P_0}{P_1} \gg \left(\frac{\kappa+1}{2}\right)^{\kappa/(\kappa-1)} . \tag{3.14}$$

For noble gases, $\kappa = 5/3$ leads to the condition $P_0 \gg 2.05 \cdot P_1$. After the expansion through the nozzle, the gas jet can be divided in different regions dependent on the magnitude of the Mach number as sketched in Fig. 3.7 (b). The region with the lowest effective gas temperature $T_{1,\text{min}}$ and a Mach number of $M_a \gg 1$ is located after the nozzle, better known as the *zone of silence*. The zone of silence extends until the boundary of the *Mach disk* ($M_a = 1$) which sits at a distance of [208, Sec. 3.5]

$$x_M = d \cdot 0.67 \sqrt{\frac{P_0}{P_1}} , \tag{3.15}$$

independent of κ, yet dependent on the nozzle diameter d. In order to prevent the supersonic gas jet from collapsing before reaching the next vacuum chamber, a small *skimmer* can be placed within the zone of silence at $x < x_M$ as shown in Fig. 3.7 (a). The skimmer is simultaneously the orifice to the next chamber. In our setup, an additional second skimmer (chamber) is placed before reaching the *target* or *main chamber*, as shown in Fig. 3.7 (a), in order to further collimate the beam and hence remove particles with higher transverse momenta. After passing the main chamber, the gas jet is guided into a fourth differential pumping stage where it is finally evacuated in a *beam dump*. The technical parameters of the jet and vacuum system in our ReMi are summarized in Tab. 3.1 as well as typically achieved pressures in the chambers as sketched Fig. 3.7 (a).

A theoretical description of the *properties of a supersonic jet* can also be derived from fundamental gas dynamics (included in [205] and [208, Sec. 3.6]). In order to derive the jet velocity v_{jet} (for $P_0 \gg P_1$), one can assume that the whole enthalpy of the stagnated gas before the nozzle - consisting of thermal energy $E_{\text{therm}} = \frac{f}{2} k_B T_0$ and compression energy $E_{\text{comp}} = k_B T_0$ - is completely converted into translational kinetic energy in the expansion process described above [207, Subsec. 4.1.1]. That leads to a jet momentum in propagation direction of

$$\frac{1}{2} m v_{\text{jet}}^2 = \frac{f}{2} k_B T_0 + k_B T_0 \;\rightarrow\; p_{\text{jet}} = p_{\parallel} = \sqrt{2 k_B T_0 m \left(1 + \frac{f}{2}\right)} . \tag{3.16}$$

This expression for p_{jet} is considered the maximum momentum of the gas jet, and can also be derived from Eq. 3.12 with the speed of sound in the gas jet as $c = \sqrt{\kappa k_B T_1/m}$ [208, Sec. 3.3] and considering $P_0 \gg P_1$ (derivation in App. C.2). After expansion, a supersonic gas jet effectively reaches temperatures at the target T_∞ ranging from several mK to a few tens of K. Additionally, the gas supply can

Gas bottle stagnation pressure (typ.)	1-3 bar
Pressure in Jet Chamber	10^{-4} mbar (Ar_{1bar}), 10^{-9} mbar (bg.)
Jet ch. turbo pump	510 l/s (for N^2)
Pressure in Collimation Chamber	10^{-6} mbar (Ar_{1bar}), 10^{-9} mbar (bg.)
Collimation ch. turbo pump	250 l/s (for N^2)
Pressure in Main Chamber	10^{-9} mbar (Ar_{1bar}), $5{\cdot}10^{-11}$ mbar (bg.)
Main ch. turbo pump	510 l/s (for N^2)
Pressure in Dump Chamber	10^{-8} mbar (Ar_{1bar}), 10^{-10} mbar (bg.)
Dump ch. turbo pump	250 l/s (for N^2)
Nozzle diameter	30 µm
Skimmer 1 diameter	200 µm
distance nozzle - skimmer 1	∼ 5 mm
Skimmer 2 diameter	400 µm
distance skimmer 1 - skimmer 2	∼ 22 mm
distance skimmer 2 - focal plane	∼ 65 mm
gas beam divergence Θ	0.85°
gas jet diameter at focal spot	∼1.4 mm

Table 3.1: Technical parameters of our jet and vacuum system.

also be externally pre-cooled with liquid nitrogen using a cold finger of a cryo-pump [62] in order to start with an initial reservoir temperature of e.g. $T_0 = 30\,\mathrm{K}$. This is not applied in our case.
In order to calculate the final temperature in the jet T_∞, it is helpful to define the *speed ratio* [205, 208] as the ratio between the jet velocity and the residual thermal velocity of the particle in the jet

$$S_{\infty,\parallel} = \frac{v_{\text{jet}}}{v_{\text{therm.}}} = A \left[\sqrt{2}\, \frac{P_0\, d}{k_\mathrm{B}\, T_0} \left(\frac{53\, C_6}{k_\mathrm{B}\, T_0} \right)^{1/3} \right] , \tag{3.17}$$

consisting of parameters that are experimentally determinable (P_0, T_0 and d) as well as three empirical parameters (A, B and C_6). The latter values can be found in [205] for some targets. The final jet temperature follows as

$$T_{\infty,\parallel} = T_0\, \frac{\kappa}{\kappa - 1}\, \frac{1}{S^2_{\infty,\parallel}} . \tag{3.18}$$

Hence, the longitudinal momentum spread of the supersonic jet at target $\Delta p_{\parallel,\infty}$ can be calculated by combining Eq. 3.11 and Eq. 3.18 to

$$\Delta p_{\parallel,\infty} = \pm \sqrt{k_\mathrm{B}\, T_{\infty,\parallel}\, m} . \tag{3.19}$$

The final temperature in the gas jet at target can also be determined experimentally as $T_{\infty,\parallel} = \Delta p^2_{\perp,ion} \,/\, [4 \ln(4)\, k_\mathrm{B}\, m]$ [210], where $\Delta p_{\perp,ion}$ is the detected ion momentum distribution in jet direction (perpendicular to the laser polarization)[23].

[23] Note that $\Delta p_{\perp,ion}$ and $\Delta p_\perp$ are different here, the former being the transverse ion momentum (relative to the laser polarization) and the latter being the jet momentum spread perpendicular to the jet direction.

target	Δp_{300K} [a.u.]	v_{jet} [m/s]	$p_{\parallel}$ [a.u.]	$T_{\infty,\parallel}$ [K]	$\Delta p_{\perp}$ [a.u.]	$T_{\infty,\perp}$ [K]
Ar	8.35	560	18.7	?	0.14	0.08
Xe	15.2	309	33.9	?	0.25	0.08
O_2	7.5	741	19.8	13	0.15	0.12
C_2H_2	6.7	823	17.8	?	0.13	0.12

Table 3.2: Properties of our supersonic jet for target species used in this thesis. In order to calculate $T_{\infty,\parallel}$, the coefficients A, B and C6 are needed in order to estimate the speed ratio $S_{\infty,\parallel}$. For oxygen those coefficients are A = 0.78, B = 0.35, C6/k_B = 8.3·10^{-43} cm^{6}K [205]. The values for Ar, Xe and C_2H_2 could not be found in available literature.

The transverse momentum spread $\Delta p_{\perp}$ of the jet, on the other hand, is determined geometrically by the last skimmers' orifice and is usually smaller than the longitudinal one $\Delta p_{\parallel}$ (see [139, Subsec. 4.1.1]). Hence, the divergence of the gas jet $\Theta = \arctan[d_{s2}/(2\,x_{\text{Nozzle-sk.2}})]$ yields a transverse momentum spread [62] of

$$\Delta p_{\perp} = \pm \tan(\Theta)\, p_{\parallel} \,. \tag{3.20}$$

With Eq. 3.19 the temperature corresponding to the transverse momentum spread can be estimated. The physical properties of our supersonic jet calculated for the targets used within this thesis (Ar, Xe, O_2, C_2H_2) are summarized in Tab. 3.2[24]. In general, jet temperatures in propagation direction are desirable in the few-K region, while the transverse spread should fall in the hundreds of mK range [211]. In terms of the longitudinal spread, our experimental setup can be further improved by pre-cooling the nozzle [62].

The reduction of particles with two skimmer stages and differential pumping has a favorable impact on the pressure in the main chamber which barely changes from its base pressure without load. Hence, next to reducing the gas jet temperature, also the particle density n in the jet at target is decreased. The number density in the supersonic gas jet can be calculated according to [209]

$$n = n_0 \left[1 + \frac{M_a(x)^2\ (\kappa - 1)}{2}\right]^{\frac{1}{1-\kappa}} \tag{3.21}$$

where $M(x)$ is the Mach number in the zone of silence as a function of the distance x from the nozzle, which can be determined with an empirical model as outlined in App. C.1. For similar ReMi setups, relatively low target densities of 10^{10} - 10^{12} 1/cm^3 can be achieved. Assuming the initial stagnation conditions used in Tab. 3.2 (P_0 = 2 bar, T_0 = 300 K) which implies an initial particle density of $n_0 \sim 5 \times 10^{19}$ 1/cm^3[25], this signifies an effective particle density reduction of 7 to 10 orders of magnitude. The low densities are important to conduct single-atom / single-molecule SFI which is essential for the coincidence capability of the ReMi detection.

[24] For P_0 = 2 bar, and A = 0.78, B = 0.35, C6/k_B = 8.3·10^{-43} cm^{6}K for oxygen [205]. The values (A, B, C6) for Ar, Xe and C_2H_2 could not be found in available literature.

[25] according to the *ideal gas law* $P = n\,k\,T$

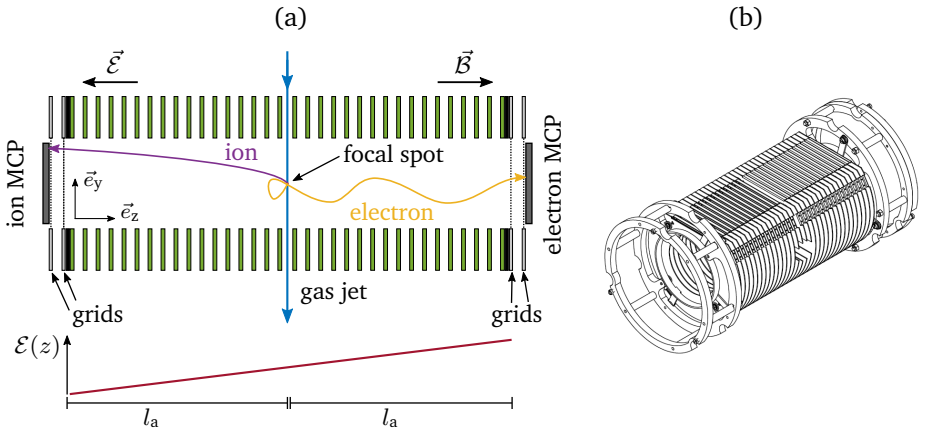

Figure 3.8: Electric field spectrometer. (a) The electric field is created by 34 metal electrode plates separated by 8 mm by applying a potential difference of both ends. Hence, the electrons and ions are separated and guided on their respective MCP detectors. Two representative trajectories of ion (purple) and electron(orange) are sketched. While the ion reaches the detector on a paraboloid trajectory, the electron needs to be guided onto a spiral (by applying a magnetic field) in order to reach its detector. **(b)** CAD plan of our spectrometer.

3.2.1.2 Spectrometer and Helmholtz coils

Upon ionization of the target species in the reaction volume all charged particle are guided onto two opposing large-scale and position-sensitive detectors (see next Sec. 3.2.1.3) by a combination of a static, homogeneous electric $\vec{\mathcal{E}}$ and magnetic $\vec{\mathcal{B}}$ field. The goal is to reconstruct the resulting trajectories of all particles on the basis of classic electrodynamics in order to deduce the initial momentum of the particles gained in the SFI process.

The electric field that accelerates the electrons ($-$) and ions ($+$) in opposing directions, is created in the *spectrometer* [sketched in Fig. 3.8 (a), and to scale in Fig. 3.8 (b)] which consists of a stack of 34 metal electrode plates each separated by 8 mm. The electric field is created by applying an appropriate potential $\pm U_{\text{sp}}$ on both ends of the spectrometer. The homogeneity of $\vec{\mathcal{E}}$ is assured by a chain of individual 180 kΩ resistors which electrically separate the individual potentials of the metal electrodes to create a constant voltage gradient throughout the whole spectrometer. The spectrometer itself measures a length of 269 mm. It is held on both ends by a support in order to be centered in the ReMi main chamber. Between the support and the spectrometer, a ring with a width of ∼10 mm is positioned at ∼9 mm from the spectrometer. The rings are individually biased in order to prevent the homogeneous electric field to be distorted by the grounded support. The effective spectrometer is closed by two high transmission copper wire meshes called *grids* positioned in two times 12 mm distance, to end with *grid2* just before the de-

tector. The grids are biased in order to extend the effective electric field[26] until just before the detector. This minimizes lensing effects on the charged particle trajectories which occur due to the high difference in potential between the spectrometer and the voltages applied to the detectors [207, Subsec. 4.1.2]. In the center of the spectrometer, a non-standard feature is implemented in our ReMi. In order to focus our laser beam relatively tight, an on-axis paraboloid is placed at its focal distance d_f away from the chamber center along the beam axis (x-Axis) on one side within the spectrometer plates. The focusing optic is mounted on an individual XY-translation stage. On the opposite side a $\sim 60\,\text{mm}$ diameter cut-out is made, where the laser beam propagates into the chamber. In order to keep the electric field homogeneous and to minimize distortions in the focal region, the gold-coated surface of the focusing optic is conditioned in three isolated sections which can be biased individually. Overall, all potentials of the spectrometer (spectrometer, ring, grid1, mirror for both sides) are biased by a *voltage divider* which can be supplied by one source. This voltage divider is designed to provide a constant voltage gradient throughout the distance between both detectors.

ReMis are usually operated at an electric field strength of $|\vec{\mathcal{E}}| = 1$ to $50\,\text{V/cm}$. Like this, momenta of ions can generally be detected in all three dimensions. Depending on its initial momentum, the ion is directed towards the detection on a parabolic trajectory [purple line in Fig. 3.8 (a)]. For high initial ion momenta, e.g. $\sim 100\,\text{a.u.}$ gained in dissociation reactions, higher field strengths can be applied to detect all fragments, yet with a sacrifice in momentum resolution. Dependent on the experimental resolution requirement this sacrifice can be taken.

Despite the fact the lower applied electric fields are sufficient to collect ion momenta in full 4π acceptance, electrons with its significantly lower mass will not reach the detector for most magnitudes of transverse momenta. Exemplarily, when applying a potential of $\Delta U = 25\,\text{V}$ to the electron side of our spectrometer, the 4π solid angular acceptance is ensured for electrons with an energy of only $0.4\,\text{eV}$ (using Eqs. 3.31 and 3.36 of Sec. 3.2.2.). For the experiments of this thesis, an acceptance of 3 to 4 order of magnitude higher is necessary. For that reason, an additional magnetic field is applied along the spectrometer axis (anti-collinear in our case, see Fig. 3.6) in order to restrict the transverse motion of the electrons to a radius limited by the initial transverse momentum of the electron and the magnetic field strength $|\vec{\mathcal{B}}|$ (see Eq. 3.22). The homogeneous magnetic field $\vec{\mathcal{B}}$ is generated by a pair of Helmholtz coils which consists of copper tubings with $n_{\text{coils}} = 24$ windings that are isolated by a plastic coating. Both coils have a diameter of $d_{\text{coil}} \sim 1400\,\text{mm}$ and are separated by $x_{\text{coils}} \sim 700\,\text{mm}$. For Helmholtz coils separated by the distance of half their diameter, the magnetic field magnitude is calculated as

$$|\vec{\mathcal{B}}| = \left(\frac{4}{5}\right)^{3/2} \frac{\mu_0\, n\, I}{x_{\text{coils}}} \text{ for } x_{\text{coils}} \overset{!}{=} \frac{d_{\text{coil}}}{2} \tag{3.22}$$

with the vacuum permeability μ_0 and the current I in the copper coils. The latter is provided by a power supply (*Bruker* B-SMPS) that provides a maximum current

[26] Usually grid1 is biased according to the linear voltage gradient of the spectrometer, while grid2 in principle can take any voltage value below the detector potential (magnitude).

of $I_{\text{max}} = 170\,\text{A}$ (with $U_{\text{max}} = 30\,\text{V}$). The copper coils are cooled by water flowing through them.

3.2.1.3 Position-sensitive multi-channel plate detectors

The distinctiveness of a ReMi as a momentum spectroscopy detection system is the coincidence capability of detecting all respective electrons and ion fragments in three dimensions. For optimal outcomes, large-scale and position-sensitive detectors are required that at the same time offer high efficiency, short dead times for multi-hit detection as well as good spatial and temporal resolutions. Our system achieves that with a combined detector system containing two stacked time-sensitive *multi-channel plates* (MCPs) interfaced with position-sensitive *delayline anodes* of the company *RoentDek* [212]. Both parts are explained in the following paragraphs.

Generally, it is technically challenging to detect single charged particles with high efficiency and temporal accuracy. In order to be detected and processed as an electric signal, the single particle signal needs to be amplified. This is done by the MCP which consists of a large array of microscopic hollow channels that serve as secondary electron multipliers. The setup of the MCP and its working principle is sketched in Fig. 3.9 (a). All channels of the MCP have a diameter of 25 µm and are embedded in a 1.5 mm thick silica disk equally spaced at a center-to-center distance of 32 µm. They all function as individual electron multipliers as their inside is coated with a semi-conducting material (e.g. GaAs) which serves as the electron multiplier. In our case, the whole MCP has a diameter of 80 mm (active diameter of $\lesssim 80\,\text{mm}$). The top and the bottom of the disk is coated with a metal to be able to apply a voltage difference of typically $\sim 1000\,\text{V}$ (per MCP). Upon impact of a charged particle on the channel wall, a secondary electron is released and accelerated towards the higher potential surface on a parabolic trajectory thereby gaining enough energy to bounce off the channel wall multiple times and again releasing electrons. This leads to an avalanche effect yielding a multiplication factor of $10^{3\,\text{to}\,4}$. In order to increase the efficiency of the MCP detector, the channels are tilted by an angle of 8° (all parameters are from [212]). Further, another increase of detection efficiency is achieved by stacking two MCPs together with the angles pointing in opposing directions as shown in Fig. 3.9 (a), better known as *Chevron* geometry. Thus, no charged particle can pass the MCP stack without hitting the wall at least once. Like this, initial charged particle impacts can yield an electron cloud of up to $10^{7\,\text{to}\,8}$ electrons which is detected as a small potential drop and hence electric pulse. The signal serves as timing information t_{MCP} which can be compared to a time zero obtained by the trigger t_{trigger} being the detected laser pulse on a photo diode (PD). The time-of-flight of the charged particle can hence be calculated as

$$t_{\text{oF}} = t_{\text{MCP}} - t_{\text{trigger}} + t_0 \tag{3.23}$$

with a constant global offset t_0.

In principal, an MCP provides a spatial information of the impact of the charged

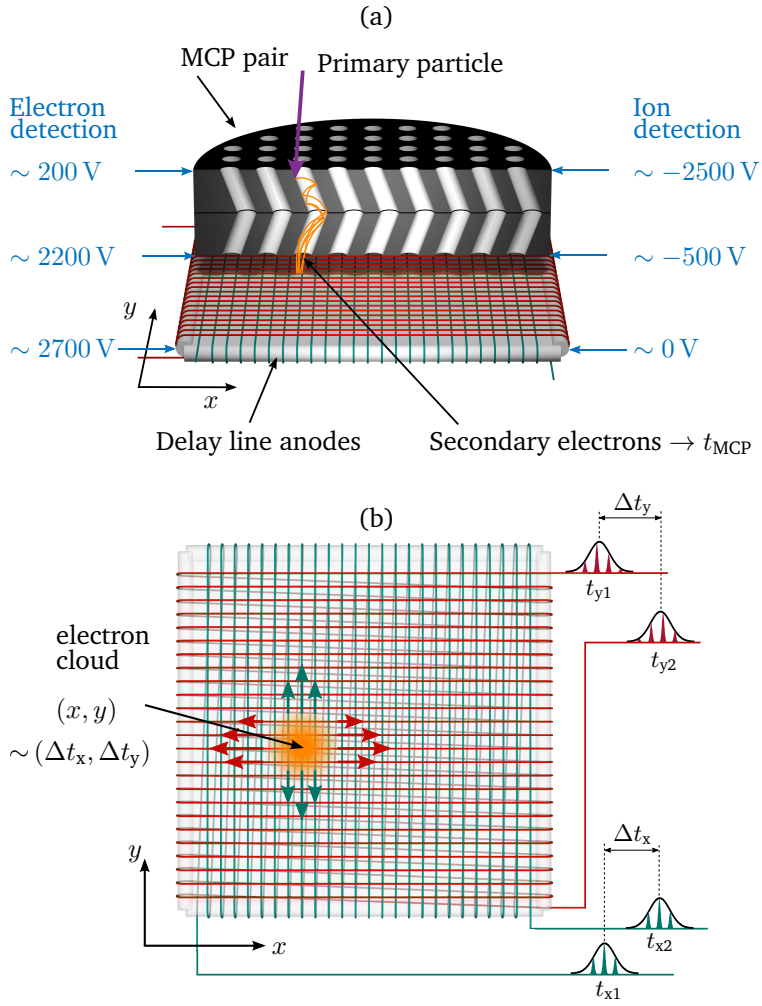

Figure 3.9: Time and position sensitive particle detection with MCP detector and delay line. The 3D sketches are a courtesy of Phillip Cörlin who used them similarly in his dissertation [139]. **(a)** An incoming, primary particle impacts the MCP creating a avalanche of secondary electrons that are detected as an electronic and further hit the delay line detector. The impacting particle reaches one of the micro channels that is positioned at an angle to the impact plane, so that a secondary electron can be created at the wall of the channel. The process repeats further down in the channel generating an avalanche of electrons triggering an electron signal on the back side of the MCP. **(b)** Two copper-wired delay lines (green and red) are coiled perpendicular to each other around an insulating plate. The electron avalanche creates electric signals in the grid traveling along both ends of each delay line. The temporal difference Δt between both detected signals of each line yields the offsets from the center of the delay line grid yielding the 2D coordinate on the detector.

particle since every channel works individually. Yet, the MCP itself does not contain a spatial read-out of the amplified electron pulse. Therefore, our detector is equipped with two perpendicularly oriented delay line anodes (DLAs). The working principle of a DLA is visualized in Fig. 3.9 (b). The delay line is a copper wire that is coiled around an insulating plate (ceramic) forming a grid of parallel, equidistant wires that are biased positively typically +200 V to +500 V compared to the rear end of the MCP stack. Hence, the secondary electron cloud impinges on the parallel wires creating a locally enhanced charge density which travels as pulsed signals to both ends of the delay line wire. The time difference of these detected signals on both ends indicate the spatial difference of the impinging electron cloud from the center of the windings. Since two crossed DLAs are used, the spatial position of the electron cloud can be determined as

$$x = v_\perp \left[(t_{\mathrm{x1}} - t_{\mathrm{MCP}}) - (t_{\mathrm{x2}} - t_{\mathrm{MCP}})\right] = v_\perp \left(t_{\mathrm{x1}} - t_{\mathrm{x2}}\right) , \tag{3.24}$$

$$y = v_\perp \left[(t_{\mathrm{y1}} - t_{\mathrm{MCP}}) - (t_{\mathrm{y2}} - t_{\mathrm{MCP}})\right] = v_\perp \left(t_{\mathrm{y1}} - t_{\mathrm{y2}}\right) , \tag{3.25}$$

with the propagation speed $v_\perp$ of the electric signals in the copper wire. Of course, multiple wires are hit at the same time by the ideally Gaussian distributed electron cloud resulting in set of equally spaced electric pulses with a Gaussian envelope. The center of the envelope serves as the appropriate time signal $t_{\mathrm{xi/yi}}$ as depicted in Fig. 3.9 (b). The sum of the associated time signals $t_{\mathrm{x/y,sum}} = t_{\mathrm{x1/y1}} + t_{\mathrm{x2/y2}}$ is constant since the copper wire has a fixed length. These sums can be used as a check for true position signals in the data analysis as described in Sec. 3.2.2.2.

3.2.1.4 Signal processing and data acquisition

Before being able to calculate the momentum vectors $\vec{p} = (p_{\mathrm{x}}, p_{\mathrm{y}}, p_{\mathrm{z}})$ of the charged particles, the electric signals as detected in the MCP/DLA combination for both ions and electrons need to be converted into relative time signals which then can be digitized to be derived into the necessary t_{oF} and respective impact position $(x_{\mathrm{i}}, y_{\mathrm{i}})$ for each particle. This procedure involves a few individual steps for both the ion and electron detection side.

A coupling box[27] converts the high voltage signals of the MCP and both DLAs to lower voltage signals that can be treated in the "counting cards". In the actual DLA setup, every copper wire is coiled twice for each direction around the plate. Both wires, called *signal* and *reference*, are insulated from each other, so that the detected pulses can be cross-checked electronically. Only if electric signals from both the signal and the reference at the respective ends of the wire are detected in the coupling box, two overall electric signals $t_{\mathrm{x1/y1}}$ and $t_{\mathrm{x2/y2}}$ for both directions are sent to the counting cards.

After the coupling boxes, five signals (t_{MCP}, t_{x1}, t_{y1}, t_{x2}, t_{y2}) are send to the counting electronics, respectively for each detector. Since each of the signals of successive

[27] The coupling boxes were home-built in the electronic workshop at the MPI-K in Heidelberg, Germany.

ionization events can arrive in different condition in terms of signal height, width or overall shape, they need to be pre-conditioned in order to be comparable in a reliable manner. Therefore, the signals are first amplified by a fast, wide-bandwidth amplifier (*Ortec - FTA820A*). Then they are processed by a *constant fraction discriminator* (CFD, *RoentDek - CFD4b*) which generates a constant time stamp for all incoming pulse forms. The way the CFD works is that it creates an attenuated, inverted replica of the incoming pulse and delays that smaller pulse by a fraction $F_{\textbf{threshold}}$ of its rise time acting as a threshold. Afterwards, both the original signal and the attenuated and inverted pulse are overlayed leading to a zero-crossing at the delay. Here a NIM-signal[28] is triggered for all incoming pulses equally. With the aid of a CFD, all incoming signals independent off signal height are processed equally leading to a reduced timing jitter between each other.

After the CFD standardization, all ten signals plus the time zero signal t_{PD} of the laser pulses detected with a PD are fed into a *time-to-digital converter* (TDC) card (*C.A.E.N. - V1290N*) where they are digitized in single channels. The TDC has a minimum time resolution of 25 ps (effectively it is around $\sim$100 ps depending on calibration [206]), a maximum readout window of $t_{\mathrm{w,max}} = 52\,\mu\mathrm{s}$, which can be set by the user, and a dead time of 5 ns which is critical for multiple-hit detection. The operation of the TDC is the so-called *trigger matching mode*, which means that upon a received *trigger*, the TDC reads out backwards in time all detected signal data that were previously recorded for the time window t_{w} set by the user. Hence, the effective and positive time signal can be calculated from the difference between any detector signal and the PD signal t_{PD} as the latter is taken as a common time zero reference. The TDC operation is controlled via a VME bus[29] which navigates the readout and the data storage in a *listmode* file before sending the data to a PC via an MBS[30] stream server (information about the ReMi electronics is collected from [206]). The transferred data can then be streamed by the MBS system directly to the analysis software *Go4* to monitor the data acquisition online (see Sec. 3.2.2).

Generally, the laser pulse as detected with a PD is taken as the trigger to initiate the TDC read-out. In the process, all charged particles should conveniently be detected between two subsequent trigger events in order to extract the real time of flight. Yet, this triggering scheme leads to timing complications when detecting charged products of SFI initiated by *high repetition rate laser sources*. When the time between subsequent trigger signals Δt_{PD} is smaller then the flight time of the ions $t_{\mathrm{oF,ion}}$ that usually have large flight times due to their mass, the detected flight times are reduced since they will be allocated with a new triggering signal. The repetition rate of our mid-IR OPCPA source is $f_{\mathrm{RR}} = 160\,\mathrm{kHz}$ which corresponds to a clock time / clock window of $t_{\mathrm{RR}} = \Delta t_{\mathrm{PD}} = 6.25\,\mu\mathrm{s}$. When choosing a *low* extraction field of $|\vec{\mathcal{E}}| = 1\,\mathrm{V/cm}$ to $3\,\mathrm{V/cm}$, the ion time of flight for e.g. an argon cation Ar^+ results as $t_{\mathrm{oF,Ar+}} \approx (36\text{-}21)\,\mu\mathrm{s} > t_{\mathrm{RR}}$ as sketched in Fig. 3.10 (a). When triggering on the PD signal, the detected time of flight for the argon ions would result as

[28] *nuclear instrumentation module standard*
[29] *Versa Module Eurocard-bus - a data communication system developed by Motorola.*
[30] *multi-branch system*, a framework for experimental data acquisition

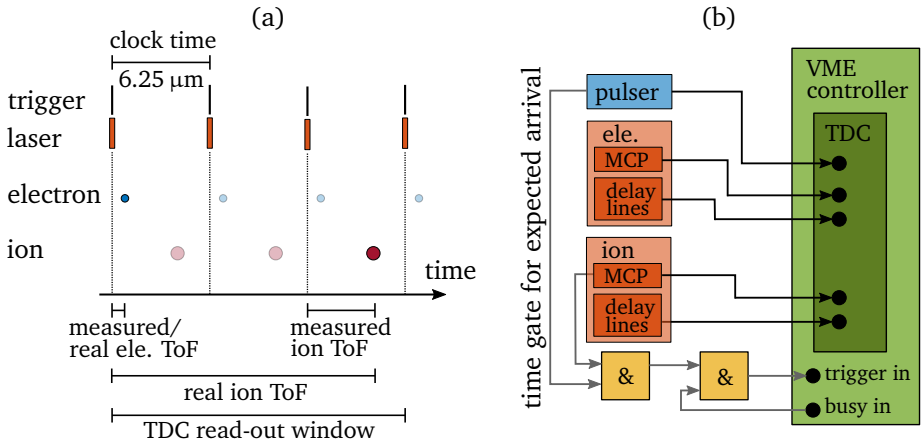

Figure 3.10: Timing and electronic trigger scheme. (a) In coincidence detection, an ion and electron are ideally detected directly after its triggering laser pulse. Using high repetition rate laser sources, the ion ToF can be larger the clock time between two subsequent laser pulses. Therefore we use a triggering scheme, as shown in **(b)**, where a detected ion hit after the expected laser pulser triggers the VME controller to read-out a user-set TDC window covering both the real ion and electron ToF. A detailed triggering scheme is shown in the appendix (see the detailed scheme in App. D).

$t_{\mathrm{oF,det}} = \mathrm{mod}_{6.25}(t_{\mathrm{oF,Ar+}})$. This yields complications especially for the coincidence information with the associated electrons of the detected ions, since the flight time of electrons is on the order of tens of ns, e.g. here $t_{\mathrm{oF,ele}} \approx (134\text{-}77)$ ns. Hence, electrons are always detected together with their respective laser trigger. In order to solve this issue, we use an electronic scheme that triggers on detected ions. As the flight time of the ions can be estimated for set measurement conditions (set $\vec{\mathcal{E}}$, with Eq. 3.30), the backwards read-out capability of the TDC in trigger matching mode is set such that all preceding clocking windows of $\Delta t_{\mathrm{n,PD}} = n \cdot t_{\mathrm{RR}}$ are included up until the window initiated by the ion related pulse trigger that includes the detected and corresponding electron count(s). The triggering scheme is sketched in Fig. 3.10 (b). Via a combination of electronic AND-circuits (see the detailed scheme in App. D) the detected ion is assigned to its current clock window $t_{\mathrm{n,PD}}$ to create a NIM signal at the end of that current clocking channel. This signal serves as the trigger for VME controller to read-out the TDC for a user-set time window $t_{\mathrm{w}} = \Delta t_{\mathrm{n,PD}}$ which hence includes both the ion and the electron related signals.

3.2.2 Data analysis

The momentum vectors of all charged particles resulting from strong-field induced ionization and fragmentation events need to be derived from the detected time signals for events as acquired in experiments within this PhD thesis. In order to handle the large amounts of data, an automated data analysis routine is needed.

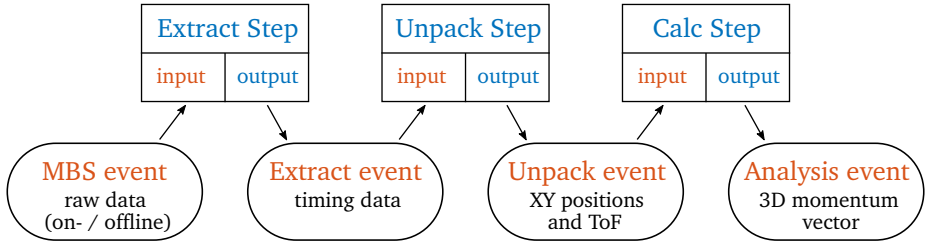

Figure 3.11: GENERiC signal flow chart. Analysis steps of the automatized program treating the raw data towards extracting the 3D momentum vector. The code is explained in detail in [206].

In our case, data processing is performed with the general analysis code for reaction microscopes *GENERiC* which was developed by Arne Senftleben (et *al.*) at the Max-Planck-Institut für Kernphysik (MPIK, Max Planck Institute for Nuclear Physics, Heidelberg, Germany) within his PhD thesis [206]. The GENERiC code can be hosted and executed in the framework *Go4*[31] which is an open-source, object-oriented, real-time, *online / offline* data analysis graphical user interface (GUI) that can integrate the MBS streaming server and generally organize a data stream into a multi-step analysis. Thereby, Go4 provides a large set of C++ classes that extends the *ROOT* framework which was developed at CERN as a data analysis and code developing environment for particle and high energy physics.

The GENERiC code is universally applicable to process all data signals extracted from the TDC of the ReMi electronics so that the momentum vector of the charged particle and so its physical attributes can be translated independent of the physical process. In Fig. 3.11, the signal flow chart of the GENERiC analysis code is sketched as it is used for the analysis of the data of this thesis. The pipeline consists of three main processing steps: the *extract* step, the *unpack* step and the *calc* step. As mentioned above, an event in the MBS contains the raw time stamps of the signals arriving from the MCP, the DLAs and the PD corresponding to one particle hit on either ion or electron detector.
In the extract step, the data of the raw events, that come directly from the main buffer of the MBS (online) or from a data file (offline), is converted to basic event objects. Like this, every TDC channel can be plotted as histograms as a function of their time bins/stamps. Those are useful for calibration of the experiment i.e. for setting the thresholds of the CFDs for all channels equally and at the same time reducing noise in all channels.
In the unpack step, the raw data of the TDC channels are translated into the ToF and position information of the incident particle on the detector by comparing the time stamp of each TDC signal to the time stamp of the reference signal of the PD (channel 0 in Fig. 3.10). Hence, ToF and XY position are calculated with both Eq. 3.23 and Eqs. 3.24, 3.25, respectively.
In the calc step, two subsequent calculation steps are performed. First, the ion and

[31] developed by the GSI Helmholtz Centre for Heavy Ion Research (German: GSI Helmholtzzentrum für Schwerionenforschung)

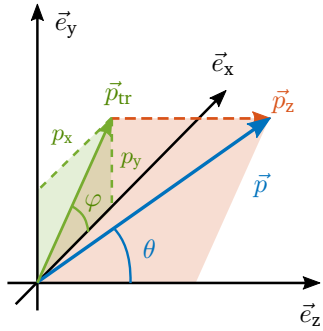

Figure 3.12: Convention of coordinate system. The coordinate system in the ReMi yielding momentum components and angles of the charged particle momentum vector as used throughout this work. The $+\vec{e}_z$ axis lies along the electron side of the spectrometer, the $-\vec{e}_y$ axis lies along the gas jet expansion direction and $\vec{e}_x$ yields the propagation direction of the laser beam.

electron momenta in three dimensions are calculated by tracing back the trajectory of the particle within the static electric and magnetic fields of the ReMi. The formulas for these kinematic conversions are described in the next section 3.2.2.1. All other physical characteristics of interest, such as the kinetic energy or the solid angle distribution of ionization are derived from the momentum vector. Then, the electron momentum vector $\vec{p}_{ele}$ is associated with its corresponding ion momentum vector $\vec{p}_{ion}$ via momentum conservation. Details are explained in Sec. 3.2.2.2. Like this, individual ionization and fragmentation channels can be selected and analyzed, yet also for false coincidences get discarded which decreases the effective event rate of the experiment in coincidence.

3.2.2.1 Momentum reconstruction

The principle idea of the ReMi is the detection of the 3D momentum vector $\vec{p}$ of charged reaction products. Hence, the key analysis step is the reconstruction of $\vec{p}$ from the experimentally determined ToF and the impact position (x,y) of the detected particle. The necessary analysis is part of the *calc* step of the GENERiC code, and is described in the following.

The convention of the coordinate system used to describe the momentum vectors in this thesis is shown in Fig. 3.12 and is expressed as follows

$$\vec{p} = \begin{pmatrix} p_x \\ p_y \\ p_z \end{pmatrix} = p \cdot \begin{pmatrix} \sin(\Theta)\,\cos(\phi) \\ \sin(\Theta)\,\sin(\phi) \\ \cos(\Theta) \end{pmatrix} = \begin{pmatrix} p_{tr}\,\cos(\phi) \\ p_{tr}\,\sin(\phi) \\ p_z \end{pmatrix} = \begin{pmatrix} \vec{p}_{tr} \\ p_z \end{pmatrix} \tag{3.26}$$

with the magnitude of the vector $p = |\vec{p}|$, the polar Θ and azimuthal ϕ angle in spherical coordinates, as well as the transverse momentum $p_{tr} = \sqrt{p_x^2 + p_y^2}$ in cylindrical coordinates. Since both the static electric $\vec{\mathcal{E}}$ and the magnetic $\vec{\mathcal{B}}$ fields are

aligned along the spectrometer axis $\vec{e}_z$, it results that the ToF and hence the momentum component p_z solely depend on $\vec{\mathcal{E}}$. The transverse components of the momentum vector $\vec{p_{tr}}$ are influenced by $\vec{\mathcal{B}}$ (and $\vec{\mathcal{E}}$ via the ToF). The overall motion of the charged particles in the collinear static fields can be described by the Lorentz force

$$m\,\ddot{\vec{r}} = \vec{F}(\vec{r}) = q\left(\vec{\mathcal{E}} + \dot{\vec{r}} \times \vec{\mathcal{B}}\right) = q\left[\begin{pmatrix}0\\0\\\mathcal{E}_z\end{pmatrix} + \begin{pmatrix}\dot{x}\\\dot{y}\\\dot{z}\end{pmatrix} \times \begin{pmatrix}0\\0\\\mathcal{B}_z\end{pmatrix}\right] \tag{3.27}$$

with the mass m and the charge q of the particle. For the condition $\vec{\mathcal{E}} \parallel \vec{\mathcal{B}}$, analytical solutions can be derived from Eq. 3.27 for both the motion of the particle longitudinal and transverse to the spectrometer axis $\vec{e}_z$.

Longitudinal momentum. The momentum component along the $\vec{e}_z$ axis of the spectrometer can be calculated by solving the differential equation along the third vector component of Eq. 3.27. With the assumption that the electric field $\mathcal{E}_z = \Delta U \,/\, l_a$ yields from the potential difference along the *acceleration length* $z = l_a$, the following equation results

$$l_a = \frac{1}{2}\,\frac{q\,\Delta U}{m\,l_a}\,t_{oF}^2 + \frac{p_{z,i}}{m}\,t_{oF} + z_0\ , \tag{3.28}$$

where $p_{z,i}$ is the *initial momentum of the charged particle* in the reaction volume, which is the measurement parameter of interest, and z_0 is the position of the reaction volume. The spectrometer of many ReMis can be equipped with an additional section with no applied electric field which is located after the acceleration section and before the detector. This *drift region* compensates for the fact that particles from the same reaction volume are detected with different ToFs because the they are ionized at different positions throughout the wide cross-section of the gas jet (in xz - plane) [63][32]. In our case, no drift region is implemented since we generally focus our laser beam to a relatively small reaction region [see Fig. 3.4 (a), $w_0 \approx 7\,\mu m$] compared to the jet diameter at the focal spot of $\sim 1.4\,mm$. For the sake of completeness, a small effective drift region could be assumed for the region between the end of the spectrometer until the detector (including ring, grid1 and grid2) where no detector plates are given. The equation of motion 3.28 can be solved for the drift region as

$$l_d = \frac{q\,\Delta U}{m\,l_a}\,t_{oF,a}\,t_{oF,d} + \frac{p_{z,i}}{m}\,t_{oF,d}\ . \tag{3.29}$$

Hence, the overall time-of-flight can be derived as [206]

$$t_{oF}(p_{z,i}) = t_{oF,a} + t_{oF,d} = m \cdot \left(\frac{2\,l_a}{\sqrt{p_{z,i}^2 + 2\,m\,q\,\Delta U} \pm p_{z,i}} + \frac{l_d}{\sqrt{p_{z,i}^2 + 2\,m\,q\,\Delta U}}\right)\ , \tag{3.30}$$

[32] The optimal compensation is achieved in the *time-focusing condition* $l_d = 2\,l_a$, when the drift region measures double the length of the acceleration region.

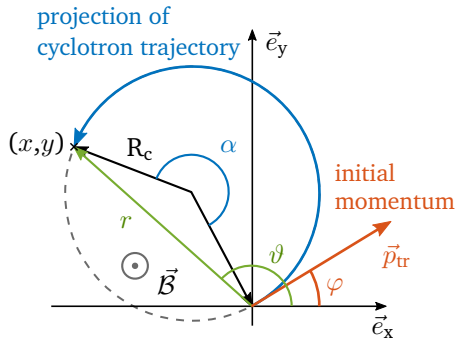

Figure 3.13: Electron cyclotron trajectory. The spiraling electron trajectory is projected onto the xy - plane of the MCP detector. The coordinate $(x,y) = |\vec{r}|$ yields the spiral radius and the cyclotron frequency or vice versa. The plot is adapted from [63].

considering the ionization is occurring at $(x_0,y_0,z_0) = 0$. The "$\pm$" sign in the denominator of the first part of Eq. 3.30 refers to particles that are accelerated in $\pm\vec{e}_z$ direction. In order to calculate the initial longitudinal momentum of the charged particle for a given t_{oF}, Eq. 3.30 has to be solved for $p_{z,i}$ which is analytically not possible. In the GENERiC code, this is solved numerically via the *Newton's method* (see [206, App. B]). With no drift zone $l_d = 0$ in our ReMi, Eq. 3.28 or 3.30 yield an analytical solution for the longitudinal momentum

$$p_{z,i} = -\frac{1}{2}\frac{q\,\Delta U}{l_a}\,t_{oF} + \frac{m\,l_a}{t_{oF}} \tag{3.31}$$

which clearly shows that the longitudinal momentum can directly be derived from the time-of-flight for specific particle and ReMi conditions. Moreover, a ReMi can easily be used for *ion mass spectroscopy* to identify different particle species and charges which is especially important when dealing with molecules that can fragment in various moieties. Generally, the center of a peak in a ToF spectrum relates to the ions with no initial momentum $p_{z,i} = 0$ (for linear laser polarization). Hence, Eq. 3.31 can be rearranged to

$$t_{oF} = \sqrt{\frac{2\,l_a^2}{\Delta U}\frac{m}{q}} \tag{3.32}$$

which reveals the dependence of the time-of-flight on the square root of the *mass-charge ratio* of the ion $\sqrt{m/q}$.

Transverse momentum. The initial transverse momentum $\vec{p}_{tr,i} = (p_{x,i},p_{y,i})$ of the charged particle perpendicular to the $\vec{e}_z$ axis of the spectrometer yields a motion in the xy plane that is solely determined by the magnetic field $\vec{\mathcal{B}}$ leading to a spiral motion on its way towards the detector. Here, the absolute value of $|\vec{p}_{tr,i}| = p_{tr,i}$ is not changed by the magnetic field, yet its direction. $\vec{p}_{tr,i}$ can be derived on the basis of the *cyclotron motion* of the charged particle, which is sketched in Fig. 3.6 as a

yellow trajectory, and the impact position on the detector. The angular or cyclotron frequency is defined as

$$\omega_c = \frac{2\,\pi}{t_c} = \frac{|q|\,\mathcal{B}_z}{m} \tag{3.33}$$

with the cyclotron period t_c. In Fig. 3.13, a projection of a typical cyclotron motion onto the detector plane is sketched in order to illustrate how to reconstruct the transverse momentum vector $\vec{p}_{tr,i}$ (red arrow). Here the angle under which the particle has moved around the cyclotron axis is defined as $\alpha = \omega_c\,t$. The radius of the cyclotron motion can be determined via geometrical considerations as

$$R_c = \frac{r}{2\,|\sin(\alpha/2)|}\,, \tag{3.34}$$

where the distance of the final position of the particle trajectory (x,y) to the MCP center (0,0) is defined as $r = |(x,y)|$. On the other hand, the radius of the cyclotron motion can also be derived from the equality of the Lorentz force with the centripetal force

$$R_c = \frac{p_{tr,i}}{\omega_c\,m}\,. \tag{3.35}$$

Hence, the transverse momentum of the charged particle can be derived from Eq. 3.34 and 3.35 as

$$p_{tr,i} = \frac{\omega_c\,m\,r}{2\,|\sin(\omega_c\,t/2)|}\,. \tag{3.36}$$

The individual momentum components $p_{x,i}$ and $p_{y,i}$ can be derived with $p_{tr,i} = \sqrt{p_{x,i}^2 + p_{y,i}^2}$ and the emission angle $\varphi = \arcsin(p_{x,i}/p_{y,i})$. The emission angle itself is related to the polar angle ϑ of the impact position on the DLA [(x,y) = (r,ϑ)] and hence can be derived as [63]

$$\varphi = \vartheta - \frac{\mathrm{mod}_{2\pi}(\omega_c\,t)}{2}\,. \tag{3.37}$$

The expression for the transverse momentum in Eq. 3.36 is generally valid for all charged particles detected with the ReMi. Earlier in this section, it was mentioned that the magnetic field was mainly integrated in the ReMi to increase the transverse momentum acceptance for particles with low masses, i.e. electrons. This can be clarified when examining the equation for heavy particles like e.g. ions. For $m \gg 1$, the cyclotron frequency (see Eq. 3.33) results in small values. Using the rule of l'Hôspital and the small-angle approximation, Eq. 3.36 can be simplified to

$$\lim_{\omega_c \to 0} p_{tr,i} = \frac{r\,m}{t}\,. \tag{3.38}$$

Thus, the transverse momentum of ions can be expressed as

$$\vec{p}_{tr,i} = \begin{pmatrix} p_{x,i} \\ p_{y,i} \end{pmatrix} = \frac{m}{t_{oF}} \begin{pmatrix} x \\ y \end{pmatrix} \tag{3.39}$$

considering $t = t_{oF}$. This also results from solving the equation of motion 3.27 for heavy particals where the influence of $\mathcal{B}_z$ can be considered small.

3.2.2.2 Momentum calibration

The key to extract momentum spectra at high precision with a ReMi is the accurate knowledge of all involved experimental parameters. This includes the magnitude of the applied fields $\mathcal{E}$ and $\mathcal{B}$, the spectrometer dimensions as in l_a and l_d, the detector geometry, the time shift introduced by electric cable lengths or trigger mismatches, the gas jet velocity, and others. Since all of these parameters can only be determined up to certain accuracy partially insufficient for precise calibration, specific experimental and physical features and insights need to be taken into account in order to accurately calibrate the reconstructed momenta of ions and electrons. The required calibration steps are shortly explained in this section. For every dataset with different experimental parameters like e.g. laser parameters, target preparation, etc., the procedure needs to be done individually. This is related to the fact that laser beam's pointing and size can alter the position of the focus, so that the SFI process takes place at a slightly different position hence changing the acceleration distances of the resulting charged particles. This alteration needs to be compensated for in the calibration in order to make different experiments comparable.

The first step of calibration should be the identification of the ion species to be investigated. This can be achieved by ion mass spectroscopy on the basis of the typical time-of-flight spectrum (see Sec. 3.2.2.1). As an example, the ToF distribution (extraction field $\mathcal{E} = 2\,\mathrm{V/m}$) of a measurement on SFI of xenon atoms with our mid-IR source is plotted in Fig. 3.14 (a). The ToF spectrum is plotted for the maximum TDC read-out window of $t_{w,max} = 52\,\mu s$ as discussed in Fig. 3.10. The main peaks resemble the different Xe isotopes (shown in the inset) with the maximum of each peak corresponding to the ToF of the respective ion with no initial momentum. The laser pulse that triggered the ionization of the Xe isotopes interacted with the atoms at time zero. Further, the intermediate seven replicas of the peaks of the Xe isotopes are artefacts that are separated by $n \times 6.25\,\mu s$. They were triggered by preceding laser pulses. In literature they are sometimes referred to as "ghost peaks" [213]. By defining a condition for a specific ToF window, the desired ion target can be selected. On the other hand, the electron ToF distribution only yields one mayor peak as plotted in Fig. 3.14 (b) so that the whole peak can be selected via another condition. The small peak in the electron ToF spectrum at around 240 ns corresponds to an artefact of the measuring process and will be rejected automatically by the coincidence condition applied in the following.
Next, the selected ion and electron peaks are transformed to momentum space as explained before in Sec. 3.2.2.1. The resulting longitudinal momentum distributions need to be centered around $p_z = 0$ per definition, which can be achieved by adjusting the involved parameters (ΔU and l_a) of Eq. 3.31. With two variable parameters for one equation to solve, the system is overdetermined. This means that when changing one parameter the result of the momentum distribution can be compensated by the other one.

Over-determination is a general issue in the momentum calibration of ReMi results. Best practice here is usually to fix one parameter at an estimated value close

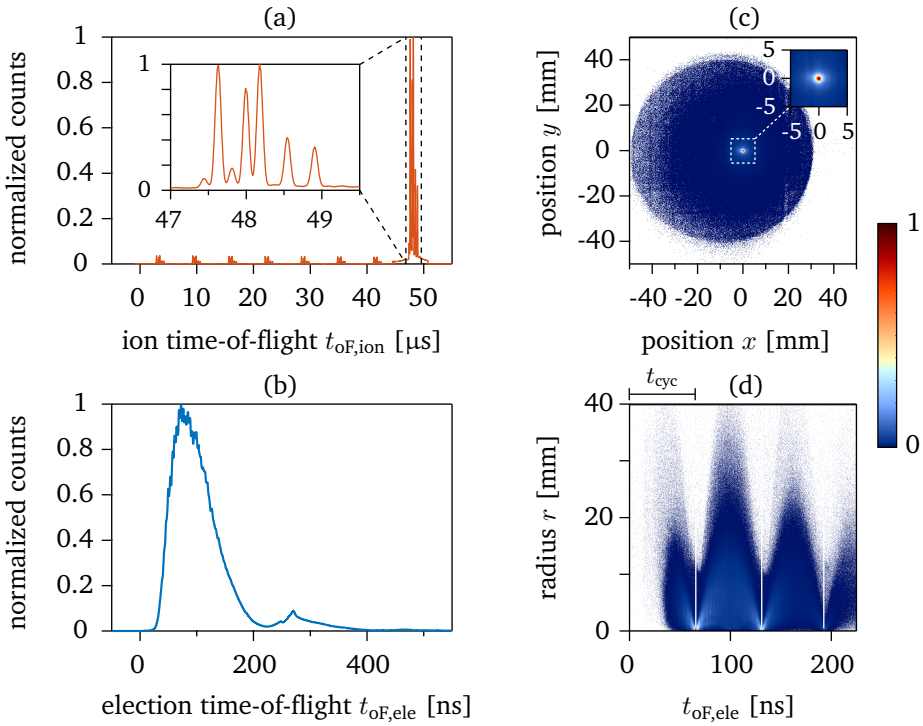

Figure 3.14: Analysis steps to calibrate experimental conditions (Part I). Time and position frame. **(a)** The ion time-of-flight spectrum allows to select a condition for the ion (fragment) of interest similar to mass-spectroscopy. The inset shows the individual Xe isotopes of this exemplary data set of SFI of Xe atoms with mid-IR pulses. **(b)** The electrons detected for all SFI events yield an electron ToF distribution along the spectrometer axis ($\vec{e}_z$). The transverse electron spread as detected by the delay-line anodes is displayed in Fig. **(c)**. A shift from the center of the MCP can be compensated in the analysis. **(d)** The radial distribution of the detected electrons as a function of time yields the magnetic field nodes or singularities after $n \times t_{\mathrm{cyc}}$ which are visible for $r \to 0$ where the electrons hit the same spot of the MCP.

to what can be expected in the experiment (e.g. the voltage ΔU displayed on the power meter) to then vary the other parameter (e.g. the acceleration length l_{a} since it is difficult to determine the exact focal spot position). There is usually no rule of which of the over-determined parameters to fix in the analysis since the resulting calibration results equally. The resulting longitudinal momentum distributions for Xe^+ ions and electrons are plotted in Fig. 3.15 (a).
In order to calibrate the transverse momentum components the respective distributions need to be centered around $p_{\mathrm{x,y}} = 0$, too. Therefore, the size of the detectors resulting from the DLA signals need to be scaled in the analysis and furthermore, the spatial distribution of the detected particles that is Gaussian for linear polarization perpendicular to the detector plane, needs to be centered by applying x- and

y-shifts as calibrations. In Fig. 3.14 (c) the xy-distribution of the electron detector is shown exemplarily. As the center of the circular distribution of the electrons hitting the MCP detectors is slightly shifted "southeast" in this example, x- and y-shifts are computationally applied. The center of the XY distribution is plotted in the inset of Fig. 3.14 (c). Since the electrons move on spiral trajectories towards the detector, it needs to be determined in which round trip N of the cyclotron cycles $l \times t_{\mathrm{cyc}}$ they impact on the detector after the flight time t_{oF}. This behavior entails a characteristic feature of ReMi detection systems that needs to be considered. When t_{oF} of the impacting electrons is a multiple integer of the cyclotron period t_{c}, all electrons impact on the MCP at the same position regardless of their initial transverse momentum $\vec{p}_{\mathrm{tr}}$ [63]. This point is shown in the inset of Fig. 3.14 (c), and depicts a singularity in momentum space. This is illustrated in Fig. 3.14 (d) where the radial position $r = \sqrt{x^2 + y^2}$ of the impact on the detector is plotted as a function of time. Here, the radius r from the center of all electrons minimizes at multiples of the cyclotron period t_{c}, so that t_{c} can be directly determined from the graph. On the basis of this information, the magnetic field magnitude $\mathcal{B}$ can be calibrated. By getting an exact measure of t_{c}, the magnetic field magnitude $\mathcal{B}$ results via Eq. 3.33. The correct $\mathcal{B}$ field value leads to a calibrated initial transverse momentum information of the detected electrons which is characterized by a 2D (super-)Gaussian distribution p_{y} over p_{x} as shown in Fig. 3.15 (b) (considering horizontal laser polarization along $\vec{e}_{\mathrm{z}}$).

After calibration of both longitudinal and transverse momenta of ions and electrons individually, the coincidence between both species are compared and sorted according to momentum conservation. Considering the sum of both ion and electron momentum, a well calibrated experiment yields a sharp peak around $\mathrm{p_{z,sum}} = 0$ as plotted in Fig. 3.15 (d). To envoke the momentum coincidence condition, only events need to be chosen that correspond to the sharp peak as marked by the green background in Fig. 3.15 (d). The position and width of the sum distributions can be optimized by fine-tuning the individual parameters. Usually, a perfectly centered $\mathrm{p_{z,sum}}$ distribution is only achieved for an equally centered electron *or* ion distribution due to disparities in the setup. In our case, we optimize with respect to the electron distribution which means that the ion distribution can be slightly off-center which can be corrected for by a overall shift of the momentum spectrum being equal to a scaling of the ToF spectrum $t' = a \cdot t$ (with $\mathrm{a} \sim 1$) [203, Sec. 4.2.3]. In our present example, the longitudinal electron momentum distribution is slightly thinner than the respective ion distribution on one side of the spectrum which explains the slight asymmetry in the sum spectrum in Fig. 3.15 (d).
Finally, the momentum axis can be scaled linearly as $\mathrm{p' = b \cdot p}$ (with $\mathrm{b} \sim 1$) to correct for last aberrations due to inhomogeneities of the static fields in order to arrive at an absolute calibration of the full 3D momentum space [203, Sec. 4.2.3]. Ideally, physical "orientation points", like e.g. ATI peaks/rings, can be used to scale the absolute calibration.

Many photo ionization experiments yield a cylindrical symmetry around the linear polarization axis. Hence, when the laser field is polarized along the $\vec{e}_{\mathrm{z}}$ axis, all momenta $\vec{p}$ in cylindrical coordinates can be simplified and integrated around

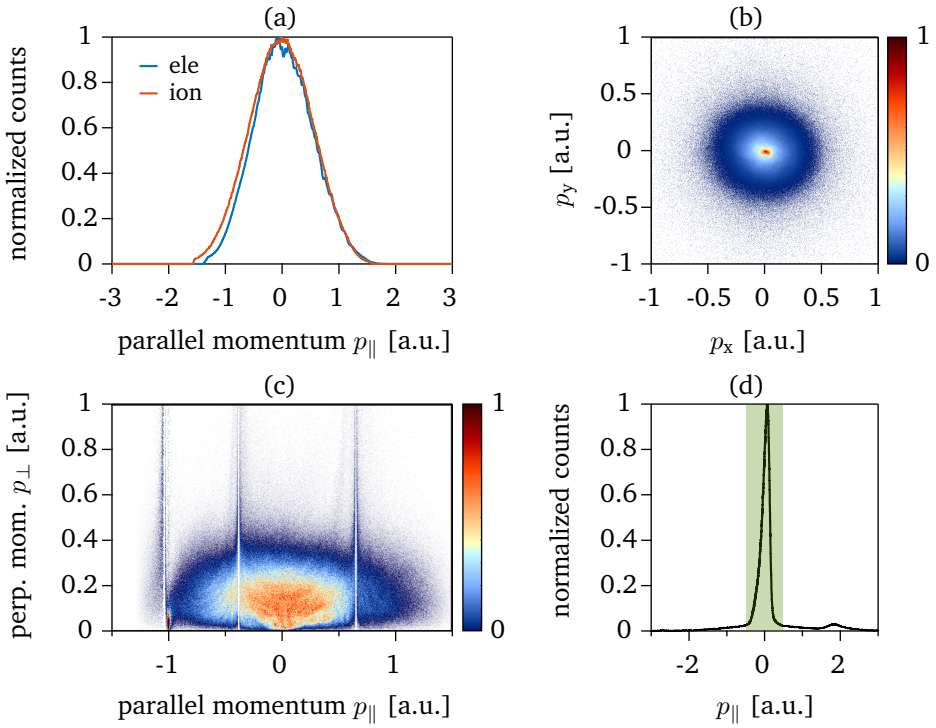

Figure 3.15: Analysis steps to calibrate experimental conditions (Part II). Momentum frame. **(a)** The momentum along the spectrometer axis for both the ions (red) and electrons (blue) is calculated from their respective ToF distributions. For horizontal polarization $\vec{\mathcal{E}} \parallel \vec{e}_z$ the component is called $p_{\parallel}$ within this thesis. **(b)** The transverse momentum distribution is calculated from the radial spread in the XY plane of the delay-line anodes. The full 3D momentum information is plotted in **(c)** in cylindrical coordinates integrated over the azimuthal symmetry around φ. **(d)** The events are selected in momentum coincidence where the momentum sum of electrons and ions yields zero (blue shaded area).

the azimuthal angle ϕ leading to an effective 2D vector. In Fig. 3.15 (c), the full electron momentum space is plotted in cylindrical coordinates after integrating around the azimuthal symmetry axis with $p_\perp = p_{\text{tr}} = \sqrt{p_x^2 + p_y^2}$ over $p_{\parallel} = p_z$. The data are extracted in full momentum coincidence and corresponds to three Xe isotopes ($^{129}Xe^+$, $^{131}Xe^+$, $^{132}Xe^+$). The nodes are clearly visible in the full momentum map and slightly distort the spectrum close by. In this specific example the distribution closely around the third node at $p_{\parallel} \sim$-1 a.u. is not fully symmetric which can happen due to inhomogeneities of the magnetic field distribution. Depending on the magnitude of the $\mathcal{B}$ field, the influence of these inhomogenities on the momentum distribution can vary, and in general have less impact for higher $\mathcal{B}$ fields[33].

[33] private conversation with Arne Senftleben and Phillip Cörlin at the MPI-K in Heidelberg, Germany

3.2.2.3 Particle coincidence

The probability to detect n particles in coincidence with a ReMi scales with $p = \epsilon^n$ [214] where ϵ is the detection efficiency of the ion or electron detection which scales between 40 % and 60 % depending on the nature of the incoming projectile and the detection quality [215]. Exemplarily for the data shown in the previous section of the momentum calibration, the probability to detect both (single) SFI products being e.g. the Xe^+_{132} ion and its corresponding electron in coincidence drops to $p = 0.5^2 = 25$ % (assuming a 50 % average detector efficiency [214]). That means that 75 % of all "clean events" [203] are discarded for the cases where only one Xe atom is ionized per laser pulse and a minimum of false coincidences can be assumed. This is crucial to measurement statistics which define the extraction error.

In the data analysis, there are two ways to impose coincidence conditions on corresponding ion-electron, ion-ion, electron-electron or fragmentation events. The common and more accurate way is to compare the momentum vectors of the regarded particle pairs (or triplets, quartets, etc.) detected for the same laser pulse (trigger) so that their momentum sum vanishes. This momentum coincidence constraint yields the cleanest view on a SFI or fragmentation event, yet is a strong constraint with regard to statistics. As high statistics are key for sufficient signal-to-noise ratios in any measurement, a second possibility is to restrict the coincidence condition only to the fact that the regarded particle pair is detected for the same laser pulse without imposing the momentum coincidence argument. Hence, the full momentum conservation constraint is "loosened" for the benefit of extracting with higher statistics in overall detected events. This analysis procedure is commonly used for the detection of processes with lower cross-sections (see e.g. [203, Ch. 6.2 & 7.4]) and in experiments where the rate of false coincidences is generally kept at low level in the experiment, i.e. ion count rate significantly lower than the repetition rate to assure less than one SFI event per pulse. This allows for good confidence that the e.g. ion-electron pair detected for the same laser pulse truly belong to each other without double-checking their momentum sum to be zero.
When applying both extraction scenarios to our exemplary data set presented above in Figs. 3.14 and 3.15, two basically similar distributions can be extracted as shown in Fig. 3.16. The shapes of both 3D momentum maps are identical with $\sim$14% more event counts for the loose coincidence case (b) compared to the momentum conservation case (a). While this does not seem like a lot, it might make a difference when looking at processes yielding low cross-sections.

Thus, for a general low level of false coincidences, the analysis using the alternative method of *loose coincidence* gives similar results compared to the *momentum conservation coincidence* events, considering the momentum sum of all involved reaction partners being zero, yet with more statistics still ensuring the elimination of electron background of other ionization and background channels [203, Ch. 6.2 & 7.4].

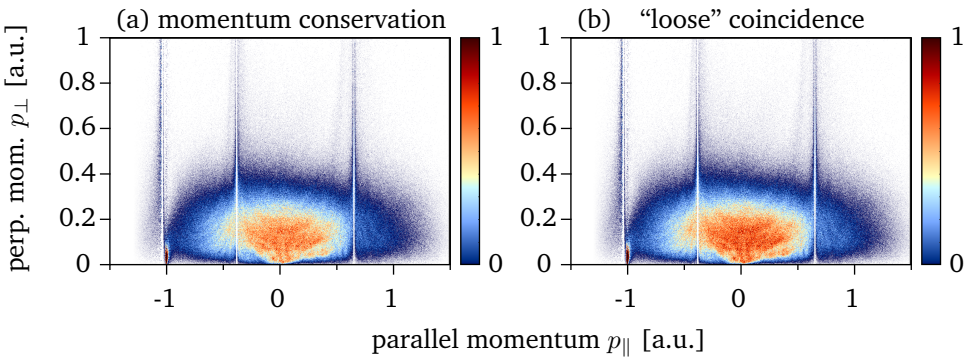

Figure 3.16: Momentum conservation and "loose" coincidence. In the data analysis, there are two options to invoke coincidence between a particle pair (or triplet, quartet etc.). **(a)** Both particles need to be detected for the same laser pulse trigger and their respective momentum vectors are required to apply to momentum conservation ergo their momentum sum needs to be zero. **(b)** On the other hand, in a "loose" coincidence scenario only the origin from the same laser pulse trigger is inferred provided that the rate of false coincidences in the experiment is kept low, i.e. less than one SFI event per pulse. In the exemplary data set of SDI on Xe atoms, both coincidence extractions lead to a similar 3D momentum distribution with ∼14% more event counts for the loose coincidence (b).

3.2.3 Capabilities of the system

The best way to characterize a ReMi is to calculate at its capabilities in terms of energy or momentum acceptance in all dimensions as well as the respective resolutions. The following sections will briefly summarize the most important equations needed to asses both features.

3.2.3.1 Electron and ion acceptance

The detection acceptance of all charged particles is basically dependent on the surface diameter of the detectors and the strength of both the static electric and magnetic field when assuming the spectrometer geometry as well as the mass and charge of the particle are known. Therefore, an experiment needs to be planned according to the momentum range to be covered to then scale the static extraction fields appropriately.

Longitudinal acceptance. For both electrons and ions, the longitudinal acceptance is solely dependent on the electric field strength $\mathcal{E}_z$. To be exact, both species have an infinite acceptance in their respective *forward direction* meaning when they are accelerated directly to their respective detector ($+\vec{\mathcal{E}} = -\vec{e}_z$ for ions and $-\vec{\mathcal{E}} = +\vec{e}_z$ for electrons, as indicated in Fig. 3.6). Yet, when their initial longitudinal momentum in *backward direction* is negative enough to overcome the electric field invoke acceleration in opposite direction, they are not detected. In other words,

the kinetic energy in longitudinal direction needs to be smaller than the potential difference between the focal region and the respective detector $E_{\text{kin}} \leq |\Delta U / q|$ in order to effectively reach the detector. Hence, the minimum detectable momentum of electrons or ions are defined as

$$p_{\text{z}} \geq -\sqrt{\frac{2\,|q\,\Delta U|}{m}} \tag{3.40}$$

in their specific coordinate systems[34].

Transverse acceptance. The calculation of momentum acceptance in transverse direction is determined differently for ions and electrons due to their different behavior in the magnetic field.
The *maximum transverse momentum for electrons* is mainly limited by the detector diameter and can be controlled by the applied magnetic field magnitude. By combining Eq. 3.33 and 3.35, the upper limit for the transverse momentum can be expressed as

$$p_{\text{tr,ele}} \leq \frac{r_{\text{max}}}{2}\, e\, \mathcal{B}_{\text{z}}\ , \tag{3.41}$$

while the upper transverse kinetic energy yields

$$E_{\text{kin,tr,ele}} \leq \frac{r_{\text{max}}^2\, e^2\, \mathcal{B}_{\text{z}}^2}{8\, m}\ . \tag{3.42}$$

The maximum radius of our MCP is $r_{\text{max}} = 40\,\text{mm}$ which is the effective maximum radius considering the electrons with no transverse momentum impact directly in the center of the detector. When discussing the transverse acceptance of electrons, the discontinuities or *nodes* as observed e.g. in Fig. 3.14 (d) need to be considered. As all electrons impact on the MCP at the same central position regardless of their initial transverse momentum $\vec{p}_{\text{tr}}$ [63] a singularity in momentum space emerges. As mentioned before, these nodes yield a precise information about the cyclotron period t_{c} of the experiment being the temporal difference between two subsequent nodes. Yet, the momentum acceptance at these nodal positions is zero since the p_{tr} information is lost (division by zero in Eq. 3.36).
On the other hand, the *transverse acceptance of ions* is limited by both the spectrometer potential and the extension of the detector. As explained before, the influence of the magnetic field on the ions can be neglected due to their higher mass. Consequently, the maximum transverse kinetic energy can be estimated from Eq. 3.38 using the flight time for electrons with initial longitudinal momentum from Eq.3.32 which results in

$$E_{\text{kin,tr,ion}} \leq \frac{r_{\text{max}}^2\, |q\,\Delta U|}{2\, l_{\text{a}}}\ . \tag{3.43}$$

[34] In order to circumvent confusion by expressing the ion and electron momenta in only the laboratory coordinate system leading to opposite signs and energy/momentum limits, the equations purposely are expressed in the species' specific coordinate system, as they will be represented in chapters of the experimental results of this thesis.

3.2.3.2 Momentum resolution

According to Eq. 3.40 to 3.43, the momentum acceptance of a ReMi could be infinitely scaled up with increased static fields, however the momentum resolution deteriorates with increasing field strengths. Next to the magnitude of the fields, the momentum resolution depends as before on the ReMi geometry, the mass and charge of the particle species, as well as in case of the ion on the jet temperature.

In general, the momentum resolution Δp of a ReMi is determined by a *Gaussian error propagation* of the equations 3.30 and 3.36 which define the longitudinal and transverse momentum, respectively (after [63] and [206, Sec. 4.8]). The main uncertainties that need to be taken into account are the uncertainty δt of the ToF extraction connected to finding the exact time zero of the triggering laser pulse (see Eq. 3.23) as well as the uncertainty δr of the determination of the exact impact point on the DLA. This leads to the following expressions for the longitudinal momentum resolution

$$\Delta p_\mathrm{z} = \left| \frac{1}{\partial t \,/\, \partial p_\mathrm{z}} \, \delta t \right| \overset{l_\mathrm{d}=0}{=} \left| -\frac{1}{2} \frac{q \, \Delta U}{l_\mathrm{a}} - \frac{m \, l_\mathrm{a}}{t^2} \right| |\delta t| \tag{3.44}$$

as well as the transverse momentum resolution

$$\Delta p_\mathrm{tr} = \frac{m \, \omega_\mathrm{c}}{2 \, |\sin(\omega_\mathrm{c} \, t/2)} \sqrt{\delta r^2 + \left(\frac{r \, \omega_\mathrm{c}}{2 \, \tan(\omega_\mathrm{c} \, t/2)} \right)^2 \delta t^2} \tag{3.45}$$

with $t = t_\mathrm{oF}$. In these expressions for both momentum resolutions, the variables t and r can be substituted with the equations of their related momentum components p_z (Eq. 3.30) and p_tr (Eq. 3.36). Thus, the respective resolutions can be presented as a function of the detected momentum variables: $\Delta p_\mathrm{z}(p_\mathrm{z})$ and $\Delta p_\mathrm{tr}(p_\mathrm{z}, p_\mathrm{tr})$. This context is important as it shows that every particle with a different initial momentum vector is detected with a different resolution. Usually, the systematic uncertainties in a ReMi our kind are estimated as δt = [0.5;1] ns and δr = [0.5;1] mm depending on the accuracy of the adjustment of the CFDs. Furthermore, other uncertainties can add to the momentum error like e.g. the acceleration length δl_a, which can vary as the focal spot position varies, and the static field strength $\delta \mathcal{E}$ and $\delta \mathcal{B}$, which can arise from instabilities of the respective power sources or inhomogeneities created in the setup. These experimental uncertainties are assumed reduced by the momentum calibration, as described in Sec. 3.2.2.2, and hence are not taken into account here. Moreover, the energy resolution can be calculated as

$$\Delta E = \frac{1}{m} \sqrt{(p_\mathrm{z} \, \Delta p_\mathrm{z})^2 + (p_\mathrm{tr} \, \Delta p_\mathrm{tr})^2} \tag{3.46}$$

with the overall momentum uncertainty of $\Delta p = \sqrt{\Delta p_\mathrm{z}^2 + \Delta p_\mathrm{tr}^2}$.

As addressed beforehand, the magnetic field node is a characteristic feature in the 3D momentum distributions detected with a ReMi. Due to the singularity in Eq. 3.36 for transverse momenta of electrons that underwent a full cyclotron trajectories for $t_\mathrm{oF} = k \, t_\mathrm{c}$ (for $k \, \epsilon \, \mathbb{N}^0$), the resolution of those transverse momenta goes to

infinity $\Delta p_{\mathrm{tr}}(k\, t_{\mathrm{c}}) \to \infty$. For measurements, where a broad "node-free" momentum distribution is desirable, the combination of the static electric and magnetic field can be chosen favorably, or on the other hand, two measurements with slightly shifted $\mathcal{E}$- or $\mathcal{B}$-fields at otherwise constant conditions can be performed. Advantageously chosen, the nodes in both measurements are shifted so that the two measurement results can be merged in order to achieve a broader and node-free momentum distribution. This procedure has been studied and applied in various investigations in [206, 216] and will be used in Ch. 4 of this thesis.

3.2.3.3 Acceptance - resolution trade-off

In general, applying higher static fields in the detection procedure with a ReMi leads to the 4π solid acceptance for ions and electrons with larger momenta as obvious regarding the Eqs. 3.40, 3.41 and 3.42. However, higher fields lead to larger momentum uncertainties as seen in Eqs. 3.44 and 3.45 which can blur out distinct structures within the momentum distribution. Hence, the magnitude of the static extraction fields when detecting charged particles with a reaction microscope needs to be chosen according to the objective of the experiment. When the focus lies on characteristic structures and local distributions within the spectrum, the fields should be chosen relatively low in order to provide an optimum resolution. In both experiments of the Part II of this thesis the setting is chosen like this. Yet, when the focus lies on detecting electrons with large momenta as generated by elastic re-scattering in SFI with mid-IR fields where kinetic energies of several keV can be reached, high fields need to be chosen. In Part III of this thesis we investigate molecular imaging based on LIED where diffraction cross-sections can be extracted from broad sections of the momentum distribution so that higher momentum uncertainty can be sacrificed.

Part II

Strong-field Ionization in Mid-IR Fields

Chapter 4

Energy Bunching for Electrons crossing the Ionization Threshold

SFI induced re-collision phenomena like HHG, NSDI as well as elastic re-scattering and diffraction are used extensively in modern attosecond science [14, 122] in order to investigate and image the structural and electronic nature of atomic and molecular systems. In order to be able to interpret and understand experimental observations, extracted physical parameters are generally compared to theoretical ionization models that are able to quantitatively reproduce the observed features of the ionization products. Hence, a fundamental understanding of the SFI process is key to further advance the research process. This chapter is the first of two parts in this thesis on the investigation of SFI as driven by long wavelength electric laser fields and hence under unambiguous quasi-static conditions ($\gamma \ll 1$) that has only been possible with the recent progress and availability of intense mid-IR sources.

The underlaying physics of the SFI process as described in Sec. 2.1.2 are believed to be relatively well understood as experimental findings generally can be reproduced with various theoretical models including the "workhorse" of the field, the SFA. Per definition, the SFA is valid specifically in the quasi-static or tunneling regime where the post-tunneling behavior of the electron wave packet is supposed to be dominated by the laser electric field rather than the Coulomb field of the parent ion. Hence, the SFA neglects the influence of the Coulomb field on the outgoing electron in its final continuum state which allows analytical solutions that predict and agree with the majority of experiments on strong-field-induced re-collision physics (see Sec. 2.1.2). However recently, SFI experiments on atomic and small molecular targets interacting with electric fields at $\lambda \geq 2\,\mu$m yielded unexpected features in the lower part of the kinetic energy spectrum of the resulting photo electrons [58, 59]. These low-energy structures (LESs) were not predicted by the SFA. Yet, including the influence of the Coulomb field on the post-tunneling behavior of the electron wave packet led to an explanation of the origin of the LESs. In the course of further investigations, a second order LES for even lower kinetic energies [59, 196], originally dubbed as *very-low-energy structure* (VLES) as well as a structure at (near-) zero kinetic energy (ZES) (by initial investigations of our group [60]) were found that have not been quantitatively characterized yet. Especially the mechanism behind the ZES due to its relatively small kinetic energy around several tens of meV is still under debate since theoretical models that propagate the Coulomb field influence are not able to reproduce the structure.

On a more fundamental level, the correspondence between quantum and classical dynamics very close to the ionization threshold is of concern as most models describing the distant re-scattering scenario are based on classical dynamics. In particular, the explanations of the LES rely on subtle properties of the classical phase space. Yet, the applicability of classical models to explain the VLES and even ZES is not obvious as the the *de-Broglie*[1] wavelength of the electron wave packet diverges drastically for kinetic energies approaching the threshold $E \rightarrow 0$.

This chapter presents a thorough experimental and theoretical study of the 3D vectorial momentum spectrum of photo-electrons emitted well below 1 eV in order to obtain a quantitative idea of the mechanisms behind all low-energy structures as well as their relations. The chapter begins with an overview of the state-of-the-art of the knowledge obtained from experimental and theoretical studies of the different LESs and its underlaying mechanisms in Sec. 4.1. Next, our experimental and theoretical results on the SFI of argon atoms are presented and compared in Sec. 4.2 after introducing the experimental conditions as well as the classical and quantum mechanical simulations. Then, the position of the LES peaks in the momentum spectrum is studied as a function of pulse duration in Sec. 4.3. Next, the VLES and its characteristic V-shape are analyzed in Sec. 4.4 before the mechanism behind the ZES is discussed in Sec. 4.5. Moreover, the universality of the structures is discussed in Sec. 4.6 by presenting similar results of other atomic targets. The experimental and theoretical data presented in this chapter and hence its main results have been published in

B. Wolter et al., PRA ***90****, 063424 (2014)* cited as [217]

and partially in

M. G. Pullen et al., J. Phys. B ***47****, 204010 (2014)* cited as [218] and
B. Wolter et al., PRX ***5****, 021034 (2015)* (highlighted in APS Physics) cited as [169].

4.1 Low-energy structures: state-of-the-Art

The idea to drive the SFI-induced electron recollision process with intense, long wavelength light sources has been intensified about a decade ago [45] with advent of stable, intense and ultrashort mid-IR sources [52]. Next to the benefits of utilizing long wavelength driving sources as described in Sec. 2.4, the ionization process in tunneling conditions is constituted in the associated Keldysh regime ($\gamma \ll 1$). Moreover, it is assumed that in unambiguous quasi-static conditions the post-tunneling behavior of the electron in only the time-varying electric laser field can solely be described in a classical manner while in mixed regimes ($\gamma \geq 1$) both quantum and classical aspects play a role during photo ionization [219]. Hence, experimental results are supposed to be predominantly interpreted in the context of the popular SFA [72, 93, 94].

[1] De Broglie first described matter with a wave-like behaviour resulting in wavelength of $\lambda = h/p$.

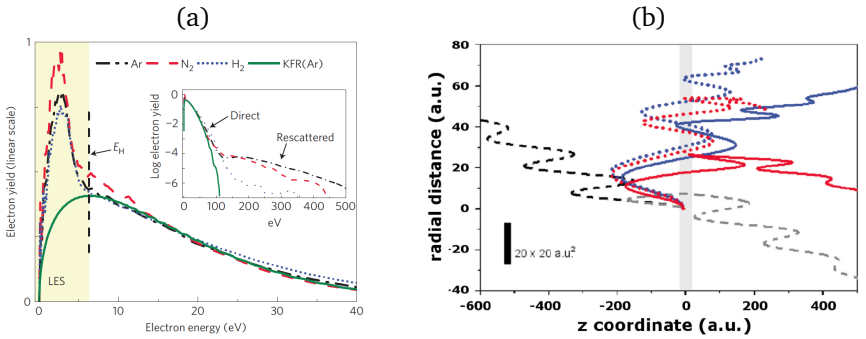

Figure 4.1: LESs: state-of-the-art. (a) The plot is taken from [58, Fig. 1] and shows the ionization surprise as found by Blaga *et al.* [58] revealed a peak-like structure for electrons with low kinetic energies on top of the expected broad distribution of direct electrons (green) which was not predicted by SFA based simulations. The LES was found universally for noble gases and small molecules. The revealment of the LES was connected to SFI with long wavelength ($\lambda \leq 2\,\mu$m) as it was never experimentally extracted by near-IR SFI investigations. **(b)** The LES was soon explained by semi-classical theories incorporating the Coulomb field influence on the electron trajectories. E.g. in the work of Lemell *et al.* [220, Fig. 5] a classical-trajectory Monte-Carlo simulation showed that electrons of the LES (blue and red lines) return to the vicinity of the nucleus (gray shaded area) and softly re-scatter with the nucleus in forward direction which leads to an agglomeration of electrons for specific energies. On the other hand, trajectories of direct electrons (black and gray dashed lines) oscillate away from the nucleus without return.

LES

The first experimental investigations of SFI with longer wavelength laser sources ($\lambda \geq 1.6\,\mu$m) were carried out by Blaga *et al.* [58] and at the same time by Quan *et al.* [59] in 2009. The main result of [58] is shown in Fig. 4.1 (a). Here, a peak-like structure was observed at low electron energies of 1 eV to 6 eV in addition to the well-known behavior of the kinetic energy distribution (KED) for SFI with a drop in yield beyond directly emitted electrons [see inset in Fig. 4.1 (a)]. This LES was observed in experiments conducted with laser pulses at λ_C between 1.7 eV to 3.6 μm and universally for various target systems (He, Ne, Ar, Kr, Xe, N_2, H_2, D_2) in [58] (black, red and blue, dashed and dotted lines), while for λ_C between 1.5 eV to 2.0 μm for Xe in [59]. The latter investigation also measured the KED of electrons for λ_C at 0.8 eV to 1.25 μm where the LES was rather suppressed. In both experimental studies the electrons were detected with a ToF spectrometer with an acceptance angle of $\pm$ (5° to 6°). The width of the LES increases with increasing laser wavelength λ and intensity I and hence a decreasing γ, while its peak position moves towards larger energies for decreasing γ scaling with $E \propto \gamma^{-1.78}$ [58]. As mentioned before, the LES could not be reproduced with the SFA as plotted in green in Fig. 4.1 (a), surprisingly, since the approximation was expected to become more accurate as the QS limit is approached. On the other hand, full 3D

TDSE calculations within the SAE approximation reproduced the LES almost exactly which pointed towards a lack of completeness in the SFA [58]. In [59], a semi-classical model considering a hydrogen-like Coulomb potential ($V = -Z_{\text{eff}}/r$ with Z_{eff} being the effective nuclear charge) was able to reproduce the LES in the KED, hence accounting the influence of the Coulomb field on the electron as part of the mechanism behind the LES. In addition to that, the experimental observation of the LES disappeared with circular polarization [221] hinting that the origin of the LES also might be connected to re-scattering [65, 221] which diminishes with increasing ellipticity of the driving field.

Consequently, many theoretical investigations were undertaken to corroborate and refine the initial insights of [58, 59]. Initial semi-classical calculations [222, 223] which included both tunneling and Coulomb field effects were able to attribute the LES to a combination of multiple forward scattering with a disturbance of the transverse electron momentum by the Coulomb field. Further investigations attributed the structure to a one-dimensional (longitudinal to the laser polarization only $\overleftrightarrow{\mathcal{E}}$) [224, 225] or two-dimensional (longitudinal and transverse to $\overleftrightarrow{\mathcal{E}}$) [220, 226] *focusing* of the electron trajectories to the vicinity of the Coulomb field. In contrary to the "head-on" *hard re-collisions* leading to elastic scattering and a plateau of large energies [see inset of Fig. 4.1 (a)], the Coulomb focusing can be understood as *soft re-collisions* of electrons close to the parent ion while oscillating in forward direction of the laser field. This scenario is re-plotted from [220] in Fig. 4.1 (b). Generally, direct electron trajectories (exemplarily in black and gray dashed lines) quiver away from the parent ion towards the detector. In doing so, some trajectories in the classical phase space (blue and red, solid and dashed lines) can return to the vicinity of the Coulomb field around $z \sim 0$ (as a gray background) where they receive a "kick" resulting in a focusing into higher angular momenta at specific low energies [220, 226]. In [224, 225], the same effect is described along the z-axis (longitudinal component) as an "energy-bunching" of electrons that miss the ionic core. Both series of studies have in common that the energy-bunching or kick process can occur for multiples of the optical cycles of the driving laser field leading to multiple order LESs (blue and red dashed lines). Moreover, the creation of the LES and hence its position in the KED can be controlled by the CEP of the laser field [220, 225].

In another approach, improved SFA (ISFA) model calculations that extended the T-Matrix element with an additional interaction of the emitted electron with the parent ion [227] or that incorporated a second-order (re-scattering) term in the S-Matrix expansion [228] were also able to show the LES. The models take a short-range Coulomb potential into account, yet it is assumed that the LES is even enhanced with a considered long-range potential [226, 227]. Furthermore, various theoretical approaches were compared in terms of the creation of LESs in [229]. The LES could be derived by taking forward scattering trajectories into account in the purely classical simple man's or rescattering model considering solely the influence of the laser field (see Sec. 2.2.1). Similarly the forward scattering quantum orbits in the SFA or the ISFA yielded the LESs. Yet, both cases revealed the LES less pronounced as for the classical trajectories derived in the influence of both the

laser and Coulomb field. [229] arrived to the conclusion that the LES is a purely forward scattering induced effect which can be drastically enhanced by considering a Coulomb potential.

VLES

In the course of the investigations of the mechanism(s) behind the LES, further experimental investigations using similar laser conditions were conducted. Wu *et al.* [196] revealed, next to the actual LES, a further structure at even lower energies of around ~ 100 meV. This very-low-energy structures (VLES) was detected with a ReMi detection system, yet the KED was analyzed only for a virtual acceptance angle of 5° to 8°. Moreover, the longitudinal momentum distribution (LMD) of the data were derived by projecting the total (and not only under an acceptance angle of 5° to 8°) transverse momentum of the 3D momentum space onto the longitudinal axis. The resulting LMD showed a distinctive double hump structure which was speculated to correspond to the VLES. The double-hump resembles structures that were previously observed using 0.8 µm radiation [230]. Theory interprets the VLES in many different ways assuming the influence of the long-range [196] or solely short-range [231] Coulomb potential as the origin of the VLES, while the structure can also be interpreted in connection to the LES as a second-order soft re-collision [220, 224]. Moreover, the before mentioned ISFA calculation including a second-order scattering term [228] was not able to reproduce the VLES which they reasoned to be connected with missing higher-order scattering terms. Therefore, a full understanding about the VLES has not been achieved yet. Also, the connection of the VLES (extracted under an acceptance angle of of 5° to 8°) with the double hump in the LMD (extracted for the full 3D spectrum) needs further investigation.

ZES

More recently, first investigations of our group using the combination of our mid-IR OPCPA source with the ReMi detection system were published [60] resolving - for the first time - the full 3D electron momentum space ($|\vec{p}| \leq 0.4$ a.u.) of SFI of argon atoms and oxygen molecules in "deep" quasi-static conditions ($\gamma = 0.3$). Here, two peculiar new structures were found for even lower kinetic energies: 1) a peak-like structure close to the origin at around 1 - 10 meV therefore called (near-) ZES and 2) a V-shaped structure centered in the transverse plane just above the ZES.
The ZES sits close to the origin at $p_{\parallel} = 0$ a.u. and $p_{\perp} \sim 0.01$ a.u. (with $\parallel$ and $\perp$ corresponding to the laser polarization along $\vec{e}_z$) and is therefore well separated from the beforehand observed VLES and LES. Moreover, the ZES lies outside of the acceptance range of a typical ToF spectrometer which explains why is has not been observed in previous measurements. Due to the extremely low kinetic energy of the electrons in the ZES, it was speculated in [60] that the origin of the ZES could be related to population trapping in high-lying Rydberg states, so different from the mechanism behind the LES and VLES, or a similar soft re-scattering far away from

the parent ion so with relatively low Coulomb field influence. Both speculations are also based on the fact that the ZES vanished for a small ellipticity of the laser polarization which prevents both processes. Interestingly, the only other experimental investigations [232, 233] of SFI of (single) noble gas atoms using a ReMi for full 3D acceptance did not resolve the ZES. Liu *et al.* [232] found a depletion of electrons around the momentum space origin for decreasing γ in contrast to the findings of the ZES. Yet they reasoned their finding also with Rydberg state population of stabilized atoms that are not further ionized. To add to the controversy, Veltheim *et al.* [233] neither could find population around the origin for the single SFI of argon atoms, yet they revealed a ZES like structure for argon dimers Ar_2 which they explained with a strong-field induced Rydberg state population scheme known as *frustrated tunnel ionization* (FTI) [234] (which will be further discussed in Sec. 4.5) and subsequent ionization by charge oscillation within the dimer ion core. Up until the investigations of this thesis, no theoretical calculation had been published that could reproduce the ZES or identify its origin in SFI of single noble gases and small molecules.

The other novelty revealed by the experimental data of [60] is the V-shaped structure in the transverse plane of the 3D momentum distribution. The V-structure is centered around $p_{\parallel} = 0$ a.u. and extends from $p_{\perp} \sim 0.01$ - 0.08 a.u. The structure reminds of the property of the VLES as discussed in [196] since it similarly results into a double-hump structure when integrated along $p_{\perp}$. Yet the difference here is that [196] integrated along the total transverse momentum space while the VLES they extracted from the KED was only identified under an acceptance angle of a few degrees. The results from [60] differ in that sense, because the V-like shape lies definitely above the acceptance cone of a ToF spectrometer (highlighted in [169, 218] and in Fig. 4.3 of the next section).

4.2 Multiple orders of low-energy structures in 3D momentum space

The intention of our experimental and theoretical investigation is to shed light on the mechanisms behind all previously found LESs and disentangle their mechanisms. In particular we were interested in 1) resolving multiple orders of LES (including the V-shaped structure and ZES) in the 3D momentum space as predicted by [220, 224]; 2) analyzing the V-shape in the 3D momentum distribution as initially found by [60]; and 3) explaining the mechanism behind the ZES. Therefore, we analyze the behavior of the LES(s), the V-shaped structure, and the ZES for argon atoms as a function of pulse duration of the mid-IR pulse. As the number of distant re-collisions with the ionic core is controlled by the number of optical cycles and the peak-to-peak amplitude after tunneling ionization, variation of the pulse duration provides a knob to manipulate the focusing properties of the recollision process. On the detection side, the ReMi detection field parameters were optimized for high resolution detection of low electron energies. In parallel, we

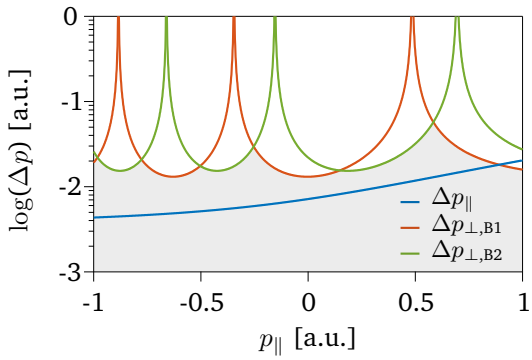

Figure 4.2: Momentum resolution with two magnetic fields. The momentum resolution four our experimental conditions as a function of $p_{\parallel}$ for two low values of the magnetic field ($\Delta p_{\parallel}$ in blue, $\Delta p_{\perp,\mathrm{B1}}$ in red, $\Delta p_{\perp,\mathrm{B1}}$ in green). The "nodes" which reveal infinite momentum uncertainty can be eliminated by stitching together the results of multiple measurements with different values of $\mathcal{B}$ leaving an effective $\Delta p_{\perp,\mathrm{eff}}$ (gray background).

worked in collaboration with theorists, namely Christoph Lemell from the group of Joachim Burgdörfer of the Technical University, Vienna, Austria, and Xiao-Min Tong from the University of Tsukuba, Ibaraki, Japan, in order to employ *classical trajectory Monte Carlo* (CTMC) as well as TDSE calculations to study the experimental results in detail in terms of classical and quantum theory.

4.2.1 Experimental parameters

The experiments were performed on argon atoms at a fixed laser peak intensity of $I = 0.9 \times 10^{14}\,\mathrm{W/cm^2}$, corresponding to a Keldysh parameter of $\gamma = 0.31$ ($z \sim 202$, $z_1 \sim 10.3$, $z_\mathrm{f} \sim 3.2 \times 10^{-4}$; in agreement with the tunneling conditions according to Reiss as described in Sec. 2.1.3) and a pondermotive energy $U_\mathrm{P} = 80.8\,\mathrm{eV}$, for three different pulse durations of 4 cycles ($\tau = 41\,\mathrm{fs}$), 6.5 cycles ($\tau = 68\,\mathrm{fs}$) and 13.5 cycles ($\tau = 140\,\mathrm{fs}$). In principle, the OPCPA source is CEP stable which is inherited by the DFG process created by two arms of the same oscillator (see Sec. 3.1). In the experiment, the CEP is purposely randomized by periodically changing the time delay[2] between both DFG arms in order to make sure to investigate the averaged SFI process[3].

The goals in terms of detection are resolving all possible structures (LESs, VLES, ZES) in the 3D momentum space by providing a very high resolution for the momentum region around the origin while keeping the $4\,\pi$ solid angle acceptance

[2]The time delay is actively shifted with a delta voltage created by a function generator where the amplitude corresponds to a 2π CEP shift between both arms, while the spectral bandwidth stays constant. The temporal period of the delta voltage signal is chosen significantly larger than the repetition time of the laser pulses, in our case 10 s.

[3]Technically, there are no CEP-dependent effects expected for laser pulses with more than 3 cycles in duration. This measure was taken to be completely sure to dismiss any CEP effect.

valid for at least a range of $p_{\parallel} \lesssim \pm 0.86$ a.u. (corresponding $E_{\text{kin}} < 10$ eV). This is achieved by standardly used extraction fields of in our case $\mathcal{E} = 1.3$ V/cm and $\mathcal{B}_1 = 4.4$ Gs. The idea in this experiment compared to [60] was to slightly lower the extraction field for higher longitudinal resolution, and to increase the "node-free" range along $p_{\parallel}$ to resolve multiple orders of LESs. Since the original investigations [58, 59] were conducted with a ToF spectrometer, the LES (at least first order) should appear for $|p_{\parallel}| < 0.9$ a.u. and perpendicular momenta under an acceptance angle of $\alpha = {}' \arctan(p_{\perp} / p_{\parallel}) < 5°$[4]. In order to achieve a "node-free" momentum range the momentum distribution is measured for two different magnetic fields $\mathcal{B}$ while keeping all other experimental parameters constant as described in [206, 216]. Two different magnetic fields result into two different cyclotron periods which shift the nodes to different positions. As a result, the nodes in the first momentum distributions that occupy an infinitely large momentum uncertainty can be filled with the data from the second measurement at a different magnetic field which provides a low momentum uncertainty in this area. In doing so, we conduct the same measurement with a slightly enhanced magnetic field of $\mathcal{B}_2 = 5.1$ a.u. The context is highlighted in Fig. 4.2 where the resolution distributions are calculated for our experimental conditions according to Eqs. 3.44 and 3.45. The transverse momentum resolution $\Delta p_{\perp}$ is shown for both magnetic field $\mathcal{B}_1$ and $\mathcal{B}_2$ in red and green lines, respectively. By combining the regions with the highest momentum resolution (gray shaded area in Fig. 4.2) the discontinuities by the nodes can be circumvented. In our case, this results in a maximum perpendicular uncertainty of $\Delta p_{\perp,\text{max}} = 0.057$ a.u. at $p_{\parallel} \sim 0.6$ a.u. and a minimum of $\Delta p_{\perp,\text{min}} = 0.013$ a.u. at $p_{\parallel} \sim 0$ a.u. corresponding to tens to single meV, respectively. The longitudinal momentum uncertainty distribution $\Delta p_{\parallel}$ (blue line) is slowly increasing for increasing $p_{\parallel}$ and is $\Delta p_{\parallel} = 0.007$ a.u. at the origin. This method to expand the node-free momentum range has been applied either by changing the electric or the magnetic field [206, 216] hence keeping the transverse or longitudinal momentum acceptance and resolution constant, respectively. In our case, we focus on a constant $p_{\parallel}$ because we are interested in the area towards the origin. It should be added that this method to circumvent the nodes is just a "means to an end" since ideally the full momentum distribution should be resolved at once. Yet, the nodes are inherent features of the ReMi which could be spread apart with respect to each other by increasing $\mathcal{E}$ or decreasing $\mathcal{B}$. This measure is unfavorable, however, in terms of managing the momentum acceptance and high resolution. Hence, the method of filling in the nodes with data from a second measurement at a different field strength is a good alternative to overcome these limitations, at best, with perfectly homogeneous field distributions.

[4] In [60], the LES was marked for momenta of 0.06 a.u. $< p_{\perp} <$ 0.3 a.u. which are mainly located outside of the ToF spectrometer acceptance and correspond to the underlying distribution of direct electrons.

4.2.2 Theoretical methods: classical and quantum simulations

The theoretical simulations were performed by our collaborators Christoph Lemell (CTMC simulation) of the group of Joachim Burgdörfer and Xiao-Min Tong (TDSE simulations). For the sake of completeness, the detailed descriptions of the theoretical methods are taken directly from our publication in [217].

We perform both quantum and classical simulations in order to probe the degree of quantum–classical correspondence at very low electron energies which is, *a priori*, not obvious. This point is highlighted by the fact that the de-Broglie wavelength of a typical low-energy electron is quite large, $\lambda_e(E = 1\ \mathrm{eV}) \approx 25$ a.u. ≈ 1.25 nm.

4.2.2.1 CTMC simulation

In the CTMC simulation, an effective potential derived from the Hartree-Fock (HF) approximation [235] is employed. The binding energy E_{bind} determining the energy shell of the microcanonical ensemble was set to the HF result of -16.0824 eV (experimental value $E_{\mathrm{bind}} = -15.76$ eV [236]). This leads to a Keldysh parameter $\gamma = \omega\sqrt{-2E_{\mathrm{bind}}}/F_0 \approx 0.32 \ll 1$ [72] suggesting a strong dominance of tunneling over multiphoton ionization for the laser parameters used in the experiment. Since the electron emission originates from the Ar3p subshell with quantum numbers $n = 3$, $\ell = 1$, and $m = 0, \pm 1$, we use the ℓ, m-dependent ADK rates [89]

$$w_{m=0} = \left(\frac{3e}{\pi}\right)^{3/2} \frac{Z^2}{n^{*9/2}} \left(\frac{4eZ^3}{\mathcal{E}\, n^{*4}}\right)^{2n^*-3/2} \exp\left(-\frac{2Z^3}{3n^{*3}\,\mathcal{E}}\right) \quad , \tag{4.1}$$

$$w_{|m|=1} = \left(\frac{3e}{\pi}\right)^{3/2} \frac{2eZ^2}{n^{*11/2}} \left(\frac{4eZ^3}{\mathcal{E}\, n^{*4}}\right)^{2n^*-5/2} \exp\left(-\frac{2Z^3}{3n^{*3}\,\mathcal{E}}\right) \quad , \tag{4.2}$$

where n^* is the effective principal quantum number derived from $E_{\mathrm{bind}} = -Z^2/2n^{*2}$ and was already defined in Eq. 2.18. Up to constant factors, the total emission rate is therefore proportional to

$$w_{\mathrm{total}} \propto F^{3/2-2n^*} \left(1 + \frac{Fn^{*3}}{Z^3}\right) \exp\left(-\frac{2Z^3}{3n^{*3}F}\right) \quad , \tag{4.3}$$

and the probability for emission during a time interval Δt proportional to

$$P(\Delta t) = 1 - \exp(-w_{\mathrm{total}}\Delta t) \quad . \tag{4.4}$$

Integration of $P(\Delta t)$ over the pulse duration gives the total emission probability for an atom in a laser pulse with maximum field strength F.

The z coordinate of the tunnel exit, z_0, was calculated from the field strength at ionization time. The perpendicular position was taken from projections of the corresponding HF wavefunctions with $m = 0$ and $|m| = 1$ onto the plane perpendicular to the polarization axis at z_0. The widths of the Gaussian momentum distributions along the polarization direction at the tunnel exit

$$\sigma^2(p_\parallel) = \frac{3\omega}{2\gamma^3} \tag{4.5}$$

and the perpendicular direction

$$\sigma^2_{\mathrm{ADK}}(p_\perp) = \frac{F/2}{\sqrt{-2E_{\mathrm{bind}}}} \quad . \tag{4.6}$$

were derived in Ref. [237]. Recently, it was suggested that the transverse width is somewhat underestimated by Eqn. 4.6 [238–240]. We have therefore allowed for a wider momentum distribution to match the experimental results with an empirically determined width of $\sigma(p_\perp) = \sqrt{2}\sigma_{\mathrm{ADK}}(p_\perp)$ similar to the observations in [238, 239]. For each set of initial conditions taken from properly normalized distribution functions, the trajectory is calculated in the combined fields of the remaining laser pulse and the ionic core. The propagation was performed using a standard fourth order Runge-Kutta algorithm and proceeds to electron-core distances of at least $r \geq 5000$ a.u. after the end of the laser pulse. Since the experimental conditions of the ReMi were set to use an extraction field of $F_{\mathrm{extr}} = 1.3$ V/cm $\approx 2.5 \times 10^{-10}$ a.u., this very weak external field was also taken into account. It is further used in the data evaluation of the CTMC simulation as it is crucial for the analysis of the ZES. For each carrier-envelope phase ($\Delta\varphi_{\mathrm{CEP}} = 15°$), 2.5×10^6 trajectories were calculated and combined for the determination of the final vectorial momentum and energy vs. angular momentum distributions. Momentum, energy, and angular momenta were also recorded for electrons with energies $E_{\mathrm{final}} < 0$ after the end of the pulse, signifying electrons recaptured into high-lying Rydberg states.

To accurately simulate the experiment we perform an average over the focal intensity distribution (as described in Sec. 3.1.3). To this end we have assumed a cylindrically symmetric beam with Gaussian intensity profile and maximum intensity I_0. The volume with an intensity larger than I_i is given by [241, 242]

$$V(I > I_i) = \frac{2\pi d_\circ^2 z_R}{3}(2\beta + \beta^3/3 - 2\arctan\beta) \tag{4.7}$$

with $\beta = \sqrt{I_0/I_i - 1}$ and $d_\circ$ the focal diameter. This expression was evaluated for small steps of the maximum electric field ($F_{i+1}(t) = F_i(t)/1.005$) resulting in thin shells of volume

$$V = V(I > I_{i+1}) - V(I > I_i) \tag{4.8}$$

with maximum local field strength F between F_{i+1} and F_i.

4.2.2.2 TDSE calculation

Quantum simulations of the interaction of strong laser pulses with atoms in all dimensions remain a challenge in the mid-IR region. This is because the quiver amplitude, and therefore the excursion from the ionic core, is on the order of $\alpha = F_0/\omega^2 \approx 250$ a.u., which requires a large domain in configuration space to be accurately calculated. Technical details of our 3D quantum-mechanical simulation have been described previously [243, 244]. In brief, the radial coordinate space is discretized in a pseudo-spectral grid and propagate the wave function which is

expanded into a set of pseudostates with quantum numbers $\tilde{n}, \ell, m$ employing the velocity gauge for the coupling to the laser field. To prevent unphysical reflections from the "boundaries" of the computing box the real space is separated into inner ($R < R_c$) and outer ($R_c < R < R_{\max}$) regions. The parts of the wavefunction reaching the outer region are projected onto Coulomb-Volkov states in momentum space and are propagated analytically henceforth. For the calculations presented here we chose an outer box radius of $R_{\max} = 1250$ a.u. and an inner radius of $R_c = 750$ a.u. R_c needs to be significantly (at least a factor of two) larger than the quiver radius. Moreover, the value of R_c determines the range of pseudostates which closely resemble atomic states with principal quantum number n, $\langle r \rangle_{\tilde{n}} < R_c$. In the present case, Rydberg states up to $n \approx 20$ are faithfully accounted for. Higher lying bound states are included in terms of pseudostates with $\ell < 80$ where the hydrogenic ℓ degeneracy is lifted. This allows for a coarse-grained representation of the spectral excitation density $\rho(E)$ close to the continuum threshold at $E = 0$. $\rho(E)$ plays an important role in representing the process of recapture into Rydberg states, which is the key to the ZES. We describe the ionization of the Ar3p electron in terms of a model potential that reproduces I_p and the oscillator strengths of the coupling to the first excited states (4d, 5d) [245]. Unphysical deexcitation to lower lying occupied states is in the present case suppressed by the large energy gap $\Delta E_{3s-3p} = 1/2$ a.u. to the closest state 3s and the large and parity-disfavored even number of photon energies required to bridge this gap ($\Delta E_{3s-3p} = 34\hbar\omega$). The maximum occupation of the 3s state was checked to remain at least 5 orders of magnitude smaller than the ionized part of the wavefunction (ionization yield $\sim 1\%$). Therefore, use of effective potentials that project onto the othogonal component to the occupied core states is not required in this case.

4.2.3 Experimental results in comparison with CTMC simulations

In Fig. 4.3 our experimental results for three different pulse durations [4 optical cycles in a), 6.5 optical cycles in b) and d), 13.5 optical cycles in c) and e)] are plotted in comparison with their CTMC simulation counterparts (f, g, h) as 3D electron momentum distributions (cylindrical coordinates integrated over the azimuthal angle, $p_\perp = \sqrt{p_x^2 + p_y^2}$ on logarithmic scale over $p_\parallel = p_z$ on linear scale). Here, Figs. 4.3 (a,b,c) show the experimental data as measured for one magnetic field (in this case $\mathcal{B}_1$)[5]. The ReMi related nodes positioned at $p_\parallel \sim$ -0.4 a.u. and $\sim +0.5$ a.u. are cut out by $\Delta p_{\text{cut}} = \pm 0.06$ a.u. In order to increase the node-free momentum range, the experiments were repeated with a second magnetic field $\mathcal{B}_2$ as described in Sec. 4.2.1, so that the respective measurements can be merged. The resulting distributions (symmetrized due to CEP randomization) are plotted in Figs. 4.3 (d,e) for the case of 6.5 and 13.5 optical cycles (the second measure-

[5] For transverse momenta $p_\perp > 0.1$ a.u. the momentum distribution shows half-ring like distortions overlayed with the data. These stem from inhomogeneities of the static fields which can be related to noise of power sources. The effect is more drastic for lower applied fields and vanishes for increasing fields.

ment for 41 fs could not be executed due to laser malfunctions at the end of the campaign).

Immediately striking is the V-shaped structure that can clearly be recognized for electrons with $|p| < 0.1$ a.u. in both the experimental [Figs. 4.3 (a-e)] and simulated [Figs. 4.3 (f-h)] momentum distributions for all pulse durations. The width of the V-shaped structures seems to increase with decreasing pulse duration which will be analyzed in Sec. 4.4. The ZES ($p_\perp \approx 0.01$ a.u.) is also clearly visible in the experimental data [Fig. 4.3 (a-e)] which confirms the findings of [60]. However, in the CTMC calculations [Figs. 4.3 (f-h)] considering only direct ionization to the continuum, the ZES is absent which will be further analyzed in Sec. 4.5. Additionally, lobes of the distribution towards lower transverse momenta are visible for $p_\parallel \approx \pm 0.4$ a.u. and $p_\parallel \approx \pm 0.6$ a.u., especially for the two measurements with shorter pulse durations (a, b, d). For the data at $\tau \sim 41$ fs (a), only one lobe is visible as the second one might be covered by the ReMi node. In the case of $\tau \sim 140$ fs (c,e), the lobes are almost not visible compared to theory (h). It is also apparent that in the unsymmetrized momentum distributions the lobes towards positive values of $p_\parallel$ are less pronounced compared to their counterparts for negative $p_\parallel$. In principle, the distribution should be symmetric around $p_\parallel = 0$ since CEP effects can be neglected. The asymmetry might be ascribed to the fact that the overall momentum uncertainty is higher in the positve $p_{\parallel,+}$ space compared to $p_{\parallel,-}$. This is due to the fact that transverse uncertainty $\Delta p_\perp$ (red and green in Fig. 4.2) spreads wider around the nodes in $p_{\parallel,+}$ as well that the longitudinal uncertainty $\Delta p_\parallel$ is generally higher in $p_{\parallel,+}$.

The lobes, that were not visible in [60][6] due to a limited $p_\parallel$-range and slightly less overall resolution, can be identified as LESs of first and second order by comparison with the CTMC simulation where they appear in a very pronounced manner. This can also be corroborated by analyzing the lobes in comparison to the original LES(s) observed in [58, 59] and detected by a ToF spectrometer. Therefore, the KED of the emitted electrons is extracted for the case of 68 fs pulses [experiment and theory, see Figs. 4.3 (d,g)] by restricting the data set to detection aperture angles of $5°$ [marked in Figs. 4.3 (d,g) as black dashed lines], $10°$, and $15°$ which are comparable to the opening aperture in a typical TOF. The result is shown in Figs. 4.4 (a,b). The structures appearing in the experimental data (a) near 5 and 1.75 eV can be attributed to first and second order LES, respectively, which is supported by our simulated spectra (b).

Let us analyze the CTMC results a bit further. In [220], LESs of increasing order were attributed to turning points of the electron trajectory close to the ionic core after an increasing number of quiver oscillations in the driving laser field. Consequently, only longer laser pulses with many cycles driving the liberated electron back to the core multiple times facilitate a high-order LES. The association of low-energy structures with two-dimensional Coulomb focusing is corroborated by the projection of the final states of the trajectories in the energy–angular momentum plane. As in Ref. [220], we can link the structures appearing at small perpendicular

[6] When looking very closely, the LES2 can almost be made out in Figs. 1 (a,f) of [60]

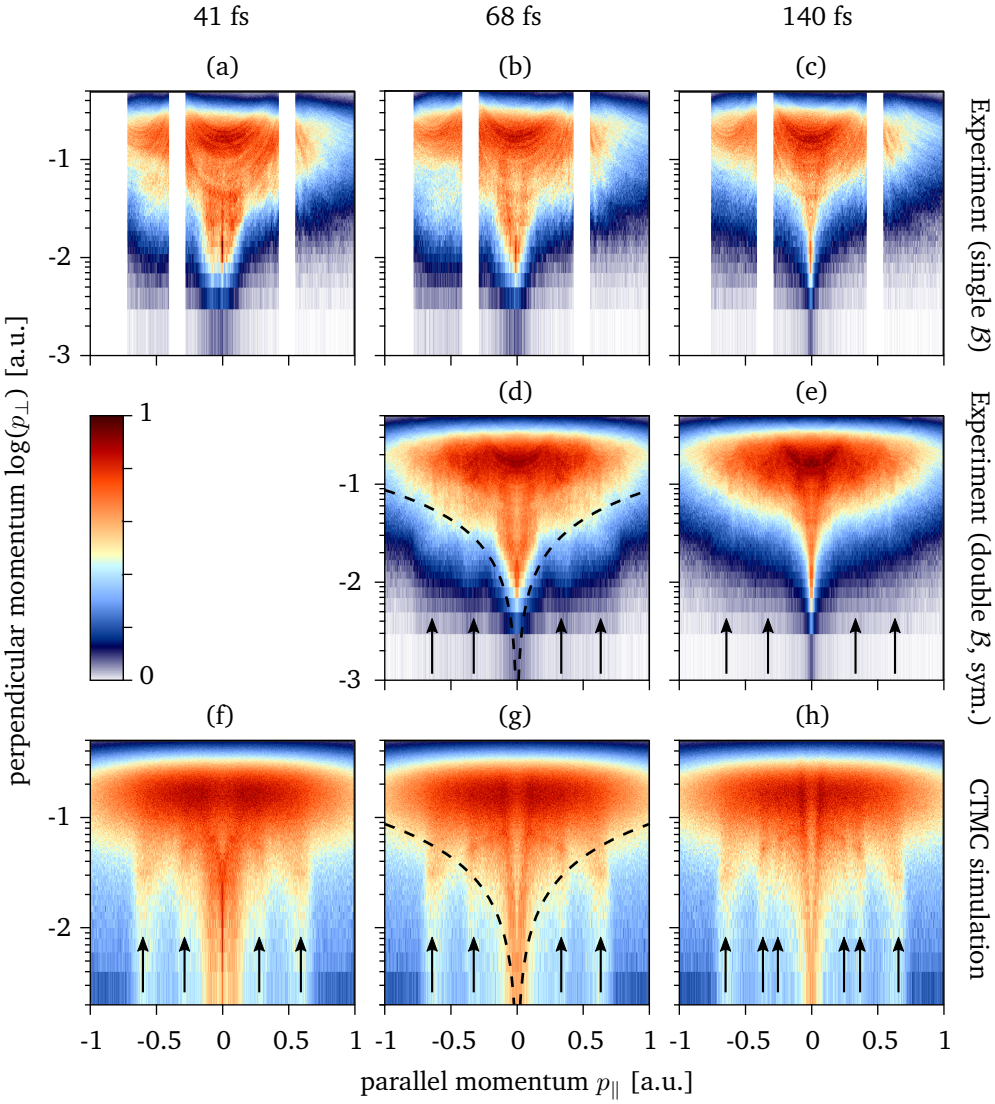

Figure 4.3: Detection of multiple LESs, VLES and ZES in 3D momentum space (a-c) Experimental 3D electron momentum distribution (detected at $\mathcal{B}_1$) of SFI of Ar atoms at a fixed laser peak intensity of $I = 0.9 \times 10^{14}$ W/cm^2 ($\gamma = 0.31$) for pulse durations of **(a)** 41 fs (4 optical cycles), **(b)** 68 fs (6.5 opt. cyc.) and **(c)** 140 fs (13.5 opt. cyc.). **(d,e)** Merged and symmetrized momentum distributions of two measurements at different magnetic fields $\mathcal{B}_1$ and $\mathcal{B}_2$ resulting in node-free momentum space between $p_\parallel = \pm 1$ a.u. **(f-h)** Comparative CTMC simulation results for respective pulse durations revealing agreement with experiments both in extent of the momentum space and in observed electron structures. In **(d,g)**, a cutout of the data for a typical ToF spectrometer with an acceptance angle of 5° (and below) is shown in black dashed lines. Black arrows mark the different orders of LESs in **(d-h)**.

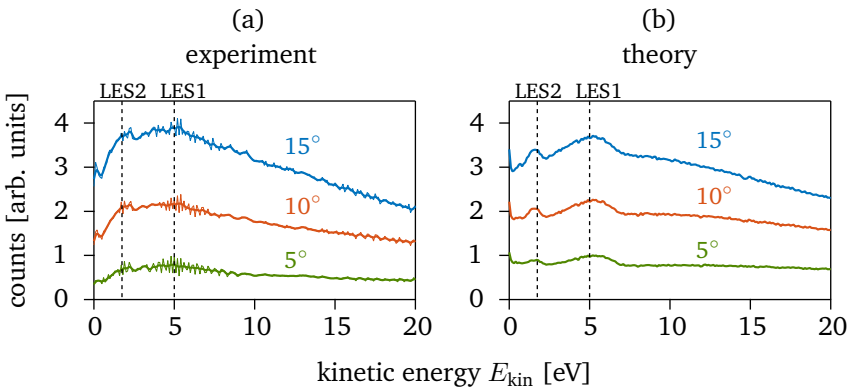

Figure 4.4: Kinetic energy spectra at ToF-like cuts. Energy spectra **(a)** resulting from the experimental momentum distributions of Fig. 4.3 (d) and **(b)** its CTMC counterpart of Fig. 4.3 (g) for electrons emitted into a cone with opening angles $\varphi = 5°$ (green), $10°$ (red), and $15°$ (blue) around the polarization axis. Structures near 5 and 1.75 eV are attributed to first and second order LES, respectively (experimental raw data: thin lines, smoothed spectra: thick lines).

momenta in Fig. 4.3 (g) (exemplarily for simulations at 6.5 cycles) to local maxima in the energy–angular momentum distribution plotted in Fig. 4.5 (a). Peaks due to focusing of varying order of recollision can be identified (LES1 – LES4, LES5/VLES). Their influence on the vectorial momentum spectrum can now be highlighted by selectively mapping these peaks onto the $(p_\parallel, p_\perp)$ plane thereby suppressing the smooth background. The resulting reduced momentum map is plotted in Fig. 4.5 (b). It thus becomes obvious in comparison with Figs. 4.3 (g) that the approximately vertical bands or lobes signify the low-order LESs (LES1 – LES4). Moreover, the V-shaped structure appears at the origin [red data points in Fig. 4.5 (b)] corresponds to the highest order (in this case fifth order) LES. In the following, we will call the V-shaped structure VLES to distinguish it from the differently, vertically shaped lower orders of LES. The V-shape of the VLES will be further analyzed in Sec. 4.4. To show the difference in final momentum between VLES and other electrons with similar kinetic energies we have also plotted the final momenta of trajectories from the same energy range as the VLES but higher angular momentum ($L \sim 22$, absolute maximum of the $E - L$ distribution) in Fig. 4.5 (b). This leads to the feature-less uniformly distributed background half-circle [gray data points in Fig. 4.5 (b) and magnified in Fig. 4.5 (c)] around zero momentum.

It should be added here that Wu *et al.* [196] named the second order LES as VLES and claimed a double hump for it in momentum space, similar to our findings for the VLES. Yet, their VLES in the KED was analyzed under an angle of 5° to 8° which does not include our VLES at the origin of the distribution. Hence, our VLES and the one found in Wu *et al.* [196] are not related, while their double hump might be related to our VLES since it was extracted from the total momentum distribution.

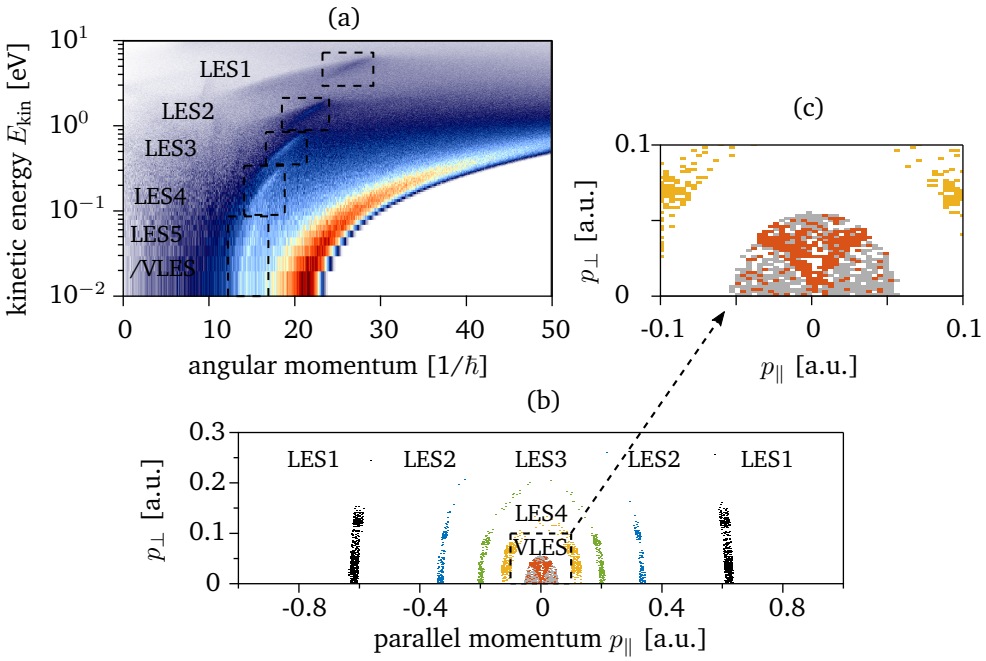

Figure 4.5: Projection of $p_\perp$-$p_\parallel$ - map onto E-L plane and identification of Coulomb focused structures. (a) Projection of the electron momentum distribution of Fig. 4.3 (g) onto the $\log E - L$ plane (normalized linear color scale). The k-th order LES peaks ($k = 1, \ldots, 4$) and the VLES resulting from two-dimensional Coulomb focusing are marked. **(b)** Mapping of the trajectories focused within the k^{th} order LES in the $E - L$ plane [dashed boxes in (a)] back onto the $(p_\parallel, p_\perp)$ plane. The near vertical stripes correspond to the low-order LES [$k = 1$ (black), 2 (blue), 3 (green), 4 (yellow)] while the VLES also visible in Fig. 4.3 (d,g) gives rise to a V-shaped distribution ("VLES", red). **(c)** The latter is shown zoomed in together with a feature-less half-circle around zero momentum which corresponds to very-low energy electrons outside the VLES region (gray, see text).

4.3 LESs: dependence on pulse duration

The mechanism behind the LES was ascertained in many theoretical publications (as described in Sec. 4.1) after its original finding in [58, 59] and related to soft re-collisions where electrons re-scatter elastically with their parent ion in forward direction and with relatively low kinetic energies $E_{\text{kin,LES}} \ll U_\text{P}$. The low return momenta makes the electrons relatively responsive to the Coulomb field of the nearby nucleus leading to an increase or decrease of momentum that results in an energy/momentum bunching forming the LESs in the spectrum. Since the soft re-collision is strongly dependent on the laser field that drives the electron trajectory after tunneling, the formation of the LES also depends on the laser field properties. Kästner *et al.* [225] described that the LES peak position in the energy and respectively momentum spectrum depends on the number of optical cycles n_cyc[7] of the laser field as well as on its CEP [225,226]. Moreover, multiple orders k of LES peaks occur for trajectories having turning points near the $z = 0$ plane [see Fig. 4.1 (b)] after the k quiver oscillation following tunneling [220]. Hence, multiple quiver oscillations k of the electron are dependent on n_cyc of the laser field. When applying the same analysis on our CTMC calculations as in Fig. 4.5 for the data of different pulse durations, we find that only the 3 orders of LES form in the case of the shortest pulse duration of 41 fs (4 optical cycles, calculated in [220, Fig. 7(b)])[8] while ~ 6 orders of LESs appear in the CTMC calculation of the case of the longest pulse duration of 140 fs (13.5 optical cycles, estimated from [220, Fig. 7(d)])[9].

It is instructive to study the variation of the peak position of the LES(s) as a function of pulse duration, i.e. the number of optical field cycles n_cyc, on the basis of both our experimental results and the CTMC calculations shown in Fig. 4.3. Therefore a cross section of the 3D momentum distribution is extracted along the $p_\parallel$ direction at $p_\perp = 0.025$ a.u. for all experiments and CTMC calculations [plotted in Fig. 4.6 (a,b)]. The chosen $p_\perp$ - level is found to be the best compromise between signal statistics and the ability to resolve the LES(s), specifically for all experimental data since the LES(s) are less pronounced than in the CTMC calculations. The cross sections are plotted in red for the data according to $\tau = 4$ cycles [from Fig. 4.3 (a,f)], blue for the data according to $\tau = 6.5$ cycles [from Fig. 4.3 (d,g)] and green for the data according to $\tau = 13.5$ cycles [from Fig. 4.3 (e,h)], respectively for experiment and CTMC simulation. As expected from the experimental 3D momentum distributions, the cross section of $\tau = 6.5$ cycles (blue) reveals a well pronounced LES1 at $p_{\parallel,\text{LES1,6.5oc}} \sim (0.626 \pm 0.05)$ a.u. and LES2 at $p_{\parallel,\text{LES2,6.5oc}} \sim (0.382 \pm 0.05)$ a.u. in Fig. 4.6 (a). These values correspond

[7] As commonly practiced, we use the definition of the FWHM of the pulse intensity throughout this section.

[8] This example calculated in [220, Fig. 7(b)] shows two distinct orders of LES and a shallow third order close to $E \sim 0$ can be seen. The number of optical cycles are defined in as the full width of an envelope function $f_\text{env.} = \sin^2(\pi\, t/\tau_\text{theo})$ applied to the electric field and compare to the FWHM of the experimental pulse intensity as $\tau_\text{FWHM} = 0.364\, \tau_\text{theo}$ [220]. Hence, $\tau_{1/e2} = 10 \rightarrow \tau_\text{FWHM} \sim 3.6$. For 4 cycles the shallow third LES is expected to be stronger.

[9] $\tau_{1/e2} = 30 \rightarrow \tau_\text{FWHM} \sim 10.9$ in [220, Fig. 7(d)] 5 orders of LESs are clearly visible and we expect a 6th LES to be formed for $\tau_\text{FWHM} \sim 13$.

to $E_{kin,\mathrm{LES1,6.5oc}} \sim (5.33 \pm 0.60)$ eV and to $E_{kin,\mathrm{LES2,6.5oc}} \sim (1.99 \pm 0.36)$ eV agrees with the extracted LES peak positions in the KED of Fig. 4.4 (a). The data for $\tau = 13.5$ cycles (green) result in $p_{\parallel,\mathrm{LES1,13.5oc}} \sim (0.65 \pm 0.075)$ a.u. and LES2 at $p_{\parallel,\mathrm{LES2,13.5oc}} \sim (0.394 \pm 0.075)$ a.u. shifted to larger momentum positions[10]. For the case of $\tau = 4$ cycles (red) the experimental data only reveal LES1 at $p_{\parallel,\mathrm{LES1,4.5oc}}$ $\sim (0.562 \pm 0.05)$ a.u. due to the discussed issue with the magnetic field node. The data are summarized in Fig. 4.6 (c) as opened squares for LES1 and opened circles for LES2 with their respective colors. Overall, a clear trend to lower momenta is noticeable for shorter pulse durations (indicated with black arrows). In comparison, the cuts from the CTMC calculations [see Fig. 4.6 (b)] reveal much more pronounced LES(s) than the experimental case, yet they result in similar peak positions as the experimental values as shown in Fig. 4.6 (c) as closed upward triangles for LES1 and closed, downward triangles for LES2 with their respective colors. The agreement between experiment and CTMC simulation is quite remarkable as mentioned earlier.

Thus, our results show experimental evidence for the soft re-collision mechanism behind the different LES orders by showing a direct dependence of LES position on the laser pulse duration. Recently, Zhang *et al.* [246] published a similar investigation on showing the LES peak dependence for measurements on argon and krypton with a laser source at wavelength of $\lambda = 2\,\mu$m for pulse durations between $n_{\mathrm{cyc}} = 2$ to 10 cycles. Moreover, they presented an analytical approach based on classical trajectories that accurately describes the peak positions as a function of n_{cyc} and which will be explained here shortly. The analytical solution divides LES peak position in momentum space into a part containing the laser and target properties and a secondary part containing the universal time dependence [246]. The first part expresses the LES peak position according to [224, 225] as

$$p_{\mathrm{LESk}} = \frac{2}{(2\,k+1)\,\pi}\frac{\mathcal{E}}{\omega} \quad , \tag{4.9}$$

and correspondent to that in energy space

$$E_{\mathrm{LESk}} = \frac{8}{(2\,k+1)^2\,\pi^2}\,U_{\mathrm{P}} \tag{4.10}$$

as a function of the electric field $\mathcal{E}$, and the frequency ω of the laser and respectively $U_{\mathrm{P}} = \mathcal{E}^2/(4\,\omega^2)$, as well as the order of the LES k. This expression is valid for a continuous wave (cw, $n_{\mathrm{cyc}} \to \infty$). The influence of the envelope and the relative electric field amplitudes on the LES position can be expressed by including the pulse duration dependence as follows [246]

$$p_{\mathrm{LESk}}(n_{\mathrm{cyc}}) = \frac{p_{\mathrm{LESk}}}{2}\left[1 + \exp(-c\,\{\frac{3}{n_{\mathrm{cyc}}}\}^2)\right] \quad \text{for } n_{\mathrm{cyc}} \geq 2 \tag{4.11}$$

with $c = \ln 2/2$[11]. The resulting behavior of the LES peak position is plotted for our experimental conditions in Fig. 4.6 (c) as dashed lines (black for LES1, gray for

[10] error is larger since the structures are less pronounced

[11] This factor compensates for the in parts for the difference in FWHM of the intensity and the electric field distribution.

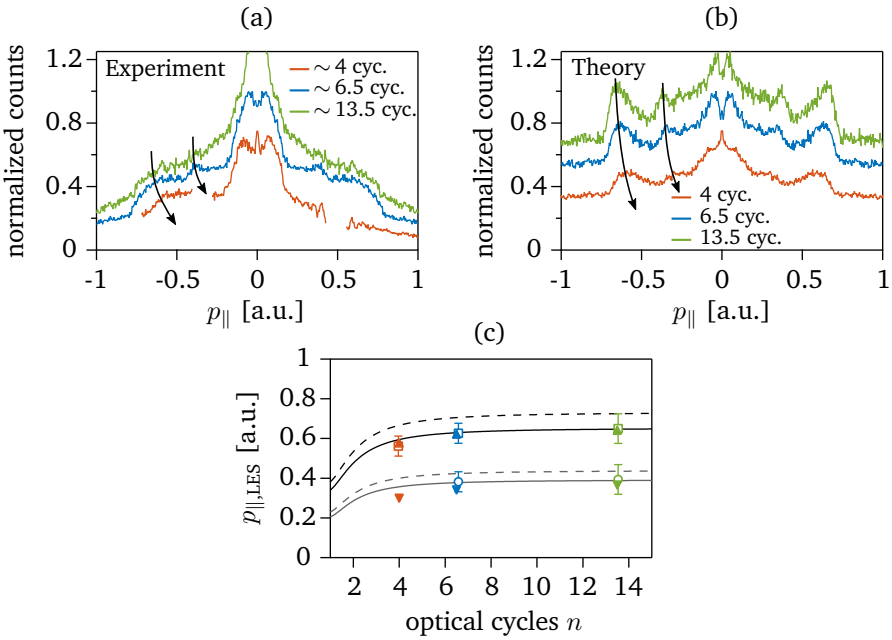

Figure 4.6: Dependence of LESs on pulse duration. The peak positions in momentum space of the first and the second order LESs are compared for the different pulse durations of 41 fs (red), 68 fs (blue) and 140 fs (green) for cut through the ($p_\perp$,$p_\parallel$) distributions along the $p_\parallel$ axis at $p_\perp = 0.025$ a.u. The cuts through **(a)** the experimental distributions of Figs. 4.3 (a,d,e) and **(b)** the CTMC simulation results of Figs. 4.3 (f,g,h) show the single peaks of the LESs which are highlighted with black arrows. The center of the peaks are determined and plotted in **(c)** (LES1 positions: exp. open squares, theo. filled upwards triangles; LES2 positions: exp. open circles, theo. filled downwards triangles). For evaluation of our results, the expected peak positions according to [246] are plotted for a plain model (black dashed line) and a corrected model (black solid line) taking into account focal averaging and a numerics related momentum shift (see text).

LES2). The trend of the analytical solution agrees quite nicely with our experimental and CTMC data, yet is shifted to higher momentum values ($\sim 12\,\%$ higher then the experiemental LES1 peak position, and $\sim 20\,\%$ higher in case of the LES2). This disagreement can be explained by on the one hand a "red shift" [246] of all LES peaks in the numerical simulation due to a small momentum reduction of the electrons before leaving the attractive Coulomb potential, and secondly, the missing influence of the averaging over the full Gaussian focal volume (as described in Sec. 3.1.3). When introducing the corrections for both effects, the peak position dependence can be expressed by

$$p_{\mathrm{LESk,corr.}}(n_{\mathrm{cyc}}) = p_{\mathrm{LESk}}(n_{\mathrm{cyc}}) \left(1 - \frac{9}{16\,\gamma^3}\,\frac{\omega}{U_\mathrm{P}} - \frac{3\,\pi\,C_{3\mathrm{D}}}{2^{11/5}}\,\frac{\omega^{2/5}}{U_\mathrm{P}^{3/5}}\right) \tag{4.12}$$

with $C_{3\mathrm{D}} = 0.073$. The equation was expanded in ω for fixed γ. The corrected

analytical solution is plotted for our experimental conditions in Fig. 4.6 (c) as solid lines (black for LES1, gray for LES2) and agrees quite accurately within error with our experimental and CTMC results. In case of the second order LES2, the CTMC appear slightly below the analytical model. The overall agreement of both theories and the experiment reveals confirms our experimental findings of the LESs and generally supports the soft re-collision related mechanism behind the LESs.

4.4 VLES: analysis of the V-shape

In Sec. 4.2.3, we found in the analysis of the CTMC simulation for a pulse duration of 68 fs that the VLES differs from lower order LESs not only by its very low energy but also by a different vectorial momentum distribution. While the lower-orders of LESs appear as almost vertical bands that are slightly tilted towards $p_{\parallel} = 0$ [see Fig. 4.5 (b)], the VLES shows its clear V-shape so a tilt away from $p_{\parallel} = 0$ which is obvious by inspecting the overall momentum distribution.

In Fig. 4.7, a magnification of only the VLESs for all measured pulse durations (a-c) and their corresponding CTMC calculations (d-f) is plotted. As mentioned before, it is apparent that the VLES becomes increasingly sharper with an increasing number of optical cycles and hence an increasing number k of soft re-collisions with the vicinity of the Coulomb field in the $z = 0$ - plane [see Fig. 4.1 (b)]. While the characteristic V-shape of the VLES is not entirely recognizable for the shortest pulse duration $\tau_p = 41$ fs, it develops for longer pulses. The reason for the absence of the V-shape is that for the shortest pulse duration (41 fs) the VLES is surrounded/overlapped by a small contribution of a third order LES close to $p_{\parallel} = 0$ [compare Fig. 7 (b)[12] in [220]] which gives the appearance of a "trident" of the center structure in Figs. 4.7 (a,d). The total width of the structure reduces as τ gets longer. In Fig. 4.8 the evolution of the full width Γ of the structures at the origin as a function of pulse duration is plotted allowing for a quantitative comparison between experiment (red squares) and simulation (blue circles). The widths are extracted along the $p_{\parallel}$ direction taken at $p_{\perp} = 2 \times 10^{-2}$ a.u. (dashed black lines in Fig. 4.7) intersecting with the $60\,\%$ level contour of the normalized data. The $60\,\%$ level was found to be the best compromise between signal statistics and the ability to resolve the structure. Both experiment and theory in Fig. 4.8 show a monotonic trend towards smaller width Γ with increasing τ. The agreement is quite remarkable given the uncertainty in the extraction of this observable and the small energies ($E < 0.15$ eV) of the electrons in that momentum region which are treated within CTMC.

Let's come back to the origin of the V-shape in contrast to the almost vertical bands of the lower-order LESs. While the LESs all have a finite offset in $p_{\parallel}$, the VLES, by contrast, features strongly transverse emission at angles centered about $\pi/2$ as seen in Figs 4.3 and Fig. 4.5 (b). A possible explanation for this can be found by

[12] The number of optical cycles are defined in [220] with a width of $1/e^2$, corresponding to $\tau_{1/e2} = 10 \rightarrow \tau_{\text{FWHM}} \sim 4$ in FWHM.

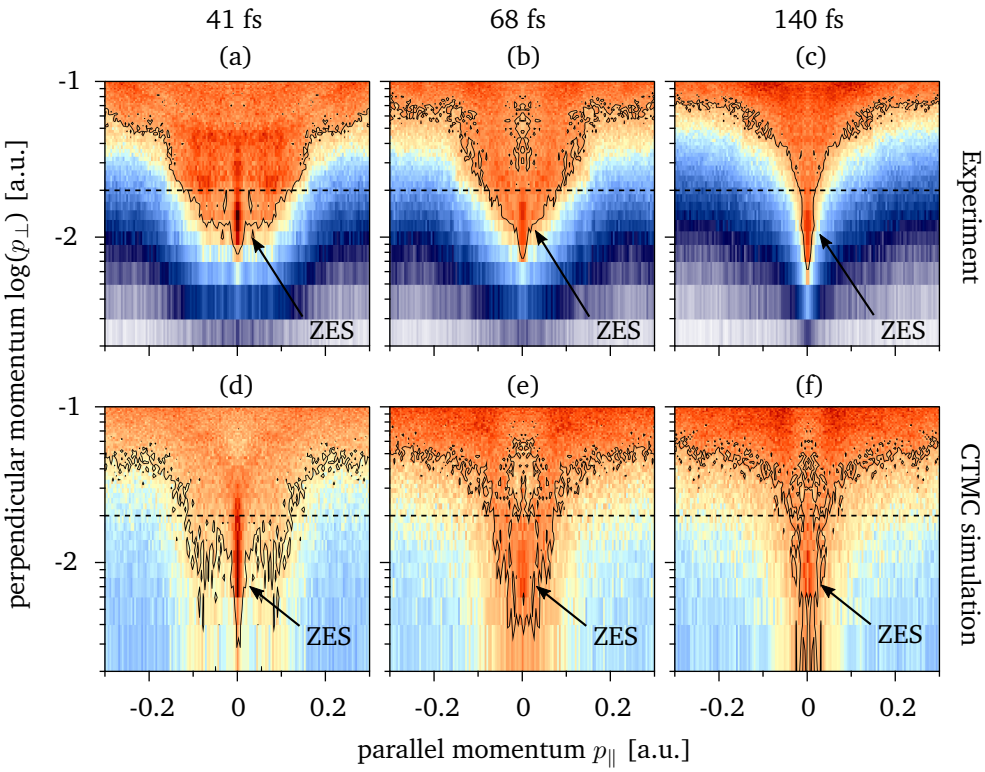

Figure 4.7: Comarison of experiment and CTMC calculations around the center of PtPl. Momentum map ($\log p_\perp$ over $p_\parallel$) of the measured (top) and simulated (bottom) emission spectra (normalized linear color scale) for different pulse durations $\tau_p = 41$ fs (4 cycles, left), 68 fs (6.5 cycles, center), and 140 fs (13 cycles, right). The ZES is marked. A contour highlights the $60\,\%$ level of the normalized data. The cut at $p_\perp = 2 \times 10^{-2}$ a.u. is used to determine the full width Γ of the structures at very low energies.

analyzing the Kepler orbits (similar to [220]) of the outgoing trajectories that electrons can lock onto due to a perturbation by a combined Coulomb and laser field. The Kepler orbits for our case of 6.5 optical cycles exhibit eccentricities ranging from $\varepsilon = \sqrt{1 + 2EL^2} \approx 1$ close to threshold (VLES), showing parabolic character, to $\varepsilon \approx 17.3$ in the center of LES1 showing strong hyperbolic character[13]. Such hyperbolas have asymptotes with inclination angles relative to the major axis ranging from $\theta = \arctan\sqrt{\varepsilon^2 - 1} = 0$ to almost $\theta \approx \pi/2$. As the major axes of LES electrons of all orders have similar tilt angles close to $\pi/2$ with respect to the laser polarization direction, increasing order of LES is associated with larger emission angles of the electrons reaching near parallel emission for VLES electrons. The analysis is described in more detail in [220, 226].

[13] Kepler orbits feature trajectories with hyperbolic character for $\epsilon > 1$, parabolic character for $\epsilon = 1$, elliptical character for $\epsilon < 1$ and circular character for $\epsilon = 0$.

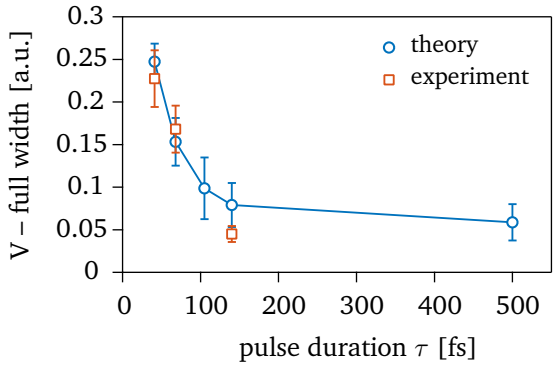

Figure 4.8: Comarison of width of center structure in experiment and CTMC calculations. Full width Γ of the structures at very low energies in $p_{\parallel}$ detected for a cut through the momentum distribution at $p_{\perp} = 2 \times 10^{-2}$ a.u. intersecting with the 60 % level contour of the normalized data (see Fig. 4.7). Blue line and circles: CTMC simulation; red squares: experimental data.

A related analysis was published by Becker *et al.* [247] as a direct investigation of the V-shape of the VLES of this work and of our publication [217] on the basis of the classical SMM and in the related quantum-orbit expansion of the SFA [219, 248]. As particular orbits can be associated with particular patterns in the 3D momentum space, Becker *et al.* already revealed beforehand the nature of the LES as being fully related to forward-scattering (FS, $\Theta_r \to 0°$) orbits [229] in contrast to high-energy electrons related to back-scattering (BS, $\Theta_r \to 180°$) electrons. The energy/momentum cutoffs of the re-scattered electrons in all directions can be calculated according to the SMM (see Eq. 2.47 in Sec. 2.2.2.3) and can be projected in the plane of final momenta as plotted in Fig. 4.9 (a) (taken from [247], p_y over p_x in Cartesian coordinates with laser polarization along $\vec{e}_x$). Here, the single cutoffs can easily be distinguished. The FS cutoffs, which correspond to the LES positions, are marked around the $p_y = 0$ – axis with $\mu \geq 1$, whereas μ stands for the LES order. The cutoff trajectories of the LES appear in hyperbolic shapes as described earlier, and its crossing with the $p_y = 0$ – axis can be calculated according to Eq. 4.9. For increasing scattering angles $\Theta_r \gg 0°$ the FS solutions connect with the BS solutions in the nature of the re-scattering process. The BS cutoffs furthermore can be divided in two different classes: those with final energies $E_{resc} > 8\,U_P$ which are marked in Fig. 4.9 (a) as β = -1, and those with $E_{resc} < 8\,U_P$ marked as $\beta = 1$. This distinction is related to the special case of electrons re-colliding with the parent ion when the electric field $\mathcal{E}$ is zero, and hence the vector potential is maximal $A_{max} = A_0 = p_{str}$ [see Fig. 2.5 (a)] resulting in case of BS in a final energy of $8\,U_P$. In Fig. 4.9 (a), the boundary between the higher energetic β = -1 and the lower energetic $\beta = +1$ cutoffs is marked with a dotted line. Moreover, β = -1 cutoffs (black, red, green and blue) are connected with the FS scattering solutions of the LESs. On the other hand, the $\beta = +1$ cutoffs (purple, yellow, pink, brown) all pass through the origin of the distribution. In Fig. 4.9 (b) (also taken from [247]), the area around the origin is magnified, showing the context in more detail. While the β = -1 BS curves

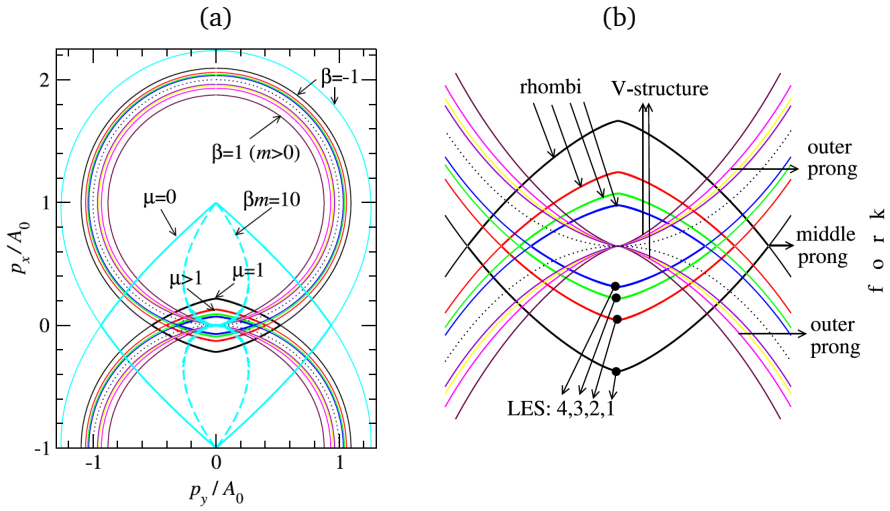

Figure 4.9: Quantum orbit analysis of VLES and LESs. The analysis was performed in [247]. Both graphs are taken from the same publication. **(a)** The angle-dependent final or cut-off energies are calculated along a quantum-orbit expansion of the SFA for the ($p_\perp$,$p_\parallel$) - plane of the final momenta. Along the longitudinal momentum axis ($p_\perp = p_y = 0$) the different structures can be perceived as kinks in the hyperbolic trajectories in forward scattering (FS, $\Theta_r \to 0$) direction. For increasing Θ_r the cut-off energies transition into back-scattering (BS, $\Theta_r \to 180°$) solutions which can be distinguished by final energies of $E_{resc} > 8\,U_P$ marked as β = -1, and those with $E_{resc} < 8\,U_P$ marked as $\beta = 1$. The structures in FS direction corresponding to β = -1 correspond to multiple orders of LESs, while the ones of $\beta = 1$ correspond to the VLES which yield a clear V-shape in contrary to the LESs. The context becomes clear in the zoomed in cut-out in **(b)** which agrees with our CTMC calculation results of Figs. 4.5 (b,c).

form a diamond like structure around the origin, the $\beta = +1$ BS curves all pass the origin in different angles forming a V-shape towards the center. This is exactly the V-shape we encounter in our measurement and which we dubbed as VLES.

This analysis explains the different shape of the VLES compared to the LES which strongly depends on when they are "born" in the phase space, either before the trajectory that returns when $\mathcal{E} = 0$ ($\beta = +1$) or after that trajectory (β = -1). The former trajectories correspond to the VLES which is obviously generated by a superposition of both forward and backward scattering orbits for very low kinetic energy, while the LESs can solely be attributed to forward scattering. A similar analysis was done by Möller *et al.* [61] where they analyzed a *fork-like structure* off-set in transverse momentum space which they revealed experimentally. This fork-structure could be related to the diamond (or rhombi) like shapes as composed by the β = -1 BS orbits around the origin, which either interfere with themselves or with the $\beta = +1$ BS orbits to create several prongs or forks as also shown in Fig. 4.9 (b).

4.5 ZES: mechanism and quantitative analysis

We now turn to the ZES, a feature found in all experimental momentum spectra of several atomic or molecular targets [60,218] as well as in the current measurement [see Fig. 4.3 (a–e)] with the local maximum appearing at $p_{\parallel} = 0$ and $p_{\perp} \approx \Delta p_{\perp}$. $\Delta p_{\perp}$ is the experimental momentum resolution perpendicular to the polarization axis as calculated in Sec. 4.2.1. This peak is, within the experimental resolution, consistent with emission at (near) zero kinetic energy and remains at the same position irrespective of the pulse duration. Yet, as we found earlier, such a structure is absent in the simulated emission spectrum when only direct ionization to the continuum is taken into account [see Fig. 4.3 (f–h)]. In [60, 218] the mechanism behind the ZES electrons was assumed to be related to high-lying Rydberg state population due to their negligible energy. Moreover, the structure showed a dependence on ellipticity, vanishing for an increasing degree of ellipticity which let to the conclusion that re-scattering is involved in the process.

Assuming the ZES electrons originate from stabilized, high-lying Rydberg states, the question remains how they are ionized to eventually reach the detector. According to the findings of [232], the Rydberg states stay populated and the region around the origin yields a low yield. As this is not the case for us, however, the presence of a weak extraction field in the interaction volume of the ReMi spectrometer, in the present case $\mathcal{E}_{\text{extr}} = 1.3$ V/cm $\approx 2.6 \times 10^{-10}$ a.u., does allow for the extraction of the high-lying states via field-ionization. Approximating the ionic potential by a Coulomb tail and using hydrogenic Rydberg states, the threshold for over-the-barrier ionization above the saddle point at (e.g. described in [249])

$$E_{\text{bind}} = -\frac{1}{2\,n^2} = -2\,\sqrt{\mathcal{E}_{\text{extr}}} \tag{4.13}$$

lies near the principal quantum number $n = 125$ meaning that our extraction field does field-ionize any Rydberg state of $n \geq 125$, which is a possible scenario. Also tunneling through the Coulomb potential that is a minorly bent by the extraction field is an additional ionization possibility for the Rydberg state electrons sitting slightly below $n = 125$.

In order to investigate the possible population of high-lying Rydberg states, the CTMC simulation allows to track also the electron trajectories that end up with *negative final energy* and so below the ionization threshold after the end of the pulse. The CTMC calculation of our experimental conditions [3100 nm, 68 fs, 10^{14} W/cm^2, see Fig. 4.3 (g)] yields an energy distribution of electrons with $E < 0$ as plotted in blue in Fig. 4.10 featuring a steep rise near $E_{\text{onset}} = -0.0035$ a.u. and a nearly constant spectral excitation density up to the ionization threshold, thus including $n = 125$. This rise can be related to the onset of Rydberg population near $n \gtrsim 1/\sqrt{2\,E_{\text{onset}}} \sim 12$. Hence, there seem to be sufficient electrons populating high-lying Rydberg states to be field-ionized by the extraction field long after the pulse and to end up in our momentum distribution as the ZES.

That leaves the question of how exactly the Rydberg state population occurs. There

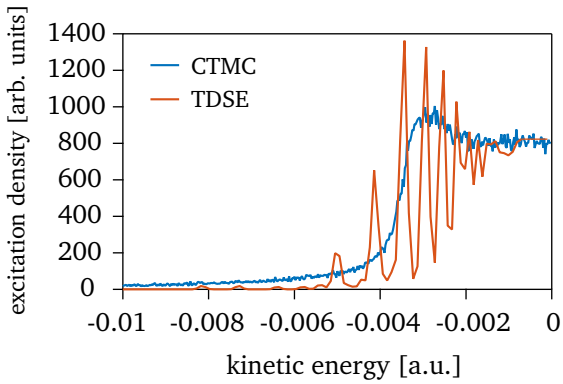

Figure 4.10: Energy distribution of bound electrons from CTMC and TDSE calculations. Energy distribution of electrons bound in high-lying Rydberg states after the end of the mid-IR laser pulse (3100 nm, 68 fs, 10^{14} W/cm^2) from classical (blue line) and quantum (red line) simulations. An onset of the Rydberg population is found at $E \sim$ -0.0035 a.u. corresponding to states with principal quantum numbers of $n \geq 12$.

are two alternative pathways contributing to the population of such high Rydberg states: direct *multi-photon like excitation* from the ground state and indirectly through *recapture of tunnel-ionized electrons*. The latter process has been referred to as FTI [234, 250] and has been unambiguously identified for Rydberg atoms exposed to a sequence of ultrashort pulses [251]. Only the second pathway is accounted for by the present CTMC simulation while the quantum simulation contains all pathways. Hence, probing the spectral distribution below the ionization threshold with both the CTMC and the TDSE simulation allows for the determination of the relative importance of the two excitation processes. This is also a sensitive probe of the classical–quantum correspondence. In Fig. 4.10 the energy distribution of electrons after the end of a IR laser pulse is plotted for the quantum in red. Strikingly, the TDSE results feature the same steep rise near $E = -0.0035$ a.u. and a similar constant spectral excitation density up to the ionization threshold (up to where the pseudostate expansion is still useful). The existence of the onset of Rydberg population near $n \gtrsim 12$ in both the quantum and classical simulations is a clear indication that recapture of tunnel-ionized electrons dominates over direct multi-photon bound state excitation. For the latter such a sharp onset is not expected. Moreover, the value for the threshold can be easily estimated from the recapture scenario. Comparing the Coulomb potential of an electrons with vanishing kinetic quiver energy at a distance corresponding to the quiver amplitude $\alpha = \mathcal{E}_{\text{peak}}/\omega^2$ at the end of the pulse with the (hydrogenic) binding energy of a Rydberg state with principal quantum number n gives

$$-\frac{1}{\alpha} = -\frac{1}{2n^2} \tag{4.14}$$

yielding $n \approx 11$ and $E_{\text{bind}} = -0.004$ remarkably close to the onset in Fig. 4.10. The CTMC simulation is thus well suited to describe the recapture process and the ZES

emerging from it. This is particularly convenient since the spectral region close to threshold contributing to field ionization ($n \gtrsim 125$) cannot be easily accurately represented by the discrete pseudostate expansion in the quantum simulation.

Within the CTMC the relative weight of the ZES compared to the surrounding low-energy spectrum can be easily determined. Since both contributions originate from the same source, we compare them to the total number N_I of the ensemble of tunnel ionized electrons during the pulse. From those, the fraction

$$P_{\mathrm{low-E}} = N_{\mathrm{low-E}}/N_I \tag{4.15}$$

contributes to the smooth low-energy spectrum defined here by electrons with positive energy and final momenta $p \leq 0.1$ a.u. The fraction of recaptured electrons

$$P_{\mathrm{ZES}} = N_{\mathrm{rec}}/N_I\,, \tag{4.16}$$

where N_{rec} is the number of electrons captured into weakly bound Rydberg states above the field-ionization threshold, contribute to the ZES. For a pulse duration of 68 fs the ratio $F_{\mathrm{ZES}} = P_{\mathrm{ZES}}/(P_{\mathrm{ZES}} + P_{\mathrm{low-E}})$ for the CTMC results gives $F_{\mathrm{ZES}} = 0.006$. In the experiment [see Fig. 4.3 (g)], ZES electrons cannot be distinguished from the low-energy background, requiring a modification of Eq. 4.16. We, instead, determine the number of electrons N_{ZES} with asymptotic momentum $p \leq 0.018$ a.u. and evaluate $F_{\mathrm{ZES}} = N_{\mathrm{ZES}}/N_{\mathrm{low-E}}$ for $N_{\mathrm{low-E}}$ corresponding to $p \leq 0.1$ a.u. For the comparison with the simulation we fold the simulated distribution of recaptured electrons with a Gaussian with widths $\sigma_{\parallel} = \Delta p_{\parallel}$ and $\sigma_{\perp} = \Delta p_{\perp}$ given by the experimental resolution centered near the origin ($p_{\parallel} = 0, p_{\perp} = \Delta p_{\perp}$) and add them to the momentum distributions [marked as ZES in Fig. 4.8 (d-f)]. We consider only over-barrier ionization neglecting tunnel ionization of Rydberg states with principal number smaller but close to $n \lesssim 125$. This results in simulated values of $F_{\mathrm{ZES}} = 0.038$ for 41 fs pulses slowly decreasing to $F_{\mathrm{ZES}} = 0.036$ for 140 fs pulses. The experimental value for F_{ZES} is slightly smaller ($F_{\mathrm{ZES}} = 0.025$ for 41 fs pulses, $F_{\mathrm{ZES}} = 0.027$ for 140 fs pulses) which might be directly related to the reduced detection probability for electrons with asymptotic momenta below the perpendicular momentum resolution of the ReMi, $p < \Delta p_{\perp}$. Overall, the *quantitative* agreement between classical simulation and experiment is remarkable again regarding the fact that the applicability of classical calculations at the tunnel exit seems initially not obvious.

Consequently, we can associate the ZES as discovered in our experiments [60, 169, 217, 218] as re-captured electrons via FTI with subsequent post-pulse ionization by the static extraction field. The FTI process itself has been investigated in various publication (e.g. [234, 251–255]). Nubbemeyer *et al.* [234] first made the connection of explaining the re-capture process in regard to the strong-field recollision model or SMM. For electrons returning to their parent ion with relatively low kinetic energy, there is the possibility to be slowed down even further by the attractive force of the Coulomb field after re-collision and hence to end up in a high-lying Rydberg state. This *re-absorption* process in FTI can be seen as a recapture similar to the re-combination in HHG. Since re-collision is part of FTI, the

probability of this process strongly decreases with increasing ellipticity in polarization as the electron returns less probable to the parent ion [253, 254]. [234] even suggests that the FTI process might occur as a substantial part of Corkum's recollision model next to HHG, NSDI and HATI, yet it is the least investigated since it involves neutral, excited atomic systems which are harder to detect with extraction field dependent techniques.

After our work on the mechanism behind the ZES was published [217], further investigations on the topic followed. Diesen *et al.* [256] investigated the dynamics of the Rydberg electrons that are released by the weak extraction field. On the basis of our work, they confirmed the occurrence of the ZES by weak-field-ionization of the static field of the ReMi and moreover explored the Stark dynamics of the slowly escaping electrons in the static field. Interestingly, they found an asymmetric shift of the ZES peak compared to the broad distribution of direct electrons in the final momentum space along the axis of the static field in opposite flight direction of the electron, hence in $+\vec{\mathcal{E}}$ direction. The ZES shift was quantified and related to the static field strength as Δp_{shift} = -0.6 $\mathcal{E}^{0.25}$. In our case, this momentum shift would hence amount to Δp_{shift} = -0.0024 a.u. < $\Delta p_{\parallel}$ which is below our longitudinal momentum resolution. Nevertheless, by careful inspection of the non-symetrized momentum distributions in Fig. 4.3 (a–c), a small asymmetry in position of the ZES can be presaged. In [60], the ZES shift seems slightly more obvious.
Further theoretical investigations on the mechanism behind the ZES were published by Pisanty *et al.* [257, 258]. Here, they used the *analytical R-matrix* (ARM) theory to investigate a kinematic mechanism underlaying the ZES similar to the soft re-collisions leading to several orders of LESs. What they found was a second series of LESs that results in much lower energies of ∼meV which is why they have been mostly overlooked by theoretical and experimental studies so far. According to [257, 258], these set of soft-recollision based ZESs scale in energy with $E_{\text{ZES}} \sim I_{\text{P}}^2/U_{\text{P}}$ while the LES energy scales with $E_{\text{LES}} \sim U_{\text{P}}$ (see [225] and Eq. 4.10). Hence, these ZESs could be shifted to higher energies for targets with higher ionization potential I_{P} or for SFI with shorter wavelength driving fields (as $U_{\text{P}} \sim \lambda^2$). Moreover, they explain that possibly both the mechanism proposed by us being FTI into Rydberg states with subsequent field-ionization and their mechanism of "ultra" soft re-collisions contribute to the ZES. A way to find out which is the dominant mechanism behind the ZES would be to investigate the intensity of the ZES both for higher I_{P} targets and for larger extraction fields.
Finally, another experimental and theoretical investigation by Quan *et al.* [259] suggested that the influence of the long-range Coulomb tail on the electrons quiver motion leads to the creation of the ZES.

It remains the question, why Liu *et al.* [232] and Veltheim *et al.* [233] did not resolve a ZES-like structure for Ar atoms as they both used a ReMi as their detection system with both a higher extraction field then us of 3 V/cm^2 and 4.78 V/cm^2, respectively. If the ZES mechanism is mainly related to FTI into Rydberg states, then they should have seen an even more pronounced ZES compared to us, yet also their resolution is slightly worse for higher fields. On the other hand, the experiments in the case of Liu *et al.* [232] were performed on xenon and krypton

which have lower I_P than argon, which would explain a less pronounced ZES after the mechanism of Pisanty *et al.* [257]. Nevertheless a ZES peak was found for Ar dimers which was explained by ionization of Rydberg states by charge oscillation within the dimer ion core. These open questions should be adressed in future investigations.

4.6 Universality of the structures

The LESs have been initially found in experimental studies on various target systems (He, Ne, Ar, Kr, Xe, N_2, H_2, D_2) [58, 59, 196]. This showed that the LES is a universal feature in SFI which was backed up by theory. As described beforehand, also the mechanisms behind the V-shaped VLES and the ZES is independent of the target system (being noble gas atoms and small diatomic molecules), hence both structures are universally relevant.

In the course of our investigation, we also measured the SFI of the lower I_P target xenon (published in [169]) at a peak intensity $I = 4 \times 10^{13}$ W/cm^2 ($U_P = 36$ eV, $\gamma = 0.4$, $z \sim 89.8$, $z_1 \sim 5.9$, $z_f \sim 1.4 \times 10^{-4}$)) and a pulse duration of $\tau = 71$ fs (7 optical cycles) at slightly higher static field of $\mathcal{E} = 2.0$ V/cm, $\mathcal{B}_1 = 4.7$ Gs and $\mathcal{B}_2 = 5.4$ Gs. The resulting electron momentum distribution corresponding to Xe^+ ions (averaged over the isotopes Xe_{129}, Xe_{131} and Xe_{132}) is plotted in Fig. 4.11 (a). The symmetric distribution shows similar characteristics to our results on Ar [compare to Fig. 4.3 (d)]. We find a broad distribution of direct electrons with pronounced low energy features, with the most distinct being the merged VLES and ZES near $p_{||} \approx 0$ a.u. and $p_\perp < 0.03$ a.u. Note that compared to our Ar measurement, the ZES in Xe does not appear as clearly [compare to e.g. Fig. 4.7 (b)]. The difference in experimental conditions in both measurements are the intensity being $I = 4 \times 10^{13}$ W/cm^2 in case of Xe compared to $I = 9 \times 10^{13}$ W/cm^2 for Ar and a slightly higher extraction field of the ReMi (2.0 V/cm in the case of Xe compared to 1.3 V/cm in the case of Ar). This slightly diminished ZES in Xe could be related to the requirement of a high I_P in the soft re-collision mechanism suggested by Pisanty *et al.* [257], yet would need a more accurate analysis.
To highlight the other individual features two normalized horizontal line-outs are plotted in Fig. 4.11 (b) at values of $p_\perp = 0.02$ a.u. (blue curve) and $p_\perp = 0.03$ a.u. (red curve). The $p_\perp = 0.03$ a.u. curve has been offset by $+0.2$ to enhance visibility. The $p_\perp = 0.03$ a.u. curve shows the richest structure with four different structures being resolvable: LES_1 at $p_{||} \approx 0.39$ a.u., LES_2 at $p_{||} \approx 0.27$ a.u., LES_3 at $p_{||} \approx 0.15$ a.u. The slight enhancement at around ≈ 0.065 a.u. seems to be an artefact. The characteristic V-shape associated with the VLES [196] is visible between $|p_{||}| \leq 0.06$ a.u. For the $p_\perp = 0.02$ a.u., only the first LES orders are visible. The positions of the LES orders (dashed black circles) agree well with predictions [225, 246]. This is highlighted in Fig. 4.11 (c), where the first three LES orders (1: green square, 2: green circle, 3: green diamond) are compared with the model of [246] as introduced in Sec. 4.3. For all orders (1: black, 2: dark gray, 3: light gray), the plain (dashed) and the corrected (solid) model agree well within

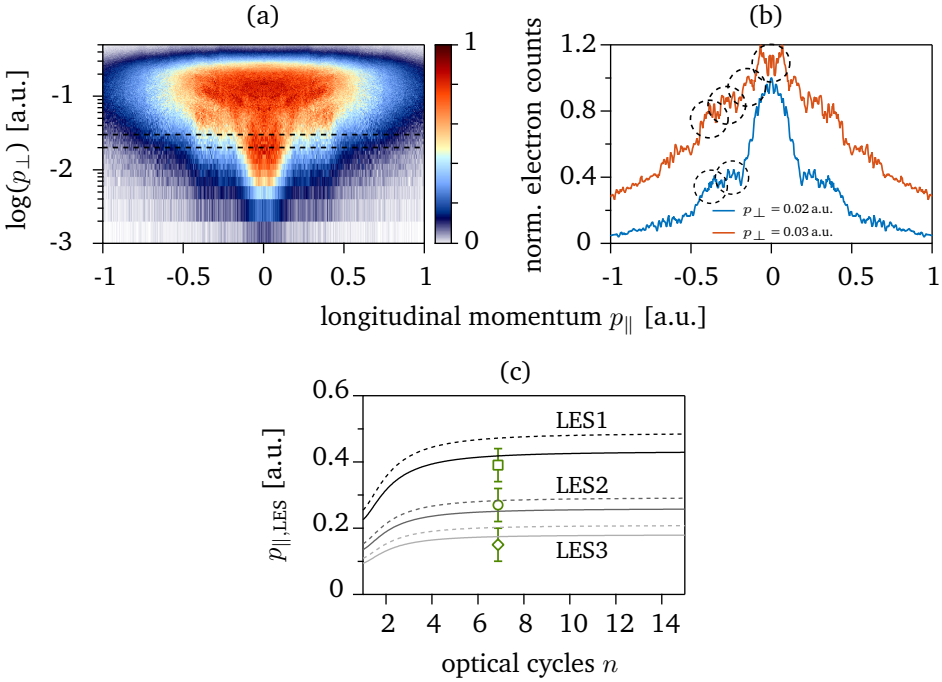

Figure 4.11: LES, VLES and ZES detected for xenon. (a) The measured electron momentum distribution corresponding to Xe^+ ions (71-fs, 4×10^{13} W/cm^2, $\gamma = 0.4$). Line outs [dashed lines in (a)] at $p_\perp = 0.02$ a.u. (blue) and 0.03 a.u. (red) are presented in **(b)** to highlight the different LES orders, the VLES and the ZES (black dashed circles). **(c)** The positions of LES1 (green square), LES2 (green circle) and LES3 (green diamond) are extracted from (b) and compared to the model calculation by [246] as introduced in Sec. 4.3 using the experimental parameters at hand.

error. Compared to the experiment with argon atoms (see Sec. 4.3), the LESs sit at lower momentum values for this measurement on Xe as a half of the intensity was utilized.

The universality of all low energy features independent of the target system is further corroborated by experimental data taken in our group on N_2 and O_2 in the course of the campaign leading to [60]. The data for O_2 are shown in the supplementary information of [60] and for N_2 in [218, Fig. 2]. In both data sets, both the VLES and ZES are clearly visible plus the LES2 can be conjectured in the momentum range shown.

Chapter 5

Double Ionization of Xenon atoms in Strong Mid-IR Fields

In the previous chapter, we have shown that investigations of SFI as driven by long wavelength laser fields that ensure unambiguous quasi-static conditions ($\gamma \ll 1$), yield new insights and mechanisms behind post-tunneling electron dynamics in strong electric fields. One aspect of strong-field physics that continues to provide many insights is multiple ionisation (MI), in first order being double ionization (DI). Especially the NSDI process relying on in-elastic scattering of the returning electron still offers surprises. Since many details about the re-collision induced (e,2e) process have been investigated in the last decades, this chapter focuses specifically on the NSDI process in xenon atoms driven with mid-IR laser pulses. So far NSDI results on Xe atoms were found to deviate in terms of their electron correlation mechanism [3, 260] from the common behavior as found in lower Z (atomic number) noble gas targets like e.g. helium, neon or argon driven in the near-IR. We investigate the NSDI regime of Xe atoms for moderate intensities ($I = 10^{13}$ W/cm^2 to 2×10^{14} W/cm^2) with mid-IR laser pulses in order to find the intensity-dependent transition between NSDI and *sequential double ionization* (SDI), relying purely on (double) tunneling ionization, when driving the SFI process in the mid-IR.

The chapter starts off with an overview over basic knowledge about NSDI in Sec. 5.1 stressing the essential analysis steps in order to interrogate the NSDI process as developed in the last decades, before discussing the precedent findings for the case of Xe atoms in Sec. 5.2 which seem to deviate from "standard" behavior. Afterwards, the experimental and theoretical results of our investigation of NSDI of Xe atoms by a mid-IR driving field are compared and discussed (in Sec. 5.3), where first the theoretical methods used in our investigation are introduced in Sec. 5.3.1 before the ion yield (Sec. 5.3.2), the re-coil ion momentum (Sec. 5.3.3) and the electron correlation distributions (Sec. 5.3.4) are analyzed as a function of peak intensity. Finally the mid-IR initiated results are put into perspective in Sec. 5.4. The experimental and theoretical data presented in this chapter and hence its main results have been submitted as

M. G. Pullen et al., Phys. Rev. A ***96****, 033401 (2017)*, cited as [261] and were also partly discussed in

B. Wolter et al., Physical Review X ***5****, 021034 (2015)* (highlighted in APS Physics) cited as [169].

5.1 Basics of non-sequential and sequential double ionization

The NSDI process is intricately linked to the re-collision of the first electron e_1 and mainly proceeds via two routes: the second electron e_2 can either be directly ionized by e_1 via the so-called (e, 2e) mechanism or it can be resonantly excited by e_1 and subsequently tunnel ionized at a later time (RESI) as briefly discussed in Sec. 2.2.2.2. The research on NSDI has been ongoing since three decades. The main experimental insights and theoretical approaches in understanding the NSDI process have been summarized in various review articles [74,102,109,135]. In this section, a general overview of the main experimental techniques is given in order to clarify our experimental approach to investigate the NSDI of xenon atoms. This section is basically a summary the most important insights on the topic of NSDI of today, and represents a possibility to get into the topic for the non-expert. The experts can easily skip this section.

The experimental milestones of investigations on NSDI are sketched in Fig. 5.1 (adapted from [102]). In the early 1980s, the initial signature of NSDI was discovered in ion yield distributions as a function of laser intensity for the SFI of xenon atoms by l'Huillier *et al.* [129]. Instead of following standard tunneling rates (e.g. PPT or ADK) the yield of the dications was already occurring for one order of magnitude lower intensities then expected resulting in a yield of only two to three orders of magnitude less the the one of the cation. Later the behavior was discovered for other noble gases [130–132] and small molecules [133,134]. In Fig. 5.1 (a) the work of Walker *et al.* [132] is shown exemplarily for helium atoms interacting with linearly polarized laser pulses at 780 nm wavelength. The expected yield of He^+ cations and He^{++} dications created by sequentially releasing two individual tunneling electrons is obtained via TDSE calculations (SAE approximation) and plotted as solid lines, respectively. While the cations[1] agree perfectly with the quantum mechanical calculation, the dications only overlap with the TDSE simulation for higher intensities (in this case $I > 10^{15}$ W/cm^2). The dashed line shows ADK rates. The unpredicted and very pronounced yield of dications below $I > 10^{15}$ W/cm^2 was accounted to a non-sequential mechanism that increases the probability for the emission of e_2 before the field alone is able to do so, e.g. by sequential tunnel ionization. Generally, the NSDI process is observed below the saturation intensity (I_{Sat}) [132], which is the point where both the cation and NS dication yield saturates due to a lack of neutral atoms in the interaction volume [134]. For intensities above I_{Sat}, both yields plateau while the SDI starts to dominate leading to a renewed increase of the dication yield. At the (second) saturation intensity

[1] Data points are taken in three different scans at different focal spot sizes leading to discontinuities in the transition regions.

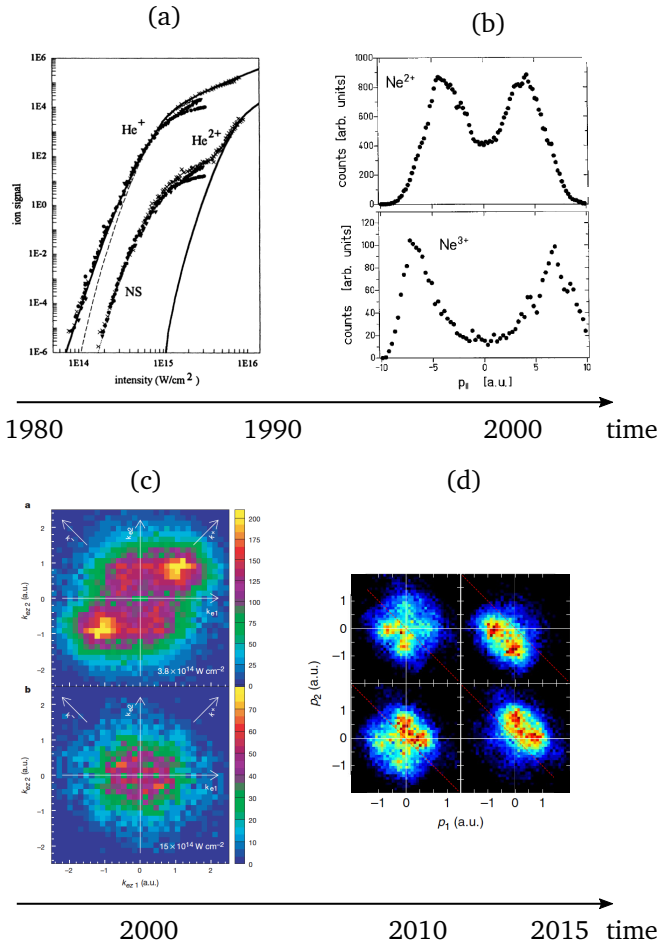

Figure 5.1: Milestones of experimental discoveries of NSDI. (a) The "knee structure" in the ion yield distribution of Xe atoms was discovered by L'Hullier *et al.* [129] showing an unforeseen yield of dications for moderate intensities to NSDI. Exemplarily, similar results on the DI of He atoms by Walker *et al.* [132] is shown here revealing a clear transition from NSDI to SDI. **(b)** The *double-hump structure* for NSDI in the momentum distribution (Ne^{2+} middle and Ne^{3+} lower panel) of Moshammer *et al.* [262] in contrary to the Gaussian like distribution (Ne^{+} upper panel) revealing the re-scattering induced impact ionization process as the origin for NSDI. **(c)** Correlated electron behavior (upper panel) in the NSDI regime measured by Weber *et al.* [263] while the SDI regime shows uncorrelation (lower panel). **(d)** CEP dependent, asymmetric electron correlations measured by Bergues *et al.* [264].

of the SDI $I_{\mathrm{Sat2,SDI}}$ the SDI regime completely dominates ands NDSI electrons are negligible. The region between I_{Sat} and $I_{\mathrm{Sat2,SDI}}$ can be defined as the *transition region*. Hence, the (monocat-, dicat- or polycat-) ion yield distribution as a function

of peak intensity gives a good indication of the double ionization behavior of an atomic or molecular system.

After these initial findings, many theoretical investigation worked on an explanation for the enhanced NSDI yield. It was concluded that only a correlated behavior of e_1 with one or multiple of the residual electrons in the system can be accountable for the enhanced probability of NSDI over SDI for low intensities. Any further, independent (uncorrelated) ionization step could be calculated exactly as the single ionization yet for a higher I_P. Hence, any deviation from that principle must be attributed to correlations of e_1 with the residual electrons.

Proposed mechanisms included e.g. the *shake-off mechanism*. It is based on the quick removal of one electron from the atomic compound which is followed by the release of a secondary electron due to the vibrational relaxation of the system, so that e_2 is basically "shaken off" [135]. Today it is known that the shake-off double ionization dominates for interaction with high kinetic energy photons [135] so multiple ionization by hard X-rays.

The other possibility behind NSDI is the re-collision based impact ionization based on the re-collision model by Corkum as discussed. Re-collision is nowadays generally accepted as the main cause regime behind the NSDI enhanced yield in the ion yield distribution in the strong-field. Yet, experimental proof for the (e,2e) process was provided by Moshammer *et al.* in 2000 [262] where they collected the recoil-ion momentum distribution (parallel to the laser polarization) of Ne ions (ionized with a $I = 1.3 \times 10^{15}$ W/cm^2 at $\lambda = 795$ nm) with a ReMi detection system as plotted in Fig. 5.1 (b-d). Here, the Ne^+ cations showed an expected narrow Gaussian distribution around the origin of ~ 3 a.u. FWHM [in Fig. 5.1 (b), upper panel]. The distribution around zero momentum for cations is related to the fact that the tunnel ionization process happens around an electric field maximum where the vector potential $A(\varphi)$ that accelerates the liberated electron is minimized (see Fig. 2.4). On the other hand, the momentum distribution of the Ne^{++} dications revealed a "double hump" shape with both peaks separated by $\sim \pm 4$ a.u. which is shown in Fig. 5.1 (b) (middle panel). Even the distribution of Ne^{+++} trications was detected which also showed two peaks separated by $\sim \pm 6.5$ a.u [in Fig. 5.1 (b), lower panel]. This double hump structure can be regarded as the second milestone in the study of electron-electron correlations in NSDI and its cause can be explained on the basis of Fig. 5.2 (a).

Since the double hump implies that at least one electron of the NSDI process transfered a non-zero momentum to the recoil-ion that electron must have been released not at a peak of the electric field. This is a strong indication for the re-collision impact ionization where e_1 (red trajectory) that tunnels (indicated by *step 1*) around a local field maximum [first green shading in Fig. 5.2 (a)] returns to the parent ion at around 0.75 of the full optical cycle [purple green shading in Fig. 5.2 (a)] where the vector potential $A(\varphi)$ maximizes (see Fig. 2.4). Upon impact e_1 promotes e_2 (orange trajectory) to the continuum (indicated as *step 2*) so that at least one of the electrons is drastically accelerated by the laser field leading to the large, non-zero momentum of the recoil-ion. The double hump also implies that after the (e,2e)

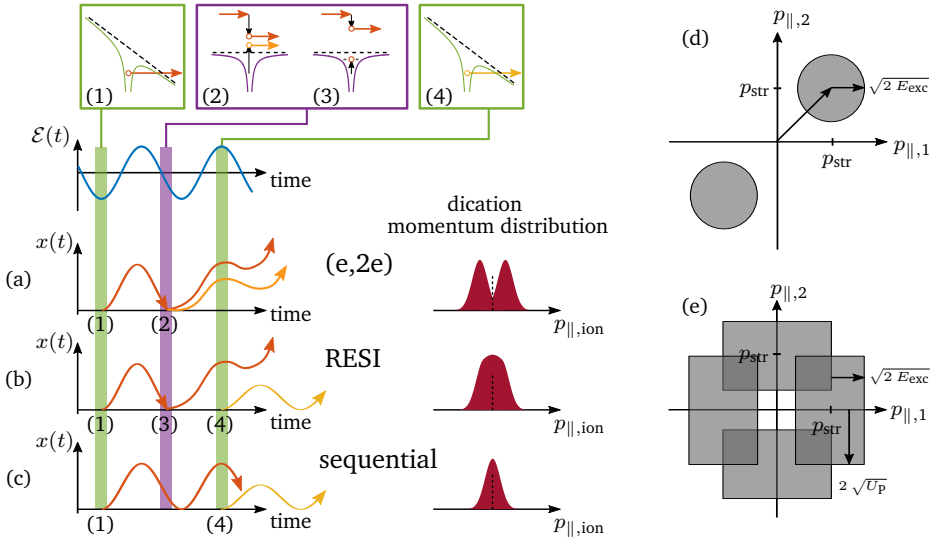

Figure 5.2: Basic DI mechanisms and characteristic behavior of experimental observables. (a) In the re-scattering induced (e,2e) [or (e,ne)] process the first electron e_1 tunnels (1) around a field maximum (green shading) and re-scatters with the parent ion after around 0.75 optical cycles (purple shading) where it lifts a second electron e_2 directly to the continuum (2). The (almost) parallel escape of all emitted electrons results in a high, non-zero recoil-ion momentum which leads to a double-hump in the momentum spectrum. **(b)** In the RESI process, the returning e_1 excites the parent ion (3) (purple shading) which is then field-ionized (4) at one of the subsequent field maxima (green shaded) leading broadened, "fill-the-valley" momentum distribution. **(c)** In SDI both electrons are liberated by tunnel ionization (1,4, green shaded areas) leading to a Gaussian-like momentum distribution. The classically allowed regions in the electron correlation distribution for **(d)** (e,2e) and **(e)** RESI are shown (explanation in the text).

impact, the electrons escape in the same vectorial direction because otherwise their momentum would cancel out leading to a recoil-ion momentum peak around the origin. Hence, the classical maximum transferred recoil momentum for a (polycat-)ion results as twice (for both electrons) the maximum streaking momentum $p_{\mathrm{str,max}}$ that can possibly be obtained by the vector potential resulting as

$$p_{\mathrm{recoil,max}} = n \cdot p_{\mathrm{str,max}} = 2\,n\,\sqrt{U_{\mathrm{P}}} \tag{5.1}$$

with n indicating the number of ionizations.

A conformation of the findings of Moshammer *et al.* [262] was published by Weber *et al.* [263] in the same year where they showed the correlated electron emission in NSDI with a kinematically complete measurement of the momenta of two corresponding electrons as a function of each other. The result constitutes the third milestone and is shown in Fig. 5.1 (c) in the upper panel. Here, the Ar^{++} dication

momentum was detected in coincidence with the momenta of its two related electrons (for an intensity of $I = 3.8 \times 10^{14}\,\mathrm{W/cm^2}$ at $\lambda = 800\,\mathrm{nm}$) in order to resolve the correlated electron momenta. Strikingly, the *electron correlation distribution* ($e2e1$ map) shows two distinct maxima for electrons with equal momentum magnitude and direction in the first and third quadrant of the $e2e1$ map. This confirms the findings of [262] that both electrons escaped in a correlated manner after impact of e_1. When increasing the intensity by a factor of 4 to $I = 15 \times 10^{14}\,\mathrm{W/cm^2}$ the $e2e1$ map changes to a non-correlated distribution with a 2D Gaussian shape centered at the origin [lower panel in Fig. 5.1 (c)]. This signifies that both electrons escape into the continuum without any relative interaction. This is a characteristic of SDI where the electrons tunnel independently for the same or consecutive electric field maxima as depicted in green shades in Fig. 5.2 (c). It shows, how an $e2e1$ distribution clearly reveals the nature and hence the regime of the DI process. Note that, the anti-correlated behavior of electrons can be weakly seen in Fig. 5.1 (c) in the upper panel for the second and the fourth quadrant. The behavior was found to be related to NSDI resulting from multiple re-collisions of e_1 to promote e_2 to the continuum [265].

Double ionization is a complex process that is known to be dependent on a number of laser parameters such as the intensity [241, 266], polarization [130], pulse duration [267] and wavelength [170, 268]. Especially by means of intensity, the process behind DI can be changed drastically. NSDI is observed below the saturation intensity (I_{Sat}), which is the point where sequential double ionisation (SDI) starts to dominate, and seems to be ubiquitous in low-Z atomic targets [269] and small molecules [134]. Yet, as mentioned beforehand, the direct promotion of e_2 to the continuum is only possible if the returning electron e_1 accumulated an energy in the electric field that is larger then the second ionization potential $E_{r,e1} \geq I_{P,2}$. If this is not the case, the process of RESI is a viable option where an intermediate excited state of the cation can be populated by the energy $E_{r,e1} \leq I_{P,2}$ of the returning electron e_1 [purple shading and indicated as *step 3* in Fig. 5.2 (b)]. Like this, an electron can tunnel through Coulomb barrier at the successive electric field maximum [second green shading and *step 4* in]. The process was suggested and shown by Feuerstein *et al.* [270]. In the ion yield distribution, RESI should account for the dications at the onset of NSDI. A kinematic analysis of RESI reveals that only e_1 gets distinctively accelerated by the close to maximum vector potential since the e_2 tunnels near the peak of the electric field resulting in almost no field acceleration. Thus, the recoil-ion momentum distribution shows a particular distribution which could be described as a double hump structure with a "filled valley" around the origin [270]. This filling the valley behavior of the recoil-ion momentum distribution was studied further and confirmed by de Jesus *et al.* [269] for several different target systems. Additionally, they revealed that RESI is more likely for targets like helium or argon rather than neon atoms because their total excitation cross-sections by electron re-collision exceed the total ionization cross-section for most electron impact energies in case of He and Ar whereas for Ne the ionization dominates for energies just after I_P. Therefore, for different intensities towards I_{Sat} the valley is filled for He and Ar and in case of Ne a clear double

hump can be seen [269]. Electrons emitted via RESI can be found in an electron correlation distribution positioned along the coordinate axes. This seems intuitive for one accelerated electron and another electron with almost zero momentum. In [270], the classically allowed regions for (e,2e) and RESI were explained as shown in Fig. 5.2 (d,e). In case of (e,2e), both electrons escape the parent ion at the same time, hence obtain the same drift momentum by the laser field p_{str} (with a possible maximum of $p_{str,max} = 2\sqrt{U_P}$). Because of energy conservation, the electrons can appear in the $e2e1$ map in a circle with the origin (p_{str},p_{str}) and a radius of $\sqrt{2\,E_{exc}}$ [270]. The excess energy is the remaining energy of the first electron $E_{exc} = E_r$ - I_P [see Fig. 5.2 (d)]. In the case of RESI, the electrons are classically allowed in a rectangle which is restricted by the momentum of e_1 as p_{str} - $\sqrt{2\,E_{exc}} \leq p_{e1} \leq p_{str} + \sqrt{2\,E_{exc}}$, while the second and tunneling electron gains a momentum $|p_{e2}| \leq p_{str,max}$ centered around $p_{e2} = 0$. In Fig. 5.2 (e), the regions are shown for both local electric field maxima within one optical cycle, hence mirrored both along the x-Axis and the y-Axis. Both RESI and (e,2e) need a minimum return energy of e_1 to overcome the respective excitation/ionization barrier. For lower intensity regimes where the return energy of e_1 is not sufficient, the beforementioned multiple re-collision can still excite the specific states yet leading to an anti-correlated electron behavior [265].

The most recent milestones in terms of the experimental interrogation of NSDI has been published by Bergues *et al.* [264] where they studied the behavior of NSDI for near-single-cycle pulses resolving the NSDI process as a function of CEP. The $e2e1$ distribution for their measurement of 750 nm pulses at $I = 3 \times 10^{14}$ W/cm^2 and 4 fs pulse duration is shown in Fig. 5.1 (d) for four different CEP positions. With it, they showed that the electron emission of both electrons can be steered with the relative CEP opening up the possibility to study single electron trajectories on subcycle (attosecond) timescales that promote the second electron to the continuum either via (e,2) or RESI.

5.2 NSDI and SDI of xenon atoms: state-of-the-art

As mentioned in Sec. 5.1 above, the enhanced double ionization yield for moderate intensities below the sequential regime can be explained by the mechanisms (e,2e) and RESI (depending on the laser intensity) which are based on the semiclassical re-collision model. As discussed in [3], the resulting double-hump structure in the re-coil ion momentum distribution that is connected to the correlation of both emitted electrons into the same hemisphere are experimentally detected universally for the low-Z noble gases, i.e. He [271–273], Ne [262, 274, 275], Ar [201, 263, 270]. Interestingly, in the case of high-Z atoms such as Xe, which is one of the most well studied atomic species, the understanding of DI is not as clear [3]. Various investigations conducted as Xe ion yields as a function of intensity in the near-IR wavelength regime (for λ 800 nm) [276–279] and as function of wavelength (for λ 800 nm to 1600 nm) [268] found disparate results for the nonsequential formation of doubly charged Xe atoms being multi-photon or Freeman

(Rydberg) resonances. Explanations were found in additional mechanisms such as multi-photon population of Rydberg and intermediate excited states [277–279] as well as multiple electron re-collisions [268, 277]. Moreover, MPI of the intermediate $5s5p^6$ cation state [171, 268, 279] in xenon was found as an essential NSDI pathway for moderate intensities. Since ion yield measurements alone are not sufficient to unambiguously understand the DI process as described in the previous Sec. 5.1, Sun *et al.* [3] conducted the complete set of measurements on the ion yield and momentum as well as the *e2e1* distribution, a "fully differential measurement" [3] as they named it, of the DI of Xe atoms. Here, unlike low-Z targets, the results were suggestive of SDI not only at high intensities above the saturation intensity of SDI $I_{\mathrm{Sat2,SDI}} \sim 2 \times 10^{14}\,\mathrm{W/cm^2}$ for Xe atoms (according to ADK rates [245] for $\lambda = 790\,\mathrm{nm}$, and $\tau = 25\,\mathrm{fs}$), but also for the low peak intensities where NSDI normally dominates [3]. Despite finding the characteristic knee structure for the NSDI regime in the yield distribution as shown in Fig. 5.3 (a), the recoil-ion momentum shows only a single (Gaussian peak) for both moderate and high intensities [see Fig. 5.3 (b)] and no correlation of electrons in the respective *e2e1* map [see Fig. 5.3 (c) with $I =$ (i) $3 \times 10^{14}\,\mathrm{W/cm^2}$, (ii) $1.6 \times 10^{14}\,\mathrm{W/cm^2}$, (iii) $7 \times 10^{13}\,\mathrm{W/cm^2}$ and (iv) $4 \times 10^{13}\,\mathrm{W/cm^2}$]. All graphs of Fig. 5.3 are taken from Sun *et al.* for illustration. These findings are in contrary to the knowledge of NSDI for low-Z atomic systems and show that its overall understanding is not complete.

As the cause behind these findings, Sun *et al.* [3] and also their theoretical follow-up investigation by Yuan *et al.* [260] proposed the screening of the valence electrons by core electrons. Therefore, the electron correlation distributions based on a semi-classical model were calculated, thereby comparing a helium-like potential with an improved Green-Sellin-Zachor (GSZ) model. The latter accounts for the repelling force of all inner-shell electrons (Z - 2 = 52 electrons in this case for xenon) that shields the nucleus ($Z = 54$ protons). The case of the Helium-like model showed the expected evolution of *e2e1* maps [260]: 1) an anti-correlated behavior for intensities below the respective threshold intensity for RESI $I_{\mathrm{RESI,thres}} \leq 6 \times 10^{13}\,\mathrm{W/cm^2}$ corresponding to returning electrons (for $\lambda = 800\,\mathrm{nm}$) with $E_{\mathrm{r,max}} \leq I_{\mathrm{P}}(5s5p^6) = 11.3\,\mathrm{eV}$ smaller than the ionization potential of the first excited cation state $5s5p^6$, 2) cross-like or RESI-type behavior for $I > I_{\mathrm{RESI,thres}}$, 3) correlated behavior reaching the direct (e,2e) threshold $I > I_{\mathrm{e2e,thres}} \sim 1.1 \times 10^{14}\,\mathrm{W/cm^2}$ to overcome $I_{\mathrm{P,2}} = 21.3\,\mathrm{eV}$, to 4) sequential behavior or non-correlation for $I > I_{\mathrm{Sat,SDI}} \sim 2 \times 10^{14}\,\mathrm{W/cm^2}$ (according to ADK rates [245] for $\lambda = 790\,\mathrm{nm}$, and $\tau = 25\,\mathrm{fs}$). In contrast to that Helium-like behavior, the model with a GSZ shielding potential shows a non-correlated behavior for all intensities with slightly decreasing momentum expansions. The latter reproduces the experimental results fairly well. By interrogating the difference between both models more closely [260], it is found that in case of the shielding model the probability of the electron returning to the core decreases with increasing intensity. In direct conclusion that means that the NSDI mechanism based on re-collision is suppressed by the shielding electrons and effectively SDI is drastically enhanced for higher intensities already well below $I_{\mathrm{Sat,SDI}} \sim 2 \times 10^{14}\,\mathrm{W/cm^2}$ in the case of xenon. For lower intensities RESI is favoured since moreover the shielding potential shows a reduction

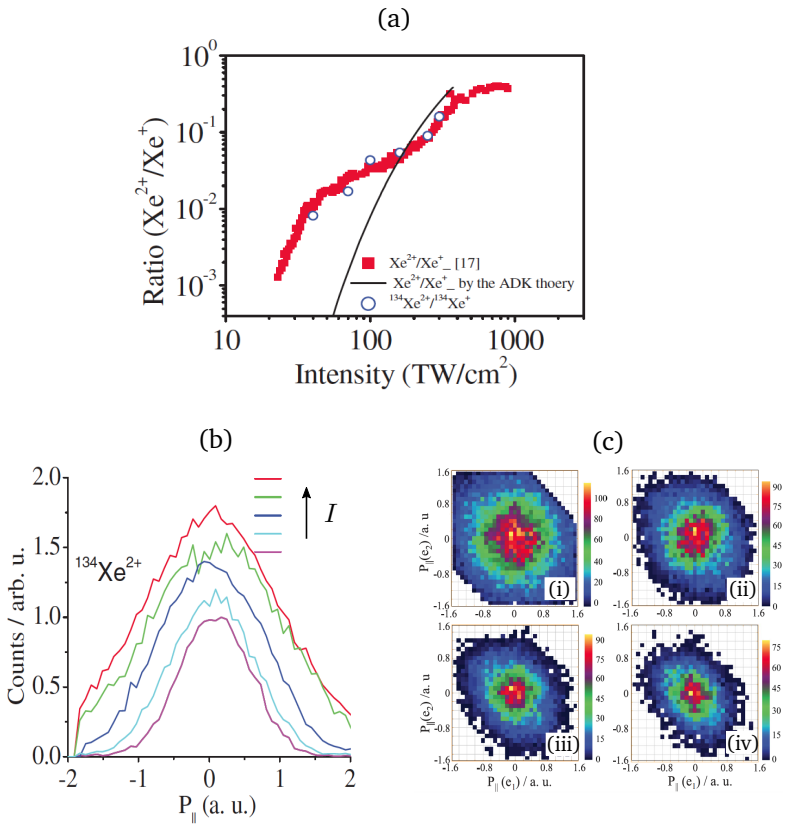

Figure 5.3: Particular findings of Sun *et al.* [3] on NSDI of Xe atoms. (a) The ratio of dications to monocations as a function of laser intensity from Chaloupka *et al.* [278] in red squares, their own data in blue circles (25 fs, 790 nm) and a calculated ADK ratio. The first and the latter are plotted in Fig. 5.4 (b) for comparison with our data. **(b)** Recoil-ion momentum distribution of $^{134}Xe^{2+}$ for intensities between $(0.4\text{-}3) \times 10^{14}$ W/cm^2 showing RESI and SDI-like behavior. **(c)** Experimental electron correlation spectra for (i) 3×10^{14}, (ii) 1.6×10^{14}, (iii) 7×10^{13} and (iv) 4×10^{13} W/cm^2 yielding only uncorrelated, SDI-like behavior.

in tunneling barrier supporting field-assisted tunneling mechanisms. This explains the "filling-the-valley" type re-coil ion momentum distributions [see Fig. 5.3 (b)]. In this process, also multiple re-scatterings are found to facilitate the excitation of intermediate states for RESI for low intensities which leads to the non-correlated correlations [3] [see Fig. 5.3 (c)].

Along the idea of the work in this thesis, it is often beneficial to scale experiments to the quasi-static regime using longer wavelengths where classical methods can accurately describe the electron interaction in SFI processes. Moreover in the near-IR regime, moderate intensities for xenon atoms below 10^{14} W/cm^2 due to the lower I_P compared to other noble gases result in ionization in the MPI regime

($\gamma > 1$) leading to (non- and) resonant structures in the resulting momentum distributions [268,277,279]. Hence, the NSDI process can be described free from MPI resonances with mid-IR driving fields. So far, two results have been reported where the goal was to investigate DI in Xe at longer wavelengths [171,173]. Gingras *et al.* explored a wide wavelength range while monitoring single and double ion yields as a function of the laser intensity. In addition to supporting the idea of resonances at shorter wavelengths, there was evidence for the occurrence of NSDI at longer wavelengths. The position of the famous "knee structure", which is traditionally (for $\lambda = 800\,\text{nm}$) near the meeting point of SDI and other mechanisms, was observed below $10^{14}\,\text{W/cm}^2$ and shifting to lower intensities as the wavelength was increased towards $\lambda = 2\,\mu\text{m}$. These results suggest that SDI should become already dominant below $10^{14}\,\text{W/cm}^2$ in the mid-IR ($\lambda > 3\,\mu\text{m}$) as the onset of (e,2e) type NSDI is shifted towards lower intensities.

Interestingly, this expectation was not observed at wavelengths of $3.2\,\mu\text{m}$ and $3.6\,\mu\text{m}$ where the measured yields for DI could still be described using inelastic electron impact cross-sections [173]. In comparison to Sun *et al.* [3], neither of the above reports included doubly-charged ion momentum distributions or electron correlation maps in order to get a "fully-differential" idea of the NSDI of Xe atoms at longer wavelength. Therefore, no single experiment has unambiguously shown the transition from NSDI to SDI in Xe for "clean" quasi-static conditions. Here is where our investigation sets in to clear up the uncertainty and debate as to the mechanisms of DI in high-Z targets.

5.3 Transition from NSDI to SDI of Xe atoms with mid-IR fields

By using ion yields, ion momenta and electron correlations as a function of peak intensity we perform a thorough, "fully differential" investigation of DI of Xe atoms in the mid-IR regime and to identify the transition from (e, 2e) NSDI to SDI for high-Z target systems in unambiguous quasi-static conditions where a classical interpretation of the post-tunneling electron trajectory is possible. Moreover, our experimental results are compared with semi-classical calculations in order to interrogate the transition between the different DI regimes regarding the previously found inconsistencies of NSDI of xenon compared to lower-Z noble gases (mentioned in Sec. 5.2 above). Moreover, an additionally undertaken time-dependent density functional theory (TDDFT) calculation allows us to study the influence of the excited $5s5p^6$ orbital [171,268,279] of the cation on the NSDI yield for lower intensity closer to $I = 10^{13}\,\text{W/cm}^2$ in our data.

5.3.1 Theoretical methods

We compare our experimental results to semi-classical (SC) and TDDFT calculations. The calculations were performed by our collaborators Xu Wang (SC) of the

group of Chi-Dong Lin at Kansas State Universtity, Manhattan, Kansas, USA, and Xiao-Min Tong (TDDFT) from the University of Tsukuba, Ibaraki, Japan who already performed the TDSE simulation of the previous chapter (see Sec. 4.2.2), respectively. The descriptions of the simulations are taken from our paper [261].

5.3.1.1 Semi-classical model

In the semi-classical method, the laser field is first discretized with a time step of size Δt. For a mid-IR wavelength of 3.2 µm, one laser cycle equals to 442 a.u. or 10.7 fs. Δt is usually set between 0.1 a.u. and 1.0 a.u. and so that the convergence of our numerical results can be checked by changing this step size.

The semi-classical model assumes quantum tunneling of the first electron. For each time step, a tunneling rate $\Gamma_{\mathrm{ADK,l,m}}$ is calculated according to higher orbital states l,m - dependent ADK rates [89, 245] which were already utilized for Ar atoms in Eq. 4.1 of the CTMC calculation of Sec. 4.2.2.1. In our case, the first electron is considered to tunnel out from its highest orbital $5p^6$ (with l = 1, m = 0 and the coefficient $C_l = 2.57$ of [151, 245]) overcoming the first ionization potential $I_{\mathrm{P,1}} = 12.13$ eV. The resulting effective charge of the ion core is $Z = 1$ a.u. The tunneling exit point, which is also the initial position of e_1, is determined in parabolic coordinates [280, 281] via numerically solving the following equation

$$-\frac{\beta_2}{2\,\eta} + \frac{m^2-1}{8\,\eta^2} - \frac{\mathcal{E}(t)\,\eta}{8} = -\frac{I_{\mathrm{P,1}}}{4} \quad , \tag{5.2}$$

where β_2 is a separation constant and η is a variable of the parabolic coordinates to be solved. The tunneling exit point in the Cartesian coordinates is then given by $z_0 = -\eta/2 \cdot sgn[\mathcal{E}(t)]$, assuming the laser polarization is along the $\vec{e}_{\mathrm{z}}$ direction. Note that $\eta \geq 0$. If $\mathcal{E}(t) > 0$, then tunneling is to the negative $\vec{e}_{\mathrm{z}}$ direction, and if $\mathcal{E}(t) < 0$ then tunneling is to the positive $\vec{e}_{\mathrm{z}}$ direction. The velocity of the first electron at the tunneling exit is assumed to be zero.

Having set the birth place and velocity of the first electron, let us turn to the second electron which is "created" in the vicinity of the ion core and has a charge of $Z = 2$ a.u. The procedure of assigning e_2 a position and a momentum is described as follows. First, a position is randomly assigned and the potential energy of e_2 is calculated, noted as E_{e2}, which includes the ion-core attraction energy and the e-e repulsion energy. If $E_{\mathrm{e2}} > -I_{\mathrm{P}} = -20.98$ eV (the second ionization potential of Xe), this position is rejected and a new position is assigned until the classically allowed condition $E_{\mathrm{e2}} < -I_{\mathrm{P}}$ is fulfilled. Then the kinetic energy of the second electron is given by $E_{\mathrm{kin,2}} = -I_{\mathrm{P}} - E_{\mathrm{e2}} > 0$. With this kinetic energy, the three momentum components of e_2 are randomly partitioned.

Now the initial positions and momenta of both electrons are assigned. Remember that we are currently at time t during the pulse. From this time t until the end of the pulse, the motion of the two electrons is governed by classical mechanics via numerically integrating the time-dependent Newtonian equation of motion [282,

283]

$$\frac{\partial^2 \vec{r}_i}{\partial t^2} = -\nabla \left[V_{ne}(r_i) + V_{ee}(r_{12})\right] - \vec{e}_z \mathcal{E}(t) \quad \text{, for } i = 1,2 \tag{5.3}$$

where $\vec{r}_i$ is the position of the ith electron, r_{12} is the distance between the two electrons, $V_{ne}(r_i)$ = -2/r_i is the nuclear-electron Coulomb potential, $V_{ee}(r_{12}) = 1/r_{12}$ is the electron-electron Coulomb potential. The trajectories (i.e., positions and momenta) of the two electrons are followed and recorded from the birth time t_i to the end of the pulse. A double ionization event happens if at the end of the pulse, both electrons have positive energies.

The weight of a two-electron trajectory can be given by $p(t) = \Gamma(t)\,\Delta t$, for low intensities where the total ionization probability by the entire pulse is small. For relatively high intensities where the total ionization probability is not small so that the population of the neutral atoms is depleted appreciably during the pulse, the weight should be modified to $p(t) = N(t)\,\Gamma(t)\,\Delta t$, where $N(t) = \exp[-\int_{-\infty}^{t} \Gamma(t')\,\Delta t]$ is the survival probability of neutral atoms at time t. The overall probability of double ionization is obtained by summing the weights of all double ionization events at the end of the pulse according to Eq.4.4. Post-selecting these double ionization events, we can trace back the trajectories of the two electrons during the pulse, or study the momentum correlation between the two electrons.

At an intensity limit of $I_{lim} \sim 4.0 \times 10^{13}$ W/cm^2 our semi-classical model calculations exceed our computational capabilities due to low statistics and hence intensities below I_{lim} can not be investigated.

5.3.1.2 TDDFT approach

The multiple ionization of Xe atoms in a mid-IR laser field is also investigated within the framework of TDDFT by solving the time-dependent Kohn-Sham equations as

$$i\frac{\partial \psi_i(\vec{r},t)}{\partial t} = H(\vec{r},t)\,\psi_i(\vec{r},t) \quad , \tag{5.4}$$

with the electron wave function $\psi_i(\vec{r},t)$ of the ith orbital and the single-particle-like Kohn-Sham Hamiltonian $H(\vec{r},t)$ [144]. The Hamiltonian is written as

$$H(\vec{r},t) = -\frac{1}{2}\nabla^2 + V_{eff}^{PP}[\phi(\vec{r},t)] + V_{ext}(\vec{r},t) \tag{5.5}$$

where $V_{ext}(\vec{r},t)$ is the electron-laser interaction and $V_{eff}^{PP}[\phi(\vec{r},t)]$ the nonlocal l-dependent pseudo-potential as detailed in [284]. To analyze the electron-electron dynamic effect, $V_{eff}^{PP}[\phi(\vec{r},t)]$ is further recasted into

$$V_{eff}^{PP}[\phi(\vec{r},t)] = V_{eff}^{PP}[\phi_0(\vec{r})] + \left(V_{eff}^{PP}[\phi(\vec{r},t)] - V_{eff}^{PP}[\phi_0(\vec{r})]\right) \quad , \tag{5.6}$$

two terms with $\phi_0(\vec{r})$ the laser field free electron density and $\phi(\vec{r},t)$ the time dependent electron density. The first term represents the single active electron potential and $(V_{eff}^{PP}[\phi(\vec{r},t)] - V_{eff}^{PP}[\phi_0(\vec{r})])$ stands for electron-electron dynamic effect. Note that the dominant contribution to the second term is the Coulomb interaction due

to the density changes. To compensate *the spurious self-interaction* [243][2], a positive charge background $\phi_+ = c^3/2 \cdot \mathrm{e}^{-c\,r}$ was added, which provides the correct Coulomb tail. $c = 0.122$ is chosen, with which the ionization potential from the simulation is $I_{\mathrm{P},1} = 12.13$ eV, close to the measured one. The above time-dependent Schrödinger equation is solved by the generalized pseudo-spectral method in the energy representation [286] and project out the time-dependent wavefunction in the outer region onto the momentum space as detailed in [244]. When the laser pulse is over, the ionization probability p_i is obtained for each orbital. In the simulation, we included all eight valence electrons (two 5s, $i = 1,2$ and six 5p states, $i = 3,4, \ldots ,8$). The total single ionization probability can be expressed as

$$P^+ = \sum_{i=1}^{8} p_i \prod_{j \neq i} (1 - p_j) \tag{5.7}$$

and the double ionization probability is

$$P^{++} = \sum_{i,j,i\neq j}^{8} p_i p_j \prod_{k \neq i,j} (1 - p_k) \quad . \tag{5.8}$$

As we know, and also confirmed in [173], the contribution of the 5s state to the single ionization is negligible. As shown in [284] for the case of Ar atoms, if we turn off the electron-electron dynamical correlation (set in the second term in Eq. 5.6) in the simulation, the ionization probability of 3s is about 4 orders smaller than the one with the term. Therefore, we conclude that for the present case, the 5s is mainly ionized through electron-electron dynamical correlation or re-scattering induced ionization and not via multi-photon resonances [268,279], not direct laser field ionization and its contribution should directly add to the double ionization, not the single ionization. Thus, we define the double ionization probability with 5s contribution as

$$P^{++}_{5s} = P^{++} + 2\, p_{5s}\, (1 - p_{5s}) \prod_{k=3} (1 - p_k) \quad . \tag{5.9}$$

Hence, ionization from the excited Xe^+ $5s5p^6$ orbital can optionally be included in the calculation. Another reason to add the 5s contribution to the double ionization is that even if there is 5s single ionization state created by the laser field directly, the 5s hole will be filled by laser enable Auger decay process [287, 288], which results in the double ionization.

5.3.2 Ion yield

In general, the transition between the non-sequential and the sequential DI regime needs to be regarded as a gradual process as already discussed in Sec. 5.1. NSDI

[2]The spurious self-interaction is a common error in many density functional theory approximations when accounting for the exchange-correlation energy. It is widely believed that this error causes failures in various approximations leading to poor description of charge transfer and transition states when describing chemical reactions [285].

predominantly occurs for intensities $I < I_{\text{Sat}}$ below the ionization saturation intensity of the neutral atom which defines the intensity where all neutral atoms in the interaction volume are ionized [134]. The mechanism of any re-scattering related NSDI process is based on the kinetic energy of the returning electron as also stated beforehand. The regime of only field-induced tunneling ionization can be roughly delimited by the secondary ionization saturation intensity $I_{\text{Sat,SDI}}$ that is the point where all cations in the interaction volume are ionized. Hence, SDI prevails for intensities $I > I_{\text{Sat,SDI}}$. The transition between NSDI and SDI happens in between $I_{\text{Sat}} < I < I_{\text{Sat,SDI}}$ where both processes appear with different probabilities while the SDI process takes over to dominate the NSDI process. These occurrence probabilities can be investigated adequately by the ion yield distributions and relative ion ratios as a function of intensity, which we conducted for Xe atoms as follows.

In the experiment, we used 3.1 µm pulses at a duration of $\tau = 75$ fs and focused them into the Xe atoms gas jet at various peak intensities. The linear laser polarization direction was chosen along the $\vec{e}_z$ axis of the ReMi spectrometer. The electric field of the ReMi was chosen to be $\mathcal{E} \sim 6$ V/cm. The initial gas pressure P_0 was set in order to detect an amount of the overall ion counts well below the repetition rate of the system. Therefore, the higher intensities in our yield distribution (half of our dynamic intensity range) were taken for a lower initial pressure then the lower intensities. The peak intensity was calibrated by comparing the longitudinal momentum spread of the $^{129}Xe^{+}$ with the momentum-dependent ADK rates (see Eq. 2.20), as well as in the background of the overall intensity calibration collected in this thesis (see Sec. 3.1.3). As in general in this thesis, the intensity error is estimated as 20% (in good conscience). The yield data for every ion were extracted by integrating over the different ion peaks in the ToF spectra. All nine stable Xe isotopes for every ion (although only the five main ones are visible in Fig. 5.6) order were considered in the yield data so that a merging of potential double peak structures is accounted for in the analysis. The integrated counts were normalized by division by the amount of detected laser trigger signals. The resulting Xe^{+} – Xe^{4+} ion yields as a function of the peak intensity are presented as a log-log plot in Fig. 5.4 (a).

The single ionization [circles in Fig. 5.4 (a)] data show the typical saturation-like behavior as the intensity is increased towards $I_{\text{Sat}} \sim 5.0 \times 10^{13}$ W/cm^2. The value for I_{Sat} is determined by fitting a *sudden onset function* (SOF) according to [289]

$$S = \alpha \, [\ln(I) - \ln(I_{\text{Sat}})] \tag{5.10}$$

to the ionization signal. The SOF is generally used to model the barrier suppression or over-the-barrier ionization (as mentioned in Sec. 2.1.1). Here, α is the *limiting slope* of the SOF. In Fig. 5.5 the fit through our cation data (blue dots in linear scale) is shown as a blue line where the interception with the intensity axis yields the saturation intensity I_{Sat} [289]. The doubly charged ion (squares) data in Fig. 5.4 (a) show a similar gradient for intensities below I_{Sat}, as is generally observed in the NSDI regime [132]. The rescaled single ionization data [Fig. 5.4 (a), black line] clearly illustrates this similarity. Approaching I_{Sat} the NSDI yield begins to plateau in a similar way to the cation yield. At intensities slightly higher than I_{Sat}, however,

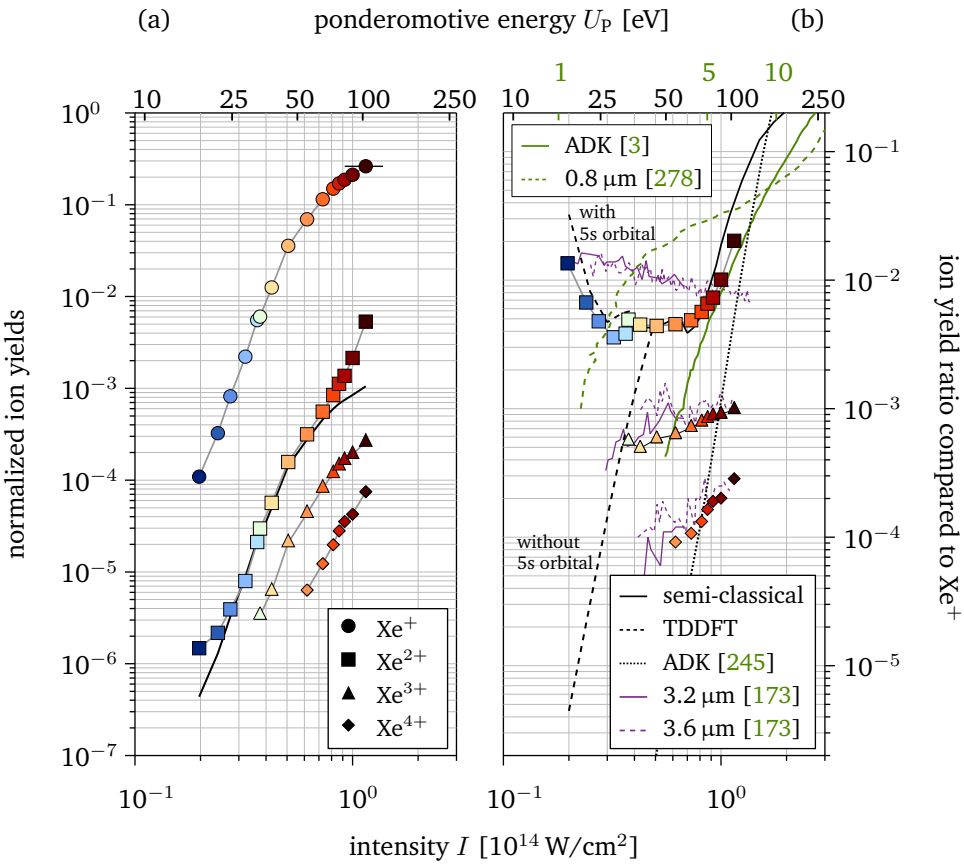

Figure 5.4: Distributions of Xe ion yields and respective ratios. (a) The number of Xe^+ (circles), Xe^{2+} (squares), Xe^{3+} (triangles) and Xe^{4+} (diamonds) ions detected as a function of the estimated peak laser intensity (bottom axis), and of the respective ponderomotive energy (top axis) for 3.1 μm (black) and 790 nm (green). The Xe^+ data are also scaled to overlap with the Xe^{2+} curve at intermediate intensities (black line).The estimated ±20 % error in the absolute intensity determination is indicated on the last Xe^+ data point. **(b)** The corresponding ion yield ratios shown alongside the semi-classical (solid black), TDDFT (dashed black, with and without 5s orbital) and ADK (dotted black) calculations. Moreover, the experimental data from [278] for Xe^{2+} at 780 nm (green dotted) and the ADK-based ratio of [3] as well as the data from [173] acquired for similar mid-IR wavelengths as in our experiment (solid and dashed purple) are shown for comparison.

the Xe^{2+} yield starts to increase again and this trend continues up until our maximum detected intensity of $I = 1.2 \times 10^{14}$ W/cm^2. Such a pronounced change in the intensity dependence of the ion yield is characteristic of the transition from NSDI to SDI [132] as discussed earlier. The yields of the triple and quadruple charged ions (triangles and diamonds, respectively) do not show this trend.

The increase in Xe^{2+} counts is more obvious when viewed as a ratio of doubly to singly charged ion yield, as presented in Fig. 5.4 (b, squares). Also by considering the ion ratio rather than the independent yields any systematic errors are reduced. The Xe^{2+}/Xe^{+} trace shows a plateau at a ratio level of ~ 4 to 5×10^{-3} up until I_{Sat}, upon which the ratio starts to increase drastically. Additionally, it is striking that the dication ratio is higher than the plateau for intensities lower than $I \sim 3 \times 10^{13}$ W/cm^2. On the other hand, the respective ratios of the Xe^{3+} and Xe^{4+} data are steadily increasing throughout our observed dynamic range with the Xe^{4+} ratio showing a steeper slope. In order to interpret the different features, we compare the data to theory (describe in Sec. 5.3.1). The semi-classical calculations shown in Fig. 5.4 (b) as a solid black line reproduce both the plateau and the gradient of the Xe^{2+}/Xe^{+} ratio above I_{Sat} quite accurately after rescaling the theoretical curve by a factor of 0.3 to compensate for the absence of focal averaging. This comparison clearly shows that also DI in the mid-IR regime can be accurately modeled using semi-classical methods. In order to compare the relative contribution of NSDI with SDI in our measurement we additionally calculated the pure ADK-based [245] Xe^{2+}/Xe^{+} ratio [black dotted line in Fig. 5.4 (b)] for our laser parameters which only accounts for the sequential, field-induced DI and omits the non-sequential, re-scattering induced as included in the semi-classical model. The curve shows the onset of SDI for intensities well below $I < 1 \times 10^{14}$ W/cm^2 and lies close to the experimental dication ratio. It reaches a comparable level of ~ 4 to 5×10^{-3} to the NSDI-plateau of our data (squares) at around 1.1×10^{14} W/cm^2 before saturation according to [289] at $I_{Sat,SDI} = 1.4 \times 10^{14}$ W/cm^2. The respective fit is shown in Fig. 5.5 as a green line. This comparison confirms that the drastic increase of the experimental dication ratio after $I > I_{Sat}$ is related to fact that the SDI yield overcomes the NSDI.

One behavior we were interested in is how the transition between NSDI and SDI behaves when changing the driving wavelength from 800 nm to 3.1 μm. Therefore, we plotted the dication ratio data of 780 nm pulses ($\tau = 100$ fs) interacting with Xe atoms from Chaloupka *et al.* [278]in Fig. 5.4 (b, green dotted line) which moreover agrees with the dication ratio of Sun *et al.* [3] (790 nm, 25 fs). Also, we plot the SDI-ADK ratio as calculated in Sun *et al.* (green solid line). It stands out that the near-IR dication ratio plateaus for higher intensities towards $I \sim 1 \times 10^{14}$ W/cm^2 which is related to the lower ponderomotive energy U_P in the near-IR case yielding lower kinetic energies of the returning electrons. This is illustrated by the upper axis of the ratio plot in Fig. 5.4 (b) where the respective U_P is indicated for 3.1 μm (black) and 790 nm (green). Moreover, the level of the plateau in the near-IR dication ratio sits almost one order of magnitude higher than the mid-IR case, which agrees with a similar study in [290] and is expected due to the lower returning probability for longer wavelength.

Yet, the behavior of the near-IR SDI-ADK ratio (green solid line) agrees remarkably well with our respective mid-IR ratio (black dotted line) which is expected since ADK rates are wavelength independent. The near-IR SDI-ADK ratio agrees even better with the experimental dication ratio data intercepting with the level of ~ 4 to 5×10^{-3} at $I \sim 8 \times 10^{13}$ W/cm^2. On the other hand, both near-IR ratios (exper-

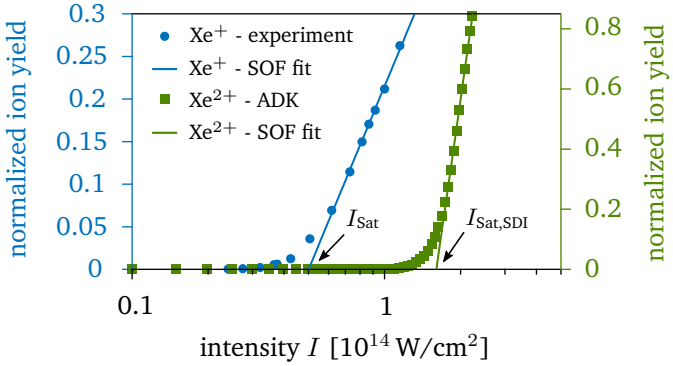

Figure 5.5: Determination of saturation intensity. The Xe^+ cation yield of Fig. 5.4 (a) and the respective, SDI-ADK calculated yield of the Xe^++ dications of Fig. 5.4 (b) is plotted in blue cirles and green squares, respectively. The saturated part is fitted with a sudden onset function [289] in both cases to extract the respective saturation intensity as the interception with the intensity axis. The fits yield a saturation of the single ionization at $I_{Sat} = 5.0 \times 10^{13}$ W/cm^2 (fit as blue line) and the saturation of the sequential double ionization process at $I_{Sat} = 1.4 \times 10^{14}$ W/cm^2 (fit as green line).

iment and SDI-ADK in green) merge around $I \sim 2 \times 10^{14}$ W/cm^2 for significantly larger intensities then in the mid-IR case. This nicely shows that the transition from NSDI to SDI is shifted to lower intensities for longer wavelength. An explanation for this can be found in the fact that re-collision induced NSDI is less probable for longer wavelength due to a lower return probability which leads to a "take-over" of the SDI process already for lower intensities well below 1×10^{14} W/cm^2 in the mid-IR case.

Another interesting part of our data are the enhanced dication ratio for low intensities. Unfortunately the semi-classical model is too computation intensive for sufficient statistics in that intensity region yet the TDDFT simulation can cover this intensity range between 2 to $5, \times 10^{13}$ W/cm^2. The respective results are also presented in Fig. 5.4 (b,dashed black line) for both simulations with and without the influence of the intermediate $5s5p^6$ orbital. Here, the calculations that include the $5s5p^6$ orbital accurately reproduce the change in ratio observed for lower intensities while the ones without drop below 4×10^{13} W/cm^2 similar to the near-IR dication ratio (green dotted line). The comparison to the data show the decisive role of the $5s5p^6$ orbital for NSDI of Xe atoms which has been proposed in literature for a while now [171, 173, 268, 279]. Due to the mid-IR driving wavelength and the associated DI in quasi-static conditions ($\gamma \ll 1$) it becomes clear that the excitation to and ionization from the $5s5p^6$ orbital is clearly connected to re-scattering instead of MPI, which were both speculated occur at 800 nm [171, 268].

Here, we directly identify the contribution of the $5s5p^6$ excited state to the NSDI yield as a function of intensity which could not be revealed in DiChiara *et al.* [173] as they conducted an investigation of the ion yield for similar wavelengths (3.2 μm

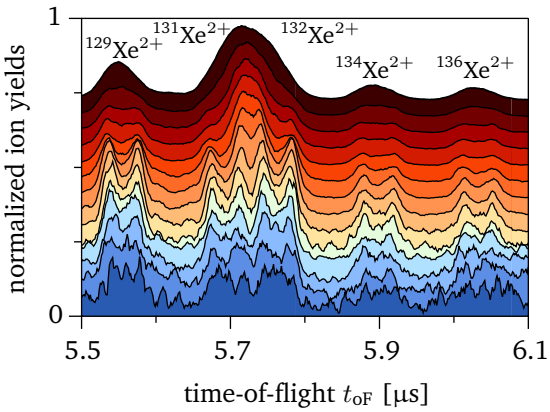

Figure 5.6: ToF spectra of five Xe dications for different intensities. Normalized and vertically shifted ToF spectra for five Xe double ion isotopes as the intensity is increased from bottom to top according to data points (squares) in Fig. 5.4 (a).

and 3.6 μm). Its presence was seemingly inferred because the Xe^{2+} data were systematically above the theoretical expectations for (e, 2e) impact ionization. Moreover the influence of the $5s5p^6$ state was assumed for all investigated laser intensities, which is in direct contrast to our results that show it dominating at low intensities only. For a direct comparison, the results of [173] are also plotted (solid purple line for 3.2 μm and dotted purple line for 3.6 μm) in Fig. 5.4 (b). While the Xe^{3+} and Xe^{4+} data of [173] agree well with our observations, the trend in doubly-to-singly charged ion yield ratio definitively does not. While for lower intensities the dication ratio is similarly high, it decreases towards 1×10^{14} W/cm^2 and above yet never shows the SDI enhancement as seen in our experimental and theoretical data and neither to the SDI-ADK ratio calculated in [3]. The reason for this is not clear but it could be related to the intensity calibration, the accuracy of which is generally limited to the several tens of percent level or worse [178].

5.3.3 Dication momentum distribtion

In order to further corroborate our insights on the DI behavior of Xe atoms in mid-IR fields from the analysis of the ion yield distributions, we turn to the ion momentum distribution as a function of intensity. Therefore, the evolution of the single ToF spectra of Xe^{2+} ions with increasing intensity is shown in Fig. 5.6 for all different intensities of Fig. 5.4. Each spectrum exemplarily contains five of the nine isotopes[3] and is normalized before being vertically shifted for visibility. The data show that, apart from the lowest intensity, a clear transition from a broadening double-peak structure at low intensities (bottom traces) to a single peak at high intensities (upper traces) is observed for each isotope. The broadening double

[3] $^{130}Xe^{2+}$ is covered in noise due to a 6 times lower probability than its neighboring isotopes and $^{124,126,128}Xe^{2+}$ are not presented.

peaks of $^{131}Xe^{2+}$ and $^{132}Xe^{2+}$ even merge for the higher intensities due to the overlap in momentum. As mentioned in Sec. 5.1, the double peak structure is suggestive of the (e, 2e) or impact NSDI mechanism where the doubly charged ion is created at a phase close to the zero-crossing of the electric field (illustrated in Fig. 5.2 (a) yielding a large drift momentum [266] due to a streaking kick by the maximized vector potential $A(\varphi_r)$. To the best of our knowledge, a double hump structure in the Xe^{2+} momentum distribution has never been reported in the literature before.

The respective, calculated ion momentum distributions for $^{129}Xe^{2+}$ are shown in Fig. 5.7 (a). The corresponding distributions of all other isotopes appear to be similar. The distributions show double-hump structures peaking around $\sim\pm1.8$ a.u. at $I = 2.7\times10^{13}$ W/cm^2 expanding to about $\sim\pm2.4$ a.u. at $I = 8.1\times10^{13}$ W/cm^2. For the low intensities a clear "valley" between the two humps is identifiable while it slowly fills up with increasing intensity. The results seem to rule out an influence of the RESI and resonant enhancement mechanisms for low intensities as both are known to *fill-the-valley* in between the double hump [3, 266]. The absence of these mechanisms is not unexpected since: 1) RESI dominates when the returning electron energies are large enough to excite the ion but too low for impact ionization or (e,2e), and 2) the contribution from resonant enhancement decreases with increasing wavelength [171]. The first point becomes clear when calculating the maximum return energies $E_{r,max} = 3.17\,U_P$ for our intensity range as plotted in Fig. 5.7 (c) (red) which range from $E_{r,max} = 28.5$ eV at $I = 1\times10^{13}$ W/cm^2 to $E_{r,max} = 341.4$ eV at $I = 1.2\times10^{14}$ W/cm^2 and lies entirely above both the ionization potential of Xe^{2+} being $I_{P,2} = 21.3$ ev and the $5s5p^6$ excited state being $I_P(5s5p^6) = 11.3$ eV. For completeness [270], the maximum recoil momenta respectively for all intensities as derived from classical considerations (see Eq. 5.1) of the (e,2e) process are plotted in Fig. 5.7 (c) (blue solid) and are indicated in Fig. 5.7 (a) (white) which delimits the ion momenta correctly. As the intensity is increased, the ion momentum distributions narrow which indicates a convergence towards purely sequential ionization [266]. The same analysis of the Xe^{3+} momentum spectra [Fig. 5.7 (b)] shows that the double hump behavior persists at the highest intensity, which indicates that non-sequential ionization is still the dominant mechanism for creating triply-charged ions[4]. Moreover the trications show a wider spread double-hump structure compared to the dications extending from about $\sim\pm3.5$ a.u. at $I = 3.6\times10^{13}$ W/cm^2 to about $\sim\pm4.4$ a.u. at $I = 1.2\times10^{14}$ W/cm^2. This means that the three emitted electrons escape from the parent triple ion into the same hemisphere in a correlated manner. Also in Fig. 5.7 (b) the maximum recoil momentum for each intensity is shown as a white line which corresponds to the calculation plotted in Fig. 5.7 (c) as a blue dotted line.

This behavior of the ion momenta clearly reflects the transition from NSDI to SDI for intensities below $I < 1\times10^{14}$ W/cm^2 which we have found in the ion yield distribution. Yet, these results also are contrary to the findings of Sun *et al.* [3] who encountered a shielding of the inner-shell electrons that led to an overall SDI-

[4]The momenta for Xe^{4+} should behave accordingly in our observed intensity regime, yet are not shown since the single isotope peaks overlap and can not be isolated satisfactorily.

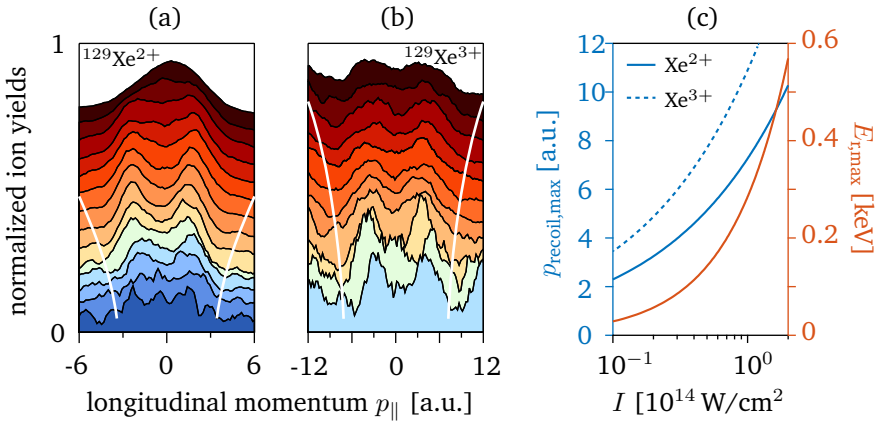

Figure 5.7: Recoil-ion momenta of $^{129}Xe^{2+}$ and $^{129}Xe^{3+}$ for different intensities. (a,b) Normalized and vertically shifted recoil-ion momenta for **(a)** $^{129}Xe^{2+}$ and **(b)** $^{129}Xe^{3+}$ as the intensity is increased from bottom to top according to the data points in Fig. 5.4 (a). The maximum classical recoil momentum for each intensity is plotted in white, respectively, and is also shown in **(c)** as blue solid and dashed lines, respectively. **(c)** Also, the maximum return energy $E_{\mathrm{r,max}}$ of electrons driven by our 3.1 µm source is shown in red.

like behavior.

5.3.4 Electron correlation distribution

Next, the correlations between both electrons e_1 and e_2 emitted from the dication need to be investigated for the different intensity dependent DI regimes we spotted in the results above. Therefore, we conducted two kinematically complete measurements with the ReMi for the intensity $I_1 = 4.0 \times 10^{13}$ W/cm^2 in the NSDI regime before saturation (at $I < I_{\mathrm{Sat}}$) and for our maximum intensity $I_2 = 1.2 \times 10^{14}$ W/cm^2 where the ion yield shows a clear SDI dependent increase. Thus the longitudinal electron correlation distribution could be extracted and compared for both cases.

The experiments were conducted by choosing an extraction field of $\mathcal{E} \sim 2$ V/cm and a magnetic field of $\mathcal{B} \sim 5$ Gs. The laser polarization was selected horizontally along the spectrometer axis along $\vec{e}_z$. The pulse duration was $\tau = 71$ fs, so close to the measurements of the yield and momentum distributions. The resulting experimental (e2,e1) correlations are shown Fig. 5.8 (a,b) and are with the $^{129}Xe^{2+}$ isotope only. The data are extracted in a two-particle-coincidence between the $^{129}Xe^{2+}$ ion and one incoming electron e_i which could either be e_1 or e_2 as they are indistinguishable in the detection plane. The momentum of the second incoming electron e_j ($i \neq j$) is then calculated via the given conservation of momenta

$$p_{\parallel,e_j} = -\left(p_{\parallel,Xe^{2+}} + p_{\parallel,e_i}\right) \quad \text{with } i \neq j \quad . \tag{5.11}$$

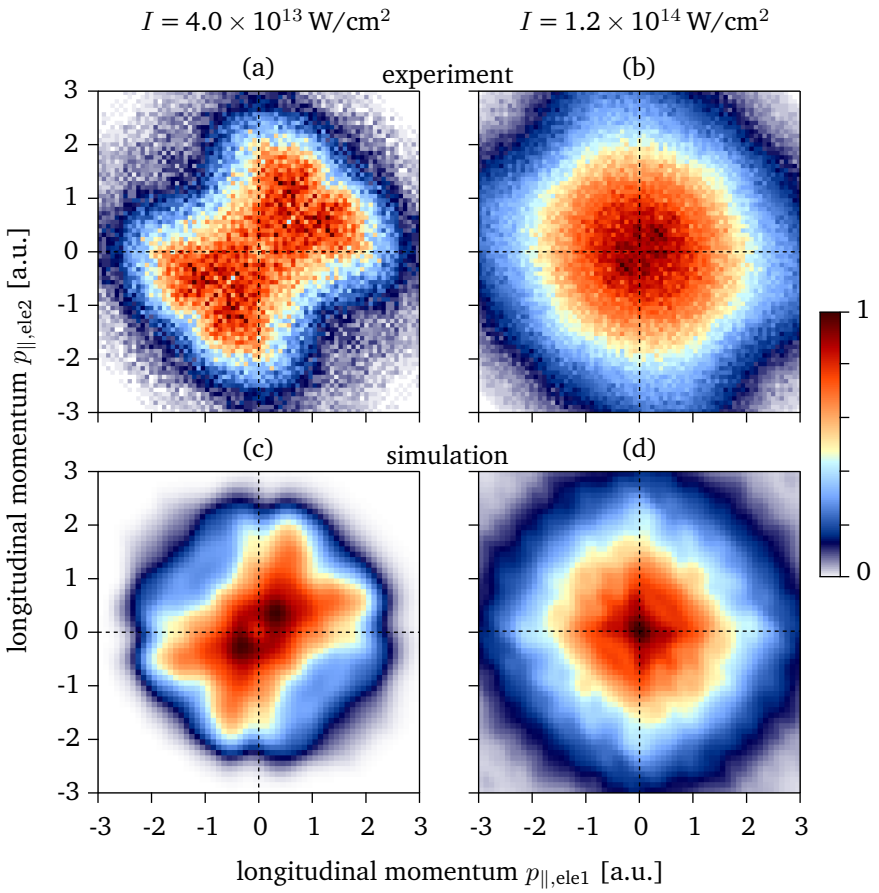

Figure 5.8: Experimental and semi-classical electron correlation distributions for moderate and high intensity. (a,b) Experimentally measured electron correlation maps for intensities of **(a)** 4.0×10^{13} W/cm^2 (left column) and **(b)** 1.2×10^{14} W/cm^2 (right column). **(c,d)** For comparison the theoretical counterparts are calculated with the semi-classical model for the respective intensities.

The resulting distributions are symmetrized along the $p_{\parallel,e1} = p_{\parallel,e2}$ diagnonal due to the indistinguishability of both electrons on the detection and along $p_{\parallel,e2} = -p_{\parallel,e1}$ diagonal since our measurement was conducted with random CEP[5].

Looking at the results in Figs. 5.8 (a,b), the lower intensity in (a) shows a pronounced correlation in the first and third quadrants indicating (e,2e) impact ionization. Moreover, a fork-like structure is observed along the diagonal which has been observed beforehand by [272,273] and can be explained by a typical Coulomb repulsion by parallelly escaping electrons. Interestingly, the lower intensity correla-

[5]For CEP dependent measurements of the e2e1 correlation distribution like e.g. by [264] the latter symmetry along the anti-diagonal is not applicable as it would wash out the CEP dependent asymmetry of the correlation distribution.

tion map shows a slight minimum at the origin which excludes a tunneling related DI process. Also it is interesting to note that the plot shows counts in the second and fourth quadrants as well, which indicates that there is a small amount of anti-correlated electron emission due to multiple re-collisions [265] involved.

As already mentioned before, these results are distinctly different from the results of Sun *et al.* [3] where no correlations were found for any of the investigated intensities at 790 nm wavelength. In fact, the observation of electron correlations during DI of Xe does not seem to exist in the literature to the best of our knowledge. On the other hand for the higher intensity measurement in Fig. 5.8 (b), a 2D Gaussian like distribution yields that no evidence of electron correlations are present indicating that this intensity I_2 is well within the SDI regime. In order to further corroborate our findings, we compare the experimental results [Fig. 5.8 (a,b)] with e2e1 correlation distributions extracted from the semi-classical simulations for similar experimental conditions. The theoretical distributions [Figs. 5.8 (c,d)] agree quite accurately with their experimental counterparts. Note that the same color scale range is taken for both the experimental and theoretical data in Fig. 5.8. Not only the expansions of the distributions agree but also the distinct features of the NSDI case are reproduced exactly, i.e. the fork-like structure, secondary forks around the axis, the local minimum at the origin or the anti-correlated counts in the second and forth quadrant.

The excellent agreement of the semi-classical model with experiment provides confidence that all interaction mechanisms are captured and thus opens up the ability to track individual electron trajectories from the model in order to get further insights. In Figs. 5.9 (a,b), representative trajectories for both emitted electrons for intensities of $I_1 = 4.0 \times 10^{13}$ W/cm^2 and $I_2 = 1.2 \times 10^{14}$ W/cm^2 are plotted in terms of their distance away from the ion as a function of laser cycles. Figs. 5.9 (c,d) show zooms of the interaction region of the electrons with the core. For the lower intensity (a) e_1 (dashed red line) is emitted at the peak of the pulse (t = 0 cycles) and is able to impact-ionize e_2 (solid blue line) upon returning to the core. This is a typical example of (e, 2e) DI where e_2 is directly ionized upon re-collision and the two electrons show correlated behavior by leaving in the same direction. The fact that both trajectories in Fig. 5.9 (a) are slowly separating over time while they leave in parallel close to the dication [see Figs. 5.9 (c)] reflects the Coulomb repulsion amongst each other which leads to the fork-like structure in Figs. 5.8 (a,c). The motions of the two electrons at the higher intensity [see Figs. 5.9 (b,d)] are tellingly different. Due to the much higher intensity, e_1 (dashed red line) can be emitted much before the peak intensity (t = 0 cycles) and does not at all return to the vicinity of the core. For e_2 (solid blue line) to also be emitted it must undergo an individual tunneling process (two cycles later in this example) in which case no correlation between the two electrons is expected. Interestingly, in this example e_2 returns to the vicinity of the parent dication half a cycle later as clearly seen in see Fig. 5.9 (d).

These results show that the trajectories of both electrons resulting from NSDI and SDI in the mid-IR regime can be accurately modeled using a simple classical approach [282]. This also means that any elastic re-scattering event that occurs

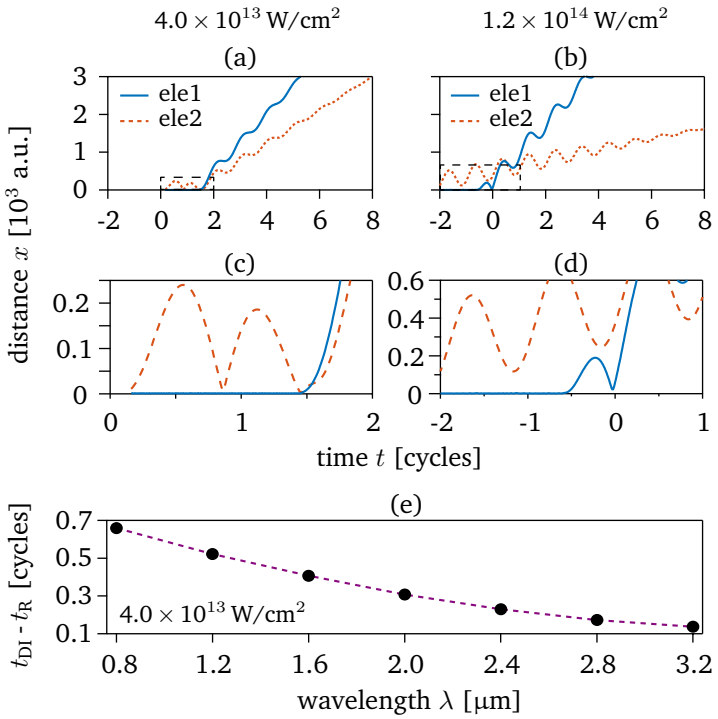

Figure 5.9: Representative trajectories for both moderate and high intensity from semi-classical model. (a - d) Example first (dashed red line) and second (solid blue line) electron trajectories for intensities of **(a,c)** 4.0×10^{13} W/cm^2 (left column) and **(b,d)** 1.2×10^{14} W/cm^2 (right column). **(c,d)** Zoom of the origin of the coordinate system being the position of the parent dication. **(e)** Time difference between the return of e_1 and the ionization of e_2 as a function of wavelength at an intensity of 4.0×10^{13} W/cm^2. Large time differences correspond to the RESI process while close to zero time difference relates to impact ionization via (e,2e).

not only after SI but also after SDI in the mid-IR can be interpreted classically. These points could be of potential interest when imaging molecular structure via LIED [289] especially when dication states ought to be imaged. We will pick up on this point in a later chapter 7.

Furthermore, the data of the single traceable electron trajectories from the semi-classical model calculations are used to complement the insights of the previous Sec. 5.3.3 on the negligible influence of the RESI process in our data. In Fig. 5.9 (e) we analyze the difference between the re-scattering time of e_1 (t_R) and the ionization time of e_2 (t_{DI}) for a constant intensity of 4.0×10^{13} W/cm^2. Larger time differences are an indication of the RESI mechanism since the second electron needs to "wait" in the intermediate excited state to be ionized by the subsequent field maximum. On the other hand smaller time differences are indicative of (e,2e) DI where the emission of e_2 occurs almost instantaneously after the impact of e_1. The

results of Fig. 5.9 (e) reveal that increasing the wavelength results in shorter time difference $\Delta t = t_{\mathrm{DI}} - t_{\mathrm{R}}$ yielding a dominance of the (e, 2e) mechanism. This can be understood in terms of an increasing U_{P}, which is proportional with the square of the wavelength, and therefore return energies greater than the second ionization potential being more readily generated as shown earlier in Fig. 5.7 (b, red).

5.4 Overcoming shielding effects of inner-shell electrons in NSDI of xenon

The main insights of our experimental and theoretical investigation of the previous section are that 1) the transition of NSDI to SDI of Xe atoms can be unambiguously identified with mid-IR laser pulses within the "fully differential investigation" including ion yield and momentum as well as electron correlation distributions, 2) SDI dominates over the (e, 2e) mechanism well below $I = 1.0 \times 10^{14}\,\mathrm{W/cm^2}$ with mid-IR driving fields due to the lower return probability of e_1, 3) the ionization pathway via the $5s5p^6$ orbital occurs primarily for lower intensities and 4) the NSDI specific (e,2e) features like the double-hump structure in the ion momentum distribution and a correlation of e_1 and e_2 in the e2e1 map can be clearly observed in contrary to investigations at 800 nm [3].

The last point is interesting since the non-existence of the double hump and electron correlation for DI of Xe with near-IR fields was convincingly explained with the missing structures by the influence of the shielding potential by the residual inner-shell electrons [3] which was modeled in agreement with the experimental findings [260]. Our results though insinuate that these shielding effects have no influence on the NSDI process when applying DI with mid-IR fields. Also the agreement of our data with the semi-classical model shows that primarily the correlation between e_1 and e_2 are governs the NSDI process while the residual valence electrons of the parent ion can be ignored. A possible explanation for this phenomena could be the 15 times[6] higher return energies in our mid-IR case compared to SFI with driven with 800 nm fields. For higher return energies the shielding potential is less repulsive which leads to a higher probability for inelastic scattering of the return electron with the parent ion. This could potentially be interrogated experimentally by a systematic study of the appearance of characteristic (e,2e) structures with increasing wavelength. On the side of the theory, it would be interesting to see what the the simulation of Yuan *et al.* [260] with the improved GSZ shielding potential returns for mid-IR driving fields.

[6] $(3.1\,\mu\mathrm{m})^2 / (0.8\,\mu\mathrm{m})^2 \sim 15$

Part III

Imaging of Molecular Structure and Dynamics

Chapter 6

Retrieval of Structural Information from Polyatomic Molecules with Laser-Induced Electron Diffraction

In the following chapters, we turn to exploring the structural imaging application of the re-collision process by LIED. As explained in Sec. 2.4, the ponderomotive up-scaling of the kinetic energy of the returning electrons when utilizing long-wavelength fields holds the potential to greatly enhance the spatial capabilities of the technique. Moreover, applying LIED with our experimental tools establishes the basis to further develop LIED into a technique that is able to accurately image structural dynamics of large, polyatomic molecules on their natural time scales.

In this chapter, we show how LIED can be taken beyond the hitherto achieved imaging of simple diatomic molecules [38, 39] as our 160 kHz, mid-IR OPCPA source combined with full three-dimensional electron-ion coincidence detection offers crucial solutions to limiting problems. The chapter is structured as follows: At first the state-of-the-art of structural imaging techniques based on *X-ray* (XRD) and *conventional electron diffraction* (CED) is introduced in Sec. 6.1 before LIED as an alternative for molecular imaging is introduced in Sec. 6.2 including its basic requirements to image "larger" molecular systems, its experimental and theoretical state-of-the-art and its intrinsic temporal properties. Further, the theoretical concepts for LIED as used within this thesis are introduced in Sec. 6.3. Next, we conducted a LIED experiment with our experimental methodology on xenon atoms in Sec. 6.4 to extract and compare differential cross-sections with CED data from literature to test and calibrate our approach. Finally in Sec. 6.5, we applied mid-IR LIED on aligned acetylene molecules in order to extract structural information of all individual nuclei positions.

The experimental and theoretical data presented in this chapter and hence its main results have been published in

B. Wolter et al., Physical Review X ***5****, 021034 (2015)* [169] (highlighted in APS Physics[1]) and

[1] https://physics.aps.org/synopsis-for/10.1103/PhysRevX.5.021034

M. G. Pullen et al., Nat. Communications **6***, 7262 (2015)* [174] (highlighted in OSA - Optics & Photononics News 2015[2] [291]).

6.1 Capabilities and limitations of X-ray and conventional electron diffraction

The most established techniques to spatially resolve the atomic constituents of a gas-phase molecule are based on X-ray or electron diffraction. In both cases, a target object is illuminated by a plane wave, a photon or electron wave, respectively, resulting in a far-field diffraction pattern that is the Fourier-transform of the object. The response of the target potential introduces phase shifts and makes partial waves interfere, causing peculiar *differential scattering cross sections* (DCSs) $\partial\sigma'/\partial\Omega$ for different angles. Here, a high energy of the impacting particle (again photon or electron, respectively) is conterminous for a short wavelength on the scale of a single atom or below. The wavelength that corresponds to the atomic scale of $\Delta x \sim 1\,\text{Å}$ is given by a photon energy of $E_\lambda \sim 12.4\,\text{keV}$[3] in the case of *X-ray diffraction* (XRD) and an electron energy of $E_e \sim 150\,\text{eV}$[4] in the case of *conventional electron diffraction* (CED). Magnitudes higher respective energies need to be used in order to achieve resolutions that are orders of magnitude better than the size of the target object. Conventional X-ray sources like e.g. hard X-rays from a synchrotron [292] as well as CED experiments [29] readily reach picometer[5] spatial resolutions when utilizing $E_\lambda \to 1\,\text{GeV}$ to $8\,\text{GeV}$ and $E_e \to 40\,\text{keV}$ to $100\,\text{keV}$, respectively.

An important parameter when comparing diffraction imaging techniques is the *scattering amplitude* $f(k,\Theta)$ with different gas-phase molecular targets. Per definition the scattering amplitude describes the relative amplitude of the outgoing spherical wave relative to the incoming plane wave. Hence it is a characteristic to interrogate the scattering response of a target. The relation between the scattering amplitude and the DCS is [95]

$$\frac{\partial\sigma'}{\partial\Omega} = |f(k,\Theta)|^2 \equiv \sigma(k,\Theta)^{6} \quad . \tag{6.1}$$

For small cross-sections the overall interaction is weaker leading to an effectively longer experiment in order to see a comparable signal. Comparing XRD and CED based techniques, electron scattering cross sections are generally five to eight orders of magnitude higher than those of X-rays [37, 293, 294] making CED more

[2] http://www.osa-opn.org/home/articles/volume_26/december_2015/extras/laser-induced_electron_diffraction_to_image_molecu/

[3] $E_\lambda = \mathrm{h\,c}/\lambda$

[4] $E_e = \mathrm{h}^2/(2\,\mathrm{m}\,\lambda^2)$

[5] $1\,\text{pm} = 10^{-12}\,\text{m} = 0.01\,\text{Å}$

[6] For simplicity the DCS is written as a single variable σ in the following although per definition is should be a differential $\partial/\partial\Omega$. Integrating the DCS over the full 4π solid angle results in the total cross-section σ_{tot}.

powerful for determining the structure of matter. An illustrative example is given in [294], where the comparison is drawn between a 7 keV X-ray of 1.75 Å wavelength and an electron with the same de-Broglie wavelength at a kinetic energy of 50 eV. The elastic cross-sections on a carbon atom are <10 b (barn) and $\sim$470 Mb, respectively showing the advantage of electron diffraction based techniques.

Besides the spatial capabilities of XRD and CED, they historically offered in its pulsed forms solely durations of hundreds of picoseconds [37] that is not suitable for resolving ultrafast namely sub-ps dynamics.

Typically ultrafast "pump-probe" type experiments are applied where a pump pulse is used to initiate an ultrafast process or reaction by promoting the molecule into an excited state to then use a probe pulse to project the molecular wave package onto a final state at a pre-determined time delay [176]. A typical pump-probe setup was illustrated in the introduction in Fig. 1.1. Repeating the measurement over a range of time delays results in a "motion picture" of the reaction [176, 295]. Today this methodology has developed into a mature and reliable experimental tool and has been used to study processes such as melting [296], dissociation [297, 298], and isomerization [27], amongst others. In order to combine the spatial capabilities of diffraction imaging with the ultrafast pump-probe techniques, several ultrafast diffraction experiments have been initiated.

In case of XRD, new sources have been developed in order to provide femtosecond X-ray pulses: X-ray free electron laser (XFEL) sources [299] that are designed to produce coherent radiation in the soft and hard X-ray regime generating pulses of durations down to <10 fs [299]. In XFELs, relativistic electrons are forced on oscillatory trajectories via *undulators* generating high energy photons. The process can be controlled such that the photons are generated coherently leading to X-ray pulses in the femtosecond regime. Nowadays, XFEL sources are built around the globe like e.g. the FLASH (**F**ree-electron **Las**er in **H**amburg) or the Stanford LCLS (**L**inac **c**oherent **l**ight **s**ource) [300]. Both facilities have been used in XRD experiments reaching 100 fs pulses at a wavelength of 6.2 Å (2 keV) in case of FLASH [301] imaging aligned molecules, and in case of LCLS [302] with 1.5 Å (8.3 keV) at 30 fs to take snapshots of a molecular motion. Hence, the spatial resolutions in both cases lie on the single Å - level. These results are great achievements for these large-scale facilities that initiated their XFEL programs within the last decade. Yet, both XRD experiments also show that the desirable, combined spatio-temporal resolutions for gas-phase pump-probe imaging of ultrafast (tens to hundreds of femtosecond scale) molecular dynamics are not achieved yet, specifically in terms of spatial resolution which is two orders of magnitude better for CED. Efforts for improvements are on their way in both XFEL facilities. As an example of how to overcome the spatial resolution boundary, a very recent investigation by Glownia *et al.* [303] showed how the vibrational wave packet of iodine I_2 can be resolved over time via interference of the diffraction signals of the vibrating excited state with the rigid ground state. By means of the interference signal a sub-Ångström spatial resolution of $\sim$0.3 Å can be achieved (with a temporal resolution of 30 fs).

method	σ [barns]	∂x [Å]
XRD	10^0 - 10^1 [37, 293, 294]	1 - 10 [35, 301], 0.3 [303]
UED	10^6 - 10^8 [37, 293, 294]	0.01 - 0.1 [33, 298, 311]
LAED	10^6 - 10^8 [37, 293, 294]	0.01 [313]
LIED	10^6 - 10^8 [37, 293, 294]	0.05 [39]

method	∂t - achieved [fs]	∂t - predicted [fs]
XRD	$\sim$10 [35, 314]	$<$10 [299]
UED	28 [34] - 230 [315]	$<$1 [307, 310]
LAED	$\sim$ 520 [313]	$<$10 [313]
LIED	$\sim$ 5 [39]	$\leq$ 1 [316, 317]

Table 6.1: Overview of properties of various molecular imaging techniques.

Similarly, CED techniques have been utilized in ultrafast pump-probe setups in order to image molecular dynamics by "pumping" the system using a short excitation pulse and then "probing" the molecular target using a short electron pulse [304–306]. The technique was dubbed *ultrafast electron diffraction* (UED). The electron pulses are created in an "electron gun" where electron bunches are generated from the cathode material by focusing pulsed optical fields onto them. Afterwards, the electron bunches are accelerated to the desired kinetic energy by a potential difference of up to e.g. $\Delta U_e \rightarrow 100\,\mathrm{kV}$ [29]. The temporal resolution of such experiments is typically limited by the repulsion of the electrons within a pulse due to their intrinsic charge. Coulomb repulsion within the electron bunch sets the pulse durations limit from the hundreds of femtoseconds to the picosecond level. Shorter temporal resolutions are currently difficult to achieve in UED but different concepts already proved a drastic decrease of electron pulse durations below the 100 fs level. Two approaches have been successfully so far. Electron pulses can be generated on the single-electron wave packet level circumventing space-charge effects leading to pulse durations of $\sim$28 fs [34]. Also pulse compression is achieved by perpendicular propagated terahertz waveforms [307] to achieve $\sim$75 fs. Another option would be to utilize relativistic electron energies [308] in order to yield $\sim$10 fs. Another UED scheme that proposed temporal resolutions $<$10 fs is *laser assisted electron diffraction* (LAED) [309]. By intersecting a picosecond electron pulse with a femtosecond optical field, UED on the target is only enforced in the temporal intersection of both pulses limiting the effective pulse duration to the femtosecond optical pulse duration. Even attosecond electron pulses are conceptualized [310]. These techniques may be used for diffraction imaging of a dynamic molecular process in the coming years. The current state-of-the-art of using UED to image coherent molecular motion was published very recently imaging the vibrational wave packet of iodine I_2 and achieves a combined resolution of $\partial x = 0.07\,\text{Å}$ spatially and $\partial t = 230\,\mathrm{fs}$ [311] based on recent work [312].

However, spatially resolving the fastest known molecular movements, e.g. proton motion within a molecular compound, has been impossible so far using established pump-probe diffraction imaging techniques such as UED and ultrafast XRD. As both

methods currently lack to *simultaneously* provide sub-Ångström spatial and few femtosecond temporal information being essential requirements for a molecular movie of hydrogen motion [318]. The current state-of-the-art of spatio-temporal capabilities of the most common diffraction imaging techniques are summarized in Tab. 6.1 as they were partially mentioned above. While XFELs allow pulse durations on the ∼10 fs level [35, 314], solely single Å spatial resolutions are currently possible [35, 301]. In addition, XFEL sources currently suffer from relatively large spectro-temporal jitter and are only available at large-scale facilities. On the other hand, UED offers few picometer spatial resolutions [33, 298], yet up until today lacked temporal resolutions, yet improvements are on the way. One specific example is LAED which promises simultanous few picometer spatial and <10 fs temporal resolution [313]. A problem both of XRD and UED is the fact that the scattering amplitudes of low-mass atoms, specifically of hydrogen, generally is orders of magnitude lower than of heavier atoms. This means that interrogating gas-phase, organic molecules with diffraction techniques typically is not susceptible to imaging the protons within the compound.

Some of these restraints have motivated the development of new dynamical imaging techniques, largely for the gas phase, such as chirped encoded re-collisions [319], photoelectron holography [320], femtosecond photoelectron diffraction [294,321], Coulomb explosion imaging [322,323] and LIED. As mentioned previously, the latter is going to be technique on which our work focuses within this thesis and which is beneficial for several reasons explained in the subsequent section.

6.2 Imaging molecular structure with LIED

Versatile laboratory scale, table-top methods that provide the combined spatial and temporal resolutions would push the limits especially for the imaging of gas-phase molecular dynamics. LIED is such a method and is based on probing an objects' structure using its own electrons that are elastically re-scattered during strong-field induced re-collisions. The basic process based on the re-collision model was already explained in Sec. 2.2. Fig. 6.1[7] sketches our approach of applying LIED with mid-IR laser fields on larger, polyatomic molecules. A molecular system is tunnel-ionized by the long wavelength electric field (red) to accelerate the liberated electron on a long excursion (green) before driving it back to the parent ion where it elastically re-scatters in all directions, henceforth containing a diffraction imprint of the positions of the single atomic scatterers. This diffraction information is perceptible in the 3D detected momentum distribution as the Fourier transform in the far-field. In the following, requirements and capabilities are explained, as well as limitations and how to overcome them.

[7] The figure was already plotted in the introduction as Fig. 1.2 and is replotted here for illustration.

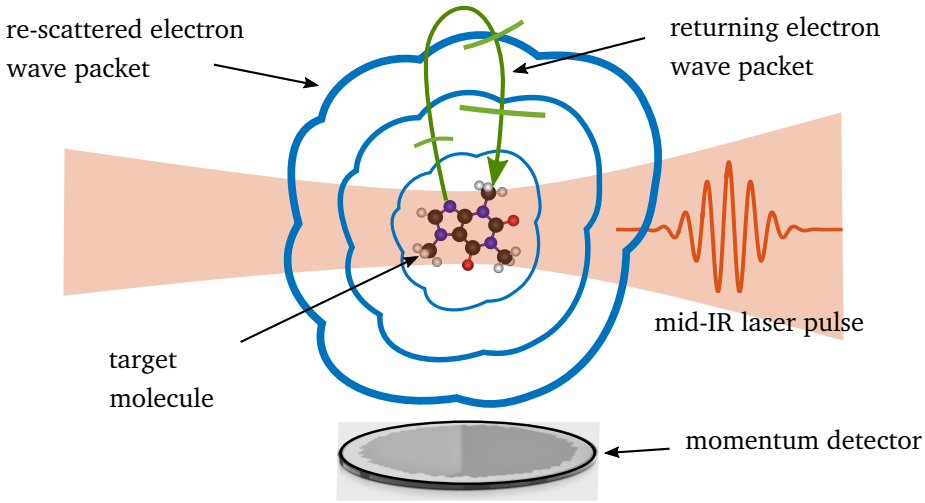

Figure 6.1: Illustration of LIED imaging of molecules. A target molecule is tunnel-ionized by a long wavelength electric laser field (red) to accelerate the liberated electron on a long excursion (green) before driving it back to the parent ion. Upon return the electron elastically re-scatters in all directions (blue), henceforth containing a diffraction imprint of the positions of the single atomic scatterers. This diffraction information is perceptible in the 3D detected momentum distribution as the Fourier transform in the far-field.

6.2.1 Basic requirements and capabilities

The challenge lies in simultaneously fulfilling the stringent conditions for LIED in order to extract structural information of molecular targets; these are: **(i)** achieving core penetrating collisions and sufficient momentum transfer with the scattered electron, **(ii)** achieving high re-collision energies and simultaneously a small fraction of target ionization, **(iii)** driving re-collision in the quasi-static regime to enable extraction of field-free diffraction images from the photo electron momentum spectra, **(iv)** ideally achieving a close-to-plane wave front of the re-colliding electron wave packet, and **(v)** detection of all scattering angles to exploit the angular dependence of target atom dependent scattering amplitudes. When these conditions are met, the method of molecular structure retrieval is similar to conventional electron (or X-ray diffraction), with the added benefit of femtosecond temporal resolution of the driving laser which will be discussed in the next section.

6.2.1.1 Core penetrating momentum transfer

In case of UED, the pulsed electron bunches are guided onto a target so that the electrons can scatter off the target, and are collected under usually small scattering angles $\Theta \lesssim 10^\circ$ (like e.g. in [298]) depending on the acceptance abilities of the detection setup. As mentioned beforehand, the spatial resolution of a measurement

is determined by the kinetic energy and hence the wavelength of the electron projectile. A measure for the degree of "interrogation" or "penetration" of the nuclei in your target system that is achieved by the electron wave is given by the *momentum transfer*

$$\vec{q} = \vec{k}(k, \Theta, \Phi) - \vec{k}_0(k_0, 0, 0) \quad , \tag{6.2}$$

which is the difference between the momentum/wave[8] vector of the scattered electrons $\vec{k}(k, \Theta, \Phi)$ and the incoming momentum vector $\vec{k}_0(k_0, 0, 0)$ (assumed to be along the main axis of laboratory system). Assuming an azimuthal symmetry in the scattering system, the magnitude of the momentum transfer is defined as

$$q = 2\, k_0\, \sin(\frac{\Theta}{2}) \quad , \tag{6.3}$$

with the wave vector defined as $k_0 = 2\,\pi/\lambda_e$[9]. In Fig. 6.2 the momentum transfer q is plotted as a function of scattering angle Θ for various electron energies. In the example of the famous paper of Ihee *et al.* [298] of the Zewail group, they used accelerated electrons at a wavelength of $\lambda_e = 0.067$ Å ($E_e = 30$ keV) for a momentum transfer range Δq of $\sim$1 to 18.5 Å^{-1} covering a scattering angle range of $\sim$0.6° to 11.3° (as shown as red background in Fig. 6.2). The larger the momentum transfer range the smaller the spatial distances that can be resolved[10]. Accordingly, if different inter-atomic distances within a molecule are almost equivalent, they cannot be distinguished in the diffraction pattern [324]. Hence, UED experiments are usually scaled in electron energy to achieve a high spatial resolution in interrogating the atoms' positions within a molecular complex due to a fixed angular acceptance of e.g. a one-dimensional detection system. Yet, also there are experiments applying low-energy electron diffraction (LEED) with typical energies ranging from 10 to 300 eV [324] reaching spatial resolution in the nm range or momentum transfers below $q \lesssim 1$ Å. Here, the focus lies more on probing the valence electron response of or electron correlations within a system where quantum-mechanical effects might play a role and which are generally hard to reproduce with theoretical simulations [324].

In the case of LIED imaging, the approach to achieve high momentum transfers to be able to probe the different nuclei of a molecular system is opposite to UED. While laser systems that are typically used for SFI, limit the electron return energies generally to the *low-energy regime* from a UED perspective, i.e. $E_\mathrm{r} < 300$ eV, high q values can be achieved with electrons that re-scatter at larger angles $\Theta_\mathrm{r} \gtrsim 40°$ [324] according to Eq. 6.3. For a typical Ti-Sapphire laser system ($\lambda = 800$ nm) at an intensity of 2.5×10^{14} W/cm^2 as used in the first experimental proof of LIED by Meckel *et al.* [38] in 2008, the maximum electron return energies lie around $E_\mathrm{r,max} \sim 50$ eV[11] [compare with Fig. 2.10 (b)]. This technically offers a momen-

[8] In atomic units, the momentum vector equals the wave vector: $\vec{p} = \hbar\,\vec{k}$ (SI).

[9] The de-Broglie wavelength in atomic units it defined as: $\lambda = \pi\sqrt{\frac{2}{E}}$.

[10] The (Fourier-) transform limit of the product between momentum transfer and spatial resolution is comparable to the relation between optical bandwidth and pulse duration of a mode-locked laser.

[11] Finally, they used electron return energies with solely $E_\mathrm{r} \leq 20$ eV to extract structural information due to missing statistics for higher E_r.

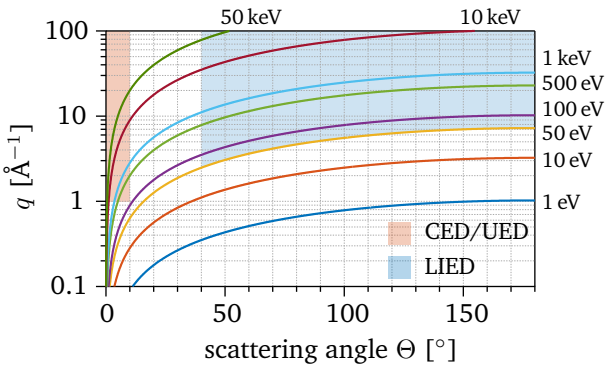

Figure 6.2: Momentum transfer as a function of scattering angle. The momentum transfer q is plotted as a function of scattering angle Θ for various electron impact energies. A standard angular detection range for UED experiments is highlighted with a red background region (like e.g. in [298]). LIED experiments offer sufficient q to resolve nuclear structure for $E_r \gtrsim 50\,\text{eV}$ and $\Theta_r > 40^\circ$ [324] as shown as blue background.

tum transfer range Δq ranging from $2.0\,\text{Å}^{-1}$ at $\Theta_r = 30^\circ$ to $7.7\,\text{Å}^{-1}$ at $\Theta_r = 180^\circ$ comparable to a UED experiment from the same year [325].

Hence, experiments on SFI that are conducted with detection systems that can detect the full 3D momentum distribution (or at least a 2D distribution along the laser polarization axis) are able to extract LIED signals that originate from returning electron wave packets that "penetrated" the atomic cores. The lower limit of scattering energies that provide sufficient momentum transfer in order to probe solely the nuclei of molecular targets without influence of valence electrons was identified to be around $E_r \gtrsim 50\,\text{eV}$ for $\Theta_r \gtrsim 40^\circ$ [324] as shown in Fig. 6.2 as blue background. Xu *et al.* [324] determined this limit by comparing experimental CED data (here detected up until $\Theta_r < 120^\circ$) with the well-established *independent atom model* (IAM, discussed further down in Sec. 6.3.2) and hence pertains also for LIED. For electron energies below $E_r < 50\,\text{eV}$ the IAM does not seem to describe the collision process with the nucleus adequately which is certainly connected to the missing influence of valence electrons. These different angular ranges of UED and LIED to achieve similar momentum transfers are compared in Fig. 6.2.

6.2.1.2 Suitable re-collision energies at low ionization fraction

Naturally, the momentum transfer range and hence the spatial resolution for LIED imaging can be scaled up by generating returning electrons with higher return energies in the SFI process. As already shown in Ch. 2, the return energy $E_r \propto U_P \propto I\,\lambda^2$ scales with intensity and the wavelength square. The intensity cannot be scaled up infinitely since the ionization process saturates due to ground state depletion for high intensities (dependent of the ionization potential). The more effective option is to drive the SFI process at longer wavelength as discussed in Sec. 2.4

which is also the strategy in this thesis. By using mid-IR laser pulses the return energies result higher as calculated in Fig. 2.10 (b) while at the same time, the effective ionization fraction is lower for a constant γ. This relation was illustrated in Fig. 2.10 (a). Mid-IR laser pulses are especially beneficial when applying LIED to molecular systems that generally have lower ionization potentials than atomic systems.

6.2.1.3 Quasi-static conditions for classical interpretation of the electron recollision

As long wavelength SFI is advantageous for high return energies in LIED, they also provide quasi-static conditions for the SFI and hence the LIED process. This results in the emission of an electron via tunneling which sets the ideal condition to then invoke classical considerations for the electron's trajectory in the time-varying electric field as derived in Subsec. 2.2.1. The use of semi-classical models is a common approach in the field of SFP as discussed in Sec. 2.4 since ab-initio TDSE simulations generally deny studying a problem by switching on and off physical processes. Hence, an interpretation of experimental data on the basis of semi-classical models is more instructive. This benefit is the basis of the *quantitative re-scattering* (QRS) model [110, 190] developed by our collaborators of the group of C. D. Lin of the Kansas State University, USA. QRS theory accurately calculates SFI distributions including the LIED signal used to evaluate and compare to experimental SFI data including elastically re-scattered electrons taking into account their classical trajectories. In order to make this comparison, the experiment has to provide quasi-static conditions.

6.2.1.4 Close-to-plane wave front of the re-colliding electron wave packet

The scattering and diffraction process between an electron wave and an atomic scatterer can in first approximation be described as a plane wave interacting with an atomic Coulomb potential. This *plane-wave approximation* is used as a first step in most scattering models (discussed e.g. in [326]). The same argument is used in the theoretical modeling of the SFI process by assuming a continuum state for the outgoing electron wave packet (see SFA in Sec. 2.1.2). In reality, using the plane-wave approximation to describe experimental results shows weaknesses especially in the SFI process, since the returning wave packets generally exhibits strong curvatures. These arise from the fact that the Coulomb potential actually has an influence on the electron wave both during from emission and upon return to the parent ion (known as Coulomb focusing). Influences of the Coulomb potential on the (quasi)-free tunnel electron were discussed in Ch. 4 of this thesis.

The use of longer wavelength laser pulses for the SFI process is beneficial to achieve a close-to-plane wave front of the re-colliding electron wave packet. This can be explained in two parts. On the one hand, the electron propagates further away from the target ion due to the longer excursions of the electric field. This leads to

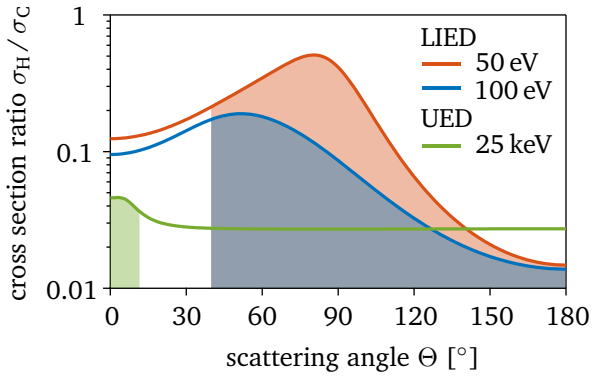

Figure 6.3: Ratio of scattering cross-sections of hydrogen and carbon. The ratio of the H and C scattering cross-sections σ_H/σ_C as a function of scattering angle Θ for typical energies used in LIED (50 eV in red and 100 eV in blue) and CED/UED (25 keV in green). Also the typically utilized angular ranges are highlighted.

an enhanced overall spread of the wave packet due to quantum diffusion [8], so that the effective wave front as seen by the ion upon return can be approximated a plane wave. The second point is that higher return energies due to ponderomotive scaling lead to less influence of the Coulomb field on the returning electron. The resulting weaker Coulomb focusing as felt by the electron wave packet is beneficial in terms of its shape and hence on its curvature (as discussed in [327]).

6.2.1.5 3D detection of re-scattered electrons for exploitation of scattering amplitudes at large angles

As mentioned earlier, to achieve sufficient spatial resolution in LIED experiments, ideally the full angular scattering range should be detected. The kinetic energy of the returning electrons in mid-IR SFI lie around some hundreds of eV so that a high momentum transfer can be achieved for backward scattering according to Eq. 6.3. Hence, momentum detection systems which resolve the full 4π solid angle are advantageous for LIED experiments.

Moreover, full angular detection of the momenta of re-scattered electrons has another benefit. The electron scattering amplitudes σ are both dependent on the impact energy E_e as well as the scattering angle Θ but also on the atomic species. Crucial is the dependence of σ on atomic species since in principle light atoms have a lower σ than heavier atoms. Therefore, it is difficult in CED and UED experiments to determine the position of light atoms within a molecular compound [324]. To exemplify the context, Fig. 6.3 shows the ratio of the scattering cross-sections of hydrogen (H) and carbon (C) as a function of Θ for different E_e comparably used in LIED (50 eV in red, 100 eV in blue) and in UED (25 keV in green). H and C were chosen here since both are the main ingredients of organic molecules and H as the lightest atom gives the biggest contrast to the argument. It is apparent in Fig. 6.3

that σ_H is smaller than σ_C (and their ratio < 1) for all Θ and E_e. For larger Θ the ratio is in favor of UED-like scattering energies of e.g. 25 keV. By comparing the typical angular ranges for LIED (red and blue shaded) and UED (green shaded) in Fig. 6.3 it becomes clear that σ_H is a factor of 20 smaller compared to carbon for typical scattering angles and energies used in UED which renders them effectively "invisible" to most diffraction based imaging techniques. On the other hand, LIED offers a better σ ratio for lighter atoms, i.e. hydrogen, since the contrast to the heavier carbon atoms is generally smaller compared to the one of CED/UED up until $\Theta \lesssim 120°$. The σ ratio for angles between 30° and 120° even approaches within one order of magnitude for LIED-like scattering energies, i.e. $\sigma_H/\sigma_C \sim 0.5$ for $E_e = 50$ eV and $\Theta = 85°$ and 0.2 for 100 eV and 50°. This shows that LIED ranges of specific combinations of scattering angles and energies that allow to resolve both light and heavy atoms assuming the whole angular scattering range can be detected.

6.2.2 Intrinsic sub-optical cycle temporal resolution

As shown before, the LIED imaging technique capitalizes on the established principles of CED/UED with the main difference that the nuclear structure of the target system is probed with one of its own electrons [36] rather than an external source of electrons. By operating within the strong-field quasi-static limit the classical re-scattering model can be invoked to associate specific emission and return times to each re-scattered electron energy [23] as described in detail in Sec. 2.2. In LIED, the electron's emission at the tunnel exit and the return to the parent ion can be regarded as a *pump* and a *probe*, respectively, of the target system. Just like in a conventional pump-probe setup (see Fig. 1.1), the temporal difference between pump and probe yield the temporal information. Since the laser-induced re-scattering process occurs within one optical cycle, the pump and probe times for each diffracted electron can each be determined with a precision at the sub-femtosecond level [328]. The research field of attosecond science relies heavily on this argument in order to investigate electron [18,329,330] and nuclear [316,319] dynamics on the attosecond temporal scale.

The re-collision model predicts the electron with the maximum return energy $E_{r,max} = 3.175\,U_P$ to be emitted at $\phi_{i,Er,max} \approx 0.05\,\tau_{cycle}$ and to return at $\phi_{r,Er} \approx 0.70\,\tau_{cycle}$ (see Sec. 2.2). In Fig. 6.4 (a) the return energy $E_{r,max}$ is plotted as a function of optical cycle for both emission $\phi_i \leq 0.25\,\tau_{cycle}$ and return times $\phi_r \geq 0.25\,\tau_{cycle}$ for long (black solid line) and short (grey dashed line) trajectories [similar to Fig. 2.4 (c)]. The emission and return times of the maximum return energy are indicated with a red dot and exemplarily the return energy of $E_r = 0.5\,U_P$ for long trajectories with a blue dot. The long trajectories are emphasized here since the ionization probability of an electron on a long trajectory is generally higher than the one of a short trajectory [see Fig. 2.5 (c,left)]. It is clear from Fig. 6.4 (a) that the energy of the returning electron decreases as ϕ_i and hence t_i (or alternatively ϕ_r and t_r) moves progressively away from $t_{i,max}$ ($t_{r,max}$). The time difference between electron emission and re-scattering $\Delta t = t_r - t_i$ depends on both the return energy and

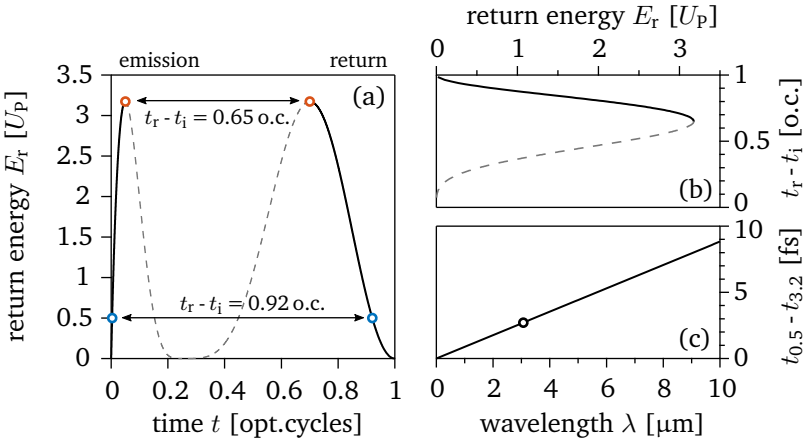

Figure 6.4: Intrinsic sub-cycle temporal resolution. (a) The return energy E_r is plotted as a function of time within an optical laser cycle for both the electron emission ($t \leq 0.25$ o.c.) and return ($t \geq 0.25$ o.c.) times and long (black solid lines) and short (grey dashed lines), respectively. The emission and return time of electrons with the maximum return energy $E_{r,max} = 3.2\,U_P$ are highlighted with red dots, and exemplarily the corresponding times of a return energy of $E_r = 0.5\,U_P$ with blue dots. **(b)** The propagation time of the detached electron within the electric field before returning is calculated as a function of return energy. Long trajectories (black solid line) return 0.65 o.c. after emission while short trajectories (grey dashed line) "fly" on shorter time scales. By defining an arbitrary time window between electrons that return with $E_r = 0.5\,U_P$ and $E_r = 3.2\,U_P$, LIED offers the probability to probe an *interaction window* at which fast molecular processes occur. The temporal width of this interaction window is plotted as a function of wavelength in **(c)**. LIED applied at $\lambda = 3.1$ μm results in a interaction window of about 3 fs centered around 8 fs propagation time indicated with a black dot.

the trajectory type. The short trajectories (grey dashed curve) return to the parent ion sooner than their longer counterparts (solid curves) known from the naming convention. In Fig. 6.4 (b) this time difference is plotted as a function of E_r and it shows that the short trajectories have a "flight" time of $\Delta t \leq 0.65$ o.c. while long trajectories lie above. The exemplary return energy of $E_r = 0.5\,U_P$ for long trajectories "travels" around 0.92 o.c.

In the attoscience field the difference in emission/return time as a function of energy is often called *atto-chirp* (e.g. in [331]) which must be compensated for in order to generate the shortest possible attosecond pulses [332]. In the case of LIED this intrinsic dispersion is an extremely powerful tool that can be harnessed to investigate molecular dynamics at unprecedented temporal precision. Since long trajectories dominate [see Fig. 2.5 (c,left)], then we can define an arbitrary *interaction window* between electrons that return with energies of $0.5\,U_P$ and $3.2\,U_P$. In our case of the mid-IR laser pulses at 3.1 μm (optical cycle of 10.3 fs) wavelength such electrons return 9.6 fs and 6.5 fs after emission, respectively, thus yielding a

roughly 3 fs interaction window centered near 8 fs. Any structural changes that occur within this time should be resolvable by merely analyzing the returning electron as a function of E_r. The size of the interaction window can be tuned by changing the driving wavelength as calculated in Fig. 6.4 (c). For a laser system with a central wavelength of $\lambda = 10\,\mu m$ with an optical cycle duration of $\tau_{10\mu m} = 33\,fs$, the interaction window would be 9 fs long.

The fastest known molecular processes certainly evolve over such timescales. These intrinsic temporal properties could be utilized in the future to image fast and complex processes. If used in combination with a traditional pump-probe scheme, then an experiment could potentially explore an unlimited temporal range that starts at a few femtoseconds to picoseconds and has a precision at the sub-femtosecond level [25].

6.2.3 State-of-the-Art

In the following, the state-of-the-art of theoretical and experimental investigations on the research of LIED is briefly stated[12].

The initial suggestion to use electrons created during strong-field ionization to image molecular structure was published by Zuo *et al.* [36] in 1996 where they originally proposed to utilize *directly* ionized electrons that do not re-scatter from the parent ion under the terminology of LIED. Moreover, they suggested that also the re-scattered electron should carry structural information which is nowadays understood under LIED. The idea was picked up in 2002 by Lein *et al.* [333] who calculated the angularly dependent ATI spectra for a diatomic molecule both quantum-mechanically and semi-classically in order to study the dependence on distance between both atoms. In the same year, Niikura *et al.* [316, 334] showed for the first time how the sub-cycle temporal resolution of the SFI re-collision process can be used to study molecular dynamics. The experiment on H_2^+ did not use electron diffraction information yet but investigated the resulting kinetic energy distribution of the ions yet they stated that the elastically re-scattered electrons carry the diffraction signal. Moreover, the high current density of laser-driven electron pulses was pointed out in these publications. In 2004, Spanner *et al.* [317] described a very important first theoretical recipe of how to extract the diffraction information directly from an electron momentum distribution thereby pointing out difficulties like (i) the imprint of the molecular orbital distribution on the electron wave packet, (ii) holographic interferences between direct and re-scattered electrons, (iii) the importance of large scattering angles in LIED while at the same time decreased signal, (iv) the influence of the vector potential of the laser field on the returning electron upon re-collision, and (v) intra-cycle interference of electrons with different return energies [25, 317].

In the following years, many theoretical investigations were conducted on the possibility to extract structural information from with molecules LIED. Yurchenko *et al.* [335] in 2004 as well as Hu and Collins [336] in 2005 showed via 3D TDSE

[12] The completeness of this overview is subject to change.

simulations the resulting diffraction patterns of 400 nm-pulses interacting with H_2^+ and 800 nm-pulses interacting with a model molecule K_2^+, respectively. LIED was also covered by utilizing the molecular SFA for molecular imaging by Hetzheim *et al.* [337] in 2007 and Busuladzic *et al.* [338, 339] in 2008. The latter observed distinct minima in their electron momentum spectra which they connected with diffraction interferences that remain after including focal averaging allowing to determine the nuclear separation of diatomic molecules. Also in 2008, Morishita *et al.*[13] [190, 340] showed that the *field-free* differential cross-section (DCS) similar to CED experiments can be extracted from the laser-induced electron momentum distribution. They concluded that the photo electron yields in the momentum spectrum $I(p_r, \Theta_r) = W(p_r)\,\sigma(p_r, \Theta_r)$ can be calculated as the product of the *field-dependent* electron wave packet $W(p_r)$ with the *field-free* elastic DCS $\sigma(p_r, \Theta_r)$ and showed this on the basis of TDSE simulations of 800 nm-pulses interacting with hydrogen, argon, neon and xenon atoms and comparing the respective. This idea of removing the laser influence on the returning electron within the momentum distribution is based on the work of Spanner *et al.* [317] as mentioned earlier. In the following, the QRS theory [110] was developed by the same group on the basis of the work of Morishita *et al.*. Chen *et al.* [110] nicely showed that in QRS theory the same photo electron momentum yield distribution can be composed of the exact elastic DCS that can be calculated by standard potential scattering theory (see e.g. [95]) and the electron wave packet information calculated by SFA calculations including the elastic scattering of the propagating electron, called *SFA2* or *improved SFA* (see Sec. 2.1). The QRS theory showed agreement with TDSE simulations and was confirmed in various publication to accurately describe HHG [190, 341] and NSDI [342]. The use of QRS theory to extract structural information from molecules was extensively described by Xu *et al.* [324]. Also, the possibility to use LIED for investigating molecular dynamics is described, which was already touched by Morishita *et al.* [340] where they showed DCS evolution of the proton migration during the creation of vinylidene from acetylene (C_2H_2) The QRS theory as utilized within this thesis will be explained in more detail in the following section.

First experimental studies were published from 2008 on. Okunishi *et al.* [343] as well as Ray *et al.* [344] published subsequently in the same issue of PRL, the first experimentally extracted (according to QRS theory) DCSs of LIED from photo electron momentum spectra of 800-nm pulses interacting with Ne, Ar, and Xe showing a fair agreement with theoretical DCSs for field free electron scattering. In the same year, Meckel *et al.* [38] published the first experimental proof of LIED applied on aligned, diatomic molecules in Science Magazine. The work nicely showed the applicability of LIED to image molecules by extracting bond lengths of O_2 and N_2 from a 3D momentum spectrum detected with a ReMi. In the same year, Okunishi *et al.* [345, 346] also published angle-resolved electon spectra on O_2 and N_2 agreeing with SFA2 simulation, yet DCSs were not extracted from the spectra nor were the molecules aligned. Further in 2009, accurate DCSs could be extracted for LIED on Ar^+ detected by Micheau *et al.* [347]. Moreover, Cornaggia reported the extraction of DCSs of larger molecules, in this case CO_2 [348]. The next milestone

[13] of the group of our collaborators of the group of C. D. Lin from the Kansas State University, USA

was published in 2011 by Okunishi *et al.* [349] when they experimentally detected a doubly DCS (2D-DCS) for LIED on O_2 and CO_2 containing accurate DCS for varying scattering angle and returning momenta which nicely agreed with theory. Further work of applying LIED with two-color fields (400 nm- and 800 nm-pulses) on Xe was published by Ray *et al.* [350].

All investigations up until 2011 were conducted with state-of-the-art near-IR laser pulses at around 800 nm. As described earlier, shifting the driving wavelength to longer wavelength is beneficial when imaging molecules with LIED due to the granting of true quasi-static conditions and the ponderomotively up-scaled return energies with at the same time low ionization fraction. These conditions were exploited for the first time by Blaga *et al.* [39] in 2012 when they published LIED results on N_2 and O_2 probed with 1.7 μm-, 2.0 μm- and 2.3 μm-pulses. Not only could they accurately extract the bond length of N_2 and O_2 yet they could also resolve a 0.1 Å contraction of the $O_2{}^+$ bond 5 fs after ionization. Spatial resolutions of 0.05 Å and temporal resolutions of 5 fs were reported. This was the first time that the intrinsic temporal resolution of LIED was utilized to image molecular dynamics, in this case the vibration of the homonuclear molecular wave packet of O_2^+. Moreover this work, as others before, proved the validity of the QRS theory. For the sake of completeness, the same group published shortly after results on the DCS extraction of atomic targets with with 1.7 μm-, 2.0 μm- and 2.3 μm-pulses. Here, Xu *et al.* [351] could accurately resolve the atomic DCSs including their characteristic minima thereby agreeing with field-free DCS from CED experiments. They could achieve agreeing DCS as a function of return energies independent of laser parameters (intensity, pulse duration, wavelength) which verifies QRS theory.

The prove of concept by Blaga *et al.* [39] established the potential of LIED as a dynamical imaging technique with sub-Ångström spatial and few-femtosecond temporal resolutions. Hence, the next steps for experiments on LIED need to be the application of mid-IR LIED to image larger, polyatomic, hetero-nuclear molecules that offer many interesting dynamics like dissociation or isomerization. This set up the starting point of this part of the thesis to apply mid-IR LIED with 3 μm-pulses in combination with coincidence momentum detection in the ReMi.

6.3 Theoretical concepts

In this section, the two main theoretical concepts for LIED imaging, as employed by us, are explained: 1) The *QRS model* sets the foundation to be able to extract the *field-free* DCS from experimentally detection strong-field photo electron momentum distributions. 2) The *IAM* is standardly used to describe the coherent scattering of an electron wave packet with a certain impact momentum on all atomic scatters of a molecular systems. The resulting molecular DCSs models the diffraction image of a CED experiment. The IAM is also applied in comparison with LIED signals of molecular systems [39].

6.3.1 Quantitative re-scattering (QRS) theory

Nowadays, LIED experiments are almost unanimously based on the QRS model [110, 190, 191], which is particularly valid within the quasi-static regime since it is based on the semi-classical re-collision model [23]. According to the QRS theory, the photoelectron momentum distribution $D(k,\Theta)$[14] as a function of the final, detected momentum k and the final, detected scattering angle Θ is related to the elastic DCS $\sigma(k_r,\Theta_r)$ as a function of returning momentum k_r and re-scattering angle Θ_r by [190, 340, 352]

$$D(k,\Theta) = W(k_r)\,\sigma(k_r,\Theta_r) \quad , \tag{6.4}$$

where $W(k_r)$ is the returning electron wave packet (RWP). The elastic DCS $\sigma(k_r,\Theta_r)$ can be calculated by standard potential scattering theory (see e.g. [95]) where elastic scattering of an electron on a spherical potential $V(r)$ can be solved via the time-independent Schrödinger equation (TISE). A nice summary of this calculation is described by Chen *et al.* [110, Part II.D] resulting in the elastic DCS as the squared sum of scattering amplitudes

$$\sigma(k,\Theta) \;=\; \left| f_C(\Theta) \;+\; \widetilde{f}(\Theta) \right|^2 \quad , \tag{6.5}$$

where the scattering amplitudes f_C corresponds to a Coulomb potential V_C = -1 / r and $\widetilde{f}(\Theta)$ to a modeled short-range potential V_S (more information on the short-range potential is given in [110, Eq. 9] and [351, Eq. 2]).

The independence of the RWP $W(k_r,\Theta_r) = W(k_r)$ from the scattering angle Θ_r and hence the validity of the de-coupled extraction of the field-free DCS was carefully tested in [110]. Here, $W(k_r,\Theta_r) = D(k,\Theta) \,/\, \sigma(k_r,\Theta_r)$ was determined for different Θ_r and by calculating $D(k,\Theta)$ from TDSE and from SFA2[15] simulations. Both in agreement showed no dependence on Θ_r for various intensities, pulse durations and target systems.

The relation between the final, detected k and Θ with the returning k_r and Θ_r in $D(k,\Theta)$ can be resolved according to the re-collision model (as described in Sec. 2.2). This context was already explained in Sec. 2.2.2.3 in Fig. 2.6[16]. Here, the returning electron scatters from the target in the laser field at time t_r, it therefore gains an additional momentum shift $-A(t_r) \equiv -A_r$ from the laser. Hence the momenta are related as

$$k_{\parallel} = k\,\cos(\Theta) = -A_r \,\pm\, k_r\,\cos(\Theta_r) \quad , \tag{6.6}$$

$$k_{\perp} = k\,\sin(\Theta) = k_r\,\sin(\Theta_r) \quad , \tag{6.7}$$

where plus (minus) sign refers to electron returning back to the target along the positive (negative) polarization direction. Again, long trajectories are considered as they dominate over short trajectories due to the higher ionization probability.

[14] D is defined in polar coordinates of 2D momentum distribution $k_{\perp}$ over $k_{\parallel}$ also known as ($p_{\perp}$,$p_{\parallel}$) map.

[15] improved SFA

[16] The variables are expressed in atomic units here, so that $p_{resc} \equiv k$, $p_r \equiv k_r$ and $\Theta' \equiv \Theta$.

Thus one needs to calculate the momentum shift A_r, corresponding to any k_r for long trajectories according to the semi-classical re-collision model. Alternatively, one can use a phenomenological relationship $A_r = k_r / 1.26$ [110] which simplifies the DCS extraction process. This constant value has been derived by Chen *et al.* [110] from the fact that the ratio $k_r / |A_r|$ is relatively constant for long trajectories as plotted in Fig. 2.5 (d).

Equations 6.4 - 6.7 above were written for atomic targets. For molecules, these DCSs contain modulations that are directly linked to the geometrical arrangement of the constituent atoms. Hence, similar equations hold for fixed-in-space molecules. Taking into account that the returning wave packet is proportional to the angularly distributed ionization rate $N(\Omega_L)$ of a molecule, we can write

$$D(k, \Theta, \Omega_L) = W(k_r, \Omega_L)\, \sigma(k_r, \Theta_r, \Omega_L) \;=\; \widetilde{W}(k_r)\, N(\Omega_L)\, \sigma(k_r, \Theta_r, \Omega_L) \quad , \tag{6.8}$$

where Ω_L is the alignment angle of the molecule with respect to the laboratory frame. The observed photoelectron spectrum is obtained by the incoherent sum of the contributions from all molecules in the interaction region. Assuming that the molecular alignment distribution is described by $\rho(\Omega_L)$, the total signal folded with the ionization and alignment distribution can be written as

$$\bar{D}(k, \Theta) \;\propto\; \widetilde{W}(k_r) \int d\Omega_L \; [\rho((\Omega_L)\, N(\Omega_L)\, \sigma(k_r, \Theta_r, \Omega_L)] \quad . \tag{6.9}$$

It is clear that Eq. 6.9 together with Eqs. 6.4 - 6.7 allow us to relate the observed photoelectron momentum spectrum with DCSs weighted by ionization rates and the alignment distribution

$$\frac{\bar{D}(k, \Theta)}{\widetilde{W}(k_r)} \;\propto\; \int d\Omega_L \; [\rho(\Omega_L)\, N(\Omega_L)\, \sigma(k_r, \Theta_r, \Omega_L)] \;\equiv\; \sigma_{tot}(k_r, \Theta_r) \quad . \tag{6.10}$$

In other words, a weighted DCS $\sigma_{tot}(k_r, \Theta_r)$ can be measured in LIED experiments up to an overall scaling factor. The validity of the QRS theory and hence on Eq. 6.4 was shown in experimental investigations of both atomic [343, 344, 350, 351, 353] and molecular [39, 345, 348, 349] targets.

6.3.2 Independent atom model (IAM)

In this thesis, we use the independent-atom model (IAM) [354] to calculate elastic *molecular* DCSs acquired in LIED experiments [324]. This approach has been found adequate for relatively large scattering angles ($\Theta_r \gtrsim 40°$) [324] and electron energies $E_r \gtrsim 50$ eV [324, 326]. Within the IAM, the DCS corresponding to an electron incident on various atomic scatterers can be expressed as

$$\sigma(k_r, \Theta_r, \Omega_L) = \sum_{i,j} f_i\, f_j^*\, e^{i\, \vec{q}\, \vec{R}_{i,j}} \quad , \tag{6.11}$$

where Ω_L is again the alignment angle of the molecule with respect to the laboratory frame, $f_i \equiv f_i(k_r, \Theta_r)$ is the scattering amplitude from the i-th atom in the

molecule, $\vec{R}_{i,j} = \vec{R}_i - \vec{R}_j$ the vectorial interatomic distance and $\vec{q} = \vec{k} - \vec{k}_r$ the momentum transfer vector (as defined in Eq. 6.2). Combining Eq. 6.10 with Eq. 6.11, the weighted DCS can be approximated as

$$\sigma_{tot}(k_r, \Theta_r) = \sum_i |f_i|^2 \int d\Omega_L \, [\rho(\Omega_L) \, N(\Omega_L)] + \sum_{i \neq j} f_i \, f_j^* \int d\Omega_L \, \left[\rho(\Omega_L) \, N(\Omega_L) \, e^{i \, \vec{q} \, \vec{R}_{i,j}}\right] \quad . \tag{6.12}$$

This equation is merely a straightforward extension of Eq. 6.11 by Xu *et al.* [324] for the case of aligned molecules. Following [324], a molecular contrast factor (MCF) is defined as the ratio of the *coherent molecular interference term* (the second term of Eq. 6.12) and the *incoherent atomic term* σ_{atom} (the first term of Eq. 6.12)

$$MCF(k_r, \Theta_r) \equiv \frac{\sigma_{tot} - \sigma_{atom}}{\sigma_{atom}} = \frac{\sum_{i \neq j} f_i \, f_j^* \int d\Omega_L \, \left[\rho(\Omega_L) \, N(\Omega_L) \, e^{i \, \vec{q} \, \vec{R}_{i,j}}\right]}{\sum_i |f_i|^2 \int d\Omega_L \, [\rho(\Omega_L) \, N(\Omega_L)]} \quad . \tag{6.13}$$

For electrons scattering from a randomly distributed, so a non-aligned set of molecules, the weighted DCS of Eq. 6.12 is averaged over the alignment angle Ω_L resulting in [324]

$$\langle \sigma_{tot} \rangle \, (k_r, \Theta_r) = \sigma_{atom} + \sum_{i \neq j} f_i \, f_j^* \, \frac{\sin(q \, R_{i,j})}{q \, R_{i,j}} \quad , \tag{6.14}$$

where q is the magnitude of the momentum transfer as defined in Eq. 6.3 and $R_{i,j}$ the magnitude of the interatomic separations. The molecular contrast factor can hence be written as [351]

$$MCF(k_r, \Theta_r) = \frac{1}{\sigma_{atom}} \sum_{i \neq j} f_i \, f_j^* \, \frac{\sin(q \, R_{i,j})}{q \, R_{i,j}} \quad . \tag{6.15}$$

It should be stressed here that the molecular interference term does not vanish after averaging over Ω_L which was originally pointed out by Fano and Cohen in 1966 [324, 355]. Therefore, the diffraction signal of electrons scattering upon isotropically distributed molecules depends only on the magnitude of the interatomic separations $R_{i,j}$.

Since the experimental DCS can be measured up to an overall factor for a fixed scattering energy, the experimental MCF can be defined as

$$MCF_{exp}(k_r, \Theta_r) = \frac{\sigma_{exp,tot} - \sigma_{atom}}{\sigma_{atom}} = \frac{\beta \, \sigma_{exp} - \sigma_{atom}}{\sigma_{atom}} \tag{6.16}$$

where β can be found by best fit to the theoretical MCF and σ_{exp} is the experimentally measured molecular DCS.

6.4 Calibration experiment of mid-IR LIED on Xenon atoms

The capacity of LIED to accurately extract field-free DCSs is investigated by applying a QRS analysis on the 3D momentum spectrum of the SFI of xenon atoms interacting with mid-IR pulses from our OPCPA system. Conducting LIED with mid-IR fields avails of the mentioned benefits that result in core penetrating electron-ion collisions at high momentum transfer. On the detection side, the coincidence capability of the ReMi adds to the signal-to-noise of the DCSs of the electron-Xe^+ scattering process. The applicability of our combination of experimental tools to LIED investigations is tested on the atomic system of xenon since atomic scatterers offer well studied DCSs at low scattering energies that are rich in structure [356, 357] which serves as calibration of our experimental system.

6.4.1 Experimental parameters and detection

In this experiment, we used mid-IR pulses with 70 fs (FWHM) duration at an intensity of $I \approx 5.5 \times 10^{13}$ W/cm^2 resulting in a ponderomotive energy of the detached electrons of roughly $U_\mathrm{P} \approx 50$ eV ($\gamma \approx 0.35$, $z \sim 125$, $z_1 \sim 8.2$, $z_\mathrm{f} \sim 2.0 \times 10^{-4}$; in agreement with the tunneling conditions according to Reiss as described in Sec. 2.1.3). As described in Sec. 3.1.3, the peak intensity can be determined by various indirect methods when - like in our case - the focal waist is not directly measurable. The above value is determined by fitting the corresponding ADK rate (see Eq. 2.20) to the longitudinal momentum distribution of Xe ions or its coinciding electrons. Due to the uncertainty of the intensity estimation, an intensity calibration was established within this thesis (see Sec. 3.1.3) containing all intensity measurements of experiments performed within this thesis that were aligned in a similar manner. From a linear regression through all data, we can extract an intensity value of $(6.1 \pm 20\%) \times 10^{13}$ W/cm^2 ($U_\mathrm{P} \approx 55$ eV, $\gamma \approx 0.33$, $z \sim 138$, $z_1 \sim 9.1$, $z_\mathrm{f} \sim 2.2 \times 10^{-4}$) when using the the measured power $P = 625$ mW and pulse duration $\tau = 70$ fs in Eq. 3.10.

In order to detect the entire 3D momentum spectrum of the emitted and re-scattered electrons which can acquire final kinetic energies of up to $E_\mathrm{kin} \leq E_\mathrm{resc,max} \approx 10\,U_\mathrm{P} \approx 500$ eV, high static electric and magnetic fields need to be applied operating the ReMi. More specifically, to achieve full 4π solid angular detection of electrons with at least $E_\mathrm{kin} = 500$ eV a potential difference of $|\Delta U_\mathrm{min}| = 500$ V between the focal region and the detector needs to be applied to overcome the the respective momentum away from the detector along the spectrometer axis $\vec{e}_\mathrm{z}$. The respective transverse momentum components in this case are caught with a magnetic field $\mathcal{B}_\mathrm{z} \approx 40$ Gs (see Eq. 3.42 for transverse energy acceptance).

As mentioned in the chapter explaining the experimental setup (see Sec. 3.2.3.2), the trade-off in order to acquire high electron energies at 4π solid angle acceptance with up-scaled static fields of the ReMi is a decreased momentum resolution.

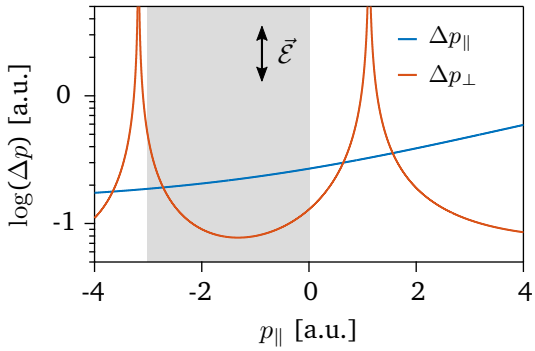

Figure 6.5: Electron momentum resolutions for high static fields. The momentum resolution for electrons detected with higher static fields of the ReMi being $|\mathcal{E}| \approx 50\,\mathrm{V/cm}^2$ and $|\mathcal{B}| \approx 3.8\,\mathrm{mT}$ as a function of p_z. In order to detect "node-free" electron momentum resolutions, the laser polarization is chosen to be vertical in the reaction chamber, so parallel with respect to $\vec{e}_y$ and perpendicular to $\vec{e}_z$.

In Fig. 6.5 the estimated momentum resolutions are plotted for our experimental conditions $|\mathcal{E}| \approx 50\,\mathrm{V/cm}^2$ and $|\mathcal{B}| \approx 38\,\mathrm{Gs}$. For the extraction of DCSs from the electron momentum distribution ideally over the full angular scattering range, the experimental parameters of both the laser and the ReMi can be deliberately chosen to position the 3D momentum distribution optimally away from the magnetic field "nodes" that are characteristic of a ReMi and can distort the data. On the one hand, the polarization of our mid-IR pulses can be chosen in vertical direction (along the $\vec{e}_y$ axis parallel to the gas jet) to prevent magnetic field "nodes" perpendicular to the $\vec{e}_z$ axis from crossing through the full momentum distribution. On the other hand, the static fields can be fine-tuned around the previously estimated values to steer at least one half space of the full distribution between two magnetic field "nodes" detecting it effectively "node-free". The possible area of interest for our resulting momentum distribution is highlighted in Fig. 6.5 in gray. Note that there are various experimental parameter combinations (different static fields, chamber geometry, etc.) that could technically carve out a wide as possible "node-free" momentum distribution while detecting large electron momenta.

In the data analysis, all electrons were selected that correspond to Xe^+_{132} cations[17], so that *false* electrons corresponding to multiple ionization and background events are ignored. We consider in our analysis all those events in which a Xe^+_{132} ion is detected for one laser pulse, and extract the corresponding electron that reaches the detector for the same laser pulse without putting the momentum conservation constraint on the coincidence. Hence, the full-2-particle momentum conservation constraint is loosened for the benefit of extracting slightly higher statistics in overall detected events. This analysis procedure is commonly used for the detection of processes with lower cross-sections (see e.g. [203, Ch. 6.2 & 7.4]) and in ex-

[17] We chose the isotope Xe^+_{132} since it is the most probable of all Xe isotopes, hence results in the highest amount of events.

periments where the rate of false coincidences is generally kept at low level in the experiment, i.e. ion count rate significantly lower than the repetition rate to assure less than one SFI event per pulse. As shown in Sec. 3.2.2.3, this leads to more statistics while still ensuring the elimination of electron background of other ionization and background channels.

In Fig. 6.6 (a), the resulting 3D electron momentum distribution is plotted corresponding to the half space indicated in gray in Fig. 6.5. The data span a six orders of magnitude dynamic range (logarithmic color scale) and extend along the polarization axis $\vec{e}_y$ up to $p_y = p_\parallel \approx \pm$(6 to 6.3) a.u. in longitudinal momentum corresponding to about $E_{kin} \approx$ (490 to 540) eV. In the perpendicular directions the data extend up to around $p_x \approx \pm$(3 to 3.5) a.u. (in the propagation direction of the laser) and up to around $p_z \approx$ -3 a.u. which is limited by the node. In order to make use of the azimuthal symmetry of the data around the polarization axis, the momentum vectors are converted to cylindrical coordinates, then integrated over the azimuthal angle ϕ before applying solid-angle correction with the appropriate Jacobian $J_{cyl./Cart.} = 1/p_\perp$. This leads to a 2D momentum map representation of the detected 3D momentum distribution plotted in Fig. 6.6 (b) which basically resembles a "cut" through the 3D distribution along the polarization axis containing all re-scattering planes of electrons detected with a momentum $p = \sqrt{p_\parallel^2 + p_\perp^2}$ at an angle Θ. It is from this data representation that we extract the DCSs.

6.4.2 Extraction of differential cross-sections (DCSs)

It is clear from Fig. 6.6 (b) that the momentum distribution shows a rich structure with a number of features being visible, especially the lobes near $|p_\parallel| = 3.5$ a.u. and $|p_\perp| = 2.5$ a.u. The extraction of DCSs from experimentally measured electron momentum distributions is based upon the QRS theory outlined above. The angularly resolved DCSs are obtained by sweeping the scattering angle Θ_r around the circumference of a circle with radius p_r ($= k_r$ in atomic units) that has been shifted in the laser polarization direction ($\vec{e}_y$) by the vector potential at the time of re-scattering A_r. After finding the appropriate values of k_r and A_r via the re-scattering model, obtaining the DCS corresponds to counting the number of electrons found at each scattering angle Θ_r [110]. Accurate results of the DCSs are achieved with a satisfactory signal-to-noise level which can be reached by choosing an adequate integration window for $k_r \pm \Delta k_r$ and $\Theta_r \pm \Delta\Theta_r$. Here we chose values of $\Delta k_r = 0.05\,k_r$ to $0.15\,k_r$ and $\Delta\Theta_r = 2°$ to $4°$ depending on the detected statistics. The momentum ranges are on the order of the momentum resolution $\Delta k_r \approx \partial k$ achieved with the herein chosen static fields of the ReMi (see Fig. 6.5)[18]. The error of the DCS depends on the electron counts N_i within each integration box and are deduced from Poissonian statistics, i.e. $\Delta N_i = \sqrt{N_i}$.

[18] Obviously, the momentum error distribution is complex since every position/bin within the momentum distribution has a different error (see Sec. 3.2.3.2). By testing the positions on the DCS circles closest to the magnetic field node, i.e. for $\Theta_r = 90°$, the momentum error compared to $p_r \approx 3$ a.u. (i.e. $E_r \approx 2.5\,U_P$) is about 16.9 % while for $p_r \approx 1.9$ a.u. (i.e. $E_r \approx 1\,U_P$) it is around 14.2 %. Hence, an integration range of up to $\Delta k_r \approx 15$ % seems appropriate.

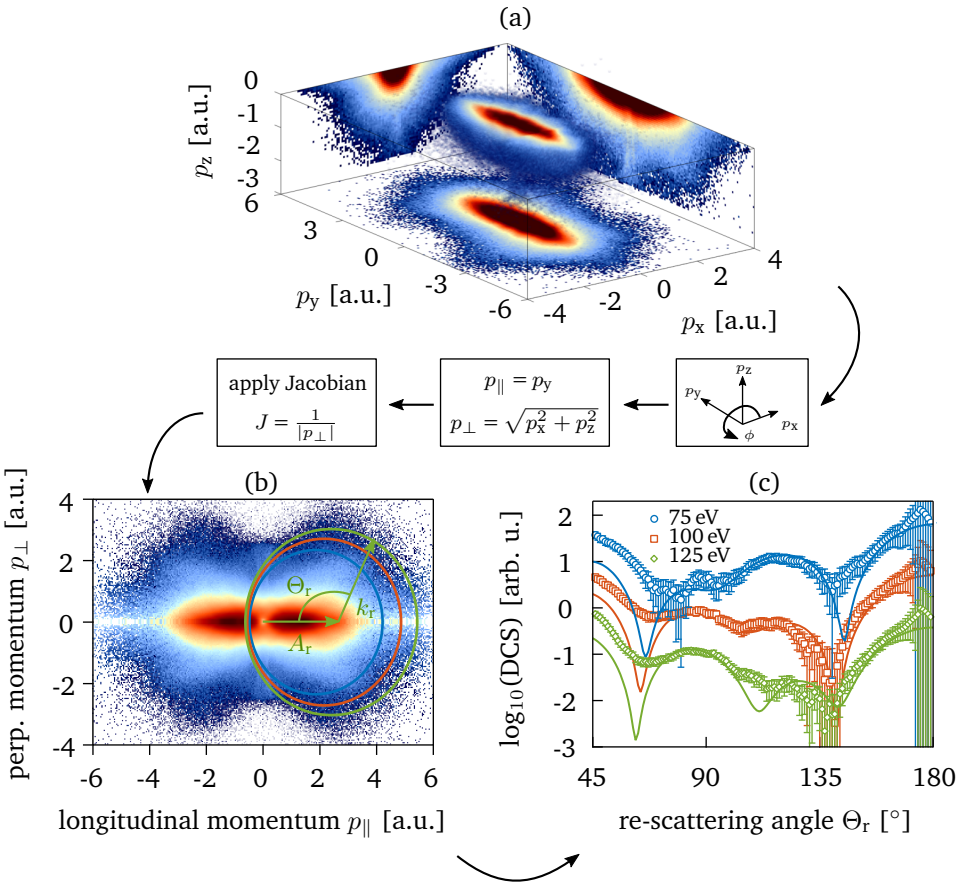

Figure 6.6: Extraction of elastic DCSs of electrons re-scattering off Xe atoms with mid-IR LIED. (a) Xe_{132} isotopes are ionized with mid-IR pulses at an intensity of $I \approx 6.0 \times 10^{13}$ W/cm^2 and pulse durations of ∼70 fs. The 3D electron momentum distribution is detected in coincidence with the respective Xe ions. **(b)** To exploit the azimuthal symmetry of the data around the polarization axis, the data are converted into cylindrical coordinates, then integrated around the azimuthal angle ϕ before the the solid-angle correction appropriate Jacobian is applied. This leads to a 2D representation of the momentum distribution as comparable to QRS theory. **(c)** The DCSs are found by tracing along the circumference of a circle with radius k_r (corresponding to the electron's return momentum) that has been shifted by the vector potential A_r at the time of re-scattering. Accurate DCSs are plotted for return energies of 75 eV (blue circles), 100 eV (red squares), and 125 eV (green triangles) as a function of re-scattering angle Θ_r. The solid lines are taken from the NIST database [358].

This extraction procedure is exemplarily applied for electron return energies of 75 eV (blue circles), 100 eV (red squares) and 125 eV (green triangles) and the respective DCSs are presented in Fig. 6.6 (c). As each returning electron of different p_r encounters a slightly different vector potential A_r, the re-scattering circles are shifted by differing amounts. For enhanced visualization of the traces, the DCS data of 75 eV (blue circles) and 125 eV (green triangles) have been scaled by factors of 10^1 and 10^{-1} compared to the 100 eV (red circles) data, respectively. As the error bars are derived from Poissonian statistics, the large error bars at $\Theta_r \approx 180°$ are due to the application of the Jacobian ($J_{180°} \to 0$) mentioned above. Also presented in Fig. 6.6 (c) are the Xe DCSs provided by NIST [358], which have been scaled to overlap with the experimental data. Our data are able to accurately resolve most of the predicted rich structure for $\Theta_r \geq 60°$. For these angles the local extrema as well as slope changes are generally well reproduced while for smaller scattering angles ($\Theta_r < 60°$) the data are "contaminated" through background arising from direct electrons. While these direct electrons cause a slight mismatch between the experimental and theoretical data, the local minima between Θ_r = (50 to 60)° are still resolvable. Overall, we observe an excellent match between our measured data and the theoretical expectations. Since the QRS model can only extract the DCSs up to a scaling factor, each extracted DCS has been normalized. Notably, the experimental scaling factor is the same for all curves in Fig. 6.6 (c).

6.4.3 Doubly differential cross-section compared to NIST data

Our accumulated data of mid-IR SFI events of Xe atoms contain DCSs as a function of *both* scattering angle $\Theta_\mathbf{r}$ as well as return momentum k_r / energy E_r. This *doubly differential cross-section* (DDCS) $\partial^2\sigma/(\partial E_r\,\partial\Theta_r)$ for our experiment is investigated in more detail in the following. A distribution of the extracted DDCS can be constructed by performing the extraction procedure from above for a finer range of return energies. In Figs. 6.7 (a,b) the theoretical [358] and experimental results for the return energy range between 50 eV and 150 eV in 1 eV steps and scattering angle range between 45° and 180° in 1° steps are presented. The color scale is logarithmic and in this case covers one and a half orders of magnitude dynamic range. The agreement is excellent with the main features being resolvable over most of the parameter space between theory (a) and experiment (b). The largest disagreement occurs for electrons roughly near $\Theta_r \lesssim 60°$ for $E_r \lesssim 65$ eV where the minimum is not resolved indicated by the black dotted curve in Figs. 6.7 (a,b). As mentioned before, this can be caused partially by the background of direct electrons. Yet, the onset of these background electrons still allows to resolve the general trend at least for return energies above $E_r > 65$ eV. For lower energies, it turns out that the mismatch is due to an experimental artifact that might have resulted from false coincidences in data analysis. This artifact was removed in subsequent experiments investigating different targets by reducing the overall ionization / event rate with lower gas pressures. Achieving agreement for $\Theta_r < 40°$ seems to be difficult in general with LIED due to stronger influence of the direct electrons. An interesting fact was stated by Xu *et al.* [351] mentioning that the angular distribution of

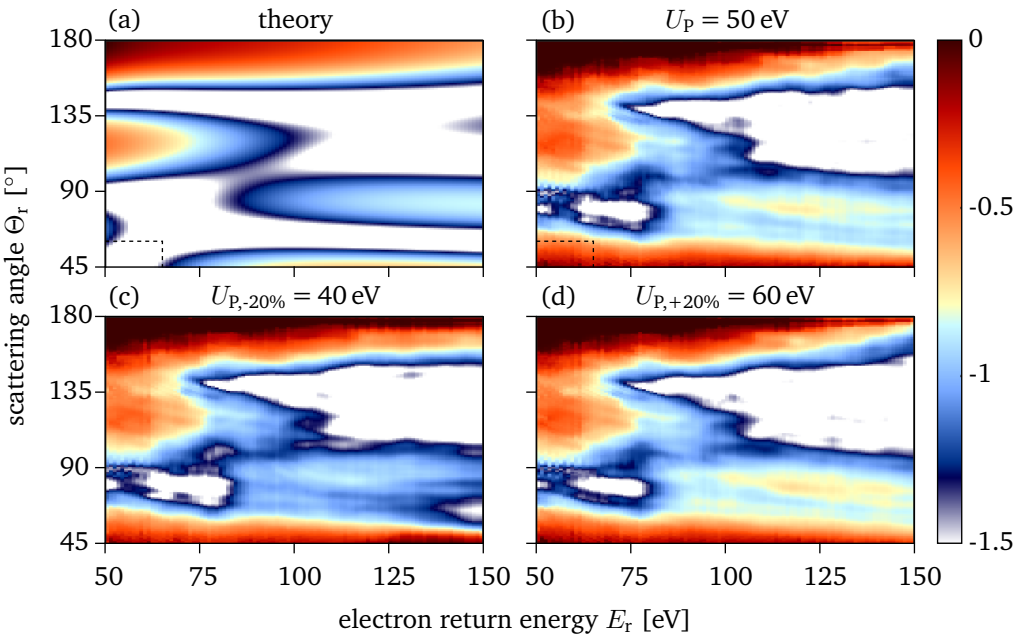

Figure 6.7: Doubly differential cross-section of mid-IR LIED on Xe atoms. **(a,b)** The **(a)** theoretical [358] and **(b)** experimental *doubly differential cross-section* (DDCS) $\partial^2\sigma/(\partial E_r\,\partial\Theta_r)$ for the 1 eV energy and 1° angular steps are presented. The color scale is logarithmic and in this case covers one and a half orders of magnitude dynamic range. Though the overall agreement is quite striking, the area towards $\Theta_r \lesssim 60°$ for $E_r \lesssim 65$ eV disagrees where a minimum is not resolved indicated by the black dotted curve. This is connected to false coincidences in the analysis which have been removed in subsequent experiments by lowering the gas pressures. **(c,d)** The DDCS distributions are extracted for **(c)** U_P =40 eV and **(d)** U_P =60 eV according to intensity changes of ±20 %. The variations result in similar results showing the intensity insensitivity.

direct electrons along the polarization axis is "squeezed" for longer wavelength. That means that "non-contaminated" DCS could be extracted down to an angle of $\Theta_r \approx 30°$ which they show for LIED with 2 μm pulses on argon atoms [351] (yet it differs for krypton and xenon atoms).

These results serve as a "calibration check" for our approach to perform LIED imaging experiments and prove a few points: 1) the mid-IR LIED measurements can be accurately performed with our experimental setup combining a 3 μm OPCPA source with a ReMi, 2) the validity of the QRS theory meaning that field-free DCSs can be extracted with mid-IR LIED over a wide range of return energies and re-scattering angles at high accuracy, 3) scattering energies of 50 eV and higher are suitable to image a target's nucleus where its long-range Coulomb potential has no influence on the electron wave packet [351], and (4) the momentum resolutions of the ReMi achieved with higher static fields (needed for the detectability of high electron

energies) are still on the order to not wash out the diffraction signal.

6.4.4 Intensity insensitivity of DCS extraction via QRS theory

The QRS theory permits the field-free extraction of DCSs from the momentum distribution of re-scattered electrons as described in Sec. 6.3.1 and investigated in Chen *et al.* [110]. This includes the fact that the DCS extraction is insensitive to the peak intensity I_{peak} of the strong ionizing field. The context is demonstrated in Figs. 6.7 (c,d) where the experimental DDCS distributions are plotted assuming the ponderomotive energies of $U_\text{P} = 40\,\text{eV}$ and $U_\text{P} = 60\,\text{eV}$, respectively. The logarithmic color scales are kept constant in all Figs. 6.7. These values correspond to the uncertainty extremes of $\pm 20\%$ of our intensity estimate being $I_{\text{peak}} = (6 \pm 1.5) \times 10^{13}\,\text{W/cm}^2$ (corresponding to $U_\text{P} \sim 50\,\text{eV}$). Note that for the $U_\text{P} = 40\,\text{eV}$ case, the return times and therefore the momentum shift A_r are assumed to be the same for all electrons with energies $E_\text{r} \geq 127\,\text{eV}$ (maximum of $3.17 \times 40\,\text{eV}$). Both resulting distributions are extremely similar with all features still visible in both cases as well as compared to the $U_\text{P} = 50\,\text{eV}$ case and the NIST data up to slight differences in relative amplitudes. Interestingly, the "island" around $\Theta_\text{r} = 90°$ for $E_\text{r} > 75\,\text{eV}$ seems to agree best with theory for $U_\text{P} = 40\,\text{eV}$.

To put it in a simpler context, the scattering event on the atomic or molecular target by an electron wave packet at a certain kinetic energy proceeds independently of the laser field amplitude that accelerated the electron to that specific kinetic energy. Yet, this is only half of the story since electrons that are tunnel-emitted by differently intense laser fields but re-scatter with the same kinetic energy attribute different emission and return times. Hence, they acquire different streaking "kicks" by the laser fields at their respective points of return. The influence of this correlation is visualized in Figs. 6.8 (a,b). Here, the resulting circles are plotted for electrons returning at $E_\text{r} = 50\,\text{eV}$ yet accelerated by laser pulses with different intensities $I_{\text{-20\%}} = 4.8 \times 10^{13}\,\text{W/cm}^2$ (red solid line), I_{peak} (black solid line) and $I_{\text{+20\%}} = 7.2 \times 10^{13}\,\text{W/cm}^2$ (green solid line). In the $I_{\text{-20\%}}$ case, 50 eV resemble a $E_\text{r} \approx 1.19\,U_\text{P}$, and in the $I_{\text{+20\%}}$ case $E_\text{r} \approx 0.79\,U_\text{P}$. The dashed lines show the respective integration ranges of $\Delta k_\text{r} = 0.15\,k_\text{r}$. The differences between the respective integration fractions are marginal ($\sim \pm 1.5\,\%$) as highlighted in Fig. 6.8 (b) and do not influence the extraction of the field-free DCS as demonstrated in Fig. 6.7.

6.4.5 Dominance of long trajectories in LIED

Electrons returning on long trajectories exit with a higher probability than their short counterparts due the fact that they tunneled closer to the respective electric field maximum. This context was discussed in Sec. 2.2.1 and demonstrated Fig. 2.5 (c,left), where the ratio of the ionization rates of long and short trajectories $\frac{\Gamma_{\text{long}}}{\Gamma_{\text{short}}}$ is plotted as a function of return energy.

The context can be tested on the basis of the present data set. In Fig. 6.8 (a) the "re-scattering circles" corresponding to electrons returning with an energy of

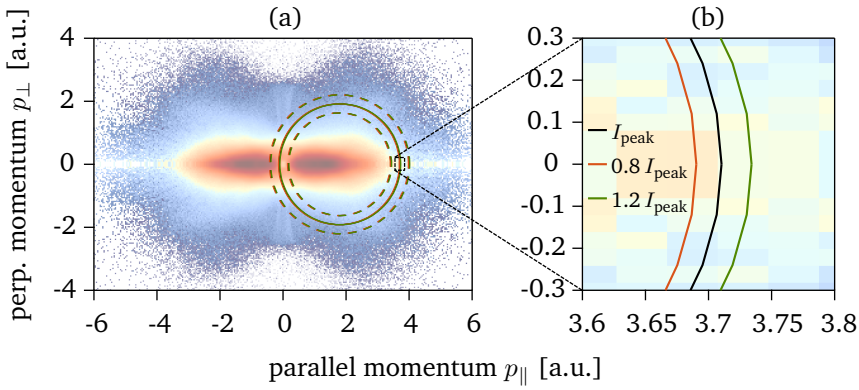

Figure 6.8: Demonstration of intensity insensitivity in LIED. (a) Our experimental electron momentum distribution of SFI of Xe atoms is re-plotted in the background (with 50 % opacity). In the foreground, the "re-scattering circles" are plotted (in the right quadrant) for electrons re-turning with $E_r = 50$ eV when accelerated by laser fields at $I_{-25\%} = 0.8\, I_{\text{peak}}$ (red solid line), $I_{\text{peak}} \sim 6 \times 10^{13}$ W/cm^2 (black solid line) and $I_{+25\%} = 1.2\, I_{\text{peak}}$ (green solid line). The dashed lines show the respective integration ranges $\Delta k_r = 0.15\, k_r$. **(b)** A fraction of the distribution of (a) is shown highlighting the three individual and closely separated circles for three different intensities.

$E_r = 0.5\, U_P$ (25 eV here), $1.0\, U_P$ (50 eV), $1.5\, U_P$ (75 eV), $2.0\, U_P$ (100 eV), $2.5\, U_P$ (125 eV), $3.0\, U_P$ (150 eV) and $3.17\, U_P$ (158.5 eV) are plotted for electrons that would "travel" on long (red) or short (green) trajectories. Since they scatter from the parent ion at different times the circles are shifted by different amounts of the resulting vector potential A_r by the laser field. The DCSs extracted from long and short trajectories are presented in Figs. 6.8 (b,c), respectively. As shown before, the long trajectory DDCS [similar to Fig. 6.7 (b)], shows agreement with the corresponding theoretical data from the NIST database [358] (see Fig. 6.7 (a)) over the entire range of Θ_r and E_r. On the other hand, the short trajectory DDCS clearly deviates from both the long trajectory DDCSs and the theoretical counterpart. In detail, the local minima around $E_r = 60$ eV to 80 eV and $\Theta_r = 65°$ to 100° as expected in the theoretical trace [see Fig. 6.7 (a)] are covered by a local maximum in the case of short trajectories while the local maxima around $E_r = 75$ eV to 150 eV and $\Theta_r = 80°$ to 100° are not existing. Moreover, the maxima around $E_r = 50$ eV to 100 eV and $\Theta_r = 90°$ to 135° are not mapped at all while new maxima around $E_r = 75$ eV to 125 eV and $\Theta_r = 130°$ to 150° develop. Overall, this lack of agreement of the short trajectory DDCS shows that such trajectories do not contribute significantly enough to the momentum distribution including the diffraction signal, thus confirming the related discussion above.

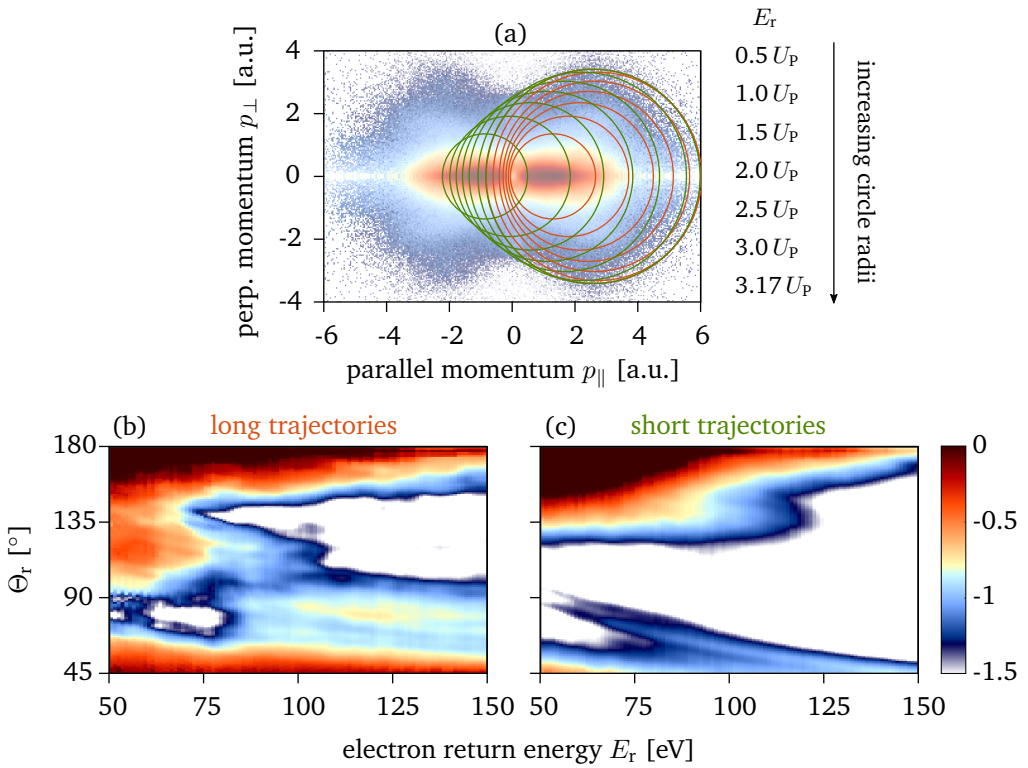

Figure 6.9: Demonstration of dominance of long trajectories in LIED. (a) Our experimental electron momentum distribution of SFI of Xe atoms is again re-plotted in the background (with 50 % opacity). In the foreground, the resulting "re-scattering circles" represent re-scattering of 0.5 U_P, 1.0 U_P, 1.5 U_P, 2.0 U_P, 2.5 U_P, 3.0 U_P and 3.17 U_P electrons returning on short (green) and long (red) trajectories. **(b)** The extracted DDCS corresponding to the long trajectories from (a) are plotted and compared with **(c)** the short trajectory counter-part. The disagreement between (b) and (c) and the beforehand shown agreement between long trajectories with theoretical data [see Figs. 6.7 (a,b)] prove the dominance of long trajectories in LIED.

6.5 Extraction of multiple bond lengths of aligned acetylene

The results presented in the previous Sec. 6.4 demonstrate that LIED driven by mid-IR radiation can be used to extract accurate field-free DCSs from gas-phase atomic targets. The ultimate goal of LIED is to investigate structural dynamics so the next logical step is to apply LIED to molecular targets. In this section, the results of its application to the polyatomic molecule acetylene C_2H_2 are presented with particular attention being paid to whether its molecular geometry can be imaged.

6.5.1 Challenges of imaging polyatomic, hetero-nuclear molecules via LIED

To harness the combined temporal and spatial resolutions of LIED and applying it to polyatomic molecules, i.e. systems with three or more atoms[19] that exhibit full prototypical molecular dynamics, requires addressing a decisive and unresolved issue, namely the fact that launching the re-collision (imaging) electron possibly initiates molecular distortion and eventually fragmentation. Therefore, a certain portion of the detected electrons present an unwanted background that can make imaging difficult or even impossible. This problem can be resolved through ion-electron coincidence detection and the retrieval of the doubly differential cross section. This ensures unambiguous imaging of the molecular structure, or fragments, of interest. In addition to this major concern, there are other experimental obstacles that must be overcome: 1) complex molecules commonly have ionization energies I_P lower than atomic systems i.e. around and below 10 eV, which necessitates the use of mid-IR driving lasers in order to avoid ionization saturation as described earlier. At the same time mid-IR sources offer the added benefit that electrons with the required high return energies are liberated at lower intensities. 2) Since each constituent atom has a unique scattering cross section, a careful selection of the electron scattering parameters namely the angular range can enhance the relative contribution of all single atomic scatterers and hence facilitates the simultaneous determination of multiple bond lengths as discussed in Fig.6.2.1. 3) In order to resolve the increased structural complexity, it is highly beneficial for the gas ensemble to be anisotropically distributed with respect to the molecular axis in order to remove averaging effects [25, 324]. Our combination of experimental tools brings the capabilities to overcome all four beforehand mentioned challenges.

6.5.2 Acetylene C_2H_2 as molecular target

To validate our experimental approach to apply mid-IR LIED on a polyatomic molecular target, we intend to simultaneously image the C-C and C-H bond sep-

[19] A molecule is a stable system that contains by definition at least two atoms. Hence, a molecule with three or more atoms is considered polyatomic.

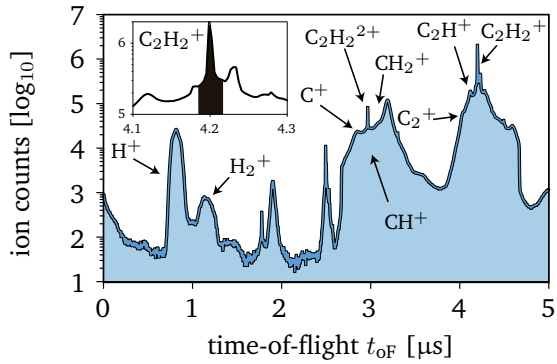

Figure 6.10: Time-of-Flight distribution of acetylene interacting with 3 µm pulses. The measured ion ToF spectrum after ionization of C_2H_2 using 70 fs, 3.1 µm laser pulses with an intensity of around 6.0×10^{13} W/cm^2 (according to an ADK fit on the longitudinal electron distribution; a full intensity determination is described in Sec. 6.5.4). The inset shows the ToF region around the peak corresponding to $C_2H_2{}^+$.

arations of aligned polyatomic molecule acetylene C_2H_2. We chose acetylene as the test molecule since it is 1) hetero-nuclear including the lightest atom hydrogen that features small small scattering amplitudes (see Fig. 6.3), 2) readily alignable via e.g. impulsive molecular alignment (e.g. in [359]), 3) linear and symmetric so that orientation is not required, and 4) its bond lengths are accurately known and calculated in various theoretical simulations for most of the primary ionization and excitation states (see e.g. [360–365]. More importantly, acetylene as the smallest organic molecule is a prototype to study molecular dynamics such as isomerization or proton migration [27], dissociation [366] and internal vibrational redistribution of energy and conical intersections [367] that could be studied using LIED.

The multitude of dissociating reactions of acetylene is shown in the ToF spectrum extracted from the experimental of the measurement described within this Sec. 6.5. The main peak of the ToF distribution with the highest ionization probability belongs to the cation $C_2H_2{}^+$ (ground-state) showing the maximum of counts at around 4.2 µs. The dication $C_2H_2{}^{++}$ (ground-state) sits around 3.0 µs. The three main two-body dissociation reactions of acetylene are [361]

1. *deprotonation*: $C_2H_2{}^{++} \rightarrow H^+ + C_2H^+$
2. *symmetric breakup*: $C_2H_2{}^{++} \rightarrow CH^+ + CH^+$
3. *isomerization*: $C_2H_2{}^{++} \rightarrow C^+ + CH_2{}^+$

with the individual branching ratios being 1) 57 %, 2) 38 % and 3) 3 % according to [361] or 1) 71 %, 2) 25 % and 3) 4 % according to [366][20]. All reaction products can be found in our ToF distribution in Fig. 6.10 and their respective peaks are

[20]The branching ratios can vary depending on the population process (single photon, multi-photon, resonant, non-resonant, or tunneling). Also different theoretical models give different results due to model differences.

indicated. Other three- and four-body reactions also exist in the spectrum at lower probabilities.

6.5.3 Impulsive molecular alignment of C_2H_2

The electron diffraction signal of aligned molecules results to have a higher signal-to-noise ratio than of isotropically distributed molecular targets [25] which results in a better spatial resolution when extracting structural information. Moreover, aligned-in-space molecules allow for a systematic study of structural behavior in different orientation configuration where the molecular wave packet can emerge differently [324] (depending on the target). Therefore, we prepared the gas-phase acetylene target in different aligned states via impulsive (non-adiabatic) molecular alignment (see Sec. 2.3.4).

In our case, we use the 98 fs, 1.7 μm output arm (signal) of the OPCPA source at $I_{1.7\mu m} = 2.0 \times 10^{13}$ W/cm^2 to impulsively align the C_2H_2 molecules by focusing the laser pulses into the supersonically expanded gas jet, which has an estimated rotational temperature of 90 K, thereby overlapping it spatially with the focus of the 3.1 μm pulses. The polarization directions of both the pump and probe radiation were kept parallel preserving the cylindrical symmetry. As the 1.7 μm pulse leaves the interaction region, the molecules periodically align along the polarization axis of the laser fields or anti-align, perpendicular to the polarization axis, at intervals that are governed by the rotational constant of the molecule [158]. We measure the degree of alignment by monitoring the ion yield as a function of the delay between the alignment pulse and the intense 3.1 μm ionizing pulse. Fig. 6.11 (a) shows the experimental results of this delay scan (black dots). This experimental trace is normalized to the level of ions triggered by only the 3.1 μm probe pulse (with the 1.7 μm output arm blocked). At time zero, so when both pulses overlap both in space and time, an ionization enhancement to about a factor of 2.1 of the normal level is reached. For increasing delays, the half-revivals at 6.8 ps and 7.1 ps for anti-alignment and alignment can be observed, respectively, as well as the full-revivals at time delays of 14.05 ps and 14.40 ps, respectively. The temporal positions of the full revivals agree nicely with literature [359, 368], while the half revivals are -0.2 ps off.

To verify our trace in more detail, we simulated the molecular alignment distribution. The simulation was performed by our collaborator A.-T. Le of the group of C. D. Lin of the Kansas State University. Here, the TDSE for the molecule in the pump laser pulse was solved while treating it as a rigid rotor [158] with a rotational constant of $B = 1.177\,\text{cm}^{-1}$ [369], polarizability of $\alpha_{\parallel} = 31.634$ a.u., and $\alpha_{\perp} = 19.445$ a.u. The polarizability was obtained from calculations using *ab initio* quantum chemistry GAUSSIAN code [370] (see below). The polarizability anisotropy is $\Delta\alpha = \alpha_{\parallel} - \alpha_{\perp} = 12.189$ a.u., which is quite close to the value of $\Delta\alpha = 1.74\,\text{Å}^3$ (11.74 a.u.) [371]. A Boltzmann distribution of the rotational levels was assumed at the initial time. Due to nuclear spin statistics, the ratio between odd and even rotational angular momentum J is taken as 3:1. The time-dependent

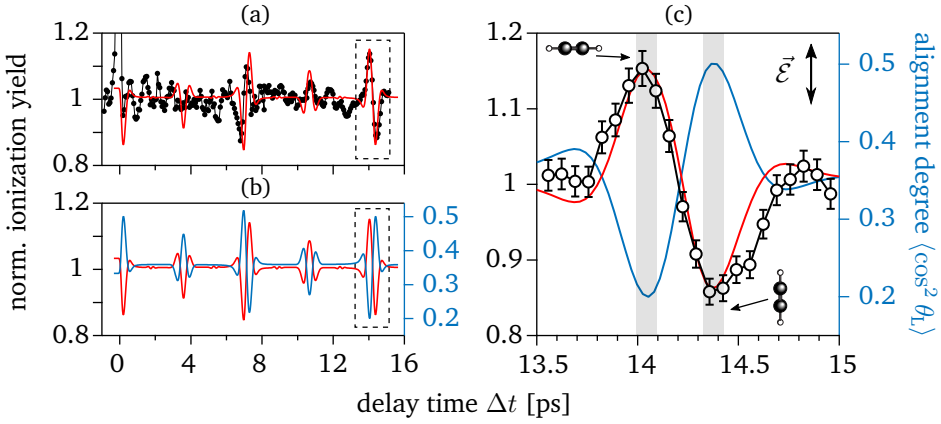

Figure 6.11: Impulsive molecular alignment of C_2H_2. (a) The experimental ionization yield is shown (black dots) as a function of delay time Δt between the 1.7 µm pump pulse and the 3.1 µm probe pulse. The data are normalized on the ion yield from only 3.1 µm pulses. The simulated ionization signal is plotted for comparison (in red). **(b)** Both the simulated ion signal (red) and alignment degree $\langle\cos^2(\theta_L)\rangle$ (blue, right axis) are plotted being out of phase at the alignment revivals. **(c)** A zoom into [see dashed boxes in (a) and (b)] the full-revival is plotted highlighting the alignment position at around 14.4 ps and the anti-alignment position at 14.05 ps (gray shadings).

alignment distribution $\rho(\theta_L,t)$ can be calculated as

$$\rho(\theta_L,t) = \sum_{J\,M} \omega_{J\,M}\ |\Psi_{J\,M}(\theta_L,\phi_L,t)|^2 \quad , \tag{6.17}$$

where $\Psi_{J\,M}(\theta_L,\phi_L,t)$ is the molecular wavefunction, evolved from initial $\Psi_{J\,M}(\theta_L,\phi_L,\,t\,=\,-\infty)\,=\,|J\,M\rangle$ and $\omega_{J\,M}$ is the weight according to the Boltzmann distribution. The degree of alignment can be estimated by $\langle\cos^2(\theta_L)\rangle$[21] and is shown in Figs. 6.11 (a,b) (red curve). To reach a good level of agreement with our experimental data we used the following parameters: a pump pulse intensity of $I_{1.7\mu m} = 2.0\times10^{13}$ W/cm^2, a wavelength of 1.7 µm, a pulse duration of 90 fs (FWHM), and rotational temperature of 90 K. These parameters have been adjusted to match the experimental time delay measurement of the ion signal (black dots) and are also close to the experimental estimates. The full range of the resulting simulated ion signal is presented in Fig. 6.11 (a, red line). The corresponding simulated degree of alignment is plotted in Fig. 6.11 (b, blue line) next to the ion signal over the full time range. The ion signal and the alignment degree are out of phase with each other as expected (see below) and as has been shown previously in high harmonic generation measurements [359]. The dashed black boxes both in Fig. 6.11 (a, b) represents the zoom-in of the full revival as replotted in Fig. 6.11 (c) which contains the region of interest (gray shading) for the data presented in this section. The agreement of the simulated ion signal (red line) over the time span

[21] alternatively $\langle\cos^2(\phi_L)\rangle$ is possible depending on definition and symmetry arguments

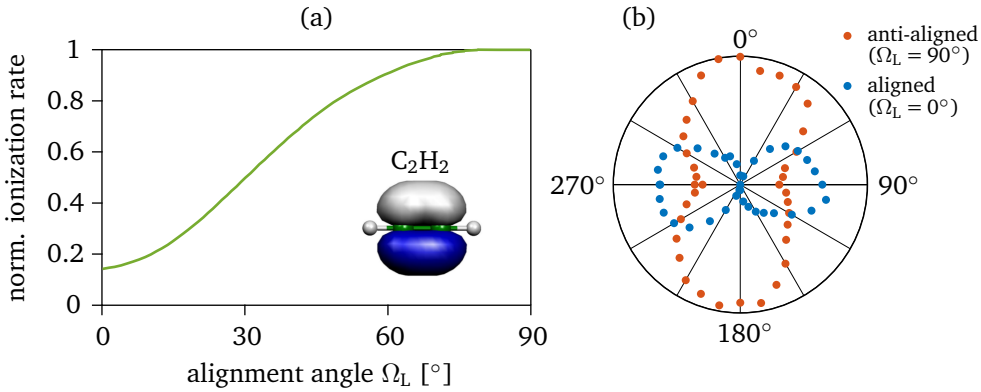

Figure 6.12: Ionization rate as a function of alignment angle of the HOMO of C_2H_2. (a) The simulated ionization rate is plotted as a function of alignment angle Ω_L (between the laser polarization and the molecular axis) of the HOMO of of C_2H_2. **(b)** The experimental normalized ionization rate is shown as a function of the angle between the polarizations of the 1.7 µm pump pulse and the 3.1 µm probe pulse for both the aligned ($\Omega_L = 0°$, $\Delta t = 14.4$ ps) and anti-aligned ($\Omega_L = 90°$, $\Delta t = 14.05$ ps) acetylene molecules.

of the full-revival is clearly visible, resulting in a maximum alignment degree of $\langle\cos^2(\theta_L)\rangle \approx 0.50$ at the full revival of alignment at 14.40 ps while the anti-aligned position at 14.05 ps results in an (anti-)alignment degree of $\langle\cos^2(\theta_L)\rangle \approx 0.2$. Note that arbitrary alignment calculates to $\langle\cos^2(\theta_L)\rangle = 0.33$.

In our simulation of the ion signal is calculated using the SFA [72, 123, 372] to get ionization rates from aligned and anti-aligned C_2H_2. The *highest occupied molecular orbital* (HOMO) is calculated using the GAUSSIAN code [370] within the density functional theory (DFT) with Becke's three-parameter Lee-Yang-Parr hybrid functional (B3LYP) and the augmented correlation-consistent polarized valence triple-zeta (aug-cc-pVTZ) basis set. A typical ionization rate versus alignment angle calculated using the SFA is shown in Fig. 6.12 (a) for a laser intensity of 1.0×10^{13} W/cm^2. Note that the ionization probability is maximal when molecules are anti-aligned, i.e., when the molecular axis is perpendicular (at 90°) to the polarization direction of the ionizing pulse. This is understood by the molecular tunneling ionization theory [151] (as shortly described in Sec. 2.3.3), which states that tunnel ionization rate is proportional to the electron density in the direction of laser polarization direction. This is illustrated in the inset of Fig. 6.12 (a) where the orbital distribution is clearly showing a dipole perpendicular to the molecular axis for the HOMO. Since the outermost electron of acetylene has π_v symmetry, ionization is maximal when the molecule is aligned at 90° with respect to the polarization direction of the ionizing radiation. The ionization rate therefore minimizes near 0°, which reflects the nodal line of the HOMO along the molecular axis. The electronic structure of acetylene is discussed in more detail in Sec. 7.1.1.

The context is experimentally confirmed as presented in Fig. 6.12 (b). The ion sig-

nal was measured as a function of the angular difference in the polarization directions of the pump and probe pulses for the delay times corresponding to alignment (blue, at 14.4 ps delay) and anti-alignment (red, at 14.04 ps delay), as indicated in Fig. 6.12 (b). When the pump and probe pulses have the same polarization, the anti-aligned signal maximizes and the aligned signal minimizes, hence confirming the predicted behavior of Fig. 6.12 (a).

6.5.4 Experimental parameters and bond extraction fitting routine

For SFI of aligned acetylene molecules and hence to generate elastically re-scattered electrons for LIED imaging, we used 3.1 µm pulses with 70 fs (6.5 cycles) duration at an intensity of 6.0×10^{13} W/cm^2 ($U_\mathrm{P} \approx 54$ eV, $\gamma \approx 0.33$, $z \sim 135$, $z_1 \sim 8.9$, $z_\mathrm{f} \sim 2.1 \times 10^{-4}$)). The value was determined by fitting the corresponding ADK rate (see Eq. 2.20) to the $p_\parallel$ - distribution of $C_2H_2^+$ ions or its coinciding electrons. When applying the calibration fit (see Sec. 3.1.3), we can extract an intensity value of $(6.5 \pm 20\%) \times 10^{13}$ W/cm^2 ($U_\mathrm{P} \approx 58$ eV, $\gamma \approx 0.31$). Via the $2U_\mathrm{P}$ cutoff of the electron distribution from all electrons in coincidence with the acetylene cation $C_2H_2^+$ as plotted in Fig. 6.16 (a, black line), one can estimate an intensity of 5.5×10^{13} W/cm^2 ($U_\mathrm{P} \approx 50$ eV, $\gamma \approx 0.34$). The values lie all close to each other within error. On the detection side we used similar parameters as in the calibration mid-LIED measurement on Xe atoms as described earlier in Sec. 6.4.1.

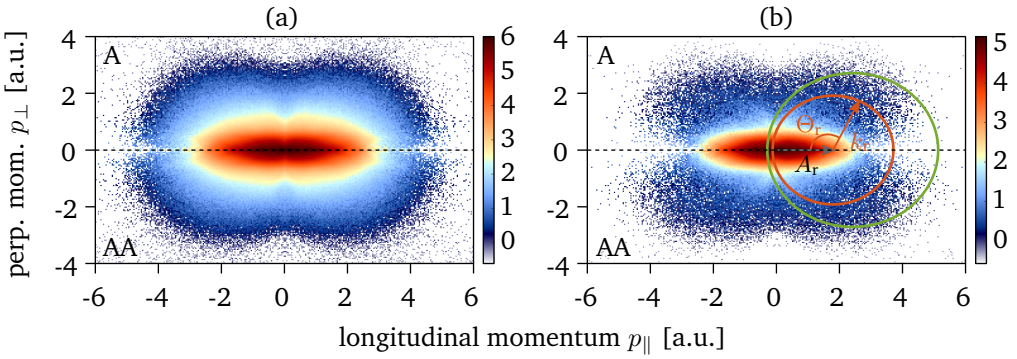

Figure 6.13: Electron momentum distributions of all channels and corresponding to C_2H_2. (a) Logarithmically scaled momentum distributions (*A* top, *AA* bottom) of electrons corresponding to all ionic fragments. **(b)** The respective logarithmically scaled electron momentum distributions of electrons corresponding to only $C_2H_2^+$ cations. The respective "rescattering circles" for a $E_\mathrm{r} = 50$ eV (red) and $E_\mathrm{r} = 100$ eV (green) are indicated. The drop in signal of rescattering electrons towards $\Theta_\mathrm{r} \to 180°$ seems to occur due to a lower probability of backscattering for molecular target systems (compare to [373, Fig. 1]).

For both aligned and anti-aligned acetylene molecules at 14.05 ps and 14.4 ps delayed from the 1.7 µm pulses, respectively [as highlighted in gray shadings in

Fig. 6.11 (c)], we extracted the overall electron momentum distributions shown in Fig. 6.13 (a). In the following, data corresponding to aligned acetylene molecules are indicated with an *A* and in the anti-aligned case with *AA*. The distributions show similar extents like the LIED experiment on Xe atoms. Since we are interested in imaging acetylene molecules, we focus the data analysis on only electrons corresponding to $C_2H_2^+$ ions which corresponds to the highest probable peak in our ToF spectrum as shown in black in the inset of Fig. 6.10. Like in the calibration measurement on Xe atoms (see Sec. 6.4.1), we apply the loose coincidence condition, hence extracting the corresponding electrons of all incoming $C_2H_2^+$ ions without setting a momentum conservation condition. As explained in [203, Ch. 6.2 & 7.4], this is a commonly used technique to enhance the statistics for similar results in case a relatively low rate of false coincidences is given (low gas pressures). In Fig. 6.13 (b), the respective electron momentum spectra are shown, yielding one order of magnitude less events and a rather smooth and rounded spread of re-scattered electron in contrary to the LIED measurement on Xe atoms. Also, it is apparent that electron counts for re-scattered electrons towards $p_\perp \lesssim 2$ a.u. and $p_\parallel \gtrsim 3$ a.u. gradually decrease towards $p_\perp \to 0$ which is different from the behavior in the Xe data set [see Fig. 6.6 (b)]. The reason therefore could be related acceptance limit of the reaction microscope and to SFI properties of acetylene as a molecular target. The latter case is related to the fact that molecules generally have a lower electron re-collision probability as experimentally observed e.g. in Xu *et al.* [373, Fig. 1] where atoms and molecules with comparable I_P are ionized under equal conditions revealing a lower yield of the plateau of re-scattered electrons for the case of the molecule. Moreover, this difference in [373] increases for larger re-scattering angles Θ_r which reflects specifically the region we observe here with less counts.

In order to get the structural information from the data, we proceed by extracting the molecular DCSs $\sigma_\mathrm{exp,tot}$ from the electron momentum distributions according to classical considerations as described earlier for the LIED experiment on Xe atoms in Sec. 6.4.2. Resulting DCSs (extracted with $\Delta k_\mathrm{r} = 0.15\, k_\mathrm{r}$ and $\Delta\Theta_\mathrm{r} = 4°$) for both alignments are shown in Fig. 6.14 (a) for the exemplary electron return energy of 60 eV for the aligned (blue on the left axis) and anti-aligned (red on the right axis) case. The error bars were calculated by Poissonian statistics on the number of counted electrons for each integration interval. The DCSs show a continuous decrease by one order of magnitude for increasing scattering angles. For scattering angles beyond around 100° to 120° the DCSs drop more drastically which is related to the decrease in counts towards the $p_\perp \to 0$ ($\Theta_\mathrm{r} \to 180°$) axis which seems to occur due to a lower probability of backscattering for molecular target systems (compare to [373, Fig. 1]) as described above. The corresponding theoretical molecular DCSs σ_tot are calculated via the IAM[22] (see Sec. 6.3.2) for C_2H_2 with close to equilibrium dimensions (*A* in blue on the left axis and *AA* in red on the right axis) and are presented in Fig. 6.14 (b). Also the incoherent atomic DCSs σ_atom are plotted in black, respectively. Both σ_tot decrease by one order of mag-

[22]The simulation was again performed by our collaborator A.-T. Le of the group of C. D. Lin of the Kansas State University.

nitude until $\sim$100° before increasing moderately for $\Theta_r \to 180°$. The latter part differs from the experimentally extracted DCSs.

Nevertheless, the diffraction information of the molecular scattering target is hidden in the difference between the molecular DCS σ_{tot} and the its atomic counterpart σ_{atom}. This coherent molecular interference term is expressed by the MCF as defined in Eq. 6.13 which is plotted in Fig. 6.14 (b) in solid lines. Features of the MCF like positions of and the phase between its extrema as well as the zero crossing(s) translate into specific structural dimensions of the scattering target object. In case of electron scattering on acetylene, the MCF contains distinct modulations on the tens of percent level for scattering angles of mainly between 30° to 120° which makes them experimentally observable with a carefully configured apparatus. On the other hand, for higher scattering angles than 120° the molecular DCS approaches its atomic counterpart for no modulations. This is advantageous for our measurements as the experimental DCSs show a similar progression as the theory up until 100° to 120° while the signal drops beyond. The experimental MCF is calculated according to Eq. 6.16 where the incoherent theoretical atomic scattering cross-sections σ_{atom} are subtracted from β-scaled experimental DCS before normalization by division over σ_{atom}. Both experimental MCFs are plotted in resulting in Fig. 6.14 (c, *A* in blue squares and *AA* in red circles with Poissonian errors, respectively). In order to extract bond lengths of the respective data, the individual bond distances (symbolically denoted in the following as $\vec{R}_a$) are varied and the theoretical DCSs σ_{tot} and hence the MCFs are calculated for each configuration. The best chi-square fit of the experimental MCF to the theoretical ones is retrieved via

$$\chi^2(\vec{R}_a) = \sum_{i\,j} \left(MCF_{exp}(k_{r,i}, \Theta_{r,j}) \; - \; MCF(k_{r,i}, \Theta_{r,j}, \vec{R}_a)\right)^2 \quad . \tag{6.18}$$

i, j gives the indices of grid points of scattering energies (or momenta) and scattering angles, respectively, available in the experiment. Note that we focus in this case of acetylene on extracting only the bond lengths assuming the molecule stays linear[23]. Thus, Eq. 6.18 gives the best overall fit for the available range of scattering energy and angle. This procedure resembles a 2D-fitting. This can be simplified to a 1D-fitting procedure which corresponds to limiting the double summation in Eq. 6.18 to a single sum over i and j corresponding to a fixed scattering angle or a fixed scattering energy, respectively. This structure retrieval using a *fitness function* $\chi^2(x_i)$ was proposed in [324].

For our exemplary case of electrons returning with an energy of 60 eV, we apply a 1D-fitting. Figs. 6.15 (a,b) show the respective χ^2 solution maps (logarithmic color scale) as a function of the C-C and C-H (assuming a symmetric stretch of both C-H bonds) bond distances. The minimum position (χ^2_{min}) are found to be for bond length of aligned $C_2H_2^+$ at $D_{CC}^{A,60} = (1.28 \pm 0.13)$ Å and $D_{CH}^{A,60} = (1.04 \pm 0.10)$ Å and

[23] Technically, any desired number number of structural parameters could be fitted against including bond angles, torsions etc. Yet, this comes with the prize of increased computational demands. For the purpose of optimization, certain structural parameters should be kept constant by physical argumentation.

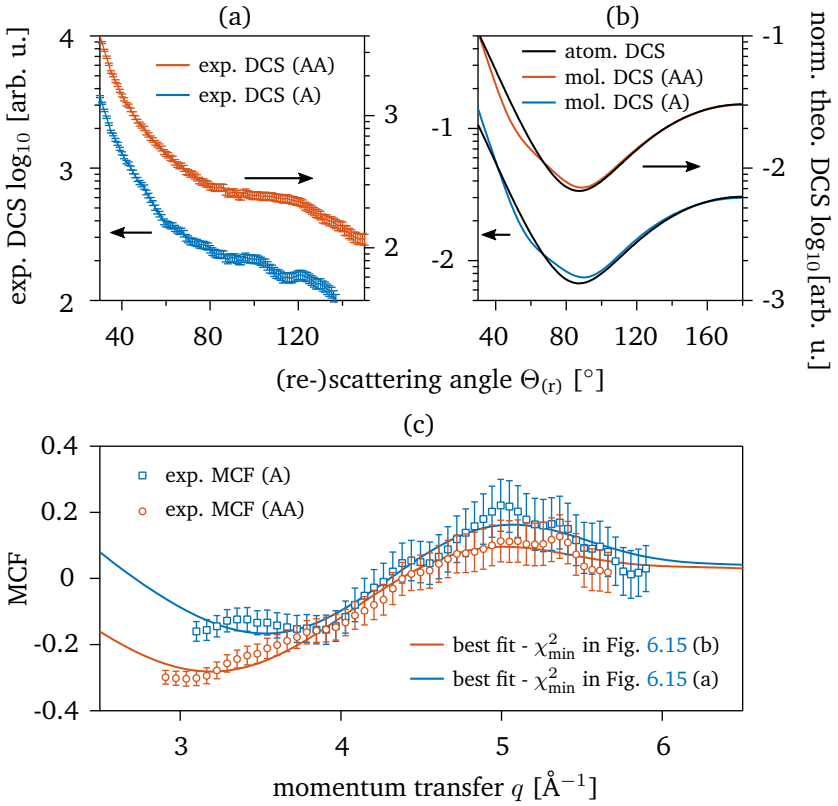

Figure 6.14: Extraction of molecular structure from electron momentum distributions. **(a)** The experimental DCSs (with Poissonian error bars) of aligned (blue to the left) and anti-aligned (red to the right) $C_2H_2^+$ extracted according to QRS theory. The drop in signal of re-scattering electrons towards $\Theta_r \to 180°$ is marked (gray background). **(b)** The theoretical atomic (black) and molecular DCSs of aligned $C_2H_2^+$ molecules (*A* in blue to the left, *AA* in red to the right). Disappearing structural modulations are expected for the case of acetylene for scattering angles larger than 110° to 120°. **(c)** The experimental MCFs are plotted (*A* in blue squares, *AA* in red circles, with Poissonian error bars). The theoretical MCFs found at the minimum value χ^2_{min} of the fitting routine for both alignments are plotted as solid lines (*A* in blue, *AA* in red) corresponding to the normalized difference of the theoretical molecular and atomic DCSs.

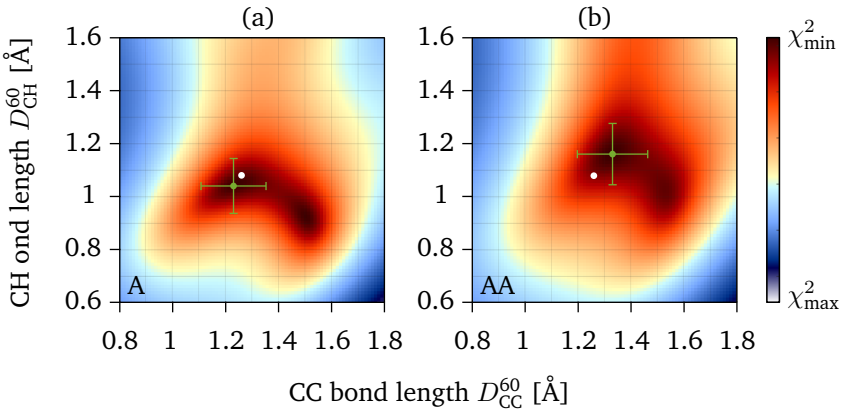

Figure 6.15: χ^2 solution maps of the fitting routine. (a,b) The logarithmically scaled χ^2 solution maps of the fitting routine comparing the experimental and theoretical MCSs [*A* in (a) and *AA* in (b)]. The minimum position χ^2_{min} is indicated by a green dot with 10 % error bars while the theoretical value for $C_2H_2^+$ cations is plotted as white dot.

for the anti-aligned case at $D_{CC}^{AA,60} = (1.33 \pm 0.13)$ Å and $D_{CH}^{AA,60} = (1.15 \pm 0.12)$ Å. Here the notation $D_{bond}^{alignment,energy[eV]}$ is used for the results of the individual fits to refer to energy-specific bond lengths. The χ^2_{min} are indicated by the green dots while the known cation equilibrium position is indicated by the white dot for $D_{CC,lit.} = 1.2482$ Å and $D_{CH,lit.} = 1.0763$ Å [363]. The fitted results in Figs. 6.15 (a,b) are marked with individual error bars on the order of ±10% which overlap with the known values in this example. The two MCFs presented in Fig. 6.14 (c) correspond to the corresponding χ^2_{min}s of Figs. 6.15 (a,b). The differences in extracted bond lengths are directly connected with the differences of the MCFs such as the position of the minimum near $q \sim 3.5$ Å^{-1}, which is shifted to lower q values in case of anti-aligned acetylene, and the modulation amplitude, which is smaller in the aligned case. Depending on the target and the degree to which it is aligned, molecular alignment or anti-alignment can lead to larger differences in the peak-to-peak amplitude of the MCFs, which is beneficial for structural imaging. These results confirm that LIED can simultaneously extract multiple bond lengths from polyatomic molecules with high accuracy. Moreover, it indicates that, in the case of acetylene, launching the re-collision electron does not cause detrimental differences between the neutral and ionic species within the short re-collision time.

6.5.5 Importance of ion-electron coincidence detection for LIED imaging

A crucial property of our experimental setup for accurate retrieval of polyatomic molecular structure via the experimental MCF is the coincidence detection capability of the ReMi. Moreover, in order to develop the time resolving capabilities of LIED, it is important that we ensure the scattering pattern originates from the

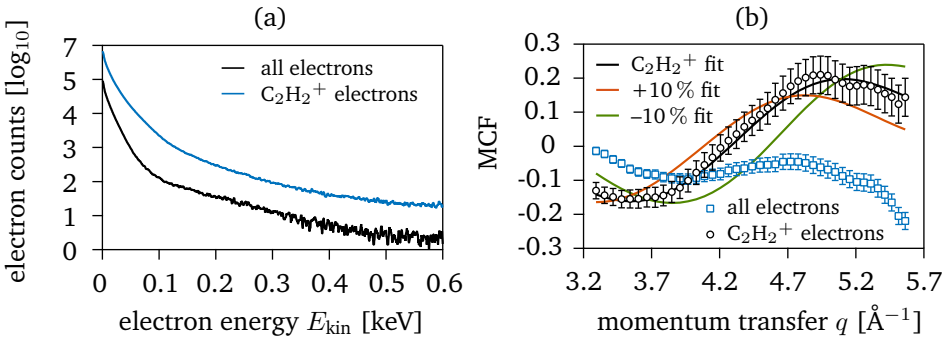

Figure 6.16: Coincidence imaging enabling accurate bond length extraction. **(a)** The electron kinetic energy distribution is plotted for all detected electrons (blue line) and for electrons coinciding with only $C_2H_2^+$ cations (black line). **(b)** The extracted MCF for returning electrons re-scattering off alignded $C_2H_2^+$ ions (black circles) and from all ion fragments detected (blue squares) at a kinetic energy of 65 eV. The solid black curve shows the best fit matching well with the $C_2H_2^+$ cation channel. The MCFs for $\pm 10\,\%$ changes in the molecular length of C_2H_2 (dashed curves) highlight the sensitivity of the LIED technique. The s.d. error bars are derived from Poissonian statistics.

(fragmentation) channel of interest only. To highlight this point, the measured electron kinetic energy spectrum for all fragments (so all detected electrons, in blue) and corresponding to the $C_2H_2^+$ fragments only (extracted in loose coincidence, in black) is plotted in Fig. 6.16 (a). The respective ToF spectrum of all the detected positively charged fragments was already shown in Fig. 6.10. There, the main peak near 4.2 µs being the acetylene cation $C_2H_2^+$ constitutes about 10 % of the total number of detected fragments. The inset shows a close-up of this peak and the black shaded area represents the region that the electrons associated with $C_2H_2^+$ are extracted from. Many other fragments can be observed and identified in the ToF and each of these peaks has associated electrons. The corresponding kinetic energy spectra show an order of magnitude difference in the number of detected electrons which is visible over the entire spectral range. It is these omnipresent extra electrons that serve as an unwanted background signal and are detrimental to structure retrieval without coincidence detection. This point is further substantiated by the fact that the characteristic kink at $2U_P$ and the plateau until $10U_P$ of the kinetic energy spectrum according to the re-collision model is more clearly visible for the electrons detected in coincidence with $C_2H_2^+$.

The influence of the unwanted electron background on the extraction of structural information via LIED is shown in Fig. 6.16 (b). Here, the MCFs are compared that were retrieved when analyzing electrons (with a return energy of 65 eV here) corresponding to all fragments (blue squares) and from $C_2H_2^+$ only (black). The $C_2H_2^+$ data result in an MCF that compares well with the equilibrium acetylene structure (theoretical fit as black line). On the other hand, using electrons from all fragmentation channels, so not having imposed any coincidence condition, results in a dramatically different MCF. This MCF cannot be accurately fitted and fails in

retrieving the $C_2H_2^+$ bond lengths. This analysis validates that electron-ion coincidence detection is a pre-requisite for the application of LIED to larger molecules.

Moreover, the high sensitivity of LIED to the exact molecular structure is also illustrated in Fig. 6.16 (b). By inducing a drastic change of the molecular structure, the MCF corresponding a 10% contraction (green dashed line) or expansion (red dashed line) of the molecule are calculated. Clearly both MCFs deviate from the measured data highlighting both the sensitivity and accuracy of the LIED technique. By using the fitting technique to extract the bond lengths from the experimental MCF we can reach an accuracy of each bond fit around $\sim$10 pm. This point needs to be stressed, as this is an order of magnitude lower than the de-Broglie wavelength of the scattering electrons ($\lambda_e \approx 1.5$ Å).

6.5.6 Complete experimental results

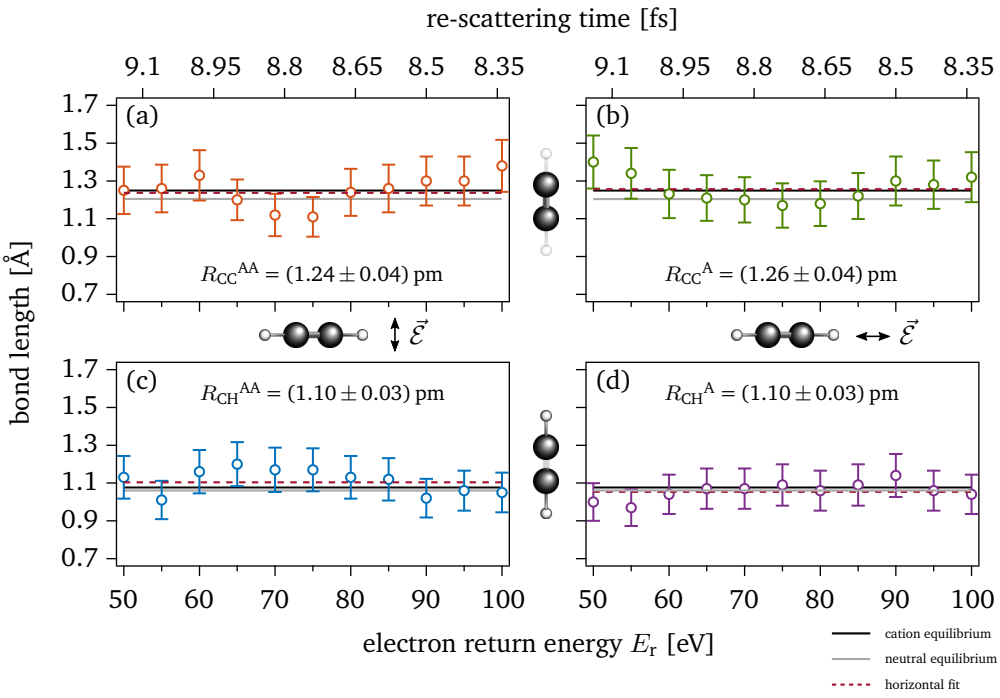

Figure 6.17: Accurate $C_2H_2^+$ bond length extraction. The C-C and C-H bond length 2D-fitting results are plotted as a function of the kinetic energy of the returning electron and vice versa its re-scattering time in the top **(a,b)** and bottom **(c,d)** quadrants both both aligned **(a,c)** and anti-aligned **(b,d)** acetylene molecules. The expected equilibrium values of the acetylene cation are shown in black lines according to [363] as well as for the neutral acetylene molecule (gray solid line) after [374]. Horizontal fits for each bond are displayed in the respective panels (burgundy dashed line).

As our experimental data contain the DDCS of all scattering events as explained in Sec. 6.4.3, we are able to retrieve the C-C and C-H bond lengths as a function of the electrons' return energies. In Fig. 6.17 all these extracted bond lengths are plotted where the resulting C-C bonds are shown in the upper (a,b) and the C-H bonds in the lower (c,d) panels separated results from anti-aligned [left panels (a,c)] and aligned [right panels (b,d)] acetylene. This measured energy range can be used to establish a high level of confidence and redundancy for the retrieved bond length. The extracted D_{CC}^{A}, D_{CC}^{AA}, D_{CH}^{A} and D_{CH}^{AA} values are consistent within error with the expected neutral (gray lines) [374] and ionic equilibrium values (black lines) [363] over the investigated energy range.

Moreover, we can illustrate the possible intrinsic sub-cycle temporal resolution [25, 316] of the LIED technique in Fig. 6.17. As explained in Sec. 6.2.2, based on operating mid-IR LIED in the quasi-static limit we can invoke the classical re-scattering model to associate a specific time to the measured electron re-scattering energy. The top axis in Fig. 6.17 shows the corresponding return time for each electron energy and indicates that a temporal resolution on the order of sub-fs could be achieved by analyzing at different re-scattering energies. With the extracted electron energies we cover a time window of ∼8.35 fs to ∼9.15 fs. Within this window, all extracted bond lengths are consistent within error with the expected equilibrium structures (neutral and ionic) [363, 374] which suggests that the $C_2H_2^+$ cation undergoes negligible re-arrangement during the ∼9 fs between ionization and re-scattering. Also no significant structural rearrangements are expected after acetylene is ionized from a neutral to a cation [363]. This allows us to fit a horizontal line to the energy dependent bond length estimates (burgundy dashed lines in Fig. 6.17) yielding an overall estimate of the C-C and C-H bond lengths. This results in estimates of $R_{CC}^{AA} = (1.24 \pm 0.04)$ Å and $R_{CH}^{AA} = (1.10 \pm 0.03)$ Å for anti-aligned molecules while the same analysis with aligned molecules gives bond lengths of $R_{CC}^{A} = (1.26 \pm 0.04)$ Å and $R_{CH}^{A} = (1.05 \pm 0.03)$ Å. This method amounts to performing 2D fitting over both electron energy and scattering angle, resulting in a few-pm spatial resolution. Again this highlights the accuracy of the LIED method.

Extending on the bond length extraction, both C-H bonds can be included individually in the χ^2 fitting routine. This results in a three dimensional solution space (D_{CC} × D_{CH} × D_{HC}) where the assumption of symmetric molecular structure has been removed. The bond lengths resulting from this fit combine to represent a more accurate molecular structure observed during LIED on the cost of higher computational effort. In Figs. 6.18 the fitting results are presented for the aligned (a-c) and anti-aligned (d-f) experimental MCF data for the example of electrons re-scattering with an energy of 60 eV (as in Figs. 6.14 and 6.15). In the aligned case, the 3D fit at χ^2_{min} gives bond lengths of $D_{CC}^{A,60} = (1.16 \pm 0.12)$ Å, $D_{CH}^{A,60} = (1.08 \pm 0.11)$ Å and $D_{HC}^{A,60} = (1.08 \pm 0.11)$ Å [blue points in Figs. 6.18 (a-c)] while the anti-aligned case results in $D_{CC}^{AA,60} = (1.31 \pm 0.13)$ Å, $D_{CH}^{A,60} = (1.21 \pm 0.12)$ Å and $D_{HC}^{A,60} = (1.25 \pm 0.12)$ Å [blue points in Figs. 6.18 (a-c)]. All bond lengths agree with the 2D solution as extracted in Fig. 6.15 showing overall slightly larger bond length in the anti-aligned case, thus highlighting the consistency of scaling this method to more structural degrees of freedom. Comparing the 3D results of both alignments,

it can be noticed that the aligned case offers two exactly similar C-H bond lengths while in the anti-aligned case, both C-H bond lengths slightly differ by $\sim$3 % yet are within error similar. Overall, the fact that the two individual C-H bonds are the same for both alignments, shows that, in this case, the two dimensional fitting routine as used earlier is already able to accurately extract the molecular structure.

We estimate the uncertainty in the structural extraction by creating an iso-surface at a value of $1.25\chi^2_{\text{min}}$ (blue shading). In the aligned case [Figs. 6.18 (a-c)], the iso-surface extends in an oval shape over the C-C range from 1.09 Å to 1.25 Å and the C-H range from 0.97 Å tp 1.17 Å, thus still being consistent with the expected C_2H_2 neutral (red) and cation (green) equilibrium structures. Moreover, the anti-aligned 3D solution space [Figs. 6.18 (d-f)] reveals a slightly difference iso-surface shape appearing like a "beltbag" extending from 1.25 Å to 1.37 Å over the C-C range and from 1.05 Å tp 1.45 Å in the C-H range. In the AA case, the extracted bond lengths seem to be slightly extended within error compared to the expected neutral (red) and cation (green) equilibrium structures in contrary to the A case. Projections of the solution spaces in the R_{CH} vs. R_{CC} and R_{CH} vs. R_{HC} planes are presented in Figs. 6.18 (b,e) and Figs. 6.18 (c,f), respectively. The different appearances of the uncertainties of the 3D solution spaces between both alignments can be reasoned by the fact that the individual molecular states are dressed by the laser field and feel the effective electric field differently when aligned parallel or perpendicular to the molecular axis. This point is investigated further in the next chapter 7.

The successful retrieval of C_2H_2 molecular structure from alignment dependent LIED provides a number of important pieces of information. Firstly, the extension of LIED to a truly polyatomic molecule demonstrates that the technique can be applied to larger and more complicated molecules in the future. Secondly, the successful application of a QRS theory based data analysis to both molecular alignments demonstrates the consistency of the underlying model. Even though in the particular case of C_2H_2 the observed differences in the alignment dependent MCFs [see Fig. 6.14 (c)] are quite small, the fact they can be resolved at all shows how powerful the method is. Simulations of other molecules have shown that the MCF amplitude can change drastically depending on the angle of the molecular axis [324]. Thus, the use of molecular alignment may play a large role in future LIED experiments. Finally, we note that these results were obtained using the coincidence detection capabilities of our experimental apparatus. The same analysis performed without electron-ion coincidence resulted in molecular structure being unobtainable.

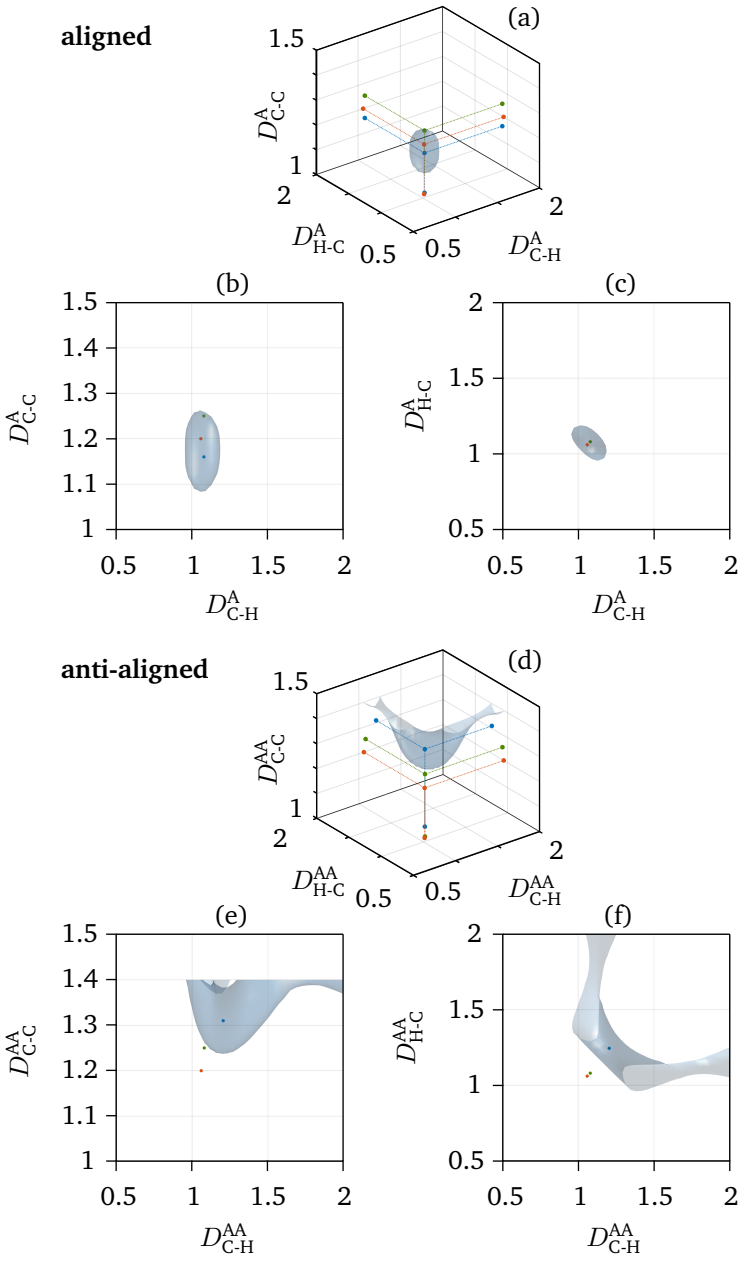

Figure 6.18: Extraction of all 3 individual C_2H_2[2] bond lengths. The fitting routine is performed over the three individual bonds of C_2H_2 ($D_{CC} \times D_{CH} \times D_{HC}$). The 3D solution space is plotted for both **(a)** aligned and **(d)** anti-aligned data sets. The position of the χ^2_{min} is represented by the blue data points. The blue isosurface is taken at a value of $1.25\chi^2_{min}$ and represents the edges of the expected uncertainty in the measurement. The expected structure of neutral (red) [374] and cationic (green) [363] acetylene are indicated. **(b,c,e,f)** Projections of the solution spaces in **(a,d)**.

Chapter 7

Imaging and Control of Selected Molecular Fragmentation

During a chemical reaction molecular compounds dynamically transition from one structural configuration to another leading to the formation, breaking and other geometrical (re-)arrangement of individual bonds between its individual atoms. The ability to image such an ultrafast motion of the structural components of a molecule is prerequisite to disentangling the complex interplay between its reactants and products [4, 6, 375, 376]. An imaging method should be able to track the motion of all atoms within a molecular compound, since the nuclei are coupled and every individual motion affects the outcome of a chemical reaction [145, 377, 378]. LIED not only allows to image the entire molecular structure at few-pm spatial resolutions but also offers an intrinsic sub-optical cycle temporal resolution (see Sec. 6.2.2) that could be utilized to resolve ultrafast molecular dynamics as speculated many times in literature [25, 37, 324, 326]. The only investigation to date[1] that made use of the both spatial and the intrinsic temporal information provided by LIED was published by Blaga *et al.* [39] where they applied LIED to image O_2 molecules inferring a 10 pm vibrational contraction of the O_2 bond 5 fs after ionization. The next step is to apply equivalent investigations using LIED to the dynamics of more complex, polyatomic molecular structure which was so far limited due to experimental difficulties that were overcome by our work in the previous chapter. Hence, we now want to use our mid-IR LIED technique to spatio-temporally resolve an ultrafast molecular reaction as the prerequisites are given.

In the last chapter, we imaged the stable cation (ground state) of acetylene for a series of electron return energies. Via classical arguments this chirped electron pulse can be regarded as imaging $C_2H_2^+$ for a time window between $\sim$8 to 9 fs after population and ionization. As expected, the stable cation ground state was found to exhibit C-C and C-H bond length close to the dimensions of the neutral molecules [$R_{CC} = 1.2038$ Å and $R_{CH} = 1.0609$ Å [363]] for all electron return energies not showing any structural change. In order to fully take advantage of our set-up, we ideally would want to image a molecular reaction that shows a significant structural change at $\sim$8 to 9 fs after population and tunnel-ionization of the respective state. Therefore, we focus in this chapter on imaging bond fragmentation of acetylene, namely the breakage of one of its hydrocarbon bonds and the

[1] October 2016

subsequent departure of one proton from the residual ethynyl C_2H^+ moiety. These "snapshots" of the entire acetylene molecule during the *deprotonation*[2] process are taken with our mid-IR LIED technique, as introduced and tested in the previous chapter (Ch. 6). Moreover the snapshots are compared for both alignment states (aligned parallel and anti-aligned perpendicular to the laser polarization axis) of the molecule.

This prototypical dissociation pathway is interesting for us for different reasons. On the one hand, it presents one of the fastest expected nuclei motions in nature since a proton is escaping the heavier carbon. Moreover, the deprotonation process has never been resolved directly during its reaction with any structural imaging method. On a more broader perspective, a detailed knowledge of reactions involving bond breakups of organic molecules is of vital importance for applications in e.g. material science and pharmaceuticals. Of particular interest within organic compounds are carbon-hydrogen bonds since they provide a scope for investigations into e.g. C-H functionalization [380]. Here the C-H bond is selectively cleaved and then synthesized into a novel moiety C-X, where carbon is bound to a different hetero-atom *X*. A challenge of this process is the precision and predictability of new bond syntheses starting with the initial C-H bond cleavage. In order to influence this deprotonation reaction it needs to be tracked and controlled. The results of this chapter constitute a reliable approach in this direction.

The chapter is arranged such that in the first Sec. 7.1 the electronic structure of acetylene is presented and the pathways towards the targeted deprotonation channel are specified. Further, the experimental isolation of the fragmentation relevant ions via the coincidence information of the ReMi detection system is presented. In the second part of this chapter, in Sec. 7.2 the electron momentum distribution data corresponding to the moieties of the deprotonation channel are investigated with respect to its containing LIED signal to extract the structural information of the specific channel. The experimental results are compared with quantum dynamical molecular wave packet simulations. The experimental and theoretical data presented in this chapter and hence its main results have been published in

B. Wolter et al., Science ***354****, 308-312 (2016)* cited as [381] (highlighted by C.-Y. Ruan in Science [382]).

7.1 Preparation and isolation of the deprotonation pathway of $C_2H_2^{++}$

During the interaction of strong laser pulses with acetylene molecules, different fragmentation reactions are triggered. In this section, the potential energy landscape of acetylene is presented as well as the possible pathways to populate the respective dissociative states. Moreover, the specific population of the (dication) de-

[2] In literature *deprotonation* is often only used for proton departure in acids, yet in many articles on acetylene, the C-H bond breakup is also referred to as deprotonation, see [66, 361, 364, 379].

protonation channel is experimentally isolated in order to extract the corresponding re-scattering electrons containing the diffraction imprint of the reaction ∼9 fs after population of the dissociative state.

7.1.1 Potential energy landscape of acetylene

A convenient approach to understand complex molecular systems and its dynamics is to study its potential energy structure in order to identify the dynamic pathways of choice. In Fig. 7.1 the PECs of acetylene are plotted as cuts along the (a) C-C and (b) C-H stretching modes of the 3D PESs. The PECs were calculated via the program package *MOLCAS*[3] by our collaborator Katharina Doblhoff-Dier of the theoretical chemistry research group of Stefanie Gräfe, Jena, Germany. Details about the simulations are given in [365]. The calculations agree nicely with other theoretical investigations in literature [361, 364]. Information about the potential energy landscape of acetylene and its population pathways (see Sec. 7.1.3) has been adapted from the dissertation of Katharina Doblhoff-Dier [383, Chs. 4 & 5] where the context is discussed in more detail.

The neutral ground state of acetylene $^1\Sigma_g^+$ is found in a stable, linear configuration with its equilibrium bond lengths of $R_{CC} = 1.2038$ Å and $R_{CH} = 1.0609$ Å [363] as discussed earlier. The bond lengths correspond to the local minima of the respective PECs (black lines) in Fig. 7.1 along the C-C bond in (a) and the C-H bond(s) in (b) which resemble the Franck-Condon points of acetylene.

The bound ground state $^2\Pi_u$ of the cation $C_2H_2{}^+$ lies $I_P = 11.4$ eV above $^1\Sigma_g^+$ and is found to be linear with slightly shifted bond lengths of $R_{CC} = 1.2482$ Å and $R_{CH} = 1.0763$ Å [363]. The corresponding minima are visible in the lower dark blue PECs in Figs. 7.1 (a,b). The first excited states of the cation $^2\Sigma_g^+$, $^2\Pi_g$ and $^2\Sigma_u^+$ lie approximately 5 eV to 8 eV above the cation ground state and are bound and slightly stretched bonds [384]. For the sake of completeness, it should be mentioned that the cation exhibits the state $^2\Sigma_u^-$ around 6 eV further above those states (not shown in Fig. 7.1) which is strongly repulsive along the C-H cut dissociating as $C_2H_2{}^+ \rightarrow H^+ + C_2H_2$ into a proton and a neutral ethynyl moiety [384]. The same publication [384] suggests that $^2\Sigma_u^-$ only reacts this way, and not resulting in a charged ethynyl and a neutral atomic hydrogen[4]. $^2\Sigma_u^-$ is loosely bound along the C-C axis.

The dication features a triplet ground state $^3\Sigma_g^-$ (dark green) and two singlet states $^1\Delta_g$ (light green) and $^1\Sigma_g^+$ (red) sitting at around 31.9 eV, 33.0 eV and 33.5 eV above the neutral ground state, respectively. All these states are *metastable* along the C-H bond axis meaning that they are bound at bond lengths of $R_{CC} = 1.344$ Å and $R_{CH} = 1.122$ Å [361] yet only for lifetimes of $\tau_{^3\Sigma g-} = 108$ ns [385] up to $\tau > 1$ µs [361]. All three states are bound along the C-C axis. At 5.5 eV and 6.3 eV above $^3\Sigma_g^-$ sit the next higher excited dication states $^3\Pi_u$ (triplet) and $^1\Pi_u$ (singlet,

[3] see http://www.molcas.org

[4] This was also confirmed by Stefanie Gräfe in a private conversation.

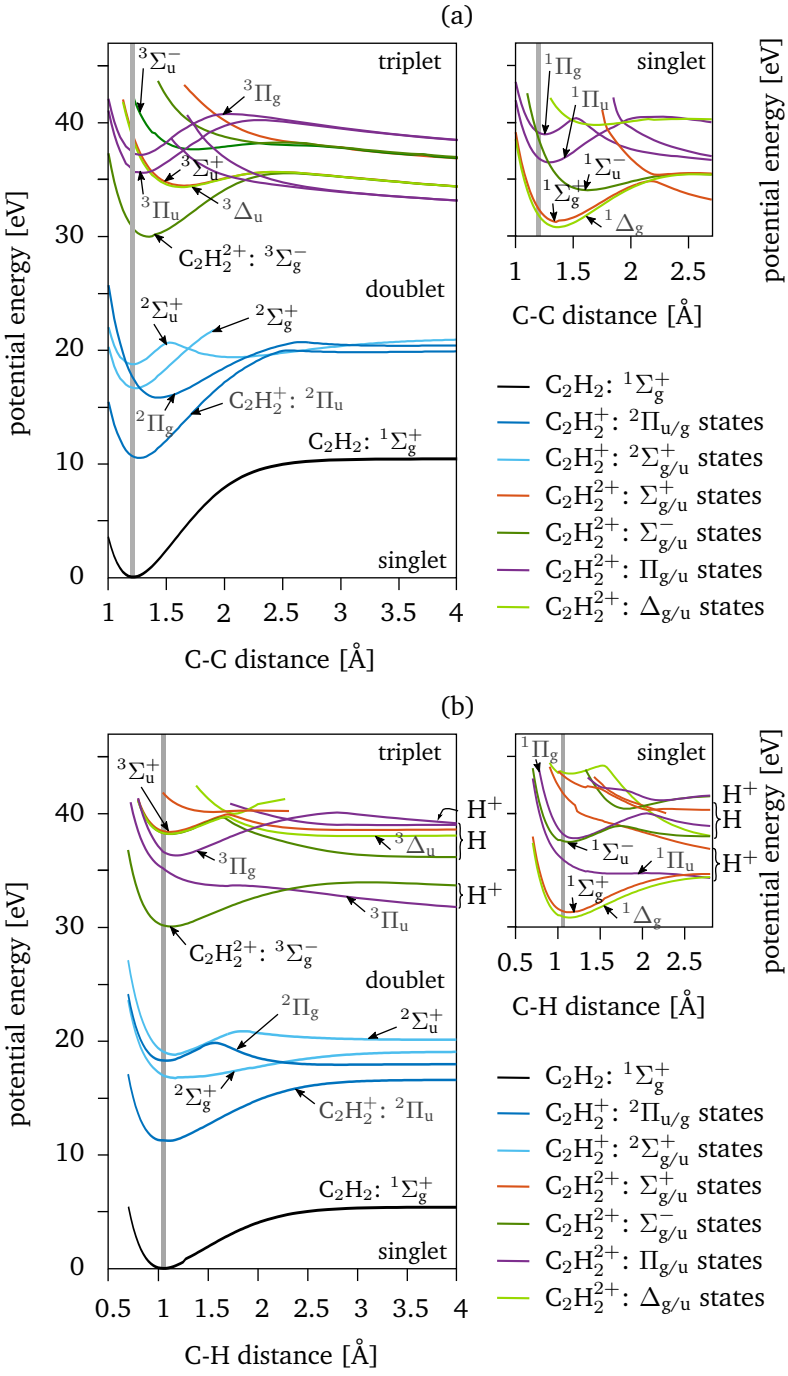

Figure 7.1: Potential energy landscape of acetylene. The main potential energy curves of acetylene are plotted along the **(a)** C-C and the **(b)** C-H stretching mode. The gray horizontal line indicates the Frank-Condon region. The PECs were calculated by Katharina Doblhoff-Dier for her publication [365, Fig. 1 & 2] and are extended here.

both in dark blue) which are strongly dissociative along the C-H axis [361, 364, 365]. Both excited states resemble the deprotonation reaction into a proton and a charged ethynyl moiety which is the dissociation with the highest branching ratio of acetylene (as mentioned in Sec. 6.5.2). The deprotonation reaction is the only possible reaction along these excited states as indicated with a H^+ in Fig. 7.1 (b), since the second possible dissociation along the C-H axis $C_2H_2{}^{++} \rightarrow C_2H^{++} + H$ only occurs for even higher states indicated with a *H*. The plotted lower dication states as presented above show all barriers towards dissociation along the C-C cut of the PECs. However, there are possibilities to overcome these barriers by e.g. a manifold of conical intersections between themselves and higher lying excited states that can effectively lower the potential barrier towards dissociation [364, 365]. This can lead to the symmetric breakup of the strongly bound C-C bond into two CH^+ moieties. Also, isomerization (as proton migration from one end of the molecule to the other) of the molecule in the $^2\Sigma_g^+$ cation state [27] can lead to a C-C breakup after further population of the excited dication state $^3\Pi_u$ [365]. In this chapter, we are specifically interested in the fast deprotonation reaction along $^3\Pi_u$ and $^1\Pi_u$.

7.1.2 Double ionization regimes of acetylene in mid-IR fields

In order to apply the LIED technique to imaging the dissociating dication of acetylene, it needs to be ensured that the emitted secondary electrons elastically re-scatter from the dissociating molecule. In other words, it needs to be assured that the $^3\Pi_u$ and $^1\Pi_u$ excited states are populated via SDI in two tunneling steps so that the emitted electrons leave the nuclei uncorrelated. Like this the second electron can enter a returning trajectory that eventually elastically re-scatters with the excited dication. The potential of the secondary electron in SDI to undergo a re-scattering trajectory was shown exemplarily in our classical simulation shown in Figs. 5.9 (b,d). The resulting electron momentum corresponding to the dication contains diffraction information that can be interpreted using the QRS model as described above. In the NSDI regime, the second electron would be correlated with the first electron and leave the Coulomb potential before the peak of the subsequent pulse. This would prevent the second electron from any re-turn to the nuclei to elastically re-scatter[5]. Hence, the SDI regime offers the possibility for the second tunnel electron to elastically re-scatter of the dissociating molecule.

In order to perform LIED on acetylene in the SDI regime, the transition between the NSDI and the SDI regime for the molecules interacting with our 3.1 μm pulses needs to be probed. Therefore, we performed an investigation similar to Ch. 5 on the DI of xenon atoms. Firstly, the yields of $C_2H_2{}^+$ (gray circles), $C_2H_2{}^{++}$

[5] In NSDI, the secondary electron is emitted before the peak of the subsequent electric field maximum since the first electron return at roughly three quarters of the optical cycle just after the return of the first electon [386]. This is the case for primary electron with zero kinetic energy at the tunnel exit according to classical calculations. If one assumes the primary electron to exit the tunnel barrier with $v_{\parallel} > 0$, there are technically solutions so that it returns after the subsequent field maximum which would allow the second electron to undergo a returning trajectory. The point could be further investigated in the future.

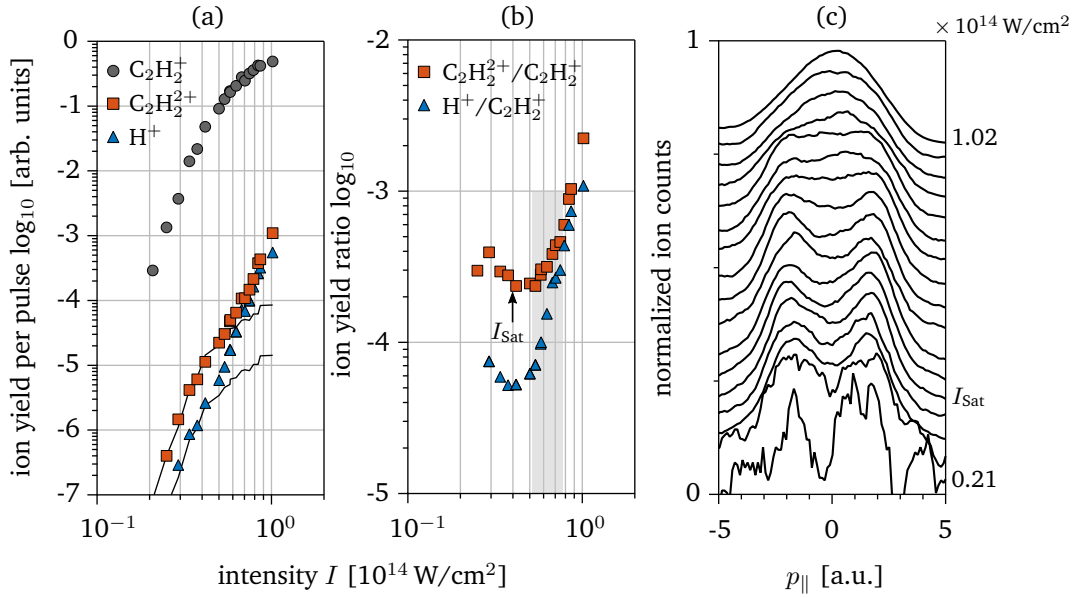

Figure 7.2: Transition from NSDI to SDI of acetylene with mid-IR pulses. **(a)** The experimental yields of $C_2H_2^+$ (gray circles), $C_2H_2^{++}$ (red squares) and H^+ (blue triangles) ions are plotted as a function of the peak intensity of our linearly polarized 3.1 µm source ($\tau \approx 70$ fs). **(b)** The respective $C_2H_2^{++}/C_2H_2^+$ (red squares) and $H^+/C_2H_2^+$ (squares) ratios as a function of the estimated peak laser intensity. The experimental intensity used in our LIED experiments is highlighted in gray with a 20 % error (shaded). **(c)** Normalized and vertically shifted $C_2H_2^{++}$ momentum distributions as the intensity is increased from bottom to top.

(red squares) and H^+ (blue triangles) ions were measured as a function of the peak intensity of our linearly polarized 3.1 µm source ($\tau \approx 70$ fs) as presented in Fig. 7.2 (a). In this measurement the C_2H_2 molecules were isotropically distributed. The yield of the cation, $C_2H_2^+$ (gray circles), shows a typical plateau-like behavior as the intensity is increased passed the point of saturation at $I_{Sat} \approx 4 \times 10^{13}$ W/cm^2 determined by fitting the cation yield with a sudden-onset function (Eq. 5.10 according to [289], see Sec. 5.3.2). In contrast to this observation, the yield of the dication, $C_2H_2^{++}$ (red squares) continues to increase as the intensity surpasses I_{Sat}. To emphasize the different trends also a scaled version of the $C_2H_2^+$ yield (black curves) is plotted that overlaps only at low intensities. As extensively discussed in Ch. 5, the point at which the dication trend starts to differ from the cation behavior is generally interpreted as the point at which the contributions of NSDI start to be exceeded by those of SDI [132]. The onset of SDI is more obvious when the data are plotted as a ratio of the ion yields, as presented in Fig. 7.2 (b). As expected from the above discussion, the $C_2H_2^{++}/C_2H_2^+$ yield ratio is quite flat at low intensities and then increases rapidly for $I > I_{Sat}$. This dramatic increase of the dication/cation ratio above I_{Sat} was similarly observed in our investigation on

the DI of xenon atoms in Ch. 5. In that experimental study, a comparison of the experimental data with classical Monte-Carlo simulations confirmed that it does indicate the transition point from NSDI to SDI. By comparing the investigations using mid-IR and 800 nm pulses (the latter taken from literature), another insight of Ch. 5 was that SDI regime predominates the NSDI regime for lower intensities. This is reasoned in the fact that the NSDI yield in the mid-IR is more than an order of magnitude lower due to lower return probabilities. We conclude that the behavior for acetylene molecules is similar yet already occurring for even lower intensities due to the lower I_P. Moreover, the saturation intensities of both the single ionization and SDI of molecular targets are generally expected to occur at slightly lower intensities than their "atomic siblings" being an atomic target with equal I_P, which has been studied in e.g. [276, Fig. 4] and [138, Sec. 4.5.2].

A similar analysis can be applied to the H^+ ion yield [blue triangles in Figs. 7.2 (a,b)] in the ToF spectrum gives which results from a C-H bond breakup in acetylene. In our case it shows very similar results, although the onset of "SDI-like" behavior seems to have been shifted to an even lower intensity near $I \sim 3$ to 4×10^{13} W/cm^2.

To further corroborate the DI regime transition for acetylene, the $C_2H_2{}^{++}$ ion momentum distributions are plotted in Fig. 7.2 (c). The double peak structure that results from NSDI is observed at low intensities. As the intensity is increased the "deep valley" of dications related to NSDI is filled up by ions corresponding to SDI peaking around $p_\parallel = 0$. Finally, the distribution transitions to a narrower single peak, which is representative of dominant SDI. This confirms the insights from the yield behaviors that for intensities of $I > I_\mathrm{Sat} \approx 4 \times 10^{13}$ W/cm^2 the SDI process starts to outweigh the NSDI process. Thus, in order to image the deprotonation reaction of acetylene with LIED in the SDI regime an intensity similar (or higher) to the one used in the previous chapter to image the cation ground state of acetylene ($I = 6.5 \times 10^{13}$ W/cm^2, see Sec. 6.5) needs to be selected. The intensity is represented by the gray shaded region in Fig. 7.2 (b). The width of the estimated intensity represents the intrinsic ± 20 % uncertainty when making absolute intensity measurements without being able to measure the beam width directly [178] (see Sec. 3.1.3).

7.1.3 Sequential ionization pathways of dication states

In this section, the pathways to populate the various dication states are discussed. The information of this section is taken from [365, 383]. The neutral ground state $^1\Sigma_\mathrm{g}^+$ consists of and fully occupies the following lowest-lying molecular orbitals: [$1\sigma_\mathrm{g}{}^2$, $1\sigma_\mathrm{u}{}^2$, $2\sigma_\mathrm{g}{}^2$, $2\sigma_\mathrm{u}{}^2$, $3\sigma_\mathrm{g}{}^2$, $1\pi_\mathrm{u}{}^4$] as sketched in Fig. 7.3. The exponents resemble the individually populated electrons on each orbital summed up to all 14 electrons of acetylene. The HOMO[6] of acetylene is a doubly degenerate $1\pi_\mathrm{u}$ orbital resulting from a superposition of p-orbitals of the carbon atoms that lie orthogonal to the molecular axis [365]. The next-lower HOMOs $3\sigma_\mathrm{g}$ (HOMO-1), $2\sigma_\mathrm{u}$ (HOMO-2) and $2\sigma_\mathrm{g}$ (HOMO-3) consist as superpositions of the carbon sp orbitals and the

[6] highest occupied molecular orbital

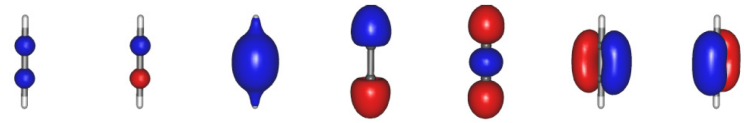

Figure 7.3: Molecular orbitals of the neutral ground state of acetylene. The lowest occupied orbitals of the neutral ground state $^1\Sigma_{g+}$ of acetylene are shown as calculated by [365].

hydrogen's $2s$. The *lowest occupied molecular orbitals* (LOMOs) of acetylene result from the carbon $1s$ orbitals [365].

The different ground and excited states of the cation and dication of acetylene as introduced earlier (see the relevant PECs along the C-H direction in Sec. 7.1.1) can be directly populated via the following tunneling pathways (sketched in Fig. 7.4). The ground state $^2\Pi_u$ of the cation is populated by detracting an electron from the HOMO ($1\pi_u$) while one electron removed from the HOMO-1 ($3\sigma_g$) results in the first excited cation state $^2\Sigma_g^+$. The further higher excited states can be directly populated from the even lower lying orbitals of the neutral ground state. In order to further ionize to the dication, the metastable (ground) states $^3\Sigma_g^-$, $^1\Delta_g$ and $^1\Sigma_g^+$ [green in Fig. 7.4 (b)] generally have two electrons missing from the doubly degenerate HOMO (each state with a different assembly of the four electron positions). The strongly dissociative excited states $^3\Pi_u$ and $^1\Pi_u$ [red in Fig. 7.4 (b)] both miss one electron from the HOMO ($1\pi_u$) and from the HOMO-1 ($3\sigma_g$)[7]. In this case, the tunneling of both electrons can either proceed from both first the HOMO and then HOMO-1 [left pathway in Fig. 7.4 (b)] or first the HOMO-1 and in a second tunneling step from the HOMO [right pathway in Fig. 7.4 (b)]. According to a rough estimate using the ADK rate [89] to calculate the probabilities of both pathways including their different subsequent I_Ps[8], the pathway on the right seems to be more probable by one order of magnitude than the one on the left, which, however, should still contribute significantly. The general physical processes determining the alignment features is not expected to change significantly depending on one of the two pathways (left and right), since the overall, symmetry-determined, structure of the orbitals will be similar in both cases. This description of the different pathways is described in more detail in [361, 365].

Due to their shape, both types of orbitals π and σ differ in angular ionization characteristics as plotted in Figs. 7.5 (a,b), so that they are experimentally distinguishable. π-type orbitals like the HOMO of acetylene are ionized preferably for the laser polarization perpendicular to the molecular axis ($0° \leftrightarrow 180°$) [see

[7] A rule of thumb here is the fact that a transition between two states being of Σ and Π type (states are named in capital greek letters) always involves the tunneling from a π orbital (in lowercase greek letters) of the neutral ground state, while a transition between two equal type states (Σ to Σ, or Π to Π) involves the release of an electron from a σ orbital.

[8] Left: first HOMO with $I_{P,1} \sim 11.4$ eV, then HOMO-1 with $I_{P,2} \sim 23.7$ eV. Right: first HOMO-1 with $I_{P,1} \sim 17.4$ eV, then HOMO with $I_{P,2} \sim 17.4$ eV.

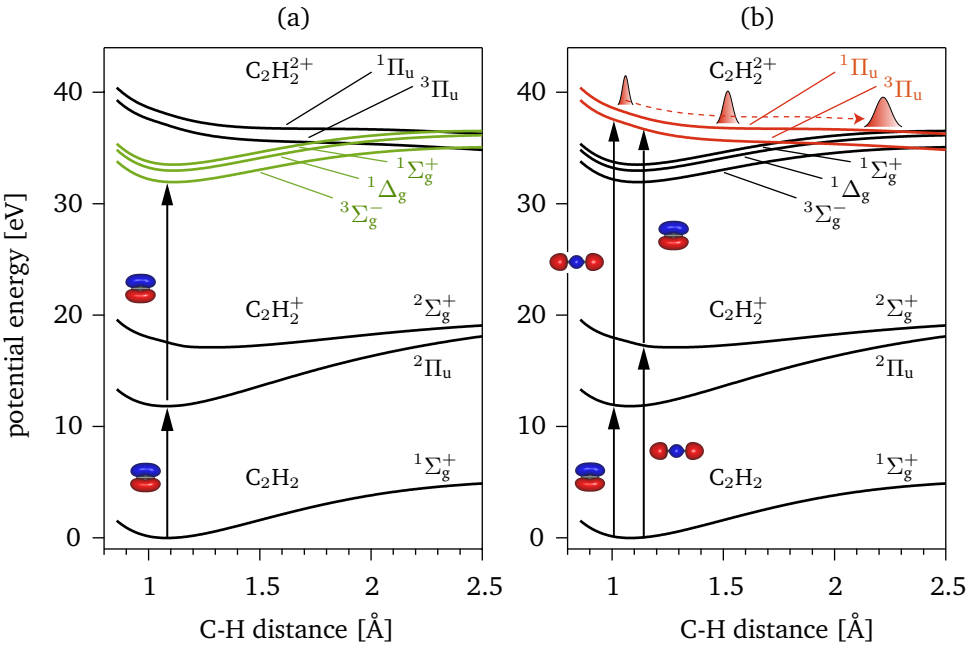

Figure 7.4: Relevant potential energy curves of acetylene and pathways to populate dication states. The PECs are shown for the cut along the C-H bond axis including the relevant states for the population of different dication states via two tunneling processes in the SDI regime. **(a)** In order to populate the metastable dication ground $^3\Sigma_g^-$ and first excited $^1\Delta_g$, $^1\Sigma_g^+$ states (all in green), two electrons are ejected from the HOMO ($1\pi_u$) of the neutral ground state of acetylene. **(b)** In order to populate the strongly dissociative excited states $^3\Pi_u$ and $^1\Pi_u$ (both in red), electrons tunnel both from the HOMO and the HOMO-1. The two possible pathways shown while the right pathway (first HOMO-1, then HOMO) has a one order of magnitude higher probability.

Fig. 7.5 (a) and also [365]] while σ-type orbitals like the HOMO-1 are ionized with the highest probability along the molecular axis ($0° \leftrightarrow 180°$) [see Fig. 7.5 (b) and also [365]]. The calculations behind the angular ionization distributions of the HOMO and HOMO-1 of acetylene were described in Sec. 6.5.3. Since the absolute ionization probability is higher from the HOMO than from the HOMO-1 by only a factor of 6 to 7 [365], SFI from HOMO-1 contributes substantially to the overall ionization of acetylene. This phenomenon has been observed experimentally and studied for several molecules [43, 153–156].

We show this dependency of the ionization probability of the various ionization and excitation states on the different molecular alignments by impulsively aligning the acetylene target molecules. Similarly to the previous chapter (see Sec. 6.5.3), we therefore overlay 1.7 µm pulses [98 fs duration and $(2.0 \pm 0.4) \times 10^{13}$ W/cm^2] into the interaction region of the gas target with the 3.1 µm pulses [70 fs duration and $(6.5 \pm 1.3) \times 10^{13}$ W/cm^2]. Having ensured that the 1700 nm pulse does not yield

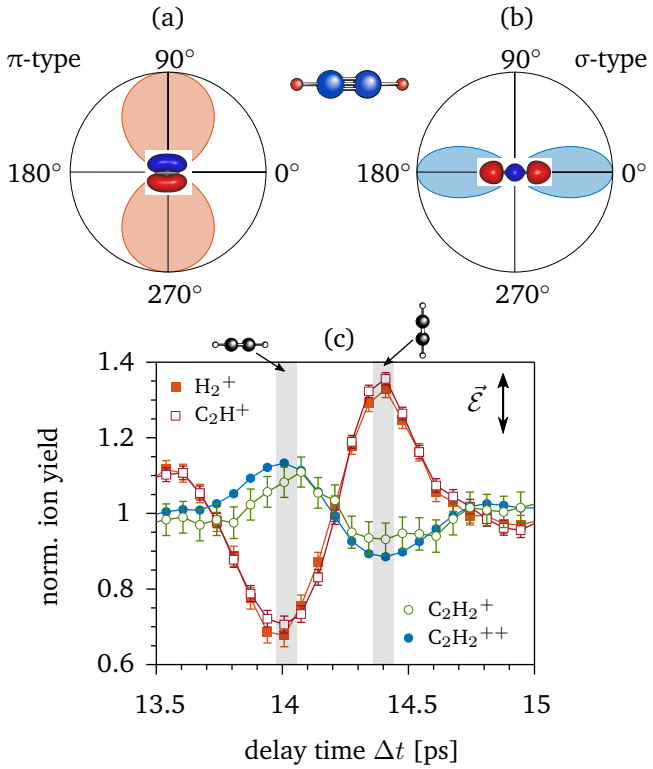

Figure 7.5: Angular ionization yield dependence of HOMO and HOMO-1. (a,b) The ionization yield of acetylene is calculated as a function of angle between the polarization and the molecular axis (between 0° and 180°) for **(a)** π-type orbitals like the HOMO and **(b)** σ-type orbitals like the HOMO-1. **(c)** The ionization yield as a function of delay time between the 1.7 µm alignment pulse and the 3.1 µm probe pulse. The cation $C_2H_2^+$ (blue) and the dication $C_2H_2^{++}$ (green) ground states show a maximum for the anti-alignment and a minimum for alignment implying SDI involving only π-type orbitals (so via the HOMO). On the other hand, the H^+ (light red) and C_2H^+ (dark red) fragments have their extrema out-of-phase with the ground states which means the two tunneling steps involve a σ-type orbital (HOMO-1) as expected in SDI of excited dication states.

ionization, the different ion fragments are collected with the ReMi using the higher static fields as utilized in the LIED measurements (see Sec. 6.4.1 and 6.5.4), and their ionization yield is mapped as a function of the delay time between the 1.7 μm and the 3.1 μm pulses. The results of the yield of $C_2H_2^+$ (blue), $C_2H_2^{++}$ (green) as well as H^+ (light red) and C_2H^+ (dark red) are plotted in Fig. 7.5 (c) over delay time around the expected full-revival of acetylene. The curves of $C_2H_2^+$ and $C_2H_2^{++}$ exhibit a maximum for the anti-alignment position around 14.05 ps and a minimum for the alignment position at around 14.40 ps according to Sec. 6.5.3. This agrees in both cases with the ionization from the HOMO releasing one and two electrons from the $1\pi_u$ orbital(s), respectively. On the other hand, both fragments H^+ and C_2H^+ corresponding to the deprotonation of acetylene resulting from excitation of the $^3\Pi_u$ and $^1\Pi_u$ excited states show curves with the extrema out of phase to the ones of the cation and dication ground state. With a maximum in ion yield for aligned molecules and a minimum for anti-aligned ones, the ionization involved one electron to tunnel from the $3\sigma_g$ being the HOMO-1. We made sure that both the proton and the C_2H^+ moiety belong together and so are triggered by the same laser pulse by a) detecting them in coincidence as shown in the next Sec. 7.1.4 and b) by adjusting the analogue triggering window of the ions to ± 2 μs around the main cation peak in the ion ToF spectrum (see Fig. 6.10). The latter results in the fact that the read-out is triggered when e.g. C_2H^+ yet not when a proton is detected. Hence, all detected protons must belong to the deprotonation of the dication since the read-out covers the whole ion ToF spectrum between two subsequent pulses yet the triggering window only the time span around the main ion. Like this, protons of the dissociation of the excited cation state $^2\Sigma_u^-$ are excluded since they are accompanied by a neutral ethynyl moiety.

The results show that we can populate the dissociative excited dication states $^3\Pi_u$ and $^1\Pi_u$ via SDI in two tunneling events from the HOMO-1 and the HOMO [see Fig. 7.4 (b)]. Moreover, this proves that the process involves SDI instead of NSDI (at least a higher probability) since in a population of $^3\Pi_u$ and $^1\Pi_u$ via re-collision of the first electron the alignment distributions of the resulting fragments would be in phase with the cation and dication ground state implying π-type ionization. This is because the re-collision ionization should be alignment independent as the population of a specific state is merely dependent on the return energy of the electron. The latter process has not been further investigated theoretically so far according to [365], yet an experimental study by Xie *et al.* [368] investigated the alignment dependence of the deprotonation dication channel. As they operated in a regime, where the excited states were populated both via NSDI and SDI, they were able to divide the alignment yield curves of the fragments for both regimes (possible by the coincidence capability of their ReMi detection system). Here, they found the behavior as described above where the SDI region showed an out-of-phase behavior in comparison with the cation and dication ground state in agreement with our results, while their NSDI region showed an in-phase alignment curve.

7.1.4 Photo-ion photo-ion coincidence (PiPiCo) analysis

In this chapter, we are specifically interested in investigating the fast deprotonation of the acetylene dication via the strongly dissociative states $^3\Pi_u$ and $^1\Pi_u$ with our mid-IR LIED imaging technique. Experimentally, the deprotonation reaction can clearly be identified and isolated by making use of coincidence selection with a ReMi detection system. In Figs. 7.6, the time-of-flight correlation between two detected ions is shown in form of a photoion-photoion coincidence (PiPiCo) distribution. In the PiPiCo distribution, a hit represents ions detected for the same triggering laser pulse. Hence, an agglomeration of counts in the PiPiCo distribution yields ion fragments from the same reaction, and more specifically a line shape results as products from a two-body dissociation reaction. If the line is sharp and pronounced in the PiPiCo distribution, it stems from a fragmentation reaction involving two ion fragments escaping in opposite directions with a specific internal energy that could be detected in momentum coincidence. A thick, blury line results from a three- or multiple body reaction where one or more reaction partners are missing in the 2D representation of the PiPiCo.

The data in Figs. 7.6 were taken with the same experimental conditions as the alignment curve above for both aligned (a) and anti-aligned (b) acetylene. The long line (upper left to lower right of Figs. 7.6) corresponds to the detected pair of H^+ and C_2H^+ in coincidence and can be divided into two different processes: a very pronounced section (centered around 820 ns/4120 ns) originating from the fast dissociation of the excited states $^3\Pi_u$ and $^1\Pi_u$ and a longer, more shallow and strongly curved tail which belongs to the meta-stable ground states $^3\Sigma_g^-$, $^1\Delta_g$ and $^1\Sigma_g^+$ of the dication that possess a long lifetime and hence a small probability to dissociate [385]. The insets of Figs. 7.6 shows a cutout of the line corresponding to proton-ethynyl pairs of the fast deprotonation that evidently holds the vast majority of hits in these time windows. The two shallow lines above and below belong to deprotonization reactions with different sums of the overall mass (above: involving a C(13u) atom; below: involving a neutral product that is not detected with the ReMi, e.g. from the three-body reaction $C_2H_2^{++} \rightarrow H^+ + C_2^+ + H$). Both of these processes as well as the slow deprotonation channel occur with less than two orders of magnitude of the probability compared to the fast deprotonation channel.

In order to extract the structural information of the dissociating molecules, the 3D momentum distribution of the photoelectrons associated with both reaction moieties needs to be isolated which is possible with the ReMi. By utilizing the coincidence information of only the electrons detected for the same trigger pulse as one H^+ / C_2H^+ pair corresponding to the pronounced line(s) in Figs. 7.6, we are able analyze the LIED diffraction signal of the reaction. Thereby it is possible to suppress electron background from other SFI and dissociation related processes and so to improve the signal-to-noise ratio in the LIED analysis. As a side note, on the bottom right of the PiPiCo distributions in Figs. 7.6, the lines corresponding to the other two main fragmentation processes being the symmetric breakup ($C_2H_2^{++} \rightarrow CH^+ + CH^+$) and the isomerization reaction ($C_2H_2^{++} \rightarrow C^+ + CH_2^+$). The lines are less developed compared to the deprotonation reaction due to the

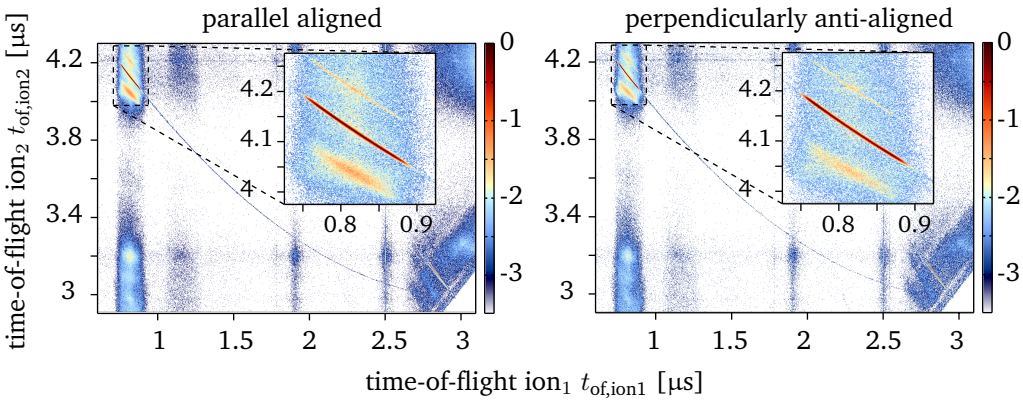

Figure 7.6: PiPiCo distributions for aligned and anti-aligned acetylene. The photoion-photoion coincidence (PiPiCo) distribution is shown for SFI of **(a)** aligned and **(b)** acetylene molecules with 3.1 µm pulses. The lines corresponding to the deprotonation reaction of the dication involving H^+-C_2H^+ pairs is shown as an inset. The two shallow lines above and below belong to deprotonization reactions with different sums of the overall mass (above: involving a C(13u) atom; below: involving a neutral product that is not detected with the ReMi, e.g. from the three-body reaction $C_2H_2{}^{++} \rightarrow H^+ + C_2{}^+ + H$). The bottom right corner reveals lines belonging to the symmetric breakup and the isomerization reactions.

lower branching ratios.

Another experimental resource to identify a dissociation reaction is the *kinetic energy release* (KER) which is potential energy brought into a molecular system by an external source, i.e. the initiating laser pulse that is then released and transfered to the products of the dissociation reaction. In the PES, the KER is the difference between the potential energies at the beginning of the dissociation and the potential energies at the asymptotic limit of that respective state [364]. The KER distributions corresponding to the detection of H^+ and C_2H^+ in coincidence for our experimental conditions are plotted in Fig. 7.7 for both alignments. Both KERs yield a similarly broad distribution peaking around ∼6 eV. This agrees nicely with [364] where a KER peaking around 6.0 eV is explained to result from dissociation along the excited $^1\Pi_u$ state, while the $^3\Pi_u$ yields a KER of 6.3 eV. In the same article it is shown that the metastable states $^3\Sigma_g^-$, $^1\Delta_g$ and $^1\Sigma_g^+$ dissociate with KERs between 3.25 eV and 3.75 eV [364]. In our data in Fig. 7.7, the contribution below <4 eV is minimized. Therefore, we can conclude that we detect the respective deptrotonation products from the strongly dissociative excited states $^3\Pi_u$ and $^1\Pi_u$. Moreover, the KERs for both alignment states of acetylene yield almost similar distributions which means that in both cases the same excited states are populated and the same dissociation reaction evolves.

It should be noted here that the data in [364] are triggered by single photon ionization in a weak field regime with linearly polarized 42-eV photons. Comparative data of KERs on the deprotonation of acetylene initiated by SFI with mid-IR laser

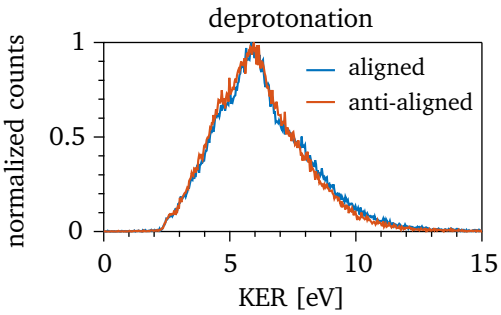

Figure 7.7: Kinetic energy release. The KER corresponding to H^+ - C_2H^+ pairs detected in coincidence are plotted for aligned (blue) and anti-aligned (red) acetylene molecues. The data correspond to the distinct line in the inset of the PiPiCo distribution plots in Figs. 7.6.

pulses are not available in literature to our knowledge. SFI induced deprotonation was investigated with 800 nm pulses by Xie *et al.* [368] as mentioned earlier and by Kübel *et al.* [387][9]. The former investigation shows the before-mentioned KER data resulting from deprotonation in both the SDI and the NSDI regime. The KER part corresponding to the SDI regime peaks at around 3.5 eV while the NSDI related KER part peaks at around 5 eV. Both don't agree with the results from [364] as described above, neither with our KER distributions. Moreover, the SDI-related out-of-phase alignment distribution (see above) corresponds to the low-KER region where dissociation from the metastable states is expected according to [364]. On the other hand, Kübel *et al.* [387] show a KER distribution shifted to higher values around 4 to 5 eV for similar intensities as [368]. These results seem not to agree with our KERs nor with the ones from [364]. The only agreement between our data and the one from Xie *et al.* [368] is that their (low-)KER corresponding to the SDI regime shows the same out-of-phase alignment trace as the the our whole KER distribution corresponding to all H^+ / C_2H^+ pairs. In contrast, their alignment distribution corresponding to the whole KER yields no alignment modulation.

7.2 Spatio-temporal imaging molecular structure during deprotonation

After successfully advancing the technique of mid-IR LIED to be able to image the polyatomic acetylene, we were interested in the question whether we could also extract structural information from one of the fragmentation channels that are triggered by SFI of acetylene. This would bring us closer to the goal of imaging a dynamic molecular reaction. Therefore, we chose to investigate the deprotonation process of the excited dictation which has the highest branching ratio for dissociations in acetylene and which was discussed in the previous Sec. 7.1 in detail.

[9] also on the ArXiv: https://arxiv.org/abs/1609.08577

What is interesting about the process is that the C-H bond break-up proceeds on ultrafast timescales in the few-femtosecond regime. A simple back of the envelope estimation of the initial speed of the C-H bond elongation, which is based on the KER peak values of ~ 6 eV of our measurement (see Sec. 7.1.4) in agreement with [364], yields an initial bond elongation or proton escape velocity of ~ 34 pm/fs[10] from the initial Frank-Condon region. In fact, we applied a quantum dynamical molecular wave packet calculation to obtain the time-scale of the deprotonation dynamics (explained and discussed in detail in Sec. 7.2.3). The results showed a velocity of the excited dication states of just below 20 pm/fs for both dressed and the field-free version of the states. This rapid dynamic makes the deprotonation reaction of acetylene the ideal candidate in order to test the combined spatio-temporal capabilities of the mid-IR LIED imaging technique.

7.2.1 Experimental parameters

The laser conditions we chose to measure the LIED signal of dissociating acetylene were similar to previous chapter. The 3.1 µm pulses were applied with a duration of ∼65 fs (6.3 cycles) and a peak intensity of 6.5×10^{13} W/cm^2 ($U_\mathrm{P} \approx 54$ eV, $\gamma \approx 0.33$, $z \sim 135$, $z_1 \sim 9.5$, $z_\mathrm{f} \sim 2.3 \times 10^{-4}$). The intensity is determined via the intensity calibration in Sec. 3.1.3 for a ±20 % error. The pulse parameters are chosen to position the experiment in an ionization regime where the population of the dictation states happens via SDI. As shown in Fig. 7.2 our intensity positions us in a regime where DI occurs sequentially (SDI) by more than a factor of 2 more than non-sequentially (NSDI). Hence, the LIED imaging electron is preferentially ejected independently from the first electron in a second tunnel ionization step before scattering off the acetylene dication. Again, we impulsively align the acetylene target molecules similarly to the previous chapter (see Sec. 6.5.3) by focusing our 1.7 µm pulses [98 fs duration and 2.0×10^{13} W/cm^2] into the interaction region.

As shown previously, the direct dissociation channel (via $^3\Pi_u$ and $^1\Pi_u$ state) that leads to the fast deprotonation of acetylene is populated with our laser conditions and can be isolated with the ReMi detection system (seen in the PiPiCo distributions of Figs. 7.6). Moreover, we made sure that every detected proton is a product of the dication deprotonation by setting the triggering window of the ions to ± 2 µs around the main cation peak ($C_2H_2^+$) in the ion ToF spectrum (see Fig. 6.10), so that the read-out of the whole ToF is triggered when e.g. C_2H^+ is detected yet not for a proton. Hence, all detected protons must belong to the deprotonation of the dication since the read-out covers the whole ion ToF spectrum between two subsequent pulses.

The electrons and especially the re-scattered electrons corresponding to this channel are detected with the conditions of the ReMi as described in Sec. 6.4.1 ($|\mathcal{E}| \approx 50$ V/cm^2 and $|\mathcal{B}| \approx 38$ Gs.) which we have used throughout all LIED measurements of this part of the thesis. The detection of four particles in coincidence is possible,

[10] $v = \sqrt{\frac{2\,\mathrm{KER}}{m_p}}$

but in momentum conservation condition a strong constraint with regard to statistics. For this reason, we consider in our analysis all those events in which both a proton and a C_2H^+ moiety are detected in the same laser pulse, so belonging to the line in the inset of the PiPiCo distribution. Then we extract all electrons that reach the detector for the same laser pulse in loose coincidence, without putting the momentum conservation constraint on the coincidence as discussed in Sec. 3.2.2.3. This loose coincidence analysis condition was also used in the LIED experiments in Ch. 6. Especially in the current case, the relieve of the full-4-particle momentum conservation constraint is beneficial for extracting higher statistics in detected electrons including the LIED signal and belonging to the deprotonation reaction.

7.2.2 Measurement of bond lengths during deprotonation

Having identified the direct deprotonation channel (via $^3\Pi_u$ and $^1\Pi_u$ state) along with its corresponding re-scattered electrons, we turn to extracting structural information from its corresponding re-scattering electrons. The resulting electron momentum distributions of this channel for our measurement of both aligned and anti-aligned acetylene are shown in Fig. 7.8 (a, left for aligned and right for anti-aligned acetylene). As described in Sec. 6.5, molecular structure is contained in the field-free molecular DCS (mDCS) which we extract according to QRS theory (see Sec. 6.3.1 and 6.4.2). The circle as drawn in black in Fig. 7.8 (a) corresponds to the angular distributed mDCS for return electron with a kinetic energy of 50 eV. The position of the molecules' nuclei is encoded in the coherent scattering term of the mDCS (extracted with $\Delta k_r = 0.15\, k_r$ and $\Delta\Theta_r = 4°$) which can be calculated in a renormalized form as the MCF (see Eq. 6.13 and 6.16). Fig. 7.8 (b) shows the resulting experimental MCF for both parallelly aligned (*A*, blue squares) and perpendicularly, (anti-)aligned (*AA*, red circles) acetylene. Striking differences are immediately apparent between the MCFs of both alignments, which indicates that different structural conditions of the target are observed. In the *A* case two extrema are visible with a minimum around $q \sim 3.5\,\text{Å}^{-1}$ and a maximum at $q \sim 4.7\,\text{Å}^{-1}$, as well as two zero-crossings at $q \sim 3.0\,\text{Å}^{-1}$ and $q \sim 4.0\,\text{Å}^{-1}$. The *AA* data however show a different progression with two minima at $q \sim 3.2\,\text{Å}^{-1}$ and $q \sim 4.6\,\text{Å}^{-1}$, a local maximum at $q \sim 4.1\,\text{Å}^{-1}$ and one zero-crossing at $q \sim 4.8\,\text{Å}^{-1}$. Both MCFs here are also different compared to MCFs of the data corresponding to the cation ground state [see Fig. **??** (e)].

The position of the individual scattering centers, and hence atomic distances, are extracted by comparing the measured MCF with a calculated MCF patterns for a range of possible positions. The theoretical MCF is calculated according to Eq. 6.13 via the IAM as described in Sec. 6.3.2. In this equation, an effective molecular alignment distribution for a cation was utilized as

$$\rho_{\text{eff}}(\Omega_L) = \rho(\Omega_L) \cdot N(\Omega_L) \tag{7.1}$$

being the product of the molecular alignment distribution $\rho(\Omega_L)$ and the angle-dependent ionization rate $N(\Omega_L)$. In the case of re-scattering from the sequentially

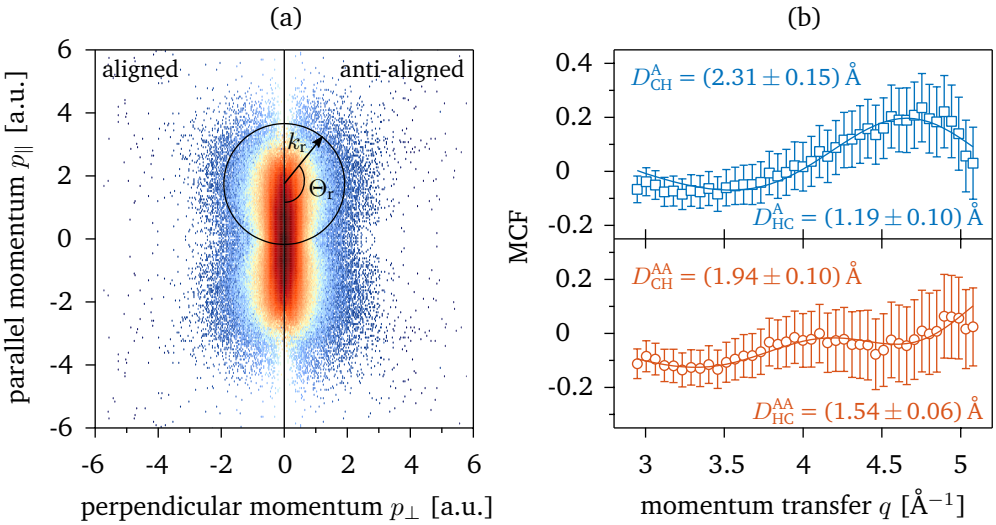

Figure 7.8: MCF extraction. (a) shows the electron momentum distribution in coincidence with the moieties corresponding to the fast deprotonation channel. The left half of the image shows data for parallel oriented, the right half of the image for perpendicularly oriented, acetylene. The molecular contrast factor (MCF) is shown for both cases, parallel (blue) and perpendicular (red) in **(b)**.

excited dication states $^3\Pi_u$ and $^1\Pi_u$ state the angular ionization distributions of both tunnel-ionization steps $N_1(\Omega_L)$ and $N_2(\Omega_L)$ need to be taken into account. Here, $N_1(\Omega_L)$ should be chosen as ionization from either the π-type HOMO or the σ-type HOMO-1, depending on the pathway, and $N_2(\Omega_L)$ is the ionization rate corresponding to a removal of an electron from the cation being the opposite of $N_1(\Omega_L)$ depending on which electron is removed from the neutral. Both calculated distributions were plotted in Figs. 7.5 (a,b) and need to be introduced in the calculation of the MCF (Eq. 6.13) as

$$N(\Omega_L) = N_1(\Omega_L)N_2(\Omega_L) \tag{7.2}$$

since both pathways are possibilities to get from the ground state of the neutral C_2H_2 to the dissociating excited dication as shown in Fig. 7.4 (b) (even though they appear with an order of magnitude different probability). Thus, the measured MCF including the effective molecular alignment distribution taking into account SDI via the HOMO and HOMO-1 are compared with these calculated MCF patterns in order to extract the full 3D solution space to determine the minimum fitted χ^2 value as a function of the C-C and both C-H distances similarly to Sec. 6.5.4. Note that the solution space results without assumptions such as partially frozen nuclei and includes all coherent, bond independent solutions for symmetric as well as asymmetric elongation of the C-H bonds. The χ^2_{min} values resemble the instant conditions of the molecular wave packet at the time of the electron's return.

The difference of the MCFs resulting for both alignments is reflected in the markedly

different resulting fitting solutions. For the aligned case [Figs. 7.9 (a-c) in blue] we measure a C-C bond length of (1.48 ± 0.17) Å which is a stretch to $\sim 123\,\%$ of the neutral acetylene's equilibrium value of 1.204 Å [363, 374]. The associated C-H distances are (2.31 ± 0.15) Å and (1.19 ± 0.10) Å corresponding to an elongation to 218 % and 112 % of the 1.06 Å equilibrium value [363]. This difference, in which one proton has more than doubled its distance to its neighbor, is a clear measure of deprotonation and the onset of bond breaking as expected for the excited state. This asymmetric stretch of only one of the C-H bonds seems intuitive when the polarization of the ionizing electric field is aligned parallel to the molecular axis. The scenario is markedly different for the anti-aligned case [see Figs. 7.9 (d-f)] for which we measure a C-C bond elongation to 116 % or (1.38 ± 0.06) Å slightly less then in the *A* - case, and measured C-H distances of (1.94 ± 0.10) Å and (1.54 ± 0.06) Å. This more symmetric scenario of C-H elongation to 183 % and 145 % of their equilibrium value is understandable considering the molecule is aligned perpendicular to the ionization field when being imaged by the LIED electrons; i.e. the molecule is pulled apart in a non-preferential direction by the strong laser field. The measured disparity of C-H distances for different alignments is interesting since it provides a control knob on the deprotonation process depending on molecular alignment.

The errors in all cases are corresponding to a χ^2 value being 25 % larger than the minimum χ^2_{min}. In order to highlight the error distribution within the 3D solution space, contours of fitting solutions that have values of $1.25\times \chi^2_{\text{min}}$ are plotted in blue in Figs. 7.9 (a-c, for *A*) and (d-f, for *AA*) where (a) and (d) show the 3D distribution and (b,c) and (e,f) the respective projections, similar to the cation ground state case of the previous chapter (see Figs. 6.18). The minima χ^2_{min} values of the 3D solution spaces are plotted in blue, while the the Franck-Condon values of the neutral [363, 374] and the meta-stable dication ground states [361] are shown in red and green, respectively. The different fitting solutions of both alignments appear clearly. There are two χ^2_{min} solutions (blue points) in our case due to a randomized CEP and hence solutions for both positive and negative electric field directions. In the aligned case, the χ^2_{min}s are positioned distinctively asymmetric in the aligned case [see HC/CH - projection in Fig. 7.9 (c)], while the solutions of the anti-aligned case [in Fig. 7.9 (f)] appear closer to the diagonal and hence to symmetric C-H bond elongations. Overall, both C-C bond solution spaces are stretched to values higher than the Franck-Condon point, which is expected according to the respective minima in the PECs along the C-C cut in Fig. 7.1 (a). In the aligned case, the uncertainty distribution of the C-C bond predicts the χ^2_{min} value at the lower end of the distribution while larger values are possible within the uncertainty. In the anti-aligned case, the uncertainty distribution for the C-C bond results symmetrically around the χ^2_{min}.

Moreover, the 3D solution spaces show fitting solutions for higher χ^2 values that are within error situated for different bond distances meaning that within error they fit the experimental data almost similarly. In the aligned case, this would be the solution for a symmetric C-H bond elongation to more than 2.3 Å hence a drastic elongation for both bonds at the same time in opposite directions. The case

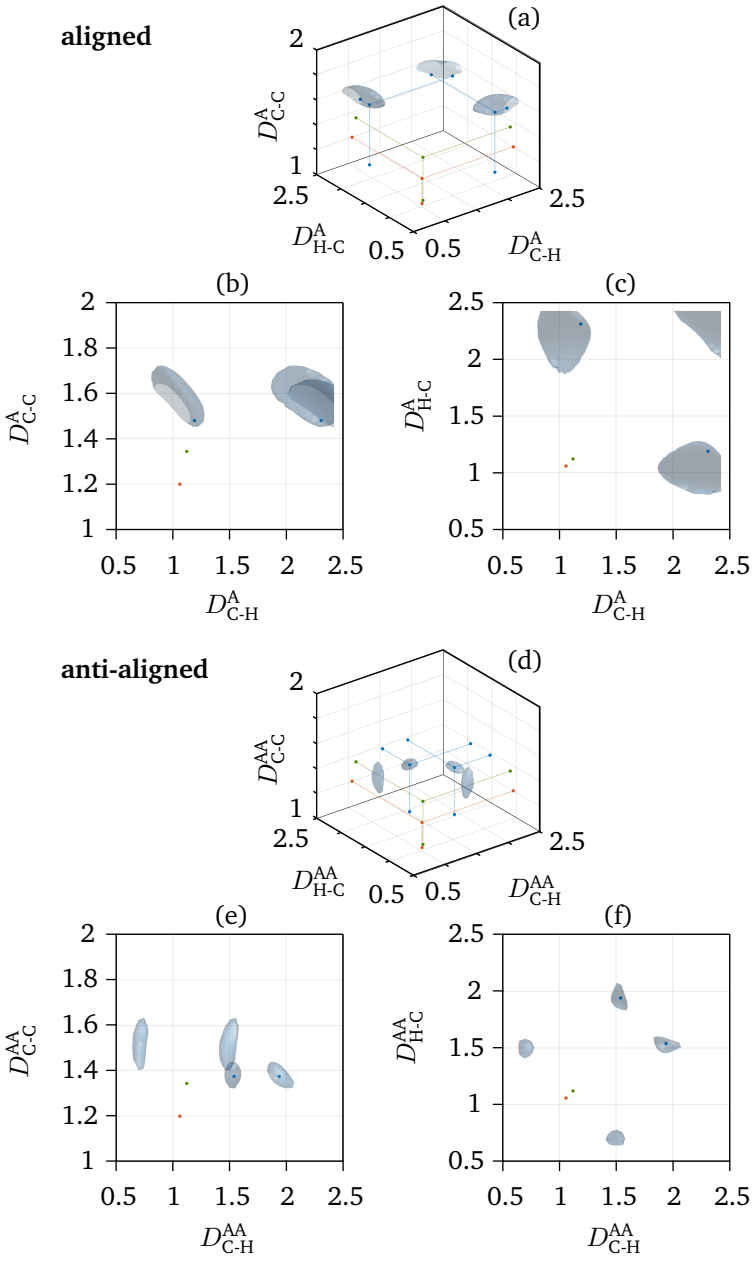

Figure 7.9: 3D χ^2 solution space of LIED imaging of the $^3\Pi_u$ and $^1\Pi_u$ states for two alignments. The minima χ^2_{min} values resulting from fitting over individual ranges of all three bonds (C-C, C-H_1 and C-H_2) are plotted in blue, while the the Franck-Condon values of the neutral [363, 374] and the meta-stable dication ground states [361] are shown in red and green, respectively, for **(a-c)** the aligned and the **(d-f)** anti-aligned cases. Moreover, the blue isosurface is taken at a value of $1.25\chi^2_{min}$ and represents the edges of the expected uncertainty in the measurement highlighting the error distributions of our experiment.

of both C-H bonds breaking at the same time is not included in our data which we took in coincidence with one H^+ and a C_2H^+ moiety. In the anti-aligned case, solutions can be found within error where one bond is stretched yet one bond is drastically contracted by around a factor of two. These solutions seem to be artifacts because no state in the PECs along the C-H bond cut [see Fig. 7.1 (b)] of acetylene shows a minimum for lower C-H distances than the Frank-Condon point. In order to verify the validity of these solutions in both cases, a larger DCS range and hence momentum transfer range or more return energies would give a more distinct solution space. In terms of return energies for our data of the deprotonation channel we are limited by suitable statistics for higher energies, and by the influence of direction electron going further below 50 eV. Moreover, theoretical modeling as performed in the next sections can give some indication of the physical (in)correctness of the artifact solutions. What is striking though is that both solution spaces do not offer solutions in the Franck-Condon regions. This is intuitively expected for the dissociating $^3\Pi_u$ and $^1\Pi_u$ states and shows that we can image the deprotonation process while it occurs.

A point that needs to be addressed is the question about the role of the first of the two sequentially tunneling electrons during the LIED imaging process of the dissociating dication wave packet. This question can be answered both from a quantum mechanical point of view where both electron wave packets are infinite in space and hence can leak into each other, and from a classical point of view of a point-like particle where the electrons are localized and can be regarded separately. In both cases, it needs to be assumed that the diffraction signal of the returning electron re-scattering off the dissociating dication as detected in our experimental data is triggered by the second electron due to the following argumentation. Firstly, the data cannot contain a diffraction signal that purely originates of re-scattering of a cation wave packet state as we detect all electrons in coincidence with the two respective ion fragments that result from a dication state. Secondly, if both electrons are tunneling for the same local electric field maximum, the question cannot be posed as both electrons have the possibility to re-scatter of the dication wave packet. On the other hand, if the second electron is tunneling for a subsequent electric field maximum with respect to the first electron, the first electron would see either the cation ground state $^2\Pi_u$ or its first excited $^2\Sigma_g^+$ as intermediate states in the sequential ionization pathways as explained in Sec. 7.1.3. Yet, both of these states are stable and slightly stretched with respect to the Franck-Condon region of the neutral ground state as shown in Fig. 7.1 (b). Hence, a diffraction signal of those states could not explain the experimental results as shown in Fig. 7.9 showing a clear, large stretch for at least one of the C-H bonds. Therefore, the second electron must be responsible for the diffraction signal as found in our experimental data.

7.2.3 Theoretical modeling of the deprotonation dynamics

Next we want to explain the difference in imaged structure between both alignments, i.e. strong asymmetric stretch of both C-H bonds in the *A* - case and and a

more symmetric stretch of both C-H bonds in the *AA* - case. Therefore, we employ a theoretical investigation using quantum chemistry and mixed quantum-classical ab-initio molecular dynamics methods in order to to realistically describe the molecular wave packet in the dressing mid-IR field with varying polarization direction and as function of time. The first method method focuses on the field free dynamics of the system, i.e. the distortion of the PESs due to the 3 μm field is not considered, whereby quantum chemistry PESs and quantum nuclear dynamics are employed to follow the dynamics of the system immediately after ionization. In the second approach the Stark deformation of the PESs due to the oscillatory electric field is explicitly taken into account by means of ab initio molecular dynamics simulations. The calculations were performed by two collaborating theory groups, namely Oriol Vendrell from Aarhus University, Aarhus, Denmark[11] and on the other hand by Katharina Doblhoff-Dier from Leiden University, Leiden, Netherlands, and Stefanie Gräfe of the Friedrich-Schiller University, Jena, Germany[12]. As their methods are sophisticated, they will be only summarized here according to the Supplementary information of our paper [381]. For further information, the reader should refer to the cited literature.

The electronic structure and dynamics of the system without Stark shifts are investigated via two approaches. The first one starts from the optimized linear structure of acetylene, obtained by second-order Møller-Plesset perturbation theory (MP2) [388] and the 6-311++G(d,p) triple-z basis [389] set as implemented in the Gaussian 09 program [370], a two-dimensional grid has been created to calculate potential energy surfaces (PESs) of the electronic singlet ground state of the neutral molecule, as well as for the ground and first excited state of the cation (doublet) and dication (triplet). The grid was expanded along the C-C bond and one C-H bond ranging from 1.0 to 2.5 Å and from 0.8 to 3.05 Å, respectively, and with a step-size of 0.15 Å and, hence, comprising 368 grid-points. The PESs have been generated using the multi-configurational CASPT2 [390] / CASSCF [391] (complete active space self-consistent field approach followed by second-order perturbation theory) methodology as implemented in the Molcas 8.0 suite of programs [392–394].

To obtain the time-scale of the deprotonation dynamics in the field-free case, we performed 2D quantum dynamical wave packet calculations, numerically solving the time-dependent Schrödinger equation for two nuclear degrees of freedom (C-H stretch) using cuts along the Born-Oppenheimer surfaces, which have been obtained by methods similar to those described above. For the propagation, we use the split-step method [395]. Since fully quantum dynamical calculations are computationally precluded when including all nuclear degrees of freedom moving in the Stark modified potentials by the presence of a strong laser field, we applied an alternative, mixed quantum-classical approach when simulating the field-driven molecular dynamics of $C_2H_2^{++}$.

The mid-IR LIED pulse exerts a maximum electric field amplitude of 0.039 a.u.

[11] at the beginning of our collaboration he was a member of the group of Robin Santra at CFEL in Hamburg, Germany

[12] earlier from the group of Stefanie Gräfe at Vienna University of Technology, Vienna, Austria

(2 V/Å) at the photon energy $E_\lambda = 0.4$ eV. Due to the strong field, the electronic wave function of the bound electrons in the $C_2H_2{}^{++}$ dication is modified beyond the perturbative regime. Moreover, the electrons adjust to the strong field adiabatically due to the long period in comparison with typical electronic time scales in molecules. The electronic structure of $C_2H_2{}^{++}$ is described in this regime by solving the TISE in the presence of the instantaneous electric field of the laser pulse

$$\left[\hat{H}_e(\vec{r},\vec{R}) + \vec{\epsilon}(t)\cdot\vec{\mu}(\vec{r},\vec{R})\right]\,\Phi_j[\vec{r};\vec{R},\vec{\epsilon}(t)] = V_j[\vec{R},\vec{\epsilon}(t)]\,\Phi_j[\vec{r};\vec{R},\vec{\epsilon}(t)] \tag{7.3}$$

where $(\vec{r},\vec{R})$ are the electronic and nuclear coordinates, respectively, H_e is the electronic molecular Hamiltonian including also the internuclear Coulomb repulsion, $\vec{\epsilon}(t)$ is the time-dependent electric field, $\vec{\mu}(\vec{r},\vec{R})$ is the dipole operator and $\Phi_j[\vec{r};\vec{R},\vec{\epsilon}(t)]$ are the adiabatic field-following electronic states. Consequently the potential energy surfaces $V_j[\vec{R},\vec{\epsilon}(t)]$ are not only a function of the nuclear coordinates $\vec{R}$, but also of the instantaneous electric field.

Within this context, the three lowest energy spin singlet electronic states ${}^1\Delta_g$, ${}^1\Sigma_g^+$ and ${}^1\Pi_u$ of the $C_2H_2{}^{++}$ ion (the respective triplet states behave equally) were computed at the complete active-space self-consistent field (CASSCF) level of theory using an active space with all 8 valence electrons and 8 molecular orbitals and employing the correlation consistent cc-pVDZ atomic basis set [396]. The two core molecular orbitals ${}^1\sigma_g$ and ${}^1\sigma_u$ were kept inactive but were allowed to relax in the self-consistent wavefunction optimization. Electronic structure calculations were performed with the GAMESS-US package [142]. The electronic state assignments agree with previous experimental [361] and theoretical results [397]. The molecular dynamics of $C_2H_2{}^{++}$ in the dissociative ${}^1\Pi_u$ electronic state were generated with our own mixed quantum-classical dynamics routines. Quasi-classical molecular dynamics trajectories were obtained by sampling initial atomic positions and momenta from the quantum distribution of the vibrational ground state of the neutral system, and propagating those classically in time in the presence of the oscillating electric field. The required nuclear gradients $\nabla_R V[\vec{R},\vec{\epsilon}(t)]$ were calculated on-the-fly along the classical trajectories as required. A total of 25 trajectories were propagated and averaged per field polarization direction and carrier envelope phase. Adiabaticity of the nuclear dynamics with respect to both nuclear displacements and variation of the electric field was checked by propagating the electronic amplitudes in the manifold of singlet electronic states along the classical trajectories [398]. Less than 1 % amplitude was transferred from the ${}^1\Pi_u$ state to other states due to either nuclear motion or electric field induced transitions.

In the field-free case good agreement was found between the quantum-dynamically calculated elongation of the C-H bond after 9 fs (corresponding to the flight time of the electron with 50 eV return energy, as further examined in Sec. 7.2.5) with in the 2D potential energy surface of the ${}^1\Pi_u$ state and the classical full dimensional calculations.

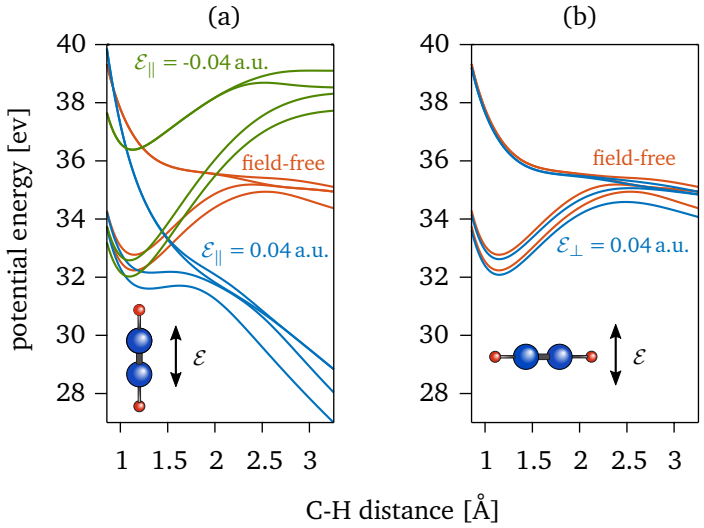

Figure 7.10: PES of the acetylene dication dressed with the mid-IR LIED field. The field-free case is shown in **(a)** and **(b)** in red. **(a)** shows how the PESs Stark-shift when dressed by the mid-IR LIED field when it is aligned with the molecular axis. For one field direction ($\mathcal{E} > 0$), all dication PESs are strongly dissociative (blue) while for the other field direction ($\mathcal{E} < 0$), the PESs present a bound scenario. Note that the trend is exactly reversed for the other C-H bond. **(b)** shows the doubly degenerate scenario for alignment perpendicular to the mid-IR LIED field for which we find slight PESs shifts, but not the dramatic Stark shifts shown in **(a)**.

7.2.4 Control over field-enhanced and field-free deprotonation

Before analyzing the time-dependent dynamics of the nuclear wave packet(s) in the dissociating dication states, the influence of the laser field on the differently aligned molecules and their electronic structure in general is regarded more closely. Therefore, the dressed PECs of the dication are presented in Figs. 7.10 for (a) aligned and (b) anti-aligned molecules in the presence of the 3 μm field. Both figures show, for clarity, only the dication's singlet ground and excited states ($^1\Delta_g$, $^1\Sigma_g^+$, $^1\Pi_u$). The triplet states ($^3\Pi_u$ and $^1\Pi_u$) behave similarly. The field-free case is depicted by the red curves and it is identical to the dication PES shown in Figs. 7.1 (b) and 7.4. For the case of the field parallel to the molecular axis in Fig. 7.10 (a), stable equilibria can be found for all regarded states including the initially highly dissociative $^1\Pi_u$ state if the sign of the field direction is such as to pull the hydrogen atom towards its neighboring carbon atom ($\mathcal{E} > 0$ in green). Once the field direction reverses, half a cycle later, all PECs ($\mathcal{E} < 0$ in blue) become strongly dissociative and the C-H bond is rapidly breaking. Note that Figs. 7.10 show the internuclear separation for only one of the two C-H bonds, i.e. the exact opposite scenario occurs at the same time for the other C-H bond; i.e. exchange the blue with green PECs. In total, during one electric field cycle (10.3 fs for 3.1 μm), one C-H is always breaking while

the other C-H bond is only oscillating in a vibrational state. This reflects nicely the results we extracted in the experimental case of aligned acetylene.

The perpendicular case is different as no preferential axis is induced by the 3 μm field and, hence, two degenerate cases exist. Thus, Fig. 7.10 (b) exhibits no field direction dependence and only minimal modification of the field-free PECs. The different scenario corresponds to slower bond dynamics with eventual breakup. The perpendicular case is therefore in stark contrast with the parallel scenario, since the mid-IR field itself does not noticeably distort the PESs and, consequently, the acetylene dication behaves like a quasi field-free electronic system. Thus, the perpendicular orientation allows imaging molecular structure with quasi-field free dynamics despite using a strong laser field. Overall, the dependence of deprotonation dynamics on the molecular alignment state permits control over the speed and visualization of molecular dissociation.

7.2.5 Spatio-temporal snapshots of the deprotonation reaction

Having applied calculations (see Sec. 7.2.3) of the evolution of the nuclear wave packet in the field-dressed dissociative states ($^3\Pi_u$ and $^1\Pi_u$) as a function of time for both alignments, we can compare the theoretical results with our experimental findings. Therefore we have to link the measured structure to the time when the snapshots were taken and hence make use of the intrinsic time resolution of LIED. In our experiment, electrons with 50 eV return energy are analyzed since they yield the highest number of counts for the largest angular coverage of the particular deprotonation channel and hence the best scattering momentum transfer. Based on the semi-classical re-scattering model, the time of return and the backscattering energy for the scattering electron are determined to have re-encountered the target after 9.15 fs (10.3 fs correspond to 1 optical cycle) and e.g. backscatter for a final maximum energy of $E_{\text{resc.}} = 188$ eV as illustrated in Fig. 7.12 (a).

In Figs. 7.11 the numerical results of the probability density of the nuclear wave packet at 9.1 fs after initialization in the $^3\Pi_u$ and $^1\Pi_u$ states at the Franck-Condon region are plotted for both (a) the aligned and the (b) anti-aligned case (logarithmic normalized color scale). Moreover, the experimental results of the fitted χ^2_{min} in the CH_1/CH_2 - plane are plotted as well in Figs. 7.11 for comparison. In both cases, the numerical results (maximum in red) come close to the experimental data points (white) within error. The different behavior of both alignment cases emerges clearly from the numerical results confirming the experimental findings. Markedly visible is the is the strong asymmetric stretch of both C-H bonds in the parallel field case while in the perpendicular case the C-H bonds are slightly more symmetric towards the diagonal in the CH_1/CH_2 - plane. Also it should be emphasized that the numerical results show distinct positions of the wave packets which clearly dismiss the validity of the artifactual solutions found in the experimental fitting solution space, i.e. the symmetric solutions in the aligned case for strong simultanous stretch of both C-H bonds, and the solutions below the Franck-Condon point in the anti-aligned case. Moreover, the corresponding numerical solutions for

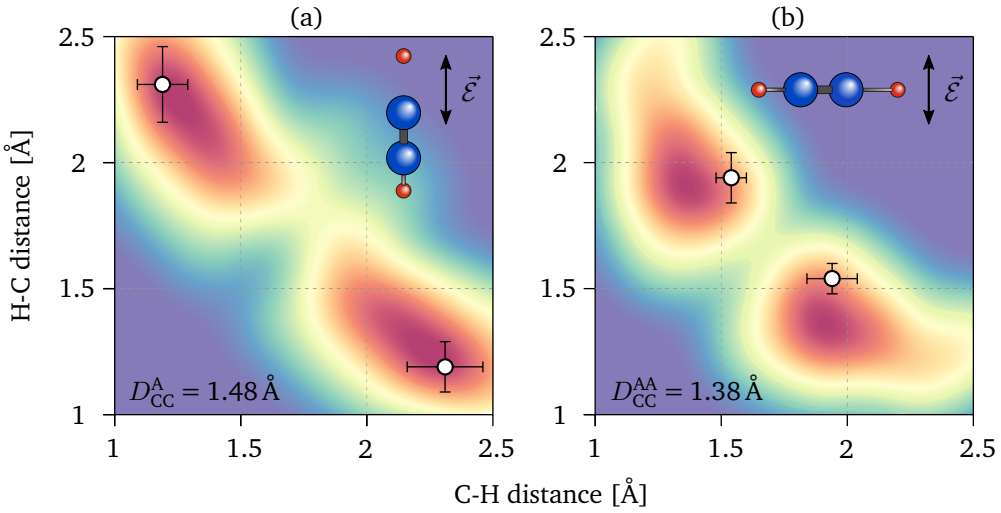

Figure 7.11: Comparison between experiment and theory of the presence of the nuclear wave packet in the $^3\Pi_u$ and $^1\Pi_u$ states. (a) and **(b)** show experimental data (white data points with error bars) overlaid with numerical results in form of the probability density plot for cuts through the 3D solution space at the location of its minima. Both the experimental data and the numerical results correspond to the electron re-encountering the target at 9.15 fs after population. This corresponds to C-C distances of 1.48 Å for the parallel case **(a)** and 1.37 Å for the perpendicular case **(b)**. **(a)** shows elongation of one C-H bond to more than twice the equilibrium bond length, corresponding to bond breakage, while the other C-H bond is still bound. **(b)** represents a more symmetric scenario nearing breakage of one of the two C-H bonds.

the C-C bonds are 1.45 Å for the aligned and 1.40 Å for the anti-aligned case which are in agreement with the corresponding experimental values [(1.48 ± 0.11) Å for *A* and (1.38 ± 0.06) Å for *AA*] within error.

To corroborate these findings, we additionally analyzed our measurement for two closely neighboring energies of 48 and 52 eV, and for which we achieve high count rates with satisfactory signal-to-noise. The overall temporal spread is negligible compared to the timescale of the reaction as these three measurements interrogate the molecular structure during a small temporal range between 9.1 fs and 9.2 fs, indicated by the vertical gray bars in Figs. 7.12.

All experimental results for the three scattering energies (circles with error bars) are summarized in Figs. 7.12 (b-g) where they underlaid with numerical probability densities of the dynamic evolution of the nuclear wave packet in dissociative excited dication states over the course of the first 20 fs comparing all bond distances for both alignments. The results from Figs. 7.11 are indicated by the pink filled circle. For parallel alignment in Figs. 7.12 (b,d,f), the molecule experiences the full electric field strength along its molecular axis and gets maximally distorted. This scenario corresponds to rapid elongation of one C-H bond [Fig. 7.12 (b)] and

breakage, which can be defined at twice its equilibrium distance[13], after ∼8 fs. The other C-H bond [Fig. 7.12 (d)] experiences an oscillatory elongation in the presence of the mid-IR field and the C-C bond [Fig. 7.12 (f)] vibrates with a period significantly longer than the mid-IR field's optical cycle.

The dynamics change markedly for perpendicular (anti-)alignment in Figs. 7.12 (c,e,g), which closely approximates a quasi field-free imaging scenario [see Fig. 7.10 (b)]. Here, we find that the C-C bond undergoes very similar vibrational excursion as for the parallel case throughout the course of the mid-IR pulse staying bound due to the stiffness of the bond. The two C-H bonds however show strong probabilities to both oscillating in phase with the LIED field and, at the same time, for dissociation of one of the two. This behavior is sensible, over the shown time range, considering that there exists no preferential direction that would result in different dynamics for one C-H bond compared with the other. Within the electron's excursion, of less than one optical cycle, an asymmetry is still found with strong probability for one C-H bond to break.

In general, all measured snapshots exhibit excellent agreement with the expected behavior of the molecule. Based on these findings we can corroborate the full spatio-temporal structure of the hydrocarbon molecule acetylene 9 fs after excitation of its dissociating excited dication states ($^3\Pi_u$ and $^1\Pi_u$). The snapshots of the spatio-temporal structure were taken with 0.6 fs temporal resolution and are capable of distinguishing the different kinetic behavior of the molecule field ionized parallel or perpendicular to the mid-IR field. The time resolution is limited to energy ranges for which sufficient counts are measured. The corresponding, extracted momentum range is averaged over ± 0.3 a.u. which determines the return time to $t_r = (9.1 \pm 0.2)$ fs. The same calculation for the ionization/emission time of the electrons results in $\Delta t_i = 0.05$ fs. Therefore this simple estimate gives $\Delta t_p = \sqrt{0.20^2 + 0.05^2} = 0.21$ fs based. Additional estimated uncertainties of the classical model need to be taken into account according to [328]. This adds an uncertainty for the ionization/emission time of 0.5 fs and 0.2 fs for the return time corresponding to our mid-IR field. Hence, we can estimate an overall temporal resolution of $\Delta t_p = \sqrt{0.20^2 + 0.05^2 + 0.2^2 + 0.5^2} \sim 0.6$ fs.

These results provide the first spatio-temporal snapshots of molecular structure with few-picometer spatial and few-femtosecond temporal resolution while a chemical bond is breaking. It demonstrates real space and time imaging of a single acetylene molecule after 9 fs while one of its bonds is broken and a proton has departed the molecule. The present investigation outlines important general aspects of LIED imaging for a molecule that is large enough to show the hallmark features of more complex molecules such as conical intersections or structural transformation. Firstly, we have imaged one of the fastest reactions, deprotonation, whilst simultaneously resolving all individual bonds of a polyatomic molecule in space and time. We take snapshots of the deprotonation reaction of acetylene within 9 fs and visualize directly the dissociation of one of the C-H bonds while the resid-

[13] The definition of when a bond is broken and when not is in the eye of the beholder. Since convoluted wave packets are involved the threshold for an exit has to be defined subjectively.

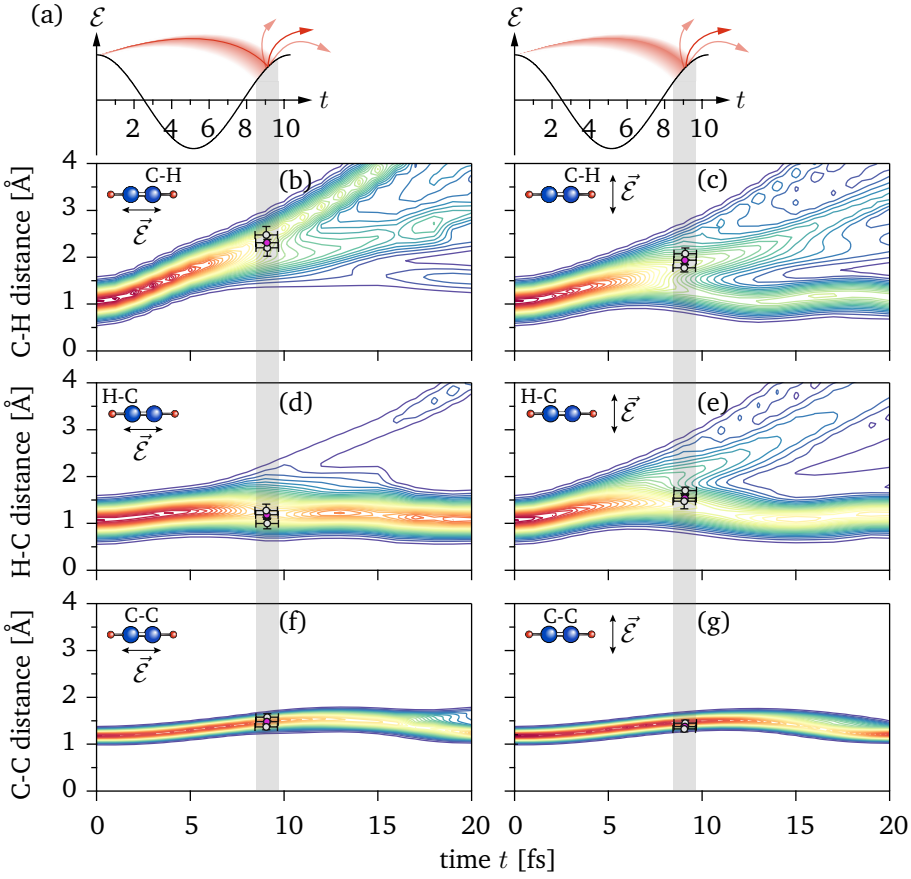

Figure 7.12: Temporal dynamics of acetylene resolved for the different bonds and as function of orientation. **(a)** shows the temporal range which was imaged for electron energies ranging up to 195 eV in accordance with the semiclassical rescattering model. Mixed quantum-classical dynamical calculations are shown in **(b-g)** for parallel **(b,d,f)** and perpendicularly oriented **(c,e,g)** acetylene. Extracted bond distances from the snapshots taken between 9.1 to 9.2 fs are overlaid onto the calculations and exhibit excellent agreement; the results corresponding to Fig. 2 are shown in pink. Differences for bond elongation between the parallel **(b,d)** and perpendicular **(c,e)** case are clearly resolved.

ual C-H and C-C bonds undergo oscillatory motion. Secondly, we demonstrate that even the simple distinction between parallelly and perpendicularly aligned molecules reveals different dissociation pathways that LIED is able to accurately spatio-temporally resolve. The found dependence of the reaction on molecular alignment permits control over the speed and occurrence of dissociation on the few femtosecond timescale. Thirdly, we show that quasi field-free molecular dynamics can be imaged with LIED when using perpendicular orientation and despite the strong laser field. Finally, our work shows that LIED provides intrinsic pump probe capabilities to access the sub- to few-femtosecond timescales of bond breaking and ultrafast proton motion.

Chapter 8

Conclusions and Outlook

In this thesis, the interaction of intense, ultrafast mid-IR waveforms with atomic and molecular gas-phase targets was studied. Of particular interest in this SFI process is the post-tunneling behavior of the detached electron in the mid-IR field and its re-collision with the parent ion. The latter yields elastic scattering and diffraction which we utilized to image and probe molecular structure and dynamics. The interest of driving strong-field re-collisions with long wavelengths is reasoned from the many benefits implied in comparison to the near-IR laser sources like e.g. the ubiquitous 0.8 μm radiation of Ti:Sapphire based laser systems which have been the workhorse of the field in the last two decades. Some of the most relevant benefits of mid-IR drivers to this study are: 1) the unambiguous creation of interaction conditions that are conducive for classical interpretations of experimental results; 2) strong-field re-collision at low peak intensity in order to avoid appreciable ground state depletion; and 3) the ability to create high energy ($E_{\text{kin}} \sim \lambda^2$) re-collision electrons for imaging applications. However, long wavelength (ponderomotive) scaling comes at the cost of a reduced signal ($\propto \lambda^{-4}$) which translates into reduced statistics or long data acquisition times. This problem becomes crucial for detection techniques which only detect a small fraction of the entire momentum space. These points are often overlooked but they present a significant roadblock to the advancement of SFP. This is because experiments will eventually become untenable due to the required acquisition times exceeding the stability of the apparatus.

The experimental methodology used in this thesis to harness the benefits and to overcome the limitations mentioned above combines two tools that are perfectly suited for mid-IR SFP: 1) an intense and high repetition rate optical parametric chirped pulse amplification based mid-IR ($\lambda = 3.1$ μm) source that creates ionization conditions deep in the quasi-static (tunneling) regime and that can generate return electron energies above 1 keV; and 2) a reaction microscope detection system that can image the 3D momentum space of the interaction in full particle coincidence. The setup allows to generate and detect electrons with return energies that span a six order of magnitude range and thus provides an accurate 3D view of strong-field interactions.

The experimental investigations performed and the results obtained in the course of this thesis can be divided into two main parts. On the one hand, peculiarities of the SFI and its electron re-scattering process when driven in the mid-IR were

subject to investigation in Part II. This involved the "ionization surprise" [65] being electrons bunching for specifically low energies when crossing the ionization threshold. These low energy structures are predominantly existent for SFI with longer wavelength, in Ch. 4. Next, the subject of mid-IR re-collision induced double ionization for the case of xenon atoms as an example of a many-electron system was investigated in Ch. 5.

On the other hand, our experimental methodology is used to overcome physical and experimental limitations of LIED imaging in order to resolve structure and dynamics of polyatomic, heteronuclear molecules. We utilized the diffraction imprint from elastically re-scattering electron wave packets to resolve the structure and dynamics of acetylene in Part III. Thereby, the ponderomotively up-scaled kinetic energies of the returning electrons are used to provide enough momentum transfer to probe the entire molecular target at once, and determine its individual bond length with few picometer spatial resolution (see Ch. 6). Lastly, mid-IR LIED is used to take spatio-temporal snapshots of the dissociation of acetylene's outer bonds in Ch. 7 witnessing the escape of a proton within 10 fs after ionization. In the following, all individual chapters are concluded in more detail with outlooks on possible future investigations.

Energy bunching for electrons crossing the ionization threshold

Atomic ionization by intense, long wavelength pulses produces low electron energy features that the strong-field approximation, which is expected to be valid in the tunneling ionization regime characterized by small Keldysh parameters ($\gamma \ll 1$), cannot describe. These features include the low-energy structure [58,59], the very-low-energy structure [59, 196], and the more recently found zero-energy structure [60]. They result from the interplay between the laser electric field and the atomic Coulomb field which influences and controls the low-energy spectrum also for small γ as was found out by several theoretical investigations [220, 222–224, 226, 228].

In Ch. 4, a joint experimental and theoretical study was presented where the vectorial momentum spectrum of photoelectrons emitted from an Ar gas target at very low energies was analyzed as a function of pulse durations (4 to 13.5 cycles). We used our ReMi detection system optimized for the detection of very low energy electrons by applying a combination of low static electric and magnetic fields. Thus, we performed a thorough study of the 3D electron momentum spectrum well below 1 eV. For each set of laser parameters, two measurements were taken with two slightly shifted static magnetic field on the ReMi (and apart from that constant detection and laser parameters), so that we were able to detect an optimized, "node"-free momentum space between for a maximum range of $p_{\parallel} = \pm 1$ a.u. In doing so, we were able to resolve three different orders of LESs together with a V-shaped structure centered around $p_{\parallel} = 0$ at once. Moreover, a pronounced agglom-

eration of counts for $p_\perp \sim 0.01$ a.u. was identified as the ZES. In order to shed light on the mechanisms behind all different structures and to disentangle their origins, we complemented our experimental results by quantum and classical simulations. The TDSE calculations were performed by Xiao-Min Tong from the University of Tsukuba, Japan, and the CTMC simulations were calculated by Christoph Lemell from Vienna University of Technology for our experimental conditions.

We obtained excellent agreement between the electron trajectories resulting from the CTMC simulations compared to our experimental data. This allowed for an interpretation of the LESs and the VLES in terms of two-dimensional Coulomb focusing of electron trajectories returning to the vicinity of the parent ion and softly re-scattering in forward direction. This "soft kick" [220] by the Coulomb field leads to energy bunching of the electron trajectories which can occur on multiple returns leading to multiple orders of LESs. We were able to detect LESs until the third order in the experimental case while yielding five orders in the CTMC data for our experimental conditions. By extracting the momentum positions of the different orders of LESs from our experiment and the CTMC simulation as a function of pulse duration we found a non-linear trend of decreased electron momentum / kinetic energy for the LESs with decreasing pulse duration. Moreover, we were able to confirm this trend by fitting our results against an analytical model as proposed by [246] which within error agrees for our experimental conditions. This result supports the soft re-collision related mechanism behind the LESs.

We also found a clear V-shaped structure in the vectorial momentum distributions of our experimental data at very low energies ($E_{\text{kin}} < 0.5$ eV), referred to as VLES as dubbed in [196]. In comparison with theory, we found that the VLES results from high-order focal points in the combined Coulomb and laser fields. Changes of structures in the vectorial momentum distributions reflect that the VLES shifts towards larger angular momenta with increasing pulse length. This leads to a narrowing of the V-shaped structure in momentum space which we can resolve experimentally. Moreover, a quantum-orbit analysis by [247] was able to confirm our results by relating the V-shaped VLES and the off-center LESs positions to differences in phase space between the single trajectories.

Next, we identified the ZES as electrons populating high-lying Rydberg states in the SFI process. We ascertained this fact as the electron trajectories belonging to the ZES ended up with negative kinetic energy in the CTMC simulations. Only by including a static electric field simulating the extraction field of the ReMi, we were able to connect them to electrons released via field ionization and distributed in the momentum spectrum around $p \sim 0$. The ZES provides, thus, quantitative information on the process of recapture of tunnel-ionized electrons and represents a projection of the Rydberg population onto the momentum plane. The recapture process was related to the frustrated re-collision population (known as FTI) instead of MPI. We corroborated this fact by comparing the negative kinetic energy spectrum between our CTMC and TDSE calculation. Moreover, the quantitative agreement between both simulations showed that the quantum-classical correspondence holds also for this low energy portion of the electron spectrum. This is not trivial in first approximation due to the large de-Broglie wavelength of electrons with

energies in the meV range.

The population of Rydberg states via FTI holds plenty of questions for future investigations. Due to the fact that without ionization by a static field the target atoms remain neutral, and hence cannot be easily detected. FTI might be one of the main effects within the re-collision model that might have been overlooked in the past. Also different ionization releases of the populated Rydberg states in dimers [233] hold unresolved questions. On the other hand, the ZES was also related to "ultra" soft re-collision far away from the Coulomb center analogous to the LES. In that regard, the position of the ZES would scale with I_P^2 which gives rise to an investigations of the ZES for atomic targets with higher I_P like e.g. helium atoms.

Non-sequential double ionization of xenon atoms in mid-IR fields

Double ionization in strong laser fields has been under highly engaged focus of the community over a decade ago. Back then, the capabilities of ReMi detection systems were used to characterize the DI mechanism not just by the ion yield as a function of intensity but also in terms of the ion momentum distribution [262] and electron correlation distributions [263]. Since then, many questions about the mechanisms behind NSDI and SDI in various target systems could be solved in great detail using a "fully differential investigation" [3] including ion yield and momentum as well as electron correlation distributions.

A topic that we found to be covered insufficiently in literature to date is the understanding of strong-field double ionization in many-electron systems throughout different intensity regimes. This depicts an important fundamental problem with potential implications for molecular imaging amongst others. Also, we found that amongst all noble gas targets that were investigated, Xe atoms were never investigated in the early years with a "fully differential investigation" up until [3]. On top of it, [3] found contradicting behavior of the NSDI regime showing no electron correlation and no double-hump behavior for a wide range of intensities where it should be expected compared to other atomic targets. Using mid-IR radiation, we investigated the transition between DI regimes in Xe atoms at an intensity below $10^{14}\,\mathrm{W/cm^2}$. Thereby, we could show for the first time that strong-field ionization of Xe atoms in the mid-IR also progresses from NSDI via the (e, 2e) mechanism at intensities near $10^{13}\,\mathrm{W/cm^2}$ to SDI as the intensity is increased towards $10^{14}\,\mathrm{W/cm^2}$.

The main insights of our experimental and theoretical investigation are that

1. the transition of NSDI to SDI of Xe atoms can be unambiguously identified with mid-IR laser pulses within a fully differential investigation,
2. SDI starts to dominate over the NSDI (e,2e) mechanism well below 1.0×10^{14} W/cm^2 with mid-IR driving fields due to the lower return probability of e_1,

3. the ionization pathway via the $5s5p^6$ orbital occurs primarily for lower intensities and
4. the NSDI specific (e,2e) features like the double-hump structure in the ion momentum distribution and a correlation of e_1 and e_2 in the e2e1 map can be clearly observed in contrary to investigations at 800 nm [3].

Especially, the latter finding is interesting since the non-existence of the double hump and electron correlation for DI of Xe with near-IR fields was convincingly explained by the influence of the shielding potential of the residual inner-shell electrons [3]. This was modeled in agreement with their experimental findings [260]. Our results though insinuate that these shielding effects have no influence on the NSDI process when driven with mid-IR fields. A possible explanation for this phenomena could be the higher return energies in our mid-IR case compared to the near-IR. The shielding potential is "felt" less repulsive by the returning electron which might lead to a higher probability for inelastic scattering of the return electron with the parent ion.

In future investigations, this context could potentially be interrogated experimentally by a systematic study of the appearance of characteristic (e,2e) structures in the NSDI regime with increasing wavelengths. In terms of theoretical investigations, it would be interesting to see what the the simulation of Yuan *et al.* [260] using the improved GSZ shielding potential returns when calculated for mid-IR driving fields.

Retrieval of structural information from polyatomic molecules with laser-induced electron diffraction

Laser-induced electron diffraction is an evolving tabletop method for molecular imaging. Our idea was to utilize LIED to image ultrafast structural changes in gas-phase polyatomic molecules as it provides sub-Ångström spatial and few- to sub-femtosecond temporal resolution. Since the momentum distribution of SFI induced elastically re-scattered electrons contains a doubly differential electron scattering cross-sections [36,317,335], the realization of LIED is dependent on the generation of high impact energies for the re-colliding electrons. The ability to extract field free DCSs despite the presence of the strong laser field is key in this context. In this thesis, we showed the first LIED experiments based on 3D momentum detection in full particle coincidence and generated in the mid-IR spectral range.

Field-free DCSs (or diffraction patterns) similar to the DCSs of conventional electron diffraction can be extracted from the 2D momentum distribution of SFI induced re-scattered electrons. In order to do so, four critical criteria need to be satisfied:

1. QS conditions for the SFI process must be achieved so that the final momentum distribution of electrons can be expressed as the product of the field-free DCS multiplied by the returning electron wave packet (QRS theory af-

ter [110]). In this case, the vector potential of the driving field can easily be calculated and taken into account, so that field-free DCSs can be extracted;

2. the returning electron wave packet must be energetic enough to generate a momentum transfer that allows to probe the core of the target and not the valence electronic structure (i.e. $E_\mathrm{r} \geq 50$ eV [110, 326]);

3. high kinetic re-collision energies need to be achieved while simultaneously providing ionization of only a small fraction of the target molecules; and

4. the re-colliding electron must propagate sufficiently far away from the interaction region such that it approximates a plane wave upon return.

These four requirements can only be simultaneously generated by intense mid-IR sources ($I \geq 5 \times 10^{13}$ W cm^{-2} and $\lambda \geq 2$ μm). Once these stringent conditions are satisfied, the achieved momentum transfers are similar between LIED and CED despite the difference in incident electron energies and scattering angles. That means in mid-IR LIED, electron energies $E_\mathrm{r} \geq 50$ eV that scatter at angles between $30^\circ < \theta_\mathrm{r} < 180^\circ$ are typically utilized while in CED the electron energies are on the order of 10^4 to 10^5 eV and scatter at forward angles ($0^\circ < \theta_\mathrm{r} < 10^\circ$). The classical momentum transfer $q = 2\,k_\mathrm{r} \sin(\theta_\mathrm{r}/2)$, where k_r is the electron incident momentum, is comparable for both methods and, as such, mid-IR strong-field induced re-scattered electrons contain structural information of the target gas.

In order to test and calibrate our experimental methodology, we applied mid-IR LIED by operating the ReMi at high static electric and magnetic fields to detect the entire 3D momentum distribution of the emitted electrons. Our first target of choice were Xe atoms as noble gases offer characteristic artifacts in their corresponding DCSs with impacting electrons. Following the QRS theory, we were able to extract the full doubly differential DCS of Xenon atoms for a return energy range of 50 eV to 150 eV and a scattering angle range between 45° and 180°. Our data accurately resolved most of the predicted rich structure and compares accurately with DCS data obtained from the NIST database. In comparison between experiment and theory, we found that for smaller scattering angles ($\theta_\mathrm{r} < 60^\circ$) the data are "contaminated" through background arising from direct electrons. While these direct electrons cause a slight mismatch between the experimental and theoretical data, characteristic minima were still resolved. Overall, we observed an excellent match between our measured data and the theoretical expectations. As the presented NIST data are calculated for neutral Xe we can infer that that the electron energies utilized here ($E_\mathrm{kin} > 50$ eV) are core penetrating. Therefore the electronic structure of the target has a negligible effect on the extracted DCSs for these experimental conditions. These results show that field free DCSs can indeed be extracted via LIED over a wide range of energies and scattering angles with our system at high accuracies.

After this preparation, we went on to use LIED to extract the entire structure of a polyatomic, hetero-nuclear molecule. Therefore, we measured momentum distributions of electrons re-scattering off aligned acetylene molecules to simultaneously measure their C-C and C-H bond lengths. Our approach takes the method beyond

the hitherto achieved imaging of simple diatomic molecules (e.g. in [38,39]). The DCS of molecules contains its structural information in form of a coherent scattering term that is filtered by the subtraction of the incoherent theoretical DCSs of all individual atomic scatterers. Oscillations, phase and zero crossings in the resulting MCFs characterize the bond lengths. By fitting a theoretical counterpart against the MCF the individual feature sizes are determined. A careful selection of experimental parameters enabled us to even image the lighter hydrogen atoms by selection of a suitable scattering energy range for which the relative cross sections contribute comparably. An excellent bond length confidence level was achieved due to the large range of re-scattering energies for which structural information is measured agreeing accurately within error with the theoretically expected bond length of acetylene [363]. Our method demonstrates a clear path to exploit the intrinsic atto- to femto-second temporal resolution of LIED for the imaging of complex molecules due to the return energy - return time relation in classical phase space. Finally, we provide a solution to selective imaging of the multiple fragmentation pathways that are inherently created when launching the re-collision electron in polyatomic molecules. We showed that the coincidence information is vital as the signal from all detected electrons only contains a completely washed out diffraction signal which did not allow for an extraction of structure. Hence, the coincidence capability is an enabling step towards time resolved imaging and permits accurate retrieval of the geometrical structure from the fragment of interest only.

As mid-IR LIED is still in its early stages of development, many possible investigations can be envisioned. On the one hand, more complex molecular structures can be interrogated towards non-linear, asymmetric molecules containing multiple different bonds. Experimentally, our method could be further improved by investigating the DCS signal for different laser parameters (higher intensities, shorter laser pulses) that shape the energy distribution of the re-scattering electrons. On the detection side, in order to achieve a large re-scattering momentum space without measurement artefacts such as nodes one could measure with constant conditions and two different magnetic fields similar to the LES chapter. This would increase the measurement time by a factor of two yet gives the possibility to increasing the momentum space range which would improve the accuracy of the fitting routine and hence the accuracy of the bond length extraction. In the long run, the technique provides an accessible and robust route towards probing ultrafast processes in complex gas-phase molecules by combining attosecond and collision physics with the future goal of realizing the molecular movie.

Imaging and control of selected molecular fragmentation

Until today sophisticated knowledge has been acquired about dynamic organic photochemistry. The ultimate goal of the field remains resolving these dynam-

ics accurately in fractions of their spatial and temporal dimensions. As shown in in this thesis, LIED has developed into viable candidate to actually image an evolving chemical reaction and so to grasp the position of all its constituents involved with regard to each other at several fractions of the overall reaction time. A first dynamic reaction in order to challenge the combined spatio-temporal abilities of our mid-IR LIED technique was the dissociation reaction of one of the C-H bonds of the acetylene dication. This deprotonation process depicts an ultrafast structural change occurring over a few femtoseconds due to the low mass of the proton compared to the resulting moiety. Traditional ultrafast imaging techniques such as X-ray and electron diffraction can not resolve the atomic movements of such fast processes, 1) due to their limited combined spatio-temporal properties and 2) because both methods lack in relative scattering amplitude of hydrogen atoms making them basically invisible for XRD and CED.

We therefore extracted the momentum information of re-scattering electrons only corresponding to the detected H^+ and C_2H^+ ions in coincidence which are the reaction products of the regarded dissociation channel. After determining DCSs of the momentum distribution and applying a similar fitting routine as in the static case we were able to resolve single frames of the deprotonation reaction resolving the primary dissociation trajectory of one C-H bond of acetylene being stretched to more than double than its initial bond length after 9 fs of the population of the reacting state, while the residual C-H bond undergoes an oscillating vibrational motion. The excited, dissociating dication state is assumed to be populated via sequential double ionization in two subsequent tunneling steps via electron ejection from both a HOMO and a HOMO-1. The actual imaging of the excited dication state is then achieved by the returning secondary electron. We selected our laser intensity to be in the SDI regime for 3 μm radiation interacting with actylene by measuring the characteristic ion yield as a function of intensity.

Moreover, we extracted the dissociating acetylene dication for different alignment distributions. Here, we saw a clear breakup of one of the C-H bonds in the case of the ionizing field parallel to the molecular axis, while a slower, more chaotic breakup was determined in the perpendicular alignment state. Our measurement results agree with theoretical investigations using quantum chemistry and mixed quantum-classical ab-initio molecular dynamics methods. This showed that in the aligned case the deprotonation process is enhanced by the laser field, while in the anti-aligned state the deprotonation evolves quasi field-free. Effectively, the alignment offers us a knob to to control the speed of the deprotonation and so to steer the reaction onto a faster or a slower pathway.

Our work provides the first spatio-temporal snapshots of molecular structure with picometer spatial and sub-femtosecond temporal resolution while a chemical bond is breaking. Moreover, resolving the sub-ångström variations in C-H bond elongation for different alignments successfully field-tested the accuracy of LIED. This present investigation outlines important general aspects of LIED imaging for a molecule that is large enough to show the hallmark features of more complex molecules such as conical intersections or structural transformation. In future investigations the two-step control of the reaction velocity could be further developed

into a gradually tuneable scheme depending on the molecular alignment degree. As a next step, the sub-fs temporal resolution of mid-IR LIED could be further characterized by probing vibrational modes of e.g. simple molecular systems like H_2, D_2 or NO. These target systems offer vibrational cycles on the order of few to tens of femtoseconds (see overview in [137, Ch. 9.5]), which are ideal to benchmark the accuracy of mid-IR LIED for a broad range of electron energies and return times. By utilizing different driving wavelength in the mid-IR, the temporal range of the return times can be further tuned.

Overall, these combined powerful tools will allow interrogating fast reactions in even more complex molecular systems. With the addition of another laser pulse to act as a coarse temporal knob, our methodology can be used to investigate in depth the evolution of chemical and biological processes from the few-femtosecond level and above. Thus, mid-IR LIED fulfills the requirements for a gas-phase "molecular movie" and we anticipate that our results will provide a launching pad for future investigations of many ultrafast molecular processes.

Appendix A

Relevant Physical Quantities in SI and Atomic Units

The theoretical background in atomic and molecular physics is often defined in *atomic units* where the physical quantities are expressed in their respective values by reference to the hydrogen atom. That means that the fundamental natural constants such as the charge of an electron (e), the mass of an electron (m_e), the vacuum permitivity/4π (ϵ_0), and the Planck's constant/2π ($\hbar$) serve as base units appointing the value of one atomic unit (see e.g. [70, Appendix A.2]):

$$\hbar = e = m_e = 4\,\pi\,\epsilon_0 = 1\,a.u. \quad . \tag{A.1}$$

This simplifies many theoretical expressions and allows to calculate with more convenient numerical values. The atomc base units can be combined to the units of key atomic properties matching the known, corresponding SI units such as energy ($E_\mathrm{h} = m_e\,e^4/\hbar^2$, length ($l = \hbar^2/m_e\,e^2$), and others [399]. The following table A.1 summarizes the basic quantities and physical constants as well as their respective conversion factors into the *SI unit*[1] system (values taken from [70, 203, 399, 400]). In this thesis, atomic units are used unless otherwise stated.

[1] French: *Système international d'unités*

physical quantity	definition	1 a.u. correponds to
mass	electron mass m_e	9.10938×10^{-31} kg
charge	elementary charge e	1.60218×10^{-19} As
length	Bohr radius a_0	5.29177×10^{-11} m
energy	$E_\mathrm{h} = m_e\, e^4/\hbar^2$	$4.3597443 \times 10^{-18}$ J
		27.21138505 eV = 1 Hartree
angular momentum	$\hbar$	$1.0545726 \times 10^{-34}$ J s
		$6.58211928 \times 10^{-16}$ eV s
time	$t = \hbar/E_\mathrm{h}$	$2.41888433 \times 10^{-17}$ s $\approx$ 24.2 as
velocity	$v_0 = a_0/t$	2.18769×10^{6} m/s
momentum	$p_0 = m_e\, v_0$	$1.99285174 \times 10^{-24}$ kg m/s
angular frequency	$\nu_0 = v_0/a_0$	4.13414×10^{16} Hz
electric field	$\mathcal{E} = e/(4\,\pi\,\epsilon_0\,{a_0}^2)$	5.14221×10^{11} V/m
intensity	$I = \mathcal{E}^2$	6.4364091×10^{19} W/m^2
laser intensity	$I_\mathrm{laser} = 0.5\,\epsilon_0\,c\,\mathcal{E}^2$	3.5094451×10^{20} W/m^2
physical constant	atomic units	SI units
proton mass m_p	1836.15 a.u.	1.67262×10^{-27} kg
atomic mass unit amu	1822.89 a.u.	1.66054×10^{-27} kg
velocity of light c	137.04 a.u.	2.99792×10^{8} m/s

Table A.1: Conversion of basic physical quantities and constants between atomic and SI units.

Appendix B

Derivation of the intensity threshold of over-the-barrier ionization

In the case of over-the-barrier or field ionization, as described in Sec. 2.1.1, the Coulomb potential can be bend by a strong, quasi-static electric field that the effective potential V_{eff} barrier is suppressed more than the amount of the ionization potential I_{P}. In this case, an electron can leave the respective state quasi-freely. The intensity threshold for field ionization can be derived as follows.

The local maximum of V_{eff} can be derived from Eq. 2.11 as

$$\frac{\partial}{\partial r} V_{\text{eff}}(r) = \frac{Z_{\text{eff}}\, e^2}{4\,\pi\,\epsilon_0\, r^2} - e\,\mathcal{E}_0 \stackrel{!}{=} 0 \tag{B.1}$$

assuming a quasi-static field $\mathcal{E}(t_0) = \mathcal{E}_0 = \text{const.}$

$$\rightarrow r_{\text{max}} = \sqrt{\frac{Z_{\text{eff}}\, e}{4\,\pi\,\epsilon_0\,\mathcal{E}_0}} \quad . \tag{B.2}$$

The electric field magnitude needed to reach over-the-barrier / field ionization to overcome the ionization potential I_{P} solely by field suppression follows as

$$V_{\text{eff}}(r_{\text{max}}) = \sqrt{\frac{Z_{\text{eff}}\, e^3\, \mathcal{E}_{\text{OB}}}{\pi\,\epsilon_0}} \stackrel{!}{=} I_{\text{P}} \quad , \tag{B.3}$$

$$\rightarrow \mathcal{E}_{\text{OB}} = \frac{\pi\,\epsilon_0\, I_{\text{P}}^2}{Z_{\text{eff}}\, e^3} \quad . \tag{B.4}$$

That leads to a threshold laser intensity I_{OB} of

$$\rightarrow I_{\text{OB}} = \frac{\pi\, c\, \epsilon_0^3\, I_{\text{P}}^4}{2\, Z_{\text{eff}}^2\, e^6} \quad . \tag{B.5}$$

Appendix C

Additional information about the supersonic gas jet

The theory behind the generation of a supersonic gas jet as well as specifications of our experimental system were depicted in Sec. 3.2.1.1. Here, additional information are given in order to complement that section.

C.1 Empirical model to determine the Mach number and the off-axis particle number density in the gas jet

The Mach number M_a which is the ratio of the jet velocity v and the speed of sound c_S as defined in Eq. 3.12 characterizes the zones of the expanded gas jet after the nozzle. In order to determine the in the jet, an empirical model was developed which allows to determine M_a as a function of x being the distance after the nozzle along the center gas propagation axis [205, 209]. The resulting formulae are listed in the following according to [209].

$$M_\mathrm{a}(\tilde{x}) = \tilde{x}^{\kappa-1}\left(b + \frac{c}{\tilde{x}} + \frac{d}{\tilde{x}^2} + \frac{e}{\tilde{x}^3}\right) \quad , \tag{C.1}$$

with the effective distance $\tilde{x} = x/d$, the nozzle diameter d, and the coefficient $\kappa = c_\mathrm{P}/c_\mathrm{V}$ being the specific heat capacity ratio. The empirical coefficients were found to be

$$b = 16.5404 - 15.8215\,\kappa + 4.7018\,\kappa^2 \quad , \tag{C.2}$$

$$c = -15.6286 + 15.1459\,\kappa - 3.7335\,\kappa^2 \quad , \tag{C.3}$$

$$d = 13.1705 - 14.4312\,\kappa + 4.0591\,\kappa^2 \quad , \tag{C.4}$$

$$e = -3.4116 + 3.7898\,\kappa - 1.0720\,\kappa^2 \quad . \tag{C.5}$$

As already defined in Eq. 3.21, the density of the number of particles within the gas jet can be calculated along the center propagation axis at a distance x from the nozzle by

$$n(x) = n_0\left[1 + \frac{M_\mathrm{a}(x)^2\ (\kappa-1)}{2}\right]^{\frac{1}{1-\kappa}} \tag{C.6}$$

as function of M_a. Again, the initial number density is determined by the ideal gas law: $P = n\,k_B\,T$. In order to calculate the number density on an off-axis position within the gas jet at an angle θ and a radius R, the following empirical formula was found [209]

$$n(R,\theta) = n(x)\,\cos^2\left(\frac{\pi\,\theta}{17.0230 - 16.1334\,\kappa + 4.5346\,\kappa^2}\right) \quad , \tag{C.7}$$

where $R = x$ for $\theta = 0°$.

C.2 Derivation of jet momentum from Mach number

The derivation of the momentum of the jet starts from Eq. 3.12, reprinted here in terms of the temperature relation

$$M_a = \frac{v}{c_S} = \sqrt{\frac{2}{\kappa - 1}\left(\frac{T_0}{T_1} - 1\right)} \quad . \tag{C.8}$$

As a reminder, temperature, pressure and particle number density ratios in an ideal gas are related by the Poisson equations

$$\left(\frac{P_1}{P_0}\right) = \left(\frac{T_1}{T_0}\right)^{\kappa/(\kappa-1)} = \left(\frac{n_1}{n_0}\right)^{\kappa} \quad . \tag{C.9}$$

The speed of sound at jet temperature is defined as [208, Eq. 3.23]

$$c_S = \sqrt{\frac{\kappa\,k_B\,T_1}{m}} \quad . \tag{C.10}$$

Plugging Eq. C.10 into Eq. C.8, and converting the jet velocity v into jet momentum $p = m\,v$ leads to

$$p_{jet}^2 = \frac{2\,\kappa\,k_B\,T_1\,m}{\kappa - 1}\left(\frac{T_0}{T_1} - 1\right) \quad . \tag{C.11}$$

Adding the relation between the specfic heat ratio and the degrees of freedom $\kappa = 1 + 2/f$ in form of

$$\frac{1}{\kappa - 1} = \frac{1}{1 + \frac{2}{f} - 1} = \frac{f}{2} \tag{C.12}$$

leads to

$$p_{jet}^2 = 2\,m\,k_B\,T_1\left(1 + \frac{f}{2}\right)\left(\frac{T_0}{T_1} - 1\right) \quad . \tag{C.13}$$

Since we are skimming the jet expansion within the zone of silence in the center of the Mach cone, where $M_a \gg 1$, and hence it can be assumed that $P_0/P_1 \gg 2.05$ for atoms ($f = 3$) or 3.95 for linear molecules ($f = 5$) according to Eq. 3.14. Taking

the Poisson equations in Eqs. C.9 into account, the relation is also valid for the temperature ratio leading to the following term for the momentum of the jet

$$p_{\text{jet}} = \sqrt{2\, m\, k_{\text{B}}\, T_0 \left(1 + \frac{f}{2}\right)} \quad , \tag{C.14}$$

which matches Eq. 3.16 for the jet momentum in the zone of silence being dependent on the temperature of the stagnation temperature T_0.

Appendix D

Electronic trigger scheme

In the experiments presented in this thesis, we used an electronic triggering scheme that sends a trigger to the TDC card in order to read out all ion and electron channels *only* when a suitable ion count has been detected. Hence, we trigger with respect to the detected ions instead of using only the laser trigger, or triggering on detected electrons (which are other possibilities). The reason behind this is to reduce the number of background electrons that might impact on the MCP detector without any respective ion. In other words, this is a hardware-based coincidence pre-selection.

The electronic triggering scheme is sketched in Fig. D.1 as it was implemented in the lab. Here, whenever an ion is detected for a specifically chosen time window (gate) between two successive laser pulses, the scheme allows to assign the respective ion signal to its current clock window $t_{\mathrm{n,PD}}$ via a series of delays, gates and logical & circuits to create a NIM signal at the end of that current clocking channel. This signal serves as the trigger for VME controller to read-out the TDC for a user-set time window $t_{\mathrm{w}} = \Delta t_{\mathrm{n,PD}}$ which hence includes all ion and the electron related signals of the set. The resulting sequence of electronic signals within the circuit of Fig. D.1 is sketched in Fig. D.2 for better understanding.

Before the final trigger is sent to the TDC card, the scheme offers a control circuit that checks if the VME controller is busy with a read-out or if it is good to go. Optionally, the laser pulse trigger can be used to read out the *analog-to-digital converter* (ADC) card. Many variations of different trigger schemes can be thought of in the lab, in order to optimize a hardware-based coincidence pre-selection. Some concepts regarding this issue were developed in the master thesis of Konstantinos Kaleris [401] which resulted during the work of this thesis.

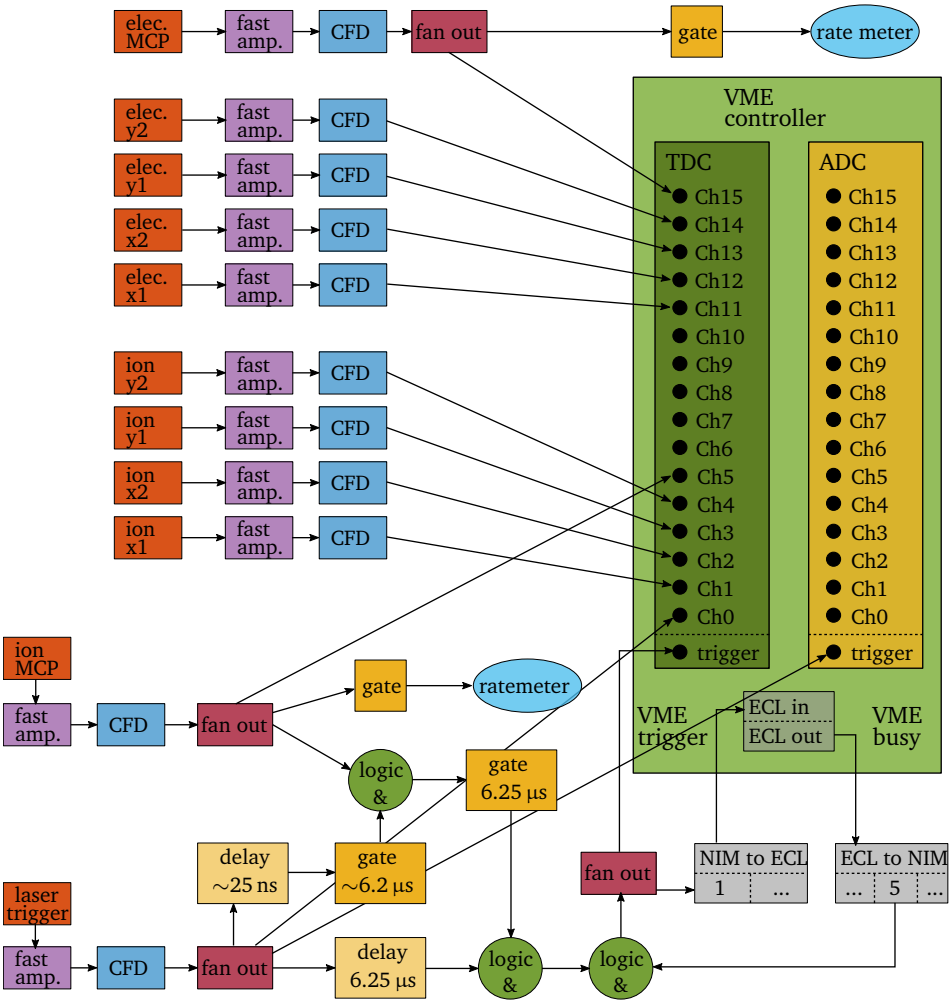

Figure D.1: Electronic trigger scheme.

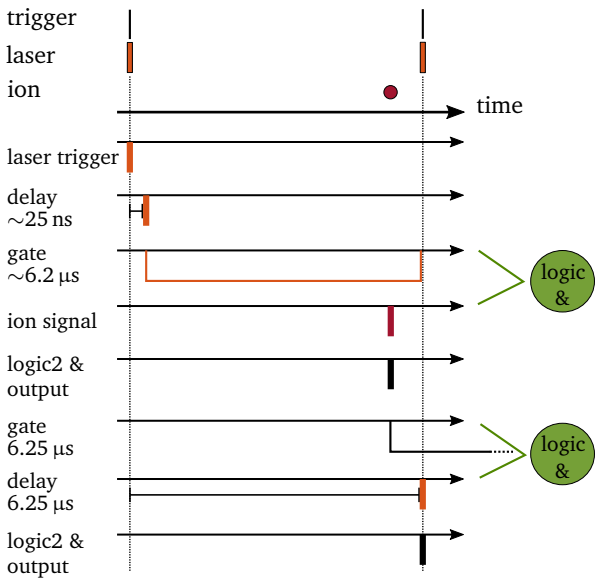

Figure D.2: Electronic trigger pulse sequence.

Acronyms

A	aligned
AA	anti-aligned
ADK	Ammosov, Delone and Krainov (model)
AMO	atomic, molecular and optical (physics)
ARM	analytic R-matrix
AT	acquisition time
ATI	above-threshold ionization
AUO	Attoscience and Ultrafast Optics (group)
BOA	Born-Oppenheimer approximation
CED	conventional electron diffraction
CEP	carrier-envelope phase
CFD	constant fraction discriminator
COLTRIMS	cold target recoil ion momentum spectroscopy
CPA	chirped pulse amplification
CTMC	classical trajectory Monte Carlo
DCS	differential cross-section
DDCS	doubly DCS
DFG	difference-frequency generation
DFT	density functional theory
DI	double ionization
DLA	delay line anode
DoF	degree of freedom
FROG	frequency-resolved optical gating
FTI	frustrated tunnel ionization
FWHM	full-width half-maximum
GAMESS	general atomic and molecular electronic structure system
GSZ	Green-Sellin-Zachor (model)
HATI	high-energy ATI
HF	Hartree-Fock (approximation)
HH	high harmonic
HHG	high harmonic generation
HNLF	highly non-linear fiber
HOMO	highest occupied molecular orbital
IAM	independent atom model
ICFO	Institute of Photonic Sciences (catalan: Institut de Ciències Fotòniques)
IR	infrared
ISFA	improved SFA (also SFA2)
KED	kinetic energy distribution

KER	kinetic energy release
KFR	Keldysh, Faisal and Reiss (model)
KLM	Kerr-lens mode-locking
LAED	laser-assisted electron diffraction
LCAO	linear combination of atomic orbitals
LEED	low-energy electron diffraction
LES	low energy structure
LIED	laser-induced electron diffraction
LOMO	lowest occupied molecular orbital
MBS	multi-branch system (stream server)
MCF	molecular contrast factor
MCP	multi-channel plate (detector)
MI	multiple ionization
mid-IR	mid infrared
MO-ADK	molecular ADK (model)
MPI	multi-photon ionization
MPIK	Max Planck Institute for Nuclear Physics, Heidelberg, Germany
NIST	National Institute of Standards and Technology
NSDI	non-sequential double ionization
OPA	optical parametric amplification
OPCPA	optical parametric chirped pulse amplification
PD	photo diode
PEC	potential energy curve
PES	potential energy surface
PiPiCo	photo-ion photo-ion coincidence
PML	passive mode-locking
PPT	Perelomov, Popov and Terent'ev (model)
QRS	quantitative re-scattering (theory)
QS	quasi-static
ReMi	reaction microscope
RESI	re-collision excitation with subsequent ionization
RWP	returning wave packet
SA	saturable absorber
SAE	single active electron (approximation)
SAM	self-amplitude modulation
SDI	sequential double ionization
SESAM	semiconductor saturable absorber mirror
SFA	strong-field approximation
SFG	sum-frequency generation
SFI	strong-field ionization
SFP	strong-field physics
SHG	second-harmonic generation
SMM	simple man's model
SOC	spin-orbit coupling
SOF	sudden onset function
SPM	self-phase modulation

TDC	time-to-digital converter
TDDFT	time-dependent density functional theory
TDSE	time-dependent Schrödinger equation
TI	tunneling ionization
TISE	time-independent Schrödinger equation
UED	ultrafast electron diffraction
VLES	very-low energy structure
XFEL	X-ray free electron laser
XRD	X-ray diffraction
XUV	extreme ultraviolet
ZES	zero energy structure
1D	one-dimensional
2D	two-dimensional
3D	three-dimensional

References

[1] F. Yan-Zhuo, Z. Song-Feng, and Z. Xiao-Xin, "Multiphoton and tunneling ionization probability of atoms and molecules in an intense laser field," Chinese Physics B **21**(11), 113,101 (2012).

[2] R. Torres, R. de Nalda, and J. Marangos, "Dynamics of laser-induced molecular alignment in the impulsive and adiabatic regimes: A direct comparison," Physical Review A **72**(023420), 1–8 (2005).

[3] X. Sun, M. Li, D. Ye, G. Xin, L. Fu, X. Xie, Y. Deng, C. Wu, J. Liu, Q. Gong, and Y. Liu, "Mechanisms of strong-field double ionization of Xe," Physical Review Letters **113**(10), 1–5 (2014).

[4] A. H. Zewail, "Femtochemistry: Atomic-Scale Dynamics of the Chemical Bond Using Ultrafast Lasers (Nobel Lecture)," Angew. Chem. Int. Ed. **39**, 2586–2631 (2000).

[5] M. Leslie, "The Man Who Stopped Time," (2001).

[6] J. R. Dwyer, C. T. Hebeisen, R. Ernstorfer, M. Harb, V. B. Deyirmenjian, R. E. Jordan, and R. J. D. Miller, "Femtosecond electron diffraction: 'making the molecular movie'." Philosophical transactions. Series A, Mathematical, physical, and engineering sciences **364**(1840), 741–78 (2006).

[7] T. H. Maiman, "Stimulated Optical Radiation in Ruby," Nature **187**, 493–494 (1960).

[8] T. Brabec and F. Krausz, "Intense few-cycle laser fields: Frontiers of nonlinear optics," Reviews of Modern Physics **72**(2), 545–591 (2000).

[9] F. Krausz, M. E. Fermann, T. Brabec, P. F. Curley, M. Hofer, M. H. Ober, C. Spielmann, E. Wintner, and A. J. Schmidt, "Femtosecond Solid-State Lasers," IEEE Journal of Quantum Eletronics **28**(10), 2097–2122 (1992).

[10] G. Steinmeyer, D. H. Sutter, L. Gallmann, N. Matuschek, and U. Keller, "Frontiers in Ultrashort Pulse Generation: Pushing the Limits in Linear and Nonlinear Optics," Science **286**(5444), 1507–1512 (1999).

[11] U. Keller, "Recent developments in compact ultrafast lasers." Nature **424**(6950), 831–838 (2003).

[12] Y. Bhattacharjee, "Measuring the Immeasurable," Nature **412**, 474–476 (2001).

[13] F. Krausz, "The birth of attosecond physics and its coming of age," Physica Scripta **91**(6), 063,011 (2016).

[14] P. Corkum and F. Krausz, "Attosecond science," Nature Physics **3**, 381–387 (2007).

[15] P. H. Bucksbaum, "The future of attosecond spectroscopy." Science (New York, N.Y.) **317**(5839), 766–9 (2007).

[16] F. Calegari, G. Sansone, S. Stagira, C. Vozzi, and M. Nisoli, "Advances in attosecond science," Journal of Physics B: Atomic, Molecular and Optical Physics **49**(6), 062,001 (2016).

[17] F. Calegari, D. Ayuso, A. Trabattoni, L. Belshaw, S. De Camillis, S. Anumula, F. Frassetto, L. Poletto, A. Palacios, P. Decleva, J. B. Greenwood, F. Martín, and M. Nisoli, "Ultrafast electron dynamics in phenylalanine initiated by attosecond pulses," Science **346**(6207), 336–339 (2014).

[18] P. M. Kraus, B. Mignolet, D. Baykusheva, A. Rupenyan, L. Horný, E. F. Penka, G. Grassi, O. I. Tolstikhin, J. Schneider, F. Jensen, L. B. Madsen, A. D. Bandrauk, F. Remacle, and H. J. Wörner, "Measurement and laser control of attosecond charge migration in ionized iodoacetylene." Science (New York, N.Y.) **350**(6262), 790–795 (2015).

[19] D. T. Attwood, *Soft X-Rays and Extreme Ultraviolet Radiation*, 1st ed. (Cambridge University Press, 2007).

[20] A. Mcpherson, G. Gibson, H. Jara, U. Johann, T. S. Luk, I. A. Mcintyre, K. Boyer, and C. K. Rhodes, "Studies of multiphoton production of vacuum-ultraviolet radiation in the rare gases," Journal of the Optical Society of America B **4**(4), 595–601 (1987).

[21] M. Ferray, A. L'Huillier, X. F. Li, L. A. Lompre, G. Mainfray, and C. Manus, "Multiple-harmonic conversion of 1064 nm radiation in rare gases," Journal of Physics B: Atomic, Molecular and Optical Physics **21**(3), L31–L35 (1988).

[22] J. Krause, K. Schafer, and K. Kulander, "High-order harmonic generation from atoms and ions in the high intensity regime," Physical Review Letters **68**(24), 3535–3538 (1992).

[23] P. Corkum, "Plasma Perspective on Strong-Field Multiphoton Ionization," Physical Review Letters **71**(13), 1994–1997 (1993).

[24] P. Hockett, C. Z. Bisgaard, O. J. Clarkin, and A. Stolow, "Time-resolved imaging of purely valence-electron dynamics during a chemical reaction," Nat Phys **7**(8), 612–615 (2011).

[25] M. Lein, "Molecular imaging using recolliding electrons," Journal of Physics B: Atomic, Molecular and Optical Physics **40**(16), R135–R173 (2007).

[26] D. P. Zhong and A. H. Zewail, "Femtosecond real-time probing of reactions. 23. Studies of temporal, velocity, angular, and state dynamics from transition states to final products by femtosecond-resolved mass spectrometry," Journal of Physical Chemistry A **102**(23), 4031–4058 (1998).

[27] Y. H. Jiang, A. Rudenko, O. Herrwerth, L. Foucar, M. Kurka, K. U. Kühnel, M. Lezius, M. F. Kling, J. van Tilborg, A. Belkacem, K. Ueda, S. Düsterer, R. Treusch, C. D. Schröter, R. Moshammer, and J. Ullrich, "Ultrafast Extreme Ultraviolet Induced Isomerization of Acetylene Cations," Physical Review Letters **105**(26), 263,002 (2010).

[28] W. Domcke and D. R. Yarkony, "Role of Conical Intersections in Molecular Spectroscopy and Photoinduced Chemical Dynamics," Annual review of physical chemistry **63**, 325–352 (2012).

[29] I. Hargittai and M. Hargittai, eds., *Stereochemical Applications of Gas-Phase Electron Diffraction - Part A The Electron Diffraction Technique* (VCH Publishers, Inc., 1988).

[30] A. H. Zewail and J. M. Thomas, *4D Electron Microscopy. Imaging in Space and Time.*, 1st ed. (Imperial College Press, 2010).

[31] A. Barty, S. Boutet, M. J. Bogan, S. Hau-Riege, S. Marchesini, K. Sokolowski-Tinten, N. Stojanovic, R. Tobey, H. Ehrke, A. Cavalleri, S. Düsterer, M. Frank, S. Bajt, B. W. Woods, M. M. Seibert, J. Hajdu, R. Treusch, and H. N. Chapman, "Ultrafast single-shot diffraction imaging of nanoscale dynamics," Nature Photonics **2**(9), 578–578 (2008).

[32] P. Thibault, "X-Ray Diffraction Microscopy," Annual Review of Condensed Matter Physics **1**, 237–255 (2010).

[33] C. J. Hensley, J. Yang, and M. Centurion, "Imaging of Isolated Molecules with Ultrafast Electron Pulses," Physical Review Letters **109**(13), 133,202 (2012).

[34] A. Gliserin, M. Walbran, F. Krausz, and P. Baum, "Sub-phonon-period compression of electron pulses for atomic diffraction." Nature communications **6**(May), 8723 (2015).

[35] H. N. Chapman, P. Fromme, A. Barty, T. A. White, R. A. Kirian, A. Aquila, M. S. Hunter, J. Schulz, D. P. DePonte, U. Weierstall, R. B. Doak, F. R. N. C. Maia, A. V. Martin, I. Schlichting, L. Lomb, N. Coppola, R. L. Shoeman, S. W. Epp, R. Hartmann, D. Rolles, A. Rudenko, L. Foucar, N. Kimmel, G. Weidenspointner, P. Holl, M. Liang, M. Barthelmess, C. Caleman, S. Boutet, M. J. Bogan, J. Krzywinski, C. Bostedt, S. Bajt, L. Gumprecht, B. Rudek, B. Erk, C. Schmidt, A. Hömke, C. Reich, D. Pietschner, L. Strüder, G. Hauser, H. Gorke, J. Ullrich, S. Herrmann, G. Schaller, F. Schopper, H. Soltau, K.-U. Kühnel, M. Messerschmidt, J. D. Bozek, S. P. Hau-Riege, M. Frank, C. Y. Hampton, R. G. Sierra, D. Starodub, G. J. Williams, J. Hajdu, N. Timneanu, M. M. Seibert, J. Andreasson, A. Rocker, O. Jönsson, M. Svenda, S. Stern, K. Nass, R. Andritschke, C.-D. Schröter, F. Krasniqi, M. Bott, K. E. Schmidt, X. Wang, I. Grotjohann, J. M. Holton, T. R. M. Barends, R. Neutze, S. Marchesini, R. Fromme, S. Schorb, D. Rupp, M. Adolph, T. Gorkhover, I. Andersson, H. Hirsemann, G. Potdevin, H. Graafsma, B. Nilsson, and J. C. H. Spence, "Femtosecond X-ray protein nanocrystallography." Nature **470**(7332), 73–7 (2011).

[36] T. Zuo, A. Bandrauk, and P. Corkum, "Laser-induced electron diffraction : a new tool for probing ultrafast molecular dynamics," Chemical Physics Letters **259**, 313–320 (1996).

[37] C. D. Lin and J. Xu, "Imaging ultrafast dynamics of molecules with laser-induced electron diffraction." Phys. Chem. Chem. Physics **14**(38), 13,133–13,145 (2012).

[38] M. Meckel, D. Comtois, D. Zeidler, A. Staudte, D. Pavicic, H. C. Bandulet, H. Pepin, J. C. Kieffer, R. Dorner, D. M. Villeneuve, and P. B. Corkum, "Laser-Induced Electron Tunneling and Diffraction," Science **320**(5882), 1478–1482 (2008).

[39] C. I. Blaga, J. Xu, A. D. DiChiara, E. Sistrunk, K. Zhang, P. Agostini, T. A. Miller, L. F. DiMauro, and C. D. Lin, "Imaging ultrafast molecular dynamics with laser-induced electron diffraction." Nature **483**(7388), 194–7 (2012).

[40] M. Uiberacker, T. Uphues, M. Schultze, A. J. Verhoef, V. Yakovlev, M. F. Kling, J. Rauschenberger, N. M. Kabachnik, H. Schröder, M. Lezius, K. L. Kompa, H.-G. Muller, M. J. J. Vrakking, S. Hendel, U. Kleineberg, U. Heinzmann, M. Drescher, and F. Krausz, "Attosecond real-time observation of electron tunnelling in atoms." Nature **446**(7136), 627–32 (2007).

[41] G. Sansone, F. Kelkensberg, J. F. Pérez-Torres, F. Morales, M. F. Kling, W. Siu, O. Ghafur, P. Johnsson, M. Swoboda, E. Benedetti, F. Ferrari, F. Lépine, J. L. Sanz-Vicario, S. Zherebtsov, I. Znakovskaya, A. L'huillier, M. Y. Ivanov, M. Nisoli, F. Martín, and M. J. J. Vrakking, "Electron localization following attosecond molecular photoionization." Nature **465**(June), 763–766 (2010).

[42] E. Goulielmakis, Z.-H. Loh, A. Wirth, R. Santra, N. Rohringer, V. S. Yakovlev, S. Zherebtsov, T. Pfeifer, A. M. Azzeer, M. F. Kling, S. R. Leone, and F. Krausz, "Real-time observation of valence electron motion." Nature **466**(7307), 739–43 (2010).

[43] O. Smirnova, Y. Mairesse, S. Patchkovskii, N. Dudovich, D. Villeneuve, P. Corkum, and M. Y. Ivanov, "High harmonic interferometry of multi-electron dynamics in molecules." Nature **460**(7258), 972–977 (2009).

[44] J. Tate, T. Auguste, H. Muller, P. Salières, P. Agostini, and L. DiMauro, "Scaling of Wave-Packet Dynamics in an Intense Midinfrared Field," Physical Review Letters **98**(1), 013,901 (2007).

[45] P. Colosimo, G. Doumy, C. I. Blaga, J. Wheeler, C. Hauri, F. Catoire, J. Tate, R. Chirla, A. M. March, G. G. Paulus, H. G. Muller, P. Agostini, and L. F. DiMauro, "Scaling strong-field interactions towards the classical limit," Nature Physics **4**(5), 386–389 (2008).

[46] M. Frolov, N. Manakov, and A. Starace, "Wavelength Scaling of High-Harmonic Yield: Threshold Phenomena and Bound State Symmetry Dependence," Physical Review Letters **100**(17), 173,001 (2008).

[47] D. Austin and J. Biegert, "Strong-field approximation for the wavelength scaling of high-harmonic generation," Physical Review A **86**(2), 1–7 (2012).

[48] T. Fuji, N. Ishii, C. Y. Teisset, X. Gu, T. Metzger, A. Baltuška, N. Forget, D. Kaplan, A. Galvanauskas, and F. Krausz, "Parametric amplification of few-cycle carrier- envelope phase-stable pulses at 2.1 μm," Optics letters **31**(8), 1103–1105 (2006).

[49] O. Chalus, P. K. Bates, and J. Biegert, "Design and simulation of few-cycle optical parametric chirped pulse amplification at mid-IR wavelengths." Optics express **16**(26), 21,297–21,304 (2008).

[50] O. Chalus, P. Bates, M. Smolarski, and J. Biegert, "Mid-IR short-pulse OPCPA with micro-Joule energy at 100kHz," Optics express **17**(5), 3587–3594 (2009).

[51] A. Thai, M. Hemmer, P. K. Bates, O. Chalus, and J. Biegert, "Sub-250-mrad, passively carrier-envelope-phase-stable mid-infrared OPCPA source at high repetition rate," Optics Letters **36**(19), 3918–3920 (2011).

[52] J. Biegert, P. K. Bates, and O. Chalus, "New Mid-Infrared Light Sources," IEEE Journal of Selected Topics in Quantum Electronics **18**(1), 531–540 (2012).

[53] A. Thai, M. Baudisch, and J. Biegert, "20 μJ, few-cycle Pulses at 3.1 μm and 160 kHz Repetition Rate from mid-IR OPCPA," in *CLEO 2012*, pp. 1–2 (2012).

[54] M. Hemmer, M. Baudisch, A. Thai, A. Couairon, and J. Biegert, "Self-compression to sub-3-cycle duration of mid-infrared optical pulses in dielectrics," Optics Express **21**(23), 28,095 (2013).

[55] M. Hemmer, A. Thai, M. Baudisch, H. Ishizuki, T. Taira, and J. Biegert, "18-μJ energy , 160-kHz repetition rate , 250-MW peak power mid-IR OPCPA," Chinese Optics Letters **11**(013202), 11–13 (2013).

[56] M. Baudisch, H. Pires, H. Ishizuki, T. Taira, M. Hemmer, and J. Biegert, "Sub-4-optical-cycle, 340 MW peak power, high stability mid-IR source at 160 kHz," Journal of Optics **17**(9), 094,002 (2015).

[57] H. Pires, M. Baudisch, D. Sanchez, M. Hemmer, and J. Biegert, "Ultrashort pulse generation in the mid-IR," Progress in Quantum Electronics **43**, 1–30 (2015).

[58] C. I. Blaga, F. Catoire, P. Colosimo, G. G. Paulus, H. G. Muller, P. Agostini, and L. F. DiMauro, "Strong-field photoionization revisited," Nature Physics **5**(5), 335–338 (2009).

[59] W. Quan, Z. Lin, M. Wu, H. Kang, H. Liu, X. Liu, J. Chen, J. Liu, X. He, S. Chen, H. Xiong, L. Guo, H. Xu, Y. Fu, Y. Cheng, and Z. Xu, "Classical Aspects in Above-Threshold Ionization with a Midinfrared Strong Laser Field," Physical Review Letters **103**(9), 093,001 (2009).

[60] J. Dura, N. Camus, A. Thai, A. Britz, M. Hemmer, M. Baudisch, A. Senftleben, C. D. Schröter, J. Ullrich, R. Moshammer, and J. Biegert, "Ionization with low-frequency fields in the tunneling regime," Scientific Reports **3**, 2675:1–4 (2013).

[61] M. Möller, F. Meyer, A. M. Sayler, G. G. Paulus, M. F. Kling, B. E. Schmidt, W. Becker, and D. B. Milošević, "Off-axis low-energy structures in above-threshold ionization," Physical Review A **90**(2), 023,412 (2014).

[62] R. Moshammer, M. Unverzagt, W. Schmitt, J. Ullrich, and H. Schmidt-Böcking, "A 4π recoil-ion electron momentum analyzer: a high-resolution "microscope" for the investigation of the dynamics of atomic, molecular and nuclear reactions," Nuclear Instruments and Methods in Physics Research B **108**, 425–445 (1996).

[63] J. Ullrich, R. Moshammer, A. Dorn, R. Dörner, L. P. H. Schmidt, and H. Schmidt-Böcking, "Recoil-ion and electron momentum spectroscopy : reaction-microscopes," Reports on Progress in Physics **66**, 1463–1545 (2003).

[64] H. Schmidt-Böcking, "Die "Blasenkammer" der Atomphysik," Physik Jounal **9**(8/9), 1–6 (2010).

[65] F. H. M. Faisal, "Ionization surprise," Nature Physics **5**(May), 319–320 (2009).

[66] T. S. Zyubina, Y. A. Dyakov, S. H. Lin, A. D. Bandrauk, and a. M. Mebel, "Theoretical study of isomerization and dissociation of acetylene dication in the ground and excited electronic states." The Journal of chemical physics **123**(13), 134,320 (2005).

[67] G. G. Paulus, "Strong-Field Photoionization by Few-Cycle Laser Pulses," in *Progress in Ultrafast Intense Laser Science IV*, K. Yamanouchi, A. Becker, R. Li, and S. L. Chin, eds., vol. 91 of *Springer Series in Chemical Physics*, chap. 2, pp. 17–40 (Springer Berlin Heidelberg, Berlin, Heidelberg, 2009).

[68] A. E. Siegman, *Lasers*, 1st ed. (University Science Books, 1986).

[69] A. Einstein, "Über einen die Erzeugung und Verwandlung des Lichtes betreffenden heuristischen Gesichtspunkt," Annalen der Physik **322**(6), 132–148 (1905).

[70] I. V. Hertel and C.-P. Schulz, *Atoms, Molecules and Optical Physics 1: Atoms and Spectroscopy*, 1st ed. (Springer Berlin Heidelberg, Berlin, Heidelberg, 2015).

[71] M. Göppert-Mayer, "Über Elementarakte mit zwei Quantensprüngen," Annalen der Physik **401**(3), 273–294 (1931).

[72] L. V. Keldysh, "Ionization in the field of a strong electromagnetic wave," Soviet Physics JETP **20**(5), 1307–1314 (1965).

[73] M. Y. Ivanov, M. Spanner, and O. Smirnova, "Anatomy of strong field ionization," Journal of Modern Optics **52**(2-3), 165–184 (2005).

[74] W. Becker, X. Liu, P. J. Ho, and J. H. Eberly, "Theories of photoelectron correlation in laser-driven multiple atomic ionization," Reviews of Modern Physics **84**(3), 1011–1043 (2012).

[75] P. Agostini, F. Fabre, G. Mainfray, G. Petite, and N. K. Rahman, "Free-Free Transitions Following Six-Photon Ionization of Xenon Atoms," Physical Review Letters **42**(17), 1127–1130 (1979).

[76] R. R. Freeman and P. H. Bucksbaum, "Investigations of above-threshold ionization using subpicosecond laser pulses," Journal of Physics B: Atomic, Molecular and Optical Physics **24**, 325–347 (1991).

[77] R. R. Freeman, P. H. Bucksbaum, H. Milchberg, S. Darack, D. Schumacher, and M. E. Geusic, "Above-threshold ionization with subpicosecond laser pulses," Physical Review Letters **59**(10), 1092–1095 (1987).

[78] J. H. Eberly and J. Javanainen, "Above-threshold ionisation," European Physical Journal **9**, 265 (1988).

[79] G. G. Paulus, F. Grasbon, H. Walther, R. Kopold, and W. Becker, "Channel-closing-induced resonances in the above-threshold ionization plateau," Physical Review A. Atomic, Molecular, and Optical Physics **64**(2), 1–4 (2001).

[80] V. S. Popov, "Tunnel and multiphoton ionization of atoms and ions in a strong laser field (Keldysh theory)," Physics-Uspekhi **47**(9), 855–885 (2004).

[81] S.-D. Liang, *Quantum Tunneling and Field Electron Emission Theories* (2013).

[82] H. Reiss, "Theoretical methods in quantum optics: S-matrix and Keldysh techniques for strong-field processes," Progress in Quantum Electronics **16**(1), 1–71 (1992).

[83] N. B. Delone and V. P. Krainov, *Multiphoton Processes in Atoms* (Springer Berlin Heidelberg, 2000).

[84] S. V. Popruzhenko, "Keldysh theory of strong field ionization: history, applications, difficulties and perspectives," Journal of Physics B: Atomic, Molecular and Optical Physics **47**(20), 204,001 (2014).

[85] A. I. Nikishov and V. I. Ritus, "Ionization of Systems Bound by Short-range Forces by the Field of an Electromagnetic Wave," Sov. Phys. JETP **23**(1), 168–177 (1966).

[86] A. M. Perelomov, V. S. Popov, and M. V. Terent'ev, "Ionization of atoms in an alternating electric field," Soviet Physics JETP **23**(5), 924–934 (1966).

[87] A. M. Perelomov, V. S. Popov, and Terent'ev M V, "Ionization of atoms in an alternating electric field: II," Sov. Phys. JETP **24**(1), 207–217 (1967).

[88] A. M. Perelomov and V. S. Popov, "Ionization of atoms in an alternating electric field. III," Soviet Physics JETP **25**(2), 336–343 (1967).

[89] M. V. Ammosov and V. P. Krainov, "Tunnel ionization of complex atoms and of atomic ions in an alternating electromagnetic field," Sov. Phys. JETP **64**(6), 1191–1194 (1986).

[90] N. B. Delone and V. P. Krainov, "Tunneling and barrier-suppression ionization of atoms and ions in a laser radiation field," Physics - Uspekhi **41**(5), 469–485 (1998).

[91] N. B. Delone, V. A. Kovarskii, A. V. Masalov, and N. F. Perel'man, "An atom in the radiation field of a multifrequency laser," Sov. Phys. JETP **23**, 472 (1980).

[92] S. Popruzhenko, V. Mur, V. Popov, and D. Bauer, "Strong Field Ionization Rate for Arbitrary Laser Frequencies," Physical Review Letters **101**(19), 193,003 (2008).

[93] F. H. M. Faisal, "Multiple absorption of laser photons by atoms," Journal of Physics B: Atomic and Molecular Physics **6**(4), L89–L92 (1973).

[94] H. R. Reiss, "Effect of an intense electromagnetic field on a weakly bound system," Physical Review A **22**(5), 1786 (1980).

[95] J. J. Sakurai, *Modern Quantum Mechanics*, 1st ed. (Addison-Wesley, 1994).

[96] H. R. Reiss, "Foundations of the Strong-Field Approximation," in *Progress in Ultrafast Intense Laser Science III*, pp. 1 – 32 (2008).

[97] H. R. Reiss, "Absorption of Light by Light," Journal of Mathematical Physics **3**(1), 59 (1962).

[98] D. Bauer, D. B. Milošević, and W. Becker, "Strong-field approximation for intense-laser atom processes: The choice of gauge," Physical Review A - Atomic, Molecular, and Optical Physics **72**(2), 1–5 (2005).

[99] M. Klaiber, K. Z. Hatsagortsyan, and C. H. Keitel, "Gauge-invariant relativistic strong-field approximation," Physical Review A - Atomic, Molecular, and Optical Physics **73**(5), 1–7 (2006).

[100] K. C. Kulander, K. J. Schafer, and J. Krause, "Single-Active Electron Calculation of Multiphoton Process in Krypton," Int. J. Quantum Chem. Quantum Chem. Symp. **25**, 415 (1991).

[101] M. Awasthi, Y. V. Vanne, A. Saenz, A. Castro, and P. Decleva, "Single-active-electron approximation for describing molecules in ultrashort laser pulses and its application to molecular hydrogen," Physical Review A - Atomic, Molecular, and Optical Physics **77**(6), 1–17 (2008).

[102] C. F. de Morisson Faria and X. Liu, "ElectronâĂŞelectron correlation in strong laser fields," Journal of Modern Optics **58**(13), 1076–1131 (2011).

[103] K. J. Schafer, "Numerical Methods in Strong Field Physics," in *Strong Field Laser Physics*, T. Brabec, ed., pp. 111–146 (Springer Berlin Heidelberg, 2008).

[104] H. R. Reiss, "Dipole-approximation magnetic fields in strong laser beams," Physical Review A **63**(1), 013,409 (2000).

[105] H. R. Reiss, "Mixed quantum and classical processes in strong fields," Physical Review A **75**(1), 013,413 (2007).

[106] H. R. Reiss, "Limits on Tunneling Theories of Strong-Field Ionization," Physical Review Letters **101**(4), 043,002 (2008).

[107] H. R. Reiss, "The tunnelling model of laser-induced ionization and its failure at low frequencies," Journal of Physics B: Atomic, Molecular and Optical Physics **47**(20), 204,006 (2014).

[108] A. Scrinzi, M. Ivanov, R. Kienberger, and D. M. Villeneuve, "Attosecond physics," Journal of Physics B: Atomic and Molecular Physics **39**, R1–R37 (2006).

[109] W. Becker and H. Rottke, "Many-electron strong-field physics," Contemporary Physics **49**(3), 199–223 (2008).

[110] Z. Chen, A.-T. Le, T. Morishita, and C. Lin, "Quantitative rescattering theory for laser-induced high-energy plateau photoelectron spectra," Physical Review A **79**(3), 033,409 (2009).

[111] G. G. Paulus, W. Becker, W. Nicklich, and H. Walther, "Rescattering effects in above-threshold ionization: a classical model," Journal of Physics B: Atomic, Molecular and Optical Physics **27**(21), L703–L708 (1994).

[112] M. Y. Kuchiev, "Atomic antenna," JETP Lett. **45**(7), 404–406 (1987).

[113] H. B. Van Linden Van den Heuvell, *Multiphoton Processes* (Cambridge University Press, 1988).

[114] T. F. Gallagher, "Above-Threshold ionization in Low -Frequency Limit," Physical review letters **61**(20), 2304–2307 (1988).

[115] K. Schafer, B. Yang, L. DiMauro, and K. Kulander, "Above threshold ionization beyond the high harmonic cutoff." Physical review letters **70**(11), 1599–1602 (1993).

[116] M. Kitzler, X. Xie, A. Scrinzi, and A. Baltuska, "Optical attosecond mapping by polarization selective detection," Physical Review A - Atomic, Molecular, and Optical Physics **76**(1), 1–4 (2007).

[117] A. Fleischer, O. Kfir, T. Diskin, P. Sidorenko, and O. Cohen, "Spin angular momentum and tunable polarization in high-harmonic generation," Nature Photonics **8**(7), 543–549 (2014).

[118] O. Kfir, P. Grychtol, E. Turgut, R. Knut, D. Zusin, D. Popmintchev, T. Popmintchev, H. Nembach, J. M. Shaw, A. Fleischer, H. Kapteyn, M. Murnane, and O. Cohen, "Generation of bright circularly-polarized extreme ultraviolet high harmonics for magnetic circular dichroism spectroscopy," Nature Photonics **9**(December 2014), 99–105 (2015).

[119] D. D. Hickstein, F. J. Dollar, P. Grychtol, J. L. Ellis, R. Knut, C. Hernández-García, D. Zusin, C. Gentry, J. M. Shaw, T. Fan, K. M. Dorney, A. Becker, A. Jaroń-Becker, H. C. Kapteyn, M. M. Murnane, and C. G. Durfee, "Non-collinear generation of angularly isolated circularly polarized high harmonics," Nature Photonics **9**(11), 743–750 (2015).

[120] J. L. Chaloupka and D. D. Hickstein, "Dynamics of Strong-Field Double Ionization in Two-Color Counterrotating Fields," Physical Review Letters **116**(14), 1–5 (2016).

[121] V.-H. Hoang, V.-H. Le, C. D. Lin, and A.-T. Le, "Retrieval of target structure information from laser-induced photoelectrons by few-cycle bicircular laser fields," Phys. Rev. A **95**, 031,402(6) (2017).

[122] F. Krausz and M. Y. Ivanov, "Attosecond physics," Reviews of Modern Physics **81**(1), 163–234 (2009).

[123] M. Lewenstein, P. Balcou, M. Y. Ivanov, A. L. Huillier, and P. Corkum, "Theory of high-harmonic generation by low-frequency laser fields," Physical Review A **49**(3), 2117–2132 (1994).

[124] G. Farkas and C. Tóth, "Proposal for attosecond light pulse generation using laser induced multiple-harmonic conversion processes in rare gases," Physics Letters A **168**(5-6), 447–450 (1992).

[125] S. Harris, J. Macklin, and T. Hänsch, "Atomic scale temporal structure inherent to high-order harmonic generation," Optics Communications **100**(5-6), 487–490 (1993).

[126] P. Agostini and L. F. DiMauro, "The physics of attosecond light pulses," Reports on Progress in Physics **67**(6), 813–855 (2004).

[127] F. Silva, S. M. Teichmann, S. L. Cousin, M. Hemmer, and J. Biegert, "Spatiotemporal isolation of attosecond soft X-ray pulses in the water window." Nature communications **6**, 6611 (2015).

[128] S. M. Teichmann, F. Silva, S. L. Cousin, M. Hemmer, and J. Biegert, "0.5-keV Soft X-ray attosecond continua," Nat Commun **7**, 1–6 (2016).

[129] A. L'Huillier, L. A. Lompre, G. Mainfray, and C. Manus, "Multiply charged ions induced by multiphoton absorption in rare gases at 0.53 μm," Physical Review A **27**(5), 2503 (1983).

[130] D. N. Fittinghoff, P. R. Bolton, B. Chang, and K. C. Kulander, "Observation of nonsequential double ionization of helium with optical tunneling," Physical Review Letters **69**(18), 2642–2645 (1992).

[131] K. Kondo, A. Sagisaka, T. Tamida, Y. Nabekawa, and S. Watanabe, "Wavelength dependence of nonsequential double ionization in He," Physical Review A **48**(4), R2531–R2533 (1993).

[132] B. Walker, B. Sheehy, L. F. DiMauro, P. Agostini, K. Schafer, and K. C. Kulander, "Precision measurement of strong field double ionization of helium," Physical Review Letters **73**(9), 1227–1230 (1994).

[133] A. Talebpour, S. Larochelle, and S. L. Chin, "Non-sequential and sequential double ionization of NO in an intense femtosecond Ti:sapphire laser pulse," Journal of Physics B: Atomic, Molecular and Optical Physics **30**(7), L245–L250 (1997).

[134] C. Cornaggia and P. Hering, "Nonsequential double ionization of small molecules induced by a femtosecond laser field," Physical Review A **62**(2), 1–13 (2000).

[135] R. Dörner, T. Weber, M. Weckenbrock, A. Staudte, M. Hattass, H. Schmidt-Böcking, R. Moshammer, and J. Ullrich, "Multiple ionization in strong laser fields," in *Advances in Atomic and Molecular Physics*, B. Bederson and H. Walther, eds., vol. 48, pp. 1–34 (2002).

[136] G. G. Paulus, W. Nicklich, H. Xu, P. Lambropoulos, and H. Walther, "Plateau in above threshold ionization spectra," Physical Review Letters **72**(18), 2851–2854 (1994).

[137] W. Demtröder, *Experimentalphysik 3 - Atome, Moleküle und Festkörper*, 3rd ed. (Springer Berlin Heidelberg, 2006).

[138] M. Oppermann, "Resolving strong field dynamics in cation states of CO2 via optimised molecular alignment," Doctor of philosophy dissertation, Imperial College, London (2013).

[139] P. Cörlin, "Tracing ultra-fast molecular dynaics in O2+ and N2+ with XUV-IR pump-probe experiments," Doctoral dissertation, Ruperto-Carola-Universtity of Heidelberg, Germany (2013).

[140] A. F. Alharbi, "High-order Harmonic Spectroscopy of Cyclic Organic Molecules," Ph.d. dissertation, University of Ottawa, Canada (2016).

[141] M. Born and R. Oppenheimer, "Zur Quantentheorie der Molekeln," Annalen der Physik **389**(20), 457–484 (1927).

[142] M. W. Schmidt, K. K. Baldridge, J. A. Boatz, S. T. Elbert, M. S. Gordon, J. H. Jensen, S. Koseki, N. Matsunaga, K. A. Nguyen, S. Su, T. L. Windus, M. Dupuis, and J. A. Montgomery Jr, "General atomic and molecular electronic structure system," Journal of Computational Chemistry **14**(11), 1347 (1993).

[143] P. Hohenberg and W. Kohn, "Inhomogeneous electron gas," Physical Review **136**, B 864 (1964).

[144] W. Kohn and L. J. Sham, "Self-Consisten Equations IncludingExchange and Correlation Effects," Physical Review **140**(4A), A1133–A1138 (1965).

[145] J. M. Bowman, "Beyond Born-Oppenheimer," Science (New York, N.Y.) **319**, 40–42 (2008).

[146] J. Franck and E. G. Dymond, "Elementary processes of photochemical reactions," Transactions of the Faraday Society **21**, 536–542 (1926).

[147] E. Condon, "A theory of intensity distribution in band systems," Physical Review **28**(6), 1182–1201 (1926).

[148] M. J. DeWitt and R. J. Levis, "Calculating the Keldysh adiabaticity parameter for atomic, diatomic, and polyatomic molecules," The Journal of Chemical Physics **108**(18), 7739 (1998).

[149] P. H. Bucksbaum, A. Zavriyev, H. G. Muller, and D. W. Schumacher, "Softening of the H2+ Molecular bond in Intense Laser Fields," Physical Review Letters **64**(16), 1883 (1990).

[150] L. Frasinski, J. Posthumus, J. Plumridge, K. Codling, P. Taday, and A. Langley, "Manipulation of Bond Hardening in H2+ by Chirping of Intense Femtosecond Laser Pulses," Physical Review Letters **83**(18), 3625–3628 (1999).

[151] X. M. Tong, Z. X. Zhao, and C. D. Lin, "Theory of molecular tunneling ionization," Physical Review A **66**(3), 033,402 (2002).

[152] A. M. M. Hussien, "Ionization of Diatomic Molecules in Intense Laser Fields," Ph.D. thesis (2015).

[153] B. K. McFarland, J. P. Farrell, P. H. Bucksbaum, and M. Gühr, "High harmonic generation from multiple orbitals in N2." Science (New York, N.Y.) **322**(5905), 1232–1235 (2008).

[154] H. Akagi, T. Otobe, A. Staudte, A. Shiner, F. Turner, R. Dörner, D. M. Villeneuve, and P. B. Corkum, "Laser tunnel ionization from multiple orbitals in HCl." Science (New York, N.Y.) **325**(5946), 1364–1367 (2009).

[155] P. Von Den Hoff, I. Znakovskaya, S. Zherebtsov, M. F. Kling, and R. De Vivie-Riedle, "Effects of multi orbital contributions in the angular-dependent ionization of molecules in intense few-cycle laser pulses," Applied Physics B: Lasers and Optics **98**(4), 659–666 (2010).

[156] J. P. Farrell, S. Petretti, J. Förster, B. K. McFarland, L. S. Spector, Y. V. Vanne, P. Decleva, P. H. Bucksbaum, A. Saenz, and M. Gühr, "Strong field ionization to multiple electronic states in water," Physical Review Letters **107**(8), 1–4 (2011).

[157] J. Wu, M. Meckel, L. P. H. Schmidt, M. Kunitski, S. Voss, H. Sann, H. Kim, T. Jahnke, A. Czasch, and R. Dörner, "Probing the tunnelling site of electrons in strong field enhanced ionization of molecules." Nature communications **3**, 1113 (2012).

[158] H. Stapelfeldt and T. Seideman, "Colloquium : Aligning molecules with strong laser pulses," Reviews of Modern Physics **75**(April), 15 (2003).

[159] P. Dooley, I. Litvinyuk, K. Lee, D. Rayner, M. Spanner, D. Villeneuve, and P. Corkum, "Direct imaging of rotational wave-packet dynamics of diatomic molecules," Physical Review A **68**(2), 023,406 (2003).

[160] C. Z. Bisgaard, "Laser-induced alignment," Ph.D. thesis, Universtiy of Aarhus (2006).

[161] J. Ortigoso, M. Rodríguez, M. Gupta, and B. Friedrich, "Time evolution of pendular states created by the interaction of molecular polarizability with a pulsed nonresonant laser field," J. Chem. Phys. **110**(1999), 3870–3875 (1999).

[162] J. G. Underwood, B. J. Sussman, and A. Stolow, "Field-free three dimensional molecular axis alignment," Physical Review Letters **94**(14), 1–4 (2005).

[163] K. Oda, M. Hita, S. Minemoto, and H. Sakai, "All-Optical Molecular Orientation," Physical Review Letters **104**(21), 213,901 (2010).

[164] B. Sheehy, T. O. Clatterbuck, C. Lyng, J. D. D. Martin, D. W. Kim, L. F. Dimauro, M. B. Gaarde, K. J. Schafer, P. Agostini, and K. C. Kulander, "Strong Field Physics in a Scaled Interaction," Laser Physics **11**(2), 226–230 (2001).

[165] T. O. Clatterbuck, C. Lyngå, P. Colosimo, J. D. D. Martin, B. Sheehy, L. F. Dimauro, P. Agostini, and K. C. Kulander, "Scaled intense laser-atom physics: the long wavelength regime," Journal of Modern Optics **50**(3-4), 441–450 (2003).

[166] K. D. Schultz, C. I. Blaga, R. Chirla, P. Colosimo, J. Cryan, A. M. March, C. Roedig, E. Sistrunk, J. Tate, J. Wheeler, P. Agostini, and L. F. Dimauro, "Strong field physics with long wavelength lasers," Journal of Modern Optics **54**(7), 1075–1085 (2007).

[167] P. Agostini and L. F. DiMauro, "Atoms in high intensity mid-infrared pulses," Contemporary Physics **49**(3), 179–197 (2008).

[168] "International Organization for Standardization, ISO 20473:2007, https://www.iso.org/obp/ui/#iso:std:iso:20473:ed-1:v1:en," .

[169] B. Wolter, M. G. Pullen, M. Baudisch, M. Sclafani, M. Hemmer, A. Senftleben, C. D. Schröter, J. Ullrich, R. Moshammer, and J. Biegert, "Strong-Field Physics with Mid-IR Fields," Physical Review X **5**(2), 021,034 (2015).

[170] A. S. Alnaser, D. Comtois, A. T. Hasan, D. M. Villeneuve, J.-C. Kieffer, and I. V. Litvinyuk, "Strong-field non-sequential double ionization: wavelength dependence of ion momentum distributions for neon and argon," Journal of Physics B: Atomic, Molecular and Optical Physics **41**(3), 031,001 (2008).

[171] G. Gingras, A. Tripathi, and B. Witzel, "Wavelength and Intensity Dependence of Short Pulse Laser Xenon Double Ionization between 500 and 2300 nm," Physical Review Letters **103**(17), 173,001 (2009).

[172] T. Popmintchev, M.-C. Chen, D. Popmintchev, P. Arpin, S. Brown, S. Alisauskas, G. Andriukaitis, T. Balciunas, O. D. Mücke, A. Pugzlys, A. Baltuska, B. Shim, S. E. Schrauth, A. Gaeta, C. Hernández-García, L. Plaja, A. Becker, A. Jaron-Becker, M. M. Murnane, and H. C. Kapteyn, "Bright coherent ultrahigh harmonics in the keV x-ray regime from mid-infrared femtosecond lasers." Science (New York, N.Y.) **336**(6086), 1287–1291 (2012).

[173] A. D. Dichiara, E. Sistrunk, C. I. Blaga, U. B. Szafruga, P. Agostini, and L. F. Dimauro, "Inelastic Scattering of Broadband Electron Wave Packets Driven by an Intense Mid-infrared Laser Field," Physical Review Letters **108**(January), 033,002 (2012).

[174] M. G. Pullen, B. Wolter, A.-T. Le, M. Baudisch, M. Hemmer, A. Senftleben, C. D. Schröter, J. Ullrich, R. Moshammer, C. D. Lin, and J. Biegert, "Imaging an aligned polyatomic molecule with laser-induced electron diffraction," Nature Communications **6**, 7262 (2015).

[175] S. Backus, C. G. Durfee, M. M. Murnane, and H. C. Kapteyn, "High power ultrafast lasers," Review of Scientific Instruments **69**, 1207 (1998).

[176] A. Stolow, A. E. Bragg, and D. M. Neumark, "Femtosecond Time-Resolved Photoelectron Spectroscopy," Chemical Reviews **104**(4), 1719–1758 (2004).

[177] A. Stolow and J. G. Underwood, "Time-resolved photoelectron spectroscopy of nonadiabatic dynamics in polyatomic molecules," in *Advances in Chemical Physics*, S. A. Rice, ed., vol. 139, chap. 6, pp. 497–583 (John Wiley & Sons, Inc., 2008).

[178] M. G. Pullen, W. C. Wallace, D. E. Laban, A. J. Palmer, G. F. Hanne, A. N. Grum-Grzhimailo, K. Bartschat, I. Ivanov, A. Kheifets, D. Wells, H. M. Quiney, X. M. Tong,

I. V. Litvinyuk, R. T. Sang, and D. Kielpinski, "Measurement of laser intensities approaching 1015 W/cm2 with an accuracy of 1%," Physical Review A - Atomic, Molecular, and Optical Physics **87**(5), 1–6 (2013).

[179] J.-C. Diels and W. Rudolph, *Ultrashort Laser Pulse Phenomena*, 2nd ed. (Elsevier, 2006).

[180] R. W. Boyd, *Nonlinear Optics*, 3rd ed. (2008).

[181] U. Keller, K. J. Weingarten, F. X. Kärtner, D. Kopf, B. Braun, I. D. Jung, R. Fluck, C. Hönninger, N. Matuschek, and J. Aus Der Au, "Semiconductor saturable absorber mirrors (SESAM's) for femtosecond to nanosecond pulse generation in solid-state lasers," IEEE Journal on Selected Topics in Quantum Electronics **2**(3), 435–451 (1996).

[182] A. Grün, "Nonlinear pulse compression," Doctoral thesis, UPC - Universitat Politecnica de Catalunya (2014).

[183] D. Strickland and G. Mourou, "Compression of Amplified Chirped Optical Pulses *," Optics Communications **56**(3), 219–221 (1985).

[184] Q. Peng, A. Juzeniene, J. Chen, L. O. Svaasand, T. Warloe, K.-E. Giercksky, and J. Moan, "Lasers in medicine," Reports on Progress in Physics **71**(5) (2008).

[185] A. Dubietis, G. Jonusauskas, and A. Piskarskas, "Powerful Femtosecond Pulse Generation By Chirped And Stretched Pulse Parametric Amplification In BBO Crystal," Optics Communications **88**(4-6), 437–440 (1992).

[186] I. Ross, P. Matousek, M. Towrie, A. Langley, and J. Collier, "The prospects for ultrashort pulse duration and ultrahigh intensity using optical parametric chirped pulse amplifiers," Optics Communications **144**(1-3), 125–133 (1997).

[187] D. J. Kane and R. Trebino, "Characterization of Arbitrary Femtosecond Pulses Using Frequency-Resolved Optical Gating," (1993).

[188] R. Trebino, *Frequency-Resolved Optical Gating : The Measurement of Ultrashort Laser Pulses*, vol. 1 (Springer Science + Business Media New York, 2000).

[189] A. E. Siegman, "quality," Proc. SPIE 1868 **1868**(3), 2–12 (1993).

[190] T. Morishita, A.-T. Le, Z. Chen, and C. D. Lin, "Accurate Retrieval of Structural Information from Laser-Induced Photoelectron and High-Order Harmonic Spectra by Few-Cycle Laser Pulses," Physical Review Letters **100**(1), 013,903 (2008).

[191] Z. Chen, A.-T. Le, T. Morishita, and C. D. Lin, "Origin of species dependence of high-energy plateau photoelectron spectra," Journal of Physics B: Atomic, Molecular and Optical Physics **42**(6), 061,001 (2009).

[192] A. Staudte, "Subfemtosecond Electron Dynamics of H 2 in Strong Fields or The Quest for the Molecular Clock," Ph.D. thesis, Johann Wolfgang Goethe - Universität, Frankfurt am Main (2005).

[193] S. L. Cousin, F. Silva, S. Teichmann, M. Hemmer, B. Buades, and J. Biegert, "High-flux table-top soft x-ray source driven by sub-2-cycle, CEP stable, 185-μm 1-kHz pulses for carbon K-edge spectroscopy," Optics Letters **39**(18), 5383–5386 (2014).

[194] F. J. Furch, S. Birkner, F. Kelkensberg, A. Giree, A. Anderson, C. P. Schulz, and M. J. J. Vrakking, "Carrier-envelope phase stable few-cycle pulses at 400 kHz for electron-ion coincidence experiments," Optics Express **21**(19), 22,671 (2013).

[195] J. Matyschok, T. Lang, T. Binhammer, O. Prochnow, S. Rausch, M. Schultze, A. Harth, P. Rudawski, C. L. Arnold, A. L'Huillier, and U. Morgner, "Temporal and spatial effects inside a compact and CEP stabilized, few-cycle OPCPA system at high repetition rates," Optics Express **21**(24), 29,656 (2013).

[196] C. Y. Wu, Y. D. Yang, Y. Q. Liu, Q. H. Gong, M. Wu, X. Liu, X. L. Hao, W. D. Li, X. T. He, and J. Chen, "Characteristic Spectrum of Very Low-Energy Photoelectron from Above-Threshold Ionization in the Tunneling Regime," Physical Review Letters **109**(4), 043,001 (2012).

[197] I. Pupeza, T. Eidam, J. Rauschenberger, B. Bernhardt, A. Ozawa, E. Fill, A. Apolonski, T. Udem, J. Limpert, Z. A. Alahmed, A. M. Azzeer, A. Tünnermann, T. W. Hänsch, and F. Krausz, "Power scaling of a high-repetition-rate enhancement cavity." Optics letters **35**(12), 2052–4 (2010).

[198] J. Ullrich, R. Dörner, V. Mergel, O. Jagutzki, L. Spielberger, and H. Schmidt-Böcking, "Cold-Target Recoil-Ion Momentum Spectroscopy: First Results and Future Perspectives of a Novel High-Resolution Technique for the Investigation of Collision Induced Many- Particle Reactions," Comments At. Mol. Phys. **30**, 415–422 (1994).

[199] J. Ullrich, R. Moshammer, R. Dörner, O. Jagutzki, V. Mergel, H. Schmidt-Böcking, and L. Spielberger, "Recoil-ion momentum spectroscopy," Journal of Physics B: Atomic, Molecular and Optical Physics **30**, 2917–2974 (1997).

[200] R. Dörner, V. Mergel, O. Jagutzki, L. Spielberger, J. Ullrich, R. Moshammer, and H. Schmidt-Böcking, "Cold Target Recoil Ion Momentum Spectroscopy : a momentum microscope to view atomic collision dynamics," Physics Reports **330**, 95–192 (2000).

[201] V. L. B. De Jesus, A. Rudenko, B. Feuerstein, K. Zrost, C. D. Schröter, R. Moshammer, and J. Ullrich, "Reaction microscopes applied to study atomic and molecular fragmentation in intense laser fields: Non-sequential double ionization of helium," Journal of Electron Spectroscopy and Related Phenomena **141**(2-3), 127–142 (2004).

[202] N. Camus, "Non-sequential double ionization of atoms with phase-controlled ultrashort laser pulses," Dissertation, Ruperto-Carola University of Heidelberg (2013).

[203] L. Fechner, "High resolution experiments on strong-field ionization of atoms and molecules: test of tunneling theory, the role of doubly excited states, and channel-selective electron spectra," Ph.D. thesis (2014).

[204] W. Demtröder, *Experimentalphysik 1 - Mechanik und Wärme*, 5th ed. (Springer Berlin Heidelberg, 2008).

[205] D. R. Miller, "Free Jet Sources," in *Atomic and Molecular Beam Methods*, G. Scoles, D. Bassi, U. Buck, and D. Lainé, eds., vol. 14-82, chap. 2 (Oxford University Press, 1988).

[206] A. Senftleben, "Kinematically complete study on electron impact ionisation of aligned hydrogen molecules," Dissertation, Ruperto-Carola University of Heidelberg, Germany (2009).

[207] K. Schnorr, "XUV Pump-Probe Experiments on Electron Rearrangement and Interatomic Coulombic Decay in Diatomic Molecules," Dissertation, Ruperto-Carola-University of Heidelberg, Germany (2014).

[208] H. Pauly, *Atom, Molecule, and Cluster Beams I - Basic Theory, Production and Detection of Thermal Energy Beams* (2000).

[209] G. Tejeda, B. Maté, J. Fernández-Sánchez, and S. Montero, "Temperature and density mapping of supersonic jet expansions using linear Raman spectroscopy." Physical review letters **76**(1), 34–37 (1996).

[210] J. Wu, A. Vredenborg, B. Ulrich, L. P. H. Schmidt, M. Meckel, S. Voss, H. Sann, H. Kim, T. Jahnke, and R. Dörner, "Nonadiabatic alignment of van der Waals–force-bound argon dimers by femtosecond laser pulses," Physical Review A **83**(6), 061,403 (2011).

[211] R. Moshammer, D. Fischer, and H. Kollmus, "Recoil-Ion Momentum Spectroscopy and "Reaction Microscopes"," in *Many-Particle Quantum Dynamics in Atomic and Molecular Fragmentation*, J. Ullrich and V. Shevelko, eds., chap. 1 (Springer Berlin Heidelberg, 2003).

[212] RoentDek Handels GmbH, "RoentDek PRODUCT LIST - particle / photon detectors," .

[213] S. Birkner, "Strong Field Ionization of Atoms and Molecules : Electron-Ion Coincidence Measurements at High Repetition Rate," Ph.D. thesis (2015).

[214] S. Roither, X. Xie, D. Kartashov, L. Zhang, M. Schöffler, H. Xu, A. Iwasaki, T. Okino, K. Yamanouchi, A. Baltuska, and M. Kitzler, "High Energy Proton Ejection from Hydrocarbon Molecules Driven by Highly Efficient Field Ionization," Physical Review Letters **106**(April), 2–5 (2011).

[215] J. Laksman, D. Céolin, E. P. Månsson, S. L. Sorensen, and M. Gisselbrecht, "Development and characterization of a multiple-coincidence ion-momentum imaging spectrometer," Review of Scientific Instruments **84**, 123,113 (2013).

[216] T. Pflüger, "Electron Impact Ionization Studies of Small Rare Gas Clusters," Ph.D. thesis (2012).

[217] B. Wolter, C. Lemell, M. Baudisch, M. G. Pullen, X.-M. Tong, M. Hemmer, A. Senftleben, C. D. Schröter, J. Ullrich, R. Moshammer, J. Biegert, and J. Burgdörfer, "Formation of very-low-energy states crossing the ionization threshold of argon atoms in strong mid-infrared fields," Physical Review A **90**(6), 063,424 (2014).

[218] M. G. Pullen, J. Dura, B. Wolter, M. Baudisch, M. Hemmer, N. Camus, A. Senftleben, C. D. Schroeter, R. Moshammer, J. Ullrich, and J. Biegert, "Kinematically complete measurements of strong field ionization with mid-IR pulses," Journal of Physics B: Atomic, Molecular and Optical Physics **47**(20), 204,010 (2014).

[219] W. Becker, F. Grasbon, R. Kopold, D. B. Milošević, G. G. Paulus, and H. Walther, "Above-threshold ionization: from classical features to quantum effects," Advances in Atomic, Molecular, and Optical Physics **48**(1979), 35–98 (2002).

[220] C. Lemell, J. Burgdörfer, S. Gräfe, K. I. Dimitriou, D. G. Arbó, and X. M. Tong, "Classical-quantum correspondence in atomic ionization by midinfrared pulses: Multiple peak and interference structures," Physical Review A - Atomic, Molecular, and Optical Physics **87**(1), 013,421 (2013).

[221] F. Catoire, C. I. Blaga, E. Sistrunk, H. G. Muller, P. Agostini, and L. F. DiMauro, "Mid-infrared strong field ionization angular distributions," Laser Physics **19**(8), 1574–1580 (2009).

[222] C. Liu and K. Z. Hatsagortsyan, "Origin of Unexpected Low Energy Structure in Photoelectron Spectra Induced by Midinfrared Strong Laser Fields," Physical Review Letters **105**(11), 113,003 (2010).

[223] T.-M. Yan, S. V. Popruzhenko, M. J. J. Vrakking, and D. Bauer, "Low-Energy Structures in Strong Field Ionization Revealed by Quantum Orbits," Physical Review Letters **105**(25), 253,002 (2010).

[224] A. Kästner, U. Saalmann, and J. M. Rost, "Electron-Energy Bunching in Laser-Driven Soft Recollisions," Physical Review Letters **108**(3), 033,201 (2012).

[225] A. Kästner, U. Saalmann, and J. M. Rost, "Energy bunching in soft recollisions revealed with long-wavelength few-cycle pulses," Journal of Physics B: Atomic, Molecular and Optical Physics **45**(7), 074,011 (2012).

[226] C. Lemell, K. I. Dimitriou, X.-M. Tong, S. Nagele, D. V. Kartashov, J. Burgdörfer, and S. Gräfe, "Low-energy peak structure in strong-field ionization by midinfrared laser pulses: Two-dimensional focusing by the atomic potential," Physical Review A **85**(1), 011,403 (2012).

[227] D. B. Milošević, "Reexamination of the improved strong-field approximation: Low-energy structures in the above-threshold-ionization spectra for short-range potentials," Physical Review A **88**(2), 023,417 (2013).

[228] L. Guo, S. S. Han, X. Liu, Y. Cheng, Z. Z. Xu, J. Fan, J. Chen, S. G. Chen, W. Becker, C. I. Blaga, A. D. DiChiara, E. Sistrunk, P. Agostini, and L. F. DiMauro, "Scaling of the Low-Energy Structure in Above-Threshold Ionization in the Tunneling Regime: Theory and Experiment," Physical Review Letters **110**(1), 013,001 (2013).

[229] W. Becker, S. P. Goreslavski, D. B. Milošević, and G. G. Paulus, "Low-energy electron rescattering in laser-induced ionization," Journal of Physics B: Atomic, Molecular and Optical Physics **47**(20), 204,022 (2014).

[230] A. Rudenko, K. Zrost, C. D. Schröter, V. L. B. D. Jesus, B. Feuerstein, R. Moshammer, and J. Ullrich, "Resonant structures in the low-energy electron continuum for single ionization of atoms in the tunnelling regime," Journal of Physics B: Atomic, Molecular and Optical Physics **37**(24), L407–L413 (2004).

[231] Z.-Y. Lin, M.-Y. Wu, W. Quan, X.-J. Liu, J. Chen, and Y. Cheng, "The Coulomb effect on a low-energy structure in above-threshold ionization spectra induced by mid-infrared laser pulses," Chinese Physics B **23**(2), 1–7 (2014).

[232] H. Liu, Y. Liu, L. Fu, G. Xin, D. Ye, J. Liu, X. T. He, Y. Yang, X. Liu, Y. Deng, C. Wu, and Q. Gong, "Low Yield of Near-Zero-Momentum Electrons and Partial Atomic Stabilization in Strong-Field Tunneling Ionization," Physical Review Letters **109**(9), 093,001 (2012).

[233] A. V. Veltheim, B. Manschwetus, W. Quan, B. Borchers, G. Steinmeyer, H. Rottke, and W. Sandner, "Frustrated Tunnel Ionization of Noble Gas Dimers with Rydberg-Electron Shakeoff by Electron Charge Oscillation," Physical Review Letters **023001**(January), 1–5 (2013).

[234] T. Nubbemeyer, K. Gorling, A. Saenz, U. Eichmann, and W. Sandner, "Strong-Field Tunneling without Ionization," Physical Review Letters **101**(23), 233,001 (2008).

[235] C. Froese Fischer, "General Hartree-Fock program," Computer Physics Communications **43**(3), 355–365 (1987).

[236] I. Velchev, W. Hogervorst, and W. Ubachs, "Precision VUV spectroscopy of Ar I at 105 nm," Journal of Physics B: Atomic, Molecular and Optical Physics **32**(L511) (1999).

[237] N. B. Delone and V. P. Krainov, "Energy and angular electron spectra for the tunnel ionization of atoms by strong low-frequency radiation," Journal of Optical Society of America B **8**(6), 1207–1211 (1991).

[238] R. Murray, W.-K. Liu, and M. Y. Ivanov, "Partial Fourier-transform approach to tunnel ionization: Atomic systems," Physical Review A **81**(2), 023,413 (2010).

[239] I. Dreissigacker and M. Lein, "Quantitative theory for the lateral momentum distribution after strong-field ionization," Chemical Physics **414**, 69–72 (2013).

[240] L. Arissian, C. Smeenk, F. Turner, C. Trallero, A. V. Sokolov, D. M. Villeneuve, A. Staudte, and P. B. Corkum, "Direct Test of Laser Tunneling with Electron Momentum Imaging," Physical Review Letters **105**(13), 133,002 (2010).

[241] S. Augst, D. D. Meyerhofer, D. Strickland, and S. L. Chint, "Laser ionization of noble gases by Coulomb-barrier suppression," Journal of the Optical Society of America B **8**(4), 858 (1991).

[242] J. Posthumus, *Molecules and Clusters in Intense Laser Fields* (Cambridge University Press, Cambridge, 2001).

[243] X.-M. Tong and S.-I. Chu, "Theoretical study of multiple high-order harmonic generation by intense ultrashort pulsed laser fields: A new generalized pseudospectral time-dependent method," Chemical Physics **217**(2-3), 119–130 (1997).

[244] X. Tong, K. Hino, and N. Toshima, "Phase-dependent atomic ionization in few-cycle intense laser fields," Physical Review A **74**(3), 031,405 (2006).

[245] X. M. Tong and C. D. Lin, "Empirical formula for static field ionization rates of atoms and molecules by lasers in the barrier-suppression regime," Journal of Physics B: Atomic, Molecular and Optical Physics **38**(15), 2593–2600 (2005).

[246] K. Zhang, Y. H. Lai, E. Diesen, B. E. Schmidt, C. I. Blaga, J. Xu, and T. Gorman, "Universal pulse dependence of the low-energy structure in strong-field ionization," Physical Review A - Atomic, Molecular, and Optical Physics **93**, 021,403 (2016).

[247] W. Becker and D. B. Milošević, "Above-threshold ionization for very low electron energy," Journal of Physics B: Atomic, Molecular and Optical Physics **48**(15), 151,001 (2015).

[248] D. B. Milošević, "Forward- and backward-scattering quantum orbits in above-threshold ionization," Physical Review A - Atomic, Molecular, and Optical Physics **063414**, 1–11 (2014).

[249] C. Nicole, I. Sluimer, F. Rosca-pruna, M. Warntjes, M. Vrakking, C. Bordas, V. Cedex, F. Texier, and F. Robicheaux, "Slow Photoelectron Imaging," Physical Review Letters **85**(19), 1–4 (2000).

[250] U. Eichmann, T. Nubbemeyer, H. Rottke, and W. Sandner, "Acceleration of neutral atoms in strong short-pulse laser fields." Nature **461**(7268), 1261–4 (2009).

[251] S. Yoshida, C. Reinhold, J. Burgdörfer, W. Zhao, J. Mestayer, J. Lancaster, and F. Dunning, "Influence of a dc offset field on kicked quasi-one-dimensional Rydberg atoms: Stabilization and frustrated field ionization," Physical Review A **73**(3), 033,411 (2006).

[252] B.-B. Wang, X.-F. Liu, P.-M. Fu, J. Chen, and J. Liu, "Coulomb Potential Recapture Effect in Above-Barrier Ionization in Laser Pulses," Chinese Physics Letters **23**, 2729 (2006).

[253] N. I. Shvetsov-Shilovski, S. P. Goreslavski, S. V. Popruzhenko, and W. Becker, "Capture into rydberg states and momentum distributions of ionized electrons," Laser Physics **19**(8), 1550–1558 (2009).

[254] A. S. Landsman, A. N. Pfeiffer, C. Hofmann, M. Smolarski, C. Cirelli, and U. Keller, "Rydberg state creation by tunnel ionization," New Journal of Physics **15**(1), 013,001 (2013).

[255] H. Lv, W. Zuo, L. Zhao, H. Xu, M. Jin, D. Ding, S. Hu, and J. Chen, "Comparative study on atomic and molecular Rydberg-state excitation in strong infrared laser fields," Physical Review A **93**(3), 033,415 (2016).

[256] E. Diesen, U. Saalmann, M. Richter, M. Kunitski, R. D??rner, and J. M. Rost, "Dynamical Characteristics of Rydberg Electrons Released by a Weak Electric Field," Physical Review Letters **116**(14), 1–5 (2016).

[257] E. Pisanty and M. Ivanov, "Slalom in complex time: Emergence of low-energy structures in tunnel ionization via complex-time contours," Physical Review A - Atomic, Molecular, and Optical Physics **93**(4), 1–17 (2016).

[258] E. Pisanty and M. Ivanov, "Kinematic origin for near-zero energy structures in mid-IR strong field ionization," Journal of Physics B: Atomic, Molecular and Optical Physics **49**(10), 105,601 (2016).

[259] W. Quan, X. Hao, Y. Chen, S. Yu, S. Xu, Y. Wang, X. Lai, C. Wu, Q. Gong, X. He, X. Liu, and J. Chen, "Long-Range Coulomb Effect in Intense Laser-Driven Photoelectron Dynamics," Scientific Reports **6**, 27,108 (2016).

[260] Z. Yuan, D. Ye, J. Liu, and L. Fu, "Inner-shell electron effects in strong-field double ionization of Xe," Physical Review A **93**(6), 063,409 (2016).

[261] M. G. Pullen, B. Wolter, X. Wang, X.-M. Tong, M. Sclafani, M. Baudisch, H. Pires, C. D. Schröter, J. Ullrich, T. Pfeifer, R. Moshammer, J. H. Eberly, and J. Biegert, "Transition from non-sequential to sequential double ionisation in many-electron systems," Phys. Rev. A **96**, 033,401 (2017).

[262] R. Moshammer, B. Feuerstein, W. Schmitt, A. Dorn, C. Schröter, J. Ullrich, H. Rottke, C. Trump, M. Wittmann, G. Korn, K. Hoffmann, and W. Sandner, "Momentum Distributions of Ne++ Ions Created by an Intense Ultrashort Laser Pulse," Physical Review Letters **84**, 447–450 (2000).

[263] T. Weber, H. Giessen, M. Weckenbrock, G. Urbasch, A. Staudte, L. Spielberger, O. Jagutzki, V. Mergel, M. Vollmer, and R. Dorner, "Correlated electron emission in multiphoton double ionization," Nature **405**(6787), 658–661 (2000).

[264] B. Bergues, M. Kübel, N. G. Johnson, B. Fischer, N. Camus, K. J. Betsch, O. Herrwerth, A. Senftleben, a. M. Sayler, T. Rathje, T. Pfeifer, I. Ben-Itzhak, R. R. Jones, G. G. Paulus, F. Krausz, R. Moshammer, J. Ullrich, and M. F. Kling, "Attosecond tracing of correlated electron-emission in non-sequential double ionization." Nature communications **3**(may), 813 (2012).

[265] Y. Liu, S. Tschuch, A. Rudenko, M. Dürr, M. Siegel, U. Morgner, R. Moshammer, and J. Ullrich, "Strong-Field Double Ionization of Ar below the Recollision Threshold," Physical Review Letters **101**(5), 053,001 (2008).

[266] A. Rudenko, T. Ergler, K. Zrost, B. Feuerstein, V. de Jesus, C. Schröter, R. Moshammer, and J. Ullrich, "Intensity-dependent transitions between different pathways of strong-field double ionization," Physical Review A **78**(1), 015,403 (2008).

[267] M. Kübel, K. J. Betsch, N. G. Kling, A. S. Alnaser, J. Schmidt, U. Kleineberg, Y. Deng, I. Ben-Itzhak, G. G. Paulus, T. Pfeifer, J. Ullrich, R. Moshammer, M. F. Kling, and B. Bergues, "Non-sequential double ionization of Ar: From the single- to the many-cycle regime," New Journal of Physics **16** (2014).

[268] P. Kaminski, R. Wiehle, W. Kamke, H. Helm, and B. Witzel, "Wavelength dependence of double ionization of xenon in a strong laser field," Physical Review A **73**(1), 013,413 (2006).

[269] V. L. B. D. Jesus, B. Feuerstein, K. Zrost, D. Fischer, A. Rudenko, F. Afaneh, C. D. Schröter, R. Moshammer, and J. Ullrich, "Atomic structure dependence of nonsequential double ionization of He, Ne and Ar in strong laser pulses," Journal of Physics B: Atomic, Molecular and Optical Physics **37**(8), L161–L167 (2004).

[270] B. Feuerstein, R. Moshammer, D. Fischer, A. Dorn, C. Schröter, J. Deipenwisch, J. Crespo Lopez-Urrutia, C. Höhr, P. Neumayer, J. Ullrich, H. Rottke, C. Trump, M. Wittmann, G. Korn, and W. Sandner, "Separation of Recollision Mechanisms in Nonsequential Strong Field Double Ionization of Ar: The Role of Excitation Tunneling," Physical Review Letters **87**(4), 043,003 (2001).

[271] T. Weber, M. Weckenbrock, A. Staudte, L. Spielberger, O. Jagutzki, V. Mergel, F. Afaneh, G. Urbasch, M. Vollmer, H. Giessen, and R. Dorner, "Recoil-ion momentum distributions for single and double ionization of helium in strong laser fields," Physical Review Letters **84**(3), 443–446 (2000).

[272] A. Rudenko, V. de Jesus, T. Ergler, K. Zrost, B. Feuerstein, C. Schröter, R. Moshammer, and J. Ullrich, "Correlated Two-Electron Momentum Spectra for Strong-Field Nonsequential Double Ionization of He at 800 nm," Physical Review Letters **99**(26), 263,003 (2007).

[273] A. Staudte, C. Ruiz, M. Schöffler, S. Schössler, D. Zeidler, T. Weber, M. Meckel, D. Villeneuve, P. Corkum, A. Becker, and R. Dörner, "Binary and Recoil Collisions in Strong Field Double Ionization of Helium," Physical Review Letters **99**(26), 263,002 (2007).

[274] M. Weckenbrock, D. Zeidler, A. Staudte, T. Weber, M. Schöffler, M. Meckel, S. Kammer, M. Smolarski, O. Jagutzki, V. Bhardwaj, D. Rayner, D. Villeneuve, P. Corkum, and R. Dörner, "Fully Differential Rates for Femtosecond Multiphoton Double Ionization of Neon," Physical Review Letters **92**(21), 213,002 (2004).

[275] Y. Liu, D. Ye, J. Liu, A. Rudenko, S. Tschuch, M. Dürr, M. Siegel, U. Morgner, Q. Gong, R. Moshammer, and J. Ullrich, "Multiphoton Double Ionization of Ar and Ne Close to Threshold," Physical Review Letters **104**(17), 173,002 (2010).

[276] C. Guo, M. Li, J. Nibarger, and G. Gibson, "Single and double ionization of diatomic molecules in strong laser fields," Physical Review A **58**(6), R4271–R4274 (1998).

[277] R. Wiehle and B. Witzel, "Correlation between double and nonresonant single ionization," Physical Review Letters **89**(22), 223,002 (2002).

[278] J. L. Chaloupka, J. Rudati, R. Lafon, P. Agostini, K. C. Kulander, and L. F. DiMauro, "Observation of a transition in the dynamics of strong-field double ionization." Physical review letters **90**(3), 033,002 (2003).

[279] J. Rudati, J. Chaloupka, P. Agostini, K. Kulander, and L. DiMauro, "Multiphoton Double Ionization via Field-Independent Resonant Excitation," Physical Review Letters **92**(20), 203,001 (2004).

[280] L. Landau and E. Lifshitz, *Quantum Mechanics (Non-relativistic theory)*, 3rd ed. (Pergamon, 1977).

[281] C. Z. Bisgaard and L. B. Madsen, "Tunneling ionization of atoms," American Journal of Physics **72**(2), 249 (2004).

[282] P. J. Ho, R. Panfili, S. L. Haan, and J. H. Eberly, "Nonsequential double ionization as a completely classical photoelectric effect," Physical Review Letters **94**(9), 1–4 (2005).

[283] T.-J. Wang, Z. Major, I. Ahmad, S. Trushin, F. Krausz, and S. Karsch, "Ultrabroadband near-infrared pulse generation by noncollinear OPA with angular dispersion compensation," Applied Physics B (2009).

[284] X. M. Tong, G. Wachter, S. A. Sato, C. Lemell, K. Yabana, and J. Burgdörfer, "Application of norm-conserving pseudopotentials to intense laser-matter interactions," Physical Review A - Atomic, Molecular, and Optical Physics **92**(4), 1–9 (2015).

[285] O. A. Vydrov, "Correcting the Self-Interaction Error of Approximate Density Functionals," Doctoral thesis, Rice University (2007).

[286] X.-M. Tong and S.-I. Chu, "Time-dependent density-functional theory for strong-field multiphoton processes: Application to the study of the role of dynamical electron correlation in multiple high-order harmonic generation," Phys. Rev. A **57**(1), 452–461 (1998).

[287] X. M. Tong, P. Ranitovic, C. W. Hogle, M. M. Murnane, H. C. Kapteyn, and N. Toshima, "Theory and experiment on laser-enabled inner-valence Auger decay of rare-gas atoms," Physical Review A - Atomic, Molecular, and Optical Physics **84**(1), 1–8 (2011).

[288] P. Ranitovic, X. M. Tong, C. W. Hogle, X. Zhou, Y. Liu, N. Toshima, M. M. Murnane, and H. C. Kapteyn, "Laser-enabled auger decay in rare-gas atoms," Physical Review Letters **106**(5), 2–5 (2011).

[289] S. Hankin, D. Villeneuve, P. Corkum, and D. Rayner, "Intense-field laser ionization rates in atoms and molecules," Physical Review A **64**(1), 1–12 (2001).

[290] S. Larochelle, A. Talebpour, and S. L. Chin, "Non-sequential multiple ionization of rare gas atoms in a Ti:Sapphire laser field," Journal of Physics B: Atomic, Molecular and Optical Physics **31**, 1201–1214 (1998).

[291] M. G. Pullen, B. Wolter, A.-T. Le, M. Baudisch, M. Hemmer, A. Senftleben, C. D. Schröter, J. Ullrich, R. Moshammer, C. D. Lin, and J. Biegert, "Laser-Induced Electron Diffraction to Image Molecular Structure," OSA - Optics & Photonics News Highlights 2015 (December), 50 (2015).

[292] D. H. Bilderback, P. Elleaume, and E. Weckert, "Review of third and next generation synchrotron light sources," Journal of Physics B: Atomic, Molecular and Optical Physics **38**(9), S773 (2005).

[293] M. Chergui and A. H. Zewail, "Electron and X-ray methods of ultrafast structural dynamics: advances and applications." Chemphyschem : a European journal of chemical physics and physical chemistry **10**(1), 28–43 (2009).

[294] R. Boll, D. Anielski, C. Bostedt, J. D. Bozek, L. Christensen, R. Coffee, S. De, P. Decleva, S. W. Epp, B. Erk, L. Foucar, F. Krasniqi, J. Küpper, A. Rouzée, B. Rudek, A. Rudenko, S. Schorb, H. Stapelfeldt, M. Stener, S. Stern, S. Techert, S. Trippel, M. J. J. Vrakking, J. Ullrich, and D. Rolles, "Femtosecond photoelectron diffraction on laser-aligned molecules: Towards time-resolved imaging of molecular structure," Physical Review A - Atomic, Molecular, and Optical Physics **88**(6), 061,402(R) (2013).

[295] V. Blanchet, M. Z. Zgierski, T. Seideman, and A. Stolow, "Discerning vibronic molecular dynamics using time-resolved photoelectron spectroscopy," Nature **401**(6748), 52–54 (1999).

[296] B. J. Siwick, J. R. Dwyer, R. E. Jordan, and R. J. D. Miller, "An atomic-level view of melting using femtosecond electron diffraction." Science (New York, N.Y.) **302**(5649), 1382–5 (2003).

[297] M. Dantus, M. J. Rosker, and A. H. Zewail, "Femtosecond real-time probing of reactions. II. The dissociation reaction of ICN," J. Chem. Phys. **89**(10), 6128–6140 (1988).

[298] H. Ihee, V. A. Lobastov, U. M. Gomez, B. M. Goodson, R. Srinivasan, C. Y. Ruan, and a. H. Zewail, "Direct imaging of transient molecular structures with ultrafast diffraction." Science (New York, N.Y.) **291**(5503), 458–462 (2001).

[299] P. Emma, R. Akre, J. Arthur, R. Bionta, C. Bostedt, J. Bozek, A. Brachmann, P. Bucksbaum, R. Coffee, F.-J. Decker, Y. Ding, D. Dowell, S. Edstrom, A. Fisher, J. Frisch, S. Gilevich, J. Hastings, G. Hays, P. Hering, Z. Huang, R. Iverson, H. Loos, M. Messerschmidt, A. Miahnahri, S. Moeller, H.-D. Nuhn, G. Pile, D. Ratner, J. Rzepiela, D. Schultz, T. Smith, P. Stefan, H. Tompkins, J. Turner, J. Welch, W. White, J. Wu, G. Yocky, and J. Galayda, "First lasing and operation of an ångstrom-wavelength free-electron laser," Nature Photonics **4**(9), 641–647 (2010).

[300] C. Bostedt, S. Boutet, D. M. Fritz, Z. Huang, H. J. Lee, H. T. Lemke, A. Robert, W. F. Schlotter, J. J. Turner, and G. J. Williams, "Linac Coherent Light Source: The first five years," Reviews of Modern Physics **88**(1) (2016).

[301] J. Küpper, S. Stern, L. Holmegaard, F. Filsinger, A. Rouzée, A. Rudenko, P. Johnsson, A. V. Martin, M. Adolph, A. Aquila, S. Bajt, A. Barty, C. Bostedt, J. Bozek, C. Caleman, R. Coffee, N. Coppola, T. Delmas, S. Epp, B. Erk, L. Foucar, T. Gorkhover, L. Gumprecht, A. Hartmann, R. Hartmann, G. Hauser, P. Holl, A. Hömke, N. Kimmel, F. Krasniqi, K.-U. Kühnel, J. Maurer, M. Messerschmidt, R. Moshammer, C. Reich, B. Rudek, R. Santra, I. Schlichting, C. Schmidt, S. Schorb, J. Schulz, H. Soltau, J. C. Spence, D. Starodub, L. Strüder, J. Thøgersen, M. J. Vrakking, G. Weidenspointner, T. A. White, C. Wunderer, G. Meijer, J. Ullrich, H. Stapelfeldt, D. Rolles, and H. N. Chapman, "X-Ray Diffraction from Isolated and Strongly Aligned Gas-Phase Molecules with a Free-Electron Laser," Physical Review Letters **112**(8), 083,002 (2014).

[302] M. P. Minitti, J. M. Budarz, A. Kirrander, J. S. Robinson, D. Ratner, T. J. Lane, D. Zhu, J. M. Glownia, M. Kozina, H. T. Lemke, M. Sikorski, Y. Feng, S. Nelson, K. Saita, B. Stankus, T. Northey, J. B. Hastings, and P. M. Weber, "Imaging Molecular Motion: Femtosecond X-Ray Scattering of an Electrocyclic Chemical Reaction," **255501**(June), 1–5 (2015).

[303] J. Glownia, A. Natan, J. Cryan, R. Hartsock, M. Kozina, M. Minitti, S. Nelson, J. Robinson, T. Sato, T. van Driel, G. Welch, C. Weninger, D. Zhu, and P. Bucksbaum, "Self-Referenced Coherent Diffraction X-Ray Movie of Ångstrom- and Femtosecond-Scale Atomic Motion," Physical Review Letters **117**(15), 153,003 (2016).

[304] G. Mourou and S. Williamson, "Picosecond electron diffraction," Applied Physics Letters **41**(44), 3 (1982).

[305] A. P. Rood and J. Milledge, "Combined flash-photolysis and gas-phase electron-diffraction of small molecules," J. Chem. Soc., Faraday Trans. 2 **80**, 1145–1153 (1984).

[306] S. Williamson, G. Mourou, and J. C. M. Li, "Time-Resolved Laser-induced Phase Transformation in Aluminium," Physical Review Letters **52**(26), 2364 (1984).

[307] C. Kealhofer, W. Schneider, D. Ehberger, A. Ryabov, F. Krausz, and P. Baum, "All-optical control and metrology of electron pulses," Science **352**(6284), 429–433 (2016).

[308] S. Manz, A. Casandruc, D. Zhang, Y. Zhong, R. A. Loch, A. Marx, T. Hasegawa, L. C. Liu, S. Bayesteh, H. Delsim-Hashemi, M. Hoffmann, M. Felber, M. Hachmann, F. Mayet, J. Hirscht, S. Keskin, M. Hada, S. W. Epp, K. Fi Ottmann, and R. J. D. Miller, "Mapping atomic motions with ultrabright electrons: towards fundamental limits in space-time resolution," Faraday Discuss. **177**(177), 467–491 (2015).

[309] R. Kanya, Y. Morimoto, and K. Yamanouchi, "Observation of laser-assisted electron-atom scattering in femtosecond intense laser fields," Physical Review Letters **105**(12), 8–11 (2010).

[310] P. Baum and A. H. Zewail, "Attosecond electron pulses for 4D diffraction and microscopy," Proceedings of the National Academy of Sciences **104**(47), 18,409–18,414 (2007).

[311] J. Yang, M. Guehr, X. Shen, R. Li, T. Vecchione, R. Coffee, A. Fry, K. Gaffney, N. Hartmann, C. Hast, K. Hegazy, K. Jobe, J. Robinson, M. S. Robinson, S. Vetter, S. Weathersby, X. Wang, and M. Centurion, "Diffractive Imaging of Coherent Nuclear Motion in Isolated Molecules," Physical Review Letters **153002**, 2016 (2016).

[312] J. Yang, J. Beck, C. J. Uiterwaal, and M. Centurion, "Imaging of Alignment and Structural Changes of Carbon Disulfide Molecules using Ultrafast Electron Diffraction," Nature Communications p. accepted (2015).

[313] Y. Morimoto, R. Kanya, and K. Yamanouchi, "Laser-assisted electron diffraction for femtosecond molecular imaging." The Journal of chemical physics **140**(6), 064,201 (2014).

[314] C. E. Liekhus-Schmaltz, I. Tenney, T. Osipov, A. Sanchez-Gonzalez, N. Berrah, R. Boll, C. Bomme, C. Bostedt, J. D. Bozek, S. Carron, R. Coffee, J. Devin, B. Erk, K. R. Ferguson, R. W. Field, L. Foucar, L. J. Frasinski, J. M. Glownia, M. Gühr, A. Kamalov, J. Krzywinski, H. Li, J. P. Marangos, T. J. Martinez, B. K. McFarland, S. Miyabe, B. Murphy, A. Natan, D. Rolles, A. Rudenko, M. Siano, E. R. Simpson, L. Spector, M. Swiggers, D. Walke, S. Wang, T. Weber, P. H. Bucksbaum, and V. S. Petrovic, "Ultrafast isomerization initiated by X-ray core ionization," Nature Communications **6**, 8199 (2015).

[315] J. Yang, M. Guehr, T. Vecchione, M. S. Robinson, R. Li, N. Hartmann, X. Shen, R. Coffee, J. Corbett, A. Fry, K. Gaffney, T. Gorkhover, C. Hast, K. Jobe, I. Makasyuk, A. Reid, J. Robinson, S. Vetter, F. Wang, S. Weathersby, C. Yoneda, M. Centurion, and X. Wang, "Diffractive imaging of a rotational wavepacket in nitrogen molecules with femtosecond megaelectronvolt electron pulses," Nature Communications **7**, 11,232 (2016).

[316] H. Niikura, F. Légaré, R. Hasbani, M. Y. Ivanov, D. M. Villeneuve, and P. B. Corkum, "Probing molecular dynamics with attosecond resolution using correlated wave packet pairs." Nature **421**(6925), 826–829 (2003).

[317] M. Spanner, O. Smirnova, P. B. Corkum, and M. Y. Ivanov, "Reading diffraction images in strong field ionization of diatomic molecules," Journal of Physics B: Atomic, Molecular and Optical Physics **37**(12), L243–L250 (2004).

[318] R. J. D. Miller, "Femtosecond crystallography with ultrabright electrons and x-rays: capturing chemistry in action." Science (New York, N.Y.) **343**(6175), 1108–16 (2014).

[319] S. Baker, J. S. Robinson, C. A. Haworth, H. Teng, R. A. Smith, C. C. Chirila, M. Lein, J. W. G. Tisch, and J. P. Marangos, "Probing Proton Dynamics in Molecules on Attosecond Time Scales," Science (New York, N.Y.) **312**, 424 (2006).

[320] F. Krasniqi, B. Najjari, L. Strüder, D. Rolles, A. Voitkiv, and J. Ullrich, "Imaging molecules from within: Ultrafast angström-scale structure determination of molecules via photoelectron holography using free-electron lasers," Physical Review A - Atomic, Molecular, and Optical Physics **81**(3), 1–11 (2010).

[321] R. Boll, A. Rouzée, M. Adolph, D. Anielski, A. Aquila, S. Bari, C. Bomme, C. Bostedt, J. D. Bozek, H. N. Chapman, L. Christensen, R. Coffee, N. Coppola, S. De, P. Decleva, S. W. Epp, B. Erk, F. Filsinger, L. Foucar, T. Gorkhover, L. Gumprecht, A. Hömke, L. Holmegaard, P. Johnsson, J. S. Kienitz, T. Kierspel, F. Krasniqi, K.-U. Kühnel, J. Maurer, M. Messerschmidt, R. Moshammer, N. L. M. Müller, B. Rudek, E. Savelyev, I. Schlichting, C. Schmidt, F. Scholz, S. Schorb, J. Schulz, J. Seltmann, M. Stener, S. Stern, S. Techert, J. Thøgersen, S. Trippel, J. Viefhaus, M. Vrakking, H. Stapelfeldt, J. Küpper, J. Ullrich, A. Rudenko, and D. Rolles, "Imaging molecular structure through femtosecond photoelectron diffraction on aligned and oriented gas-phase molecules," Faraday Discuss. **171**, 57–80 (2014).

[322] H. Xu, T. Okino, and K. Yamanouchi, "Tracing ultrafast hydrogen migration in allene in intense laser fields by triple-ion coincidence momentum imaging," Journal of Chemical Physics **131**(15) (2009).

[323] H. Ibrahim, B. Wales, S. Beaulieu, B. E. Schmidt, N. Thiré, E. P. Fowe, É. Bisson, C. T. Hebeisen, V. Wanie, M. Giguére, J.-C. Kieffer, M. Spanner, A. D. Bandrauk, J. Sanderson, M. S. Schuurman, and F. Légaré, "Tabletop imaging of structural evolutions in chemical reactions demonstrated for the acetylene cation." Nature communications **5**, 4422 (2014).

[324] J. Xu, Z. Chen, A.-T. Le, and C. Lin, "Self-imaging of molecules from diffraction spectra by laser-induced rescattering electrons," Physical Review A **82**(3), 033,403 (2010).

[325] P. Reckenthaeler, M. Centurion, W. Fuß, S. Trushin, F. Krausz, and E. Fill, "Time-Resolved Electron Diffraction from Selectively Aligned Molecules," Physical Review Letters **102**(21), 213,001 (2009).

[326] C. D. Lin, A.-T. Le, Z. Chen, T. Morishita, and R. Lucchese, "Strong-field rescattering physicsâĂŤself-imaging of a molecule by its own electrons," Journal of Physics B: Atomic, Molecular and Optical Physics **43**(12), 122,001 (2010).

[327] C. I. Blaga, "Atoms and Molecules in Strong Midinfrared Laser Fields," Ph.D. thesis, Stony Brook Universtiy (2009).

[328] D. Shafir, H. Soifer, B. D. Bruner, M. Dagan, Y. Mairesse, S. Patchkovskii, M. Y. Ivanov, O. Smirnova, and N. Dudovich, "Resolving the time when an electron exits a tunnelling barrier." Nature **485**(7398), 343–6 (2012).

[329] M. F. Kling and M. J. J. Vrakking, "Attosecond electron dynamics." Annual review of physical chemistry **59**, 463–92 (2008).

[330] F. Lépine, M. Y. Ivanov, and M. J. J. Vrakking, "Attosecond molecular dynamics: fact or fiction?" Nature Photonics **8**(3), 195–204 (2014).

[331] M. Nisoli and G. Sansone, "New frontiers in attosecond science," Progress in Quantum Electronics **33**(1), 17–59 (2009).

[332] Z. Chang, "Chirp of the single attosecond pulse generated by a polarization gating," Physical Review A - Atomic, Molecular, and Optical Physics **71**, 023,813 (2005).

[333] M. Lein, J. Marangos, and P. Knight, "Electron diffraction in above-threshold ionization of molecules," Physical Review A **66**(5), 051,404 (2002).

[334] H. Niikura, F. Legare, R. Hasbani, D. M. Villeneuve, and P. B. Corkum, "Sub-laser-cycle electron pulses for probing molecular dynamics," Nature **417**, 917–922 (2002).

[335] S. N. Yurchenko, S. Patchkovskii, I. V. Litvinyuk, P. B. Corkum, and G. L. Yudin, "Laser-induced interference, focusing, and diffraction of rescattering molecular photoelectrons," Physical Review Letters **93**(November), 223,003 (2004).

[336] S. X. Hu and L. A. Collins, "Imaging molecular structures by electron diffraction using an intense few-cycle pulse," Physical Review Letters **94**(7), 2–5 (2005).

[337] H. Hetzheim, C. Figueira De Morisson Faria, and W. Becker, "Interference effects in above-threshold ionization from diatomic molecules: Determining the internuclear separation," Physical Review A - Atomic, Molecular, and Optical Physics **76**(2), 1–9 (2007).

[338] M. Busuladžić, A. Gazibegović-Busuladžić, D. B. Milošević, and W. Becker, "Angle-resolved high-order above-threshold ionization of a molecule: Sensitive tool for molecular characterization," Physical Review Letters **100**(20), 8–11 (2008).

[339] M. Busuladžić, A. Gazibegović-Busuladžić, D. B. Milošević, and W. Becker, "Strong-field approximation for ionization of a diatomic molecule by a strong laser field. II. the role of electron rescattering off the molecular centers," Physical Review A - Atomic, Molecular, and Optical Physics **78**(3), 1–11 (2008).

[340] T. Morishita, A. T. Le, Z. Chen, and C. D. Lin, "Potential for ultrafast dynamic chemical imaging with few-cycle infrared lasers," New Journal of Physics **10**, 025,011 (2008).

[341] A. T. Le, T. Morishita, and C. D. Lin, "Extraction of the species-dependent dipole amplitude and phase from high-order harmonic spectra in rare-gas atoms," Physical Review A - Atomic, Molecular, and Optical Physics **78**(2), 1–5 (2008).

[342] Z. Chen, Y. Liang, and C. D. Lin, "Quantitative rescattering theory of correlated two-electron momentum spectra for strong-field nonsequential double ionization of helium," Physical Review A **82**(6), 063,417 (2010).

[343] M. Okunishi, T. Morishita, G. Prümper, K. Shimada, C. D. Lin, S. Watanabe, and K. Ueda, "Experimental retrieval of target structure information from laser-induced rescattered photoelectron momentum distributions," Physical Review Letters **100**(April), 143,001 (2008).

[344] D. Ray, B. Ulrich, I. Bocharova, C. Maharjan, P. Ranitovic, B. Gramkow, M. Magrakvelidze, S. De, I. Litvinyuk, A.-T. Le, T. Morishita, C. Lin, G. Paulus, and C. Cocke, "Large-Angle Electron Diffraction Structure in Laser-Induced Rescattering from Rare Gases," Physical Review Letters **100**(14), 143,002 (2008).

[345] M. Okunishi, R. Itaya, K. Shimada, P. G, K. Ueda, M. Busuladžić, A. Gazibegović-Busuladžić, D. B. Milošević, and W. Becker, "Angle-resolved high-order above-threshold ionization spectra for N2 and O2 : measurements and the strong-field approximation," Journal of Physics B: Atomic, Molecular and Optical Physics **41**(20), 201,004 (2008).

[346] M. Okunishi, R. Itaya, K. Shimada, G. Prümper, K. Ueda, M. BusuladžÌĂić, A. Gazibegović-BusuladžÌĂić, D. B. Milošević, and W. Becker, "Two-source double-slit interference in angle-resolved high-energy above-threshold ionization spectra of diatoms," Physical Review Letters **103**(4), 1–4 (2009).

[347] S. Micheau, Z. Chen, A. T. Le, J. Rauschenberger, M. F. Kling, and C. D. Lin, "Accurate retrieval of target structures and laser parameters of few-cycle pulses from photoelectron momentum spectra," Physical Review Letters **102**(7), 1–4 (2009).

[348] C. Cornaggia, "Electron-Ion elastic scattering in molecules probed by laser-induced ionization," Journal of Physics B: Atomic, Molecular and Optical Physics **42**(16), 161,002 (2009).

[349] M. Okunishi, H. Niikura, R. R. Lucchese, T. Morishita, and K. Ueda, "Extracting Electron-Ion Differential Scattering Cross Sections for Partially Aligned Molecules by Laser-Induced Rescattering Photoelectron Spectroscopy," Physical Review Letters **106**(6), 063,001 (2011).

[350] D. Ray, Z. Chen, S. De, W. Cao, I. V. Litvinyuk, A. T. Le, C. D. Lin, M. F. Kling, and C. L. Cocke, "Momentum spectra of electrons rescattered from rare-gas targets following their extraction by one- and two-color femtosecond laser pulses," Physical Review A - Atomic, Molecular, and Optical Physics **83**(1), 1–8 (2011).

[351] J. Xu, C. I. Blaga, A. D. Dichiara, E. Sistrunk, K. Zhang, Z. Chen, A.-t. Le, T. Morishita, C. D. Lin, P. Agostini, and L. F. Dimauro, "Laser-Induced Electron Diffraction for Probing Rare Gas Atoms," Physical Review Letters **109**(December), 233,002 (2012).

[352] Z. Chen, T. Morishita, A.-T. Le, and C. Lin, "Analysis of two-dimensional high-energy photoelectron momentum distributions in the single ionization of atoms by intense laser pulses," Physical Review A **76**(4), 043,402 (2007).

[353] T. Morishita, T. Umegaki, S. Watanabe, and C.-D. Lin, "High-resolution spatial and temporal microscopy with intense-laser-induced rescattering electrons," Journal of Physics: Conference Series **194**(1), 012,011 (2009).

[354] H. S. W. Massey, *Electronic and Ionic impact Phenomena* (Oxford University, London, 1969).

[355] H. D. Cohen and U. Fano, "Interference in the photo-ionization of molecules," Physical Review **150**(1), 30–33 (1966).

[356] J. F. Williams and B. A. Willis, "The scattering of electrons from inert gases. I. Absolute differential elastic cross sections for argon atoms," Journal of Physics B: Atomic, Molecular and Optical Physics **8**(10), 1670 (1975).

[357] J. F. Williams and A. Crowe, "The scattering of electrons from inert gases. II. Absolute differential elastic cross sections for neon, krypton and xenon atoms," Journal of Physics B: Atomic, Molecular and Optical Physics **8**(13), 2233 (1975).

[358] A. Jablonski, F. Salvat, and C. J. Powell, "NIST Electron Elastic-Scattering Cross-Section Database," NIST Standard Reference Database **64**, 1 (2010).

[359] R. Torres, N. Kajumba, J. G. Underwood, J. S. Robinson, S. Baker, J. W. G. Tisch, R. D. Nalda, W. A. Bryan, R. Velotta, C. Altucci, I. C. E. Turcu, and J. P. Marangos, "Probing Orbital Structure of Polyatomic Molecules by High-Order Harmonic Generation," Physical review letters **98**, 203,007 (2007).

[360] K. M. Ervin, S. Gronert, S. E. Barlow, M. K. Gilles, A. G. Harrison, V. M. Bierbaum, C. H. DePuy, W. C. Lineberger, and G. B. Ellison, "Bond strengths of ethylene and acetylene," Journal of the American Chemical Society **112**(15), 5750–5759 (1990).

[361] R. Thissen, J. Delwiche, J. M. Robbe, D. Duflot, J. P. Flament, and J. H. D. Eland, "Dissociations of the ethyne dication C2H2+2," The Journal of Chemical Physics **99**(9), 6590 (1993).

[362] M. Peric, B. Ostojic, and B. Engels, "Ab initio study of the electronic spectrum of C2H2+: Investigation of structure of spectra involving low-lying doublet electronic states," Journal of Chemical Physics **109**(8), 3086–3095 (1998).

[363] O. Dopfer, R. V. Olkhov, M. Mladenovic, and P. Botschwina, "Intermolecular interaction in an open-shell pi-bound cationic complex: IR spectrum and coupled cluster calculations for C2H2+-Ar." The Journal of chemical physics **121**(4), 1744–53 (2004).

[364] B. Gaire, S. Y. Lee, D. J. Haxton, P. M. Pelz, I. Bocharova, F. P. Sturm, N. Gehrken, M. Honig, M. Pitzer, D. Metz, H.-K. Kim, M. Schöffler, R. Dörner, H. Gassert, S. Zeller, J. Voigtsberger, W. Cao, M. Zohrabi, J. Williams, A. Gatton, D. Reedy, C. Nook, T. Müller, A. L. Landers, C. L. Cocke, I. Ben-Itzhak, T. Jahnke, A. Belkacem, and T. Weber, "Photo-double-ionization of ethylene and acetylene near threshold," Physical Review A **89**(1), 013,403 (2014).

[365] K. Doblhoff-Dier, M. Kitzler, and S. Gräfe, "Theoretical investigation of alignment-dependent intense-field fragmentation of acetylene," Physical Review A **94**(1), 013,405 (2016).

[366] Y. H. Jiang, A. Senftleben, M. Kurka, A. Rudenko, L. Foucar, O. Herrwerth, M. F. Kling, M. Lezius, J. V. Tilborg, A. Belkacem, K. Ueda, D. Rolles, R. Treusch, Y. Z. Zhang, Y. F. Liu, C. D. Schröter, J. Ullrich, and R. Moshammer, "Ultrafast dynamics in acetylene clocked in a femtosecond XUV stopwatch," Journal of Physics B: Atomic, Molecular and Optical Physics **46**(16), 164,027 (2013).

[367] M. E. A. Madjet, O. Vendrell, and R. Santra, "Ultrafast dynamics of photoionized acetylene," Physical Review Letters **107**(26), 1–5 (2011).

[368] X. Xie, K. Doblhoff-Dier, H. Xu, S. Roither, M. S. Schöffler, D. Kartashov, S. Erattupuzha, T. Rathje, G. G. Paulus, K. Yamanouchi, A. Baltuška, S. Gräfe, and M. Kitzler, "Selective control over fragmentation reactions in polyatomic molecules using impulsive laser alignment," Physical Review Letters **112**(April), 163,003 (2014).

[369] G. Herzberg, *Electronic spectra and electronic structure of polyatomic molecules* (Van Nostrand, New York, 1966).

[370] M. J. Frisch, G. W. Trucks, H. B. Schlegel, G. E. Scuseria, M. A. Robb, J. R. Cheeseman, J. A. Montgomery, T. Vreven, K. N. Kudin, J. C. Burant, J. M. Millam, S. S. Iyengar, J. Tomasi, V. Barone, B. Mennucci, M. Cossi, G. Scalmani, N. Rega, G. A. Petersson, H. Nakatsuji, M. Hada, M. Ehara, K. Toyota, R. Fukuda, J. Hasegawa, M. Ishida, T. Nakajima, Y. Honda, O. Kitao, H. Nakai, M. Klene, X. Li, J. E. Knox, H. P. Hratchian, J. B. Cross, V. Bakken, C. Adamo, J. Jaramillo, R. Gomperts, R. E. Stratmann, O. Yazyev, A. J. Austin, R. Cammi, C. Pomelli, J. W. Ochterski, P. Y. Ayala, K. Morokuma, G. A. Voth, P. Salvador, J. J. Dannenberg, V. G. Zakrzewski, S. Dapprich, A. D. Daniels, M. C. Strain, O. Farkas, D. K. Malick, A. D. Rabuck, K. Raghavachari, J. B., Foresman, J. V. Ortiz, Q. Cui, A. G. Baboul, S. Clifford, J. Cioslowski, B. B. Stefanov, G. Liu, A. Liashenko, P. Piskorz, I. Komaromi, R. L. Martin, D. J. Fox, T. Keith, A. M. A. Laham, C. Y. Peng, A. Nanayakkara, M. Challacombe, P. M. W. Gill, B. Johnson, W. Chen, M. W. Wong, C. Gonzalez, and J. A. Pople, "Gaussian 03, Revision C.02," (2004).

[371] A. Rizzo and N. Rahman, "The linear and nonlinear susceptibilities of acetylene relevant for high order harmonic generation," Laser Physics **9**(1), 416–421 (1999).

[372] A. T. Le, R. R. Lucchese, S. Tonzani, T. Morishita, and C. D. Lin, "Quantitative rescattering theory of high-order harmonic generation from molecules," Physical Review A - Atomic, Molecular, and Optical Physics **80**, 013,401 (2009).

[373] J. Xu, C. I. Blaga, K. Zhang, Y. H. Lai, C. D. Lin, T. A. Miller, P. Agostini, and L. F. DiMauro, "Diffraction using laser-driven broadband electron wave packets," Nature Communications **5**, 4635 (2014).

[374] K. Kuchitsu, *Structure of Free Polyatomic Molecules - Basic Data* (Springer Berlin Heidelberg, 1998).

[375] W. E. King, G. H. Campbell, A. Frank, B. Reed, J. F. Schmerge, B. J. Siwick, B. C. Stuart, and P. M. Weber, "Ultrafast electron microscopy in materials science, biology, and chemistry," Journal of Applied Physics **97**(11) (2005).

[376] A. H. Zewail, "4D Ultrafast electron diffraction, crystallography, and microscopy," Annual review of physical chemistry **57**, 65–1003 (2006).

[377] R. G. Woolley, "Quantum chemistry beyond the Born-Oppenheimer approximation," Journal of Molecular Structure: THEOCHEM **230**, 17–46 (1991).

[378] G. A. Worth and L. S. Cederbaum, "BEYOND BORN-OPPENHEIMER: Molecular Dynamics Through a Conical Intersection," Annual Review of Physical Chemistry **55**, 127–158 (2004).

[379] A. S. Alnaser, M. Kübel, R. Siemering, B. Bergues, N. G. Kling, K. J. Betsch, Y. Deng, J. Schmidt, Z. A. Alahmed, a. M. Azzeer, J. Ullrich, I. Ben-Itzhak, R. Moshammer, U. Kleineberg, F. Krausz, R. de Vivie-Riedle, and M. F. Kling, "Subfemtosecond steering of hydrocarbon deprotonation through superposition of vibrational modes." Nature communications **5**(May), 3800 (2014).

[380] J. A. Labinger and J. E. Bercaw, "Understanding and exploiting C-H bond activation." Nature **417**(6888), 507–14 (2002).

[381] B. Wolter, M. G. Pullen, A.-T. Le, M. Baudisch, K. Doblhoff-Dier, A. Senftleben, M. Hemmer, C. D. Schröter, J. Ullrich, T. Pfeifer, R. Moshammer, S. Gräfe, O. Vendrell, C. D. Lin, and J. Biegert, "Ultrafast electron diffraction imaging of bond breaking in acetylene," Science (New York, N.Y.) **354**(6310), 308–312 (2016).

[382] C.-Y. Ruan, "Molecular imaging at 1-femtosecond resolution," Science **354**(6310), 283–284 (2016).

[383] K. Doblhoff-Dier, "Strong-Field Dynamics in Small Molecules," (September 2014), 171 (2014).

[384] M. Hochlaf, S. Taylor, and J. H. D. Eland, "Quartet states of the acetylene cation: Electronic structure calculations and spin-orbit coupling terms," Journal of Chemical Physics **125**(21) (2006).

[385] M. Alagia, C. Callegari, P. Candori, S. Falcinelli, F. Pirani, R. Richter, S. Stranges, and F. Vecchiocattivi, "Angular and energy distribution of fragment ions in dissociative double photoionization of acetylene molecules at 39 eV." The Journal of chemical physics **136**(20), 204,302 (2012).

[386] N. Camus, B. Fischer, M. Kremer, V. Sharma, A. Rudenko, B. Bergues, M. Kübel, N. G. Johnson, M. F. Kling, T. Pfeifer, J. Ullrich, and R. Moshammer, "Attosecond Correlated Dynamics of Two Electrons Passing through a Transition State," Physical Review Letters **108**(7), 073,003 (2012).

[387] M. Kübel, C. Burger, R. Siemering, N. G. Kling, B. Bergues, A. S. Alnaser, I. Ben-Itzhak, R. Moshammer, R. de Vivie-Riedle, and M. F. Kling, "Phase- and intensity-dependence of ultrafast dynamics in hydrocarbon molecules in few-cycle laser fields," Molecular Physics **0**, 1–11 (2017).

[388] M. Head-Gordon and J. A. Pople, "MP2 energy evaluation by direct methods," Chemical Physics Letters **153**(6), 503–506 (1988).

[389] R. Krishnan, J. S. Binkley, R. Seeger, and J. A. Pople, "Self-consistent molecular orbital methods. XX. A basis set for correlated wave functions," J. Chem. Phys. **72**, 650 (1980).

[390] J. P. Finley, "Similarities between single reference perturbation theory based on a CASSCF wavefunction and multireference perturbation theory based on a reference space spanned by a CAS," Chemical Physics Letters **283**(5-6), 277–282 (1998).

[391] K. P. Lawley, ed., *Advances in Chemical Physics: Ab Initio Methods in Quantum Chemistry Part 2, Volume 69* (John Wiley & Sons, Inc., 1987).

[392] G. Karlström, R. Lindh, P. Å. Malmqvist, B. O. Roos, U. Ryde, V. Veryazov, P. O. Widmark, M. Cossi, B. Schimmelpfennig, P. Neogrady, and L. Seijo, "MOLCAS: A program package for computational chemistry," Computational Materials Science **28**(2), 222–239 (2003).

[393] V. Veryazov, P. O. Widmark, L. Serrano-Andrés, R. Lindh, and B. O. Roos, "2MOLCAS as a development platform for quantum chemistry software," International Journal of Quantum Chemistry **100**(4 SPEC. ISS.), 626–635 (2004).

[394] C. Steffen, K. Thomas, U. Huniar, A. Hellweg, O. Rubner, and A. Schroer, "TmoleX–A Graphical User Interface for TURBOMOLE." Journal of computational chemistry **31**, 2967–2970 (2010).

[395] M. D. Feit, J. A. Fleck, and A. Steiger, "Solution of the Schrtidinger Equation by a Spectral Method*," Journal of Computational Physics **47**, 412–433 (1982).

[396] T. H. Dunning Jr, "Gaussian basis sets for use in correlated molecular calculations. I. The atoms boron through neon and hydrogen," J. Chem. Phys. **90**(1989), 1007 (1989).

[397] E. M. L. Ohrendorf, F. Tarantelli, and L. S. Cederbaum, "Dicationic states of hydrocarbons and a statistical approach to their Auger spectra," J. Chem. Phys. **92**, 2984 (1990).

[398] J. C. Tully, "Molecular dynamics with electronic transitions," The Journal of Chemical Physics **93**(2), 1061 (1990).

[399] Frank Weinhold and Clark R. Landis, "Atomic Units (a.u.) and Conversion Factors," in *Discovering Chemistry with Natural Bond Orbitals*, pp. 307–308 (John Wiley & Sons, Inc., 2012).

[400] M. Meckel, "Laser-Induced Electron Tunneling and Diffraction," Dissertation, Johann-Wolfgang-Goethe-Universität in Frankfurt am Main (2011).

[401] K. Kaleris, "Strong field ionization of atoms and small molecules with ultra-short mid-IR pulses: technical aspects and data analysis," Master thesis, KIT - Karlsruhe Institute of Technology (2013).

Contributions

All experiments conducted within this thesis were performed in the *Attoscience and Ultrafast Optics* laboratory at ICFO in Castelldefels, Barcelona, Spain, which is designed and supervised by Prof. Dr. Jens Biegert (JB). The experimental methodology used in these experiments involved the use of the group's high repetition rate, 3 μm OPCPA source that was designed and initially built by JB and Dr. Olivier Chalus (OC). Further upgrades of the source were performed by Dr. Michaël Hemmer (MH), Alexandre Thai (AT), Dr. Matthias Baudisch (MB), Dr. Hugo Almeida (HA) and Ugaitz Elu (UE). The ReMi used for 3D coincidence momentum detection was built up in the lab by Dr. Thorsten Ergler (TE) and Dr. Philip Bates (PB) and calibrated by Dr. Judith Dura (JD) in collaboration with the Max-Planck-Institute for Nuclear Physics (MPI-K) from Heidelberg, Germany, in person of Prof. Dr. Joachim Ullrich (JU), Dr. Robert Moshammer (RM), Dr. Claus Dieter Schröter and Dr. Arne Senftleben (AS). Throughout the time of this thesis, the ReMi was upgraded and maintained by the author. The general analysis code (GENERiC) used in the experiments to analyze the raw signals detected by the ReMi and convert them into physical variables was developed by AS. The Barcelona branch of the code was maintained and extended by the author.

The CTMC simulations in Ch. 4 were calculated by our collaborators Dr. Christoph Lemell (CL) and Prof. Dr. Joachim Burgdörfer (JBD) of the Vienna University of Technology. The TDSE simulations of the same Ch. 4 were performed by Prof. Dr. Xiao-Min Tong (XMT) of the University of Tsukuba in Japan. The experiment of Ch. 4 was set up by the author together with MB. The data of this experiment was acquired by the author, MB, MH and Dr. Michael Pullen (MP), and its analysis was performed by the author. The semi-classical calculations of Ch. 5 were performed by Dr. Xu Wang (XW) of the Kansas State University, Manhattan, Kansas, USA, under supervision of Prof. Dr. Joe Eberly (JE) of the University of Rochester, New York, USA. The experiment of Ch. 5 was set up by the author, MB and MP. Its data was acquired by the author, MB, MP, MH, HA and Dr. Michele Sclafani (MS), and its analysis was performed by the author together with MP. The experiments conducted in Ch. 6 and 7 were setup by the author, MB and MP. The different data sets were acquired by the author, MB and MP, together with MH. Its data analysis, interpretation and visualization were performed by the author and MP. Theoretical simulations for Ch. 6 and 7 were calculated by various groups: the dynamic molecular alignment distribution of acetylene and the molecular DCSs via the IAM model were calculated by Dr. Anh-Thu Le (AT) under supervision of Prof. Dr. Chi-Dong Lin (CDL) of the Kansas State University in Manhattan, Kansas, USA; the potential energy landscape of acetylene was calculated by Dr. Katharina Doblhoff-Dier (KDD) under supervision of Prof. Dr. Stefanie Gräfe (SG) of the Friedrich-Schiller

University in Jena, Germany; the quantum chemistry and mixed quantum-classical ab-initio molecular dynamics calculations were performed in combined efforts of KDD, SG and Dr. Oriol Vendrell (OV) of Aarhus University, Denmark.

Measurements, additional calculations and analysis of data sets not mentioned here and presented in this thesis were done by the author. Illustrations of the experimental setup are based on authorized designs of Dr. Lutz Fechner (LF) and Dr. Phillip Cörlin (PC) of the MPI-K in Heidelberg. Some details of the illustrations used in this thesis were created by Itsaso Arana Corral (IAC).

Acknowledgements

Last but not least, I would like to thank all people that helped and supported me throughout the last years and without whom this thesis would not have been made possible.

First of all I would like to thank my supervisor Prof. Dr. Jens Biegert for giving me the opportunity to pursue my PhD thesis in his group at ICFO. I am grateful for the great deal of trust he put into me throughout the years while working on the reaction microscope. I highly appreciate to be given the unique opportunity of working on a forefront project in our field. Above all, Jens provided an extremely well-equipped laboratory, gave opportunities of presenting our work at numerous international conferences plus organized great group retreats with skiing (& some physics) in the Pyrenees.

Strong-field physics has evolved in a highly multi-disciplinary field over the last decades, where setups are extremely complex and experiments can only be successful when being performed in a great team. I was lucky enough to be part of a group of smart and motivated people that helped to make this work possible.

First and foremost, I am truly thankful for the scientific, technical and moral support of two gentleman with whom I closely worked on the experiments of this thesis and who were essential in the constant progress we made throughout the years: After one year without a postdoc on the project, Michael G. Pullen - better known as Mick - joined the team in October 2013. He immediately had an impact with his wide understanding of strong-field physics and his thoroughness in interpreting the physics contained in the "deluge" of data we measured over the years. Mick taught me quite a bit about endurance and always gave me moral support in stressful times. Matthias Baudisch was my counterpart on the OPCPA in all experiments from the beginning. He always worked tirelessly to make sure the OPCPA was running at optimum and was ready for experiments on the ReMi. Matze always offered a different view on a problem plus provided the team with plenty of poise within all these years which was tremendously helpful. Thanks to you two for everything.

Many thanks goes also to the following colleagues. Some came and some went, yet all were directly involved in the work of this thesis: Michël Hemmer, who always helped out with the OPCPA, and was never shy of taking a night shift during our measurement campaigns; Michele Sclafani, who it always was a pleasure to work and share the office with especially due to his unconventional view on things and who taught me at least *three* things in the lab ◡̈; Judith Dura, who I inherited the ReMi project from and who gave me the most thorough (and intense) introduction into the world of ReMis in the three month of overlap we shared; always a great

help was Ugaitz Elu who took over the reigns of Matze on the OPCPA, and the other newcomers Hugo Almeida and Aurelien Sanchez.

I would also like to thank the rest of the AUO group members for fruitful discussions, helping hands and an awesome group dynamic: Alexander Grün, Seth Cousin (it's been a pleasure!), Dane Austin, Stephan Teichmann (no need to apologize!), Francisco Silva, Alexandre Thai, Alexander Britz, Barbara Buades, Daniel Sanchez, Konstantinos Kaleris, Noslen Suarez, Iker León, Idoia Martí, Ioachim Pupeza, Nicola Di Palo, Daniel Rivas, Julius Huijts (thanks for reading my thesis!), Biplop Nandy, Lenard Vamos, Tobias Steinle, Themistoklis Sidiropoulos, and Antonio Picon.

Fortunately, I could participate in interesting and fruitful collaborations and am thankful for the help and insights of the following people: Arne Senftleben of the MPI-K team from Heidelberg, Germany, later University of Kassel, Germany, who taught me a lot about the ReMi as well as the interpretation of data on molecules; the rest of the MPI-K team namely Robert Moshammer, Thomas Pfeifer, Joachim Ullrich, Claus Dieter Schröter, Nicolas Camus, Thomas Pflüger, Phillip Cörlin, and Lutz Fechner; Christoph Lemell of the Vienna University of Technology, Austria, who helped me tremendously with my first publication on low-energy structures, Joachim Burgdörfer also from Vienna; Anh-Tu Le and Chii-Dong Lin from Kansas State University, Manhattan, Kansas, USA, who were vital for our work on mid-IR LIED; Katharina Doblhoff-Dier, University of Leiden, Netherlands, Stefanie Gräfe, University of Jena, Germany, and Oriol Vendrell, Aarhus University, Denmark, who provided the quantum chemistry calculations on the deprotonation reaction paper.

Very important for experimental work is the technical support of the institute. At ICFO we can count on the help of Xavi Menino and his team of the mechanical workshop, José Carlos Cifuentes and his team in the electronic workshop as well as Carlos Dengra for the facility management. A big thank you deserves Juli Céspedes who always helped me in maintaining the group's servers and the iMacs plus implementing and administering the group's Confluence server. Also the rest of the IT team lead by Goncal Badenes needs to be mentioned. Moreover, I would like to thank Anne Gstöttner, Cristina Garcia, Manuela Furkert, Ingrid Solsona, Mery Gil and Laia Miralles from HR, as well as Mará José Martínez, Mónica Montaña, Mercedes Santacana, Santiago Martín, Magdalena Lara, Elena Enrique, Jonas Padonou and Adrián Guardia.

My time at ICFO will always stay in my memory, mainly due to the many interesting people from all over the world. Lunches, coffee breaks, going running at the beach or El Garaf, football sessions in Gava, and beers after work were especially fun with Peter Weber, Mussie Beian, Esteban Bermúdes, Dominik Kufer, Jan Gieseler, Michael Geiselmann, Gabriele Navickaite, Nicolas Maring, Emanuele Distante, Jana Nieder, Ioannis Tsioutsios, Johannes Güttinger, Alexandros Tavernarakis, Achim Woessner, Simon Coop and James Douglas.

Life in Barcelona is exciting and perfect to get your mind off the stressful side of a PhD. A big part in this during the last 5 years played Peter, Stephan, Mussie, Anjana, Arantxa, Ana, Gaval, Guiru, Patty, Marta, and the football team of Athletic

Catalunya. Of course friends and family need to be mentioned that came to visit on multiple occasions to enjoy the beach, nightlife and festivals together, and thereby kept the contact alive whilst living in different countries: Michi, Denis, Tim, Jonas, Gabri, Uli, and of course my brother Basti and his wife Franzi. It would have been only half the fun without you.

My life's trajectory started in Berlin, then led to Colmberg, Heilbronn, Karlsruhe, Edinburgh, via Berlin back to Karlsruhe, and - for now - to Barcelona. The biggest influence and constant for me throughout this path have been my parents who gave me all the advice, support, freedom and love that a son could ask for. Both in happy times but especially when life got difficult, this support provided a safety net and a source of strength for me, and allowed me to become the person I am today. I cannot put into words how grateful I am to you for that. - *Mein Lebensweg begann in Berlin, führte mich dann nach Colmberg, Heilbronn, Karlsruhe, Edinburgh, über Berlin wieder nach Karlsruhe, und - bis jetzt - nach Barcelona. Der größte Einfluss und die Konstante auf diesem Weg waren meine Eltern, die mir all die Ratschläge, Unterstützung, Freiheit und Liebe gaben, die sich ein Sohn wünschen kann. In fröhlichen Momenten und besonders, wenn das Leben mal schwierig wurde, gab mir dies stets Sicherheit und eine Quelle der Stärke und erlaubte mir, die Person zu werden, die ich heute bin. Ich kann nicht in Worte fassen, wie dankbar ich euch dafür bin.*

Last but not least, I want to thank my lovely and wonderful girlfriend Itsaso. I am a lucky bastard to have met you as you make me happy every day while taking me for who I am. Your love and support in the last years helped me greatly to successfully finish this part of my life and I am excited about what our future holds for us (especially the near one ◡̈).